NASA SP-319

EVOLUTIONARY AND PHYSICAL PROPERTIES OF METEOROIDS

A colloquium held at
ALBANY, N.Y.
June 14–17, 1971

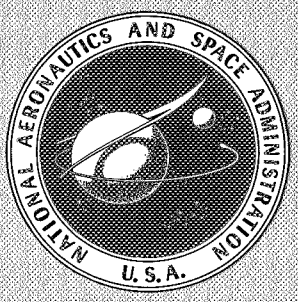

NATIONAL AERONAUTICS AND SPACE ADMINISTRATION

NASA SP-319

EVOLUTIONARY AND PHYSICAL PROPERTIES OF METEOROIDS

The proceedings of the International Astronomical Union's Colloquium #13, held at the State University of New York, Albany, N.Y., on June 14–17, 1971

Edited by

Curtis L. Hemenway
Dudley Observatory

Peter M. Millman
National Research Council of Canada

Allan F. Cook
Smithsonian Astrophysical Observatory

Scientific and Technical Information Office 1973
NATIONAL AERONAUTICS AND SPACE ADMINISTRATION
Washington, D.C.

For sale by the Superintendent of Documents, U.S. Government Printing Office
Washington, D.C. 20402 - Price $4.30 (paper cover)
Stock Number 3300-00499

Library of Congress Catalog Card Number 72-600319

PREFACE

The Fourteenth General Assembly of the International Astronomical Union was held in Brighton, England, in 1970. During the conference, arrangements were made to hold a colloquium on "The Evolutionary and Physical Problems of Meteoroids." An invitation was issued by the State University of New York at Albany (SUNYA) and the Dudley Observatory to host the meeting. C. L. Hemenway, P. M. Millman, and A. F. Cook were selected to organize the program. IAU Colloquium No. 13 was held June 14–17, 1971, at the State University of New York at Albany. Forty papers were presented and are included in this volume.

The organizing committee and participants are indebted to Maurice Dubin, Chief, Cosmic Dust Branch, Office of Space Science, National Aeronautics and Space Administration, Washington, D.C.; Louis Benezet, President of SUNYA; and the Executive Committee of the International Astronomical Union for financial support of the Colloquium.

We also express our appreciation for the assistance of Rita Spenser, Betty Sterrett, and the graduate students in astronomy at SUNYA—particularly Larry Relyea, Charles Bowman, and Marty Richardson. The SUNYA staff took care of local arrangements for the meeting. We are also indebted to the staff of NASA's Technical Publications Division for undertaking the publication of this Colloquium and providing editorial assistance.

Curtis L. Hemenway
Peter M. Millman
Allan F. Cook

Page intentionally left blank

Contents

1. Photographic Fireball Networks

IAN HALLIDAY
National Research Council of Canada
Ottawa, Ontario

Three networks for the photography of bright fireballs are now in operation; in the central United States, central Europe and western Canada. A detailed comparison is made of the parameters which describe the three networks. Although only two meteorites for which photographic orbital data is available have been recovered, the networks are contributing valuable data on fireball orbits, influx rates and problems of meteor physics.

A MAJOR DIFFICULTY IN OBSERVATIONAL METEOR ASTRONOMY is the unpredictable nature of the events of interest. The population of observable meteoritic events is defined by the product of the flux of suitable particles, the area of the atmosphere under observation and the duration of observations. Where the flux of suitable meteoroids is reasonably high, as in radar meteor astronomy or direct photography of faint meteors, moderate observing intervals suffice to accumulate considerable data. For bright fireballs, however, the flux is so low that very large areas must be monitored for long intervals to obtain any statistically significant volume of observations.

There are now three networks for fireball photography in operation. Planning for the Prairie Meteorite Network in the central plains of the United States began about a decade ago. The basic aims, principles of operation and instrumentation were described by McCrosky and Boeschenstein (1965). The successful photography of the flight of the Pribram meteorite, using conventional meteor cameras (Ceplecha, 1961), led to the establishment of a network of all-sky cameras in Czechoslovakia for fireball photography (Ceplecha and Rajchl, 1965). This network has since been expanded to include the southern area of Germany and is known as the European Network. During the early stages of operation, a photographic network will bring successive stations into operation gradually and a variety of instrumental problems tends to reduce the efficiency of operation for at least several months, so that it is difficult to define a single date when a network became active. The Prairie Network and the European Network may be considered to have begun operations about 1964 (McCrosky and Ceplecha, 1969).

A third network now operates in western Canada, known as the Meteorite Observation and Recovery Project, or MORP Network. The effective beginning of routine operations for this network may be taken as early in 1971. The MORP network has had an advantage in that it could draw on the early experience of the other networks, although the major decisions on instrumentation were taken in 1966 and 1967 when only quite preliminary results were available from the operation of the first two networks.

NETWORK PARAMETERS

Let us examine the various parameters which describe the design and operation of a meteorite camera network. Each one involves some sort of compromise in its selection and the choices adopted in the three networks now in operation may be compared. Local geographical conditions,

distribution of population, the availability of engineering design facilities and of financial support are some of the considerations which influence the decisions. Much of the discussion to follow is summarized in table 1 where each heading below is assigned a row in the table.

Number of Stations and Station Spacing

Calculation of the meteor trajectory requires a minimum of two-station photography but the confidence in the results may be strengthened in some cases if more than two stations observe a meteor. As the anticipated expense of the instrumentation and operation of a typical station gradually increases during the planning stage, there is a temptation to increase the station separation to limit the total number required and hence the total cost. If the camera focal length is large then positional accuracy may be maintained to a greater range from each station, although the danger of one-station observations due to scattered clouds (or instrumental failure) will increase as the station spacing approaches the point where only two stations could provide coverage for a given event. The number of stations in each network is shown in the first row of table 1 while the second row shows a typical separation of any station from an adjacent one. The European Network is characterized by many closely-spaced stations compared to the other two networks.

Figures 1, 2 and 3 are maps of the three networks, drawn to the same scale, showing the location of all stations of the present networks.

Number of Cameras

The Prairie Network employs four wide-angle cameras per station, the European Network has a single all-sky camera, while the MORP stations each have five cameras. A small area near the zenith is obscured by the mounting for the camera itself above the convex mirror in the all-sky version. The other networks cover the sky to altitudes of about 60° but have small gaps in the coverage between adjacent cameras near the horizon.

Focal Length

The three networks differ widely in the focal lengths of their camera systems, as shown in the table. The European Network (effective focal length = 5.7 mm) records the all-sky photographs on 35-mm film, the MORP cameras use 70-mm film, while the much longer focal length of the Prairie Network cameras is used with a 9½-inch (24 cm) film format.

Occulting Rate

The selection of a frequency at which the meteor trail is chopped involves an interesting compromise. A knowledge of the deceleration of the meteoroid in the atmosphere is required to estimate the physical size of the body for the ballistic calculations of the terminal, dark portion of the flight path. The deceleration value will be more secure if it is based on many measures per second, especially since there may be sudden changes in deceleration due to fragmentation of the body.

TABLE 1.—*Comparison of Network Parameters*

Row	Parameter	Prairie	European	MORP
(i)	No. of stations	16	46	12
(ii)	Station spacing, km	250	87	193
(iii)	No. of cameras per station	4	1	5
(iv)	Focal length, mm	152	5.7	50
(v)	Occulting rate, s^{-1}	13.3	12.5	4
(vi)	Dash length, mm	0.236	0.034	0.330
(vii)	Meteor timing	(a) Photometer (b) Shutter code	Visual observers	Photometer
(viii)	Area of atmosphere, km^2	11.4×10^5	10.8×10^5	8.3×10^5
(ix)	Search area, km^2	13.6×10^5	4.4×10^5	7.1×10^5

FIGURE 1.—Map of the Prairie Network showing the location of 16 stations. The curved outline defines the search area as described in the text.

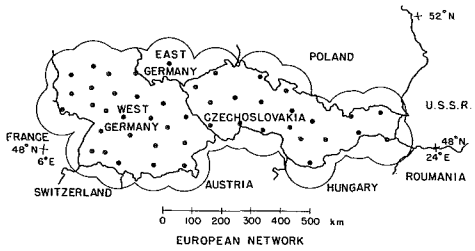

FIGURE 2.—Map of the European Network showing the location of 46 stations and the search area.

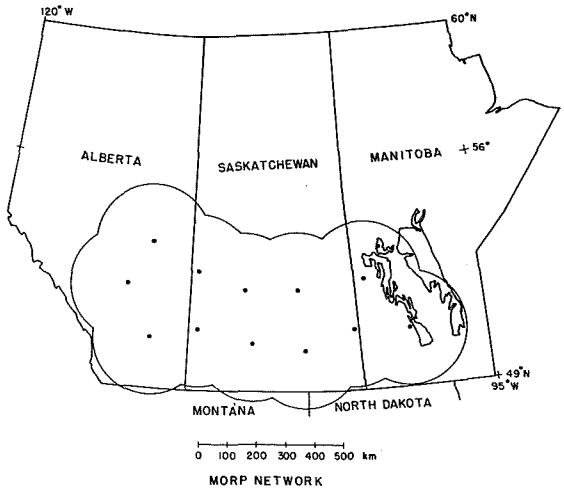

FIGURE 3.—Map of the MORP Network showing the location of 12 stations and the search area.

On the other hand, there is a real danger of overexposure in the important, lower part of the trail, hence if the segments are very short they may blend together. Due to the effects of trailing fragments or persistent luminosity in the wake of the main meteoroid it is common for the beginning (upper) end of each segment to be confused whereas the lower end of the segment is sharp, especially if the occulted interval is relatively long. As a result the best deceleration values may come from restricting the calculations to the lower end of each segment. If the segments are so short that they are measured as separate dots rather than dashes, there is some danger of a progressive shift in their measured positions as the wake effects increase, in the sense of yielding a spuriously large deceleration. If, however, only the lower ends are used, there is a possibility of a spuriously small deceleration while the meteor luminosity is increasing due to a lengthening of each segment from increased exposure effects.

Both the Příbram (Ceplecha, 1961) and the Lost City (McCrosky, 1970) fireballs showed separate fragments in the photographs and such fragmentation is the rule for stone meteorites. It is important to be able to study the individual tracks and to identify recovered meteorite fragments with the corresponding photographic tracks. If the fragments develop an appreciable lateral separation their tracks may be resolved if the orientation is favorable and the range from the station is small or the camera focal length is sufficiently large. If the separation is entirely along the trajectory (and such separations exceeding a kilometer are quite possible) then the visibility of the lesser pieces is improved as the exposure interval becomes a smaller fraction of the complete shutter cycle. For a slow occulting rate a larger separation of fragments is observable before the image of a trailing fragment becomes confused with the preceding image of the leading or main piece.

The MORP cameras have a slow occulting rate in an attempt to realize some of these advantages at the expense of a smaller number of measured points. For the first seven years of its operation the Prairie Network used an occulting

rate of 20 breaks per second. Its cameras are controlled by a photometer to reduce the lens opening with a diaphragm and filter if the meteor becomes exceptionally bright, in order to prevent overexposure. The occulter in the MORP system is nearly a focal-plane wheel with three equal segments containing filters of approximate densities 0, 3 and 5, so that the transition from density 3 to 5 may be observable even if both ends of the dense segment are badly overexposed.

Meteor Dash Length

As shown above in considering spurious deceleration effects, the length of a single meteor segment or dash on the film (not including the occulted portion) is of interest. Let us consider the case, which is important for meteorites, of a slow object at a low meteoric height. If we assume the body has been decelerated to 10 km/s then the transverse component will normally be about 8 km/s. For each network take such an object midway between two typical stations at a height of 30 km. The length of one dash will then be as shown in the table. For an actual meteorite fall we can expect the terminal velocity of luminous flight to be even lower by at least a factor of 2 and also the range will normally be greater than assumed above for at least one of the two best photographs. In the Prairie and MORP networks the gap between dashes is twice the length of the dash, in the absence of photographic overexposure effects, so that it is possible to photograph a complete segment of a fragment between the main segments, as shown in figure 4. For the European Network the dashes and the gaps between them are of equal length.

Meteor Timing

Accurate time is required for the reduction of reference points on the star trails, and although the time of appearance of the meteor is not required in the solution for the atmospheric trajectory, it is needed to determine the right ascension of the radiant and the meteor orbit. The Prairie Network uses a signal from a photometer to detect the presence of a bright meteor and, moreover, the occulter is an oscillating blade rather than a rotating disk, which is programmed with

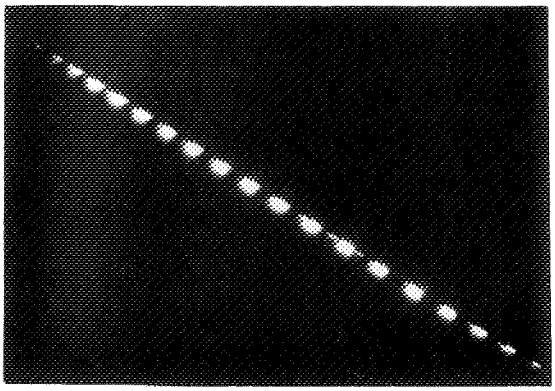

FIGURE 4.—A bright fireball photographed from the MORP station at Watson, Saskatchewan on August 18, 1971. Seven other stations also recorded this event. Note the fragmentation near the bottom of the trail, the bright, decelerating fragment about eight segments before the end and the effects of wake in the upper portion of the trail.

an ingenious code so that the omission of certain dashes in the meteor trail defines the time of the meteor to not worse than 5 s. The MORP system employs a meteor detector in which a photometer views the sky through two concentric perforated cones and interprets a flickering signal as a probable meteor. The European Network relies on the high population density within the network to provide a time from visual observations of bright fireballs.

Area of Atmosphere

In calculating the areas covered by the photographic networks it is important to distinguish between the area of the atmosphere effectively surveyed for bright meteors and the area of the Earth's surface over which a meteorite search might be conducted with a reasonable chance of success. The criteria used to define the two cases are rather arbitrary. Both the European and MORP networks are elongated rather than roughly circular, hence the computed areas are quite sensitive to the limit of effective coverage beyond the stations on the perimeter of the network.

Any meteor that drops a meteorite must be quite luminous at an altitude of 60 km. Following McCrosky and Ceplecha (1969) the area of the

atmosphere surveyed by a network is taken to be the area for which at least two stations will observe the meteor at an elevation of at least 10° above the horizon when at a height of 60 km. This limit corresponds to a ground distance of 298 km from each station (allowing for Earth curvature) and all three networks should record bright meteors effectively under these conditions. Actually many meteors will be recorded at altitudes below 10° although the Prairie and MORP networks have some gaps between the coverage of adjacent cameras near the horizon. Due to the large spacing between individual stations in the Prairie Network the two-station requirement of the criterion used here greatly restricts the fringe area included in the region just beyond each station on the edge of the network.

Search Area

The effective search area should include the interior area of a network and an external fringe based to some extent on the network's ability to retain positional accuracy comparable to that found in the interior of the network. It should also take some recognition of the suitability of the terrain for a search. The search areas shown in table 1, and indicated on the maps of figures 1 to 3, include all points for which a meteorite fall would be closer to one station of the network than the typical spacing of stations within that network. For the Prairie Network this leads to a larger search area than atmospheric area because of the one-station requirement whereas the MORP and European networks have reduced search areas because of their smaller station spacings. A criterion based on the effective range being proportional to camera focal length might have been considered and would have increased further the effective search area of the Prairie Network relative to the others.

Although at first sight it seems anomalous to include in the search area for the Prairie Network events which were excluded in the atmospheric coverage, the two problems are separate and the anomaly is due more to the strict nature of the elevation criterion than to any likelihood of grossly inadequate observations for the search area. The Prairie Network enjoys a further advantage in that essentially all the search area is suitable for an actual search. In the European Network the search area in table 1 still includes regions of the Alps and Carpathian Mountains in addition to substantial forested areas. The MORP search area includes a narrow fringe of forest on parts of its western and northern boundaries and some large lakes in Manitoba. The lakes, however, offer good conditions for a search during several months per year when they are covered with ice. (Some 13 percent of Canadian meteorites have been recovered from ice surfaces.)

The three networks combined survey 3.0×10^6 km^2 of atmosphere, with a search area estimated at 2.5×10^6 km^2, or 1.7 percent of the land area of the Earth.

NETWORK OPERATION

The routine operation of a meteorite camera network is a large undertaking although we will dismiss it here with only brief attention. All networks use a local operator assigned to each station whose duties include routine checks of the equipment, changing films when necessary and keeping local records. The European Network is directed from Ondřejov Observatory in Czechoslovakia and the Max-Planck Institute für Kernphysik in Heidelberg, Germany. The Prairie Network is directed from the Smithsonian Astrophysical Observatory in Cambridge, Mass. with a field headquarters at Lincoln, Nebraska, while the MORP Network is directed from the National Research Council of Canada, Ottawa, Ontario, with its field headquarters in Saskatoon, Saskatchewan. The operations of film processing, searching, measuring and computer reduction are performed either at the field headquarters or at the main institution headquarters. The operation of a meteorite network presupposes the intention of conducting meteorite searches. The best method of conducting such searches requires some advance planning although these plans may require modification due to the local circumstances of a particular event.

METEORITE INFLUX RATES

In the planning stage of the Prairie Network the expected meteorite fall rate was estimated

by McCrosky (McCrosky and Ceplecha, 1969) as 4.5 meteorites/yr, each 1 kg or larger, in an area of 10^6 km^2 during the hours of darkness. This was based on the estimated rates published by Hawkins (1960) rather than those of Brown (1960) which, at this mass limit, would predict only 15 percent as many as Hawkins estimated. McCrosky reduced the estimate of observable falls by a factor of 3 as a generous allowance for poor weather conditions and hence he expected to observe one or two meteorite falls per year in the Prairie Network, which is somewhat larger than 10^6 km^2.

In the six years from 1964 to 1970 the Prairie Network photographed and recovered one meteorite, Lost City (McCrosky, 1970). Four other events are mentioned by McCrosky and Ceplecha (1969) which may have produced meteorites and McCrosky et al. (1971) have described another probable meteoritic event less than a month after Lost City. On this basis it is difficult to justify a rate higher than one observable meteorite fall per year in an area of about 1.4×10^6 km^2. McCrosky and Ceplecha's (1969) data indicate that 46 percent of nighttime hours were usable so that if six meteorites were observed the fall rate may be estimated as high as 4×10^{-10} (km^{2}h)$^{-1}$, during the hours of darkness. The recovery rate, however, based on the Lost City event alone, is about 7×10^{-11}(km^{2}h)$^{-1}$ for clear nighttime hours.

Two other rough calculations of recovery rates of new falls are considered for comparison. Beginning with the Příbram fall in 1959 there appear to be 45 recorded meteorite falls to the end of 1970, of which 11 were in western Europe, south of the Baltic Sea and west of the U.S.S.R. This area of 3.6×10^6 km^2 thus yielded new meteorites at a rate of 3×10^{-11} (km^{2}h)$^{-1}$, a result in general accord with the observational data used by Hawkins. Only one of the 11 meteorites was appreciably smaller than 1 kg in size. Due to incomplete recovery this estimate is obviously a lower limit to the true rate.

In western Canada four fresh chondrites were recovered in that part of Alberta south of latitude 57°N (4.4×10^5 km^2) between 1952 and 1967. In one case (the Vilna meteorite) the mass recovered was less than a gram but there is some reason to believe large pieces may also have fallen. The indicated recovery rate is 6×10^{-11} (km^{2}h)$^{-1}$. All four falls were during clear, dark hours, however, so that if one assumes 50 percent clear weather and an average of 10.5 hr of darkness per day, a nighttime fall rate of 3×10^{-10} (km^{2}h)$^{-1}$ would be obtained, in good agreement with the rate derived if the Prairie Network observes one meteorite fall per year.

Obviously it will require several more years of operation of the networks to yield reliable values of the influx rate of meteorites. With an expectation of about 1800 clear, dark hours per year the three networks combined should attempt 1.8 searches per year if we adopt the search areas of table 1 and an influx rate of 4×10^{-10} (km^{2}h)$^{-1}$ for suitable meteoroids.

STATUS OF THE CAMERA NETWORKS

When the meteorite camera networks were proposed and constructed they were expected to yield at least partial answers to a variety of problems. Since this type of program is definitely a long-term operation it is still premature to assess the performance of the networks but it is of interest to examine some of the original questions in the light of experience gained with the networks.

The Prairie Network soon established that bright fireballs were not as rare as had been expected and McCrosky (1968) studied the orbital characteristics of 100 members of the group. Kresák (1970) has suggested that a scarcity of long-period, high-inclination orbits is at least partially due to the rejection of meteors with durations less than one second rather than to the absence of such meteors among fireballs. The flux of fireballs as a function of their photometric mass has been given by McCrosky and Ceplecha (1969) from Prairie Network data. Further observations are unlikely to alter these distributions substantially except possibly for such factors as corrections for observational selection or the dependence of photometric masses on details of the physical theory of meteors.

In terms of meteorite recoveries from the networks, Lost City is the only success to date and the recovery rate is disappointingly low. Both Pribram and Lost City are bronzite chon-

drites which constitute the second most common group of meteorites (Millman, 1969). It might be expected that a hypersthene chondrite, the most common type, should be recovered from the networks before long, but for the rarer types such as achondrites, irons, or stony-irons it may well take many years to get a single recovery for even a very few of the dozen types of meteorites in these classes. Orbital data on these rare classes are of great interest, so partial success in providing these data remains a prime goal of the networks.

In the discussion of meteorite influx rates above, the uncertainty in using data from the camera networks was seen to be caused by the difficulty in distinguishing between those events which may have dropped meteorites that remained undiscovered by the search and events which, although equally bright, left no solid pieces of appreciable size. A solution to this problem also has very practical implications in the organization of costly meteorite searches. General criteria for a meteorite fall include low initial and terminal velocities, deep penetration into the atmosphere and the absence of spectacular terminal flares. Levin and Simonenko (1969) suggest that there must be a sharp cut-off near $v_\infty = 20$ to 22 km/s for the upper limit of the velocity at which all but the very largest meteorites can penetrate the atmosphere. If the terminal velocity of the luminous path of a meteor exceeds a value of 8 to 10 km/s then it seems established that the luminosity becomes unobservable because the residual mass is insignificant and, for meteorites of a few kilograms or larger to survive, the luminosity should still be observable at or below 5 km/s. McIntosh (1970) has applied the conventional meteor theory to derive a plot of end-point heights versus surface-to-mass ratios. Even small meteorites should remain luminous to heights of 25 km or lower. Although major atmospheric breakups of meteorites will be marked by bright flares due to the sudden increase in effective area, the light curve of an individual meteorite fragment should decay gradually as the object is decelerated in the late stages of flight. If a spectacular terminal flare is observed, it appears safe to conclude that the meteoroid crumbled completely and no meteorite of a size large enough to warrant a search is to be expected.

When the meteorite resulting from a fireball event is recovered, the density of the object is known and one unknown is removed from the equations for the dynamics of the flight. The dynamical mass, determined from the observed deceleration, still requires some knowledge of the drag coefficient and a shape factor for the meteoroid, whereas the photometric mass depends critically on the luminous efficiency of the ablation process. Considerable progress has been made in experimental determination of the luminous efficiency for artificial meteors (Ayers, McCrosky and Shao, 1970). At low meteoric velocity most of the luminosity is due to iron so the known chemical composition of a recovered meteorite should provide a reasonably good estimate of the luminous efficiency.

Considering the two available test cases, the photometry of Pribram was complicated by overexposure of the photographs but the data appear to require a very massive initial object which suffered repeated fragmentation during its atmospheric flight, with the fragmentation beginning at normal meteor heights. For Lost City (McCrosky et al., 1971) fragmentation was less severe but there is evidence for a significantly flattened shape with drag forces quite different from the usual assumption for a spherical shape. The two smaller fragments of the meteorite appear to have been affected by aerodynamic lift forces during their flight. More test cases are obviously required.

The operation of a photographic fireball network involves various contacts with the local population. Since witnesses of a fireball or of an actual meteorite fall may be able to contribute very valuable information to supplement the instrumental data from the network, it is desirable to promote a good relationship with the public and a considerable effort is devoted to this aspect of the MORP operation. An information booklet on meteorites is available, meteorite displays are arranged, lectures are given to local organizations, newspaper articles on meteorites and the network are encouraged and suspected meteorites are examined for identification. One new meteorite, a 4-kg chondrite which had been found several years previously, was submitted to the MORP headquarters early in 1971 as a result of this publicity.

Viewing the photographic meteorite networks with the knowledge gained to date it may be concluded that although the rate of acquiring orbital and ballistic data on recovered meteorites is lower than had been expected, the meteorite networks are contributing very significant data on the various problems in meteor astronomy.

REFERENCES

AYERS, W. G., MCCROSKY, R. E., AND SHAO, C.-Y., 1970. Photographic observations of 10 artificial meteors, *Smithson. Astrophys. Obs. Spec. Rept.* No. 317, 1–40.

BROWN, H., 1960. The density and mass distribution of meteoritic bodies in the neighborhood of the earth's orbit, *J. Geophys. Res.*, **65**, 1679–1683.

CEPLECHA, Z., 1961. Multiple fall of Pribram meteorites photographed, *Bull. Astr. Inst. Czech.*, **12**, 21–47.

CEPLECHA, Z., AND RAJCHL, J., 1965. Programme of fireball photography in Czechoslovakia, *Bull. Astr. Inst. Czech.*, **16**, 15–22.

HAWKINS, G. S., 1960. Asteroidal fragments, *Astron. J.*, **65**, 318–322.

KRESÁK, Ľ. 1970. On the orbits of bright fireballs, *Bull. Astr. Inst. Czech.*, **21**, 1–9.

LEVIN, B. J., AND SIMONENKO, A. N., 1969. Meteorite radiants and orbits, in *Meteorite Research*, edited by P. M. Millman, D. Reidel Publ. Co., Dordrecht, Holland, 552–558.

MCCROSKY, R. E., 1968. Orbits of photographic meteors, in *Physics and Dynamics of Meteors*, edited by L. Kresák and P. M. Millman, D. Reidel Publ. Co., Dordrecht, Holland, 265–279.

——, 1970. The Lost City meteorite fall, *Sky and Telescope*, **39**, 158–162.

MCCROSKY, R. E., AND BOESCHENSTEIN, H. JR., 1965. The Prairie Meteorite Network, *Smithson. Astrophys. Obs. Spec. Rept.* No. 173, 1–23.

MCCROSKY, R. E., AND CEPLECHA, Z., 1969. Photographic networks for fireballs, in *Meteorite Research*, edited by P. M. Millman, D. Reidel Publ. Co., Dordrecht, Holland, 600–612.

MCCROSKY, R. E., POSEN, A., SCHWARTZ, G., AND SHAO, C. -Y., 1971. Lost City meteorite—its recovery and a comparison with other fireballs, *J. Geophys. Res.*, **76**, 4090–4108.

MCINTOSH, B. A., 1970. On the end-point height of fireballs, *J. Roy. Astron. Soc. Can.*, **64**, 267–281.

MILLMAN, P. M., 1969. Astronomical information on meteorite orbits, in *Meteorite Research*, edited by P. M. Millman, D. Reidel Publ. Co., Dordrecht, Holland, 541–551.

2. A Determination of Meteor Mass Distribution From Meteor Echoes

G. FORTI*
Smithsonian Astrophysical Observatory
Cambridge, Massachusetts

Meteor counts from the observations of the Harvard-Smithsonian Radio Meteor Project at four magnitudes in the range of about +9 to +15 in the visual scale were used to determine the exponent of the mass-distribution law under certain assumptions. Since for these data no range measures were available, and since the pattern of the transmitting/receiving antennas was very broad, the same range and radiant distribution were assumed for all counts within the same half-hour during which individual counts at different magnitudes were obtained. These echo counts, covering in five successive days 24 hr with overlapping periods, yielded for the exponent a value of 1.95±0.02, close to other determinations. Individual values, however, presented a considerable scatter, probably reflecting changes in radiant and mass distribution over the year. From the same data, it appeared that the mass exponent changed during the day, yielding generally a higher value for the evening hours.

THE NUMBER OF METEOROIDS entering the Earth's atmosphere increases as the numerical value of the magnitude increases. If the number N_m of meteoroids having mass m and larger can be expressed as

$$N_m \propto m^{-s+1}$$

then, assuming a linear dependence between the mass and the electron line density q produced by a meteoroid, the distribution of meteor trails with line density q and larger will be

$$N_q \propto q^{-s+1}$$

If the number N_q is known at different limiting values of q, a determination of the mass exponent s† can be attempted. The mass exponent s has been computed from meteor data at different magnitudes; its value ranges between 2.5 and 2.2. Hawkins and Upton (1958) find a value 2.34 for s over a magnitude interval −1 to +4; Šimek and McIntosh (1968), 2.35 between magnitudes +5 and +10; Kaiser (1961), 2.17 between magnitudes +8 and +11; and Öpik (1958), ~2.2 between magnitudes +2 and +5. The recent results of McIntosh and Šimek (1969) do not change the conclusions of their earlier paper.

Meteor counts at four different limiting magnitudes, from approximately +9 to +15 absolute visual magnitude, were recorded during normal operations of the Harvard-Smithsonian Radio Meteor Project, Havana, Ill., lat. 40°13′N, long. 90°01′W, and s was derived from these observations. The radar operates at a wavelength of 7.331 m, with a peak power of about 3 MW and antenna gains near 20 db over an isotropic radiator.

* Present address: Osservatorio Astrofisico Di Arcetri, Firenze, Italy.

† s has also been termed the differential mass index.

The electron line density is known to be dependent on the meteor's velocity and zenith angle as well as on its mass, and the observed velocity and radiant distribution vary over the day. In consequence, diurnal average values of s are more meaningful here than values at particular times of day. It has not been possible to correct the data for observational height limitations, which must have some effect. The diffusion ceiling and recombination floor on heights (Southworth, paper no. 3 this volume) will eliminate some relatively small and large line densities, respectively. Nonetheless, since we unexpectedly observed many large and small line densities compared with intermediate densities, diffusion and recombination appear to be unimportant to an overall determination of s.

ECHO COUNTS

The observed meteor rates are automatically recorded by the radar equipment, which counts the meteor echoes received in given intervals of time, down to four different limiting receiver sensitivities covering the useful dynamic range of the system. The magnitude range is about $+9<M<+15$ in the radar scale, which corresponds roughly with the visual absolute magnitude scale.

Counts are obtained every half-hour, with each receiver level sampled at least once. Counts for the faintest meteors, detected down to the receiver noise, are increased by spurious echoes, even though the equipment was specifically designed to keep these events to a minimum. Spurious counts are probably recorded at the lowest level of receiver sensitivity as well, owing to airplane echoes from a nearby airport. Both limitations must be considered in the analysis of the data. During the recording, the transmitted peak power is monitored, as well as the receiver sensitivities at each level. Observations are usually carried out on five consecutive days, each with an average of about 10 hr of continuous recording. The periods of recording are shifted to cover a full 24 hr with overlapping observations.

From these counts, it is possible to derive a diurnal variation of rate that represents the observations of a whole week. The sums of the counts of each half-hour at each level of sensitivity are normalized to this observed diurnal-rate curve to allow for the fact that these data are obtained on different days and over different periods of the day, during which the meteor rates can change considerably.

ANALYSIS AND RESULTS

Rates are discussed here in terms of a convenient parameter

$$L=10^{10}\sqrt{P_R/P_T}$$

where P_T is the transmitter power and P_R is the limiting receiver sensitivity; both varied slightly from time to time. With a mean antenna power gain of 110 and a mean slant range of 135 km, the mean limiting electron line density is

$$q=4.5\times10^9\,L$$

Denoting by N_L the hourly number of meteor echoes exceeding a given L, a least-squares fit of $\log_{10} N_L$ versus $\log_{10} L$ has been made for the data covering the period October 1968 to November 1969.

A linear fit was made for each of the 24 weeks of observations and for selected groups of hours from the reconstructed daily rates. Proper weights were introduced in the least-squares solutions to take into account false events and statistical fluctuations in N_L. The variation of the exponent s with time is plotted in figure 1, where the dotted line indicates the results from the mean rate over 24 hr, and the solid and the dashed lines show s from the mean of 4 hr in the morning (5^h to 8^h) and in the evening (17^h to 20^h), respectively. The slope $1-s$, derived from a fit combining all the data, is shown in figure 2, where the mean N_L over 24 hr is plotted versus L. The values of s for the different mean rates, together with their errors, are given in table 1.

The morning observations include a relatively large number of retrograde orbits, and the evening hours, of direct low-eccentricity orbits. The large counts from the ecliptic streams of moderate eccentricity are included only in the 24-hr averages. Since there are still other diurnal variations, it is difficult to interpret the apparent diurnal changes in s.

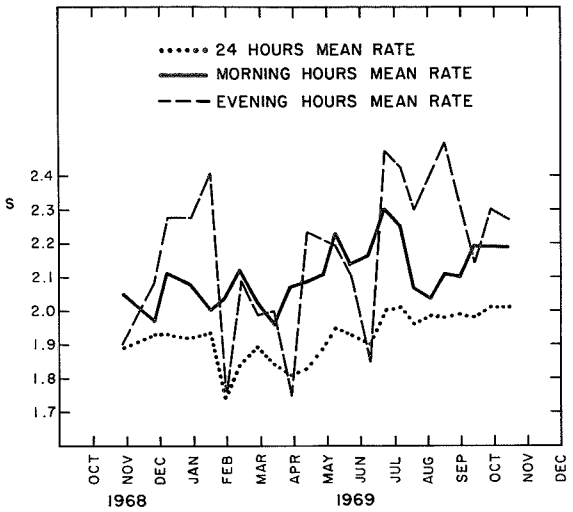

FIGURE 1.—Exponent s as a function of the date.

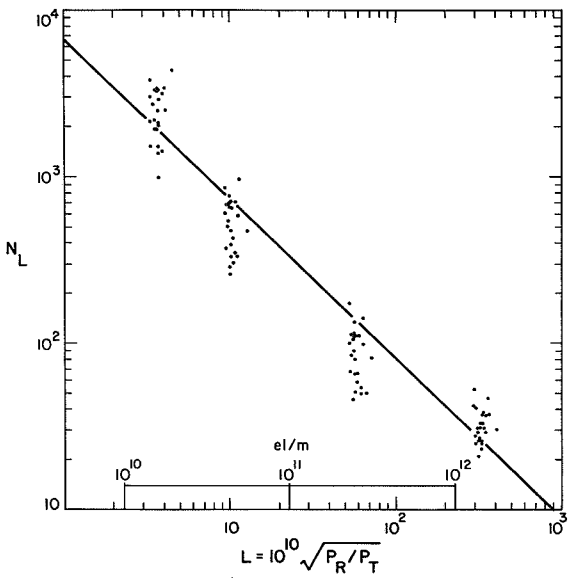

FIGURE 2.—Counts N_L plotted against L. Straight line: s from linear fit.

A mean daily variation of meteor rates, plotted in figure 3, was deduced from all the data for each of the four limiting magnitudes. Similar theoretical curves were obtained by Elford and Hawkins (1964) from the study of the orbits of sporadic meteors and from the geometry of the radar system.

The curves of figure 4, where the mean rate for each week of observations is plotted versus

TABLE 1.—*Exponent* s *and its Error for Different Mean Rates*

Magnitude interval	Mean rate	First-order polynomial	
		s	Standard error
$+9<M<+15$	24 hours	1.95	0.02
	Morning hours	2.14	0.05
	Evening hours	2.26	0.10
$+11<M<+15$	24 hours	2.19	0.04
	Morning hours	2.23	0.07
	Evening hours	2.49	0.14
$+9<M<+13$	24 hours	1.82	0.03
	Morning hours	1.96	0.05
	Evening hours	1.85	0.08

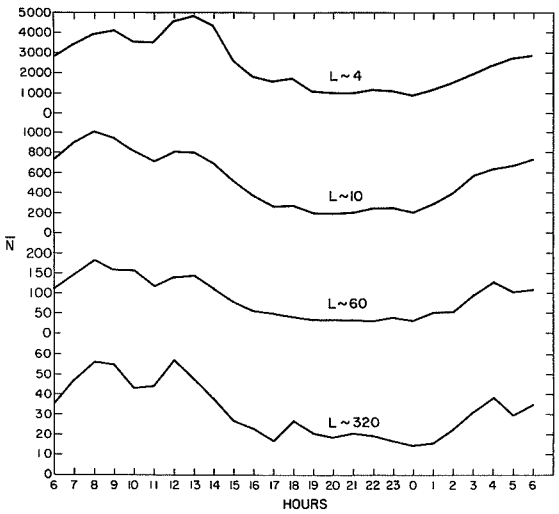

FIGURE 3.—Diurnal variation in the echo rates from all the data.

the time of the year, are in good agreement with the distribution of sporadic meteors over the year as found by Kresáková and Kresák (1955) from telescopic observations and by Weiss (1957) from radar echoes. This accordance among different surveys seems to indicate that the distribution of sporadic meteors does not change significantly with the years.

CONCLUSIONS

The observed rate of radio meteors depends on many factors, the most important being the

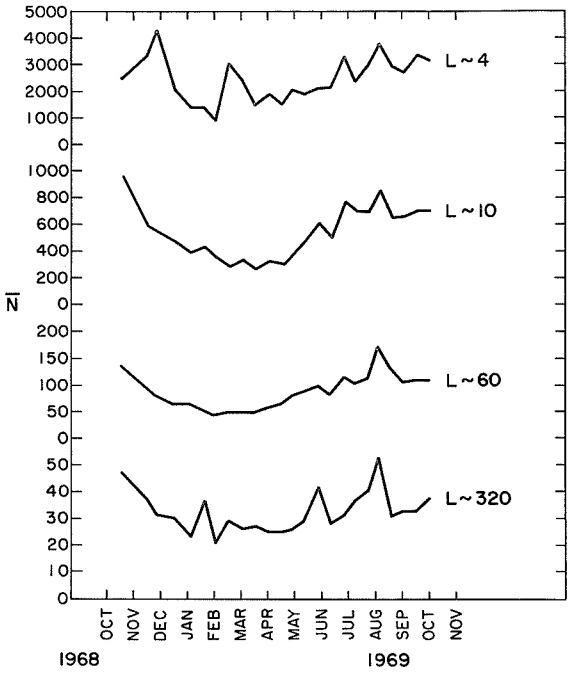

FIGURE 4.—Mean rates as a function of time of the year.

equipment parameters, the ionizing process, and the radiant distribution. To calculate the mass exponent s from the echo counts obtained in Havana, it was necessary to make some assumptions and assign certain values to unknown constants. First, since no range measures are available for these counts, the same range distribution was assumed at each limiting magnitude; second, with the antenna pattern very broad and the side lobes conspicuous, the same radiant distribution was assumed for all the counts of each half-hour of recording. The true count of meteor echoes exceeding a certain minimum electron line density is undoubtedly different from the observed count because of the lack of knowledge of range and antenna gain for each returned echo. Once these parameters are assumed, the exponent s can be calculated with some confidence.

The value found for s is 1.95 ± 0.02; it is lower than the determinations cited above but close to the values of Kaiser (1961) and Öpik (1958). When the exponent is determined over a different magnitude range, different values of s are obtained, as can be seen in table 1.

The variations of s with time as seen in figure 1 (dotted line) are probably due to changes in the radiant distribution and the mass distribution. Known streams do not contribute substantially to the observed rates, since they are observed only for short period of time, if at all. However, unknown showers might be responsible for this scatter.

ACKNOWLEDGMENTS

I wish to thank M. Schaffner and R. B. Southworth for stimulating discussions and C. S. Nilsson for lending me one of his computer programs. This work was done under NASA contract NSR 09-015-033.

REFERENCES

ELFORD, W. G., AND HAWKINS, G. S., 1964. Meteor echo rates and the flux of sporadic meteors, *Harvard Radio Meteor Project Res. Rept.* No. 9.

HAWKINS, G. S., AND UPTON, E. K. L., 1958. The influx rate of meteors in the Earth's atmosphere, *Astrophys. J.*, **128**, 727–735.

KAISER, T. R., 1961. The determination of the incident flux of radio meteors. II. Sporadic meteors, *Monthly Notices Roy. Astron. Soc.*, **123**, 265–271.

KRESÁKOVÁ, M., AND KRESÁK, Ľ., 1955. On the activity of telescopic meteors and some related problems, *Contrib. Astron. Obs. Skalnaté Pleso*, **1**, 40–77.

MCINTOSH, B. A., AND ŠIMEK, M., 1969. Mass distribution of meteoroids as determined by radar observations of underdense meteor trails, *Can. J. Phys.*, **47**, 7–22.

ÖPIK, E., 1958. Statistical results from the Arizona expedition for the study of meteors, *Contrib. Armagh Obs.*, No. 26, 1–82.

ŠIMEK, M., AND MCINTOSH, B. A., 1968. Meteor mass distribution from underdense-trail echoes, in *Physics and Dynamics of Meteors*, edited by Ľ. Kresák and P. M. Millman, D. Reidel Publ. Co., Dordrecht, Holland, 362–372.

SOUTHWORTH, R. B., Recombination in radar meteors, this volume.

WEISS, A. A., 1957. The distribution of the orbits of sporadic meteors, *Australian J. Phys.*, **10**, 77–102.

3. Recombination in Radar Meteors

RICHARD B. SOUTHWORTH
Smithsonian Astrophysical Observatory
Cambridge, Massachusetts

RECOMBINATION OF THE ELECTRONS in the ionized column has often been considered (see, for example, Öpik, 1955), but the uncertainties in the atomic and molecular species present and in the rate constants have made it difficult to predict. Furthermore, recombination has not been recognized in the observations, so that it has been judged to be negligible (McKinley, 1961). More recently, however, a relatively high rate constant has been found for dissociative recombination of certain molecular ions. We have now observed recombination at comparable rates in our radar meteor recordings.

RECOMBINATION RATE

Recombination rates for all meteoric atoms are too slow to interest us here. Mehr and Biondi (1969) have obtained reliable laboratory measures for dissociative recombination of the most likely molecules in the meteor environment, N_2^+ and O_2^+. We do not know what atoms or molecules are first ionized in the meteoric process. However, if metallic ions, such as are seen in meteor spectra, are created first, we may plausibly expect fast charge transfer to the atmospheric molecules (Öpik, 1958). Then, recombination can be expressed by

Mehr and Biondi (1969) found

$$\frac{dn}{dt} = -\alpha n n_i \qquad (1)$$

where n is the electron volume density in cm^{-3}, and n_i is the volume density of ion species that recombine at rate α cm^3 s^{-1}.

$$\alpha(O_2^+) = 1.9\times10^{-7}\left(\frac{T_e}{300}\right)^{-0.70},$$

$$300° \text{ K} < T_e < 700° \text{ K} \qquad (2)$$

$$\alpha(N_2^+) = 1.9\times10^{-7}\left(\frac{T_e}{300}\right)^{-0.39},$$

$$300° \text{ K} < T_e < 4500° \text{ K} \qquad (3)$$

where T_e is the electron temperature, and the gas and ion temperatures were held at 300° K. As a first approximation, one may take the ambient temperature ~200° K for T_e. If all ions recombine at rate α, we have $n_i = n$. Here, we will use

$$\frac{dn}{dt} = -2\times10^{-7}\, n^2 \qquad (4)$$

allowing for other ions that do not recombine so fast and for some atmospheric heating. The observations are not sensitive to an uncertainty in α of much less than a factor of 2.

ANALYTIC APPROXIMATION

If we neglect the effect of recombination on the radial distribution of electrons in the column, we can compute the effect of recombination on the total line density on the electrons as follows. The density at distance r from the column axis is taken to be gaussian with radius ρ:

$$n = \left(\frac{q}{\pi\rho^2}\right)\exp\left(\frac{-r^2}{\rho^2}\right) \qquad (5)$$

where q is the electron line density. Initially, we have $q = q_0$ the original line density, and $\rho = r_0$ the initial radius. The effect of diffusion (neglecting recombination) is

$$\rho^2 = r_0^2 + 4Dt \qquad (6)$$

and the effect of recombination is

$$\frac{dq}{dt} = -2\pi\alpha \int_0^\infty n^2 r\, dr = -\frac{\alpha q^2}{2\pi\rho^2} \tag{7}$$

When we combine equations (6) and (7),

$$\frac{dq}{q^2} = -\alpha \frac{dt}{2\pi r_0^2 + 8\pi D t} \tag{8}$$

then, integrating with respect to time, we find

$$\frac{1}{q} = \frac{1}{q_0} + \frac{1}{q_{\text{lim}}} \tag{9}$$

where

$$q_{\text{lim}} = \frac{8\pi D}{\alpha \ln[1 + (4Dt/r_0^2)]} \tag{10}$$

Qualitatively, the result of recombination is to reduce any initial line density to less than an upper bound q_{lim}.

The exponential decay of the radar signal with time, caused by diffusion, is often used to measure the meteor's height. Diffusion alone reduces the received signal voltage by the factor

$$L = \exp\left[-\left(\frac{2\pi}{\lambda}\right)^2 (r_0^2 + 4Dt)\right] \tag{11}$$

(McKinley, 1961), where λ is the radar wavelength (733.1 cm for our equipment). Differentiating (11), we have

$$D = -\left(\frac{\lambda}{4\pi}\right)^2 \frac{dL}{L dt} \tag{12}$$

which is used to find D and thence height from the observed decay dL/Ldt.

If there is recombination in addition to diffusion and if the recombination is not taken into account (to do so is difficult in practice), the height will be overestimated. The error in height can be estimated from equations (12) and (8) as

$$\Delta h_D = H \ln \frac{D'}{D} = H \ln\left[1 + \frac{\lambda^2 \alpha q}{32\pi^3 D(r_0^2 + 4Dt)}\right] \tag{13}$$

where H is the atmospheric scale height, and D' the incorrectly inferred value of D.

EXACT INTEGRATIONS

Numerical integrations were performed to find the actual distribution of electrons under combined recombination and diffusion. The electron density was computed at small intervals of space and time for 1 s after formation of the ionized column. The initial electron distribution was assumed to be gaussian, with radii approximating Manning's (1958) or Öpik's (1955) estimates, as tabulated by Southworth (1962).

Table 1 shows some results for a variety of values of diffusion D ($\text{cm}^2\,\text{s}^{-2}$), initial radius r_0 (cm), and initial line density q_0 (cm^{-1}). The tabulated cases cover the brighter end of the range of line densities observed with our equipment; fainter meteors are little affected by recombination. To fix ideas, diffusion has been translated into height h_d (km) by use of Greenhow and Neufeld's (1955) results as expressed by McKinley (1961):

$$\log_{10} D = 0.067 h_D - 1.6 \tag{14}$$

line density has been translated into radar magnitude M by Kaiser's (1955) relation

$$M = 35 - 2.5 \log_{10} q \tag{15}$$

At each height, the smaller value of initial radius is approximately Manning's estimate, and the larger value is approximately Öpik's.

Results are tabulated for 0.03 s after formation of the ionized column; this time is representative for our observations of the electrons in the principal Fresnel zone. The accuracy of approximations (10) and (13) is similar at other times.

The tabulated values of M_{lim} are deduced from M_0 and the accurately computed M by equations (9) and (15); ΔM_{lim} is the difference $(M'_{\text{lim}} - M_{\text{lim}})$ between M_{lim} and analytic approximation M'_{lim} deduced by equations (10) and (15). One sees that the error in the analytic approximation is small for all tabulated cases, and one can infer that it is small for all meteors observed with our equipment.

The integrations also yield the rates of decay caused by combined diffusion and recombination. These have been converted into height differences Δh_D by use of equation (14) and compared with predicted values from (13). The differences between approximation and integration are small for all cases computed.

The effect of recombination on the relative distribution of electrons in the column was carefully

TABLE 1.—*Results of Numerical Integrations Compared with Approximation*

		Initial values		Integration results 0.03 s after formation			Differences, integration minus approximation	
D	h_D	r_0	M_0	M	M_{lim}	Δh_D	M_{lim}	Δh_D
10^3	68.7	0.2	5.0	9.19	9.16	17.9	0.34	1.7
			7.5	9.53	9.35	16.9	0.16	1.0
			10.0	10.52	9.48	12.1	0.02	0.4
			12.5	12.57	9.50	4.0	0.00	0.1
		1.4	5.0	8.37	8.32	22.2	0.45	2.3
			7.5	8.94	8.59	19.9	0.18	1.3
			10.0	10.31	8.75	13.1	0.02	0.4
			12.5	12.54	8.77	4.1	0.01	0.0
10^4	83.4	2.0	5.0	6.71	6.46	6.5	0.17	0.5
			7.5	7.90	6.61	3.2	0.02	0.0
			10.0	10.04	6.62	0.5	0.01	0.0
		14.0	5.0	5.90	5.27	8.8	0.16	1.1
			7.5	7.65	5.43	3.4	0.02	0.0
			10.0	10.02	5.44	0.5	0.00	0.0
10^5	98.1	20.0	5.0	5.25	3.54	0.6	0.02	0.2
			7.5	7.53	3.56	0.1	0.01	0.0
		140.0	5.0	5.04	1.38	0.6	0.01	0.4
			7.5	7.50	1.39	0.1	0.00	0.0

examined; it turned out to be small in all the tabulated cases. The gaussian distribution represented by equations (5) and (6) was always a good approximation. An apparent magnitude computed from (5) and (6) would always have been between 0.0 and 0.2 mag too bright.

OBSERVED IONIZATION CURVES

For each observed meteor, we compute an "ionization curve" showing the initial radar magnitude of the ionized column as a function of position along the column; the position is represented by the time that the meteoroid passed that position. Each of the maxima and minima (collectively "extrema") of the Fresnel pattern from each station yields one point on the ionization curve. The deviations from a smooth curve of the extrema after the first maximum measure the amount of ionization in the later Fresnel zones. The effective length of the ith extremum ($i>1$) is

$$F_i \approx \frac{1}{\pi}\sqrt{\frac{\lambda R}{2[i-(\frac{3}{4})]}} \qquad (16)$$

and is measured

$$t_i \approx \frac{1}{4V}\sqrt{\frac{\lambda R}{2[i-(\frac{3}{4})]}} \qquad (17)$$

after the meteoroid passes the center of the zone. Here, $R\sim 150$ to 300 km is the distance to the ionized column, and V is the meteor velocity.

We have observed recombination in three ways. We first saw it in ionization curves derived as just described. Figure 1 is an example. The digits represent radar magnitudes derived from the principal Fresnel zone (left-most digit) and later zones as observed at stations 2, 3, 4, and 6, all corrected for diffusion in the interval since the zone was formed. Recombination is seen in the upward slope of the first few digits for each station; these show that the electron line density appears greater when measured sooner after formation, even after correction for diffusion. (The later digits for each station show fragmentation.) It is not plausible that the ionization curve should have a bump just after the principal zone for each station, on this and on many other

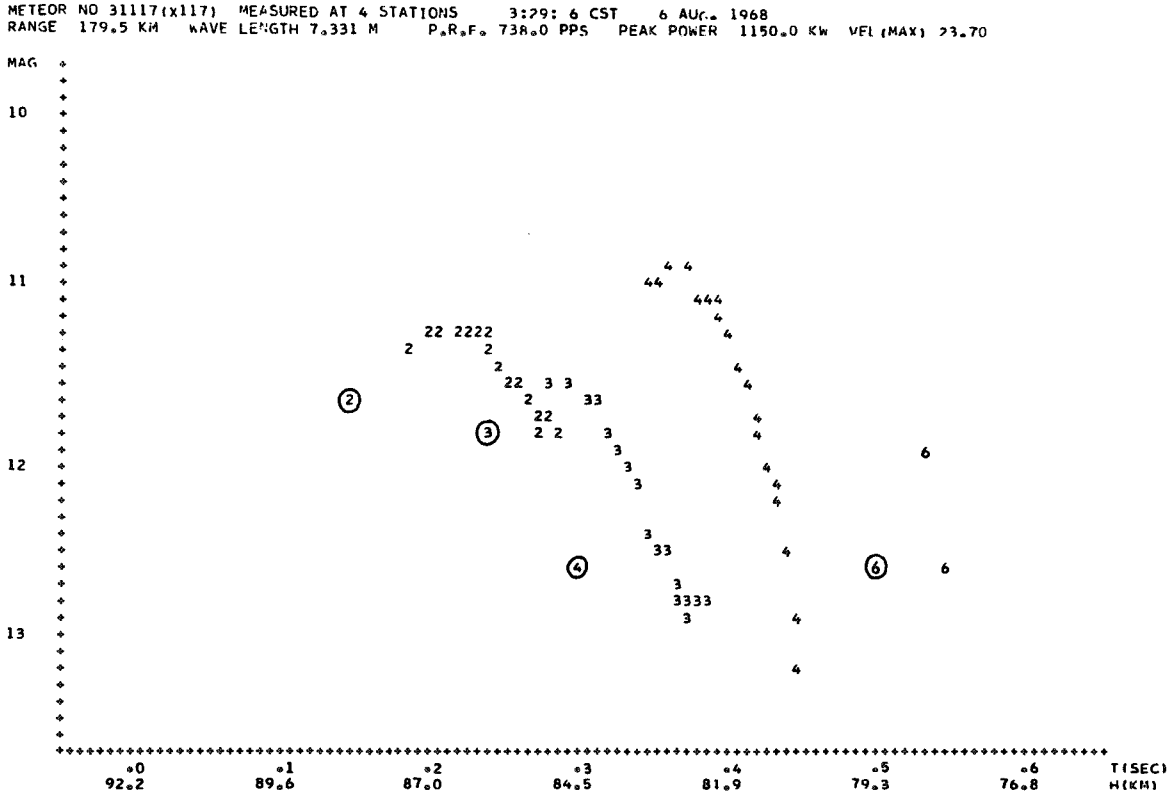

FIGURE 1.—An observed ionization curve, showing recombination and fragmentation. The circled digits represent values from the principal Fresnel zones for stations 2, 3, 4, and 6. The following digits represent values from the later zones at each station.

similar meteors. Some process that removes electrons from the column for only a few hundredths of a second is required, and recombination suits.

HEIGHT MAGNITUDE DISTRIBUTION

Diffusion heights were computed from 13 672 meteors observed in 1962 to 1965 by using Greenhow and Neufeld's (1955) profile (14). Their result was chosen because it is in harmony with atmospheric models, not because it seemed a good determination. (We believe that their statistical analysis is faulty because selection effects were ignored.) Greenhow and Hall's (1960) more careful diffusion measures are vitiated by recombination, as we discuss later. The effect of recombination on our diffusions is small for many of the relatively faint meteors that we observe.

We observe apparent diffusion at three to seven different points on each meteor trail and combine these values into a mean value of the diffusion height at the maximum of the ionization curve of each meteor. We also find an internal standard error of that height, the apparent atmospheric scale height, and its standard error. In the present analysis, we use the errors primarily to eliminate inconsistent and distorted data.

Figure 2 shows the distribution of diffusion height at the maximum of the ionization curve, as a function of the magnitude at the maximum, for 10 163 meteors. Meteors whose standard error in height exceeded 4 km or that yield an unreasonable scale height have been omitted. True height will differ from these diffusion heights by up to about 3 km, depending on height and probably also on time. True heights are not available for these meteors; but diffusion heights are preferable for the present purposes because we are examining

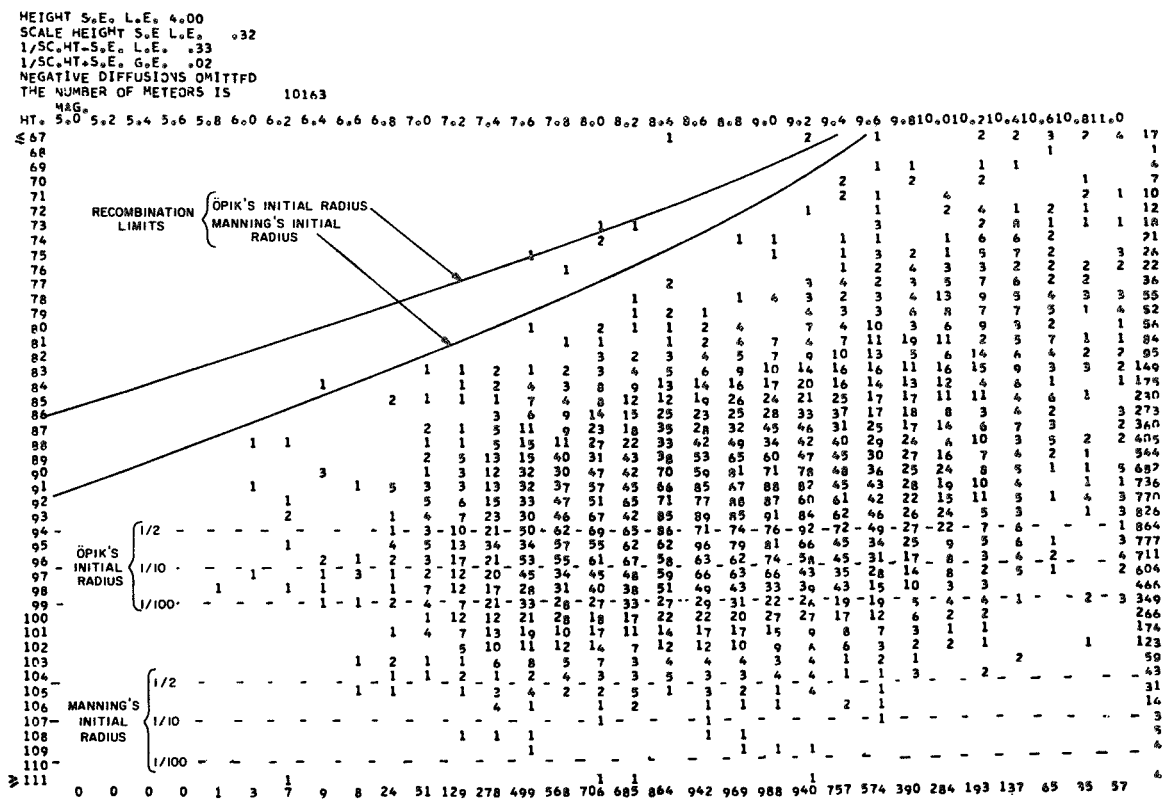

FIGURE 2.—Diffusion heights at maximum ionization of 10 163 meteors, as a function of radar magnitude at maximum ionization. The recombination limits are from equation (8). The initial radius limit is shown for received voltage attenuations of 1/2, 1/10, and 1/100 (corresponding approximately to 1/2, 1/10, and 1/100 in number of meteors observed). Considering that the standard errors of these heights are 4 km or less, these are good fits to the recombination limit and initial radius limit using Manning's initial radius.

effects that depend directly or inversely on atmospheric density, like diffusion, so that density changes with time do not smear the diagram.

Our second observation of recombination is in the lower bound to heights in figure 2. Figure 2 shows curves of $M_{\lim}=35-2.5\log_{10} q_{\lim}$, using Manning's and Öpik's values of r_0 (exact values from Southworth, 1962) and $t=0.03s$ (an average time for the center of the measured part of the Fresnel pattern, for different velocities and lengths of Fresnel pattern). The upper bound (eq. (10)) on observable radar magnitudes is well confirmed, as is Manning's initial radius. Öpik's initial radius is clearly disproved (for our magnitude range) by the observation of many meteors far above his ceiling in figure 2. The actual upper bound to our observed heights is caused by diffusion, which cuts off our observations at lower heights than initial radius.

Attachment of electrons to neutral atoms or molecules has been proposed (Davis, Greenhow, and Hall, 1959) to explain an observed lower bound on radar heights of bright photographic meteors. Attachment cannot explain the lower bound to height in figure 2, because attachment to atmospheric atoms or molecules would give a lower bound independent of magnitude, and atmospheric species vastly outnumber meteor atoms or molecules for these meteors. On the other hand, recombination seems to be an adequate explanation for Davis, Greenhow, and Hall's observations. The importance of attachment should be reconsidered with recombination taken into account.

Our third observation of recombination appears in figure 3. This is similar to figure 2, except that more stringent limits have been placed on the scale height and on the standard error of the height of maximum. The relative distribution in figure 3 is essentially similar to that in figure 2 except that a band of meteors just above the recombination limit has been eliminated. This band represents the meteors where recombination is large enough to disturb the consistency between diffusion heights at different stations on the same meteor.

FRAGMENTATION

If the meteoroid is not a single body but has broken into fragments, the composite Fresnel pattern of the group can be constructed as the sum of individual Fresnel patterns. Differences in fragment size will cause differences in deceleration of the various fragments and will spread them along their common trajectory. In the composite Fresnel pattern of several or more fragments, this corresponds to smoothing out the later oscillations; and in the ionization curves constructed from observations and from single-body theory, this corresponds to progressively fainter magnitudes for the later Fresnel zones. This effect is obvious in figure 1 and in a large proportion of our meteors. It corresponds to fragment spreads of the order of 50 to 200 m along the trajectory; smaller fragment separations are below our resolution. A more complete study of fragmentation will be made at a later date.

SYSTEMATIC ERRORS CAUSED BY RECOMBINATION

Greenhow and Hall (1960) have made the most careful attempt, to date, to observe atmospheric density changes from study of meteors. They

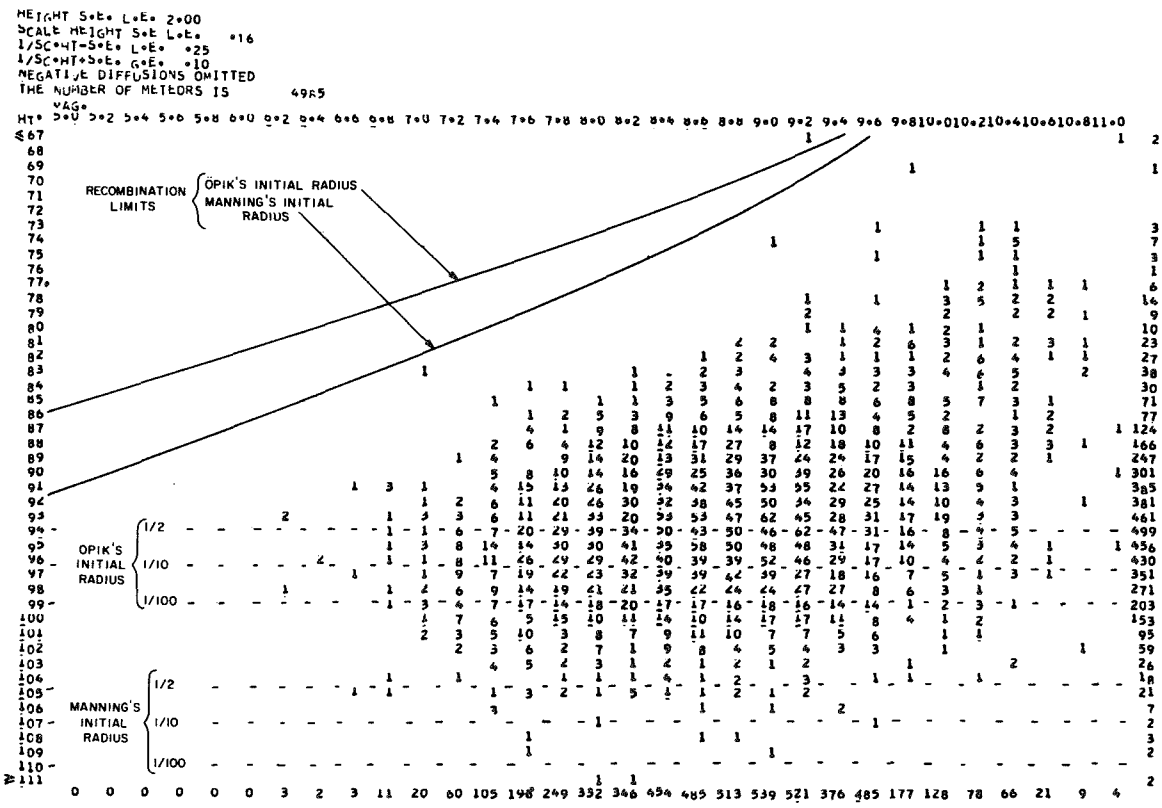

FIGURE 3.—Diffusion heights at maximum ionization of 4985 meteors as a function of radar magnitude at maximum ionization. These meteors are a subset of the meteors in figure 2, with standard errors in height of 2 km or less and with more closely restricted scale heights.

measured diffusion from radar meteors as functions of height (85 to 118 km) and time. Their rate of observation and lowest observed height show that they were observing magnitudes near the left edge of figure 2. It is not possible to correct their published observations for recombination; indeed, we could not correct more than a few if we had their original data. However, we can recognize the qualitative effects of recombination on their measures.

Three of Greenhow and Hall's principal results are out of harmony with other measures of the atmosphere: (1) the mean scale height was 9 km; (2) the density at their mean height of 96 km varied regularly through the day, with a minimum near 0600 hours and a maximum near 1800; and (3) the scale height varied regularly through the day, with a minimum near 0600 and a maximum near 1800. *A priori*, it is suspicious that these variations should be in phase with the diurnal variation of meteor velocities, where high velocities predominate in the morning and low velocities in the evening. In fact, all three effects are readily explained in terms of recombination: (1) their mean scale height is too high because their lower meteors were much affected by recombination and their higher meteors hardly at all; (2) their density at 96 km varied because the faster meteors observed in the morning were observed sooner after the column was formed, so that the measured diffusion contained more recombination than the slow meteors in the evening at the same height; and (3) their scale height varied because the fast meteors in the morning were higher, so that the slope of the overall sample was less perturbed by recombination, while the evening sample consisted mostly of meteors with appreciable recombination. Figure 4 gives a schematic representation of these effects.

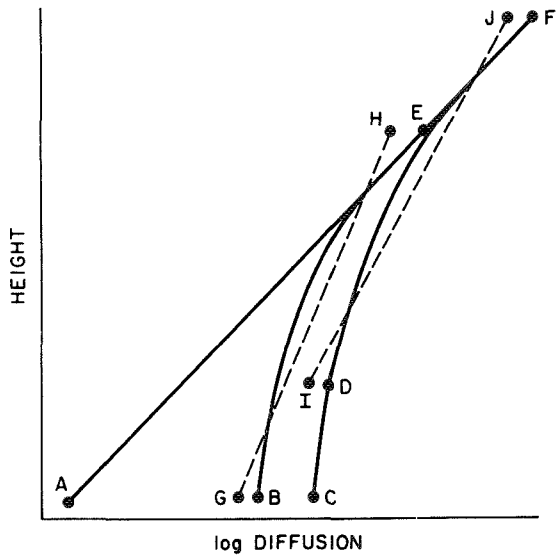

FIGURE 4.—Schematic explanation of Greenhow and Hall's results: *AF*—true diffusion; *BF*—diffusion plus recombination in the evening; *CF*—diffusion plus recombination in the morning; *GH*—linear fit to evening sample *BE*; *IJ*—linear fit to morning sample *DF*.

SELECTION EFFECTS

Recombination causes a quite unexpected selection effect against bright, low meteors. Since these are predominantly slow meteors, all existing statistics on velocity distributions of radar meteors have been significantly biased. The unrecorded meteors are mostly in direct orbits near the ecliptic plane, and it will also be necessary to revise present calculations on meteor space density (Southworth, 1967). With the Havana equipment, we will usually be able to recognize meteors that have been affected by recombination; but we will often be unable to correct for it, because most of the recombination occurs before we observe the meteor. Simultaneous observations with the image orthicon and the radar are the best way to determine how many meteors are missed or undervalued because of recombination.

IONIZING PROBABILITY

Theoretical treatment of ionizing probability in meteors suffers from grave difficulties; the energy levels are too high or too low for present techniques, the physical processes are little known, and the meteor composition is not known. In practice, the ionizing probability has been evaluated by comparing radar observations with photographic or visual observations. Verniani and Hawkins (1964) wrote the latest and most thorough discussion, combining simultaneous radar-visual observations (Millman and McKinley, 1956) with the handful of available radar-photographic observations (Davis and Hall, 1963). They found a large scatter in the data

but agreed on

$$\beta = 10^{-20}\, v^{-4} \qquad (18)$$

for the probability that an ablated meteor atom would be ionized (assuming that only meteor atoms are ionized in the first instance), where velocity v is in centimeters per second.

Unfortunately, recombination essentially vitiates all existing determinations of ionizing probability made by use of visual or photographic meteors. If we extend the recombination limit (using Manning's initial radius) in figure 1 to greater heights, we reach magnitude +4 at 100 km and magnitude +2 at 110 km, implying that virtually all visual and photographic meteors are affected by recombination to some extent. Of course, this extension can hardly be quite correct; the initial radius probably depends on magnitude, and the early history of the ionized column doubtless depends on the ratio of meteoric atoms and molecules to atmospheric atoms and molecules. Recombination depends very strongly on both these factors. If, however, we guess that Öpik's initial radius may be a better approximation for brighter meteors, we still find that most visual and photographic meteors experience recombination. Further, if we assume that we know the initial radius and the physical processes, a rediscussion of the observations considering recombination is still unpromising because the uncertainties in magnitude, and in radar and optical height, make it difficult even to recognize unrecombined meteors, and correction for recombination is impossible. The most hopeful view is that radar-visual observations of faint high meteors may be little affected by recombination. However, we retain uncertainties in the initial radius and in the early history of the ion column; the former uncertainty is an additional difficulty for analysis of radar echoes from high meteors.

The only observational treatment of ionizing probability made without use of optical observations was done by Evans and Hall (1955). They conclude, using the slope of the height-velocity curve and a theoretical height-magnitude relation, that ionizing probability is independent of velocity. This conclusion is invalidated by the observed independence of height and magnitude, as seen in figure 2.

If we assume that recombination is the only significant effect omitted from past determinations of ionizing probability, it appears that equation (18) must represent a lower bound. However, equation (18) might not be a poor approximation if there were a self-selection effect whereby recombining meteors tended to give radar echoes below equipment-sensitivity limits and thus tended to be omitted from statistics of simultaneous observations. In view of the other uncertainties dependent on magnitude (initial electron radius, fragment spread, early history of the column), we can conclude very little from the data analyzed so far.

Simultaneous radar and image-orthicon observations are the only resource now available to us for determining ionizing probability in our magnitude range and for finding masses for our radar meteors.

CONCLUSIONS

We have observed recombination in the ionized columns generated by faint radar meteors (radar magnitudes 6 to 9) as: (1) a rapid loss of returned signal in the first few milliseconds after formation of the column, before the slower decay caused by diffusion; (2) an apparent absence of bright, low meteors; and (3) anomalies in apparent diffusion rates. Recombination at rates characteristic of dissociative recombination of ionized atmospheric molecules N_2^+ and O_2^+ is completely consistent with the observations. Since no other likely constituent of the atmosphere or of the meteoroid has a fast enough recombination rate, it appears either that the molecules are ionized in the initial formation of the ionized column or that there is rapid charge exchange.

Recombination is a sufficient cause for the differences between Greenhow and Hall's (1960) diffusion measures and other atmospheric studies.

Manning's (1958) estimate of the initial radius of meteor columns is much more nearly correct than Öpik's (1955) for radar magnitudes 6 to 11.

Bright, low, slow meteors have been missed in radar observations, so that existing statistics are significantly biased. All past determinations of the ionizing probability based on bright meteor observations are invalid.

ACKNOWLEDGMENTS

This work was supported in part by contract NSR 09–015–033 from the National Aeronautics and Space Administration.

REFERENCES

DAVIS, J., GREENHOW, J. S., AND HALL, J. E., 1959. The effect of attachment on radio echo observations of meteors, *Proc. Roy. Soc. London, A*, **253**, 130–139.

DAVIS, J., AND HALL, J. E., 1963. Meteor luminosity and ionization, *Proc. Roy. Soc. London, A*, **271**, 120–128.

EVANS, G. C., AND HALL, J. E., 1955. Meteor ionizing and luminous efficiencies, in *Meteors*, edited by T. R. Kaiser, Pergamon Press, New York, 18–22.

GREENHOW, J. S., AND HALL, J. E., 1960. Diurnal variations of density and scale height in the upper atmosphere, *J. Atmos. Terr. Phys.*, **18**, 203–214.

GREENHOW, J. S., AND NEUFELD, E. L., 1955. The diffusion of ionized meteor trails in the upper atmosphere, *J. Atmos. Terr. Phys.*, **6**, 133–140.

KAISER, T. R., 1955. The interpretation of radio echoes from meteor trails, in *Meteors*, edited by T. R. Kaiser, Pergamon Press, New York, 55–64.

MANNING, L. A., 1958. The initial radius of meteoritic ionization trails, *J. Geophys. Res.*, **63**, 181–196.

MCKINLEY, D. W. R., 1961. *Meteor science and engineering*, McGraw-Hill Book Co., New York, 309 pp.

MEHR, T. J., AND BIONDI, M. A., 1969. Electron temperature dependence of recombination of O_2^+ and N_2^+ ions with electrons, *Phys. Rev.*, **181**, 264–271.

MILLMAN, P. M., AND MCKINLEY, D. W. R., 1956. Meteor echo durations and visual magnitudes, *Can. J. Phys.*, **34**, 50–61.

ÖPIK, E. J., 1955. Meteors and the upper atmosphere, *Irish Astron. J.*, **3**, 165–181.

ÖPIK, E. J., 1958. *Physics of meteor flight in the atmosphere*, Interscience Publishers, New York, 174 pp.

SOUTHWORTH, R. B., 1962. Theoretical Fresnel patterns of radio meteors, *Harvard-Smithson. Radio Meteor Proj. Res. Rept.* No. 14, 60 pp.

——, 1967. Space density of radio meteors, in *The Zodiacal Light and the Interplanetary Medium*, edited by J. L. Weinberg, *NASA* SP–**150**, Supt. of Documents, U.S. Govt. Printing Office, Washington, 179–188; also in *Smithson. Astrophys. Obs. Spec. Rept.* No. 239, 75–98.

VERNIANI, FRANCO, AND HAWKINS, G. S., 1964. On the ionizing efficiency of meteors, *Astrophys. J.*, **140**, 1590–1600.

Page intentionally left blank

4. Combined Observations of Meteors by Image-Orthicon Television Camera and Multi-Station Radar

A. F. Cook, G. Forti, R. E. McCrosky,
A. Posen, R. B. Southworth, and J. T. Williams
Smithsonian Astrophysical Observatory
Cambridge, Massachusetts

Observations from multiple sites of a radar network and by television of 29 individual meteors from February 1969 through June 1970 are reported. The primary purpose of the program was to compare ionization with luminosity. Only 12 of the meteors did not appear to fragment over all the observed portion of their trajectories. From these 12, the following relation for the radar magnitude M_R to the panchromatic absolute magnitude M_p, in terms of velocity of the meteor V, was found:

$$M_R - M_p = +2.85 - 3.8(\log V - 6.41)$$

$$\pm 0.16 \pm 1.3$$

The double-signed quantities are standard deviations. The standard deviation for a single meteor is ± 0.5. This result applies for meteors fainter than panchromatic absolute magnitude +4.7 and in the velocity range 14.7 to 36.0 km s^{-1}.

A very tentative fit to the data on the duration of long-enduring echoes versus visual absolute magnitude is made. The assumption that brighter meteors produce a higher ratio of ionization to light is required.

The exponential decay characteristic of the later parts of several of the light curves is pointed out as possible evidence of mutual coalescence of droplets into which the meteoroid has completely broken.

RADAR EQUIPMENT, OBSERVATIONS, AND REDUCTIONS

Radar

An eight-station multistatic phase-coherent pulsed Doppler radar system located in the area between Peoria and Springfield, Illinois, was used to observe meteors. The system had the following composition:

(a) A main site for the transmitter and a dual-channel receiver

(b) Five outlying sites arranged about the main site within 24 km, each equipped with a single-channel receiver

(c) Two remote sites about 34 and 47 km from the main site, each also equipped with a single-channel receiver

The system was able to collect phase-coherent meteor echoes from a volume in the upper atmosphere that is not sharply bounded but measures roughly 50 km × 50 km horizontally and 20 km vertically over the range 80 to 100 km above mean sea level. The volume under radar patrol lies approximately above Decatur, Illinois.

When a meteor passed through this volume, echoes were received at the main site if the trail was tangent to a sphere centered at the main site. This sphere had a radius equal to the minimum range of the meteor from the main site; i.e., the meteor was observed via back scattering from the electrons of its trail. An echo was received at any

particular remote site if the trail was tangent to an ellipsoid with foci at the remote site (receiver) and the main site (transmitter).

At the main site, a nominal 4-MW peak power VHF transmitter was operated; the transmitter rarely ran at over 2 MW. The frequency employed was 40.92 MHz. The dual-channel receiver provided range, angle of arrival relative to a vertical reference plane, a Fresnel pattern, and radial velocity (Doppler information) on the back-scattered echoes received from a trail.

At each of the outlying and remote sites, a single-channel receiver provided range, a Fresnel pattern, and Doppler shift for forward-scattered echoes received from the trail.

The measurements were conveyed by microwave links to the main site, processed in a digitizer, and recorded by a multichannel digital tape recorder. All the data on the digitized tape were later processed at the Smithsonian Astrophysical Observatory's CDC 6400 computer in Cambridge, Massachusetts.

The computer program reads the tape (34 channels of information), processes the data to obtain positional information on the meteor trail and on its motion due to winds, and prints out the results.

Geographic Layout

Four of the five outlying stations are located approximately along a line with the main site bearing about 125° east of north in the order 1, 2, 3, 5, and 6, where site 3 is the main site. Site 4 is offset approximately perpendicularly from this line. The approximate spacing between sites is 12 km. Finally, the two remote sites, 7 and 8, are offset almost perpendicularly to the line 1, 2, 3, 5, and 6 at a distance of about 35 km so that stations 7, 6, and 8 also lie nearly in a straight line.

Rectangular coordinates x, y, and z are given in table 1 on axes east, north, and vertical from the main site, respectively; i.e., the system is an alt-azimuth system referred to the horizon and true north of the main site.

Simplified System Description

Figure 1 is a simplified block diagram of the radar, exhibiting station 3 near Havana, Illinois, and any one of the other stations. At sites 1 to 6,

TABLE 1.—*Rectangular Coordinates of Radar Receiving Stations and Ranges from the Transmitter at Havana*[a]

Site number	x (km)	y (km)	z (km)	R_{G3n} (km)
1	−19.89	+11.83	−0.01	23.14
2	−9.66	+8.15	+0.02	12.64
3	0.00	0.00	0.00	0.00
4	+5.04	+10.26	−0.01	11.43
5	+9.65	−6.31	+0.03	11.53
6	+22.10	−7.02	+0.01	23.19
7	+41.85	+22.03	−0.12	47.29
8	+0.67	−34.41	−0.06	34.42

[a] The x axis is toward the east point, the y axis toward the north point, and the z axis toward the zenith as seen from the transmitter, and the origin is at the transmitter.

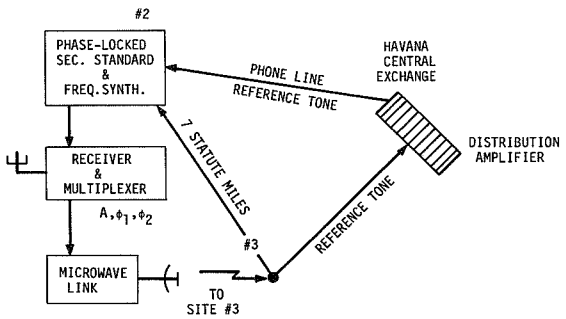

FIGURE 1.—General system layout.

trough antennas were directed toward azimuth 113° east of north. At sites 7 and 8, Yagi antennas were directed toward azimuths 139° and 94° east of north, respectively. The transmitter at site 3 (the main site) had a nominal peak power of 4 MW, which was never attained (2 MW being the usual power), and transmitted at 40.92 MHz (7.33 m). Both of the two troughs used for reception were also used for transmission.

The system at the main site produced the transmitted frequency, the mixer and reference frequencies for the receiver at the main site, and the 2.5-kHz reference frequency, sent by telephone line, for the outlying sites (1, 2, 4, 5, 6) and the remote sites (7, 8).

The transmitted pulse radiated from the transmission antenna at the main site was reflected by meteors (and aircraft), and these reflections were received at any or all of the sites. The echoes

received at the outlying and remote sites were transmitted back to the main site via microwave links.

At the main site, all the echoes were analyzed by echo-pattern recognizers. When an echo was accepted for recording, that echo was gated through gating circuits to the digitizer and a cathode-ray-tube film recorder. The main unit supplied the pulse-repetition frequency to the transmitter and range information and control to both the digitizers and the cathode-ray-tube film recorder.

Calibration of the receivers was carried out as follows: The antenna was disconnected from the receiver, and simulated echoes of known amplitude were sent to the receivers from the calibrator. Control signals for the calibrator were received from the main station via the microwave link in the form of switching tones and the pulse-repetition frequency. The tones were decoded by a tone receiver, which controlled the calibrator.

The receiver produced three outputs: The amplitude A pulse was proportional to the logarithm of the amplitude A_1 of the echo. It was sent to the main station via the microwave link on a 2.3-MHz subcarrier. Phase 1 (ϕ_1) and phase 2 (ϕ_2) pulses were proportional to $A_1 \cos \phi$ and $A_1 \sin \phi$, where ϕ is the phase of the echo relative to the transmitted phase. They were multiplexed in time and sent to the master station via the microwave link.

The receiver at the main site produced the same three outputs (A, ϕ_1, ϕ_2), as well as ϕ_3 and ϕ_4, the phase signals from the second trough of the double trough.

Reduction of Radar Data

Location of the Meteor and Measurement of Wind

Multiple Receiver System.—The epoch of the radar echo from the main site locates the meteor on a sphere about the main site of the observed range. The epoch of the echo from an outlying or remote site locates the meteor on an ellipsoid, with foci at the main site and the outlying or remote site, having the loop range (from the main site to the meteor, then to the remote site, and finally back to the main site) observed. The Fresnel patterns combined with the ranges yield the velocity of the meteor. In favorable cases, the deceleration can be determined. If three stations have received echoes from a meteor and if the stations do not lie on a straight line, the intervals between the epochs of passage through the minimum loop range as determined from the Fresnel pattern determine the radiant of the meteor (a double solution occurs but with one direction below the horizon). From the radiant and range, it is, in principle, possible to locate the meteor on a circle or an ellipse on the appropriate sphere or ellipsoid at each epoch. Projection of these on a plane perpendicular to the radiant would then locate the trail. The projected circles and ellipses do not intersect at large enough angles for this procedure to work in practice.

Extra information is required and was obtained by using an interferometric arrangement at the main site and measuring the angle of arrival of the echo from a vertical plane. A cone is thus determined for each echo at the main site. Its intersection with the plane of the circle that is normal to the radiant and has a radius equal to the range will be two straight lines, one above and one below the horizon; we can reject the latter. This intersection at a right angle between the circle and the line locates the trail to an accuracy set primarily by the accuracy of measurement of the angle of arrival. In practice, the phase difference measured in the interferometer is uncertain by a whole number of waves, so that up to three solutions are possible. The solution that lies in the antenna beam and at a reasonable height above sea level is the one chosen.

Scattering Properties of the Meteoric Trail.—We assume that all the trails were underdense, i.e., that the radio wave was scattered by individual free electrons each of which oscillated as if no others were present. The minimum range point is the so-called specular reflection point.

This situation has been treated by many authors, but we shall rely here on McKinley (1961). Of the whole trail, the effective length that contributes to the scattering is $\sqrt{2R_0\lambda} \simeq 1.5$ km in the back-scattering case (R_0 is the minimum range; λ, the wavelength). In the forward-scattering cases for the outlying and remote receivers, the lengths may be slightly different. Different stations received scattered signals from different parts of the trail.

Winds in the upper atmosphere displaced the specular reflection points, and physical processes altered the amplitude of the received echoes. Both these effects are small enough to be neglected in the initial approximation and are included later when the data are good enough to allow their measurement. Account was taken of diffusion and recombination.

Position of the Meteoric Trail.—The five outlying stations and the main site were located so as to permit approximate determinations of radiants and very rough determinations of meteor positions. If either of the two remote sites is involved in an observation along with any two of the main and outlying sites, then a rather good radiant and a fair determination of position can be expected. In all cases, an optical observation by the image-orthicon camera from Sidell, Illinois, greatly strengthens the determination. The present discussion is confined to the radar observations alone. Determination of trajectories, including optical observations, will be discussed further below. A least-squares fit is made if the meteor was observed at four or more receiving stations that do not all lie along a straight line.

Wind Measurements.—The received echo at each station conveys information concerning mainly the principal Fresnel zone, some 1.5 km in length. In general, each station observed a different portion of the trail. The spacing for the main site and the five outlying stations is typically up to 3.5 km in distance along the trail and up to 2.5 km in height. Larger spacings may occur for the two remote sites.

Measurements of phase at each station furnish a pseudoradial component of the wind velocity averaged over the first Fresnel zone. This measured component is directed along the bisector of the directions of the center of the principal Fresnel zone as seen from the main site and an outlying or remote site. This wind component is assumed to be horizontal, so that the pseudoradial horizontal wind needed to produce the observed pseudoradial wind is computed. It lies along the horizontal projection of the pseudoradial direction of measurement. The first derivative of the pseudoradial wind component with respect to distance along the trail is also found from the phase information and is transformed into a derivative with respect to height of the pseudoradial horizontal wind.

If the meteor was observed at a remote site during the interval covered by observations from the main site and the outlying sites, a mean direction and fit for the pseudoradial horizontal wind can be found for the main site and outlying sites and interpolated to the epoch of the observation from the remote site. Combination with the pseudoradial horizontal wind from the remote site allows a determination of the horizontal wind at that point in the atmosphere.

Finally, the pseudoradial horizontal wind and its derivative with height are used to correct the determination of the meteor's radiant and position.

Phase-Coherent System

Figure 1 exhibits a block diagram of the main site near Havana, and one of the outlying or remote sites. The transmitter at the main site had a nominal power of 4 MW, which was never attained, and transmitted at 40.92 MHz (7.33 m).

The establishment of reference phase for the received signals imposed the following design requirements: The relative phase jitter between the transmitter and the local oscillators of the various superheterodyne receivers must not be larger than 10 percent of the minimum detectable Doppler shift. At a signal-to-noise ratio of 20 db and for a meteor duration of 0.05 s, the minimum detectable Doppler shift for the radiated waveform is 0.25 Hz (Grossi, 1963). Consequently, a relative stability of 5 parts in 10^{10} was needed.

This requirement was met by the following system: A single master oscillator at 1 MHz operated at the main site, from which, by frequency synthesis, the frequencies required for the transmitter and the local oscillators of the dual-channel receivers were obtained. Division down of the 1-MHz frequency to 2.5 kHz (400:1) yielded a reference signal for distribution by telephone line to the other seven sites. The telephone lines were not free from phase jitter. Accordingly, the phase of the reference tone arriving by telephone line at each station was compared to a local secondary standard (VCO). The output of this phase comparator was passed through an integrator with a 10-min time constant, thereby locking the phase of the local secondary standard to the 10-min average of the incoming reference tone.

This procedure effectively suppressed the phase jitter in the telephone lines.

Range measurements for the waveform employed at a signal-to-noise ratio of 20 db, a pulse width of 6 μsec, a pulse-repetition period of 1355 μsec, and target detectability lasting 0.05 s are, in principle, possible to a standard deviation of ± 10 m. The actual tolerable range error was taken to be ± 100 m for purposes of design. Actual performance on these meteors has been closer to a standard deviation of ± 1 km. These numbers apply to the half loop range and are to be doubled for total loop range.

Mathematical Outline of Radar Reductions

Wind-Phase Information

If a meteor perchance leaves a trail of electrons that is not underdense but resonant, the corresponding phase shift varies with time in a way not possible for winds; such cases can thus be eliminated at once.

We shall begin by considering the case of back scatter. We let the x axis lie along the trajectory of the meteor, the origin lie at the minimum range point, and the radar station lie on the negative y axis. The distance D from any point (x, y) to the radar station is

$$D=[(R+y)^2+x^2]^{1/2}=(R^2+2Ry+x^2+y^2)^{1/2}$$

and expansion by the binomial theorem followed by linearization in x^2 and y yields

$$D\cong R+y+\frac{x^2}{2R} \tag{1}$$

The phase ϕ is taken with respect to an element at the origin (which differs only by a constant from that of the transmitted wave):

$$\phi=\frac{4\pi(D-R)}{\lambda}\cong\frac{2\pi x^2}{\lambda R}+\frac{4\pi y}{\lambda} \tag{2}$$

Only the y component of the wind need be considered, and we expand this component in a Maclaurin series about the origin, retaining only the first two terms:

$$\dot{y}\cong -ax_w+ax$$

i.e., we have defined the radial component of the wind in such a way that we can write

$$\dot{y}\cong a(x-x_w) \tag{3}$$

where x_w is now that point in x at which the radial component of the wind would vanish if we consider only the first two terms in the Maclaurin series.

We denote time by t and the epoch at which the meteor passes the origin by t_0. Then the coordinates of the meteor, x_m, y_m, are

$$x_m=V(t-t_0) \qquad y_m=0 \tag{4}$$

The coordinate of any element of the ionized trail can then be found from its radial speed and the interval τ since it was generated by the meteoroid:

$$y=\dot{y}\tau=a(x-x_w)\left(t-t_0-\frac{x}{V}\right) \tag{5}$$

$$y=-\left(\frac{a}{V}\right)\{x^2-[x_w+V(t-t_0)]x+x_wV(t-t_0)\}$$

The phase of the echo from an element at x is found by substitution of equation (5) into equation (2):

$$\phi=\left(\frac{2\pi}{\lambda R}\right)\left(1-\frac{2aR}{V}\right)\left\{x+\frac{aR[t-t_0+(x_w/V)]}{1-(2aR/V)}\right\}^2$$
$$-2\pi\left(\frac{a^2R}{\lambda}\right)\left(\left\{\frac{[t-t_0+(x_w/V)]^2}{1-(2aR/V)}\right\}+2x_w\frac{t-t_0}{aR}\right) \tag{6}$$

We introduce a dimensionless parameter α for the wind shear:

$$\alpha\equiv\frac{aR}{V} \tag{7}$$

so that we rewrite equation (6) as

$$\phi=\left(\frac{2\pi}{\lambda R}\right)(1-2\alpha)\left\{x+\frac{\alpha[x_w+V(t-t_0)]}{1-2\alpha}\right\}^2$$
$$-\left(\frac{2\pi}{\lambda R}\right)\alpha\left(\left\{\frac{\alpha[x_w+V(t-t_0)]^2}{1-2\alpha}\right\}+2x_wV(t-t_0)\right) \tag{8}$$

The second term on the right-hand side of equation (8) is independent of x and, therefore, applies to the phase of the integrated echo. We denote this term, the phase variation due to the

wind, by the symbol Φ,

$$\Phi \equiv -\left(\frac{2\pi}{\lambda R}\right)\alpha\left(\left\{\frac{\alpha[x_w+V(t-t_0)]^2}{1-2\alpha}\right\} + 2x_w V(t-t_0)\right) \quad (9)$$

The first term on the right-hand side of equation (8) is best examined by comparison with the phase ϕ' at vanishing wind shear:

$$\phi' \equiv \left(\frac{2\pi}{\lambda R}\right)x'^2 \quad (10)$$

We see that

$$x' \equiv (1-2\alpha)^{1/2}\left\{x+\frac{\alpha[x_w+V(t-t_0)]}{1-2\alpha}\right\} \quad (11)$$

Thus, the amplitude of the Fresnel pattern (see the derivation given by McKinley, 1961, pp. 186–198) appears as for a meteor of velocity V' that passes through minimum range at an epoch t'_0, where

$$V' = V(1-\alpha)(1-2\alpha)^{-1/2} \quad (12)$$

$$t'_0 - t_0 = -\alpha x_w (1-\alpha)^{-1} V^{-1} \quad (13)$$

The Fresnel patterns yield V' and t'_0, which we now wish to employ, by means of equation (9), in interpreting the phase variation due to the wind. Accordingly, we solve equations (12) and (13) for V and $t_0 - t'_0$ and substitute into equation (9) to find

$$\Phi - \Phi_0 = -\frac{2\pi}{\lambda R}\left(\frac{\alpha}{1-\alpha}\right)^2[V'(t-t'_0)]^2 - \frac{4\pi}{\lambda R}\left[1-\left(\frac{\alpha}{1-\alpha}\right)^2\right]\frac{\alpha x_w}{(1-2\alpha)^{1/2}}V'(t-t'_0) \quad (14)$$

where Φ_0 is the phase variation due to the winds at epoch t'_0, the apparent epoch of minimum range. Equation (14) is then the expression for the change in phase since that epoch due to the winds. Evidently we can evaluate $[\alpha/(1-\alpha)]^2$ and $\alpha x_w/(1-2\alpha)^{1/2}$. From equations (12) and (13) it is apparent that we have

$$V = V'\left[1-\left(\frac{\alpha}{1-\alpha}\right)^2\right]^{1/2} \quad (15)$$

$$t_0 - t'_0 = \frac{\alpha x_w}{(1-2\alpha)^{1/2}}\frac{1}{V'} \quad (16)$$

From equation (12) or (15) we see that $\alpha \ll \frac{1}{2}$ is required. Not only does accuracy become lost as α approaches $\frac{1}{2}$, but at $\alpha = \frac{1}{2}$ the curvature of the trail equals that of the wavefront and we receive an echo simultaneously from all along its length. Near this condition we would receive an anomalously strong echo. In fact, from equation (15) it is apparent that the received amplitude should be rescaled by a factor

$$\left[1-\left(\frac{\alpha}{1-\alpha}\right)^2\right]^{1/2}$$

to allow for the altered lengths of the Fresnel zones. For α locally greater than $\frac{1}{2}$ and varying in the usual roughly sinusoidal way with height, we would receive multiple echoes and the meteor would not have been accepted for reduction.

The actual point of tangency between the radar wavefronts and the ionized column plainly lies at $x' = 0$, so from equation (11) we have

$$x_0 = -\frac{\alpha}{1-2\alpha}[x_w+V(t-t_0)] \quad (17)$$

$$y_0 = -\frac{1}{2R}\frac{\alpha^2}{1-2\alpha}[x_w+V(t-t_0)]^2 - \frac{\alpha x_w}{R}V(t-t_0) \quad (18)$$

where we have obtained y_0 by multiplying equation (9) by $\lambda/4\pi$. Elimination of time yields the parabola

$$y_0 = -\frac{1}{2}(1-2\alpha)\frac{x_0^2}{R} + (1-2\alpha)\frac{x_w}{R}x_0 + \alpha\frac{x_w^2}{R} \quad (19)$$

which is concave toward the station. It is evident that α must be quite small or our reflection would migrate to quite a different part of the trail from the minimum range point corresponding to the absence of wind.

Observations of the wind phase yield the quantities G and H', defined as

$$G \equiv \left|\frac{\alpha}{1-\alpha}\right| \quad (20)$$

$$H' \equiv \left[1-\left(\frac{\alpha}{1-\alpha}\right)^2\right]\frac{\alpha x_w}{(1-2\alpha)^{1/2}} \quad (21)$$

There are two roots for α, from equation (20):

$$\alpha = \frac{G}{1+G} \quad -\frac{G}{1-G} \quad (22)$$

and two corresponding roots for x_w, from equation (21):

$$H \equiv \frac{H'}{(1-G^2)^{1/2}} \qquad x_w = \pm \frac{H}{G} \tag{23}$$

We recall the definition (7) to find, for the wind shear,

$$a = \frac{V}{R}\frac{G}{1+G} \qquad -\frac{V}{R}\frac{G}{1-G} \tag{24}$$

The two expressions from equation (3) for the wind are

$$\dot{y} = \frac{V}{R}\frac{G}{1+G}\left(x - \frac{H}{G}\right) \qquad -\frac{V}{R}\frac{G}{1-G}\left(x + \frac{H}{G}\right) \tag{25}$$

which are equal at

$$x = -H \qquad \dot{y} = -\frac{V}{R}H \tag{26}$$

the point at which the meteor passed through minimum range on the trail distorted by the wind field. This measured radial component of the wind and the two alternative values for the shear (eq. (24)) of this component along the trail comprise all the information that we can obtain from phase measurement from one station. The corrected velocity becomes

$$V = V'(1-G^2)^{1/2} \tag{27}$$

and the corrected epoch of passing minimum range becomes

$$t_0 - t'_0 = (1-G^2)^{1/2}\frac{H}{V'} \tag{28}$$

both independent of the selected root for a in equation (24).

The case in which the transmitter and the receiver are at different sites is very similar to the foregoing. The essential difference is that the wind component observed lies along the direction bisecting the angle between the directions of the meteor from the two stations at the epoch of minimum loop range. Another difference is that the effective range is the harmonic mean of the ranges of the meteor from each station, and the wind velocity $\dot{y}$ by equation (25) and shear a by equation (24) are to be increased by a factor sec $(\psi/2)$, where ψ is the angle between the directions of the meteor from the two stations.

Geometrical Reduction

The geometrical reduction starts with the corrected epoch of minimum range t_0 and the corrected velocity V from each station. There remains the problem of locating for each echo an "effective station" on the bisector of the directions of the transmitter and receiver from the meteor and at the harmonic mean of the two ranges. The uncorrected epoch of minimum range and the uncorrected velocity are deduced from the epochs of the maxima and minima (extrema) of the Fresnel pattern. For a meteor of constant radar magnitude without diffusion, the relation between the epoch of minimum range and those of the extrema is derived in McKinley (1961, pp. 186–225). Southworth (unpublished) finds from numerical integrations that both the diffusion and the slope of the ionization curve have an effect in the sense that the distance x_1 from the minimum range point to the first Fresnel maximum is given by

$$x_1 = \frac{1}{2}\left[0.861 - 1.535C + 2.75C^2 - 3.0C^3 + \left(\frac{\sqrt{2}}{2}\right)CS\right]F \tag{29}$$

where F is defined as the length of the first Fresnel zone:

$$F \equiv \left(\frac{R\lambda}{1-2\alpha}\right)^{1/2} \tag{30}$$

S denotes the slope of the ionization curve in magnitudes per length F, and C is defined as

$$C \equiv \frac{8\pi D}{\lambda^2 V}\left(\frac{\lambda R}{2}\right)^{1/2}(1-2\alpha)^{-1/2} \tag{31}$$

or in terms of the time to cross the first Fresnel zone T_F,

$$T_F \equiv \left(\frac{R\lambda}{1-2\alpha}\right)^{1/2} V^{-1} \tag{32}$$

and the decay time T_D for a drop in voltage amplitude of the signal by a factor e,

$$T_D = \frac{\lambda^2}{16\pi^2 D} \tag{33}$$

we have

$$C = \frac{\sqrt{2}}{4\pi}\frac{T_F}{T_D} \tag{34}$$

Southworth has found that the amplitudes of the Fresnel patterns can be analyzed by smoothing out the oscillations after the first maximum and treating the smoothed curve as representing the decay of the amplitude from the principal Fresnel zone. The later oscillations then yield the amplitude of each successive Fresnel zone as it is formed. Such an analysis yields C, S, and the radar magnitude at the specular reflection point and the extrema. It also yields the distance x_1 along the trail to the first Fresnel maximum and thus the epoch of passage t_0 through minimum range. This epoch and the corrected velocity V for each radar site comprise the information for finding the radiant of the meteor. For its geometric position in the atmosphere, we require the difference in phase between the two troughs at the main site in order to place the meteor on a small circle in the sky at the epoch of minimum range.

The distance traveled between specular reflection points from one radar receiver to another is the integral of the velocity over the interval of time between the reflections. The ratio of this distance to that between the effective stations is the scalar product of the unit vector in the direction of the first site as seen from the second and the unit vector toward the radiant. The locus on the celestial sphere of all radiants satisfying this observation is a small circle about the direction of the first site as seen from the second. A second pair of sites, not nearly in the same relative direction, gives a second small circle. One of the two intersections of the circles is usually below the horizon (unless they are nearly tangent, i.e., unless the radiant is very near the horizon, a poorly determined or indeterminate case), so it can be eliminated forthwith. The remaining intersection is our desired radiant.

The specular reflection point of the meteor as seen from the main site must lie on the great circle with the radiant as its pole. Also, the difference in phase between the signals received at the two troughs yields a small circle. Again, the intersection below the horizon is eliminated. There is often an ambiguity of a few whole waves in the phase difference. Each possibility yields a different direction for the specular reflection point. These can be combined with the observed range to find heights above mean sea level. Usually, only one value is plausible and the meteor is thus unambiguously located. If two values of height are both plausible, the meteor is rejected from further analysis.

The loop range for each receiving station is defined as the distance from the transmitter at station 3 to the meteor, plus the distance back to the receiver, plus the distance via microwave link back to station 3. This last quantity is zero at station 3, for which the loop range is merely twice the distance to the meteor. A pattern-recognition program was operated to measure the time and amplitude of each extremum of the Fresnel patterns. The spacings in the patterns are required to match from station to station. The oscillations from a smoothed curve are also found for each pattern. Next, the wind phase Φ is measured at each station at which an amplitude pattern was measured. The recorded phases from the phase detectors are in the analog form

$$s \equiv A_1 \sin \Phi \tag{35}$$

for odd pulses and

$$c \equiv A_1 \cos \Phi \tag{36}$$

for even pulses, where A_1 denotes amplitude, and Φ, the phase. Missing alternate values are interpolated.

Initially, the phases are found at the Fresnel maxima, multiples of 2π being added to preserve continuity where needed. They are then fitted by the polynomial

$$\Phi = E_0 + E_1 p + E_2 p^2 \tag{37}$$

where p is the pulse number. Next, the phase at each observed pulse after the first maximum is corrected (subscript c) for the oscillating part of the Fresnel pattern by subtraction of a rotating vector:

$$s_c = s - C_F \sin (\phi_F + E_0 + E_1 p + E_2 p^2)$$

$$c_c = c - C_F \cos (\phi_F + E_0 + E_1 p + E_2 p^2)$$

$$\tan \phi_c = \frac{s_c}{c_c} \tag{38}$$

Here, C_F is the amplitude of the oscillating part interpolated between extrema, and ϕ_F is the phase of the oscillating part, defined as 0 at the first extremum, π at the second, 2π at the third, etc., also interpolated. The corrected phases are fitted again with equation (37) and the process is

repeated. If E_2 is poorly determined or significantly positive, it is set arbitrarily equal to zero and a linear expression involving E_0 and E_1 alone is used instead.

The amplitude of the Fresnel pattern is next analyzed at each station with the measured range as part of the input.

The effective station positions are initially estimated at the midpoints of the straight-line segments joining them to station 3. Velocities and times are corrected by equations (27) and (28). They are then fitted to an expression of the form

$$V = B + C\bar{K} \exp(\bar{K}t) \tag{39}$$

$$\bar{K} = \frac{5}{4} \frac{\bar{V}}{H^*} \cos Z_R \tag{40}$$

where $H^* = 5.3$ km is an effective scale height, the factor $\frac{5}{4}$ is derived from experience with faint photographic meteors (it should be unity for classical nonfragmenting meteors), and the expression (39) is that found very convenient by Whipple and Jacchia (1957) for photographed meteors. Distances between specular reflection points are found by integration of equation (39), and the radiant is fitted to these and the effective stations. The specular reflection point from station 3 is found from the difference in phase at the two troughs with slight adjustment in the range from station 3 to give the best fit to all the loop ranges.

The next iteration and all successive ones begin by placing the effective stations on the bisector of the directions from the meteor to the transmitter and the receiver at a distance equal to the harmonic mean of the distances to the transmitter and the receiver. Also, the wind velocity $\dot{y}$ by equation (25) and the shear a by equation (24) are increased by the factor sec $(\psi/2)$, where ψ is the angle subtended by the transmitter and receiver from the specular reflection point. Iterations continue to convergence or failure.

TELEVISION EQUIPMENT AND REDUCTION OF COMBINED OPTICAL AND RADAR DATA

Image-Orthicon Television System

We have employed an image-orthicon television system loaned by the Naval Research Laboratory (NRL). It is a U.S. Navy shipboard system, AN/SXQ–3, originally modified by G. T. Hicks and G. G. Barton of NRL to accept a lens of 105-mm focal length and 125-mm aperture. The image-orthicon tube is a General Electric 7967. The camera is fitted to a motor-driven alt-azimuth mounting. In addition, there are a control console, two helical-scan Ampex VR–7500 video tape recorders, a monitoring kinescope, and a remote 14-inch kinescope suitable for photographic recording.

The normal video format of the SXQ is 30 interlaced 875-line frames per second with separate vertical and horizontal drive signals. To facilitate magnetic tape recording of the video for our purposes, vertical and horizontal sync pulses were generated from the drive signals. We added these pulses to the video through a separate distribution amplifier. This modification made practical the use of an inexpensive helical-scan video tape recorder (Ampex VR–7500) for routine recording of observations. The recorders were slightly modified to improve the playback quality of the 875-line video by increasing the tape speed by 4 percent. Figure 2 displays a schematic arrangement of the equipment.

In order to preserve a nearly constant sensitivity independent of sky conditions, much of the automatic gain-control (AGC) circuitry was eliminated or bypassed. These modifications permitted a less frequent calibration of the sensitivity of the system.

We also modified the camera beam-current control to expand the adjustment in the very low light-level region. This enabled the image erasing beam to be carefully adjusted to erase the image-orthicon target charge slightly more slowly than the rate of deposit for images within the useful dynamic range. The resulting "image lag" not only was tolerated but in fact became a useful part of the scheme for the photometry of slower moving images.

Observing Techniques

Radar meteors are observed when the meteor is at a minimum range, i.e., when the meteor is 90° from the radiant and moving with maximum angular velocity. Optical detection systems are most sensitive for meteors near the radiant when the writing speed at the focal plane is at minimum. An optical observing site was established

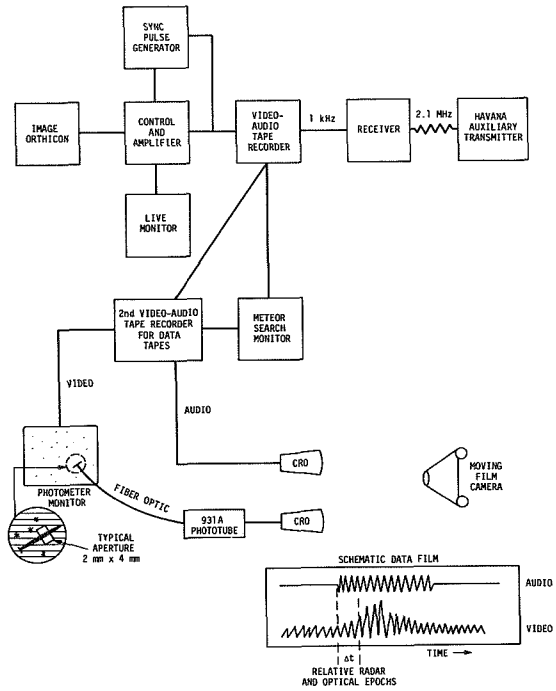

FIGURE 2.—Image-orthicon observing and data-reduction system.

near Sidell, Illinois (Long. 87°51.2′W, Lat. 39°56.6′N; $x = +185.38$ km, $y = -28.45$ km, $z = -2.67$ km). From this site, an optical system directed at elevation 49° and azimuth 263° has a maximum probability of observing objects in the meteor region at about 90-km altitude that are also observable by the Havana radar.

When operated at full sensitivity, the radar observes meteors at about 100 times the image-orthicon rate. This mismatch has two deleterious consequences. First, the problem of selecting those meteors that are true simultaneous radar and optical observations is difficult since, almost assuredly, *some* radar object will be under observation whenever the image orthicon records a meteor. Second, since the radar logic constrains the system to observing one meteor at a time, the radar data-recording system is quite likely to have been pre-empted by a faint, uninteresting meteor that occurred shortly before the brighter object was observed optically. Consequently, the radar receivers were attenuated at their input by 13 to 25 db when simultaneous observations were being attempted. To further ease the arduous task of selecting possible simultaneous observations, the audio channel of the video tape recorded a 1000-Hz signal transmitted by an auxiliary transmitter at Havana whenever the radar data system began a record of a new meteor.

Observations were generally made during moonless skies and between 11 p.m. CST and morning twilight. Observing was usually curtailed when atmospheric extinction was variable or exceeded about 1 mag. Well-regulated line power and a 1-hour warmup ensured stability. The output was observed visually on a live monitor and recorded on tape. About 75 percent of the meteors were discovered on the live monitor, and the remaining during subsequent playbacks of the tape. Possible simultaneous observations and calibration tests were copied repeatedly on data tape for future use.

Calibration

A two-step calibration procedure was followed. A pinhole light source was set up in the loft of a nearby barn. Direct current for the source was supplied from and monitored at the image-orthicon site. The source could be attenuated remotely from the site by sequential advancement of a neutral-density step wedge located between the source and the pinhole. A total of 10 steps of 0.5-mag attenuation per step were available. These calibration observations were made with the camera slewing in altitude. Slew rates of 1° to 15° per second were used. These rates bracket the angular rates of most meteors observed simultaneously, and the fundamental calibration was thus performed on a moving source comparable to a meteor.

The second calibration step was used to define an absolute scale, in terms of stellar magnitude, for the relative response determined for the artificial light source. Stars of known brightness were recorded while the image orthicon was slewed. In general, unreddened A0 stars in or near the observing field were chosen, but on some occasions stars of spectral class as early as B8 or as late as A3 (and rarely as late as A5) were used.

In summary, the first calibration step determined what in photography is called the characteristic curve, and the second supplied the zero point for this curve in terms usually employed to define meteor luminosity. This last procedure simultaneously accounted for changes in the

image-orthicon system sensitivity and for variations in sky conditions.

Photometric Reductions

Photometry of meteors observed by photographic techniques presents problems not often encountered in astronomy or, indeed, in most areas of any science. The obvious (but seldom noted) fact that we can observe our objects only once immediately places stringent signal-to-noise restrictions on the data. The unexpected nature of the meteor event may introduce problems of dynamic range. Both problems are more serious in television techniques: System noise is much higher than for photographic emulsions, and the dynamic range is lower.

We considered two general techniques for our photometry. The first was to photograph the image-orthicon outputs—both meteor and calibration—and proceed in the manner familiar to us from our photographic work. There, we compare by eye the meteor and standard source images. We rejected this approach, however, because kinescope techniques are incapable of recording the fainter images.

The second approach was to deal directly with the electrical signal, generated from the video tape, which contains the maximum amount of undistorted information. However, observing the signal from each pixel on the meteor trail is not sufficient. It is necessary also to subtract the average signal of that pixel at a time before or after the meteor appears, i.e., to detect and account for that part of the signal that is due to night sky, stars, or system noise. Furthermore, an image orthicon does not read out its entire signal in a single frame. Since, as we learned, the integrated signal is a better and more useful measure than the peak signal is, the problem of interpreting the electrical signal is increased.

We bypassed most of these problems by physically isolating the pixels of interest on a television monitor and generating a new electrical analog signal with a phototube observing the isolated region. It might appear that this technique suffers seriously by introducing nonlinearities of the phosphor of the monitor and indeterminate effects produced by the phosphor decay. In fact, none of the effects is important so long as our calibration data are treated by the same system of analysis as the meteor data. In a sense, we bring both the meteor and the calibration into the laboratory and observe them photoelectrically at our leisure.

In practice, all but a small area of the monitor screen—that part through which the meteor or calibration source will pass—is covered. The phototube records the luminosity of this area. The phototube output is registered on a chart recorder or displayed on a cathode-ray oscilloscope and photographed. The integrated intensity of the meteor pulse above the background is taken to be proportional to the original intensity of the source or meteor for the time interval required to pass through the aperture. It is the *integrated* intensity, rather than the peak intensity, that is pertinent since an image orthicon, and particularly one adjusted for high sensitivity, reads out the signal much more slowly than the signal is impressed on the target. We also demonstrated that the integrated intensity divided by the time the source was in the aperture was nearly independent of the angular velocity of the source, or, in terms used in photography, this system obeys the reciprocity law. (This fortunate circumstance could hardly have been anticipated since the entire photometric system contains a number of nonlinear components.) Therefore, the instantaneous intensity can be determined once the angular velocity of the meteor is known. No second-order corrections are required when the meteor and calibration source are of different angular velocities.

Photometry is performed on as many independent points on the meteor trail as is necessary to define the light curve.

Procedure for Reducing Observations of Meteors Observed by Both Radar and Television Camera

The procedure we employed in the analysis of television and simultaneous observations is one in which the position read from a plot of the meteor on a copy of a portion of a chart of the *Atlas des nördlichen gestirnten Himmels* (Schönfeld and Krüger, 1899) is combined with the radar observations to find the trajectory in the atmosphere. The zero points of the time scales for the radar and optical records as established by the start of the radar return recorded on the audio channel of

the video tape are exhibited on the light curve. The threshold for the kinescoped film is established to fit the duration on the film so that the epochs of beginning and end of the meteor as kinescoped are found. We then have positions (beginning of meteor, beginnings and ends of frames, end of meteor) at specified epochs. The reduction requires that two well-determined positions and their epochs be selected. These are often the beginning and end and will be referred to by those terms for convenience.

The linear velocity of the meteor is taken from results of the processing of the Fresnel patterns or of the complete radar reduction. Then a series of values of the range from Sidell to the end point of the meteor is introduced. A solution for the trajectory (rectangular coordinates and radiant) is found for each of these end ranges. The bisector of the directions of the transmitter and receiver from the meteor is also found for the minimum range epoch of each radar return. The cosine of the angle between this direction and the radiant is then determined. The correct solution is that at which this angle is a right angle and its cosine vanishes and is found by interpolation with respect to the end range. Errors of observation cause these values of the end range to vary from one radar station to another. An appropriate mean is adopted. Also, the loop ranges are computed from each station as a check, and the phase is computed for site 3 (the transmitter). Comparison of this phase with that measured between the two troughs at site 3 and of the computed loop ranges with their observed values serves to eliminate chance coincidences between a radar observation of one meteor and an optical observation of another. The computed loop range is usually near a minimum with respect to end range from Sidell and so cannot be used to determine that end range.

We are given at two epochs (beginning and ending) the right ascension and declination of the meteor as observed from Sidell: t_b, α_b, δ_b; t_e, α_e, δ_e. We are also given for each radar station n the epoch t'_n of the first Fresnel maximum, the loop range R_{3n}, and the velocity V deduced from the Fresnel pattern. We further know the alt-azimuth coordinates x_n, y_n, z_n (to the East, North, and zenith, respectively) of each station referred to site 3 as the origin, and the coordinates of Sidell x_s, y_s, z_s. If a full radar reduction is available, the epoch of specular reflection t_n is also given.

We initially find the Greenwich Sidereal Time from the *American Ephemeris* and subtract the longitude of Havana ($+6^h0^m5.27^s$) to determine the Local Sidereal Time θ_0. Also, we find the epochs of specular reflection t_n (if not given) at each site by application of the correction

$$\Delta t'_n = -0.4\,\frac{\sqrt{\lambda(R_{3n}-R_{G3n})}}{V} \qquad t_n = t'_n + \Delta t'_n \tag{41}$$

where R_{G3n} is the range of site n from site 3:

$$R_{G3n} = (x_n^2 + y_n^2 + z_n^2)^{1/2} \tag{42}$$

We commence by transforming our optical directions to hour angle and declination for the meridian of Havana as seen from Sidell:

$$t = \theta_0 - \alpha \tag{43}$$

The direction cosines on the local equatorial system are

$$\begin{aligned} \ell_E &= -\cos\delta\sin t \\ m_E &= -\cos\delta\cos t \\ n_E &= \sin\delta \end{aligned} \tag{44}$$

Here the x_E axis is directed to the east, the y_E axis to the intersection of the meridian and the equator below the horizon, and the z_E axis to the north celestial pole.

We next rotate to the alt-azimuth system of Havana:

$$\begin{aligned} \ell &= \ell_E \\ m &= m_E\sin\phi + n_E\cos\phi \\ n &= -m_E\cos\phi + n_E\sin\phi \end{aligned} \tag{45}$$

At Havana, the latitude $\phi = +40°15'$, $\sin\phi = +0.6457$, and $\cos\phi = +0.7636$. These directions are from Sidell at

$$\begin{aligned} x_s &= +185.38 \text{ km} \\ y_s &= -28.45 \text{ km} \\ z_s &= -2.67 \text{ km} \end{aligned}$$

We choose as an independent variable the range R_e at the end point of the meteor from Sidell. For

such a chosen value, the end point lies at

$$\begin{aligned} x_{me} &= R_e \ell_e + x_s \\ y_{me} &= R_e m_e + y_s \\ z_{me} &= R_e n_e + z_s \end{aligned} \tag{46}$$

Next we require the various angles in the triangle formed by Sidell and the meteor. The pole of the trail is given by

$$\begin{aligned} \ell_p \sin \alpha_{be} &= m_b n_e - m_e n_b \\ m_p \sin \alpha_{be} &= \ell_e n_b - \ell_b n_e \\ n_p \sin \alpha_{be} &= \ell_b m_e - \ell_e m_b \end{aligned} \tag{47}$$

where α_{be} is the angular distance from the beginning to the end. Then we have, by application of the law of sines,

$$\sin \theta_b = \frac{R_e}{V(t_e - t_b)} \sin \alpha_{be} \tag{48}$$

$$\theta_e = \theta_b + \alpha_{be} \tag{49}$$

Here we can use either solution of equation (48), i.e., $0 \leq \theta_b \leq 90°$ or $90° \leq \theta_b \leq 180°$. In either case,

$$R_b = V(t_e - t_b) \frac{\sin \theta_e}{\sin \alpha_{be}} \tag{50}$$

The beginning of the meteor then lies at

$$\begin{aligned} x_{mb} &= R_b \ell_b + x_s \\ y_{mb} &= R_b m_b + y_s \\ z_{mb} &= R_b n_b + z_s \end{aligned} \tag{51}$$

The radiant has the direction cosines

$$\begin{aligned} \ell_R &= \frac{x_{mb} - x_{me}}{V(t_e - t_b)} \\ m_R &= \frac{y_{mb} - y_{me}}{V(t_e - t_b)} \\ n_R &= \frac{z_{mb} - z_{me}}{V(t_e - t_b)} \end{aligned} \tag{52}$$

At the epochs of specular reflection t_n, the meteor was at

$$\begin{aligned} x_{mn} &= x_{me} \frac{t_n - t_b}{t_e - t_b} + x_{mb} \frac{t_e - t_n}{t_e - t_b} \\ y_{mn} &= y_{me} \frac{t_n - t_b}{t_e - t_b} + y_{mb} \frac{t_e - t_n}{t_e - t_b} \\ z_{mn} &= z_{me} \frac{t_n - t_b}{t_e - t_b} + z_{mb} \frac{t_e - t_n}{t_e - t_b} \end{aligned} \tag{53}$$

The loop range from sites 3 and n is given by

$$\begin{aligned} R_{3n} &= R_3 + R_n + R_{G3n} \\ R_n &= [(x_{mn} - x_n)^2 + (y_{mn} - y_n)^2 + (z_{mn} - z_n)^2]^{1/2} \\ R_3 &= (x_{mn}^2 + y_{mn}^2 + z_{mn}^2)^{1/2} \end{aligned} \tag{54}$$

Finally, we wish to determine how close the meteor was to minimum loop range. This can be done by formation of the derivative

$$\frac{dR_{3n}}{dt} = \frac{dR_3}{dt} + \frac{dR_n}{dt}$$

$$\frac{dR_n}{dt} = \frac{(x_{mn} - x_n)(dx/dt)}{R_n} + \frac{(y_{mn} - y_n)(dy/dt)}{R_n} + \frac{(z_{mn} - z_n)(dz/dt)}{R_n}$$

The derivatives are

$$\frac{dx}{dt} = -V\ell_R$$

$$\frac{dy}{dt} = -Vm_R$$

$$\frac{dz}{dt} = -Vn_R$$

Then we have

$$\frac{dR_n}{dt} = -\frac{V}{R_n}[(x_{mn} - x_n)\ell_R + (y_{mn} - y_n)m_R + (z_{mn} - z_n)n_R]$$

$$\begin{aligned} \frac{dR_{3n}}{dt} = -\frac{V}{R_3 R_n} \{ & R_n(x_{m3}\ell_R + y_{m3}m_R + z_{m3}n_R) \\ & + R_3[(x_{mn} - x_n)\ell_R + (y_{mn} - y_n)m_R \\ & + (z_{mn} - z_n)n_R] \} \end{aligned} \tag{55}$$

$$\frac{dR_{33}}{dt} = -\frac{2V}{R_3}(x_{m3}\ell_R + y_{m3}m_R + z_{m3}n_R) \tag{56}$$

To put these on a dimensionless basis, we divide by $(-2V)$:

$$\mathbf{R}\cdot\mathbf{N}_n = \frac{1}{2R_3R_n}\{R_n(x_{mn}\ell_R+y_{mn}m_R+z_{mn}n_R) + R_3[(x_{mn}-x_n)\ell_R+(y_{mn}-y_n)m_R + (z_{mn}-z_n)n_R]\} \quad (57)$$

$$\mathbf{R}\cdot\mathbf{N}_3 = \frac{1}{R_3}(x_{m3}\ell_R+y_{m3}m_R+z_{m3}n_R) \quad (58)$$

Here $\mathbf{R}$ is a unit vector toward the radiant, $\mathbf{N}_n$ is the unit vector bisecting the directions to the meteor from sites 3 and n, and $\mathbf{N}_3$ is the unit vector toward the meteor from site 3.

The observation of phase gives us $\sin\phi_A$, where ϕ_A is the phase angle from the trough at site 3. The direction cosines from station 3 are

$$\ell_{33} = \frac{x_{m3}}{R_3} = \frac{2x_{m3}}{R_{33}}$$

$$m_{33} = \frac{y_{m3}}{R_3} = \frac{2y_{m3}}{R_{33}} \quad (59)$$

$$n_{33} = \frac{z_{m3}}{R_3} = \frac{2z_{m3}}{R_{33}}$$

and the direction cosines of the southerly perpendicular to the trough are (direction toward $A=203°$) $-\sin 23°$, $-\cos 23°$, 0, or -0.3907, -0.9205, 0.0000. The scalar product of these two unit vectors is $\sin\phi_A$:

$$\sin\phi_A = -0.3907\frac{x_{m3}}{R_3} - 0.9205\frac{y_{m3}}{R_3} = -\frac{0.7814x_{m3}+1.8410y_{m3}}{R_{33}} \quad (60)$$

We repeat this process at successive ranges. We commence at $R_e=80$ km and increase in 10-km steps to 180 km and then stop. Interpolation in R_e to fit the condition $\mathbf{R}\cdot\mathbf{N}_n=0$ is then carried out and a suitable compromise made between the various stations in arriving at a final end range R_e. Finally, the computation is repeated at the adopted end range, and the height above mean sea level is found in the usual way from the deduced rectangular coordinates of the meteor.

The deduced ranges are used with the apparent light curve to find the light curve in absolute magnitude (standard range 100 km). The observed radar magnitude (a line density of 10^{12} per centimeter corresponds by definition to a meteor of radar magnitude +5) is then corrected for the antenna pattern established by Sekanina (1972, private communication).

Results from Simultaneous Radar and Television Observations

Twenty-nine meteors were observed and reduced simultaneously by radar and television from February 1969 through June 1970. Tables 2 to 6 list the results of these observations. The following quantities are presented in the tables:

V is the velocity of the meteor
h_B and h_E are the beginning and end heights
$M_{p\ \max}$ denotes the image-orthicon magnitude (approximately panchromatic) at maximum brightness

$$\int_{-\infty}^{+\infty} I_p\,dt, \qquad I_p \equiv 10^{-0.4M_P}$$

is the integrated brightness (including linear extrapolations of magnitude versus time below threshold), where I_p denotes the instantaneous panchromatic brightness in units of zero absolute magnitude (reference range of 100 km)
Z_R is the zenith distance of the radiant from the zenith at Havana
Ceplecha's (1968) class with respect to beginning height is read from his figure 1
α_R and δ_R are the right ascension and declination of the geocentric radiant (cleared of zenith attraction and diurnal aberration)
V_G is the geocentric velocity of the meteor
M_R denotes the radar magnitude and
M_p is the image-orthicon magnitude

The observed velocity was used for the velocity outside the atmosphere without correction for deceleration by atmospheric drag. The orbital elements are denoted by the usual symbols (semimajor axis, eccentricity, distance from the Sun at perihelion, argument of perihelion, longitude of the ascending node, inclination, and longitude of perihelion, respectively). The designations of the showers are those of Cook (1973).

TABLE 2.—*Circumstances of the Observed Meteors*

Meteor number	1969 UT	Radar	Optical	V (km s^{-1})	Radar		Optical	
					h_B (km)	h_E (km)	h_B (km)	h_E (km)
1	Feb. 14^{d}10^{h}57^m 23.50^s–24.48^s	23.76^s–24.13^s	23.50^s–24.48^s	31.2	90.6– 82.7		94.7 – 75.7	
2	Apr. 20 8 19 14.12–14.99	14.12–14.88	14.44–14.99	14.7	102.1– 94.6		98.8 – 93.1	
3	July 19 7 44 6.88 – 7.86	7.13 – 7.50	6.88 – 7.86	17.1	86.4– 82.6		89.0 – 79.5	
4	July 19 8 30 6.87 – 8.16	7.81 – 8.16	6.87 – 8.16	19.8	92.5– 90.6		97.6 –(90.6)	
5	Aug. 18 7 42 53.16–54.63	53.72–53.95	53.16–54.66	26.0	101.7– 96.4		110.8 –(86.0)	
6	Sept. 18 8 52 55.65–56.48	55.65–55.91	55.72–56.48	20.4	97.1– 93.8		96.2 – 86.7	
7	Oct. 8 6 18 37.20–38.86	37.42–37.82	37.20–38.86	17.9	94.1– 88.7		97.1 – 74.6	
8	Oct. 15 8 52 2.70 – 3.26	2.72 – 3.09	2.70 – 3.26	21.8	97.6– 92.1		97.9 –(88.6)	
9	Oct. 15 9 55 30.54–31.08	30.66–30.98	30.54–31.08	28.8	104.5– 98.8		106.0 –(97.0)	
10	Oct. 22 10 44 6.03 – 7.25	6.21 – 6.59	6.03 – 7.25	32.9	98.5– 90.6		102.2 – 77.0	
11	Nov. 8 8 43 2.15 – 3.43	2.77 – 2.85	2.15 – 3.43	19.3	84.6– 83.4		94.3 – 74.4	
12	Nov. 16 7 33 7.42 – 8.25	7.42 – 7.87	7.60 – 8.25	16.2	93.4– 87.7		91.1 – 82.8	
13	Nov. 16 9 45 23.58–24.10	23.83–23.99	23.58–24.10	30.2	96.7– 93.2		102.3 – 90.7	
14	Dec. 13 11 11 38.29–38.50	38.29–38.50	38.29–38.50	36.0	87.7– 81.7		87.7 –(81.7)	
15	Dec. 16 9 45 46.89–48.02	46.94–47.24	46.89–48.02	30.1	99.2– 92.3		100.4 – 74.4	
	1970 UT							
16	Jan. 10 10 26 3.38 – 4.43	3.38 – 3.75	3.38 – 4.43	44.5	110.0–103.0		(110.0)–(91.7)	
17	Feb. 12 7 50 11.22–12.04	11.22–11.92	11.35–12.04	16.9	97.8– 89.2		96.2 –(87.7)	
18	Feb. 12 9 24 24.48–25.28	24.48–24.74	24.66–25.28	25.5	96.3– 92.0		93.4 – 83.4	
19	Feb. 12 10 11 44.54–45.39	45.04–45.39	44.54–45.34	30.4	102.3– 95.4		112.2^s– 96.4	
20	Feb. 12 10 16 7.08 – 7.82	7.15 – 7.26	7.08 – 7.82	19.3	91.1– 89.6		92.0 – 82.2	
21	Feb. 12 10 36 6.12 – 6.82	6.12 – 6.45	6.14 – 6.82	32.0	95.8– 88.2		95.3 – 79.6	
22	Feb. 12 10 52 1.60 – 2.53	1.75 – 1.93	1.60 – 2.53	23.5	97.1– 93.9		99.8 – 83.3	
23	Mar. 16 10 40 58.47–59.14	58.54–59.10	58.47–59.14	35.7	93.6– 83.7		94.8 – 83.2	
24	Apr. 3 9 59 43.50–44.59	43.53–43.72	43.50–44.59	27.1	94.1– 89.9		94.7 – 70.0	
25	Apr. 7 7 48 48.43–49.55	48.43–49.22	48.61–49.55	20.2	95.1– 84.5		92.7 – 80.1	
26	Apr. 7 9 55 20.38–21.11	20.53–20.75	20.38–21.11	35.5	102.6– 96.8		106.6 – 87.2	
27	Apr. 10 8 9 11.34–12.07	11.36–12.07	11.34–11.84	20.2	100.3– 91.1		100.8 –(94.1)	
28	May 5 9 19 16.73–17.50	16.73–17.28	16.80–17.50	17.5	94.2– 87.0		93.3 – 84.1	
29	May 7 5 36 54.52–56.03^b	54.52–55.07	54.91–56.03^b	14.7	95.7– 90.6		92.1 – 81.7^b	

[a] Extrapolated out of field.

[b] Light curve extrapolated to threshold. Ending could have been as early as 55.69^s.

Heights are referred to mean sea level. Magnitudes below threshold are indicated by an inequality sign.

Velocities are probably uncertain by a few tenths of a kilometer per second (none of these relatively bright radar meteors is a first-class example of a well-observed radar meteor); no measurable decelerations were found. Heights are uncertain by a kilometer or two, or occasionally three. The threshold absolute magnitude quoted is an average for the beginning and end of the trail if both were observed, or it refers to the beginning alone if only it was observed and the meteor left the field while under observation. Masses are based on the suggested luminous efficiency of stone by Ayers, McCrosky, and Shao (1970).

Most of the observations appear to have been affected by fragmentation. Unmistakable evidence can be seen for this in the light curves shown in figures 3 and 4. Only the light curve of meteor no. 2 looks classical throughout. Meteors nos. 21 and 25 look classical except for an apparent exponential decay near the end, reminiscent of terminal blending. All sites received their radar

TABLE 3.—*Radiant and Photometric Data for the Observed Meteors*

Meteor number	$M_{p\,max}$	Integrated intensity,[a] $\int_{-\infty}^{+\infty} I_p\,dt$ (0 mag s)[a]	Cos Z_R	Ceplecha's class	Threshold M_p	α_R (deg)	δ_R (deg)	V_G (km s^{-1})
1	+5.5	3.4×10^{-3}	0.618	B	+7.4	166	+11	29.4
2	+5.8	2.7×10^{-3}:	0.745	Above C_1	+6.9	166	+53	10.0
3	+5.0	7.7×10^{-3}	0.612	B	+6.2	273	0	13.3
4	+3.9	—	0.273	C_1	+5.8	299	−35	16.6
5	$\ll$0	—	0.705	Above C_1	+5.8	281	+54	23.7
6	+4.9	6.2×10^{-3}:	0.613	C_1	+6.2	302	+65	17.2
7	+4.3	1.27×10^{-2}	0.751	Above C_1	+6.7	332	+18	14.4
8	+5.6	—	0.688	C_1	+6.1	23	+ 7	19.1
9	+4.9	—	0.659	Above C_1	+5.2	30	+16	26.9
10	$\sim$0	—	0.629	C_1	+4.9	46	+17	31.3
11	+6.1	2×10^{-3}::	0.807	C_1	+8.0	47	+19	16.0
12	+7.4	—	0.790	C_1	+7.8	27	+25	12.2
13	+4.3	5.6×10^{-3}:	0.738	C_1	+6.6	67	+18	28.4
14	+5.7	—	0.805	Below A	+7.1	120	+23	34.5
15	+6.2	—	0.778	C_1	+7.0	94	+27	28.2
16	~-1	—	0.438	Above C_1	+4.8	130	− 9	43.3
17	+6.3	—	0.736	C_1	+6.9	123	+12	13.1
18	+4.6	—	0.635	B	+6.6	140	+13	23.2
19	+5.2	5.4×10^{-3}:	0.652	Above C_1	+6.4	159	+ 8	28.6
20	+6.3	—	0.751	B–C_1	+7.0	137	+56	16.0
21	+6.5	2.1×10^{-3}:	0.731	B	+7.6	164	+20	30.2
22	+6.3	2.7×10^{-3}:	0.764	C_1	+7.4	166	+25	20.9
23	+6.1	2.1×10^{-3}:	0.497	A–B	+7.2	211	−14	34.1
24	+6.3	—	0.820	B	+6.9	207	+30	25.0
25	+4.5	8.2×10^{-3}:	0.673	C_1	+6.6	178	+ 5	17.2
26	+5.2	7.0×10^{-3}::	0.744	Above C_1	+6.2	207	+23	34.0
27	+4.1	—	0.654	Above C_1	+6.0	187	+ 2	17.1
28	+5.0	6×10^{-3}:	0.764	C_1	+5.8	214	+33	13.8
29	+5.7	6×10^{-3}:	0.640	C_1	+6.6	111	+64	9.9

[a] Uncertain integrated intensities are indicated by a colon (10 to 25 percent contribution by extrapolated parts of light curve) and very uncertain values by two colons (25 to 50 percent contribution).

returns from the classical portions of the light curves. Meteor no. 14 appears to have a classical light curve until its departure from the field of view. Meteors nos. 7, 12, 19, and 24 show strongly distorted light curves, but the early observations for each appear to have caught the meteor so soon that fragmentation had not yet degraded the radar echo. Meteors nos. 1, 9, 15, and 23 all exhibit exponential decay during the later parts of their light curves. Such a decay suggests mutual shadowing of drops against the air stream leading to mutual coalescence. This process has been discussed by Cook (1968) as an explanation for exponential decay in terminal blending. The values of M_R-M_p during the decay of light from these four meteors are so small as to suggest that this process is indeed active with a corresponding narrow spread in lines of flight of the drops. These 12 meteors appear not to have had all their radar returns weakened by fragmentations. They are no. 1 (sites 3, 4, 5), no. 2 (all sites), no. 7 (sites 4, 5), no. 9 (sites 3, 4), no. 12 (sites 3, 4), no. 14 (all sites), no. 15 (sites 4, 5), no. 19 (site 8), no. 21 (all sites), no. 23 (both sites), no. 24 (both sites), and no. 25 (all sites).

Average values were formed for M_R-M_p for each meteor. Means for the two obvious groups in velocity (meteors nos. 2, 7, 12, 25 and meteors nos.

TABLE 4.—*Orbits of the Observed Meteors*

Meteor number	a (AU)	e	q (AU)	ω (deg)	Ω (deg)	i (deg)	π (deg)	Shower
1	1.55	0.82	0.28	306	325	7	272	Northern Virginid
2	2.31	0.57	1.00	190	30	10	220	
3	2.09	0.58	0.88	231	116	9	347	
4	1.56	0.56	0.68	85	296	8	21	
5	5.1	0.81	0.99	198	145	36	342	κ Cygnid
6	1.39	0.30	0.97	212	175	30	27	
7	3.53	0.74	0.90	219	195	10	54	
8	1.60	0.64	0.58	95	22	2	116	
9	1.93	0.81	0.37	294	202	4	135	Northern Piscid
10	1.75	0.87	0.23	131	29	1	160	Southern Taurid
11	1.29	0.53	0.60	278	226	1	144	
12	1.80	0.54	0.84	236	234	4	109	
13	1.88	0.82	0.33	118	54	5	172	Southern Taurid
14	0.97	0.94	0.06	341	261	7	242	
15	2.51	0.84	0.40	288	264	4	192	Northern χ Orionid
16	56	0.99	0.31	112	110	55	221	
17	1.98	0.57	0.84	53	143	3	196	
18	3.79	0.84	0.62	79	143	2	222	Southern δ Leonid?
19	1.71	0.81	0.32	120	143	0	263	
20	2.54	0.66	0.87	225	323	16	188	
21	2.11	0.84	0.34	296	323	15	259	
22	1.20	0.60	0.47	293	323	14	256	
23	0.88	0.95	0.05	164	175	4	339	
24	3.57	0.80	0.73	247	13	27	260	
25	3.68	0.78	0.82	234	17	2	251	
26	−3.01	1.21	0.64	250	17	30	267	
27	2.49	0.69	0.78	243	20	2	263	σ Leonid
28	2.04	0.55	0.93	219	44	16	263	
29	2.10	0.53	0.99	159	46	10	205	

1, 9, 14, 15, 19, 21, 23, 24) yield a difference of higher-velocity group minus lower-velocity group of -1.0 ± 0.3 (standard deviation) mag. A linear fit with standard deviations was, therefore, found:

$$M_R - M_p = +2.85 - 3.8 \quad (\log V - 6.408)$$
$$\pm 0.16 \pm 1.3 \qquad (61)$$

with the standard deviation for a single meteor being ±0.5 mag. We note that measures consistent with this result are found over the range in height from 81.7 to 100.7 km above sea level. No measurements at all are found below these heights. This floor is presumably imposed by dissociative recombination. Meteor no. 9 was measured above this height with an underdense echo that was affected either by fragmentation or by diffusion, or by both. For meteor no. 16, the observation at 109.2 km (site 8) must have been affected by diffusion, and all the others must have been points at which the electron trail was overdense. Estimates of the strength of the radar return that should have occurred suggest that the known uncertainty of the antenna pattern at higher altitudes has taken its toll here. Meteors nos. 5 and 25 were also vulnerable to this difficulty. These data suggest that diffusion affects measurements above a height of 101 km.

We must combine these results with the two really numerous comparisons between visual and radar meteors. The Geminids and Perseids were studied by Millman and McKinley (1956), who found a relationship between $\log T_D$ and M_V (T_D is the duration of an overdense echo in seconds, and M_V is the visual absolute magnitude). McKinley (1961, pp. 228–230) has discussed these results on the basis of Greenhow and Neufeld's (1955) relation for the coefficient of

TABLE 5.—*Radar and Optical Measurements of the Observed Meteors*[a]

Meteor number	Site	Epoch	Height (km)	M_R	M_p	$M_R - M_p$	Remarks
1	1	23.81[s]	88.8	+ 9.7	+5.6	+4.1	Fragmentation
	2	23.91	86.9	+10.3	+5.8	+4.5	Fragmentation
	3	23.99	85.4	+ 9.3	+6.2	+3.1	
	5	24.11	83.1	+ 9.5	+6.8	+2.7	Perhaps only a few fragments
	4	24.13	82.7	+10.0	+6.8	+3.2	
2	4	14.37	99.5	+ 9.6[b]	$>$+6.8	$<$+2.8	
	3	14.44	98.8	+ 9.4[b]	+6.8	+2.6	
	5	14.69	96.1	+10.0	+5.8	+4.2	
	7	14.83	94.6	+ 9.9	+5.7	+4.2	
3	3	7.17	86.0	+10.4	+4.9	+5.5	All stations appear to be affected by fragmentation (see light curve)
	5	7.27	84.9	+12.1[b]	+5.1	+7.0	
	4	7.39	83.7	+12.2	+5.2	+7.0	
	6	7.50	82.6	+13.3	+5.3	+8.0	
4	3	8.04	91.3	+ 8.4	+4.1	+4.3	Strong fragmentation
	6	8.16	90.6	+ 9.9	+4.1	+5.8	
5	5	53.78	99.4	+12.1[b]	+4.0	+8.1	
	7	53.80	99.1	+10.9[b]	+3.9	+7.0	
	6	53.95	96.4	+10.5	−0.5::	+11.0::	
6	8	55.91	93.8	+11.2	+4.9	+6.3	Fragmentation and broad flares
7	4	37.57	92.0	+ 7.8	+5.0	+2.8	
	5	37.58	91.8	+ 8.2	+4.7	+3.5	
	6	37.82	88.7	+ 8.5	+4.4	+4.1	Fragmentation
8	1	2.78	96.7	+10.5	+6.0	+4.5	Fragmentation throughout
	2	2.86	95.6	+10.2	+5.8	+4.4	
	3	2.92	94.7	+ 9.8	+5.7	+4.1	
	4	3.09	92.1	+ 9.5	+5.7	+3.8	
9	1	30.71	103.6	+ 8.3	+5.0	+3.3	Fragmentation (rapid brightening, slow decline)
	8	30.81	101.7	+ 9.1	+4.9	+4.2	
	2	30.82	101.5	+ 8.7	+4.9	+3.8	
	3	30.90	100.0	+ 8.0	+4.9	+3.1	
	4	30.98	98.5	+ 6.5	+5.0	+1.5	
10	7	6.59	90.6	+ 9.8	+2.3:	+7.5:	Pronounced flare
11	1	2.85	83.4	+10.6	+6.8	+3.8	
12	3	7.66	90.3	+11.4	+7.8	+3.6	
	4	7.69	89.9	+10.4	+7.7	+2.7	
	5	7.87	87.7	+11.6	+7.5	+4.1	Fragmentation
13	8	23.99	93.2	+ 9.6	+5.9	+3.7	Fragmentation
14	1	38.34	86.3	+ 7.6	+6.6	+1.0	
	2	38.42	84.0	+ 8.1	+6.0	+2.1	
	3	38.50	81.7	+ 8.5	+5.8	+2.7	
15	2	47.04	96.9	+11.0	+6.5	+4.5	Light curve indicates fragmentation; last two values of $M_R - M_p$ imply relative proximity among fragments
	8	47.12	95.1	+12.0	+6.4	+5.6	
	3	47.13	94.9	+10.6	+6.4	+4.2	
	4	47.19	93.5	+ 8.6	+6.3	+2.3	
	5	47.24	92.3	+ 7.8[b]	+6.3	+1.5	
16	8	3.43	109.2	+ 9.5:[b]	+3.5	+6.0	Undoubtedly an overdense echo undergoing rapid diffusion
	1	3.56	106.6	+ 7.9:[b]	+1.1	+6.8	
	3	3.64	105.1	+ 7.3:[b]	−0.7::	+8.0::	
	4	3.75	103.0	+ 6.4:[b]	−0.6::	+7.0::	
17	2	11.44	95.1	+10.2	+6.5	+3.7	Fragmentation
	3	11.54	93.9	+10.8	+6.3	+4.5	
	6	11.92	89.2	+10.3	+6.8	+3.5	

TABLE 5.—*Radar and Optical Measurements of the Observed Meteors* (Continued)

Meteor number	Site	Epoch	Height (km)	M_R	M_p	M_R-M_p	Remarks
18	3	24.59	94.4	+10.2	(+6.5)	(+3.7)	Large flare
	5	24.69	92.8	+13.0	(+6.4)	(+6.6)	
	4	24.74	92.0	+12.5	+6.4	+6.1	
19	8	45.12	100.7	+ 9.0	+6.2	+2.8	
	3	45.29	97.4	+11.6	+6.6	+5.0	Fragmentation (rapid rise, slow fall)
	5	45.35	96.2	+11.1	+6.6	+4.5	
	4	45.39	95.4	+10.9	(+6.7)	(+4.2)	
20	8	7.20	90.1	+10.7	+6.4	+4.3	Fragmentation (near peak),
	6	7.26	89.3	+11.0	+6.3	+4.7	rapid rise, slow fall
	7	7.26	89.3	+10.6	+6.3	+4.3	
21	2	6.15	95.1	+10.5	+7.2	+3.3	
	8	6.18	94.4	+10.5	+7.0	+3.5	
	3	6.23	93.2	+ 9.4	+6.8	+2.6	
	4	6.31	91.4	+ 8.3	+6.6	+1.7	
	5	6.31	91.4	+ 8.9	+6.6	+2.3	
	6	6.45	88.2	+ 9.2	+6.5	+2.7	
22	2	1.81	96.0	+ 9.8	+6.2	+3.6	Maximum of strongly
	8	1.93	93.9	+11.4	+6.3	+5.1	fragmenting meteor
23	1	59.03	84.9	+ 9.0	+7.1	+1.9	Very near turning down end
	5	59.10	83.7	+ 9.8	+7.2	+2.6	after slow fall; drops reconsolidated?
24	1	43.62	92.1	+10.2	+6.5	+3.7	Echoes from stations 8, 4, 5,
	2	43.72	89.9	+ 9.4	+6.5	+2.9	6 give wild velocities, so either they are overdense (unlikely) or wind field spoils them
25	1	48.61	92.7	+11.6[b]	+6.4	+5.2	
	3	48.78	90.4	+ 8.8[b]	+5.8	+3.0	
	5	48.87	89.2	+ 9.4:[b]	+5.2	+4.2:	
	4	48.98	87.7	+ 8.3[b]	+4.7	+3.6	
	6	49.22	84.5	+10.2:[b]	+5.6	+4.6:	
26	8	20.75	96.8	+12.7:[b]	+5.3	+7.4:	Fragmentation
27	3	11.79	94.7	+ 8.8	+4.5	+4.3	Fragmentation
	6	12.07	91.1	+10.1	$>+4.6$	$<+5.5$	
28	1	16.78	93.6	+12.6[b]	(+5.7)	(+6.9)	Fragmentation?
	8	17.28	87.0	+ 8.9	+5.5	+3.4	Fragmentation
29	4	54.63	94.6	+12.0	$\gg+6.4$	$\ll+5.6$	
	3	54.81	93.0	+10.2	$>+6.4$	$<+3.8$	
	5	55.07	90.6	+ 9.4	+5.8	+3.6	Fragmentation

[a] Parentheses denote magnitudes extrapolated from observed light curves. Uncertain magnitudes are indicated by a colon and very uncertain values by two colons.

[b] Steep gradient in antenna pattern or noise in pattern.

ambipolar diffusion of electrons and ions. He finds for the Geminids

$$M_V=45.5-2.87\log q \qquad (62)$$

where q here is in electrons per meter. The definition of radar magnitude M_R is (McKinley, 1961, pp. 230–231)

$$M_R=40-2.5\log q \qquad (63)$$

and thus we have

$$M_V=-0.42+1.148M_R \qquad (64)$$

For the Perseids, McKinley derives the expression

$$M_V=40.0-2.45\log q \qquad (65)$$

TABLE 6.—*Masses of the Observed Meteors*[a]

Meteor number	Initial mass (g)	Meteor number	Initial mass (g)
1	1.0×10^{-3}	16	—
2	4.9×10^{-3}:	17	—
3	8.3×10^{-3}	18	—
4	—	19	1.8×10^{-3}:
5	—	20	—
6	5.3×10^{-3}:	21	6×10^{-4}:
7	1.43×10^{-2}	22	1.7×10^{-3}:
8	—	23	4×10^{-4}:
9	—	24	—
10	—	25	7.2×10^{-3}:
11	2×10^{-3}::	26	1.4×10^{-3}::
12	—	27	—
13	1.9×10^{-3}:	28	7×10^{-3}:
14	—	29	1.1×10^{-2}:
15	—		

[a] Uncertain mass (10 to 25 percent of total in extrapolations of light curve) is indicated by a colon; very uncertain mass (25 to 50 percent of total in extrapolations of light curve) is indicated by two colons.

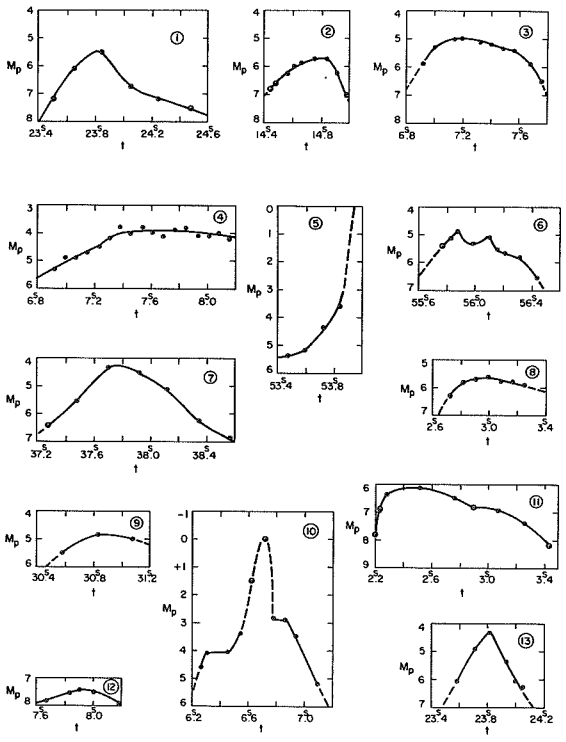

FIGURE 3.—Light curves of meteors nos. 1 to 13.

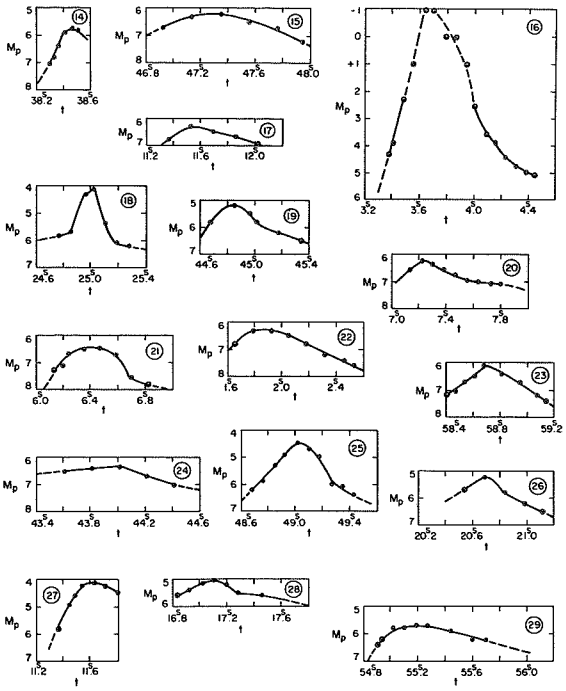

FIGURE 4.—Light curves of meteors nos. 14 to 29. Light curve of meteor no. 18 is drawn 0.6 magnitude too bright.

from which we have

$$M_V = +0.8 + 0.98 M_R \tag{66}$$

The lines of regression, $\log T_D$ vs M_V and M_V vs $\log T_D$, cross at $M_V = +0.4$, $M_R = -0.4$. The deviation from unity of the coefficient of M_R for the Geminids is not significant, as it amounts to less than the unit of a half-magnitude used in quoting magnitudes even over a range of ± 3 mag from $M_V = +0.8$, $M_R = +1.0$, the crossing point of the lines of regression.

Lindblad (1963) found for the Perseids

$$\log T_D = -0.50 M_V + 1.08 \tag{67}$$

where the echo duration T_D is in seconds. He also quotes

$$q = \frac{T_D}{4.5 \times 10^{-14}} \tag{68}$$

Here q is in cm^{-1}. Combination of these equations yields

$$\log q = 14.427 - 0.50 M_V \tag{69}$$

$$M_R = -1.07 + 1.25 M_V \tag{70}$$

Lindblad's lines of regression cross at $M_V = +1.1$, $M_R = +0.3$. We have two alternatives. In the first we accept Millman and McKinley's coefficient of M_V; i.e., it is taken as unity. Then we have the comparisons presented in table 7.

TABLE 7.—*Comparisons of Observations*

Authority	log V	M_R	M_V	$M_R - M_V$
McKinley	6.556	+1.0	+0.8	+0.2
McKinley	6.781	−0.4	+0.4	−0.8
Lindblad	6.781	+0.3	+1.1	−0.8

A linear fit through these two points (the second and third points coincide) yields

$$M_R - M_V = -0.3 - 4.4(\log V - 6.668) \quad (71)$$

Our two points from the groups of radar and television meteors are given in table 8.

TABLE 8.—*Data for Two Points*

Point	log V	$M_R - M_p$
1	6.234	+3.5±0.2
2	6.497	+2.5±0.2

The mean of the higher of these values of log V and that for the Geminids falls at log $V = 6.526$. We extrapolate both fits to that value to find $M_R - M_V = +0.3$, $M_R - M_p = +2.4$. The former value requires adjustments to panchromatic magnitudes via the color index (photographic minus visual) of −1.0 mag for faint Super-Schmidt meteors (Jacchia, 1957) and of −0.2 mag for the panchromatic index (Millman and Cook, 1959). This yields $M_R - M_p = +1.5$.

This discrepancy in $M_R - M_p$ of +0.9 mag, going from the visual observations of overdense radar meteors to the television observations of underdense radar meteors, drives us to our second alternative, which is to adopt Lindblad's coefficient of M_V. This deviates from unity by 0.25 and thus demands 3.6 mag to close the gap, leading to a fit at $M_V = +4.4$, $M_{ph} = +3.4$, $M_p = +3.2$, where M_{ph} is the photographic absolute magnitude.

A physical argument for such a behavior is that ionization should increase as we move with increasing brightness into a regime of slip flow of a meteor's own vapors.

Attention is called to the large number of light curves exhibiting a fast rise and exponential decay. This pattern suggests mutual shadowing of droplets vis-à-vis the air stream leading to mutual coalescence, a process discussed by Cook (1968) as an explanation of exponential decay in terminal blending. In this picture, no solid meteoroid is left.

ACKNOWLEDGMENTS

This work was supported in part by contract NSR 09-015-033 from the National Aeronautics and Space Administration.

REFERENCES

AYERS, W. G., MCCROSKY, R. E., AND SHAO, C. -Y., 1970. Photographic observations of 10 artificial meteors, *Smithson. Astrophys. Obs. Spec. Rept.* No. 317, 43 pp.

CEPLECHA, ZDENĚK, 1968. Discrete levels of meteor beginning height, *Smithson. Astrophys. Obs. Spec. Rept.* No. 279, 54 pp.

COOK, A. F., 1968. The physical theory of meteors, in *Physics and Dynamics of Meteors*, IAU Symp. No. 33, edited by L. Kresák and P. M. Millman, Dordrecht, Holland, D. Reidel Publ. Co., 149–160.

——, 1972. A working list of meteor streams, this volume.

GREENHOW, J. S., AND NEUFELD, E. L., 1955. The diffusion of ionized meteor trails in the upper atmosphere, *J. Atmos. Terr. Phys.*, **6**, 133–140.

GROSSI, M. D., 1963. High altitude wind measurements by collecting and processing meteor radar echoes, *Record of Conference on Direct Aeronomic Measurements in the Lower Ionosphere*, Univ. of Ill., Urbana, 82–88.

JACCHIA, L. G., 1957. On the color index of meteors, *Astron. J.*, **62**, 358–362.

LINDBLAD, B. A., 1963. The relation between visual magnitudes of meteors and the duration of radar echoes, *Smithson. Contrib. Astrophys.*, **7**, 27–39.

McKinley, D. W. R., 1961. *Meteor Science and Engineering*, New York, McGraw-Hill Book Co., 309 pp.

Millman, P. M., and Cook, A. F., 1959. Photometric analysis of a spectrogram of a very slow meteor, *Astrophys. J.*, **130**, 648–662.

Millman, P. M., and McKinley, D. W. R., 1956. Meteor echo durations and visual magnitudes, *Can. J. Phys.*, **34**, 50–61.

Schönfeld, Eduard, and Krüger, Adalbert, 1899. *Atlas des nördlichen gestirnten Himmels*, second edition, edited and corrected by Friedrich Küstner, Bonn, Marcus und Weber.

Whipple, F. L., and Jacchia, L. G., 1957. Reduction methods for photographic meteor trails, *Smithson. Contrib. Astrophys.*, **1**, 183–206.

5. Mass Influx Obtained From Low-Light-Level Television Observations of Faint Meteors

ROBERT J. NAUMANN
K. STUART CLIFTON
George C. Marshall Space Flight Center
Huntsville, Alabama

Since the advent of low-light-level television (LLLTV) systems, it has been recognized that such devices offer the ability to observe meteors as faint as 10th magnitude which allows the extension of optical meteor data to masses as small as 10^{-4} gram. The Space Sciences Laboratory at Marshall Space Flight Center has been actively engaged in such observations using image orthicons and intensified SEC vidicons.

The results of these observations are presented along with an interpretation in terms of mass-flux. This interpretation includes the development of a relationship between peak luminosity of a meteor and mass, velocity, and zenith angle that was derived from single body meteor theory and compares favorably with results obtained from the Artificial Meteor Program. Also included in the mass-flux interpretation is an analysis of the observation response of a LLLTV system to fixed and moving point sources.

THE PRESENT MODEL of the meteoroid mass distribution is based on an extrapolation from ground-based photographic observations of the larger meteoroids with masses of the order of grams to satellite-borne penetration measurements of meteoroids with masses in the microgram range. The mass range representing the greatest damage potential to manned space vehicles is from 1 to 100 mg. The fact that the meteoroid population in this region must be inferred from an extrapolation over 6 orders of magnitude between two points that are determined by completely different properties of meteoroids through interactions that are poorly understood physically and cannot be adequately tested experimentally has caused some concern among those responsible for establishing the meteoroid environment. Also, there are legitimate scientific reasons for extending the ground-based optical measurements to fainter meteors. Of primary interest is the determination of the slope of the mass distribution curve or the population index parameter. This will greatly improve the confidence in the extrapolation as well as reduce the range over which the extrapolation must be carried out, and will provide a badly needed consistency check between the ground-based and satellite measurements.

This paper discusses the techniques and results of using LLLTV observations to determine the meteoroid mass distribution in the region from grams to milligrams.

DESCRIPTION OF THE SYSTEM

Recent developments in low-light-level television systems have allowed the observation of much fainter meteors than could be photographed. This improvement results primarily from the much higher quantum efficiency of the photodetector which results in much smaller integration

times. This is particularly important in meteor work since it is advantageous to have the integration time shorter than the event duration. Our system consists of a Commercial Electronics camera chain using a Westinghouse WL-32000 Intensifier-SEC vidicon tube with a 105-mm $f/.75$ Rayxar lens. This affords a 13 by 16° field of view. The effective integration time of the system is very close to the standard frame time of $\frac{1}{30}$ s, which is ideal for meteor work.

The ultimate theoretical sensitivity for the system is $m_v = 14.26$. This was estimated by requiring a star to produce 1 photoelectron at the photocathode per integration time. The system is invariably limited by sky background which, even under ideal conditions, is 2 orders of magnitude above dark current. Stars as faint as $m_v = 11$ have been observed. This is close to the theoretical limit of 11.6 for a sky background of 300 $m_v = 10$ stars/deg^2 and a $S/N = 5$.

For moving objects, such as meteors, this limiting magnitude would apply to meteors moving nearly parallel to the optical axis so that they remain within a resolving element for one integration time. For most meteors, the S/N will be decreased because the time they contribute to a resolving element is limited by the writing speed of their image. It is estimated that if the system has an observing limit of 11 magnitude for stars, it will see all meteors brighter than $m_v = 6.4$ and 50 percent of the meteors brighter than $m_v = 8.15$.

ANALYSIS PROCEDURES

Even though the dynamic range of a TV image is limited, photometry of point images can still be performed over as much as 6 orders of magnitude by making use of the fact that the image spreads after it reaches saturation (Beyer et al., 1966). Thus, the amount of light associated with the image is a monotonic, if not linear, function of input. The difficulty lies in the fact that obtaining light curves from the TV monitor is a time consuming and laborious task, especially for the faint meteors. Until the special video processing systems presently being developed for this purpose are available, it will not be possible to obtain light curves on a sufficient sample of meteors to establish a good distribution.

An alternative procedure, which is less time consuming, was adopted for interim use. This consists of treating the video system as a threshold detector and simply counting those meteors that are above the detection threshold. By varying the threshold through reduction of the lens aperture setting, a cumulative distribution in peak meteor magnitude is obtained.

Figure 1 shows the results of this mode of operation during two observing periods at Climax, Colorado. The camera was oriented toward the zenith. Care was taken to program the aperture settings to assure a uniform distribution of observing time at each aperture setting throughout the night. The higher rates in the period from July 31 through August 9 may be attributed to the presence of the Perseids and the δ-Aquarids during this period. The details of these data will be published separately.

Taking the area of the sky within the field of view to be 445 km^2, the observed rates for the non-shower period can be expressed

$$\log \phi = -15.352 + .5053 m_v \qquad (1)$$

where ϕ is the observed rate of meteors (number/

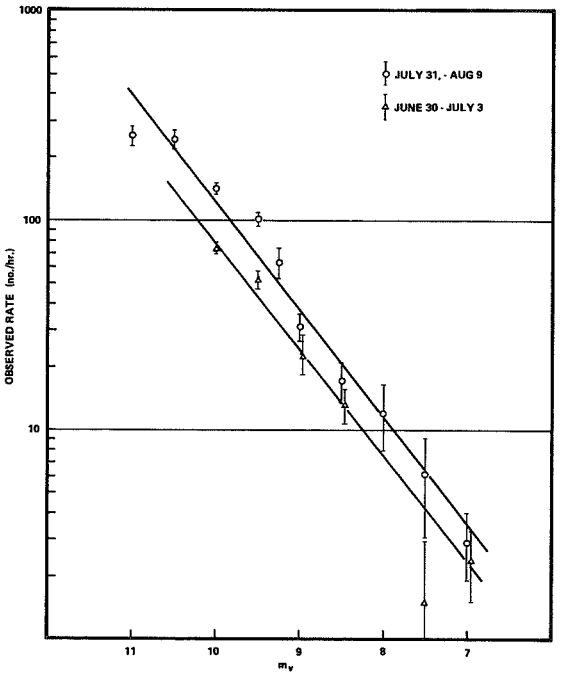

FIGURE 1.—Observed meteor rates as a function of limiting magnitude. Error bars represent 1σ limits based on the statistical sample.

m^2/s) when m_v is the limiting magnitude. This limiting magnitude is taken to be the magnitude of the faintest AO star detectable on the video screen. In a sense, this limiting magnitude represents the faintest meteor that could be detected, although practically all detectable meteors will have to be brighter than this because of their writing speed.

RELATIONSHIP BETWEEN PEAK LUMINOSITY AND METEOR MASS

A statistical analysis by Jacchia, Verniani, and Briggs (1965) of the peak brightness of meteors in terms of their mass, velocity, and entry angle yielded the result

$$I_P = 10^{-4.636} m_0^{0.9} v^{3.5} (\cos\theta)^{0.6} \tag{2}$$

where I_P is the peak intensity in units of zero magnitude stars, m_0 is the initial meteor mass in grams, v is the entry velocity in km/s, and θ is the entry angle or the angle between the velocity vector and zenith.

A similar result can be derived from classical single body meteor theory by assuming that the rate of mass loss is equal to the energy input divided by the heat of vaporization L. In the free molecular regime,

$$\dot{m} = -\frac{A\rho v^3}{2L} = -\frac{Sm^{2/3}\rho v^3}{2L\rho_m^{2/3}} \tag{3}$$

where S is the shape factor ($S=1.208$ for a sphere), ρ_m is the density of the meteoroid, and ρ is the atmospheric density. This neglects radiation losses, which are small compared to the heat input even at the boiling point of Fe (3160° K); and neglects any change in shape factor with time. Neglecting deceleration, which amounts to only a few percent velocity change in the time it takes a small meteoroid to completely burn up, and assuming an exponential atmosphere, equation (3) becomes

$$\dot{m} = -\frac{Sm^{2/3}v^3}{2L\rho_m^{2/3}} \rho_H e^{-x/h} \tag{4}$$

where $x = -vt\cos\theta$, h is the scale height, and ρ_H is the atmospheric density at $x=0$. This differential equation may be solved by separation of variables. It is convenient to define $t=0$ at meteor burnout, or $m=0$. The solution is then

$$m = m_0(1-e^{\beta t})^3 \tag{5}$$

where

$$\beta = \frac{v\cos\theta}{h}$$

and m_0, the initial mass, is

$$m_0 = \left(\frac{Sv^3\rho_H}{6L\rho_m^{2/3}\beta}\right)^3$$

Differentiating the solution,

$$\dot{m} = -3\beta m_0(1-e^{\beta t})^2 e^{\beta t} \tag{6}$$

The peak $\dot{m}$ is obtained by equating $\ddot{m}$ from equation (6) to 0 to find the time t_p when $\dot{m}$ is maximized. This yields

$$e^{\beta t_p} = 1/3$$

Putting this in equation (5),

$$\dot{m}_p = -\tfrac{4}{9}\beta m_0 \tag{7}$$

The radiant intensity from a meteor is given by

$$I = -\frac{\tau}{2}\dot{m}v^2 \tag{8}$$

where τ is the luminous efficiency. Using equation (7),

$$I_P = \frac{\tau}{2}\frac{4}{9}\frac{m_0 v^3}{h}\cos\theta \tag{9}$$

The luminous efficiency for Fe has been determined experimentally from Trailblazer (Ayers et al., 1970) and is expressed by

$$\tau = 10^{-17.95} v(\text{cm/s}) \tag{10}$$

Figure 2 compares the light curve obtained with this model with an observed light curve from one of the Fe Trailblazer meteors.

For stony meteors, Cook, Jacchia, and McCrosky (1963) recommend

$$\tau = 10^{-18.91} v(\text{cm/s}) \tag{11}$$

which is consistent with estimates of Ayers, McCrosky, and Shao based on Trailblazer measurements. Putting this value in equation (9), and choosing $h=5.4$ km which corresponds to 80 km, results in

$$I_P = 10^{-5.297} m_0 v^4 \cos\theta \tag{12}$$

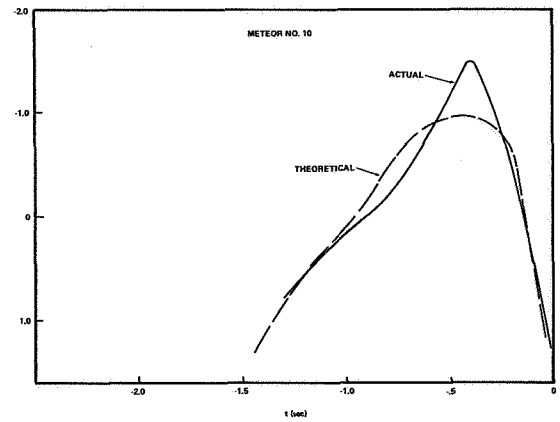

FIGURE 2.—Comparison of theoretical light curve compared with the measured light curve of an artificial meteor.

with the units the same as in equation (2). For the case of a 1 g meteor at 22 km/s, typical of cases from which equation (2) was obtained,

$$I_P = \begin{cases} 1.154 & \text{(eq. 2)} \\ 1.182 & \text{(eq. 12)} \end{cases}$$

The fact that the simple theory yields almost identical results as the empirical approach, together with the desirability of having some theoretical basis for determining the functional relationship of luminous intensity with mass, velocity, and entry angle, are the bases for choosing equation (12) as the functional observing relationship for the analysis.

SYSTEM RESPONSE TO MOVING TARGETS

As was stated previously, the detection threshold of a moving object is increased because the photons are spread over a number of resolving elements instead of contributing to the signal in a single element. A first order attempt to derive the system response to moving targets is to simply require that the minimum detectable moving object deliver the same number of photons during the time it resides in a resolving element as a minimum detectable stationary object in one integration time. The residence time is

$$t = \frac{A_r^{1/2}}{F\omega} \tag{13}$$

where A_r is the area of a resolving element, F is the focal length of the lens, and ω is the angular rate.

The criterion for detectability is

$$I_L \frac{A_r^{1/2}}{F\omega} = I_T \tau \tag{14}$$

where I_T is the threshold intensity for stationary objects, I_L is the limiting intensity for moving objects, and τ is the integration time. The photocathode is 40 mm in diameter, or 24 mm from the top to bottom raster line. Since there are 525 lines, a resolving element is taken to be a square 24/525 mm per side. Taking $F=105$ mm and $\tau = 1/30$ s,

$$I_L = I_T 76.57\omega; \qquad \omega \geq 0.01306 \text{ rad/s} \tag{15}$$

Figure 3 compares this model of the response to moving point sources with measurements made in

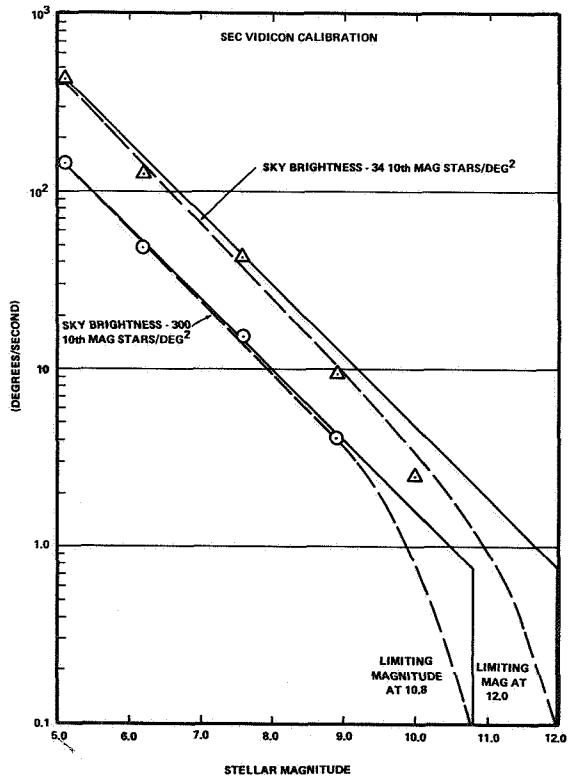

FIGURE 3.—Response of the SEC Vidicon to moving point images. The solid curves represent the predicted response based on the detection criteria used in the analysis.

our laboratory. The measurements consisted of projecting point sources onto a mirror mounted on a rate table which reflected the image onto a projection screen. The point source consisted of a precision 50μ pinhole mounted in a 35-mm slide projector. Neutral density filters were used to vary the image intensity, and the various images were calibrated by a photomultiplier photometer. The background lighting was provided by a small flood lamp with a controllable aperture. The angular rate of the mirror was adjusted for each filter until the image could no longer be detected on the monitor screen.

The agreement between the simple model and the observed results justifies the model. The only discrepancy occurs in the transition at the point where the image spends τ in a resolving element. Since the image in the experiment is smaller than the resolving element but is not an infinitesimal, some rounding off of the theoretical model in this transition region is to be expected, which, of course, is the observed result.

Since the angular rate

$$\omega = \frac{v \sin\theta}{r} \tag{16}$$

and using $r = 80$ km typical of meteor heights, equation (15) becomes

$$I_L = \begin{cases} I_T 0.957 v \sin\theta \\ I_T \end{cases} \tag{17}$$

whichever is greater.

RELATION BETWEEN INCIDENT FLUX AND OBSERVED FLUX

The number of meteors observed per unit area time is given by

$$\phi = \int_{\text{hemisphere}} d\Omega \cos\theta \int_0^\infty dv \int_{m_T(I_T,\theta,v)}^\infty dm n_{mv} \tag{18}$$

where n_{mv} is the directional mass velocity distribution (number per unit area, time, solid angle with masses between m and $m+dm$ and velocities between v and $v+dv$). The integration is carried out from the threshold m_T required to produce an observed signal, which is a function of the threshold response of the system I_T, θ, and v. Given only the observed ϕ, clearly there is not sufficient information to solve the integral equation. Several simplifying assumptions are in order. First, to a good approximation the velocity and mass distributions are independent. Second, it will be assumed that the velocities are isotropically distributed, i.e., n_{mv} is independent of θ and ϕ. Equation (18) becomes

$$\phi = 2\pi \int_0^{\pi/2} \cos\theta \sin\theta \, d\theta \int_0^\infty n_v \, dv \int_{m_T(I_T,\theta,v)}^\infty n_m \, dm \tag{19}$$

Even assuming n_v is known, there still is insufficient information to define n_m. However, the fact that the observed ϕ can be expressed as a power law, equation (1), suggests the cumulative mass flux N_m (number per unit area time with mass m or greater) can be expressed

$$N_m = \pi \int_{m_T}^\infty N_m \, dm = C m_T^{-\alpha}$$

where α is the population index. With this assumption equation (19) becomes

$$\phi = 2C \int_0^{\pi/2} \cos\theta \sin\theta \, d\theta \int_0^\infty n_v \, dv m_T^{-\alpha}(I_T,\theta,v) \tag{20}$$

The threshold mass is from equation (12)

$$m_T = I_L 10^{5.297} v^{-4} (\cos\theta)^{-1}$$

But from equation (17)

$$m_T = \begin{cases} I_T 10^{5.297} v^{-4} (\cos\theta)^{-1} & \theta \le \theta_0 \\ 0.957 I_T 10^{5.297} v^{-3} \tan\theta & \theta \ge \theta_0 \end{cases} \tag{21}$$

where

$$\theta_0 = \sin^{-1}\left(\frac{1}{0.957}\right)$$

Equation (20) becomes

$$\phi = 2C I_T^{-\alpha} 10^{-5.297\alpha} \cdot \left[\int_0^\infty v^{4\alpha} n_v \, dv \int_0^{\theta_0(v)} (\cos\theta)^{1+\alpha} \sin\theta \, d\theta + (0.957)^{-\alpha} \int_0^\infty v^{3\alpha} n_v \, dv \cdot \int_{\theta_0(v)}^{\pi/2} (\cos\theta)^{1+\alpha} (\sin\theta)^{1-\alpha} \, d\theta \right] \tag{22}$$

It is convenient to introduce an average $\bar{m}$ defined as the mass of a just detectable meteor having average velocity and $\theta=45°$. From equation (21)

$$\bar{m}=0.957 I_T 10^{5.297} v^{-3} \tan 45° \qquad (23)$$

Equation (22) becomes

$$\phi=\frac{2C\bar{m}^{-\alpha}}{v^{3\alpha}}\left[(0.957)^{\alpha}\int_0^{\infty} v^{4\alpha} n_v\, dv \cdot\int_0^{\theta_0(v)} (\cos\theta)^{1+\alpha}\sin\theta\, d\theta+\int_0^{\infty} v^{3\alpha} n_v\, dv \cdot\int_{\theta_0(v)}^{\pi/2} (\cos\theta)^{1+\alpha}(\sin\theta)^{1-\alpha}\, d\theta\right] \qquad (24)$$

The first integral is the contribution from those meteors moving nearly along the line of sight that remain in a single resolving element for one integration time. Since θ_0 is typically 3°, this contribution is small and can be ignored. The integral over θ in the second integral must be evaluated numerically unless α is an integer. The lower limit $\theta_0(v)$ is a function of v, however, as may be seen in figure 4. This dependence is not strong for $\alpha\approx 1$. Therefore, an average value of $v=20$ km/s will be used which yields $\theta_0=3°$.

The velocity distribution was adopted from the work of Dohnanyi (1966), expressed as

$$n_v=\begin{cases} C_N v^{1.6} & 11.2\leq v\leq 16.6 \\ C_N 1.61\times 10^{7} v^{-4.3} & 16.6\leq v\leq 72.2 \end{cases} \qquad (25)$$

The normalization constant $C_N=.001153$. The $\langle v\rangle$ using this distribution is 19.2 km/s. The weighted average $\langle v^x\rangle/\langle v\rangle^x$ is shown in figure 5.

Equation (24) can be written

$$\phi=2\frac{\langle v^{3\alpha}\rangle}{\langle v\rangle^{3\alpha}} I(\theta_0) N_{\bar{m}_T} \qquad (26)$$

where $N_{\bar{m}_T}$ is the cumulative isotropic mass flux of meteoroids having mass $\bar{m}_T$ or greater, $\bar{m}$ is given by equation (23), and $I(\theta)$ is

$$I(\theta_0)=\int_{\theta_0}^{\pi/2} (\cos\theta)^{1+\alpha}(\sin\theta)^{1-\alpha}\, d\theta$$

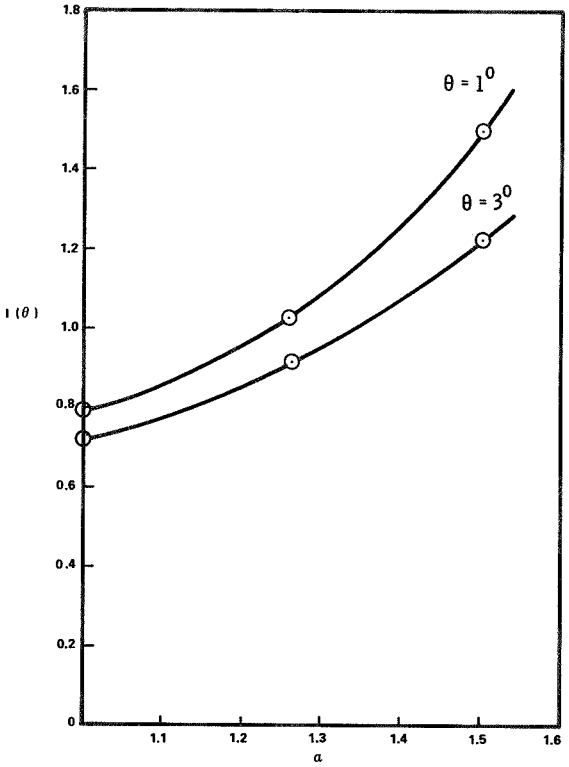

FIGURE 4.—The value of the integral $I(\theta_0)$ in equation (26) as a function of θ_0 and α.

Since $I_T=10^{-0.4\, m_v}$ and the observational results were found to be as follows, from equation (1):

$$\log\phi=-15.352+0.5053 m_v$$

$$\log\phi=-15.352-1.263\log I_T \qquad (27)$$

Differentiating the log of equation (22)

$$\frac{d(\log\phi)}{d(\log I_T)}=-\alpha$$

From equation (27) α is found to be 1.263. Using this value in figures 4 and 5,

$$\frac{\langle v^{3.76}\rangle}{\langle v\rangle^{3.76}}=2.48$$

$$I(\theta)=0.933$$

Combining equations (23), (26) and (27)

$$\log N_{\bar{m}_T}=-15.352-1.263(\log\bar{m}_T-1.466) \qquad (28)$$
$$-\log 2-\log 2.48-\log 0.933$$

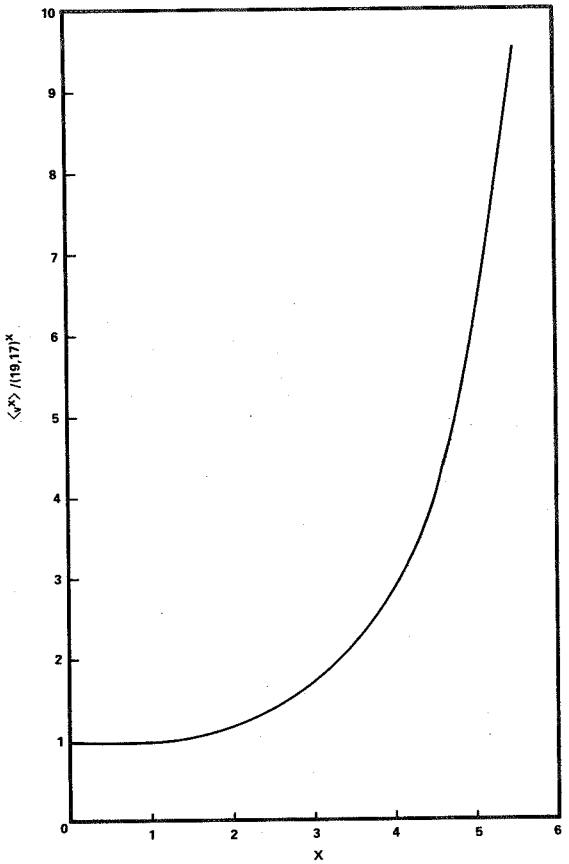

FIGURE 5.—The value of the moments of the velocity distribution computed from Dohnanyi's velocity distribution.

or

$$\log N_{\bar{m}_T} = -14.24 - 1.263 \log \bar{m}_T$$

The observed range from $m_v = 7$ to $m_v = 10$ corresponds to a mass range of $10^{-1.334}$ to $10^{-2.534}$ g. The results of equation (28) are compared with the existing distribution of meteors in figure 6. The result from the July 31 to August 9 expedition is also shown which contains the Perseids and δ-Aquarids. No attempt was made to alter the distributions in velocity and angle to account for the shower component.

COMPARISON WITH OTHER DATA

Figure 6 shows the relationship of the data obtained in this work with the current meteoroid mass distribution adopted by NASA (Cour-

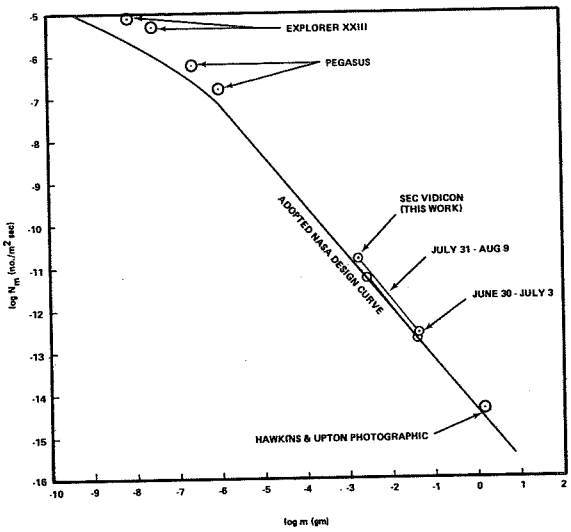

FIGURE 6.—Comparison of the results of this study with other work and with the adopted NASA meteoroid environmental design criteria. The observed data represent encounter frequency, whereas the design criteria are weighted to express penetration frequency.

Palais, 1969). Also shown for comparison is the Hawkins and Upton (1958) datum point based on photographic meteors, and the points obtained from the Pegasus (Clifton and Naumann, 1966) and Explorer XXIII penetration experiments (D'Aiutolo, 1965). These data have been analyzed in terms of encounter frequency, i.e., number incident per unit area time on a surface without regard to angle of incidence or velocity. The NASA design curve refers to the number capable of penetrating a surface per unit area time which can just be penetrated by a meteoroid with the specified mass under conditions of normal impact at the average velocity (assumed to be 20 km/s) and average density (assumed to be 0.5 g/cm^3). Integrating over the velocity and angular distributions weighted appropriately for penetration mechanics results in the penetration frequency being less than the encounter frequency by a factor of approximately 2 (Naumann, 1966).

The penetration data from Pegasus and Explorer XXIII were analyzed using recent calibration data (Naumann et al., 1969). The discrepancy between these data points and the NASA model is partially due to the difference between encounter frequency and penetration frequency,

but also includes the departure from linear size scaling in thin metallic targets. Again, the design curve was derived from the actual penetration data, using the conventional penetration formula, and will serve adequately as a design criterion so long as the same formula is used to convert back to penetration results. However, this departure should be considered in developing a true mass distribution.

CONCLUSIONS

A technique has been developed using the SEC vidicon LLLTV system as a threshold detector for faint meteors to obtain mass flux distribution data in the mass range from 1 to 100 milligrams. The analysis technique is based on peak intensities using the most recent values of luminous efficiency obtained from the Trailblazer measurements. The data are quite consistent with present photographic data at 1 gram and the satellite data at 1 microgram, and tend to confirm the adopted NASA meteoroid model.

It is recognized that these observations represent only one time during the year and may be subject to seasonal variations. Such effects are the object of a current investigation.

REFERENCES

Ayers, W. G., McCrosky, R. E. and Shao, C. -Y., 1970. Photographic observations of 10 artificial meteors, *Smithson. Obs. Spec. Rept.* No. 317.

Beyer, R. R., Green, M., and Goetze, G. W., 1966. Point-source imaging with SEC target, in *Advances in Electronics and Electron Physics*, **22A**, Academic Press, New York, 251–260.

Clifton, K. S., and Naumann, R. J., 1966. Pegasus satellite measurements of meteoroid penetration, *NASA Tech. Memo* **X-1316**.

Cook, A. F., Jacchia, L. G., and McCrosky, R. E., 1963. Luminous efficiency of iron and stone asteroidal meteors, *Smithson. Contrib. Astrophys.*, **7**, 209–220.

Cour-Palais, B. G., 1969. NASA space vehicle design criteria-environment. Meteoroid environment model—1969. (Near Earth to lunar surface), *NASA* **SP-8013**, Supt. of Documents, U.S. Govt. Printing Office, Washington.

D'Aiutolo, C. T., Kinard, W. H., and Naumann, R. J., 1965. Recent NASA meteoroid penetration results from satellites, *Smithson. Contrib. Astrophys.*, **11**, 239–251.

Dohnanyi, J. S., 1966. *Bellcomm* TR-66-340-1.

Hawkins, G. S., and Upton, E. K. L., 1958. The influx rate of meteors in the Earth's atmosphere, *Astrophys. J.*, **128**, 727–735.

Jacchia, L. G., Verniani, F., and Briggs, R. E., 1967. An analysis of the atmospheric trajectories of 413 precisely reduced photographic meteors, *Smithson. Contrib. Astrophys.*, **10**, 1–139.

Naumann, R. J., 1966. Near-Earth meteoroid environment, *NASA Tech. Note* **TN D-3717**.

Naumann, R. J., Jex, D. W., and Johnson, C. L., 1969. Calibration of Pegasus and Explorer XXIII detector panels, *NASA Tech. Rept.* **TR R-321**.

6. Determination of Meteor Parameters Using Laboratory Simulation Techniques

J. F. Friichtenicht and D. G. Becker
TRW Systems Group
Redondo Beach, California

Atmospheric entry of meteoritic bodies is conveniently and accurately simulated in the laboratory by techniques to be described which employ the charging and electrostatic acceleration of macroscopic solid particles in the 0.02 to 1 μ diameter range. Velocities from below 10 to above 50 km/s are achieved for particle materials which are elemental meteoroid constituents (e.g.: Fe, Si, Mg) or mineral compounds with characteristics similar to those of meteoritic stone (e.g.: $FeTiO_3$). The velocity, mass, and kinetic energy of each particle are measured nondestructively, after which the particle enters a target gas region. Because of the small particle size, free molecule flow is obtained at target pressures ≦10 torr. At typical operating pressures (0.1 to 0.5 torr), complete particle ablation occurs over distances of 25 to 50 cm; the spatial extent of the atmospheric interaction phenomena (luminous trails, ionized wakes, etc.) is correspondingly small, simplifying many experiments. Procedures have been developed for measuring the spectrum of light from luminous trails and the values of fundamental quantities defined in meteor theory: heat transfer coefficient λ, drag coefficient Γ, ionization probability β, and photographic luminous efficiency τ_{pg}. Results of these measurements are presented, with emphasis on recent, improved evaluations of τ_{pg} and β over wide velocity ranges; it is shown that the laboratory values of τ_{pg} for iron are in excellent agreement with those for 9 to 11 km/s artificial meteors produced by rocket injection of iron bodies into the atmosphere. Also discussed in some detail is the relevance of these measurements to the interpretation of meteor observations and the methods of inferring from them numerical values of τ_{pg} and β for natural meteors.

Simulated meteors, in the sense that we shall use the term, are phenomena which occur when macroscopic particles of known composition are accelerated to meteoric velocities *in the laboratory* and then injected into simulated "atmospheres" of known gas composition and density. These may be contrasted with artificial meteors, which are created by rocket injection of manmade bodies into the Earth's atmosphere. In this paper we intend to limit ourselves to a discussion of laboratory meteor simulation techniques and experiments, referring to artificial meteor experiments and to natural meteor observations only to compare results. We do not intend to imply by this decision that meteor simulation is generally superior to the other two methods; rather, we regard each of them as having its own unique advantages and each as being most suitable in turn in different experimental contexts.

Initially received with caution and some skepticism, laboratory meteor simulation is now beginning to be recognized as an experimental

technique of much potential value for attacking a number of unresolved or poorly resolved problems in meteor physics, certain of which have proven stubbornly unyielding to conventional observational methods. For fundamental measurements of basic meteor processes, this technique possesses two very important advantages. One is that it frees the experimenter from the necessity of waiting upon nature: It makes it possible for him to create "meteors" in the convenience of his own laboratory, in any desired quantity, and with all variables under his complete control. The other is that it enables him to separate complex meteor interactions into individual components more easily examined. As an example, he may choose to employ monoconstituent particles or monoconstituent atmospheres, changing the constituents one by one and thereby obtaining basic data from which the interaction of a multiconstituent meteoroid with a complex atmosphere may, hopefully, be synthesized. The price paid for these advantages is that the experimenter accepts the burden of demonstrating that the simulation is a meaningful approximation to a natural meteor and of developing methods for achieving the desired synthesis. These are questions that we plan to deal with later at length.

A key factor affecting the accuracy of the simulation is the flow conditions in the atmospheric gas. Most meteor phenomena appear in the extreme upper atmosphere, where low density results in free molecule flow. It is readily shown that to produce free molecule flow under practical laboratory conditions, particle size should be quite small. Calculations of mean free path as a function of pressure indicate that a 1-μ diameter particle experiences free molecule flow at pressures as high as several torr, and at such pressures a meteor is produced with a total trail length of a few tens of cm. A 1-cm diameter particle, on the other hand, requires gas pressures below about 10^{-3} torr for free molecule flow, and then the meteor which it produces will have a trail length measured in kilometers, far too long to be contained in reasonable laboratory apparatus.

Besides being small in size, the particles must obviously attain meteoric velocities; optimally, particles should be available at any and all velocities between 10 and 70 km/s. These considerations rule out light gas guns and other ballistic accelerators. Of the available microparticle hypervelocity systems, only electrostatic acceleration presently appears to combine small particle size with truly meteoric velocities. The latter technique provides in addition a large, continuous flux of particles, which allows considerable volumes of data to be acquired in a relatively brief operating time.

Early efforts to accelerate microparticles to hypervelocities began in the late 1950's and were largely motivated by a desire to study possible impact and erosion damage to spacecraft that might result upon their passage through the "dust cloud" that was then thought by many to encircle the Earth. Shelton et al. (1960) developed a method of electrically charging micron-sized spherules of a conducting powder by contact and succeeded in accelerating them in an electrostatic field. They also developed detectors that utilized the particle charge to provide nondecelerative measurement of the mass, velocity, and lateral position (with respect to the flight axis) of each particle. Friichtenicht (1962) adapted the Shelton particle charger to a commercial 2 MV Van de Graaff proton accelerator, obtaining thereby a conveniently operated research tool capable of accelerating 1μ diam iron microparticles to velocities up to about 15 km/s. This is the basic facility still employed for meteor simulation; it has, however, been further improved through the introduction of newer particle detectors developed by Hansen and Roy (1966) and time-of-flight coincidence techniques employing special instrumentation described by Roy and Becker (1971). These improvements have significantly increased the signal-to-noise ratio for particle detection, and their use has revealed the formerly unsuspected presence of numerous submicron-sized particles with velocities in the 50 km/s range in the Van de Graaff "beam." A second approach to higher particle velocities has been to increase the accelerating voltage. Becker et al. (1965) have described a linear accelerator to accomplish this; the linac became operational in 1967, but to date it has proved most useful in other types of experiments and will not be discussed further.

Until fairly recently, carbonyl iron and carbon black were the only commercially-available powders with properties suited to the Shelton particle charger. Since iron is a major meteoroid con-

stituent, the early meteor simulation experiments were conducted almost exclusively with this material. But within the last few years there have occurred major advances in the manufacture of fine powders which have greatly increased the number of usable particle materials. Some of these are also meteoroid constituents, some are of interest for purposes of comparison, and some are compounds similar to certain components of meteoritic stone.

Although, as we have noted, microparticle acceleration was first developed to create an experimental tool for cratering and erosion studies, it was observed during the early 1960's that when a hypervelocity microparticle entered a low-pressure gas environment, it produced a luminous trail visible to the naked, dark-adapted eye. The similarity to natural meteor phenomena was obvious, and this observation provided the impetus for attempts to simulate meteors. The first detailed laboratory study of the interaction of high velocity microparticles with gases was performed by Slattery, Friichtenicht, and Hamermesh (1964). They examined deceleration, particle heating, and production of luminous trails, and experimentally determined values for the drag coefficient Γ and heat transfer coefficient Λ as defined in meteor theory for velocities from below 4 to 6–7 km/s. Later, Friichtenicht, Slattery, and Tagliaferri (1968) measured the luminous efficiency of iron particles interacting with air at velocities from 20 to 35 km/s, and Friichtenicht (1969) determined the heat transfer coefficient in this velocity regime. Detailed spectral measurements of the iron luminosity were also performed by Tagliaferri and Slattery (1969). Finally, recent experiments by Becker and Friichtenicht (1971) have resulted in a more accurate evaluation of iron luminous efficiency over the entire velocity range from 11 to 47 km/s. These new data can, as we shall see, be directly compared over part of the velocity spectrum with results obtained by other methods, and such a comparison supplies important evidence regarding the accuracy of the simulation process. Becker and Friichtenicht also measured the luminous efficiency of copper from 11 to 47 km/s, thereby laying the groundwork for an understanding of the relationship between luminous efficiency and particle composition.

The discovery that visual and photographic meteors could be simulated led to attempts to simulate the ionized wakes of radiometeors. Such wakes were found to exist in the laboratory. They were studied in the specific meteor context by Slattery and Friichtenicht (1967), who found values for the ionization probability of simulated iron micrometeors entering air and argon atmospheres at 20 to 40 km/s, and in a more general context of collisional ionization theory by Friichtenicht, Slattery, and Hansen (1967). These measurements were extended by Friichtenicht and Becker (1971) to copper at 16 to 38 km/s and to lanthanum hexaboride at 20 to 112 km/s; the latter values are important to the understanding of collisional ionization processes involving compounds and to the behavior of the phenomenon at high velocities.

In the following discussion we will review in detail the laboratory techniques that are employed in these and other simulated meteor experiments. We will also examine the most recent results that have been obtained in our programs of measurement of the important meteor parameters. We hope to demonstrate from those results that, as we have long believed, these laboratory techniques do in fact provide a meaningful and accurate simulation of natural meteor processes.

TECHNIQUES FOR MICROPARTICLE ACCELERATION AND DETECTION

Since meteor simulation ultimately depends upon the ability to accelerate microparticles and to measure their parameters after acceleration, let us begin by examining the equipment and techniques that fulfill these functions. We will also consider certain accessory instrumentation which provides greater control over the accelerated particles and/or improves the signal-to-noise ratio for particle detection.

It was seen in the introduction that the meteor simulation process is based upon the particles being electrically charged. This charge is imparted to them by the device shown in figure 1, which we term a "particle injector" (since it injects the charged particles into the accelerating field) and which is identical in concept to the injector first constructed by Shelton et al. (1960). The principal components of the injector are the powder reservoir, the tongue, and the charging chamber;

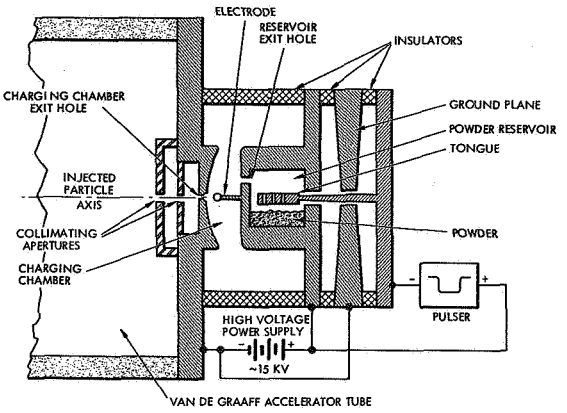

FIGURE 1.—Simplified diagram of particle injector. With no pulse applied to tongue, powder remains at rest. When tongue is pulsed negatively, powder is set in motion. Some particles diffuse through reservoir exit hole and enter charging chamber. There they eventually come in contact with electrode tip, which is at high field. On contact the particle receives a high charge, and the fields propel it out through the chamber exit hole and collimating apertures. Ground plane creates high fields along tongue shaft to inhibit backward diffusion of powder.

the latter includes a needle-like charging electrode and a shaped ground plane containing an exit aperture. Normally the powder reservoir and the tongue above it are both maintained at a positive potential of ~15 kV, the reservoir is field-free, and the powder is at rest. When particles are to be charged, the tongue is pulsed toward ground for a few milliseconds. This imposes an electric field within the reservoir, under whose influence the powder is set into violent motion. A number of particles will diffuse through the reservoir exit hole and will find themselves in the charging chamber. (Diffusion of particles backward along the shaft supporting the tongue is discouraged by high fields in this region.) In the chamber particles oscillate back and forth between the surfaces, exchanging charge at each surface and moving essentially as they would if specularly reflected. The shape of the chamber is such that particles move inward toward the charging electrode, whose tip has been formed into a ball with a diameter comparable to that of the particles. The electrode tip is obviously a region of very high field. When a particle contacts this tip, it receives a correspondingly high charge and is then propelled by this field through the chamber exit hole. Note that the entire procedure takes place *in vacuo*.

The injector will normally be mounted on the end of the accelerator tube of the 2 MV Van de Graaff (Friichtenicht, 1962). Each injected particle is then accelerated through the full potential across the tube. The injector design is such that the electrostatic focusing system present in the Van de Graaff (which, it will be recalled, was originally designed for use with a proton or positive ion source) functions normally. At a distance of a meter or so from the Van de Graaff baseplate, the particle "beam" can be focused to a diameter on the order of 2 mm. This "beam" is not continuous, but instead consists of from one to a few hundred particles for each tongue pulse applied to the injector. Pulsing of the injector is controlled by circuitry in the Van de Graaff control console and in the high voltage terminal of the machine; these are coupled by insulated rods originally present in the Van de Graaff as purchased and by a pulsed light beam system developed by us for this purpose. The potential applied to the charging electrode, the amplitude of the tongue pulse, and the pulse repetition rate can all be adjusted from the control console. Varying the pulse amplitude determines the number of particles injected with each pulse. The repetition rate can be set at any of six fixed values from 10 to 600 pulses/minute, or the injector may be pulsed manually by a pushbutton. The high particle flux is a very important feature of the system, since it results in a short data acquisition time—especially when, as will be seen, only a small fraction of the total flux is usable in the experiment.

It is evident that the operation of the particle injector depends upon the conducting properties of the powder with which it is filled. It was once thought that the powder must be a good conductor, but more recent research has shown that materials with bulk resistivities as high as about 10^{10} ohm-cm can be employed. Other important requirements for a usable powder are that it flow readily, to prevent agglomeration and subsequent clogging of the injector apertures and to insure that single particles, rather than clumps, are charged, and that its particles be reasonably uniform in size. Table 1 lists those materials which have so far been successfully tested. The table is

by no means exhaustive and is limited almost entirely by the time available in which to try different materials. Included in the list are three of the major metallic constituents of meteoritic stone: silicon, iron, and aluminum. The fourth, magnesium, has not yet been tested, but the properties of this metal are so similar to those of aluminum that little difficulty is expected in its use. Not all of the tabulated materials have been used extensively enough for us to acquire detailed data on their performance. For those that have been, we list in table 2 the maximum velocities that have been measured and the corresponding particle masses and radii. It is clear that most materials attain velocities in the neighborhood of 50 km/s, and that this value is considerably exceeded in a few cases.

TABLE 1.—*Materials Usable for Contact Charging and Acceleration*[a]

Metallic elements	Intermetallic elements	Alloys	Compounds
Ag	C	316 stainless steel[b]	$CaTiO_3$[b]
Al	Si		CrB
Co[b]			$FeTiO_3$
Cu			LaB_6
Fe			MoB
Ni			NiAl
Ta[b]			PbTe
Ti[b]			SiC[b]
U			TiC[b]
W[b]			TiN[b]
			TiO[b]

[a] Includes only materials actually tested as of January 1971.

[b] Materials so noted have been bench-tested in standard injectors; all others have been accelerated by the Van de Graaff as well.

We may now examine the factors that determine accelerator performance in more detail. A particle with a total charge q and a mass m that has been accelerated through a potential V_a attains a velocity v given from energy conservation as

$$v=\left(2\frac{q}{m}V_a\right)^{1/2} \tag{1}$$

First, the Shelton injector charges all particles to a constant surface field intensity, and so the charge q should be proportional to particle area, or equivalently to r^2 where r is the particle radius. (We assume here that the particles are spherical.) Since the mass m is proportional to r^3, we would expect v to vary as $r^{-1/2}$. Actual data for iron (the material which has been used for the longest time and for which we have the most complete data) are presented in figure 2, where the quantity $v/V_a^{1/2}$ has been plotted as a function of r. The data deviate somewhat from the theoretical behavior predicted by Shelton et al. and can instead be approximated by the expression

$$v/V_a^{1/2}=4.6\times10^{-3}\,\rho^{-1/2}r^{-3/4} \tag{2}$$

in which ρ is the particle density (7.85×10^3 kg/m^3 for iron) and all units are MKS. Our experience with other materials tends to indicate

TABLE 2.—*Maximum Velocities Achieved for Various Particle Materials Accelerated Through 1.5 MV*

Material	Velocity (km/s)	Mass (kg)	Radius (microns)
Aluminum	54.8	4.28×10^{-19}	0.034
Carbon	35.0	1.80×10^{-18}	0.058
Chromium boride (CrB)	50.7	4.26×10^{-19}	0.025
Copper	48.7	3.62×10^{-19}	0.021
Iron (carbonyl)	68.6	3.52×10^{-19}	0.022
Iron metatitanate ($FeTiO_3$)	43.4	3.51×10^{-19}	0.026
Lanthanum hexaboride (LaB_6)	112.0	9.94×10^{-20}	0.021
Lead telluride (PbTe)	39.3	7.06×10^{-19}	0.027
Molybdenum boride (MoB)	55.7	1.92×10^{-19}	0.018
Nickel aluminide (NiAl)	71.6	1.68×10^{-19}	0.019
Silicon	50.3	5.47×10^{-19}	0.038
Silver	30.8	7.98×10^{-19}	0.026

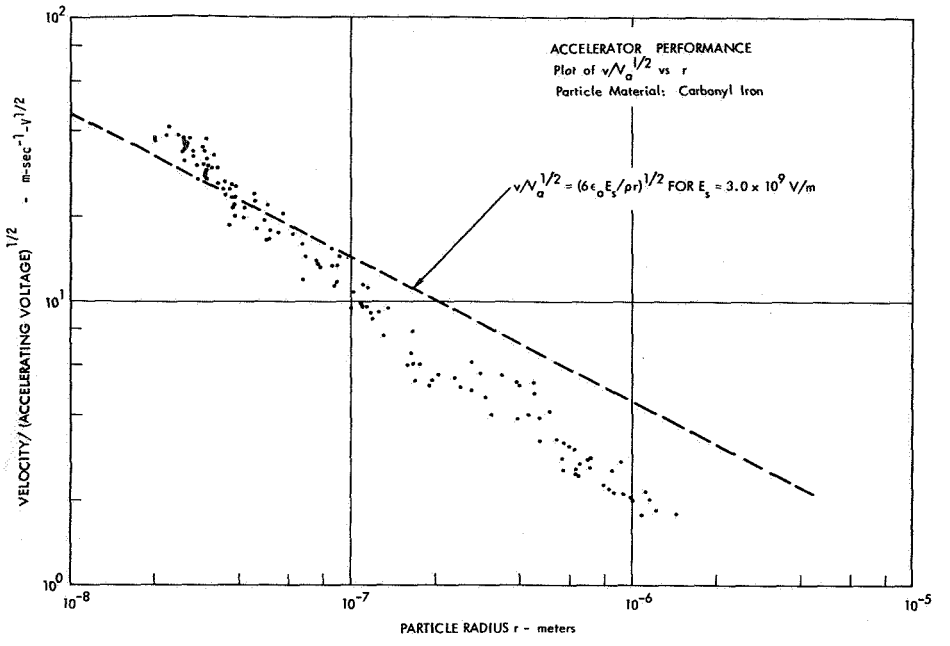

FIGURE 2.—Plot of $v/V_a^{1/2}$ vs r for iron particles. Straight line is theoretical relationship proposed by Shelton et al. (1960); data are actually proportional to $r^{-3/4}$.

that they generally follow equation (2) except for a constant factor. These data show that the highest velocities are attained by the smallest particles, and this is the reason why a powder should contain particles of sufficiently uniform size to at least exclude larger, more massive particles that would attain relatively low velocities. Another consequence of the data follows from our remarks about the relationship between charge and radius. Although the highest velocity particles have the highest charge-to-mass ratios, they also have the lowest absolute value of charge. They are therefore the hardest to detect, which accounts for the fact that these small, fast particles were not even known to be present until steps were taken to improve the signal-to-noise ratio for particle detection.

A basic particle detector appears in figure 3(a). The detector consists of three concentric tubes, the outer two being grounded with the inner one connected to a charge-sensitive preamplifier. When a charged particle enters this structure, it induces an equal charge on the inner tube which remains for only as long as the particle is actually within the inner tube. This induced charge is amplified as a voltage signal by the preamplifier. The preamplifier output, seen in figure 3(b), is a square pulse whose amplitude is proportional to particle charge q and to the ratio C_i/G, where C_i and G are the capacitance to ground of the detector structure and the preamplifier gain, both of which are known constants. The width of the pulse is of course inversely proportional to particle velocity and depends otherwise only on the known length of the inner tube. (The grounded outer tubes remove fringing effects and insure that the edges of the pulse are sharp.) Knowing the charge, velocity, and accelerating potential, the particle mass can be computed from equation (1); if the particles are spherical and their density is known, the radius is easily found.

Two other useful types of particle detector can be seen in figure 3. In figure 3(c), the inner tube has been split into two parts, between which is placed a system of horizontal and vertical plates. This detector produces a four-part output signal. On passage of a particle through the tubes, the signal has an amplitude proportional to q as before. However, the signal in the regions of the plates is also proportional to the distance between the particle flight axis and the grounded plate; a particle whose flight axis coincides with the de-

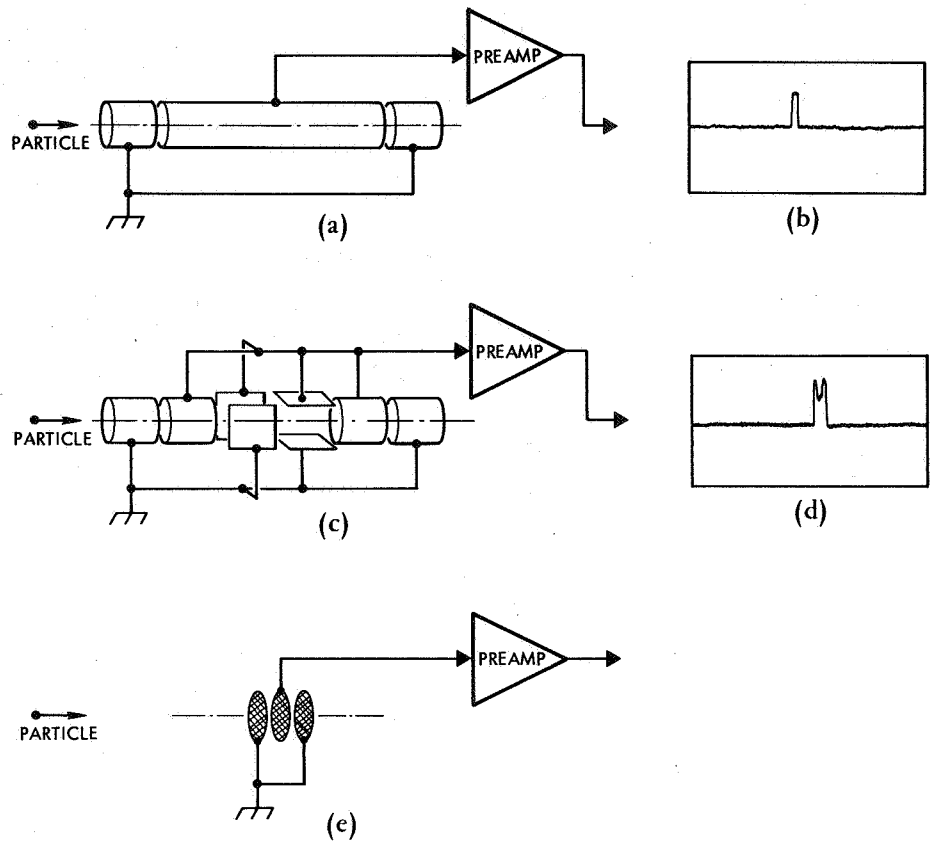

FIGURE 3.—Three types of particle detectors, with some representative output signals. (a) Detector for charge and velocity measurement. (b) Output signal from (a); amplitude is proportional to particle charge and width to transit time through the central tube. (c) Detector for lateral position measurement. (d) Output signal from (c); ratio of inner to outer parts of composite pulse gives lateral position with respect to horizontal and vertical axes; particle is centered when ratio = 0.5. (e) Timing mark detector, with tubes replaced by close-spaced grids; output is a sharp pulse whose peak coincides with particle passage through the central grid.

tector symmetry axis produces a signal whose amplitude is half that from the tubes. A typical composite output signal is shown in figure 3(d), and it is clear that this signal permits one to determine the lateral position of the particle in two coordinates. Such detectors are employed for focusing (by adjusting until the lateral positions of all particles are the same) and for system alignment (by moving the detector and other apparatus until the particles are centered in the detector bore). In figure 3(e), the detector inner tube has degenerated to a screen. A particle entering this detector produces a narrow pulse as it passes the screen, which can be used as a position marker. A pair of such detectors placed a known distance apart form a time-of-flight range for accurate particle velocity measurement.

It can be shown that the signal-to-noise ratio for particle detection is proportional to $C_i^{-1/2}$, which implies that the detector input capacitance must be made as small as possible. This is achieved in part mechanically and in part electronically by the "bootstrapped" preamplifier developed by Hansen and Roy (1966). The grid detector of figure 3(e) has an especially low structural capacitance and is therefore attractive in timing operations with small, high velocity particles.

Selection of Particle Parameters

We have found that it is essentially impossible to obtain powders with particle size variations less than about two orders of magnitude. A typical powder usually contains particle radii from about 1 or 2μ down to perhaps 0.02μ, and further size sorting is impractical. (Particles with radii greater than a few microns can be eliminated and should be, unless there is a specific reason for working with relatively massive low-velocity particles.) According to figure 2, the velocities of particles charged and accelerated from such a powder mix will vary over a wide range. In principle, if one is performing an experiment covering a wide velocity spectrum, one can simply accept all particles at random, relying on the velocity distribution inherently resulting from particle size variations to cover the range. In practice, however, low velocity particles will predominate, both because of their greater actual number and the fact that their larger signals will be much more prominent in the detectors. (Remember that large, slow particles have a higher absolute value of charge.) Therefore, in many cases it would be preferred that all of the instrumentation in an experiment respond only to particles with velocities in a specified range. Additionally, there arise instances in which out-of-range particles may unduly perturb the experiment, and then it is necessary to physically prevent the unwanted particles from interacting. Equipment has been developed to fulfill all of these functions, and the presence of this equipment has become essential to the proper operation of most simulated meteor experiments.

Several different means have been employed to achieve selection of desired velocities. The one in current use is the time interval selector and proportional delay generator discussed by Roy and Becker (1971); the reader is referred to their paper for a detailed description of the workings of this instrument. Operationally, it functions as follows: Two inputs are provided, which are connected to the outputs of a pair of particle detectors of the type in figure 3(e), assembled as a time-of-flight range. The instrument examines the flight time of all particles passing through this range. When it is determined that a given measured flight time lies within the range for which the instrument is preset, then and only then are a series of output-trigger pulses generated. One pulse appears instantaneously as soon as the flight time measurement is completed, and the others are separately delayed in time by a multiple or submultiple of the measured flight time; the multiplying factors are constants and can be set by the experimenter to any value between 0.1 and 10.0. A little thought will show that these proportional delays appear when the particle has reached a given point in space irrespective of the particle velocity. One of the two delays may be used to trigger a downstream charge detector [of the type shown in fig. 3(a)] just as the particle reaches it, and the other is usually used to trigger the instrumentation that records interaction effects just as the particle enters the experimental region. In this way, not only is data acquisition limited to a preset velocity interval, but also flight-time coincidence is introduced. That is, all downstream instrumentation is active only for that brief time in which a desired particle is expected, which reduces the effective bandwidth for data recording and thereby lowers the effective system noise level. Without such coincidence techniques, many of the small, fast particles would not be observed.

The fact that the particles are charged makes it relatively easy to remove unwanted particles from the "beam." A transverse electrostatic field can be used to deflect all particles away from a suitable aperture. When a desired particle appears, the time interval selector output trigger causes the removal of the field for a time sufficient to permit the desired particle to pass undeflected. Figure 4 illustrates the simple scheme that we have employed to accomplish this. A pair of parallel plates is installed along the particle flight path. The passive plate is held at a low dc voltage, and the active plate is connected both to a high-voltage dc power supply and to the plate of a pulse tube which is biased at cutoff. The potential difference between the plates is then almost 10 kV, and if the plates are 10 to 15 cm long, the transverse field is more than ample to deflect all particles away from the exit aperture, whose diameter is about 1 cm. When a trigger pulse is received from the time interval selector warning that an in-range particle is about to enter the deflector, the trigger activates a pulse generator.

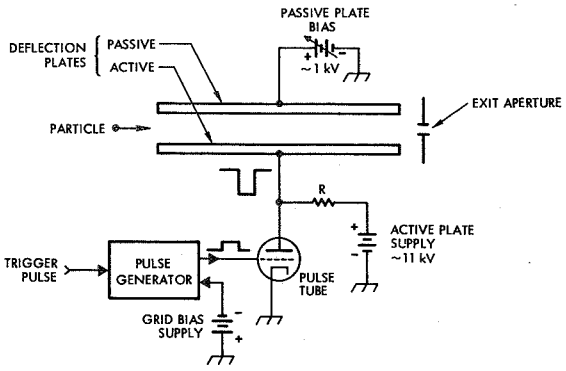

FIGURE 4.—System for controlled particle deflection. Pulse tube is normally in cutoff and 10-kV potential difference appears across deflection plates; all entering particles are deflected from exit aperture. When a trigger arrives signaling the approach of an acceptable particle, pulse generator applies a positive pulse to tube grid, causing current to be drawn through R and dropping the active plate potential to ~1 kV so that particle passes undeflected. Passive plate bias is adjusted for zero residual deflection of acceptable particles.

This unit produces a positive pulse whose width is set to exceed the time required for the particle to pass completely through the plates and whose amplitude is sufficient to drive the pulse tube into saturation. The pulse is applied to the pulse tube grid, causing current to be drawn in the plate circuit so that almost all of the supply voltage is dropped across plate resistor R. The active plate thus falls to a low voltage, which is equal to the small dc voltage on the passive plate. (The latter voltage is determined by experiment, adjusting it until there is no residual deflection of acceptable particles.) The transverse field between the plates hence drops to zero until after the desired particle has passed.

There occasionally arise a few experiments in which it is desired that all particles have almost the same mass. Equation (1) shows that the particle mass can be controlled by limiting both the particle velocity and the charge. Since the latter is proportional to the amplitude of the particle detector output signal, it can be controlled simply by feeding this signal through an appropriate window discriminator that generates an output trigger only if the amplitude lies within the limits of the window. This trigger and the one from the time interval selector are combined in a coincidence circuit; if and only if both triggers are present, the circuit turns off the particle deflector.

Integration of the Equipment Into a Facility

In figure 5, all of the equipment described above has been combined and assembled to form the basic meteor simulation facility. By now the operation of the various parts of this facility will be familiar. Particles are charged in the particle injector, accelerated and focused by the 2 MV Van de Graaff, and then enter the analysis region. There they encounter a pair of detectors set up as a time-of-flight range. The detector outputs are fed to the time interval selector and proportional delay generator, which searches for particles with in-range velocities. If mass selection is desired, the time-of-flight range is immediately followed by a charge detector connected, as we have seen, to a window discriminator. The undelayed output of the time interval selector and the window discriminator output are combined as previously discussed in a coincidence circuit, whose output triggers the deflector. Downstream from the deflector is another particle charge detector. Its output will be recorded and employed later to compute the actual particle mass and velocity prior to its entrance into the experimental region. Data recording is generally by a multitrace oscilloscope operated in the single-sweep mode and fitted with a trace-recording camera. One oscilloscope trace is triggered by the first proportionally-delayed trigger from the time interval selector unit; this trigger always occurs at position x_1, located just before the entrance to the charge detector. The second trace records the data from the experimental interaction; it is triggered by the second proportionally-delayed trigger when the particle reaches position x_2. The second delay multiplying factor is adjusted to make location x_2 coincide with the point in space where the interaction under study first begins.

There are several possible variations to the basic system, depending upon the nature of the experiment. The first charge detector, window discriminator, and coincidence circuit are of course omitted when, as in the majority of experiments, mass selection is unnecessary. The deflector may also be omitted if out-of-range particles will not disturb the experiment. (In any event, data from

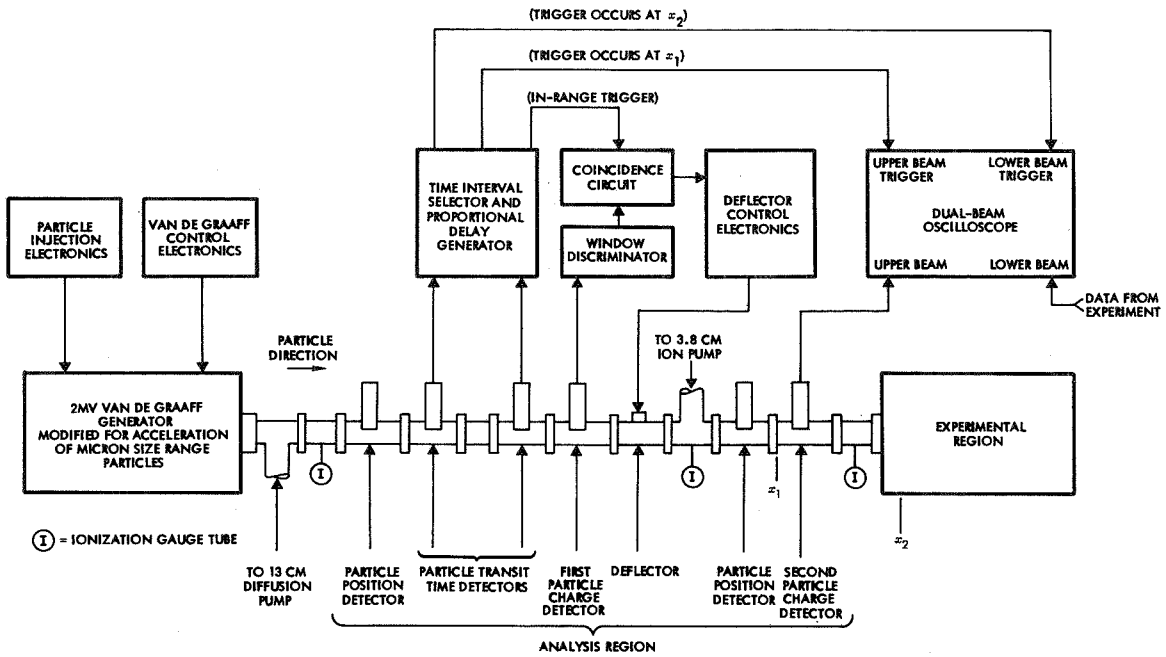

FIGURE 5.—Facility employed for simulated meteor experiments; see text for functions of major components and modifications used in certain cases. Position detectors are used only for initial alignment and focusing of the particle "beam."

such particles will not be recorded because the data recording oscilloscope will not have been triggered.) Finally, it has been observed in certain instances that if the vacuum in the analysis region is not sufficiently good, some particles may lose charge during their passage through the analysis region. Any loss of charge results in a false mass measurement and is to be avoided. If we suspect that this phenomenon is likely to occur in a given case, we often replace the single downstream charge detector with two detectors spaced a considerable distance apart and determine the charge from both detector outputs. When the values disagree, the datum is rejected.

The vacuum within the analysis region, the Van de Graaff accelerator tube, and the particle injector is maintained in the 10^{-5} to 10^{-6} torr range by a 13 cm (nominal 4-in. size) oil diffusion pump assisted by a 3.8 cm ion pump.

Data Reduction System

Because of the large volume of data generated in most of our simulated meteor experiments, we have developed a system of semiautomatic data reduction. We showed above that the raw data are usually contained in one or more oscilloscope trace photographs. The traces include the detector signal [fig. 3(b)] whose amplitude and width must be reduced to particle charge and velocity, and also various other signals containing data relating to the interaction under study. Reduction of the latter almost always involves measurement of one or more pairs of time/amplitude coordinates. The photographs are placed in a Telereader* unit, which projects them onto a screen with a pair of X-Y movable crosshairs. When these crosshairs are moved, their positions are continuously digitized in the Telereader; the origin for the position coordinate system can be set by the experimenter to coincide with an appropriate feature of the oscillogram. The experimenter moves the crosshairs so as to measure the particle detector signal width and amplitude and the coordinates of interest in the interaction signal.

* Registered trademark.

When each measurement is complete, the digitized data are automatically transferred to punch cards, each of which is simultaneously tagged with an identifying number in order that a given interaction and the parameters of the specific particle producing it are always uniquely correlated. The completed card deck is then fed to a high-speed digital computer where the data are operated on and combined with supplied constants. For each particle and its corresponding interaction, the computer prints out particle velocity, charge, mass, energy, radius, and momentum, and the interaction data reduced to meaningful physical units and normalized, if desired, to any of the particle parameters the experimenter may select.

This system has most of the advantages of fully automatic data acquisition, requiring as it does only manual read-in of the data. We regard this too as an advantage, however, because it enables the experimenter to utilize his own scientific judgment in determining whether any given datum may be spurious and in deciding how a given oscillogram must be interpreted. Our experiences with complete automation in which individual data cannot be judged indicates that such systems are less than satisfactory and can introduce serious errors.

INSTRUMENTATION FOR SIMULATED METEOR MEASUREMENT

Having seen how microparticles are accelerated to meteoric velocities, controlled, and detected, we next must investigate how these particles are made to create a simulated meteor and how the properties of the meteor may be measured. It is apparent that the particles must interact with a gaseous environment in order that a meteor be produced. As we have already seen that the analysis phase of the particle flight occurs *in vacuo*, it follows that the first problem is to introduce the particle into a downstream gas region without deteriorating the upstream vacuum. Simultaneously, the pressure and composition (if other than air) of the target must be controllable. Finally, the results of the particle-gas interaction must be observed, recorded, and measured; in all of the experiments to be discussed later, the result to be observed is either photon emission or ionization.

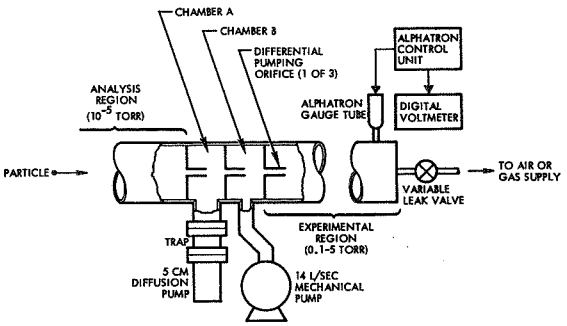

FIGURE 6.—Sketch of differential pumping and target gas control systems. If the pressure in the experimental region is to be below 1 torr, chamber B and the mechanical pump can be eliminated.

A differential pumping system is employed to allow the particles to make a transition from high vacuum to gas. The system is shown schematically in figure 6. The analysis region and the experimental region are separated by two intermediate chambers linked by small orifices. The chamber nearest the "gas" side of the system is pumped by a 14 l/sec mechanical pump, and the one nearest the "vacuum" side is connected to a trapped 5-cm oil diffusion pump. The orifices connecting the chambers are designed to have gas conductances much lower than the pumping speeds of the pumps. (Typical orifice dimensions are 1.3 to 2.5 mm diameter and 2.5 to 5 mm length.) Gas is admitted to the experimental region through a precision variable leak valve. The pressure in this region is carefully monitored, usually by an Alphatron* vacuum gauge whose control unit has been modified to digital voltmeter readout for greater accuracy and which has been calibrated against a McLeod gauge. If the pressure in the experimental region is to be less than about 1 torr, the mechanically-pumped chamber can be dispensed with. Because of the small orifice diameter through which all particles must pass, excellent focus of the particle "beam" and good axial alignment of the orifices with the "beam" axis are essential.

None of the simulated meteor phenomena that we have studied to date have shown any particular dependence on absolute gas pressure, although we have always investigated for the possible presence

* Registered trademark.

of such effects. Therefore, adjustment of the gas pressure is not especially critical, provided that it is known and that two limits are observed. The upper limit is set by the requirement that the particle experience free molecule flow. Suppose we assume, conservatively, that free molecule flow ceases when the mean free path ℓ in the gas falls below $10d$, where d is the particle diameter. If the gas molecules are approximated by rigid spheres, the mean free path and gas pressure p are shown in standard texts (cf. Hirschfelder et al., 1954) to be related according to

$$\ell = \frac{kT}{1.3p\sigma} \tag{3}$$

where k is Boltzmann's constant, T the absolute temperature, and σ the gas kinetic cross section, generally approximated as 3×10^{-15} cm^2 for air. Using this expression with $T=300°$ K, $\ell=10d$, and $d=1\mu=10^{-4}$ cm, we find that $p=8$ torr. This, then, is the upper pressure limit. The lower pressure limit is set merely by the fact that the meteor phenomenon must be completely contained within the experimental apparatus, since data analysis is considerably simplified when it is known that particle ablation has been complete and that the meteor has been observed over its entire length. The minimum pressure that produces this condition is most easily found by trial and error; it is typically on the order of 0.1 torr for fast, small particles in air, rising to perhaps 0.5 torr for 1μ diameter particles at $\sim$10 km/s.

The phenomenon of meteor luminosity is generally studied through the use of one or more photomultiplier tubes (PMT) placed transverse to the particle flight axis. Since the luminous trails of the smaller particles are quite faint, the PMT's must be sensitive. They must also cover the entire spectral range of interest, which in our experiments has been the photographic meteor spectrum from 3300 Å to 5200 Å. We have obtained satisfactory service from RCA types 8575 and 6199, Centronic type P4242B, and one or two others. Our PMT windows are generally acrylic plastic, which has a sharp cutoff at 3400 Å. (This is close enough to the edge of the photographic spectrum for most purposes.) Again because of the very low light intensities, it is necessary to integrate the photocurrent at the PMT anode in order to obtain usable signals. We therefore measure total light energy rather than intensity, and our data analyses must take this into account.

Figure 7 shows the simple setup that we employ to measure the total light energy radiated from a simulated photographic meteor. Note that two PMT's are used, each viewing the luminous trail through a long window, and that one PMT has markers placed in its field of view to block the light as the meteor passes behind the marker. It is clear that neither PMT integrated output directly measures the total radiated energy, since the solid angle subtended by the PMT at the instantaneous particle position is small and is also constantly changing. However, a theoretical relationship can be derived between the PMT output signal and the total radiated energy which permits one to compute the latter after measuring the fraction of the energy collected at the time that the meteor disappears behind the marker. Another feature of the setup is that an additional delayed pulse from the time interval selector-proportional delay generator (see fig. 5) is generated at position x_3 near the end of the chamber. This pulse is added to one of the PMT outputs and serves to insure that the meteor has terminated, i.e., that all possible light has been collected, before it passes

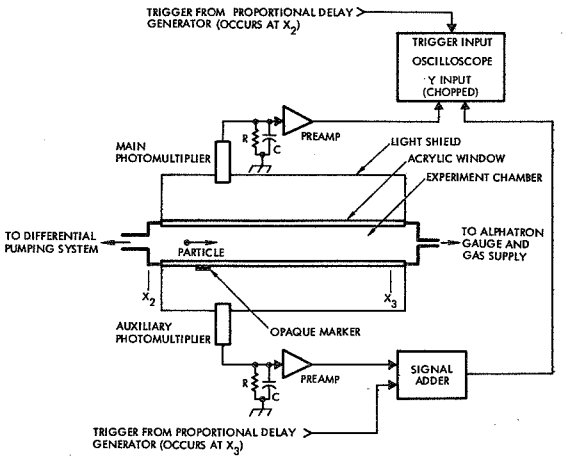

FIGURE 7.—Equipment employed for the measurement of total light energy radiated by a simulated meteor. Photomultiplier (PMT) signals are integrated by resistors R and capacitors C at the PMT anodes; the RC time constant is typically $\sim$500 μsec. Opaque marker and auxiliary PMT are used to obtain data for a solid angle correction, as discussed in the text and by Becker and Friichtenicht (1971).

out of view of the PMT's. (We require, for a datum to be valid, that there be no further increase in the PMT output signal after the appearance of the marker pulse.) Figure 8 is a typical oscillogram obtained from this setup.

Most experiments in which luminosity is the observable require that the spectrum of emitted light be known. We measure spectra using the system indicated in figure 9. Here up to six PMT's view the luminous trail simultaneously, all providing identically integrated outputs. Five of the tubes are fitted with narrow-band interference filters and the sixth is left unfiltered. The peak amplitude of any filtered PMT output normalized to the output of the unfiltered tube gives the relative amount of light emitted within the filter bandwidth. These data can be averaged for numerous simulated meteors in a given velocity interval. Using commercial filters, we obtain relative spectral intensity measurements at 300 Å intervals within the photographic meteor spectrum. Our data analysis requires only the integral of the relative spectrum, and as the integral is fairly insensitive to spectral changes, these measurements are sufficiently accurate for our needs.

When the experiment deals with the ionized wake of a simulated radiometeor, we change to the ionization chamber setup displayed schematically in figure 10. There are actually two ionization chambers in linear sequence, each having 9-cm wide parallel plates separated by 5 cm and fitted with secondary suppression grids. The plates are equally and oppositely biased so that the particle flight axis lies in the zero equipotential plane. Charge-sensitive preamplifiers can be connected

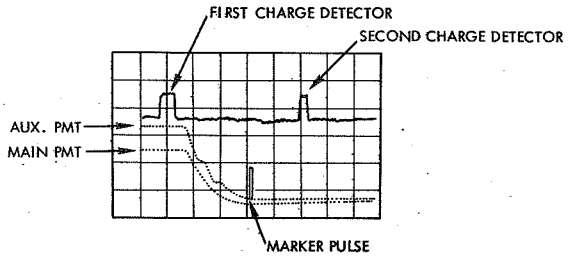

FIGURE 8.—Typical oscillogram obtained from equipment shown in figure 7. Top trace is particle detector signal; two charge detectors were used here with their outputs added, and velocity can be found from the transit time between them. Lower traces are the PMT outputs "chopped" together; these begin when particle is at x_2 and delayed marker appears when particle is at x_3. Steps on auxiliary PMT trace are produced by opaque markers (see text and fig. 7). For this simulated meteor, all sweep speeds were 10 μsec/division; deflection factors were 0.02 V/division and 0.05 V/division for the first and second charge detectors, 1.0 V/division for both PMT outputs, and 5.0 V/division for the marker pulse.

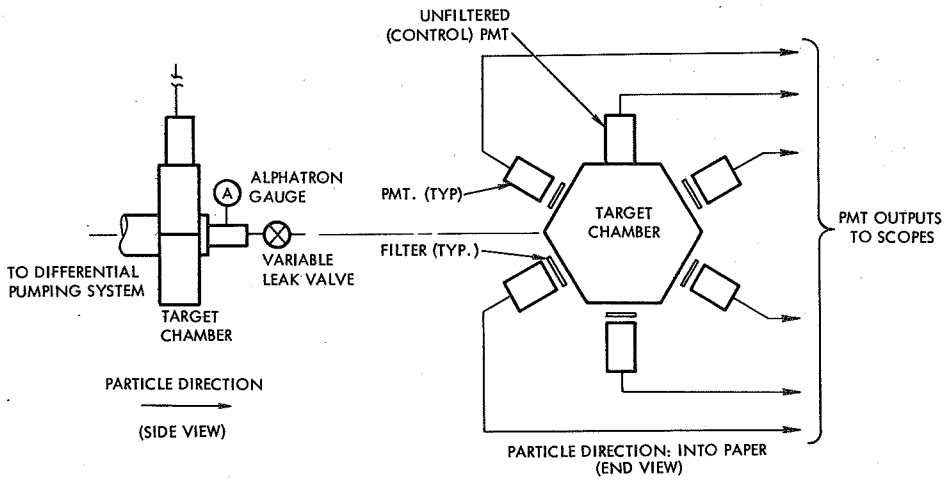

FIGURE 9.—Equipment for the measurement of simulated meteor spectra. Each PMT output is separately integrated and has an appearance similar to the main PMT trace in figure 8. Relative spectrum is derived from ratios between emitted light in passband of each filter and total emitted light as measured by unfiltered PMT.

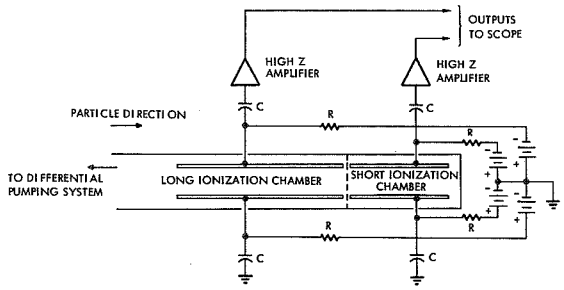

FIGURE 10.—Equipment for the measurement of ionization probability. Long ionization chamber collects all positive and negative charges in meteor wake; total number of positive charges is found from the output of the preamplifier. Short chamber checks length of the wake; any charges collected in it signify excessive wake length, and such data are rejected.

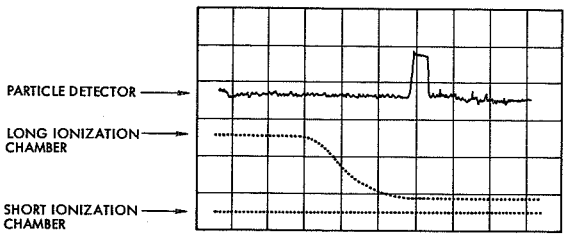

FIGURE 11.—Typical oscillogram obtained from equipment shown in figure 10. Note that short ionization chamber produced no signal, implying that this datum is acceptable. For particle charge detector trace, sweep speed was 5 μsec/division and deflection factor was 0.02 V/division; for ionization chamber traces, corresponding values were 5 μsec/division and 2.0 V/division.

either to the negative plate for measurement of total positive ion charge, or to the positive plate for measurement of total electron and negative ion charge. The former connection is most often used in order to avoid problems that might arise from the short electron collection time and possible production of secondaries; the "unused" plate is ac grounded by capacitors. The preamplifiers are similar in many respects to those employed in particle detection. They integrate the total charge collected at the plate, providing a proportional output voltage whose peak amplitude is in effect proportional in turn to the total number of collected ions (assuming, as is expected at the energies involved, that all ions are singly charged). The first ionization chamber has plates 45 cm long and serves for the actual data acquisition. The second chamber, with 22 cm long plates, is installed to determine whether the first chamber has collected all of the charge in the wake: The presence of any signal in the second chamber is regarded as grounds for rejection of the datum.

As before, the outputs of the ionization chamber preamplifiers are fed to an oscilloscope whose sweep is started by the time interval selector-proportional delay generator when the particle reaches position x_2 at the entrance to the first chamber. A typical oscillogram appears in figure 11.

EXPERIMENTAL RESULTS

Our researches to date have been largely concentrated on those aspects of the meteor problem which appear to meet two informal criteria. The first is obvious—the phenomenon under study should be one for which accurate data are lacking and/or interpretation of existing data is controversial, and for which our techniques seem to have a reasonable probability of supplying the missing data or resolving the controversy. The second is more subjective—we require that our techniques compare favorably with possible alternative research methods in terms of data returned per unit time or per unit expenditure. These considerations have guided our work toward the following areas of study: (a) luminosity effects, including measurements of luminous efficiency and the spectra of luminous trails; (b) ionization effects, particularly the measurement of ionization probabilities for various combinations of particle and atmosphere compositions; (c) other particle-gas energy exchange mechanisms, notably ablation and deceleration, and measurement of drag and heat transfer coefficients. Within the specific context of meteor simulation, those experiments that can be grouped under (c) are probably farthest from fulfilling our self-imposed criteria and will receive the least emphasis in the discussion to follow. Nevertheless, such experiments are still important, since a knowledge of ablation and deceleration mechanisms applicable to these particular particles is necessary to the reduction and analysis of data obtained from experiments in the other two groups.

In the introduction we alluded to a fourth experimental problem, which is to determine the

limits of accuracy of the simulation process and of the extrapolation of results to natural meteors. This problem is difficult to deal with directly, but much indirect evidence can be derived from the experiments themselves. In general, we feel that confidence can be placed in the relevance of the experimental results to the degree that the postulated deceleration and ablation mechanisms yield reasonable results for the drag and heat transfer coefficients, and to the degree that the results can be shown to agree with those obtained by other experimental means.

Deceleration and Ablation

Details of the deceleration and ablation processes have been studied by Slattery et al. (1964), Friichtenicht (1969), and Hersh et al. (1969). These studies employed air, oxygen, and argon atmospheres with carbonyl iron as the particle material. The sphericity of these particles has been verified numerous times by microscopic examination, permitting us to use the spherical shape factor in all data analyses with confidence. The studies have left little doubt that deceleration becomes negligible above 15–25 km/s, that the particles ablate by vaporization from about 10 km/s to the upper extremes of velocity, and that other ablation mechanisms such as sputtering and fragmentation are not important. Additional supporting data for the latter conclusion are visual and photometric observations of luminous trails and computations by Öpik (1958, ch. 5 and 6). In all cases the oxygen results are quite consistent with those for air.

The drag coefficient Γ in our usage is the same as that defined in conventional meteor theory. Under free molecule flow conditions and with all particles assumed spherical, the meteor drag equation is

$$m(dv/dt) = -\Gamma A \rho_a v^2 \qquad (4)$$

where m, v, and A are the mass, velocity, and projected area of the particle, and where ρ_a is the density of the gas with which it interacts. All drag experiments have been conducted at velocities low enough that particle heating by gas molecule bombardment is insufficient to produce significant mass ablation; then m and A remain constant at their initial values $m_0 = 4\pi r_0^3 \rho/3$ and $A_0 = \pi r_0^2$, where r_0 is the initial particle radius and ρ is the particle density. If the particle enters the gas at time $t=0$ with an initial velocity v_0, the velocity at time $t=\tau$ is given by integration of equation (4):

$$\frac{1}{v} = \left[\Gamma \rho_a \left(\frac{9\pi}{16}\frac{1}{m_0 \rho^2}\right)^{1/3}\right]\tau + \frac{1}{v_0} \qquad (5)$$

If x is the distance travelled by the particle from $t=0$ to $t=\tau$, a second integration gives

$$x = \left[\Gamma \rho_a \left(\frac{9\pi}{16}\frac{1}{m_0 \rho^2}\right)^{1/3}\right]^{-1} \times \ln\left\{\left[\Gamma \rho_a \left(\frac{9\pi}{16}\frac{1}{m_0 \rho^2}\right)^{1/3}\right] v_0 \tau + 1\right\} \qquad (6)$$

Note that in equations (5) and (6), all quantities within the square brackets are constant for any one material.

Slattery et al. (1964) used a series of particle velocity detectors within the gas region to obtain the velocity of a decelerating particle as a function of time. Particle parameter measurement prior to gas entry gave m_0 and v_0; ρ_a was found from gas pressure measurements, with the absolute gas pressure held in the area of 1 torr to insure free molecule flow. Naturally, ρ was known (7.85×10^3 kg/m^3 for iron particles). For each particle, reciprocal velocity was plotted as a function of time and a best-fit straight line was prepared by the method of least squares. The slope of this line was equal to the quantity in square brackets in equation (5), and from the slope Γ was determined. Data were obtained for ten particles interacting with air at initial velocities between 4.0 and 6.7 km/s. A total of 17 additional data points were also obtained with an oxygen atmosphere and 12 with argon; the latter results were very similar to those for air and require no further discussion.

Hersh et al. (1969) measured the total particle flight time between two detectors spaced apart a distance x and reduced their data according to equation (6). They employed an air atmosphere only, but in all other respects the experiment was essentially identical to that outlined above. Over 100 particles were observed, with initial velocities ranging from about 0.8 to 3.5 km/s.

In figure 12, drag coefficient data from both experiments are plotted together as a function of

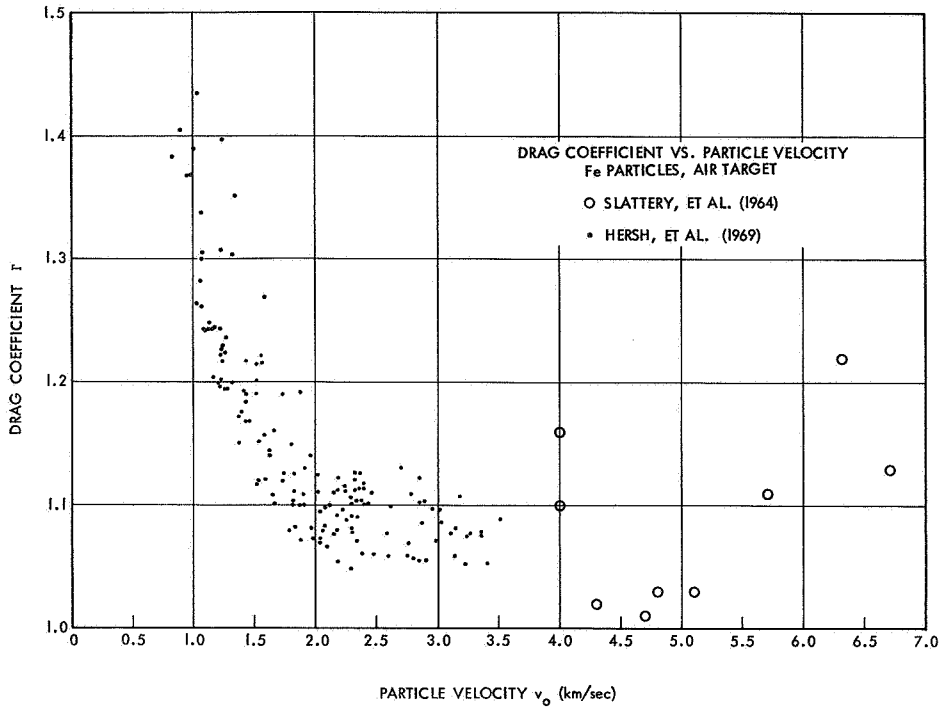

FIGURE 12.—Drag coefficient Γ as a function of initial particle velocity v_0. Data are from Slattery et al. (1964) and Hersh et al. (1969). The better controls and more refined techniques in the latter experiment resulted in a much smaller degree of scatter.

initial velocity v_0. The principal significance of these data in the context of meteor simulation is that Γ tends toward unity as v_0 approaches the lower limit of meteoric velocities, a result consistent with the assumption of particle sphericity and in agreement with the drag coefficient deduced for natural meteors from observations and other deceleration experiments (cf. Whipple and Hawkins, 1959). Hersh et al. have also related their work to details of the particle-gas molecule collision process as contained in theoretical models of free molecule flow and have found good agreement with the models; the interested reader is referred to their paper for further information.

Slattery et al. also measured a heat transfer coefficient for low velocity iron particles. In their experiment, as we have noted, there was insufficient particle heating to produce mass ablation, but the particle did acquire sufficient internal energy to melt. It was possible to determine the time at which melting was complete by examining the behavior of the particle charge, and therefore the total time τ from entry into the gas to melting could be measured. The heat transfer coefficient Λ for melting could then be determined by balancing the energy required to raise the particle temperature 1500° K to the melting point against the internal energy input from gas molecule collisions. If C is the specific heat of iron,

$$m_0 C(1500) = \tfrac{1}{2}\Lambda A_0 \rho_a \int_0^\tau v^3\, dt \qquad (7)$$

As in the drag experiments, initial velocity v_0 and mass m_0 were found from a particle parameter measurement just prior to gas entry, and v was obtained as a function of time by direct measurement in the gas. A_0 was computed from m_0 in the usual way, assuming spherical, constant-density particles. Data were obtained for 13 particles entering an air atmosphere at $3.8 \leq v_0 \leq 6.7$ km/s and for additional particles entering oxygen and argon atmospheres.

At meteoric velocities the particle of course ablates, and we return to the definition of the heat transfer coefficient λ given in meteor theory by the

energy-balance equation

$$\zeta(dm/dt) = \tfrac{1}{2}\lambda A \rho_a v^3 \qquad (8)$$

in which ζ is the heat of ablation. The expected result for natural meteors is that complete ablation occurs with relatively little deceleration. This is also true for simulated meteors with $v_0 \geq 20$ km/s or so (as we will later verify by computation). If we limit ourselves to particles with this velocity or greater, we can let $v = v_0 =$ constant. However, A varies as the particle ablates away. If x is the position coordinate of the ablating particle measured along its trajectory with $x = 0$ at entrance into the gas, it is clear that $A/A_0 = f(x)$. Then, if ablation is complete at some position x_f, equation (8) requires that

$$\lambda = 2\zeta m_0/\rho_a v_0^2 \int_0^{x_f} (A/A_0)\, dx \qquad (9)$$

Friichtenicht (1969) designed an experiment to measure λ for 25 to 40 km/s iron particles in air utilizing the principles outlined above. The experimental problem reduces to evaluation of the integral in equation (9), and to accomplish this Friichtenicht observed the luminous trail with instrumentation like that in figure 7. The integrated PMT output (see fig. 8) is proportional to the total radiated energy as a function of time, which can be shown from standard meteor luminosity theory to depend only upon m/m_0. Since the particles do not decelerate appreciably, the time scale can be converted directly to x, and the data are plots of m/m_0 vs x. But $A/A_0 = (m/m_0)^{2/3}$, and hence each particle datum is readily transformed to a plot of A/A_0 vs x from which the integral in equation (9) can be computed.

There remains the problem of specifying a value for ζ. Friichtenicht reasoned that for relatively dense particles of this size range, vaporization is the most likely ablation mechanism. Therefore, in his experiment he set ζ equal to the sum of the heats of fusion and vaporization of iron. He argued that a particle with an unpolished surface in free molecule flow should have $\lambda \approx 1$ (Öpik, 1958, pp. 52–54); if his results gave a λ near unity, this would tend to confirm that the assumption of vaporization as the primary ablation mechanism was correct.

Friichtenicht's measurements of λ for 50 iron particles are combined with those of Slattery et al. in figure 13. It is seen that the heat transfer coefficient is approximately unity for melting at low velocities and declines slightly for ablation at higher velocities. These results appear to be reasonable and tend to support the hypothesis of vaporization as a primary ablation mechanism. Combined with the drag data, they also support the contention that deceleration and ablation processes of simulated meteors are similar to those undergone by natural meteors.

Before leaving this subject, we would do well to reconsider, in the light of the values given above for Γ and λ, whether our assumption of negligible deceleration for an ablating particle with $v_0 \geq 20$ km/s is correct. Dividing equation (8) by (4) and integrating the result from $v = v_0$ to a final velocity $v = v_f$, we obtain the familiar expression

$$m_f = m_0 \exp\left[-\tfrac{1}{2}\sigma(v_0^2 - v_f^2)\right] \qquad (10)$$

where m_f is the residual mass when $v = v_f$ and σ, the ablation constant, is equal to $\lambda/2\Gamma\zeta$. Table 3 gives values of the fractional velocity change $(v_0 - v_f)/v_0$ computed from equation (10) for 99 percent mass ablation ($m_f/m_0 = 0.01$) at various initial velocities. Deceleration can clearly be ignored for v_0 greater than 20 to 25 km/s. In the 10 to 20 km/s range, deceleration is moderate but must be considered.

Luminosity

Because of the fact that so much of our information regarding natural meteors has been obtained by photographic observations, there is considerable interest in both the atomic-scale mechanisms of meteor light emission and the macroscopic-scale relationships existing between the emitted light and the gross properties of the meteoroid. Advances in the quantum theory of atomic collisions have led to a reasonable understanding of the former, although detailed calculations are very complex. Ideally, the latter can be derived theoretically from computations of the populations of all possible excited states if the constituent elements of the meteoroid are known. In practice, the effort is heroic in scope and has apparently been attempted only by Öpik (1933, 1955); his results come very close to certain others derived from observations, but, perhaps because of the complexity of their derivation, they have usually been regarded as somewhat tentative

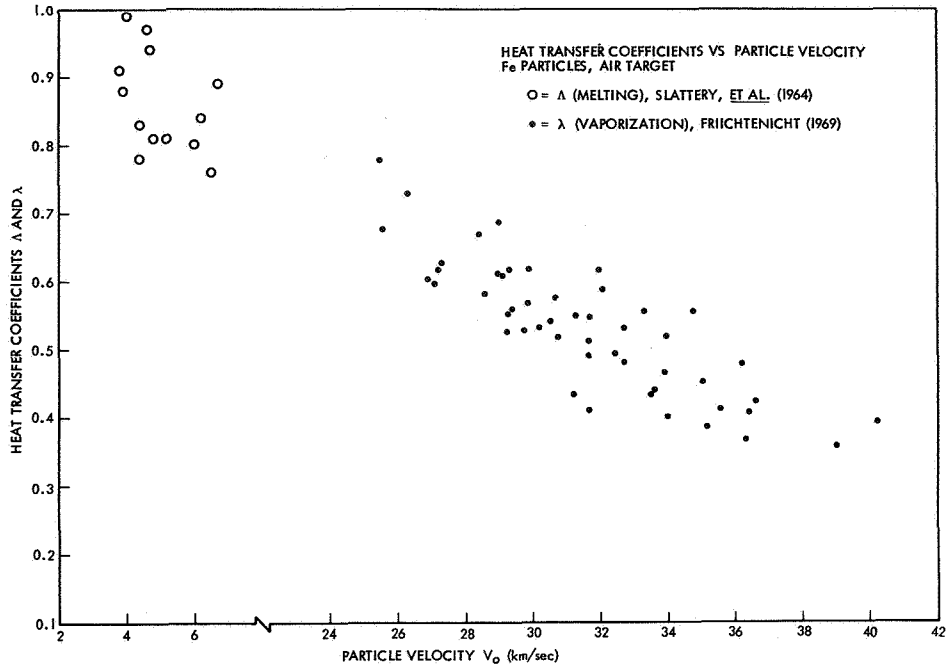

FIGURE 13.—Plot of the heat transfer coefficients Λ for melting and λ for ablation as functions of initial particle velocity v_0. Data are from Slattery et al. (1964) and Friichtenicht (1969).

TABLE 3.—*Deceleration for 99 Percent Mass Ablation* ($m_f/m_o = 0.01$)

Initial velocity (km/s)	Final velocity (km/s)	Fractional velocity change
40.0	38.4	0.04
30.0	27.7	0.09
25.0	22.2	0.11
20.0	16.4	0.18
15.0	9.7	0.35

and in need of more positive experimental verification. Primary emphasis seems instead to have been placed on observation and experiment. Meteor luminosity has been studied in this manner by numerous workers, including notably Verniani (1965), who statistically analyzed a large number of Harvard Meteor Project observations, and Ayers et al. (1970), who report results from artificial meteor experiments first introduced by McCrosky and Soberman (1963). Simulated meteor luminosity experiments were initially performed by Friichtenicht, Slattery, and Tagliaferri (1968). Their work has been improved and extended by Becker and Friichtenicht (1971), whose results we will present below.

As we know, a fraction of the kinetic energy of atoms ablated from a meteoroid is converted into atomic or molecular excitation and eventually into radiation. That fraction is the luminous efficiency of the meteor. It is generally more convenient to deal only with the portion of the radiation which is sensed by a detector with specified spectral response characteristics. The detector of major interest is a meteor camera with blue-sensitive astronomical film, whose combined spectral response has been claimed by Davis (1963) to closely approximate that of the International Photographic System. According to tabulations by Allen (1955), developed from a detailed study by Seares and Joyner (1943), the spectral response function $P(\lambda)$ in this system extends from 3300 to 5200 Å, with a peak at 4600 Å. The energy balance between the radiant intensity I_{pg} observed by a detector with a response function $P(\lambda)$ and the kinetic energy of the ablated atoms is expressed by the meteor

luminosity equation:

$$I_{pg} = -\tfrac{1}{2}\tau_{pg} v^2 dm/dt \qquad (11)$$

in which τ_{pg} denotes the photographic luminous efficiency. If τ_{pg} is accurately known and if a meteor observation measures I_{pg} and v as functions of time, then, by integrating the luminosity equation, these data can be used to solve for the initial meteoroid mass (called the photometric mass when computed in this way). It is evident that the accuracy of photometric mass computations is ultimately limited by the accuracy to which τ_{pg} is known.

If valid, the luminosity equation implies a principle with important consequences for the interpretation of simulated meteor experiments which was, to our knowledge, first pointed out explicitly by Becker and Friichtenicht in their 1971 paper. Assume that the elemental constituents of a meteoroid are well mixed and that the body ablates uniformly. In such a case the relative abundances of the various constituents remaining in the unablated body are constant during the ablation process. This means that if A_k is the initial relative abundance of some constituent k and if m_k is the total mass of that constituent, then the relation $m_k = A_k m$ holds not only initially, but also throughout meteoroid ablation, as a result of which $dm_k/dt = A_k\, dm/dt$. The total luminous intensity I_{pg} of the meteor can be theoretically thought of as a sum of radiant intensities $I_{pg}(k)$, each arising from deexcitation of ablated atoms of one constituent, and it is possible to write a luminosity equation for each such constituent individually, viz.:

$$I_{pg}(k) = -\tfrac{1}{2} A_k \tau_{pg}(k) v^2\, dm/dt \qquad (12)$$

where $\tau_{pg}(k)$ is the luminous efficiency of constituent k. Let all equations of this kind be summed; the left side of the sum, $\Sigma I_{pg}(k)$, must equal I_{pg}. But if this is so, the right side of the sum must equal the right side of equation (11), and we have that

$$\tau_{pg}(M) = \sum_k A_k \tau_{pg}(k) \qquad (13)$$

in which $\tau_{pg}(M)$ denotes the luminous efficiency of the meteor as a whole. We conclude that $\tau_{pg}(M)$ can be evaluated as a weighted sum of luminous efficiencies of those constituent elements which contribute to the radiation within the photographic spectral range. Fortunately, meteor spectra (cf. Millman, 1963) have already identified these elements as iron, silicon, magnesium, and occasionally calcium, and their relative abundances in meteoritic stone are fairly well known (cf. Öpik, 1958, p. 160). It thus seems feasible to compute $\tau_{pg}(M)$ from the results of measurements of τ_{pg}(Fe), τ_{pg}(Si), τ_{pg}(Mg), and τ_{pg}(Ca), and this has been a major motivating force behind our work.

The procedures and techniques that we use for measuring τ_{pg} of simulated meteors are those developed by Friichtenicht, Slattery, and Tagliaferri (1968), with minor modifications; the equipment and data format are described in the instrumentation section and figures 7 and 8, in this paper. We will discuss the reduction of data in broad outline only, referring the reader to Becker and Friichtenicht (1971) for additional detail. Measurements are made of the integrated intensity, initial mass, and initial velocity of each simulated meteor. In order to use the integrated intensity, one may integrate the luminosity equation, replacing dm/dt by an equivalent obtained from differentiation of equation (10) and assuming a small (but not negligible) deceleration, to get

$$E_{pg} = \tau_{pg}[E_0 - E_F - \sigma^{-1}(m_0 - m_F)] \qquad (14)$$

where $E_0 = m_0 v_0^2/2$ and $E_F = m_F v_F^2/2$ are respectively the initial and final values of the kinetic energy of the particle and where $E_{pg} \equiv \int I_{pg}\, dt$. (By small deceleration we mean that τ_{pg}, which may contain a velocity dependence, is considered constant for any one simulated meteor.) The particle ablates completely, so that $E_F \approx 0$ and $m_F \approx 0$. The drag and heat transfer data presented earlier show that $\Lambda/\Gamma \approx 1$ at low velocities, from which $\sigma \approx \tfrac{1}{2}\zeta$; at high velocities, $\sigma^{-1} m_0 \ll E_0$ and can be ignored. Then,

$$\tau_{pg} = E_{pg}(E_0 - 2\zeta m_0)^{-1} \qquad \text{(low velocities)} \qquad (15a)$$

and

$$\tau_{pg} = E_{pg}/E_0 \qquad \text{(high velocities)} \qquad (15b)$$

For the particle materials used so far, $2\zeta m_0$ becomes a negligible correction above 20 to 25 km/s, and this is the velocity range at which the transition is made from one expression to the other.

Our data are acquired photometrically, and conversions must then be applied to transform them to the photographic spectral response for direct comparison with other results. The conversions necessitate a measurement of the relative spectrum $f(\lambda)$ of the emitted light. Our detector, it will be recalled, is a PMT (usually an RCA 8575) viewing through an acrylic plastic window, and it has a relative spectral response $D(\lambda)$ which extends from 3400 to 5800 Å and peaks at about 4500 Å. Because PMT spectral response functions vary among different tube types, we normalize our data to an equivalent 3400–5800 Å "flat" detector by applying the conversion factor

$$\left[\int_{3400}^{5800} f(\lambda)\, d\lambda\right] \Big/ \left[\int_{3400}^{5800} f(\lambda) D(\lambda)\, d\lambda\right] \quad (16)$$

Luminous efficiencies normalized to this "flat" response are denoted by τ_s. The τ_s data are transformed in turn to τ_{pg} according to

$$\tau_{pg} = \tau_s \left[\int_{3300}^{5200} f(\lambda) P(\lambda)\, d\lambda\right] \Big/ \left[\int_{3400}^{5800} f(\lambda)\, d\lambda\right]$$

Note that the limits of the $D(\lambda)$ and $P(\lambda)$ spectral ranges almost coincide. The probability that the emitted spectrum $f(\lambda)$ contains a strong line falling within one range and outside of the other is therefore very small, and since $f(\lambda)$ appears in both numerator and denominator of both conversion factors, they are determined primarily by $D(\lambda)$ and $P(\lambda)$, both of which are accurately known, and only weakly by $f(\lambda)$. Hence, the measurement of $f(\lambda)$ need not be very accurate, and velocity effects (which might cause the spectra of different particles to differ somewhat) can be ignored.

Spectral measurements are performed as described in the instrumentation section and figure 9 of this paper, following the method originated by Tagliaferri and Slattery (1969) when they measured the spectrum of simulated iron meteors ablating in air. The result of their measurement is reproduced in figure 14, along with a part of a natural meteor spectrum due to Millman and Cook (1959).

Another conversion which must be applied to our data is one which involves units of measurement. In the laboratory, all quantities are measured in consistent physical units, leading to a τ that is dimensionless. But meteor astronomers find it more convenient to measure m and v in cgs units and I_{pg} in magnitudes relative to a zero-magnitude meteor, and they require τ_{pg} in units of s/erg, 0-mag. The intensity I_{op} of a zero-magnitude meteor is by convention equal to the radiant flux within a "flat" 3300 to 5200 Å passband from a star of zero apparent photographic magnitude which emits a solar spectrum. Davis and Hall (1963) find that $I_{op} = 5 \times 10^9$ ergs/s, from which

$$\tau_{pg}(\text{physical units}) = 5 \times 10^9\, \tau_{pg}(\text{s/erg, 0-mag}) \quad (18)$$

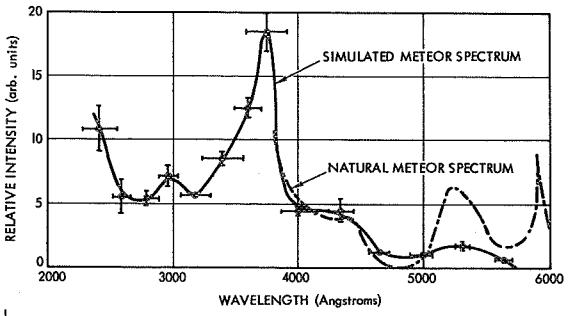

FIGURE 14.—Spectrum of iron simulated meteor in air atmosphere as measured by Tagliaferri and Slattery (1969). The natural meteor spectrum, shown for comparison, was obtained by Millman and Cook (1959).

In our most recent experiments, τ_{pg} of iron simulated meteors in an air atmosphere was measured for 167 individual particles with initial velocities ranging from 11.1 to 46.3 km/s. We also obtained τ_{pg} data for 120 copper simulated meteors in air, with initial velocities between 10.2 and 47.4 km/s. Copper, of course, is not a meteoroid constituent; rather, it was selected because it is a useful material with which to begin to examine elemental differences in luminous efficiency. Copper has an atomic mass only 10 percent greater than that of iron but a considerably different electronic structure. It has occasionally been claimed that the predominance of iron lines in low-velocity meteor spectra can be explained by the fact that iron atoms, being the heaviest of the major meteor constituents, possess a greater kinetic energy and are therefore most likely to be excited upon collisions with gas molecules. If this were a significant effect, one

would expect τ_{pg}(Cu) to exceed τ_{pg}(Fe) by ~10 percent. If τ_{pg}(Cu) and τ_{pg}(Fe) should differ widely, on the other hand, it would indicate that mass differences do not significantly contribute to differences in emission from one constituent to the next and that such differences are probably more closely involved with electronic structure.

Figures 15 and 16 present, respectively, the results of the τ_{pg}(Fe) and τ_{pg}(Cu) experiments. In each figure, the data for each 1 km/s interval of velocity have been averaged and plotted as a single point, with error bars denoting the standard deviations of the averages. The smooth curves in the figures are least-squares best fits for $v_0 \geq 18$ km/s in the case of τ_{pg}(Fe) and $v_0 \geq 14$ km/s in the case of τ_{pg}(Cu), and visually-estimated best fits at lower velocities. Values of τ_s and τ_{pg} read from these smooth curves are listed in table 4. For iron, τ_{pg}(Fe) first rises with increasing particle velocity, reaching a peak value 2.3×10^{-12} s/erg, 0-mag at $v_0 \approx 18$ km/s. At higher velocities τ_{pg}(Fe) $\propto v_0^{-3/4}$, falling to 2.1×10^{-12} s/erg, 0-mag at 20 km/s and 1.3×10^{-12} s/erg, 0-mag at 40 km/s. The behavior of copper is somewhat similar, but there are very important differences; τ_{pg}(Cu) peaks at 13 to 14 km/s, with a peak value of only 9.5×10^{-14} s/erg, 0-mag, and thereafter τ_{pg}(Cu) $\propto v_0^{-1/2}$, declining to 7.3×10^{-14} and 5.3×10^{-14} s/erg, 0-mag at 20 and 40 km/s. The differences are, then, that the peak velocities are not the same, that the velocity dependences in the high velocity regime differ, and, significantly, that τ_{pg}(Cu) is at least a factor of 20 lower than τ_{pg}(Fe) at any velocity between 18 and 47 km/s.

These results certainly permit one to conclude that differences in atomic mass are totally unrelated to the relative intensity of radiation emitted within the photographic spectral range from atoms of the different constituent species in a meteoroid. However, the macroscopic nature of the results do not allow any definite connections to be made between the behavior of τ_{pg} and specific details of the electronic structure of the two elements.

Interestingly enough, the data for τ_{pg}(Fe) correspond very well to predictions of Öpik (1958, p. 139) of the behavior of the visual luminous efficiency τ_v of dustball meteors with dilute comae. We demonstrate this correspondence in table 5, where the ratio τ/τ_{peak} is compared at

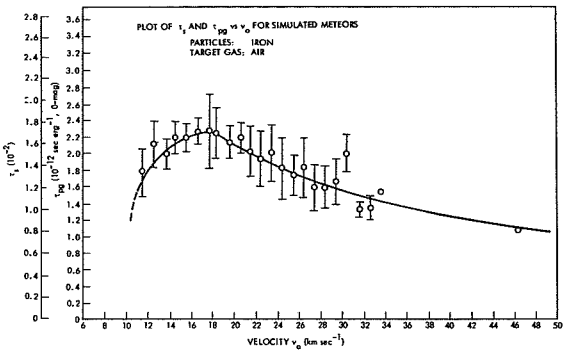

FIGURE 15.—Luminous efficiency of iron simulated meteors as a function of velocity v_0. Data for each 1 km/s velocity interval have been averaged; error bars extend ± one standard deviation of the average. When no bars are shown, the velocity interval contained only one datum.

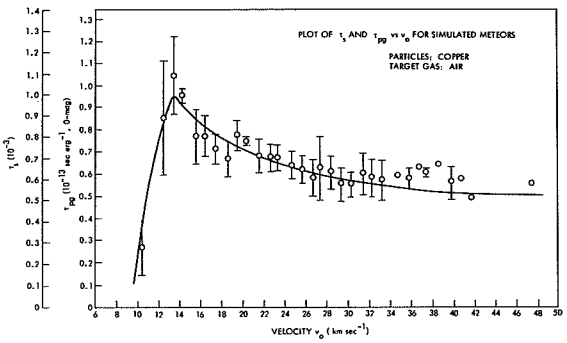

FIGURE 16.—Luminous efficiency of copper simulated meteors as a function of velocity v_0. See figure 15 for plotting and error bar conventions.

various velocities for Öpik's computation and for our experiment. We do not regard the small differences in the velocity of τ_{peak} as significant, since in both cases the peak is rather broad. The rapid rise in τ from low velocities is present in both results, and the $v^{-3/4}$ relationship at high velocities that we observed experimentally compares favorably with Öpik's predicted velocity exponent, which is −0.88.

Perhaps the most significant findings from this experiment appear when the data for τ_{pg}(Fe) are replotted in the log-log presentation employed by Ayers et al. (1970) in reporting their artificial meteor results. Such a plot appears in figure 17, where we have included for direct comparison

TABLE 4.—*Values of τ_s and τ_{pg} for Iron and Copper Micrometeors*[a]

Velocity (km/s)	Iron		Copper	
	τ_s (physical)	τ_{pg} (s/erg, 0 mag)	τ_s (physical)	τ_{pg} (s/erg 0 mag)
10	—	—	0.00026	2.6×10^{-14}
11	0.0115	1.5×10^{-12}	0.00057	5.6×10^{-14}
12	0.0133	1.8×10^{-12}	0.00079	7.8×10^{-14}
14	0.0155	2.1×10^{-12}	0.00096	9.5×10^{-14}
16	0.0168	2.2×10^{-12}	0.00087	8.5×10^{-14}
18	0.0170	2.3×10^{-12}	0.00080	7.8×10^{-14}
20	0.0159	2.1×10^{-12}	0.00074	7.3×10^{-14}
22	0.0149	2.0×10^{-12}	0.00070	6.9×10^{-14}
24	0.0140	1.9×10^{-12}	0.00067	6.6×10^{-14}
26	0.0132	1.8×10^{-12}	0.00064	6.3×10^{-14}
28	0.0125	1.7×10^{-12}	0.00062	6.1×10^{-14}
30	0.0118	1.6×10^{-12}	0.00060	5.9×10^{-14}
32	0.0112	1.5×10^{-12}	0.00058	5.7×10^{-14}
34	0.0107	1.4×10^{-12}	0.00057	5.6×10^{-14}
36	0.0103	1.4×10^{-12}	0.00055	5.4×10^{-14}
38	0.0098	1.3×10^{-12}	0.00054	5.3×10^{-14}
40	0.0094	1.3×10^{-12}	0.00054	5.3×10^{-14}
42	0.0091	1.2×10^{-12}	0.00053	5.2×10^{-14}
44	0.0088	1.2×10^{-12}	0.00053	5.2×10^{-14}
46	0.0085	1.1×10^{-12}	0.00053	5.2×10^{-14}

[a] Data taken from smooth curves, figures 15 and 16.

TABLE 5.—*Values of Normalized Luminous Efficiency Measured for Iron and Predicted for Dustball Meteors*

Velocity (km/s)	Dustballs[a] $\tau_v/\tau_v(peak)$	Iron[b] $\tau_{pg}/\tau_{pg}(peak)$
10.4	0.71	~0.47[c]
14.8	1.00	0.95
18.0	—	1.00
20.9	0.96	0.90
29.6	0.64	0.70
41.8	0.45	0.53
59.2	0.37	~0.41[d]

[a] Data from Öpik (1958).
[b] Data from current experiment.
[c] Visual extrapolation.
[d] Extrapolation assuming $\tau_{pg}(\mathrm{Fe}) \propto v^{-3/4}$.

both the Ayers et al. results and also data for Harvard Meteors 1242 and 19816 as reduced by Cook et al. (1963). Both of these meteors are believed to be of asteroidal origin; in order to place them on the same scale as the τ_{pg}(Fe) data, we have plotted both natural meteor points in terms of $\tau_{pg}(M)/A_{\mathrm{Fe}}$, using the value of $\tau_{pg}(M)$ given by Cook et al. and $A_{\mathrm{Fe}}=0.15$ from Öpik (1958). Considering that our τ_{pg}(Fe) data are accurate to ±40 percent or better and that Ayers et al. quote uncertainties for theirs in the 15 to 25 percent range, we regard the agreement between the simulated meteor and artificial meteor results as excellent. Reasonable agreement with the two natural meteor points also exists. Since the artificial meteor data (and, of course, the natural meteor data) were obtained from actual entry of bodies into the Earth's atmosphere, we believe that the agreement shown in figure 17 is extremely strong evidence that our procedures properly simulate natural meteor processes.

The reader will have noted that our observations of the velocity dependence of τ_{pg}(Fe) differ rather markedly from at least some current beliefs about the velocity dependence of $\tau_{pg}(M)$. The latter has been studied through the statistical

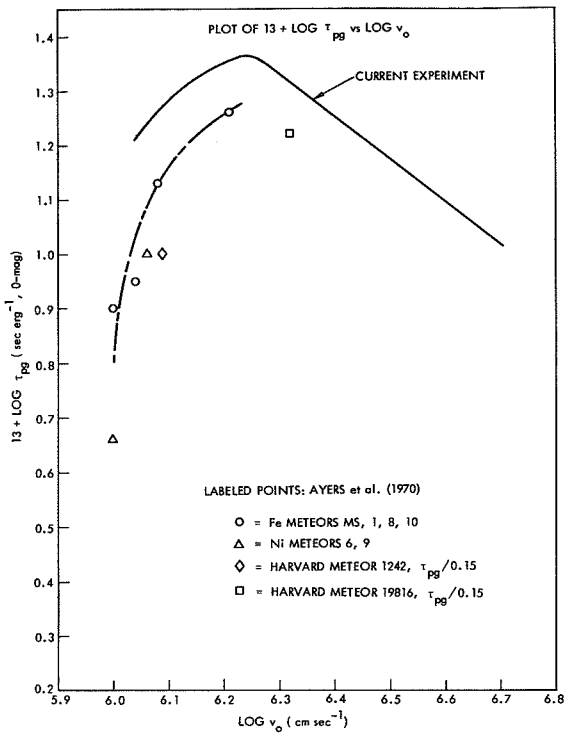

FIGURE 17.—Log τ_{pg} as a function of log v_0. Data from the currently-described experiment (Becker and Friichtenicht, 1971) are compared with artificial meteor results (Ayers et al., 1970) and two natural meteor data points (Cook et al., 1963); for the latter, τ_{pg} has been divided by 0.15, the relative abundance of iron in meteoritic stone, to permit a comparison with τ_{pg}(Fe).

analysis of meteor observations by Ceplecha and Padevět (1961) and Verniani (1965), who reached different conclusions; these have been debated at some length by Verniani (1965, 1970), Ceplecha (1966, 1968), and various others. We do not wish to join this debate at the present time. However, it is necessary to point out that the failure of τ_{pg}(Fe) to behave as a function of velocity according to Verniani's thesis that $\tau_{pg}(M) \propto v$, or according to any other proposed velocity dependence of $\tau_{pg}(M)$, is not an argument against either the accuracy or the relevance of our results. If, as we believe, equation (13) is valid, then it is neither necessary or even likely that the functional dependence of $\tau_{pg}(M)$ on velocity be the same as that of any one $\tau_{pg}(k)$. As one hypothesis, if $\tau_{pg}(k)$ of the lighter meteor constituents (which are known to emit more strongly from high velocity meteors) should behave similarly to τ_{pg}(Fe) except to peak at higher velocities, a superposition of them and τ_{pg}(Fe) could easily lead to a $\tau_{pg}(M)$ that is roughly proportional to v over a major part of the meteor velocity spectrum. There is some highly preliminary supporting evidence for such a hypothesis in our results, since τ_{pg}(Fe) was found to peak at a higher velocity than τ_{pg}(Cu).

We are presently preparing to extend our experiments to other materials with the intent of investigating some of these possibilities. One planned experiment is to check the validity of equation (13) by measuring separately the luminous efficiencies of titanium and the compound $FeTiO_3$. Since oxygen does not radiate within the photographic spectral range, we would expect to find that $\tau_{pg}(FeTiO_3) = 0.37\tau_{pg}(Fe) + 0.32\tau_{pg}(Ti)$ if equation (13) holds. Provided that this experiment proves successful, we will then attempt to measure τ_{pg}(Si), τ_{pg}(Mg), and τ_{pg}(Ca), after which we would be able to compute $\tau_{pg}(M)$ as proposed earlier.

Ionization

The ionized wakes produced by ablating meteoroids are known to be responsible for radiometeor phenomena. In recent years the study of these phenomena has been improved to the point where radiometeor observations have become an important research tool, complementing photographic observational methods. Moreover, the formation of the ionized wake is another basic mechanism of energy transfer from the meteoroid to the atmosphere and must therefore be understood before the description of the energy transfer process can be considered complete.

Meteor ionization can be treated in terms of the fraction of the meteoroid kinetic energy that is expended in ion-electron pair production, leading to an equation analogous to the luminosity equation (11):

$$I_q = -\tfrac{1}{2}\tau_q v^2 \, dm/dt \qquad (19)$$

where I_q is the energy per unit time expended in ionization and τ_q is the ionizing efficiency. In the case of ionization, however, it is more convenient to deal with the electron line density $\alpha = I_q/\phi v$,

where ϕ is the mean energy required to create a single ion-electron pair. A still more fundamental quantity is the probability β that a single meteoroid atom will produce an ion-electron pair as a result of a collision with an atmospheric molecule before the former has been reduced to thermal energy. The ionization probability and electron line density are related according to

$$\alpha = -(\beta/\mu v)(dm/dt) \qquad (20)$$

in which μ is the mean mass of a meteoroid atom, from which it follows that

$$\tau_q = (2\phi/\mu v^2)\beta \qquad (21)$$

The radiometeor problem essentially reduces to the need for an evaluation of β, since ϕ and μ are known for all meteoroid constituents. Once this is accomplished, radiometeor measurements of α and v would permit the meteoroid mass to be found.

Our remarks at the beginning of the luminosity discussion regarding the difficulty of obtaining τ_{pg} from theoretical first principles apply to ionization as well, although here the problems are not quite as complex. Predictions of τ_q and/or β based on the theory of collisional ionization have been offered by, among others, Öpik (1958), Derbeneva (1966), Furman (1967), and Sida (1969). The deduction of τ_q from observational data has been attempted by Verniani and Hawkins (1964), whose method required the simultaneous photographic and radio observation of the meteors. Their results appear to lead to a current reasonable best estimate of β for cometary meteors, but they suffer from the combined errors and uncertainties in both observational techniques (notable among which is the uncertainty in τ_{pg}). The most recent review of the subject to have come to our attention is by Verniani (1970); in it the author examines a number of theoretical and experimental results and concludes that the best estimate derived by himself and Hawkins, namely that

$$\beta/\mu = 2.6\times10^{-6}\, v^4 \qquad \text{(cgs units)} \qquad (22)$$

should continue to be used in radiometeor data reduction. As in the case of luminosity, our work is not of a type that would lead us directly to challenge any value of β proposed for composite meteoroids by others; we will, however, permit ourselves to observe that in our view, β is still sufficiently unknown that any proposed value is probably best regarded as an estimate only until much better data become available.

The basic approach that we have taken to the study of ionization probability through the medium of simulated meteor experiments is the same as that pursued in our luminosity work: to evaluate β from a series of experiments in which monoconstituent particles are made to interact with air and monoconstituent gases, in the hope that the results will lead to a firmer knowledge of the behavior of β for different single elements and may eventually allow a β for multiconstituent meteoroids to be derived therefrom. The experimental techniques employed were described in the instrumentation section and figures 10 and 11; they were developed by Slattery and Friichtenicht (1967), who were the first to measure β for simulated meteoroids. The concept of this kind of experiment and the reduction of the data are both relatively simple. We operate only with initial velocities in excess of 20 to 25 km/s, where, as we already saw, deceleration can be neglected. The total charge Q due to ions is collected in an ionization chamber. The energy per particle atom is low enough that all ions can be assumed singly charged, so that N_I, the total number of ion-electron pairs created, is equal to Q/e, where e is the electron charge. The mass μ of a particle atom is known and the initial mass m_0 is measured prior to the start of ablation, and thus the total number of particle atoms N_A can be found as the ratio m/μ. The ionization probability is then computed from

$$\beta = N_I/N_A \qquad (23)$$

To date, simulated meteor measurements of β have been reported by Slattery and Friichtenicht (1967) for iron particles interacting with air and argon, and by Friichtenicht and Becker (1971) for copper and lanthanum hexaboride (LaB_6) particles interacting with air. The choice of the latter two materials may seem strange until it is recalled why copper was selected for comparison with iron in our luminosity studies; the same criteria apply here as well. Lanthanum hexaboride was selected for two reasons: First, at the time the experiments were performed, it was the only compound that had been successfully accelerated

to meteoric velocities (now, however, see tables 1 and 2), and we were anxious to observe the behavior of a compound material. Second, it had been discovered that LaB_6 particles often achieved velocities in excess of 100 km/s, and it was, we felt, highly desirable to examine the velocity dependence of β at extreme velocities. Most prior theoretical and observational treatments have had as their result $\beta \propto v^n$, with n at least $+2$ and possibly as large as $+5$. One might expect that at some limiting velocity β would become proportional to v^2, i.e., to energy of the projectile atom. A transition to a $\beta \propto v^2$ law had not previously been observed for any material, and there was a chance that such a transition could be detected in LaB_6 ionization.

Figures 18, 19, and 20 show, respectively, the simulated meteor results obtained for β(Fe), β(Cu), and $\beta(LaB_6)$ as functions of particle velocity v_0 measured just prior to the entrance of the particle into the gas. Each figure also shows a straight line fit to the data by least squares for $20 \leq v_0 \leq 45$ km/s in figure 18; $16 \leq v_0 \leq 38$ km/s in figure 19; and $20 \leq v_0 \leq 112$ km/s in figure 20. The equations of the least-squares fits (velocity in cm/s in all cases) are

$$\beta(\mathrm{Fe}) = 1.50 \times 10^{-21} v_0^{3.12} \qquad (24a)$$

found by Slattery and Friichtenicht, and

$$\beta(\mathrm{Cu}) = 2.17 \times 10^{-35} v_0^{5.24} \qquad (24b)$$

and

$$\beta(\mathrm{LaB_6}) = 6.31 \times 10^{-21} v_0^{3.08} \qquad (24c)$$

found by Friichtenicht and Becker. The above may be compared to the result of Verniani and Hawkins (1964) for β of cometary meteors:

$$\beta(\mathrm{com}) = 1.0 \times 10^{-28} v_0^{4.0} \qquad (25)$$

obtained from equation (22) by assuming an average meteoroid atom to have a mass $\mu = 23$.

The obvious functional similarity between β(Fe) and $\beta(LaB_6)$ is not repeated with β(Cu), but it is nevertheless interesting that in the important 20 to 40 km/s velocity range, the ionization probabilities of iron, copper, and LaB_6 do not differ very greatly. Respective values are 0.07, 0.02, and 0.16 at 20 km/s; 0.24, 0.19, and 0.56 at 30 km/s; and 0.60, 0.85, and 1.36 at 40 km/s.

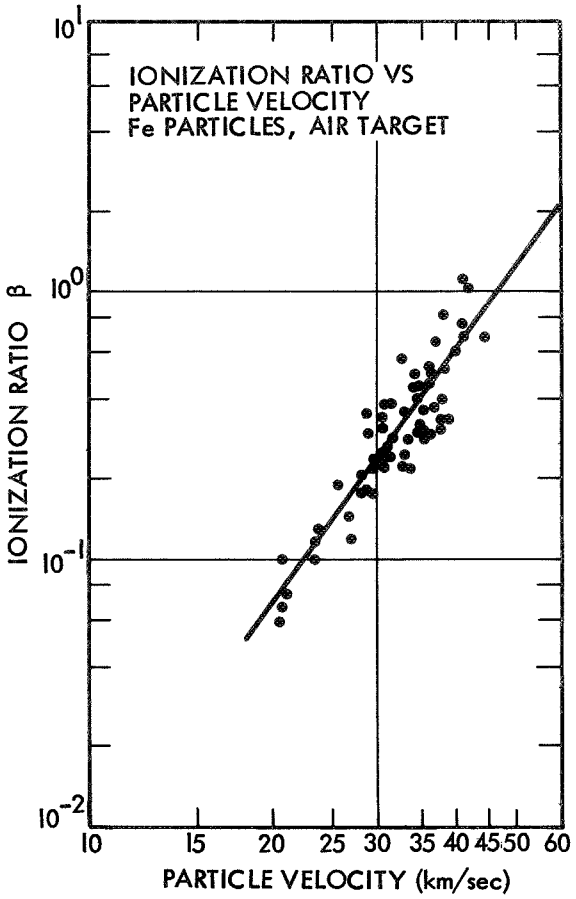

FIGURE 18.—Ionization probability of iron-simulated meteors as a function of v_0. Data are from Slattery and Friichtenicht (1967). Straight line shown has been fit by least squares; its equation is $\beta(\mathrm{Fe}) = 1.50 \times 10^{-21} v_0^{3.12}$

The LaB_6 results at very high velocities appear to have some rather interesting features. One is that the least-squares fit expressed by equation (24c) seems to hold even at 112 km/s, and there is no evidence that β is approaching a proportionality to v^2 at this high a velocity. Another is that $\beta(LaB_6)$ clearly exceeds unity at high velocities and attains a value as large as 50 at 112 km/s. An ionization "probability" greater than unity requires an other-than-probabilistic interpretation; in our usage as defined by equation (23), it means that some ablated meteoroid molecules suffer more than one ionizing collision with atoms or molecules of the atmospheric gas and that it is the latter that undergo ionization.

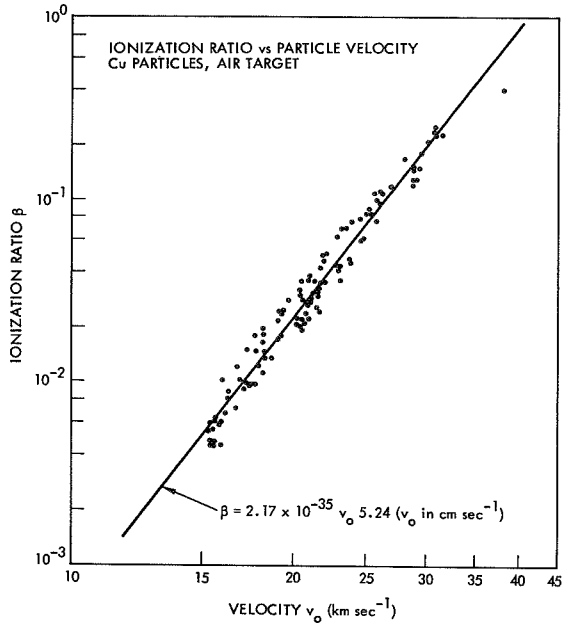

FIGURE 19.—Ionization probability of copper simulated meteors as a function of v_0. Data are from Friichtenicht and Becker (1971). Least-squares fit is shown.

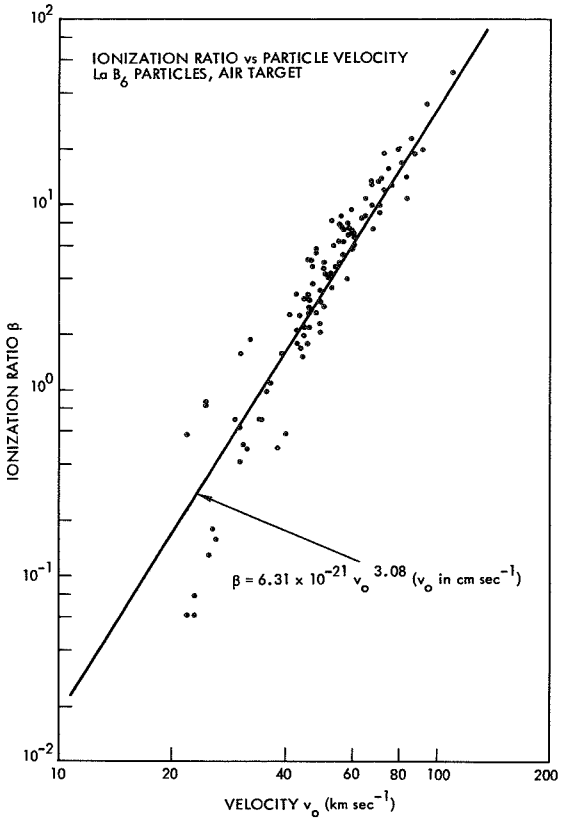

FIGURE 20.—Ionization probability of lanthanum hexaboride simulated meteors as a function of v_0. Data are from Friichtenicht and Becker (1971). Straight line with equation shown is a least-squares fit. As noted in text, separate least-squares fits were attempted above and below 40 km/s, but the results were the same within the accuracy of the experiment.

Friichtenicht and Becker (1971) support this conclusion in a discussion of the possible influence of competing energy exchange mechanisms.

At present, most theories of meteor ionization do not appear to consider either atmospheric ionization in general or the possibility of ionization of multiple atmospheric atoms by a single projectile atom in particular as likely. Instead, the theories usually regard the projectile atom as the one undergoing ionization (in some cases, multiple ionizations), primarily because of the fact that in the meteor problem, the projectile atom almost always has a lower first ionization potential. Although 112 km/s is considerably above the highest velocity that cometary meteors attain, $\beta(LaB_6)$ is still greater than unity for $40 \leq v_0 \leq 70$ km/s, and these are velocities which are possible for natural meteors. There may be, then, a need for some modification of current meteor ionization theory at high velocities.

It should be noted here that Friichtenicht, Slattery, and Hansen (1967) have extended the simulated meteor ionization experiments to a wide variety of other gases, from which they obtain a considerable amount of information that may prove useful in the study of collisional ionization on the atomic scale. In this sense the simulated meteor becomes a form of atomic beam. This work will not be discussed here because its immediate relevance to the gross behavior of meteors is slight; however, it has opened some interesting possibilities for new methods of experimentally studying atomic interactions.

We are not particularly concerned that our results for β are consistently larger than those that seem to be regarded as appropriate to cometary meteors, since we feel that the situation may be

similar to the problem of the velocity dependence of τ_{pg}. The weighting factors that would have to be applied to elemental β values in order to synthesize a β for a meteoroid are as yet unknown, and for this reason we think that it is too early to conclude that our results are in any way inconsistent. We continue to believe that such a synthesis is possible and that it would be preferable in many respects to the assumption of an "average" meteoroid atom as is now done in reducing observational material. However, just as the interpretation of radiometeor observations is less advanced than that of photographic observations (cf. Verniani, 1970), so too is the interpretation of simulated meteor ionization experiments less advanced than that of the luminosity experiments. Now in the planning stage are experiments designed to measure β for silicon, magnesium, and various other materials, which may provide information helpful in improving that interpretation.

CONCLUSIONS

Throughout this paper we have attempted to concentrate on basic methods and techniques for accelerating microparticles to meteoritic velocities and for employing these particles in practical simulated meteor experiments. In addition, we have presented the results of those experimental efforts which seem to us especially relevant to a number of unresolved problems in the study of meteors. Of these, primary emphasis has been given to luminosity experiments, because in this area our results as of the present time are most complete and most easily compared to natural meteor observations and to the work of other experimenters. However, we believe that our experimental work with meteor ionization may prove to be of equal or greater ultimate significance, largely because of the fact that the study of ionization seems to be generally less developed at this time than that of luminosity.

We have taken some pains to point out that the principal task which we have set for ourselves is the acquisition of basic data relating to the behavior of macroscopic particles ablating under meteoric conditions. Although we attempt to reproduce those conditions as accurately as possible in terms of flow regimes and other phenomena encountered by the particle, there is no attempt to reproduce a meteoroidal composition in the particle. For this reason it is seldom desirable or correct to compare our results directly to natural meteor observations, nor, do we feel, is it correct to imply the existence of errors in our work solely on the basis of lack of agreement when such a comparison is made. Instead, we regard our data as being most useful for two other purposes. One is to obtain a better understanding of meteoric processes and phenomena by examining them on a simpler and more controlled basis. The other is to acquire information from which values of meteoric constants defined in the theory may be synthesized.

Finally, throughout these discussions we have presented evidence which appears strongly to support our contention that meteoric processes are in fact accurately simulated in the experiments. We have noted that drag coefficients and heat transfer coefficients determined for simulated meteors are reasonable in themselves and are consistent with hypothesized ablation mechanisms and gas flow conditions. We have also discussed the agreement between our determination of τ_{pg}(Fe) and that found from artificial meteor experiments involving actual atmospheric entry of various bodies.

In closing, the authors wish to thank M. Dubin for his considerable support and encouragement of our work.

REFERENCES

ALLEN, C. W., 1955. *Astrophysical Quantities*, 1st ed., Athlone Press, London, 178.

AYERS, W. G., MCCROSKY, R. E., AND SHAO, C. -Y., 1970. Photographic observations of 10 artificial meteors, *Smithson. Astrophys. Obs. Spec. Rept.*, No. 317.

BECKER, D. G., AND FRIICHTENICHT, J. F., 1971. Measurement and interpretation of the luminous efficiencies of iron and copper simulated micrometeors, *Astrophys. J.*, **166**, 699–716.

BECKER, D. G., FRIICHTENICHT, J. F., HAMERMESH, B., AND LANGMUIR, R. V., 1965. Variable-frequency radially-stable micrometeoroid accelerator, *Rev. Sci. Instr.*, **36**, 1480–1481.

CEPLECHA, Z., 1966. Dynamic and photometric mass of meteors, *Bull. Astrom. Inst. Czech.*, **17**, 347–354.

——, 1968. Discrete levels of meteor beginning height, *Smithson. Astrophys. Obs. Spec. Rept.*, No. 279.

CEPLECHA, Z., AND PADEVĚT, V., 1961. The beginning of rapid evaporation of meteors of different dimensions, *Bull. Astrom. Inst. Czech.*, **12**, 191–195.

COOK, A. F., JACCHIA, L. G., AND MCCROSKY, R. E., 1963. Luminous efficiency of iron and stone asteroidal meteors, *Smithson. Contrib. Astrophys.*, **7**, 209–220.

DAVIS, J., 1963. On the color index of meteors, *Smithson. Contrib. Astrophys.*, **7**, 233–236.

DAVIS, J., AND HALL, J. E., 1963. Meteor luminosity and ionization, *Proc. Roy. Soc. London, A*, **271**, 120–128.

DERBENEVA, A. D., 1966. Ionization coefficient for meteoritic atoms, *Geomagnetizm i Aeronomiya*, **6**, 455–457.

FRIICHTENICHT, J. F., 1962. Two-million-volt electrostatic accelerator for hypervelocity research, *Rev. Sci. Instr.*, **33**, 209–212.

——, 1969. Evaporation of high-velocity particles in free-molecule flow, *J. Am. Inst. Aeronaut. Astronaut.*, **7**, 598–601.

FRIICHTENICHT, J. F., AND BECKER, D. G., 1971. Measurements of the ionization probability of Cu and LaB_6 simulated micrometeors, *Astrophys. J.*, **166**, 717–724.

FRIICHTENICHT, J. F., SLATTERY, J. C., AND HANSEN, D. O., 1967. Ionization from Fe atoms incident on various gas targets, *Phys. Rev.*, **163**, 75–80.

FRIICHTENICHT, J. F., SLATTERY, J. C., AND TAGLIAFERRI, E., 1968. A laboratory measurement of meteor luminous efficiency, *Astrophys. J.*, **151**, 747–758.

FURMAN, A. M., 1967. Meteor trail ionization theory, IV. Ionization efficiency through collision of vaporized meteoroid particles with air molecules, *Astron. Zh.*, **10**, 844–853.

HANSEN, D. O., AND ROY, N. L., 1966. A solid-state low-noise preamplifier, *Nucl. Instr. Methods*, **40**, 209–212.

HERSH, A. S., FRIICHTENICHT, J. F., AND SLATTERY, J. C., 1969. Drag coefficients of microscopic spheres in free molecule flow, in *Rarefied Gas Dynamics*, edited by L. Trilling and H. Y. Wachman, Academic Press, New York, **1**, 757–766.

HIRSCHFELDER, J. O., CURTISS, C. F., AND BIRD, R. B., 1954. Molecular theory of gases and liquids, J. Wiley and Sons, Inc., New York, Ch. 1.

MCCROSKY, R. E., AND SOBERMAN, R. K., 1963. Results from an artificial iron meteoroid at 10 km/sec, *Smithson. Contrib. Astrophys.*, **7**, 199–208.

MILLMAN, P. M., 1963. A general survey of meteor spectra, *Smithson. Contrib. Astrophys.*, **7**, 119–127.

MILLMAN, P. M., AND COOK, A. F., 1959. Photometric analysis of a spectrogram of a very slow meteor, *Astrophys. J.*, **130**, 648–662.

ÖPIK, E. J., 1933. Atomic collisions and radiation of meteors, *Acta et Commentat. Univ. Tartu* (Dorpat), **A26**, No. 2.

——, 1955. Meteor radiation, ionization, and atomic luminous efficiency, *Proc. Roy. Soc. London, A*, **230**, 463–501.

——, 1958. *Physics of Meteor Flight in the Atmosphere*, Interscience Publishing Co., New York, 174 pp.

ROY, N. L., AND BECKER, D. G., 1971. A time interval selector and proportional delay generator, *Rev. Sci. Instr.*, **42**, 204–209.

SEARES, F. H., AND JOYNER, M. C., 1943. Effective wave lengths of standard magnitudes; color temperature and spectral type, *Astrophys. J.*, **98**, 302–330.

SHELTON, H., HENDRICKS, C. D., JR., AND WUERKER, R. F., 1960. Electrostatic acceleration of microparticles to hypervelocities, *J. Appl. Phys.*, **31**, 1243–1246.

SIDA, D. W., 1969. The production of ions and electrons by meteoric processes, *Monthly Notices Roy. Astron. Soc.*, **143**, 37–47.

SLATTERY, J. C., AND FRIICHTENICHT, J. F., 1967. Ionization probability of iron particles at meteoric velocities, *Astrophys. J.*, **147**, 235–244.

SLATTERY, J. C., FRIICHTENICHT, J. F., AND HAMERMESH, B., 1964. Interaction of micrometeorites with gaseous targets, *J. Am. Inst. Aeronaut. Astronaut.*, **2**, 543–548.

TAGLIAFERRI, E., AND SLATTERY, J. C., 1969. A spectral measurement of simulated meteors, *Astrophys. J.*, **155**, 1123–1127.

VERNIANI, F., 1965. On the luminous efficiency of meteors, *Smithson. Contrib. Astrophys.*, **8**, 141–172.

——, 1970. Structure and fragmentation of meteoroids, *Space Sci. Rev.*, **10**, 230–261.

VERNIANI, F., AND HAWKINS, G. S., 1964. On the ionizing efficiency of meteors, *Astrophys. J.*, **140**, 519–564.

WHIPPLE, F. L., AND HAWKINS, G. S., 1959. Meteors, *Handbuch der Physik.*, **52**, 519–564.

Page intentionally left blank

7. Laboratory Determination of the Luminous Efficiency of Meteor Constituents

HOWARD F. SAVAGE AND CHARLES A. BOITNOTT
Ames Research Center, NASA
Moffett Field, California

A crossed beam apparatus has been used to measure the emission and ionization cross sections for the prominent spectral features of Na, Ca, Mg, and Fe in collisions with N_2 and O_2 over the velocity range of 30 to 120 km/s. From the emission and ionization cross sections, the absolute luminous efficiencies in air were determined over the range of meteor velocities. The maximum luminous efficiencies for the brightest features were: greater than 1 percent for the Na D*-lines, 0.2 percent for the CaI(2) singlet, 0.06 percent for the MgI(2) and MgI(3) triplets, and 0.4 percent for Fe over the visible spectral range. These luminous efficiencies are valid for free molecular flow conditions for velocities above about 30 km/s and are directly applicable to spectroscopic observations of faint meteors. The luminous efficiency of a typical stone will be presented and compared with the efficiencies determined by other investigators. In contrast to previous work, the luminous efficiency found for stone in the present investigation decreases with velocity above about 50 km/s.*

METEOR LUMINOSITY RESULTS primarily from the excitation of vaporized meteoric constituents during decelerating collisions occurring with atmospheric molecules. The naturally occurring process of meteor vapor excitation during the cascade of energy-transferring collisions can be simulated in the laboratory by observing the emission probability under controlled single collision conditions and integrating over all collisions to obtain the total radiating efficiency.

The major aim of our research at Ames Research Center is to make appropriate laboratory measurements of the light emissions due to collisions between air molecules and typical meteoric atoms to allow for a direct calculation of the spectral luminosity of meteors. The efficiency of converting kinetic energy to luminous energy is the luminous efficiency, τ, and for a particular spectral feature the two are related by

$$I_\lambda = -\tfrac{1}{2}\tau_\lambda v^2 \frac{dm}{dt}$$

where v is the meteor velocity, dm/dt is the mass loss rate of the element and λ is the wavelength of the spectral feature.

The spectral luminous efficiency for free molecular flow conditions can be determined from the relationship given by Sida (1969)

$$\tau_\lambda = \frac{2E_\lambda}{E_0}\int_{E_t}^{E_0}\frac{\sigma_\lambda}{\sigma_m}\frac{dE}{E}$$

where E_0 is the initial kinetic energy, E_λ is the photon energy, E_t is the threshold energy for exciting the wavelength λ, σ_m is the momentum transfer cross section, and σ_λ is the cross-section for the emission of a photon of wavelength λ in a collision between an air molecule and a meteor atom. The mathematical formulation of τ in slip

flow is too complex for present analysis and will not be considered here.

An appreciable fraction of the ablated meteor atoms is expected to be ionized during the deceleration process. The ions formed can produce either ion lines or, if neutralization occurs, neutral lines upon subsequent collisions. Therefore, an accurate determination of τ_λ must take into account the fraction of ions present during the deceleration process. The luminous efficiency equation can be evaluated using an effective emission cross section given by:

$$\sigma_\lambda(E) = \sigma_{\lambda i}(E)\frac{N_i(E)}{N_0} + \sigma_{\lambda n}(E)\left[1 - \frac{N_i(E)}{N_0}\right]$$

where $\sigma_{\lambda i}(E)$ is the emission cross section for collisions of ions with air molecules and $\sigma_{\lambda n}(E)$ is the emission cross section for those collisions involving neutral metal atoms. The ion concentration generated in decelerating the ablated atoms from initial energy E_0 to energy E can be found from the relation $N_i(E)/N_0 = 1 - e^{-\beta(E)}$ where the ionization probability $\beta(E)$ is determined from the relation given by Sida (1969)

$$\beta(E) = 2\int_E^{E_0} \frac{\sigma_i}{\sigma_m}\frac{dE}{E}$$

where σ_i is the ionization cross section. Finally, the measurable quantities in our experiments, which are related to σ_λ and σ_i, are the number of photons and ions produced in the collision of a beam of N_2 or O_2 with a perpendicular beam of metal atoms. The definitive relationship for these cross sections is $\Phi_\lambda = F(1 - e^{-Nx\sigma_\lambda})$, where Φ_λ is the number of photons per second emitted at a wavelength λ when a gas beam of intensity F passes a distance x through a metal beam of density N. A similar expression relates σ_i to the number of ions produced.

APPARATUS

The crossed molecular beam apparatus used to make these measurements shown in figure 1 has been described in detail in our previous reports (Boitnott and Savage, 1970; Savage and Boitnott, 1971). Briefly nitrogen or oxygen is ionized in the source and focused through the analyzing magnet to select the desired ion. The ion energy is set by

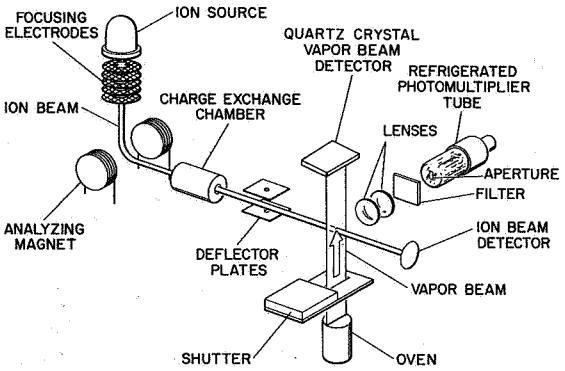

FIGURE 1.—Schematic of emission cross-section apparatus.

the potential at the ion source. The resulting N_2^+ or O_2^+ beam is then focused into a charge exchange cell which contains enough N_2 or O_2 to resonantly charge exchange about half of the original ion beam. In such a charge exchange process, there is no energy exchange or scattering as long as the densities are low enough so that there are no secondary collisions. The electrostatic deflection plates remove the remaining ions from the beam leaving only N_2 or O_2 to be injected into the test chamber. Intersecting at right angles to the N_2 or O_2 beam is the metal atom beam which emanates from a slit in an oven (the flux of metal atoms being determined by the oven temperature). The measurements were generally made with metal atom densities of the order of 10^{10} cm^{-3} while the background density of gas in the test chamber was about 5×10^{10} cm^{-3}. For Na, the flux was measured with a hot tungsten oxide surface ionizer as described in our Na paper (Boitnott and Savage, 1970); and the Mg, Ca, and Fe fluxes were measured with an oscillating quartz crystal.

A portion of the photons generated by the collisions pass through a bandpass filter and are counted. The bandpass of these filters is typically 100 Å and is centered on the multiplet of interest. Now, with the photon count, calibration factors, metal atom density, and gas beam intensity, the emission cross section is determined. Then with the ionization cross section determined from the ion count, we can work through the equations previously discussed and determine the luminous efficiency for the spectral feature being observed.

The conditions of the experiment which can be controlled are:

(1) The densities of the colliding beams
(2) The energy involved in the collision
(3) The collision partners
(4) The photon wavelength observed.

In regard to the densities of the beams, all of our measurements have been made under free molecular flow conditions. As for the energy, unfortunately, our lowest energy is limited to about 150 eV so that the luminous efficiency calculations must be made with extrapolation of the pertinent cross sections. Therefore, the efficiency values below about 30 km/s are much more uncertain than at the higher velocities.

EMISSION CROSS SECTIONS

The emission cross sections of the most prominent multiplets of Na, Mg, and Ca are shown in figure 2 over the range of energies investigated. The wavelengths of the lines of each multiplet shown in figures 2, 3, and 4 are listed in table 1. The data shown for Fe are for the total radiation in the wavelength range between 3500 and 4200 Å. The number of lines in the Fe spectrum is so numerous and closely spaced that bandpass filters could only make measurements for collections of multiplets and could not easily isolate individual multiplets. At wavelengths greater than 4200 Å, the blackbody radiation from the source oven made meaningful measurements very difficult.

Cross sections for Mg and Ca shown in figure 2 are typical with other multiplets of these elements

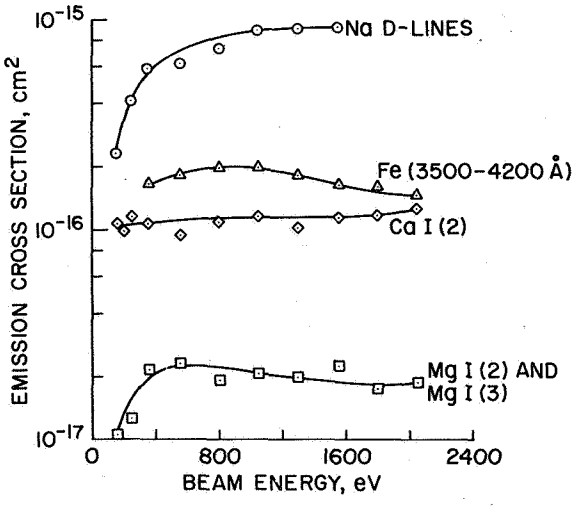

FIGURE 2.—Emission cross sections due to N_2 collisions for the prominent multiplets of Na, Mg, and Ca and of Fe over the range 3500 to 4200 Å.

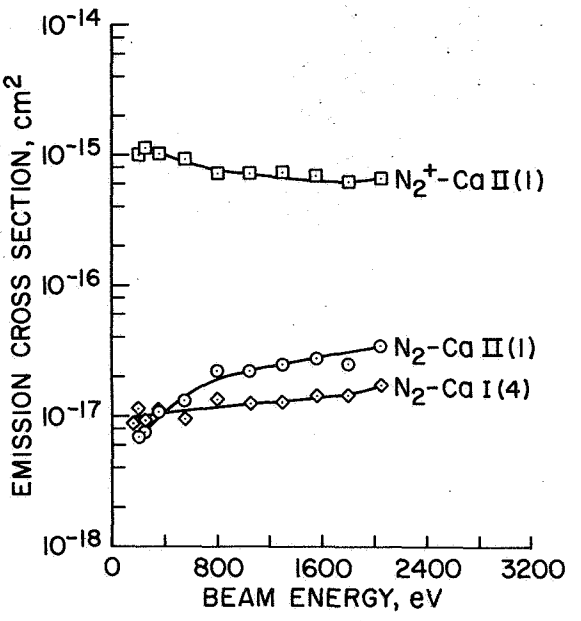

FIGURE 3.—Emission cross sections of Ca due to N_2 and N_2^+ collisions.

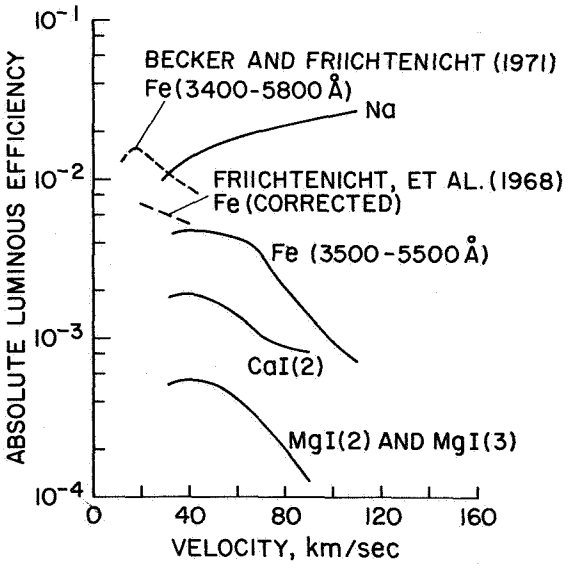

FIGURE 4.—Absolute luminous efficiencies for the prominent multiplets of Na, Mg, and Ca and of the visible spectrum of Fe.

TABLE 1.—*Wavelengths of Multiplet Lines*

Multiplet	Line wavelengths, Å
Na *D*-lines	5890, 5896
CaI(2)	4227
CaI(4)	4425, 4435, 4455
CaII(1)	3934(*K*), 3938(*H*)
MgI(2)	5167, 5173, 5183
MgI(3)	3829, 3832, 3838

showing similar characteristics but with smaller magnitudes. Collisions involving O_2 instead of N_2 generally had lower cross sections, by as much as a factor of 5, and did not necessarily show the same variations with energy (Savage and Boitnott, 1971; Boitnott and Savage, 1970).

Of considerable interest are the CaII(1) lines, H and K, since they frequently appear enhanced in meteor spectra and are thought to indicate slip flow conditions. The emission cross sections are shown in figure 3 as a function of energy for both N_2 and N_2^+ in collisions with neutral Ca. In addition to the large difference in magnitude between the ion and neutral collision partners, the variation with energy is completely different. The high H and K emission for N_2^+ collisions with neutral Ca is due to near resonant charge exchange including excitation of the Ca ion in a single collision. Without getting into a complete discussion of the H and K line enhancement as the meteor gets lower in the atmosphere, we want only to show that even in the free molecular flow regime there is considerable H and K emission as a result of neutral-neutral collisions. For the luminous efficiency and a more complete discussion of the H and K enhancement, see Boitnott and Savage (1971). The cross sections indicate, that in the free molecular flow regime, the multiplets CaI(4) and CaII(1) should be of nearly equal intensity. Any enhancement of the H and K lines should take place as the meteor enters the denser atmosphere where there are secondary collisions between neutral calcium and metal or gas ions, i.e., slip flow conditions.

LUMINOUS EFFICIENCIES

The absolute luminous efficiencies for the most prominent multiplets of Na, Mg, and Ca are shown in figure 4 along with the total luminous efficiency for the visible spectra of iron. For the luminous efficiencies of the other multiplets of Mg and Ca, see Boitnott and Savage (1971). To obtain the total for iron, allowances were made for the visible spectrum above 4200 Å by comparing our bandpass data in the 3500 to 4200 Å range with the spectrum obtained by Tagliaferri and Slattery (1969) and with the natural meteor data of Harvey (1970). The decrease in the efficiencies of Fe, Mg, and Ca at the higher velocities is caused by the high relative probability of ionization at these velocities. This has the effect of removing neutral atoms which might be excited during a later collision in the deceleration process. Also the emission cross sections for the neutral atom lines due to collision between metal ions and air molecules are very low in comparison to those for neutral-neutral collisions. There is generally good agreement between our data and the free molecular flow meteor simulation experiments of Friichtenicht et al. (1968) and Becker and Friichtenicht (1971). The data of Friichtenicht et al. has been increased by 20 percent to account for the more accurate spectral distribution found later by Tagliaferri and Slattery (1969).

The luminous efficiencies we have determined for the multiplets of Na, Mg, and Ca and the

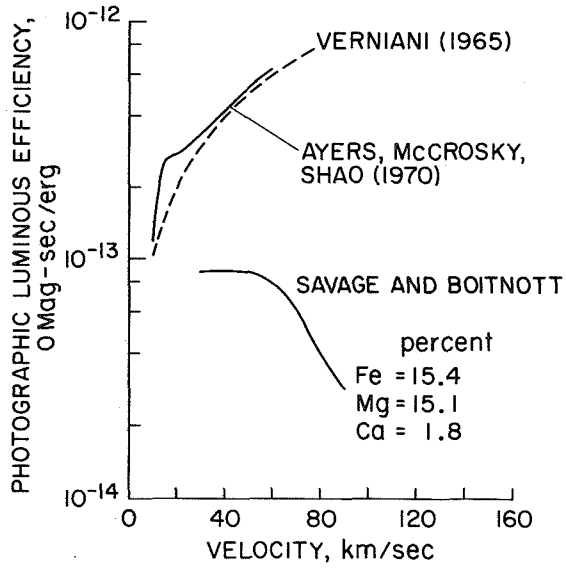

FIGURE 5.—The photographic luminous efficiency of a stone for blue sensitive film.

total for iron are directly applicable to the determination of the relative abundances of these elements in those free molecular flow photographic meteors for which good resolution spectra are available. With an assumption on the relative abundances of the weak and nonradiating elements which make up the rest of the meteor, the mass can be determined.

As an exercise, we have calculated the photographic luminous efficiency of blue sensitive film (Ayers, 1965) for a meteor with the assumed composition of meteoric stone (fig. 5). Variations in the composition would have only minor effects on the magnitude of τ without changing the general trends. Other vaporized elements present in the meteor are assumed to provide negligibly weak radiation and are neglected. In addition, any contribution by air molecules is not included in the calculations. Such radiation is toward the red and is seen in spectra using panchromatic film as are the Na *D*-lines.

For comparison, we show the luminous efficiency deduced by Verniani (1965) from 413 photographic meteors where he assumed that τ is proportional to the V^n, for all velocities, and concluded that $n=1$. Also shown is the best guess efficiency of Ayers et al. (1970) which is primarily based on low velocity, near continuum flow, artificial meteor data. The reasons for the large differences are not clear to us at this time.

In summary, we have measured in the laboratory the fundamental emission and ionization cross sections needed to determine the spectral luminous efficiencies of Na, Mg, and Ca and the total efficiency for iron. We are encouraged by the good agreement with the luminous efficiency of iron measured by Friichtenicht et al., and Becker and Friichtenicht, and feel that the luminous efficiencies obtained can be applied to the quantitative analysis of meteor spectra in free molecular flow conditions.

REFERENCES

Ayers, W. G., 1965. Luminous efficiency of an artificial meteor at 11.9 kilometers per second, *NASA* TN **D-2931**.

Ayers, W. G., McCrosky, R. E., and Shao, C. -Y., 1970. Photographic observations of 10 artificial meteors, *Smithson. Astrophys. Obs. Spec. Rept.* No. 317.

Becker, D. G., and Friichtenicht, J. F., 1971. Measurement and interpretation of the luminous efficiencies of iron and copper simulated micrometeors, *Astrophys. J.*, **166**, 699–716.

Boitnott, C. A., and Savage, H. F., 1970. Light-emission measurements of sodium at simulated meteor conditions, *Astrophys. J.*, **161**, 351–358.

Boitnott, C. A., and Savage, H. F., 1971. Light-emission measurements of calcium and magnesium at simulated meteor conditions. II. Spectral luminous efficiencies, *Astrophys. J.*, **167**, 349–355.

Friichtenicht, J. F., Slattery, J. C., and Tagliaferri, E., 1968. A laboratory measurement of meteor luminous efficiency, *Astrophys. J.*, **151**, 747–758.

Harvey, G. A., 1970. Spectra of faint optical meteors, unpublished.

Savage, H. F., and Boitnott, C. A., 1971. Light-emission measurements of calcium and magnesium at simulated meteor conditions. I. Cross-section measurements, *Astrophys. J.*, **167**, 341–348.

Sida, D. W., 1969. The production of ions and electrons by meteoritic processes, *Monthly Notices Roy. Astron. Soc.*, **155**, 37–47.

Tagliaferri, E., and Slattery, J. C., 1969. A spectral measurement of simulated meteors, *Astrophys. J.*, **155**, 1123–1127.

Verniani, F., 1965. On the luminous efficiency of meteors, *Smithson. Contrib. Astrophys.*, **8**, 141–172.

Page intentionally left blank

8. Evidence from Spectra of Bright Fireballs

ZDENĚK CEPLECHA
Astronomical Institute of the Czechoslovak Academy of Sciences
Ondřejov, Czechoslovakia

Spectral data with dispersions from 11 to 94 Å/mm on 4 fireballs of actual brightness of −4 to −12 magnitude and with velocities of about 30 km/s at 70 to 80 km heights are used for studies of meteor radiation problems. Previously published analyses need revision for two main reasons: (a) the absolute values of oscillator strengths of Fe I lines from laboratory data were recently recognized to be 1 order of magnitude lower, (b) the luminous efficiency factor τ of Fe I is now much better known from several different experiments. The radiation of fireballs is found to be strongly affected by self-absorption. But if the emission curve of growth is used for correction of the self-absorption of Fe I lines, a great discrepancy between spectral data and efficiency data for total Fe I light is found. If one assumes that the self-absorption is superposed on another effect, a decrease of the dimensions of the radiating volume with increasing lower potential E_1, *the spectral data on Fe I lines will be in agreement with the luminous efficiency of total Fe I meteor radiation. Formulas for emission curve of growth and Boltzmann distribution including this effect are derived. This effect is important for fireballs brighter than about −1 or −2 magnitude, while self-absorption seems to be important even for fainter meteors. The optically thin radiation of all Fe I lines might be expected for meteors fainter than +5 magnitude. Excitation temperature of 5500° K and relaxation time of 0.02 s were found as typical values for the Fe I radiation of fireballs studied. The light of fireballs is emitted during a relatively long relaxation time, which is many orders of magnitude longer than the time necessary for spontaneous radiation of excited Fe I atoms. The dimensions of the radiating volume of Fe I gas for lines with* $E_1 = 0$ *were found to be 0.3×9 m at 0 absolute magnitude and 2×60 m at −10 absolute magnitude. It was not possible to determine any realistic abundances of other elements due to small numbers of lines for an analysis independent of Fe I, while the Fe I curve of growth cannot be used for other elements, because the radiation originates mainly from the effective surface of the radiating volume. A general formula for meteor radiation is also derived and compared with the conventional luminosity equation.*

THERE IS ENOUGH LIGHT available to obtain spectra of bright fireballs with dispersions well below 100 Å/mm. On the other hand, there are not so many bright fireballs which is, in part, the reason that published spectral data on line intensities are rather scarce. Preparing this paper I used, almost exclusively, my own observational material resulting from ten years of systematic operation of three grating spectrographs employed in the registration of meteors at the Ondřejov Observatory in Czechoslovakia. On an average, about one year was necessary to get a good spec-

trum of a fireball (over 100 spectral lines in the visible region) using these cameras. The direct double-station cameras (30 in number) provided us with all the necessary geometrical and velocity data on these fireballs. The reduction of four spectra is now completed; three of them have been published already (Ceplecha and Rajchl, 1963; Ceplecha, 1964, 1965, 1966) and one spectrum, S 1132, containing 990 spectral lines, is in print (Ceplecha, 1971).

The summary of the spectra I am using in this study is in table 1. All the objects were of approximately the same velocity, about 30 km/s. Thus the observational data presented here are to be referred to this particular velocity, to heights of 70 to 80 km and to an actual brightness interval of −4 to −12 absolute magnitude (the maximum absolute magnitudes are in the interval from −9 to −12 mag). I also used qualitative data on one more spectrum, belonging to a fireball of approximately −18 magnitude. The reduction of this spectrum is not yet finished and only preliminary data are available. The spectrum belongs to a body with a significant terminal mass of about 600 g, but no meteorite was found.

NEED FOR REVISION OF PREVIOUS STUDIES

Some studies of spectra in table 1, which I published previously, need a revision from two main aspects:

(1) The absolute values of the oscillator strengths of Fe I lines from laboratory data were recently recognized to be one order of magnitude

TABLE 1.—*List of Meteor Spectra Used for Analysis in This Paper*

Spectrum No.	S 6	S 526	S 912	S 1132	(S 1135)
Meteor No.	130960	32281	36221	38421	
Date	Sept. 13, 1960	Nov. 13, 1961	Sept. 26, 1962	Apr. 21, 1963	
Time (GMT)	$18^h\ 59^m$	$21^h\ 49^m\ 46^s$	$23^h\ 18^m\ 16^s$	$1^h\ 13^m\ 48^s$	
[a]M_{pan}	−10.5	−9.6	−10.3	−12.4	
Appearance on spectral plate	flare of 0.025 s	trail of 0.6 s with many flares	trail of 0.4 s with steep but smooth light curve	flare of 0.022 s	trail of 0.4 s with terminal flare
Spectral order	2 to 7	1+2	1	1	prism
Dispersion (Å/mm)	38 to 11	94+47	58	57	
No. of spectral lines	166	161	189	990	
α_R (deg)	≈5	58.2	22.2	264.6	
δ_R (deg)	≈0	16.5	7.1	56.8	
cos z_R	≈0.2	0.785	0.718	0.965	
v_∞ (km/s)	≈30	28.86	31.92	32.57	
a (AU)	Southern Taurid	2.30	1.63	5.51	
e		0.814	0.849	0.819	
q (AU)		0.427	0.247	0.997	
ω (deg)	1950.0	105.5	129.9	190.8	
Ω (deg)		51.1	3.2	30.0	
i (deg)		5.0	4.9	49.0	

[a] M_{pan} is the total absolute maximum magnitude from panchromatic plates, while magnitudes in table 2 are the actual absolute magnitudes at each point of Fe I radiation only.

lower than previously accepted (Grasdalen et al., 1969; Garz and Kock, 1969).

(2) The luminous efficiency factor τ of Fe I is now much better known from several different experiments (Ayers et al. 1970, Friichtenicht et al. 1968).

The absolute abundances of Fe I derived from spectral data on fireballs were previously recognized by me to be about 1 or 2 orders of magnitude greater than that derived from total Fe I light, using a luminous efficiency factor (Ceplecha, 1965, 1968). The "spectroscopic" mass of meteors studied is increased by an additional order of magnitude over the "photometric" mass, if we use the new Fe I oscillator-strength data. The main purpose of this paper is a comparison of the spectral data on Fe I absolute abundances with corresponding data derived from the total Fe I light curve calibrated by the luminous efficiency factor.

THE LUMINOSITY EQUATION

Before dealing with the main problem of this paper, I will derive a new general form of luminosity equation, which will help to relate the conventional luminosity equation to the gas mass in the radiating volume.

Let us denote by m_A the total gas mass that has entered the radiating volume since the meteor beginning. Let us denote by m_Z the total gas mass that has left the radiating volume since the meteor beginning. Then, at each instant, the total gas mass m_G inside the radiating volume is

$$m_G = m_A - m_Z \tag{1}$$

Assuming that the excitation temperature and self-absorption are roughly constant during the meteor flight, which is applicable to radiation of one element in one state, we have for the intensity I of the radiation:

$$I = k m_G \tag{2}$$

where the proportionality factor k is a luminous efficiency of the radiating gas measured in ergs s^{-1} g^{-1}. Even if k is some function of time, it changes substantially less than m_G and the proportionality, equation (2), may be considered a good approximation to the reality. This approximation is no worse than the conventional luminosity equation (4).

Substituting equation (1) in equation (2) we have

$$I = k(m_A - m_Z) \tag{3}$$

This is a meteor luminosity equation more general than the conventional equation

$$I = -\frac{\tau}{2} v^2 \frac{dm}{dt} \tag{4}$$

Our task now is to relate the general equation (3) to the special equation (4). The additional assumptions to be applied to equation (3) can be derived from the following considerations: We differentiate (3)

$$dI = k(dm_A - dm_Z) \tag{5}$$

We can assume that dm_A and dm_Z are the same functions of time with different phase only

$$dm_Z(t) = dm_A(t - t_R) \tag{6}$$

where t_R is constant: it is the time spent by an average atom inside the volume of radiating gas, and I will refer to it as the relaxation time in this paper. Now if equation (6) is substituted in equation (5) and Taylor's series with the first derivative used, we have

$$dI = k t_R \, d(dm_A/dt) \tag{7}$$

If we replace m_A by the ablated meteor mass

$$m_A = m_\infty - m \tag{8}$$

and integrate, we have

$$I = -k t_R (dm/dt) + k_R \tag{9}$$

But there is practically no light at the beginning of the ablation of the meteor and $k_R = 0$. Thus equation (9) is equivalent to equation (4), if

$$k t_R = \frac{\tau v^2}{2} \tag{10}$$

Variation in v and τ during the trajectory of one meteor is neglected. We can summarize:

(1) The conventional luminous equation (4) is only a very special case of the more general equation (3).

(2) The conventional luminous equation (4) represents an average smooth change of light.

(3) Equation (3) can easily explain the big fluctuations of the observed light curves (see fig. 1) with dm/dt being a smooth function of time. If $dm_Z < dm_A$, I increases; if $dm_Z > dm_A$, I decreases. Thus dm_A, dm_Z may be smooth functions of time, while the light intensity is flaring. Figure 1 shows this clearly even for $t_R = \text{const.}$; but without this limiting assumption, the general form of equation (3) is even more sensitive for producing big changes in light emission from small smooth changes of dm/dt.

SELF-ABSORPTION IN SPECTRA OF FIREBALLS

I have already published studies of three spectra of meteors in table 1 using the method of emission-curve-of-growth, which takes into account the optical thickness of individual spectral lines (Ceplecha 1964, 1965, 1967). After publication of this method, there were some doubts as to whether the method is applicable to fireball spectra or not. The importance of self-absorption and damping processes for fireball radiation may be well demonstrated using figure 2. Even though figure 2 is presented here only for spectrum S 6, the same relative positions of individual multiplets result, using any of the other 3 spectra of table 1 at any of the measured points. The upper level potential E_2 is plotted along the x-axis and the total number of atoms of Fe I in all levels of the upper term, $N(\text{term})$, is plotted along the y-axis. The observed

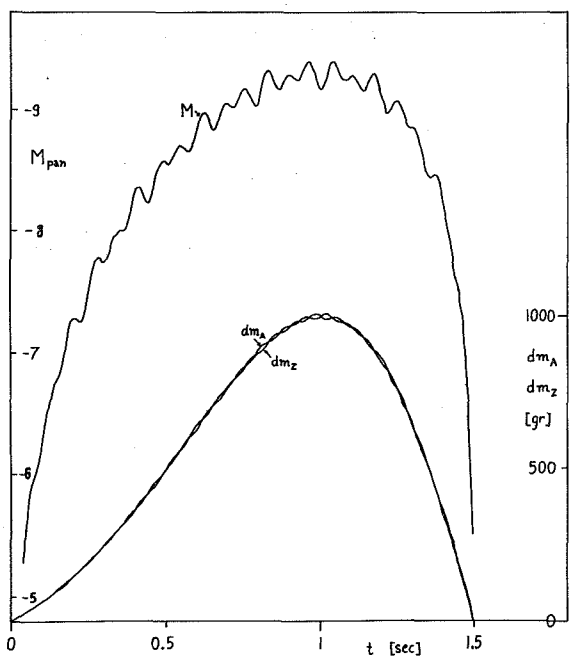

FIGURE 1.—Theoretical light curve computed from arbitrarily chosen but smooth values of dm_A, dm_Z. This shows the flaring effect. Formula (3) was used with simplifying assumption (6): log $t_R = -2.7$, $v = 30$ km/s, log $k = 3.42$. This is just an example representing formula (3) with limitation (6). General form of formula (3) is even more able to describe the flaring effect.

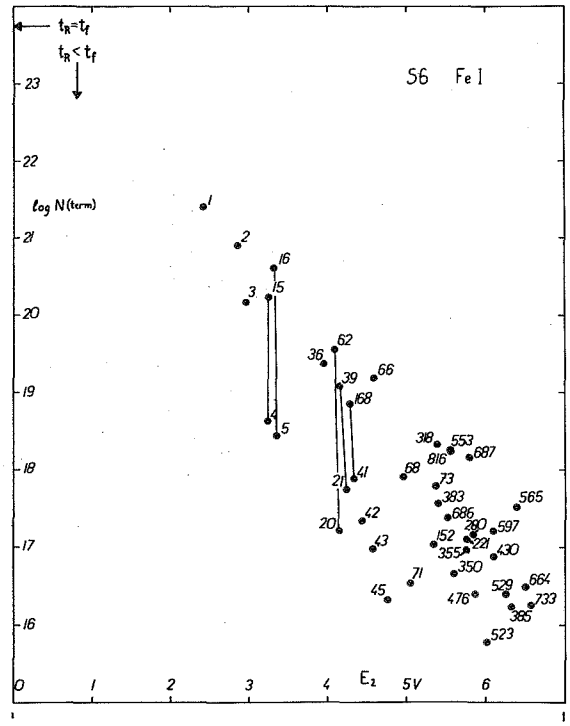

FIGURE 2.—Numbers of Fe I atoms, $N(\text{term})$, occupying all levels of the upper term were computed for S 6 spectrum of a flare on assumption that the radiation observed in corresponding lines was optically thin ($I_0 = I$). log $N(\text{term})$ is plotted against the upper potential E_2. A straight line corresponds to Boltzmann distribution of levels. One average value for each multiplet is given. The numbering of the points corresponds to the notation of multiplets after Moore (1945). A self-absorption for multiplets with the same upper level term is evident: multiplet 4 against 15, 5 against 16, 20 against 62, 21 against 39, 41 against 168. The parameter t_R is the relaxation time, t_f the duration of the flare. The extrapolation of the Boltzmann straight line to $E_2 = 0$ must be equal to or lower than the point $t_R = t_f$.

radiation is assumed to be optically thin here, which means

$$\log N(\text{term}) = \frac{I_0 \lambda^3 m_e G_2}{8\pi^2 h e^2 g f} \qquad (11)$$

I_0 is optically thin radiation: here the observed I was used for figure 2 instead. G_2 is the total statistical weight of the upper term. Each point in figure 2 corresponds to an average value for the whole multiplet assuming that no self-absorption is present ($I_0 = I$). Some of the multiplets with more observed lines point to a dependence of $\log N(\text{term})$ on $\log gf$ as is apparent from figure 3. In figure 2, multiplets with the same upper level term yield greater $\log N(\text{term})$, if their lower level is higher. Thus multiplet 4 ($E_1 = 0$) shows an absorption of more than one order of magnitude relative to multiplet 15 ($E_1 = 0.9$ V), multiplet 5 more absorption than multiplet 16, multiplet 20 more than 62, multiplet 21 more than 39 and multiplet 41 more absorption than multiplet 168. This clearly means that we see only a part of the light produced inside the radiating gas volume and emitted in multiplets 4, 5, 20, 21, 41. From other spectra than S 6, multiplets 2, 23, 42, 43 and many others show clear evidence of self-absorption. But there is no reason for the assumption that multiplets 15, 16, 62, 39, 168, giving the greatest population observed for the same upper level, are optically thin. If we visualize a Boltzmann distribution of levels in figure 2, we have a straight line, the slope of which corresponds to the excitation temperature T:

$$\log N(\text{term}) = -\Theta E_2 + \text{const.}, \text{ where } \Theta = \frac{5040}{T} \qquad (12)$$

The extrapolation of this straight line to $E_2 = 0$ gives the total number of atoms in the ground state, which is almost the number of all atoms of Fe I for all reasonable temperatures. On the other hand, spectrum S 6 belongs to a short bright flare, the duration of which (0.025 s) combined with the luminous efficiency of Fe I (Ayers et al., 1970, $\log \tau_{\text{pan}} = -11.94$) gives an upper limit for $\log N$. This is equivalent to an assumption that the duration of the flare is identical with the relaxation time t_R. If the relaxation time is less, the limit will be lower and the discrepancy higher. From figure

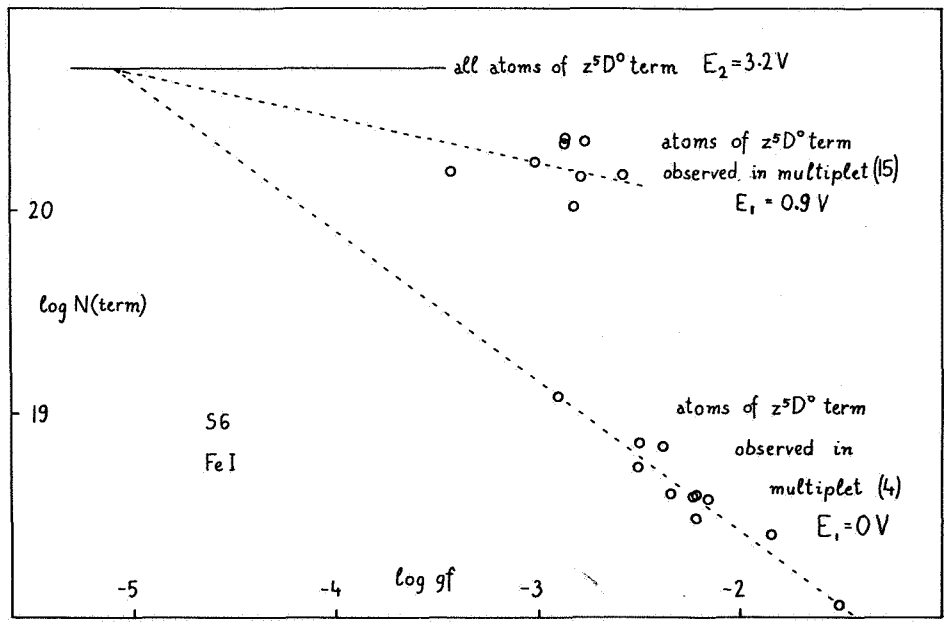

FIGURE 3.—Log N(term), from individual lines of multiplets 4 and 15 (upper term z^5D^0), is plotted against log gf of the lines, assuming optically thin radiation as in figure 2. Self-absorption is evident. The dotted lines are only schematic, but indicate that lines with log $gf \approx -5$ and less might be expected optically thin for z^5D^0 of this spectrum.

2, it is also evident that multiplets giving the greatest $\log N(\text{term})$ must be affected by some further absorption effect. As a byproduct we can guess that the relaxation time t_R of Fe I lines with $E_1=0$ is of the order of 10^{-2} or 10^{-3} s, if reasonable excitation temperatures are used. There is no reasonable way to make t_R less than 10^{-4} s. This time is by orders of magnitude longer than the time necessary for spontaneous radiation of the corresponding excited states of the Fe I atoms. Some quasiequilibrium conditions may be reached during this relatively long time. There is no doubt, inspecting figure 2, that self-absorption is at least partly responsible for the observed effects.

But if we use the emission curve of growth to correct for self-absorption, we get a relaxation time, t_R, still greater than the duration of the flare. I tried to use a model with exponential decrease of temperature along the radiating volume to avoid this discrepancy, but it was not much help. This suggests that another additional effect is present.

The observed radiation and deduced number of atoms are related to the whole volume of radiating gas. As we know that the wake phenomenon is strongly dependent on the excitation, we may expect the same dependence also for the "head" radiation. Then we actually do see the radiation of different spectral lines belonging to different volumes of radiating gas with different relaxation times. The low potential lines perhaps radiate from a larger volume with longer relaxation time. I will present here a simple theory of this effect and derive corresponding changes of the emission curve of growth and of the Boltzmann distribution. I will apply the theoretical results to the spectra of table 1.

EMISSION CURVE OF GROWTH WITH RESPECT TO CHANGES OF THE VOLUME OF RADIATING GAS WITH THE E_1 POTENTIAL

I will use the same simple model of radiating gas volume that I published previously (1964), which is a cylindrical volume with great density on the surface, termed the "cylindrical shock-wave" model. I assume that the length ℓ and radius R of the cylindrical volume are proportional, p being the proportionality factor. Then

$$\ell = pR \tag{13}$$

The intensity of the wake phenomenon seems to depend on the lower level E_1 of the corresponding line. Thus I assumed a dependence of ℓ and R on the lower level E_1 having an exponential form

$$\ell(E_1) = \ell(0)\ \exp\left[-2q\chi_1/(k_BT)\right] \tag{14}$$

where χ_1 is the energy of the lower level (potential E_1) and q is an exponential factor describing the decrease of the length of the radiating volume with increasing lower potential. Here $\ell(0)$ is the length of the radiating volume corresponding to the ground state. Following equation (18) of my previous paper (1964), we have

$$\log N(E_1) = \log N(0) - 5q\Theta E_1 \tag{15}$$

for the total number of all atoms of the ground state inside a volume corresponding to the E_1 level. Here $N(0)$ is the total number of atoms of the ground state inside the radiating volume belonging to the ground state.

The Boltzmann distribution for this case is then represented by

$$\log \frac{I_0\lambda^3}{gf} = -\Theta(E_2+5qE_1) + \log \frac{8\pi^2he^2}{m_eU} + \log N(0) \tag{16}$$

where I_0 is the optically thin intensity radiated by the assumed changing volume in all directions. The observed intensities I are to be converted to I_0 by using the emission curve of growth given in our partial case by

$$\log \frac{I}{\lambda B_\lambda} + 4q\Theta E_1 + \log \frac{c}{8\pi^2 v_m\left[R^2(0)+R(0)\ell(0)\right]\cos\alpha} = \log F(X) \tag{17}$$

where

$$\log X = \log gf\lambda - \Theta E_1 - q\Theta E_1 + \log \frac{3e^2N(0)}{16m_ecUv_m\left[R^2(0)+R(0)\ell(0)\right]\cos\alpha} \tag{18}$$

and the function $F(X)$ describes the actual shape of the curve of growth. This is the same function as previously published [Ceplecha, 1964, equation (22)]. The damping part of the emission curve of growth is also well described by

$$\lim_{X\to\infty} \log F(X) = \tfrac{1}{2} \log X + \text{const.} \qquad (18a)$$

in this case and generally.

The procedure used for application of the above derived formulas to the observed spectral lines is exactly the same as published previously (Ceplecha, 1964). The results of the computations are: the excitation temperature T, the number of all atoms of one element in one state inside a radiating volume corresponding to $E_1=0$, and Y_{lim} proportional to the surface of this volume. A set of these values is obtained for each chosen value of q. If the ratio p of ℓ to R is assumed, the volume of radiating gas for $E_1=0$ is determined and the terminal density $n_0(\delta_0)$ at the end of the cylindrical volume as well as the average density $\bar{n}(\bar{\delta})$ may be computed. The whole procedure of numerical computations was programmed for the Minsk–22 digital computer.

We have actually added one more parameter, q, to be determined from observation. But this parameter may be guessed from the spectra of flares of short duration. If dm/dt is determined from equation (4), and compared with the results from the emission curve of growth, we can determine the relaxation time

$$t_R = \frac{m_G}{dm/dt} \qquad m_G = \mu N \qquad (19)$$

Here m_G is determined from the curve of growth and dm/dt from the light curve. We have an additional condition for short duration flares

$$t_R \leq t_f \qquad (20)$$

where t_f is the duration of the flare.

RESULTS FOR FE I

The actual solution of the problem was possible for Fe I lines almost exclusively. Any other element, except for Na I, Ca I and O I in spectrum S 1132, had not a sufficient number of spectral lines for such a solution. Only the lines without any blends were used for all the computations. The gf-values used were from Corliss and Bozman (1962) and Corliss and Warner (1964), but corrected by -1.00 in the log to the newly established approximate absolute scale (Grasdalen et al., 1969; Garz and Kock, 1969). The excitation potentials were taken from Moore (1945).

I started with S 6 and S 1132 and found a temperature of 5500° K as the lowest possible to satisfy the equation (20) condition in both spectra. With this temperature, t_R of S 6 is equal to the duration of the flare of S 6, and t_R of S 1132 is about $\frac{1}{5}$ of the duration of the flare of S 1132. Any temperature higher than 5500° K may be a solution of the problem as well, but there is another rough estimation possible using the computed density inside the radiating volume: the terminal n_0 should not exceed too much the density of the surrounding air. If n_0 of Fe I is not greater than 10 times the surrounding air, the temperature should not exceed some 8000° K. If n_0 is of the order of the surrounding air, we arrive at about 5000° to 6000° K. Thus 5500° K was taken as a standard temperature and all the solutions for q were made with this temperature. A graphical example of one solution for S 1132 is given in figures 4 and 5. The curve of growth, figure 4, and the Boltzmann distribution, figure 5, are used simultaneously for the temperature determination. This means that the actual position of the theoretical curve of growth and the Boltzmann straight line are dependent on the positions of points in both figures 4 and 5.

All points of the meteor spectra of table 1 were used for the solution of q for Fe I lines, using the above estimated temperature. The following values were determined and are listed in table 2; number of all atoms of Fe I inside the radiating volume; Y_{lim} proportional to the surface of the radiating volume; dm/dt from the light curve of total Fe I radiation ($\log \tau_{\text{pan}} = -11.94$ was used for I being in 0 magnitude units combined with c.g.s.; Ayers et al., 1970); the ratio of Fe I radiation to total radiation; the relaxation time t_R; rough guesses for the ratio p of ℓ to R; characteristic velocity v_m; the terminal densities n_0, δ_0 and the average densities n, δ of Fe I atoms.

The most important result is that using equations (16) to (18), which describe the combination of self-absorption and changing volume of radiating gas in a simple model, we are able to put the spectral data on Fe I lines in agreement with the luminous efficiency of the total Fe I meteor radiation. If temperatures are close to 5500° K, the values of q are from 0.010 to 0.068, depending partly on the total brightness. Extrapolating to fainter meteors, there is clear evidence that the

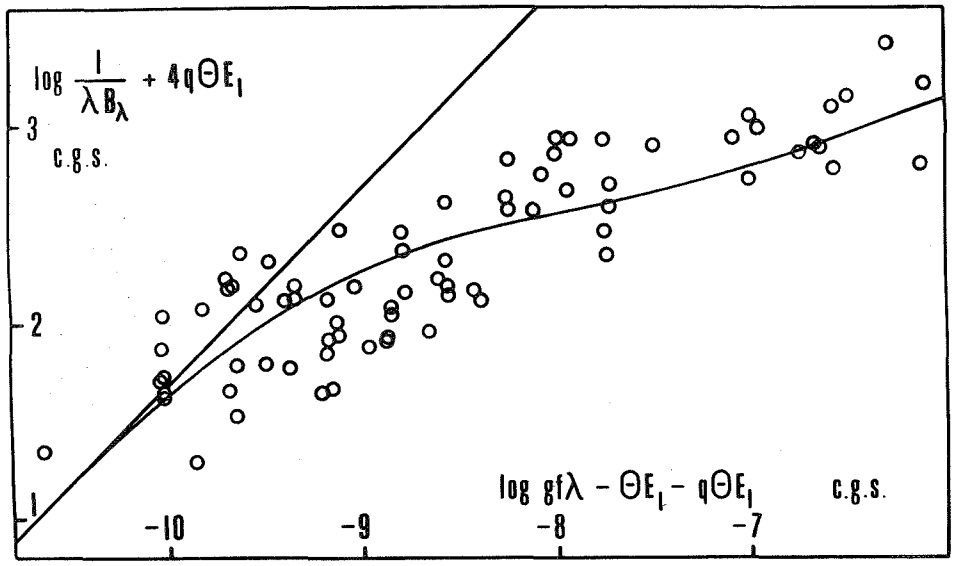

FIGURE 4.—Spectrum S 1132: The emission curve of growth with respect to the decrease of volume of radiating gas with the E_1 potential. The position of the theoretical curve of growth depends on the Boltzmann distribution presented in figure 5.

effect of a change of the radiating volume with E_1 potentials may be negligible for meteors fainter than about -2 or -1 absolute magnitude. On the other hand, the self-absorption effect is important even for fainter meteors. If we compare multiplet 4 with multiplet 15 for the fireballs of table 1, and also for the relatively fainter object of -1.5 magnitude published by Harvey (1970), we see that the relative self-absorption in bright lines of multiplet 4 decreases from about $\Delta \log I = 1.5$ at -10 magnitude to about $\Delta \log I = 0.8$ at 0 magnitude. Extrapolating, we would expect optically thin radiation in multiplet 4 for fainter meteors than +5 magnitude, but possibly starting with even fainter objects. As multiplet 4 is one of the most affected by self-absorption, the meteor radiation in the 0 to +5 magnitude interval may be optically thin for the majority of Fe I lines, that is lines with $E_i \neq 0$ and sufficiently small gf values. But this very preliminary statement should be checked in each particular case in future studies.

The resulting relaxation times are in the interval $-2.58 \leq \log t_R \leq -1.15$, most of the values being quite close to an average value of $\log t_R = -1.7$. This is independent of the actual brightness or any other changing parameters. Thus the relaxation time of 0.02 s seems to be a typical value for 30 km/s fireballs in the -4 to -12 absolute magnitude interval. The light of fireballs is emitted during a relatively long relaxation time of the gas. This is essentially the same result as found by Harvey (1970) for the spectrum of a -1.5 magnitude meteor.

Even if we are working with the absolute values of light intensities, it is an advantage that the computed values of the relaxation time are not dependent on absolute photometry [see equation (19)]. They reflect the ratio of the luminous efficiency factor to absolute gf-values, using relative photometry for comparison by means of the curve of growth.

The resulting length of the radiating volume is between 10 and 70 m, and it clearly depends on the actual brightness of the fireball. Extrapolating, a 10-m long volume of radiating gas is typical for about -1 magnitude and 100 m is typical for about -12 magnitude. It should be mentioned that the exceptional spectrum, S 1132, has values of t_R and ℓ smaller than for the other meteors.

The diameter $2R$ of the radiating volume (for $E_1 = 0$) is between 0.4 m and 2.6 m and clearly depends on the brightness of the object at the point examined (see fig. 6). A diameter of 28 cm seems to be typical for 0 magnitude and a diameter of 2 m typical for -10 absolute magnitude. All these values look reasonable. The values of the characteristic velocity were computed assuming

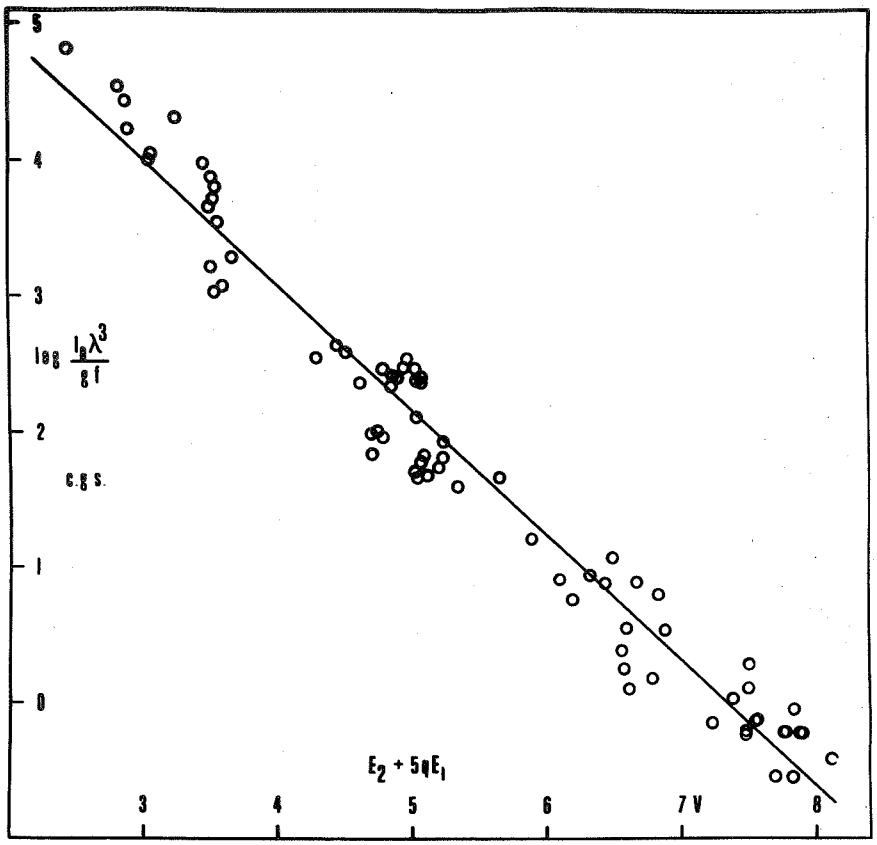

FIGURE 5.—Spectrum S 1132: The Boltzmann distribution with respect to the decrease in volume of radiating gas with the potential E_1. The slope of the resulting average straight line defines the temperature, which is used for computation of the curve of growth in figure 4. (All numbers in the abscissae (V) scale should be increased by one.)

that the atoms moved only along the direction of the meteor motion. The resulting characteristic velocities, v_m, of several km/s in most cases, are also what one would expect as the zigzag path of the atom means a greater actual velocity than v_m. The resulting densities of the iron atoms, if compared with the standard air densities (1962) at corresponding heights, are also quite reasonable.

I tried also to use an exponential change of ℓ with the upper potential E_2. Expressions analogous to equations (16), (17) and (18) were derived, but in this case the numerical solutions resulted in excitation temperatures too high to be admissible for Fe I atoms. Very high densities of the radiating gas relative to the surrounding air point to a great discrepancy in this case. It is clear that the assumption of a dependence of the radiating volume on E_2 potentials is not able to explain the discrepancy between the total light and the spectral data.

Values in table 2 should be considered as one set of possible values only. We chose the ratio p as a constant value. If p is taken as a function of E_1 and of time, one can obtain solutions which fit the observed points even better, but the number of free parameters is then too high. Also other models than that published in this paper can be used, and thus slightly different expressions for the x- and y-axes of the curve of growth and for the x-axis of the Boltzmann distribution, can be obtained. Perhaps some solutions may be found better fitting the observational points with such models.

TABLE 2.—*Results for Fe I from Emission Curve-of-Growth With Respect to Changes of the Volume of Radiating Gas with the* E_1 *potential*

Spectrum	Point[a]	h (km)	[b] log ρ (g/cm^3)	v (km/s)	Fe I total light curve data			Fe I emission-curve-of-growth data for $E_1=0$			
					[c] M_{pan}	Part from all radiation (%)	[d] dm/dt (g/s)	No. of obs.[e]	T (° K)	q	log N ($E_1=0$)
S 6		76	−7.4	29	−9.98	64	3.31	88	5540±160	0.041	23.70±0.13
S 526	D	73.1	−7.24	28.3	−6.41	53	1.90	37	5500±270	0.045	22.78±0.19
	E	72.7	−7.22	28.1	−7.42	37	2.31	57	5510±240	0.051	22.90±0.17
	F	72.1	−7.18	28.0	−7.71	49	2.43	60	5510±230	0.064	22.84±0.17
	G	71.7	−7.16	27.9	−8.49	35	2.74	79	5510±200	0.068	23.10±0.16
	H	71.2	−7.13	27.8	−7.24	51	2.25	56	5500±220	0.056	22.66±0.16
	I	70.6	−7.09	27.6	−4.70	43	1.24	16	5460±190	0.031	21.56±0.13
	J	70.1	−7.06	27.5	−8.55	37	2.78	76	5520±230	0.060	23.10±0.17
	K	69.2	−7.01	27.2	−6.15	46	1.83	38	5470±220	0.031	22.49±0.15
	(M	68.6	−6.98	26.9	−3.75	36	0.88	10	5500±240	0.010	20.33±0.16)
S 912	D	77.2	−7.51	31.7	−7.32	100	2.17	22	5500±450	0.012	22.42±0.29
	E	76.3	−7.45	31.6	−7.76	100	2.34	30	5520±410	0.024	22.70±0.27
	F	75.7	−7.41	31.5	−8.32	100	2.57	38	5470±370	0.024	22.81±0.25
	G	74.8	−7.35	31.3	−8.68	100	2.72	50	5470±350	0.034	22.90±0.24
	H	74.0	−7.30	30.8	−10.24	95	3.36	115	5520±190	0.046	23.67±0.15
	I	73.9	−7.29	30.6	−10.10	100	3.31	108	5520±180	0.044	23.57±0.14
	J	73.5	−7.27	30.0	−10.22	100	3.37	115	5500±190	0.046	23.77±0.14
S 1132		77.0	−7.49	32.1	−12.00	67	4.03	75	5490±130	0.055	23.65±0.12

But the main purpose of this paper is to demonstrate that it is possible to use a simple model of fireball radiation which agrees well with both the total light efficiency and the spectral distribution of the light in absolute values. And this is adequately verified by the values of table 2.

RESULTS FOR OTHER ELEMENTS THAN FE I

With a few exceptions, the whole procedure used for Fe I lines could not be repeated for lines of other elements. The main reason is the low number of lines available for an independent solution.

A solution for 7 Na I lines of spectrum S 1132 was possible with the result $T=5670°\pm170°$ K and $Y_{lim}=1.4$ for $q=0.05$. The curve of growth starts from the region of strong self-absorption and continues to the damping region. Thus no reliable value of total number of Na I atoms inside the corresponding radiation volume could be determined. But even if this is not the case, the unknown value of the luminous efficiency factor of sodium prevents one from estimating the relaxation time of Na I. The dimensions of the radiating volume of Na I were certainly less than that of Fe I as is clear from Y_{lim} being 1.2 less in log for Na I than for Fe I. Thus about 4 times less linear dimensions of the radiation volume are found for Na I atoms than for Fe I.

A solution for 7 Ca I lines of spectrum S 1132 was also possible with the result $T=4750°$ K$\pm300°$ and $Y_{lim}=2.6$ for $q=0.05$. The dimensions of the radiating volume are the same as for iron in this case. A slightly better position of the emission curve of growth than for Na I makes possible an estimation of the number of Ca I atoms in the whole radiating volume: log $N=20.8$ and log $m_G=-1.4$, which is about 0.1 percent of the Fe I gas mass.

A solution for 10 multiplets of O I of spectrum S 1132 was possible with a rough result of temperature 19 000°±4000° K and $Y_{lim}=0.6$ for

TABLE 2.—*Results for Fe I from Emission Curve-of-Growth with Respect to Changes of the Volume of Radiating Gas with the* E_1 *Potential*—Continued

Spectrum	Point[a]	Fe I emission-curve-of-growth data for $E_1=0$										
		log m_G (g)	[f] Y_{lim} (cm²)	log t_R (s)	log p	log R (cm)	log ℓ (cm)	log v_m (cm/s)	log n_0 (cm^{-3})	log δ_0 (g/cm³)	log $\bar{n}$ (cm^{-3})	log $\bar{\delta}$ (g/cm³)
S 6		1.67	2.4	−1.64	1.81	1.95	3.75	5.39	14.82	−7.21	15.55	−6.48
S 526	D	0.75	1.2	−1.15	1.81	1.73	3.54	4.69	14.56	−7.47	15.28	−6.75
	E	0.87	1.5	−1.44	1.81	1.73	3.54	4.98	14.67	−7.36	15.39	−6.64
	F	0.81	1.7	−1.62	1.81	1.74	3.55	5.17	14.59	−7.44	15.31	−6.72
	G	1.07	1.9	−1.67	1.81	1.79	3.60	5.27	14.70	−7.33	15.43	−6.60
	H	0.63	1.5	−1.62	1.81	1.68	3.48	5.10	14.60	−7.43	15.33	−6.70
	I	0.47	1.15	−1.71	1.81	1.53	3.33	5.04	13.94	−8.09	14.67	−7.36
	J	1.07	1.8	−1.71	1.81	1.74	3.55	5.26	14.84	−7.19	15.56	−6.47
	K	0.46	1.1	−1.37	1.81	1.62	3.43	4.80	14.59	−7.44	15.31	−6.72
	(M	−1.70	1.1	−2.58	1.81	1.22	3.03	5.61	13.64	−8.39	14.36	−7.67)
S 912	D	0.39	2.0	−1.78	1.81	1.83	3.63	5.41	13.91	−8.12	14.64	−7.39
	E	0.67	2.1	−1.67	1.81	1.89	3.70	5.37	13.99	−8.04	14.72	−7.31
	F	0.78	2.2	−1.79	1.81	1.89	3.69	5.49	14.12	−7.91	14.84	−7.19
	G	0.87	2.3	−1.85	1.81	1.90	3.71	5.56	14.17	−7.86	14.89	−7.14
	H	1.64	2.5	−1.72	1.81	2.01	3.82	5.54	14.60	−7.43	15.33	−6.70
	I	1.54	2.4	−1.77	1.81	1.96	3.77	5.54	14.65	−7.38	15.38	−6.65
	J	1.74	2.4	−1.63	1.81	2.01	3.81	5.45	14.72	−7.31	15.44	−6.59
S 1132		1.62	2.6	−2.41	1.20	2.12	3.32	5.73	14.86	−7.17	15.59	−6.44

[a] Notation of points: see the corresponding paper.
[b] log ρ air densities from the U.S. Standard Atmosphere, 1962.
[c] M_{pan} is close to absolute panchromatic magnitude, found by comparing stars with meteor spectrum by means of panchromatic emulsion.
[d] log $\tau_{pan} = -11.94$.
[e] No. of obs. is the number of Fe I spectral lines used for the solution.
[f] $Y_{lim} = (\log(I/(\lambda B_\lambda) + 4q\Theta E_1)$ limit for optically thick radiation.

$q=0.05$. The linear dimensions of the radiating volume of O I atoms are 10 times less than that of Fe I. The number of O I atoms inside this volume is log $N \approx 20.4$, giving log $m_G \approx -2.2$ (g). A rough estimate of the corresponding atoms of Fe I inside the same small volume gives about 1 to 10 percent of O I mass relative to iron mass.

No other solutions or even rough estimates for all the detailed meteor spectra of table 1 were found. In my previous papers, I used a method of estimating the abundances of other elements than iron from the curve of growth constructed for Fe I and applied to a small number of lines, the only ones available for the corresponding element. But this is possible only on the assumption that (a) the excitation temperature T is the same as that for Fe I; (b) the dimensions of the radiating volume and the characteristic velocity are the

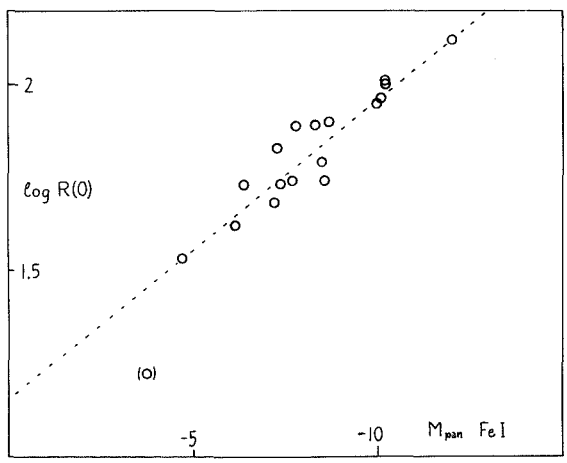

FIGURE 6.—The dependence of the radiating-volume radius (log R) of Fe I on the total actual brightness of Fe I as derived from the spectral analysis of fireballs with 30 km/s velocity.

same as that for Fe I; (c) the damping constant is the same as that for iron. The independent solutions given above even if only rough guesses, point clearly to the non-validity of all three assumptions. Nevertheless, I tried to find some abundances of other elements than iron by assuming that the prepositions (a), (b) and (c) are valid. The results were very frustrating.

In summary, it does not seem possible to determine any realistic abundances of other elements than Fe I for fireballs from -4 to -12 magnitude. The radiation we receive from these fireballs originates mainly from the effective surface of the radiating volume, and we do not see most of the light originating inside the volume. Thus we are able only to compare some total numbers of atoms radiating from a completely unknown surface of the radiating volume. This also strongly depends on what line of what element we observe. The situation should be somewhat better for meteors as faint as 0 magnitude, but this is necessary to check by construction of the emission curve-of-growth for each particular case. As mentioned before, the optical thickness still seems to be an important factor for most spectral lines of 0 magnitude meteors.

CONCLUSIONS

(a) The radiation of fireballs ($v \approx 30$ km/s, $h \approx 70$ to 80 km, $M_{\text{pan}} \approx -4$ to -12 mag) is strongly affected by self-absorption and to some extent by damping.

(b) Self-absorption should still be quite significant at 0 absolute magnitude. Optically thin radiation may be expected for meteors fainter than $+5$ absolute magnitude.

(c) If iron lines of short-duration flares are studied by the emission curve of growth and the resulting absolute abundances compared with the total luminosity by means of the luminosity equation factor, the resulting relaxation time is longer than the duration of the flare.

(d) If we assume that the dimensions of the volume of radiating gas decrease with increasing lower potential E_1, a relaxation time shorter than the duration of the flare can be found. In this way, the spectral data on Fe I lines can be made to agree with the luminous efficiency of the total Fe I meteor radiation.

(e) Parameter q, relating the dimensions of the radiating volume to the lower potential E_1, was found partly dependent on meteor brightness. The effect of change of the radiating volume with potential E_1 is negligible for meteors fainter than about -2 to -1 absolute magnitude.

(f) Excitation temperatures $T \approx 5500°$ K were found to be an optimum solution for Fe I in all the fireball spectra studied. This is effectively a lower limit, since somewhat higher values are also possible.

(g) A relaxation time of 0.02 s was found as a typical value, independent of the actual brightness of the fireball. The light of fireballs is emitted during a relatively long relaxation time, which is many orders of magnitude longer than the time necessary for spontaneous radiation of excited Fe I atoms.

(h) The dimensions of the radiating gas volume depend on the fireball brightness. Fe I gas: 0.3×9 m at 0 absolute magnitude, 2×60 m at -10 absolute magnitude.

(i) The terminal densities at the end of the radiating volume of iron vapor roughly correspond to the standard air densities at the corresponding heights.

(j) Practically, it was not possible to determine any realistic abundances of other elements than iron for the fireballs studied. A few lines are available for the same independent procedure as used for Fe I. The curve of growth derived for Fe I cannot be used for other elements. The radiation we receive from fireballs originates mainly from the effective surface of the radiating volume, which prevents a sufficiently accurate comparison for various elements of the total numbers of atoms inside the whole volume.

(k) The relaxation time and other problems contained in this paper could be studied much easier, if meteor spectra with a very short exposure time (instantaneous exposure) were available.

ACKNOWLEDGMENT AND ERRATUM

My thanks are due to R. E. McCrosky, who pointed out a discrepancy in the photometric data published in my paper (1966) on an iron meteoroid. (Private communication and McCrosky, 1968.) In preparing this paper I checked all the numbers in the S 912 photometry and found a mistake of exactly 1 in the logarithm of the factor converting from magnitudes to the absolute scale of I in

erg/s. In the phrase "3.59 magnitude≡2.73 times less intensity than 0 magnitude" the value 2.73 should be 27.3.

All data in my 1966 paper given in magnitudes or "bolometric" magnitudes are OK, all data given in log I (erg/s) must be corrected by subtraction of 1.00. Table 6 starts correctly with 11.91 for log I of point H of line No. 1 and so on till 12.85 for log I of point J of line No. 189. In figure 2: the y-axis must be changed from 12.5 to 11.5 and from 13.5 to 12.5.

The results in my 1967 paper were derived using the wrong numbers mentioned above, but the systematic error in the absolute values of the oscillator strengths of Fe I acted in the opposite direction. In any case, the problem of the analysis of meteor spectra has been studied from new and more general aspects in this paper, using the correct log I for S 912.

In my previous papers, I used the notation "bolometric" magnitudes, to indicate that bolometric magnitudes of stars were used for computation of the absolute c.g.s. scale of intensities. However, the meteor spectral lines were compared with stars using a panchromatic emulsion, and it is usual to speak about "panchromatic" magnitudes in such a case, particularly, if A O comparison stars are used.

LIST OF MATHEMATICAL SYMBOLS

α	Angle between the line of vision and the meteor motion
B_λ	Planck's function related to wavelength units
c	Velocity of light
δ_0	Terminal density of the radiating volume (g/cm³)
$\bar{\delta}$	Average density at the end of the radiating volume (g/cm³)
e	Charge of electron
E_1	The lower level potential (V)
E_2	The upper level potential (V)
$F(X)$	Function giving the curve of growth
f	Absorption oscillator strength
$g \equiv g_1$	Statistical weight of the lower level
G_2	Total statistical weight of the upper term
h	Planck's constant
χ_1	Energy of the lower level
I	Intensity of optical meteor radiation
I_0	Optically thin intensity
k	Luminous efficiency of the radiating gas per unit gas mass
k_B	Boltzmann's constant
ℓ	Length of the radiating volume
λ	Wavelength
m	Meteor mass
m_∞	Initial meteor mass
m_A	Total gas mass, which entered into the radiating volume from the beginning of the meteor luminous trajectory till time t
m_e	Mass of electron
m_G	Total gas mass inside the radiating volume
m_Z	Total gas mass which left the radiating volume from the beginning of the meteor's luminous trajectory till time t
μ	Mass of one atom
n_0	Terminal number of atoms per cm³ at the end of the radiating volume
$\bar{n}$	Average number of atoms per cm³ of the radiating volume
N	Total number of atoms of one element in one state inside the radiating volume
$N(\text{term})$	Total number of atoms being in all upper levels of one term inside the radiating volume
p	ℓ/R
q	Exponential factor giving the decrease of the length of the radiating volume with increasing potential E_1, definition (14).
R	Radius of the radiating cylindrical volume
t	Time
t_f	Duration of a flare
t_R	Relaxation time of meteor radiation: time spent by an average atom inside the volume of radiating gas
T	Excitation temperature
τ	Luminous efficiency factor
$\Theta = \frac{5040}{T}$	Boltzmann temperature
U	Partition function
v	Meteor velocity
v_m	Characteristic velocity
X	x-axis of the curve of growth
Y_{lim}	Limit value of y-axis of the curve of growth for very strong self-absorption

REFERENCES

ALLEN, C. W., 1963. Astrophysical quantities, The Athlone Press, London.

ANON, 1962. U.S. standard atmosphere, 1962, U.S. Committee on Extension of the Standard Atmosphere Supt. of Documents, Washington.

AYERS, W. G., MCCROSKY, R. E., AND SHAO, C. -Y., 1970. Photographic observations of 10 artificial meteors, *Smithson. Astrophys. Obs. Spec. Rept.*, No. 317.

CEPLECHA, Z., 1964. Study of a bright meteor flare by means of emission curve of growth, *Bull. Astron. Inst. Czech.*, **15**, 102–112.

——, 1965. Complete data on bright meteor 32281, *Bull. Astron. Inst. Czech.*, **16**, 88–101.

——, 1966. Complete data on iron meteoroid (meteor 36221), *Bull. Astron. Inst. Czech.*, **17**, 195–206.

——, 1967. Spectroscopic analysis of iron meteoroid radiation, *Bull. Astron. Inst. Czech.*, **18**, 303–310.

——, 1968. Meteor Spectra, in *Physics and Dynamics of Meteors*, edited by L. Kresák and P. M. Millman, D. Reidel Publ. Co., Dordrech, Holland, 73–83.

——, 1971. Spectral data on terminal flare and wake of double-station meteor No. 38421, *Bull. Astron. Inst. Czech.*, **22**, 219–304.

CEPLECHA, Z. AND RAJCHL, J., 1963. The meteor spectrum with dispersion from 11 to 38 Å/mm, *Bull. Astron. Inst. Czech.*, **14**, 29–49.

CORLISS, C. H. AND BOZMAN, W. R., 1962. *Experimental transition probabilities for spectral lines of seventy elements*, NBS Monograph 53, Supt. of Documents, Washington.

CORLISS, C. H. AND WARNER, B., 1964. Absolute oscillator strengths for Fe I, *Astrophys. J. Suppl. Ser.*, **8**, 395.

FRIICHTENICHT, J. F., SLATTERY, J. C., AND TAGLIAFERRI, E., 1968. A laboratory measurement of meteor luminous efficiency, *Astrophys. J.*, **151**, 747–758.

GARZ, T. AND KOCK, M., 1969. Experimentelle Oszillatorenstärken von Fe I-Linien, Astron. Astrophys., **2**, 274–279.

GRASDALEN, G. L., HUBER, M., AND PARKINSON, W. H., 1969. Absolute *gf*-values for Fe I and and Fe II lines, *Astrophys. J.*, **156**, 1153–1173.

HARVEY, G. A., 1970. Spectra of faint optical meteors, presented at 13th Plenary Meeting of COSPAR, Leningrad, unpublished.

MCCROSKY, R. E., 1968. Meteors without sodium, *Smithson. Astrophys. Obs. Spec. Rept.* No. 270.

MOORE, C. E., 1945. A multiplet table of astrophysical interest, *Contrib. Princeton Obs.* No. 20.

WIESE, W. L., SMITH, M. W., AND CLENNON, B. M., 1966. Atomic transition probabilities, *National Standard Reference Data Series*, NBS 4, Washington.

WIESE, W. L., SMITH, M. W., AND MILES, B. M., 1969. Atomic transition probabilities, *National Standard Reference Data Series*, NBS 22, Washington.

9. Spectral Analysis of Four Meteors

GALE A. HARVEY
Langley Research Center, NASA
Hampton, Virginia

Four meteor spectra from the NASA LRC Faint Meteor Spectra Patrol are analyzed for chemical composition and radiative processes. The chemical compositions of the Taurid, Geminid, and Perseid meteors were found to be similar to that of a typical stony meteorite. The chemical composition of the sporadic meteor was found to be similar to that of a nickel-iron meteorite. The radiation from optical meteors (+1 to −10 absolute photographic magnitude) was found to be similar to that of a low-temperature gas, except that strong, anomalous ionic radiation is superposed on the neutral radiation in bright (< −3 mag), fast meteors.

DURING THE 1960S, THE ACTIVITY IN SPACE resulted in a strong effort directed toward determining the meteoroid environment and its attendant hazard to spacecraft. By 1971, lack of definitive meteoroid damage to spacecraft had shown that the meteoroid environment did not present a significant danger to most missions. At the same time, the measured uncertainties in the mass flux of meteoroids, over a wide range of mass, had been reduced from orders of magnitude to factors of 3 to 10 (Ayres et al., 1970; Cook et al., 1963; D'Aiutolo et al., 1967; Harvey, 1970). However, the multitude of observations (Grygar et al., 1968; Harvey, 1971a; Lindblad, 1963; Millman, 1967) during this time period clearly indicated that meteoroids were very heterogeneous in nature and that the simplified concept of a mass-flux representation of the meteoroid environment had limitations. By 1970, the statistical or gross meteoroid environment was fairly well determined. However, many of the techniques that are applied to the study of the overall environment are not well suited to a refined study of individual meteoroids.

Meteor spectra research being conducted by NASA Langley Research Center is intended as a detailed study of individual meteoroids. This research is based on the techniques and principles of quantitative spectroscopy. The data for this research are obtained from the NASA LRC Faint Meteor Spectra Patrol (Harvey, 1971a). This patrol provides statistical quantities (several hundred per year) of meteor spectra. These spectra are used for detailed measurements of composition, for statistical studies of composition, and for study of meteor radiation.

This paper presents the results of the detailed analysis of four of the better (>100 lines) meteor spectra obtained from the patrol. The approach used in these analyses is to measure the population of excited states of the meteoric gas, and to use the parameter obtained from these measurements to obtain quantitative elemental chemical composition of the initial meteoroid. Meteor radiation processes are discussed. The "effective radiation temperatures" and "derived meteoroid compositions" are presented. Prior to this present effort only three meteor spectra are known to have been quantitatively analyzed for composition (Ceplecha, 1964, 1965; Harvey, 1970).

The NASA LRC Faint Meteor Spectra Patrol (Harvey, 1971a) has been obtaining meteor

spectra since November 1968. The patrol uses specially designed Maksutov slitless spectrographs and a photoelectric meteor-detection-shutter system. By the end of 1970, approximately 500 meteor spectra had been obtained by the patrol. Four of these were selected as useful for detailed spectroscopic analysis and as generally representative of the brighter meteors that had been photographed. Further, the meteoroids that produced these four spectra are also generally representative of the meteor velocity range. One of the spectra is of a slow sporadic meteor. The other three spectra are of Taurid, Geminid, and Perseid meteors, respectively.

SPORADIC METEOR

The spectrum of the slow, sporadic meteor is shown in figure 1. This spectrum was recorded during the night of April 4, 1969, and no position or orbital data are available. A velocity of 20 km/s or less is estimated for the meteor on the basis of a lower "effective radiation temperature" measurement than that obtained for the 28 km/s Taurid. The meteor spectrum was photographed with a 150-mm aperture, $f/1.3$ Maksutov slitless spectrograph equipped with a 407 line/mm diffraction grating. Typical slow-meteor values of 90 km initial height, trajectory-optical axis angle of 45°, and a duration of 2 s, were used to compute the intensity of this meteor. By comparing the computed intensity of this meteor in the blue and near ultraviolet region with that of an artificial meteor (Harvey, 1967a), an absolute photographic magnitude brighter than −10 is obtained for the meteor. As can be seen in figure 1, this bright meteor was recorded in the third, fourth, and fifth orders of the spectrum with dispersions of 40, 32, and 24 Å/mm, respectively. One hundred and twenty-two of the strongest lines at point A in the spectrum have been identified in a preliminary wavelength analysis and are listed in table 1. The first column of table 1 lists the wavelengths measured from the microdensitometer tracing, column two lists the identified wavelengths (Corliss and Bozman, 1962; Moore, 1945), column three lists the multiplet numbers from Moore (1945), column four lists the statistical weight-Einstein transition probability products from Corliss and Bozman (1962). Columns five and six list the upper and lower energy levels of the atomic transitions as listed in Moore (1945). Most of the lines are from ground state multiplets of iron. The large number of lines and the good spectral resolution lend themselves to a detailed analysis. The spectrum was recorded on a blue sensitive emulsion and covers the wavelength interval of 3100 Å to 4600 Å in partially overlapping orders.

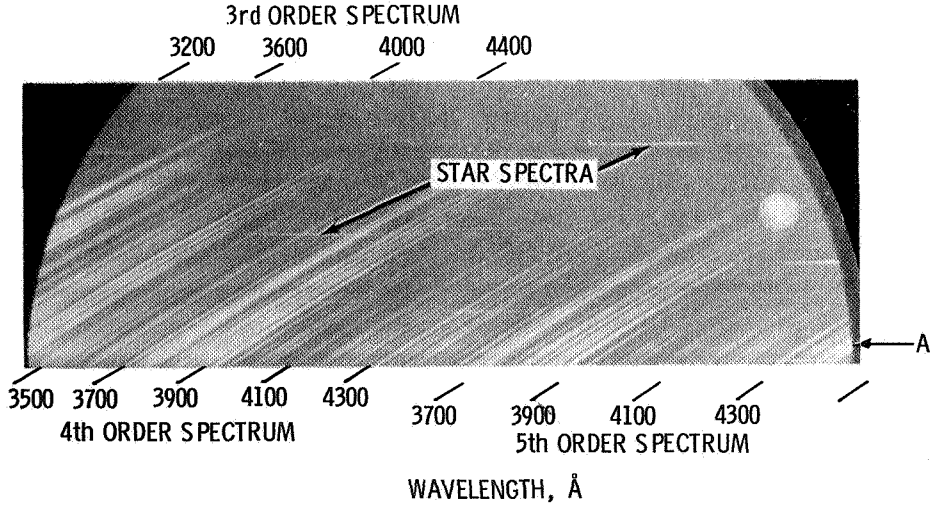

FIGURE 1.—Enlargement of spectrogram of a sporadic meteor.

TABLE 1.—*Wavelength Identifications of Sporadic Meteor*

λ measured (Å)	λ identified (Å)	Multiplet no.	gA ($\times 10^8$/s)	E_1 (eV)	E_2 (eV)
3424.8	3424.29	81 Fe	17	2.17	5.77
3426.5	3426.39	82 Fe	7.4	2.17	5.77
	3426.64	82 Fe	7.7	2.19	5.79
	3427.12	81 Fe	34	2.17	5.77
3429.0	3428.20	81 Fe	8.8	2.19	5.79
3433.0	3433.04	23 Co	9.1	0.63	4.22
	3433.60	52 Cr	44	2.53	6.13
3436.5	3436.19	52 Cr	26	2.53	6.13
3440.6	3440.61	6 Fe	2.8	0.00	3.59
	3440.99	6 Fe	0.64	0.05	3.64
3444.0	3443.88	6 Fe	0.34	0.09	3.67
3446.0	3445.15	81 Fe	17	2.19	5.77
	3446.26	20 Ni	3.8	0.11	3.69
3447.5	3447.28	82 Fe	5.3	2.19	5.77
3450.5	3450.33	82 Fe	8.9	2.21	5.79
3452.5	3452.28	25 Fe	0.49	0.95	4.53
	3452.89	17 Ni	1.0	0.11	3.68
3461.9	3461.65	17 Ni	3.2	0.03	3.59
3466.0	3465.86	6 Fe	0.52	0.11	3.67
3472.0	3471.27	82 Fe		2.21	5.77
	3472.54	20 Ni	1.2	0.11	3.66
3475.5	3475.45	6 Fe	0.64	0.09	3.64
3476.5	3476.70	6 Fe	0.28	0.12	3.67
3482.5	3483.01	24 Fe		0.91	4.45
3490.6	3490.58	6 Fe	0.58	0.05	3.59
3492.2	3492.96	18 Ni	3.9	0.11	3.64
3497.8	3497.84	6 Fe	0.19	0.11	3.64
3501.7	3502.28	21 Co	11	0.43	3.95
3505.0	3506.31	21 Co	9.4	0.51	4.03
3512.5	3512.64	21 Co	7.4	0.58	4.09
3514.0	3513.82	24 Fe	1.7	0.86	4.37
3514.8	3515.05	19 Ni	4.5	0.11	3.62
3522.0	3521.26	24 Fe	1.7	0.91	4.42
3526.0	3524.54	18 Ni	4.6	0.03	3.53
	3526.04	6 Fe	0.13	0.09	3.59
3557.5	3558.52	24 Fe	3.5	0.99	4.45
3566.0	3565.38	24 Fe	7.8	0.95	4.42
	3566.37	36 Ni	6.4	0.42	3.88
3569.5	3570.10	24 Fe	18	0.91	4.37
3578.5	3578.69	4 Cr	8.3	0.00	3.45
3581.2	3581.20	23 Fe	23	0.86	4.30
3585.5	3585.32	23 Fe	1.7	0.95	4.40
	3585.71	23 Fe	1.3	0.91	4.35
3586.8	3586.99	23 Fe	2.0	0.99	4.43
3589.6	3589.11	23 Fe	0.26	0.86	4.29
3593.2	3593.49	4 Cr	7.0	0.00	3.43
3605.5	3605.33	4 Cr	5.2	0.00	3.42
	3605.46	294 Fe	51	2.72	6.14
3606.7	3606.68	294 Fe	65	2.68	6.10
3608.9	3608.86	23 Fe	10	1.01	4.43
3618.8	3618.77	23 Fe	9.5	0.99	4.40
3631.5	3631.46	23 Fe	8.6	0.95	4.35
3647.8	3647.84	23 Fe	6.1	0.91	4.29

TABLE 1.—*Wavelength Identifications of Sporadic Meteor*—Continued

λ measured (Å)	λ identified (Å)	Multiplet no.	gA ($\times 10^8$/s)	E_1 (eV)	E_2 (eV)
3649.5	3649.30	5 Fe	∼.025	0.00	3.38
3680.0	3679.92	5 Fe	0.29	0.00	3.35
3683.0	3683.06	5 Fe	0.055	0.05	3.40
3687.5	3687.46	21 Fe	2.5	0.86	4.20
3705.3	3705.57	5 Fe	0.38	0.05	3.38
3708.0	3707.82	5 Fe	0.14	0.09	3.42
3709.0	3709.25	21 Fe	2.9	0.91	4.24
3717.0	3716.45	388 Fe	15	2.93	6.25
3720.2	3719.94	5 Fe	2.5	0.00	3.32
3722.0	3722.56	5 Fe	0.40	0.09	3.40
3725.0	3724.38	124 Fe	5.9	2.27	5.58
3727.0	3726.92	385 Fe	8.7	3.03	6.34
3735.0	3734.87	21 Fe	20	0.86	4.16
3737.3	3737.13	5 Fe	1.5	0.05	3.35
3743.0	3743.36	21 Fe	2.3	0.99	4.28
3746.0	3745.56	5 Fe	1.2	0.09	3.38
3749.0	3749.49	21 Fe	13	0.91	4.20
3758.5	3758.24	21 Fe	10	0.95	4.24
3761.0	3760.05	177 Fe	5.5	2.39	5.68
	3760.53	76 Fe	0.97	2.21	5.49
3764.0	3763.79	21 Fe	6.2	0.99	4.26
3787.0	3786.68	22 Fe	0.11	1.01	4.27
3788.0	3787.88	21 Fe	1.7	1.01	4.26
3790.5	3790.10	22 Fe	0.21	0.99	4.24
3796.0	3795.00	21 Fe	2.3	0.99	4.24
3799.5	3797.52	607 Fe	21	3.22	6.47
	3798.51	21 Fe	.93	0.91	4.16
	3799.55	21 Fe	1.5	0.95	4.20
3815.84	3815.84	45 Fe	16	1.48	4.71
3821.5	3820.43	20 Fe	12	0.86	4.09
3825.0	3824.44	4 Fe	0.28	0.00	3.23
	3825.88	20 Fe	8.9	0.91	4.14
3829.5	3829.35	3 Mg	11	2.70	5.92
3830.2	3832.51	3 Mg	23	2.70	5.92
3834.0	3834.22	20 Fe	3.9	0.95	4.17
3838.3	3838.26	3 Mg	39	2.70	5.92
3840.7	3840.44	20 Fe	2.6	0.99	4.20
3850.5	3849.97	20 Fe	1.7	1.01	4.21
3857.2	3856.37	4 Fe	0.31	0.05	3.25
3860.0	3859.91	4 Fe	1.4	0.00	3.20
3865.0	3865.53	20 Fe	1.1	1.01	4.20
3879.0	3878.02	20 Fe	1.4	0.95	4.14
	3878.58	4 Fe	0.33	0.09	3.27
3887.0	3886.28	4 Fe	0.63	0.05	3.23
3897.0	3895.66	4 Fe	0.14	0.11	3.28
3900.5	3899.71	4 Fe	0.21	0.09	3.25
3903.5	3903.90	429 Fe	4.2	2.98	6.14
3905.5	3905.53	3 Si	0.86	1.90	5.06
3906.5	3906.48	4 Fe	0.055	0.11	3.27
3923.1	3922.91	4 Fe	0.18	0.05	3.20
3928.0	3927.92	4 Fe	0.26	0.11	3.25
3930.5	3930.30	4 Fe	0.27	0.09	3.23
3933.5	3933.67	1 Ca II	0.91	0.00	3.14

TABLE 1.—*Wavelength Identifications of Sporadic Meteor*—Continued

λ measured (Å)	λ identified (Å)	Multiplet no.	gA ($\times 10^8$/s)	E_1 (eV)	E_2 (eV)
3942.2	3942.44	364 Fe	2.5	2.83	5.96
3969.3	3968.47	1 Ca II	0.45	0.00	3.11
	3969.26	43 Fe	4.4	1.48	4.59
4004.5	4005.25	43 Fe	3.6	1.55	4.63
4031.0	4030.76	2 Mn	1.4	0.00	3.06
4033.0	4033.07	2 Mn	0.95	0.00	3.06
4036.0	4034.49	2 Mn	0.54	0.00	3.06
4045.8	4045.82	43 Fe	22	1.48	4.53
4063.5	4063.60	43 Fe	9.9	1.55	4.59
4071.5	4071.74	43 Fe	9.1	1.60	4.63
4133.0	4132.06	43 Fe	2.7	1.60	4.59
4143.9	4143.42	523 Fe	16	3.03	6.01
	4143.87	43 Fe	2.9	1.55	4.53
4202.0	4202.03	42 Fe	2.0	1.48	4.42
4206.0	4206.70	3 Fe		0.05	2.99
4216.0	4216.19	3 Fe	0.0031	0.00	2.93
4226.5	4226.73	2 Ca	1	0.00	2.92
4251.0	4250.79	42 Fe	1.5	1.55	4.45
4254.5	4254.35	1 Cr	2.0	0.00	2.90
4257.8	4258.32	3 Fe		0.09	2.99
4271.8	4271.76	42 Fe	5.2	1.48	4.37
4274.5	4274.80	1 Cr	1.5	0.00	2.89
4290.0	4289.72	1 Cr	0.95	0.00	2.88
4291.5	4291.66	3 Fe		0.09	2.99
4293.5	4294.13	41 Fe	0.71	1.48	4.35
4299.0	4299.24	152 Fe	5.2	2.41	5.29
4308.0	4307.91	42 Fe	5.9	1.55	4.42
4325.8	4325.76	42 Fe	6.1	1.60	4.45
4376.0	4375.93	2 Fe	0.0094	0.00	2.82
4383.5	4383.55	41 Fe	7.7	1.48	4.29
4404.75	4404.75	41 Fe	4.4	1.55	4.35
4427.3	4427.31	2 Fe	0.0091	0.05	2.84
4461.65	4461.65	2 Fe	0.0052	0.09	2.85
4482.17	4482.17	2 Fe	0.0053	0.11	2.86

TAURID METEOR

The spectrum of the Taurid meteor is shown in figure 2. This spectrum was obtained during the night of November 4, 1969. The meteor occurred at 22:25 hours, local time. A beginning height of 100 km was assumed for the meteor. This height is in general agreement with beginning heights of meteors of similar brightness and velocity (Jacchia et al., 1967). A terminal height of 68 km was calculated from the beginning height and relevant geometry. The meteor began 8° from the radiant, and the trajectory made an angle of 10° with the optical axis of the spectrograph. Hence the meteor was nearly "head-on" and was very favorable for photographic recording. An absolute meteor magnitude of −4 was obtained for this meteor by comparing its intensity in the blue and near ultraviolet region with that of an artificial meteor (Harvey, 1967a). The Taurid meteor spectrum was recorded on the same spectrograph as the sporadic meteor spectrum. However, the Taurid spectrum (as well as the Geminid and Perseid spectra) were recorded on "meteor recording film SO–153," which is similar to extended red emulsion type 2485. That is, the spectrum covers the wavelength interval 3100 Å to 7000 Å. Two hundred

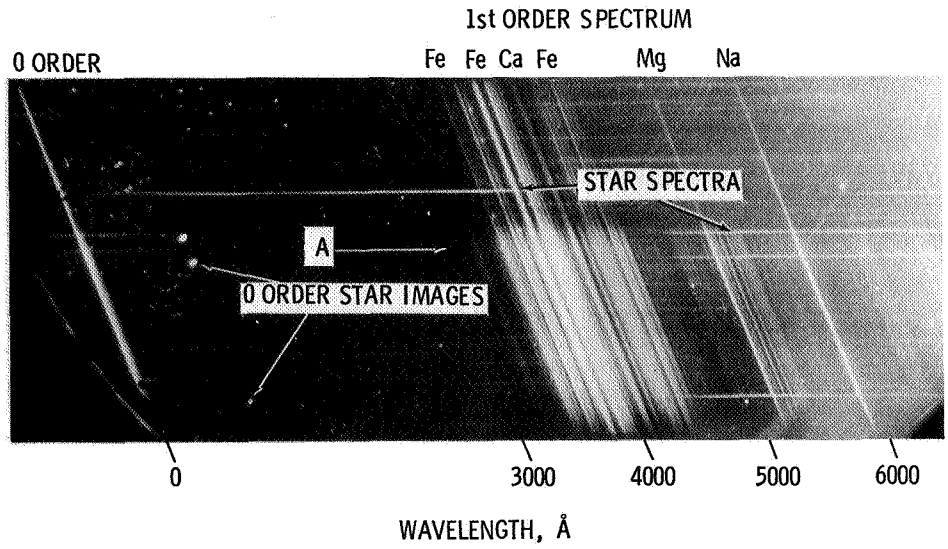

FIGURE 2.—Enlargement of a spectrogram of a Taurid meteor.

and thirty-seven of the strongest lines at position *A* in the spectrum have been identified and are listed in table 2. The strongest features in the spectrum are multiplets 4, 5, and 20 of neutral iron, 2 of neutral magnesium, and the sodium *D* lines. The spectrum suffers from mutliple zero-order star images and a dense and nonuniform background.

GEMINID METEOR

The spectrum of the Geminid meteor is shown in figure 3. This spectrum was obtained on the night of December 12, 1969. The meteor occurred at approximately 03:40, local time. The meteor began 51° from the Geminid radiant and ended 63° from the radiant. An estimated beginning height of 100 km was again used from which a terminal height of 68 km was computed. An absolute meteor magnitude of −5 was obtained for this meteor by the same method used for the Taurid. The Geminid spectrum was recorded by the same spectrograph as the Taurid spectrum. One hundred and fifty-seven of the strongest lines at position *A* have been identified in the preliminary wavelength analysis and are listed in table 3. The strongest features in the spectrum are multiplets 4, 5, and 20 of neutral iron, 2 of magnesium, and the sodium *D* lines. This Geminid spectrum is a "clean" spectrum in that it is not degraded by star images, poor resolution, or nonuniform background.

PERSEID METEOR

The spectrum of the Perseid meteor is shown in figure 4. The spectrum was obtained on the night of August 12, 1969. The meteor occurred between 02:30 and 4:00, local time. The meteor was approximately 90° from the radiant and traveling nearly perpendicular to the optical axis of the spectrograph when photographed. A beginning height of 105 km was obtained from the maximum of the auroral green line. A terminal height of 92 km was calculated. A maximum brightness of −9 absolute meteor magnitude was obtained for this Perseid meteor by the same method as used for the Taurid and Geminid meteors. This spectrum was also recorded on the same spectrograph which recorded the other three spectra. As can be seen in figure 4, the upper third of the spectrum is similar to that of the Geminid and Taurid meteors. However, in the latter part of the spectrum, the ionic lines of calcium, magnesium, and silicon become dominant. Ninety-four of the strongest lines at position *A* have been identified in the preliminary wavelength analysis and are listed in table 4. The entries of table 4 are from the same source as tables 1 to 3 except that the gA values for Si

TABLE 2.—*Wavelength Identifications of Taurid Meteor*

λ measured (Å)	λ identified (Å)	Multiplet no.	gA ($\times 10^8$/s)	E_1 (eV)	E_2 (eV)
3098	3099.97	28 Fe	8.6	0.91	4.89
	3100.30	28 Fe	3.9	0.99	4.97
	3100.67	28 Fe	3.6	0.95	4.93
	3101.55	25 Ni	4.6	0.11	4.09
3135	3134.11	25 Ni	5.8	0.21	4.15
3184	3184.90	7 Fe	0.086	0.05	3.93
3193	3191.66	8 Fe	0.087	0.00	3.87
	3193.21	7 Fe	0.14	0.00	3.86
3200	3199.92	27 Ti	14	0.05	3.90
3214	3214.40	7 Fe	0.086	0.09	3.93
3224	3225.79	155 Fe	107	2.39	6.21
3233	3234.52	2 Ti II	16	0.05	3.86
3244	3243.06	22 Ni	0.62	0.03	3.83
3251	3251.24	93 Fe		2.19	5.98
3254	3254.36	620 Fe		3.25	7.05
3265	3265.62	91 Fe	18	2.17	5.95
3270	3271.00	91 Fe	22	2.19	5.96
3284	3284.59	91 Fe		2.19	5.95
3291	3290.99	95 Fe		2.21	5.96
	3292.59	91 Fe		2.21	5.96
3301	3302.32	2 Na	0.65	0.00	3.74
	3302.99	2 Na	0.33	0.00	3.74
3306	3306.0	91 Fe	38	2.91	5.92
	3306.4	91 Fe	40	2.21	5.95
3320	3320.26	9 Ni	0.39	0.16	3.88
3332	3331.62	191 Fe		2.42	6.13
3335	3334.22	190 Fe		2.42	6.12
3342	3341.88	24 Ti	13	0.00	3.69
3352	3344.51	11 Ca		1.88	5.56
	3350.21	11 Ca		1.88	5.56
	3350.36	11 Ca		1.88	5.56
	3354.64	24 Ti	9.7	0.02	3.71
3363	3361.92	11 Ca		1.89	5.56
	3362.13	11 Ca		1.89	5.56
3365	3365.77	38 Ni	0.63	0.42	4.09
	3366.17	8 Ni	0.35	0.16	3.83
3375	3374.22	17 Ni	0.20	0.03	3.68
3384	3383.69	85 Fe		2.19	5.84
	3383.98	83 Fe	9.1	2.17	5.81
3399	3399.34	85 Fe	25	2.19	5.82
3404	3404.36	83 Fe	17	2.19	5.81
3407	3407.46	83 Fe	33	2.17	5.79
3414	3413.14	85 Fe	26	2.19	5.80
3424	3424.29	81 Fe	17	2.17	5.77
3425	3426.39	82 Fe	7.4	2.19	5.79
	3426.64	82 Fe	7.7	2.19	5.79
3429	3427.12	81 Fe	34	2.17	5.77
3440	3440.61	6 Fe	2.8	0.00	3.59
	3440.99	6 Fe	0.64	0.05	3.64
3450	3450.33	82 Fe	8.9	2.21	5.79
	3451.92	81 Fe	8.8	2.21	5.79
3460	3458.47	19 Ni	4.9	0.21	3.78
3462	3461.65	17 Ni	3.2	0.03	3.59

TABLE 2.—*Wavelength Identifications of Taurid Meteor*—Continued

λ measured (Å)	λ identified (Å)	Multiplet no.	gA ($\times 10^8$/s)	E_1 (eV)	E_2 (eV)
3466	3465.86	6 Fe	0.52	0.11	3.67
3476	3475.45	6 Fe	0.64	0.09	3.64
3491	3490.58	6 Fe	0.58	0.05	3.59
	3492.96	18 Ni	3.9	0.11	3.64
3499	3497.84	6 Fe	0.19	0.11	3.64
3514	3513.82	24 Fe	1.7	0.86	4.37
3526	3526.04	6 Fe	0.13	0.09	3.59
3534	3536.56	326 Fe	56	2.86	6.35
3541	3541.09	326 Fe	65	2.84	6.32
	3542.08	326 Fe	61	2.85	6.34
3554	3554.93	326 Fe	73	2.82	6.29
3560	3558.52	24 Fe	3.5	0.99	4.45
3565	3565.38	24 Fe	7.8	0.95	4.42
3570	3570.10	24 Fe	18	0.91	4.37
3578	3578.69	4 Cr	8.3	0.00	3.45
3581	3581.20	23 Fe	23	0.86	4.30
3586	3586.99	23 Fe	2.0	0.99	4.43
3588	3589.11	23 Fe	0.26	0.86	4.29
3594	3594.64	322 Fe	21	2.84	6.27
3604	3603.21	295 Fe	33	2.68	6.11
	3605.46	294 Fe	33	2.72	6.14
3607	3606.68	294 Fe	65	2.68	6.10
3609	3608.86	23 Fe	10	1.01	4.43
3611	3610.16	321 Fe	48	2.80	6.21
3619	3618.77	23 Fe	9.5	0.99	4.40
3620	3619.39	35 Ni	7.5	0.42	3.83
3632	3631.46	23 Fe	8.6	0.95	4.35
	3632.04	496 Fe	26	3.06	6.46
3639	3638.30	294 Fe	28	2.75	6.14
3646	3645.82	496 Fe	20	3.10	6.48
3648	3647.84	23 Fe	6.1	0.91	4.29
3659	3659.52	180 Fe	9.9	2.44	5.82
3671	3669.52	291 Fe	32	2.72	6.08
3680	3679.92	5 Fe	0.29	0.00	3.35
3683	3683.06	5 Fe	0.055	0.05	3.40
3687	3687.46	21 Fe	2.5	0.86	4.20
3694	3794.01	394 Fe	72	3.03	6.37
3700	3701.09	385 Fe	85	2.99	6.32
3706	3705.57	5 Fe	0.38	0.05	3.38
3708	3707.82	5 Fe	0.14	0.09	3.42
3720	3719.94	5 Fe	2.5	0.00	3.32
3723	3722.56	5 Fe	0.40	0.09	3.40
3733	3733.32	5 Fe	0.36	0.11	3.42
	3634.87	21 Fe	20	0.86	4.16
3737	3737.13	5 Fe	1.5	0.05	3.35
3747	3745.56	5 Fe	1.2	0.09	3.38
	3745.90	5 Fe	0.31	0.12	3.42
3749	3748.26	5 Fe	0.71	0.11	3.40
	3749.49	21 Fe	13	0.91	4.20
3759	3758.24	21 Fe	10	0.95	4.24
3764	3763.79	21 Fe	6.2	0.99	4.26
	3765.54	608 Fe	50	3.22	6.50
3768	3767.19	21 Fe	4.6	1.01	4.28

TABLE 2.—*Wavelength Identifications of Taurid Meteor*—Continued

λ measured (Å)	λ identified (Å)	Multiplet no.	gA ($\times 10^8$/s)	E_1 (eV)	E_2 (eV)
3775	3774.82	73 Fe	0.59	2.21	5.48
	3775.57	33 Ni	0.57	0.42	3.69
	3776.45	74 Fe	0.53	2.17	5.43
3786	3786.68	22 Fe		1.01	4.27
3791	3790.10	22 Fe	0.21	0.99	4.24
3795	3795.00	21 Fe	2.3	0.99	4.24
3797	3798.51	21 Fe	0.93	0.91	4.16
	3799.55	21 Fe	1.5	0.95	4.20
3813	3812.96	22 Fe	1.0	0.95	4.19
3817	3815.84	45 Fe	16	1.48	4.71
3821	3820.43	20 Fe	12	0.86	4.09
3825	3824.44	4 Fe	0.28	0.00	3.32
	3825.88	20 Fe	8.9	0.91	4.14
3831	3827.82	45 Fe	15	1.55	4.77
	3829.35	3 Mg	11	2.70	5.92
	3832.51	3 Mg	23	2.70	5.92
3838	3838.26	3 Mg	39	2.70	5.92
3849	3849.97	20 Fe	1.7	1.01	4.21
	3850.82	22 Fe	0.22	0.99	4.19
3855	3856.37	4 Fe	0.31	0.05	3.25
	3856.37	1 Si II		6.83	10.03
3860	3859.91	4 Fe	1.4	0.00	3.20
3862	3862.59	1 Si II		6.83	10.03
3874	3873.76	175 Fe	2.8	2.42	5.61
3878	3878.02	20 Fe	1.4	0.95	4.14
	3878.58	4 Fe	0.33	0.09	3.27
3886	3886.28	4 Fe	0.63	0.05	3.23
3896	3895.66	4 Fe	0.14	0.11	3.28
3900	3899.71	4 Fe	0.21	0.09	3.25
3905	3905.53	3 Si	0.20	1.90	5.06
	3906.48	4 Fe	0.055	0.11	3.27
3921	3920.26	4 Fe	0.14	0.12	3.27
3922	3922.91	4 Fe	0.18	0.05	3.20
3929	3927.92	4 Fe	0.26	0.11	3.25
	3930.30	4 Fe	0.27	0.09	3.23
3936	3935.82	362 Fe	3.5	2.82	5.96
3940	3940.88	20 Fe	0.041	0.95	4.09
3944	3944.03	1 Al	0.66	0.00	3.13
3956	3956.68	278 Fe	9.1	2.68	5.80
3969.3	3969.26	43 Fe	4.4	1.48	4.59
4000	3997.40	278 Fe	11	2.72	5.80
	3998.06	276 Fe	3.7	2.68	5.77
4005	4005.25	43 Fe	3.6	1.55	4.63
4010	4009.72	72 Fe	1.4	2.21	5.29
4030	4030.76	2 Mn	1.4	0.00	3.06
	4033.07	2 Mn	0.95	0.00	3.06
	4034.49	2 Mn	0.54	0.00	3.06
4040	4041.36	5 Mn	34	2.11	5.16
4045	4045.82	43 Fe	22	1.48	4.53
4060	4058.93	5 Mn	7.4	2.17	5.21
4063	4063.60	43 Fe	9.9	1.55	4.59
4071	4071.74	43 Fe	9.1	1.60	4.63
4082	4082.94	5 Mn	7.1	2.17	5.19

TABLE 2.—*Wavelength Identifications of Taurid Meteor*—Continued

λ measured (Å)	λ identified (Å)	Multiplet no.	gA ($\times 10^8$/s)	E_1 (eV)	E_2 (eV)
	4083.63	5 Mn	6.9	2.15	5.18
4100	4100.75	18 Fe		0.86	3.86
4108	4107.49	354 Fe	5.6	2.82	5.82
4120	4118.55	801 Fe	33	3.56	6.55
4132	4132.06	43 Fe	2.7	1.60	4.59
4140	4139.93	18 Fe		0.99	3.97
	4143.87	43 Fr	2.9	1.55	4.53
4155	4154.50	355 Fe	5.3	2.82	5.79
	4156.80	354 Fe	5.3	2.82	5.79
4172	4172.75	19 Fe		0.95	3.91
4178	4177.60	18 Fe		0.91	3.86
4189	4187.04	152 Fe	6.9	2.44	5.39
	4187.80	152 Fe	6.5	2.41	5.36
4201	4202.03	42 Fe	2.0	1.48	4.42
4206	4206.70	3 Fe		0.05	2.99
4215	4216.19	3 Fe	0.0031	0.00	2.93
4226.7	4226.73	2 Ca	1	0.00	2.92
4235	4235.94	152 Fe	7.9	2.41	5.33
4240	4238.82	693 Fe	9.4	3.38	6.29
4251	4250.79	42 Fe	1.5	1.55	4.45
4253	4254.35	1 Cr	2.0	0.00	5.36
4261	4260.48	152 Fe	15	2.39	5.29
4272	4271.76	42 Fe	5.2	1.48	4.37
4276	4274.80	1 Cr	1.5	0.00	2.89
4283	4282.41	71 Fe	2.0	2.17	5.05
4291	4289.72	1 Cr	0.95	0.00	2.88
	4291.47	3 Fe		0.09	2.99
4300	4299.24	152 Fe	5.2	2.41	5.29
4308	4307.91	42 Fe	5.9	1.55	4.42
4325	4325.76	42 Fe	6.1	1.60	4.45
4338	4337.05	42 Fe	0.23	1.55	4.40
4354	4352.74	71 Fe	1	2.21	5.05
4368	4368.30	5 O		9.48	12.31
4376	4375.93	2 Fe	0.0094	0.00	2.82
4383	4383.55	41 Fe	7.7	1.48	4.29
4405	4404.75	41 Fe	4.4	1.55	4.35
4416	4415.12	41 Fe	2.8	1.60	4.40
4427	4427.31	2 Fe	0.0099	0.05	2.84
4454	4454.78	4 Ca	7.5	1.89	4.66
	4455.89	4 Ca	0.97	1.89	4.66
4462	4461.65	2 Fe	0.0052	0.09	2.85
	4462.05	28 Mn	16	3.06	5.83
4482	4482.17	2 Fe	0.0053	0.11	2.86
4489	4489.74	2 Fe		0.12	2.87
4496	4494.57	68 Fe	1.2	2.19	4.93
4529	4528.62	68 Fe	1.8	2.17	4.89
	4531.15	39 Fe	0.076	1.48	4.20
4570	4571.10	1 Mg		0.00	2.70
4581	4581.40	23 Ca	0.96	2.51	5.21
4586	4585.87	23 Ca	1.5	2.51	5.21
4601	4602.94	39 Fe	0.088	1.48	4.16
4692	4691.41	409 Fe		2.98	5.61
4703	4702.98	11 Mg		4.33	6.95

TABLE 2.—*Wavelength Identifications of Taurid Meteor*—Continued

λ measured (Å)	λ identified (Å)	Multiplet no.	gA ($\times 10^8$/s)	E_1 (eV)	E_2 (eV)
4737	4736.78	554 Fe	2.5	3.20	5.80
4761	4761.53	21 Mn		2.94	5.53
	4762.38	21 Mn	12	2.88	5.47
4768	4765.86	21 Mn		2.93	5.52
	4766.43	21 Mn	8.4	2.91	5.50
4825	4823.52	16 Mn	4.0	2.31	4.87
4861	4859.75	318 Fe	1.3	2.86	5.40
4872	4871.32	318 Fe	3.7	2.85	5.39
	4872.15	318 Fe	2.2	2.87	5.40
4878	4878.22	318 Fe	0.77	2.87	5.40
4892	4890.77	318 Fe	2.2	2.86	5.39
	4891.50	318 Fe	4.7	2.84	5.36
4905	4903.32	318 Fe	0.62	2.87	5.39
4919	4919.00	318 Fe	2.9	2.85	5.36
4920	4920.50	318 Fe	6.5	2.82	5.33
4939	4938.82	318 Fe		2.86	5.36
4958	4957.31	318 Fe	2.2	2.84	5.33
	4957.61	318 Fe	6.4	2.80	5.29
4967	4966.10	687 Fe		3.32	5.80
4988	4985.55	318 Fe		2.85	5.33
4995	4994.13	16 Fe		0.91	3.38
5006	5006.13	318 Fe	1.3	2.82	5.29
5014	5012.07	16 Fe	0.0067	0.86	3.32
5041	5041.76	36 Fe	0.023	1.48	3.93
5054	5051.54	16 Fe	0.0061	0.91	3.35
5070	5068.79	383 Fe	0.60	2.93	5.36
5081	5083.34	16 Fe	0.0052	0.95	3.38
5110	5110.41	1 Fe	0.0014	0.00	2.41
5125	5123.72	16 Fe		1.01	3.42
5133	5133.68	1092 Fe	13	4.16	6.56
5138	5139.26	383 Fe	1.6	2.99	5.39
	5139.48	383 Fe	2.0	2.93	5.33
5152	5153.40	8 Na	0.38	2.10	4.49
5170	5166.29	1 Fe		0.00	2.39
	5167.34	2 Mg	1.2	2.70	5.09
	5167.49	37 Fe		1.55	3.91
	5168.90	1 Fe		0.05	2.44
	5171.60	36 Fe		1.48	3.86
	5172.70	2 Mg	3.5	2.70	5.09
5184	5183.62	2 Mg	6.4	2.70	5.09
5207	5204.58	1 Fe		0.09	2.46
5218	5216.28	36 Fe	0.064	1.60	3.97
5227	5227.19	37 Fe	0.27	1.55	3.91
5244	5241.76	36 Fe		1.48	3.93
5250	5250.65	66 Fe		2.19	4.54
5261	5263.33	553 Fe		3.25	5.60
5270	5269.54	15 Fe	0.098	0.86	3.20
	5270.36	37 Fe	0.20	1.60	3.94
5281	5281.80	383 Fe	1.3	3.03	5.36
	5283.63	553 Fe		3.23	5.56
5328	5328.05	15 Fe	0.087	0.91	3.23
5340	5341.03	37 Fe	0.042	1.60	3.91
	5341.06	4 Mn	0.26	2.11	4.42
5371	5371.49	15 Fe	0.062	0.95	3.25

TABLE 2.—*Wavelength Identifications of Taurid Meteor*—Continued

λ measured (Å)	λ identified (Å)	Multiplet no.	gA ($\times 10^8$/s)	E_1 (eV)	E_2 (eV)
5397	5397.13	15 Fe	0.032	0.91	3.20
5403	5405.78	15 Fe	0.038	0.99	3.27
5423	5420.36	4 Mn	0.14	2.13	4.49
5429	5429.70	15 Fe	0.039	0.95	3.23
5445	5446.92	15 Fe	0.031	0.99	3.25
5454	5455.61	15 Fe	0.022	1.01	3.27
5472	5470.64	4 Mn	0.10	2.15	4.41
5497	5497.52	15 Fe	0.0084	1.01	3.25
5507	5506.78	15 Fe	0.0100	0.99	3.23
5528	5528.46	9 Mg	1.6	4.33	6.56
5569	5569.62	686 Fe	2.4	3.40	5.62
5574	5572.85	686 Fe	3.4	3.38	5.60
5580	5581.97	21 Ca		2.51	4.72
5585	5586.76	686 Fe	4.2	3.35	5.56
5591	5588.76	21 Ca		2.51	4.72
	5594.47	21 Ca		2.51	4.72
5602	5601.48	21 Ca		2.51	4.72
	5602.85	21 Ca		2.51	4.72
	5602.96	686 Fe	0.96	3.42	5.62
5614	5615.65	686 Fe	4.7	3.32	5.52
5660	5658.54	686 Fe		3.38	5.56
5690	5688.22	6 Na	1.8	2.10	4.27
5710	5708.44	10 Si		4.93	7.09
5772	5772.26	17 Si		5.06	7.20
5790	5789.8	FeO B			
5798	5797.91	9 Si		4.93	7.06
5859	5857.46	47 Ca	3.6	2.92	5.03
5891	5889.95	1 Na	1.8	0.00	2.10
5894	5895.92	1 Na	0.90	0.00	2.09
5946	5948.58	16 Si		5.06	7.14
6155	6154.11	5 Na		2.10	4.10
6217	6218.9	FeO A			
6347	6347.09	2 Si II		8.09	10.03
6439	6439.07	18 Ca		2.51	4.43

II were computed from the absorption oscillator strengths of Griem (1964). A large number of features in the 3100 Å to 3600 Å region remain unidentified. This spectrum suffers greatly from multiple zero-order star images and poor imagery.

DATA REDUCTION

The data reduction of the meteor spectrograms consisted of two parts: the wavelength identifications, and the absolute spectral photometry. The method used for the wavelength reductions was to obtain 40× densitometer tracings of the spectra. Wavelength scales were then constructed and positioned according to the known wavelengths of strong lines in the spectra. The wavelengths of the meteor radiation were read directly from the constructed scale. These wavelengths were read to the nearest angstrom. This method allows convenient checking of wavelength and relative intensity of lines during identification. Numerous sources were used in checking the wavelengths of the identified lines. The primary ones were Ceplecha (1964), Halliday (1961, 1969), Harvey (1967a) and Moore (1945). The identifications in the 3100 Å to 3600 Å region were particularly difficult, and many features have remained unidentified. The wavelengths

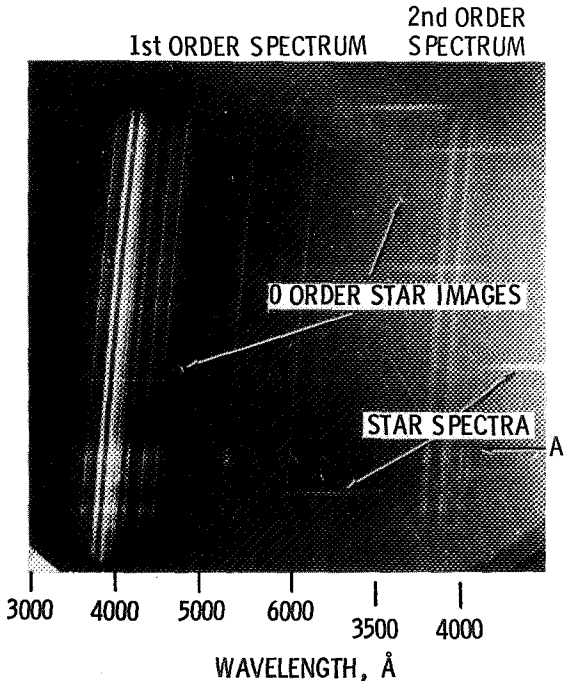

FIGURE 3.—Enlargement of a spectrogram of a Geminid meteor.

and identifications of features in the four spectra are listed in tables 1 to 4.

The spectral photometry used in the data reduction follows closely that of Harvey (1967b). This photometry is based on calibration of the meteor irradiance with the irradiance from a quartz-iodine lamp that is a standard of spectral irradiance. Again the 3100 Å to 3600 Å spectral region has proven to be difficult to work in because of the relatively low energy of the standard lamp and the high atmospheric attenuation in this region.

As mentioned in the data section, assumed heights and shower velocities were used for the three shower meteors. Factors which have further degraded the accuracy of the reduced meteor spectral irradiance are: lack of measured atmospheric attenuation, the relatively unstable character of the film emulsion and developer, poor imagery, and the dense and nonuniform fog background of the spectral plates. The attenuation used here was taken from Elterman (1964).

The reduced absolute spectral irradiances are

TABLE 3.—*Wavelength Identifications of Geminid Meteor*

λ measured (Å)	λ identified (Å)	Multiplet no.	gA ($\times 10^8$/s)	E_1 (eV)	E_2 (eV)
3363	3361.92	11 Ca		1.89	5.56
	3362.13	11 Ca		1.89	5.56
3368	3369.57	6 Ni	2.1	0.00	3.66
3371	3370.79	304 Fe	32	2.68	6.34
	3371.99	7 Ni	0.41	0.16	2.84
3378	3379.02	85 Fe		2.17	5.82
3388	3388.17	23 Co	2.2	0.58	4.22
3400	3399.34	85 Fe	25	2.19	5.82
	3401.52	26 Fe		0.91	4.54
3407	3405.12	23 Co	15	0.43	4.05
	3407.46	83 Fe	33	2.17	5.79
3408	3409.18	23 Co	7.3	0.51	4.13
3412	3413.14	85 Fe	26	2.19	5.80
3416	3414.76	19 Ni	5.7	0.03	3.64
	3417.84	81 Fe	18	2.21	5.82
3420	3418.51	81 Fe	18	2.21	5.82
	3422.66	85 Fe	9.3	2.21	5.82
3425	3424.29	81 Fe	17	2.17	5.77
3441	3440.61	6 Fe	2.8	0.00	3.59
	3440.99	6 Fe	0.64	0.05	3.64
3449	3450.33	82 Fe	8.9	2.21	5.79
3459	3458.47	19 Ni	4.9	0.21	3.78

TABLE 3.—*Wavelength Identifications of Geminid Meteor*—Continued

λ measured (Å)	λ identified (Å)	Multiplet no.	gA ($\times 10^8$/s)	E_1 (eV)	E_2 (eV)
3462	3461.65	17 Ni	3.2	0.03	3.59
	3462.80	23 Co	9.7	0.63	4.19
3466	3465.86	6 Fe	0.52	0.11	3.67
3472	3472.54	20 Ni	1.2	0.11	3.66
3474	3474.02	4 Co	3.6	0.00	3.55
	3475.45	6 Fe	0.64	0.09	3.64
3485	3485.34	78 Fe	5.9	2.19	5.73
3490	3490.58	6 Fe	0.58	0.05	3.59
3495	3495.29	238 Fe	11	2.55	6.08
3497	3497.11	78 Fe	7.4	2.19	5.70
	3497.84	6 Fe	0.19	0.11	3.64
3499	3500.57	238 Fe		2.58	6.10
	3500.85	6 Ni		0.16	3.69
3514	3513.82	24 Fe	1.7	0.86	4.37
3521	3521.26	24 Fe	1.7	0.91	4.42
3524	3524.54	18 Ni	4.6	0.03	3.53
3527	3526.04	6 Fe	0.13	0.09	3.59
	3526.17	24 Fe	0.69	0.95	4.45
3531	3533.20	326 Fe	23	2.87	6.36
3536	3536.56	326 Fe	56	2.86	6.35
3542	3541.09	326 Fe	65	2.84	6.32
	3542.08	326 Fe	61	2.85	6.34
3566	3565.38	24 Fe	7.8	0.95	4.42
3570	3570.10	24 Fe	18	0.91	4.37
	3570.24	326 Fe		2.80	6.25
3581	3581.20	23 Fe	23	0.86	4.30
3596	3594.64	322 Fe	21	2.84	6.27
3606	3605.46	294 Fe	51	2.72	6.14
	3606.68	294 Fe	65	2.68	6.10
3608	3608.86	23 Fe	10	1.01	4.43
3618	3618.77	23 Fe	9.5	0.99	4.40
3621	3621.46	294 Fe	50	2.72	6.12
3631	3631.46	23 Fe	8.6	0.95	4.35
3640	3638.30	294 Fe	28	2.75	6.14
	3640.39	295 Fe	45	2.72	6.11
3644	3644.41	9 Ca	1.8	1.89	5.28
3649	3647.84	24 Fe	6.1	0.91	4.29
	3649.30	5 Fe		0.00	3.38
3660	3659.52	180 Fe	9.9	2.44	5.82
3671	3669.52	291 Fe	32	2.72	6.08
3680	3679.92	5 Fe	0.29	0.00	3.35
3685	3684.11	292 Fe	21	2.72	6.07
	3686.00	385 Fe	34	2.93	6.28
3687	3687.46	21 Fe	2.5	0.86	4.20
3696	3694.01	394 Fe	72	3.03	6.37
	3695.05	229 Fe	12	2.58	5.92
3698	3697.43	389 Fe		2.99	6.32
3707	3705.57	5 Fe	0.38	0.05	3.38
	3707.82	5 Fe	0.14	0.09	3.42
3720	3719.94	5 Fe	2.5	0.00	3.32
	3722.56	5 Fe	0.40	0.09	3.40
3738	3733.40	5 Fe	0.36	0.11	3.42
	3734.87	21 Fe	20	0.86	4.16

TABLE 3.—*Wavelength Identifications of Geminid Meteor*—Continued

λ measured (Å)	λ identified (Å)	Multiplet no.	gA ($\times 10^8$/s)	E_1 (eV)	E_2 (eV)
	3737.13	5 Fe	1.5	0.05	3.35
3747	3745.56	5 Fe	1.2	0.09	3.38
	3745.90	5 Fe	0.31	0.12	3.42
	3748.26	5 Fe	0.71	0.11	3.40
	3749.49	20 Fe	13	0.91	4.20
3759	3758.24	21 Fe	10	0.95	4.24
3763	3763.79	21 Fe	6.2	0.99	4.26
3788	3787.88	21 Fe	1.7	1.01	4.26
3794	3795.00	22 Fe	2.3	0.99	4.24
3798	3798.51	21 Fe	0.93	0.91	4.16
	3799.55	21 Fe	1.5	0.95	4.20
3806	3805.34	608 Fe	45	3.29	6.53
	3806.70	607 Fe	21	3.25	6.50
3815	3815.84	45 Fe	16	1.48	4.71
3830	3827.82	45 Fe	15	1.55	4.77
	3829.35	3 Mg	11	2.70	5.92
3833	3832.51	3 Mg	23	2.70	5.92
3838	3838.26	3 Mg	39	2.70	5.92
3847	3846.80	664 Fe	20	3.24	6.45
3860	3859.91	4 Fe	1.4	0.00	3.20
3871	3872.50	20 Fe	1.0	0.99	4.17
3879	3878.02	20 Fe	1.4	0.95	4.14
	3878.58	4 Fe	0.33	0.09	3.27
3887	3886.28	4 Fe	0.63	0.05	3.23
	3887.05	20 Fe	4.2	0.91	4.09
3896	3895.66	4 Fe	0.14	0.11	3.28
3900	3899.71	4 Fe	0.21	0.09	3.25
3905	3905.53	3 Si	0.86	1.90	5.06
	3906.48	4 Fe	0.055	0.11	3.27
3924	3922.91	4 Fe	0.18	0.05	3.20
3935	3930.30	4 Fe	0.27	0.09	3.23
	3933.67	1 Ca II	0.91	0.00	3.14
3945	3944.03	1 Al	0.66	0.00	3.13
3948	3948.78	604 Fe	11	3.25	6.38
3962	3961.53	1 Al	1.3	0.00	3.13
3969	3968.47	1 Ca II	0.45	0.00	3.11
	3969.26	43 Fe	4.4	1.48	4.59
3983	3983.96	277 Fe	5.4	2.72	5.81
3999	3997.40	278 Fe	11	2.72	5.80
	3998.06	276 Fe	3.7	2.68	5.77
4005	4005.25	43 Fe	3.6	1.55	4.63
4008	4007.27	277 Fe		2.75	5.83
4011	4009.72	72 Fe	1.4	2.21	5.29
4032	4030.76	2 Mn	1.4	0.00	3.06
4035	4033.07	2 Mn	0.95	0.00	3.06
	4034.49	2 Mn	0.54	0.00	3.06
4046	4045.82	43 Fe	22	1.48	4.53
4063	4063.60	43 Fe	9.9	1.55	4.59
4069	4067.98	559 Fe		3.20	6.23
4072	4071.74	43 Fe	9.1	1.60	4.63
4101	4100.74	18 Fe		0.86	3.86
4109	4107.49	354 Fe	5.6	2.82	5.82
4115	4114.45	357 Fe		2.82	5.82

TABLE 3.—*Wavelength Identifications of Geminid Meteor*—Continued

λ measured (Å)	λ identified (Å)	Multiplet no.	gA ($\times 10^8$/s)	E_1 (eV)	E_2 (eV)
4119	4118.55	801 Fe	33	3.56	6.55
4122	4121.32	28 Co	3.7	0.92	3.91
	4121.81	356 Fe		2.82	5.81
4133	4132.06	43 Fe	2.7	1.60	4.59
4136	4134.68	357 Fe	5.5	2.82	5.80
4144	4143.87	43 Fe	2.9	1.55	4.53
4151	4152.17	18 Fe		0.95	3.93
4153	4154.50	355 Fe	5.3	2.82	5.79
	4154.81	694 Fe		3.35	6.32
4171	4172.75	19 Fe		0.95	3.91
4176	4175.64	354 Fe	4.7	2.83	5.79
4181	4181.76	354 Fe	10	2.82	5.77
4184	4184.90	355 Fe	3.9	2.82	5.77
4190	4187.04	152 Fe	6.9	2.44	5.39
	4187.80	152 Fe	6.5	2.41	5.36
	4191.44	152 Fe	4.4	2.46	5.40
4200	4199.10	522 Fe	25	3.03	5.97
4202	4202.03	42 Fe	2.0	1.48	4.42
4209	4210.35	152 Fe	2.2	2.47	5.40
4218	4216.19	3 Fe	0.0031	0.00	2.93
	4219.36	800 Fe	27	3.56	6.48
4227	4226.73	2 Ca	1	0.00	2.92
	4227.43	693 Fe	38	3.32	6.24
4234	4233.61	152 Fe	5.9	2.47	5.39
4237	4235.94	152 Fe	7.9	2.41	5.33
4252	4250.79	42 Fe	1.5	1.55	4.45
	4250.13	152 Fe		2.46	5.36
4254	4254.35	1 Cr	2.0	0.00	2.90
4260	4260.48	152 Fe	15	2.39	5.29
4272	4271.76	42 Fe	5.2	1.48	4.37
4282	4282.41	71 Fe	2.0	2.17	5.05
4291	4289.72	1 Cr	0.95	0.00	2.88
	4291.66	3 Fe		0.09	2.99
4294	4294.13	41 Fe	0.71	1.48	4.35
4300	4299.24	152 Fe	5.2	2.41	5.29
4302	4302.53	5 Ca	7.1	1.89	4.76
4308	4307.91	42 Fe	5.9	1.55	4.42
4315	4315.09	71 Fe	1.5	2.19	5.05
4319	4318.65	5 Ca	2.5	1.89	4.75
4326	4325.76	42 Fe	6.1	1.60	4.45
4336	4337.05	41 Fe	0.23	1.55	4.40
4339	4339.45	22 Cr	0.93	0.98	3.82
	4339.72	22 Cr	0.30	0.96	3.80
4351	4351.77	22 Cr	2.0	1.03	3.86
4353	4352.74	71 Fe	1.0	2.21	5.05
4358	4358.51	412 Fe		2.94	5.77
4377	4375.93	2 Fe	0.0094	0.00	2.82
4384	4383.55	41 Fe	7.7	1.48	4.29
4404	4404.75	41 Fe	4.4	1.55	4.35
4415	4415.12	41 Fe	2.8	1.60	4.40
4426	4427.31	2 Fe	0.0099	0.05	2.84
4434	4434.96	4 Ca	3.5	1.88	4.66
	4435.69	4 Ca	0.96	1.88	4.66

TABLE 3.—*Wavelength Identifications of Geminid Meteor*—Continued

λ measured (Å)	λ identified (Å)	Multiplet no.	gA ($\times 10^8$/s)	E_1 (eV)	E_2 (eV)
4442	4442.34	68 Fe		2.19	4.97
4455	4454.78	4 Ca	7.5	1.89	4.66
	4455.89	4 Ca	0.97	1.89	4.66
4462	4461.65	2 Fe	0.0052	0.09	2.85
4467	4466.55	350 Fe	5.3	2.82	5.58
4482	4482.17	2 Fe	0.0053	0.11	2.86
4531	4531.15	39 Fe	0.076	1.48	4.20
4580	4581.40	23 Ca	0.96	2.51	5.21
4585	4585.87	23 Ca	1.5	2.51	5.21
4646	4647.44	409 Fe		2.94	5.59
4878	4878.22	318 Fe	0.77	2.87	5.40
4890	4890.77	318 Fe	2.2	2.86	5.39
	4891.50	318 Fe	4.7	2.84	5.36
4920	4919.00	318 Fe	2.9	2.85	5.38
	4920.50	318 Fe	6.5	2.82	5.33
4960	4957.31	318 Fe	3.2	2.84	5.33
	4957.61	318 Fe	6.4	2.80	5.29
5007	5006.13	318 Fe	1.3	2.82	5.29
5108	5110.41	1 Fe	0.0014	0.00	2.41
5167	5166.29	1 Fe		0.00	2.41
	5167.34	2 Mg	1.2	2.70	5.09
	5167.49	37 Fe	0.26	1.48	3.87
	5168.90	1 Fe		0.05	2.44
5173	5171.60	36 Fe	0.12	1.48	3.86
	5172.70	2 Mg	3.5	2.70	5.09
5184	5183.62	2 Mg	6.4	2.70	5.09
5270	5269.54	15 Fe	0.098	0.86	3.20
	5270.36	37 Fe	0.20	1.60	3.94
5329	5328.05	15 Fe	0.087	0.91	3.23
5893	5889.95	1 Na	1.8	0.00	2.10
	5895.92	1 Na	0.9	0.00	2.09

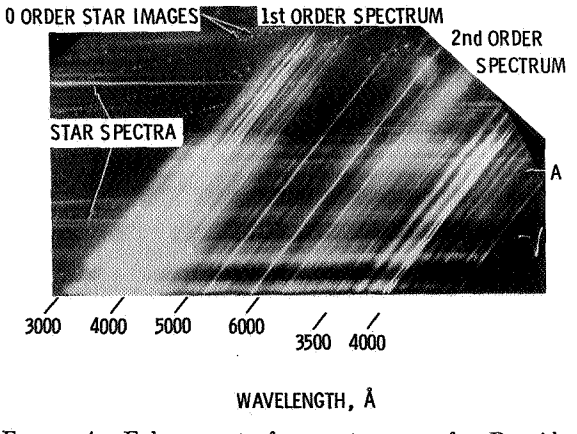

FIGURE 4.—Enlargement of a spectrogram of a Perseid meteor.

probably within a factor of 2 of the actual values, except perhaps for those in the near-ultraviolet region. In many cases, relative measurement of two lines in a spectrum (upon which most of the analysis is based) is estimated to be of the order of 5 to 10 percent accuracy. However, in some cases, especially where imagery is poor, the relative photometry suffers from blending of lines and the relative measurements are less accurate. The spectral irradiances of the four meteors are shown in figures 5 to 8.

DATA ANALYSIS

The data analysis is based on the assumption that the population distribution of the excited states is a Boltzmann distribution. Agreement in temperatures calculated from pairs of lines from

TABLE 4.—*Wavelength Identifications of Perseid Meteor*

λ measured (Å)	λ identified (Å)	Multiplet no.	gA ($\times 10^8$/s)	E_1 (eV)	E_2 (eV)
3090	3091.58	28 Fe	3.2	1.01	5.00
3102	3099.97	28 Fe	8.6	0.91	4.89
	3100.30	28 Fe	3.9	0.99	4.97
	3100.67	28 Fe	3.6	0.95	4.93
	3101.55	25 Ni	4.6	0.11	4.09
3135	3134.11	25 Ni	5.8	0.21	4.15
3192	3191.66	8 Fe	0.087	0.00	3.87
	3193.21	7 Fe	0.14	0.00	3.86
3240	3239.44	157 Fe	65	2.41	6.22
3265	3265.62	91 Fe	18	2.17	5.95
3298	3302.32	2 Na	0.65	0.00	3.74
	3302.99	2 Na	0.33	0.00	3.74
3348	3344.51	11 Ca		1.87	5.56
	3350.21	11 Ca		1.88	5.56
	3350.36	11 Ca		1.88	5.56
3370	3369.57	6 Ni	2.1	0.00	3.66
3385	3383.69	85 Fe		2.19	5.84
	3383.98	83 Fe	9.1	2.17	5.81
3422	3418.51	81 Fe	18	2.21	5.82
	3422.66	85 Fe	9.3	2.21	5.82
	3424.29	81 Fe	17	2.17	5.77
3441	3440.61	6 Fe	2.8	0.00	3.59
	3440.99	6 Fe	0.64	0.05	3.64
3472	3474.02	4 Co	3.6	0.11	3.66
	3475.45	6 Fe	0.64	0.09	3.64
3487	3485.34	78 Fe	5.9	2.19	5.73
3495	3495.29	238 Fe	11	2.55	6.08
3566	3565.38	24 Fe	7.8	0.95	4.42
	3570.10	24 Fe	18	0.91	4.37
3581	3581.20	23 Fe	23	0.86	4.30
3608	3608.86	23 Fe	10	1.01	4.43
3618	3618.77	23 Fe	9.5	0.99	4.40
3630	3631.46	23 Fe	8.6	0.95	4.35
3649	3647.84	24 Fe	6.1	0.91	4.29
3685	3684.11	292 Fe	21	2.72	6.07
	3686.00	385 Fe	34	2.93	6.28
3706	3705.57	5 Fe	0.38	0.05	3.38
	3707.82	5 Fe	0.41	0.09	3.41
3720	3719.94	5 Fe	2.5	0.00	3.32
	3722.56	5 Fe	0.40	0.09	3.40
3735	3733.40	5 Fe	0.36	0.11	3.42
	3734.87	21 Fe	20	0.86	4.16
	3737.13	5 Fe	1.5	0.05	3.35
3746	3745.56	5 Fe	1.2	0.09	3.38
	3745.90	5 Fe	0.31	0.12	3.42
	3748.26	5 Fe	0.71	0.11	3.40
	3749.49	20 Fe	13	0.91	4.20
3760	3758.24	21 Fe	10	0.95	4.24
3796	3795.00	22 Fe	2.3	0.99	4.24
3836	3827.82	45 Fe	15	1.55	4.77
	3829.35	3 Mg	11	2.70	5.92
	3832.51	3 Mg	23	2.70	5.92
	3838.26	3 Mg	39	2.70	5.92
3860	3859.91	4 Fe	1.4	0.00	3.20

TABLE 4.—*Wavelength Identifications of Perseid Meteor*—Continued

λ measured (Å)	λ identified (Å)	Multiplet no.	gA ($\times 10^8$/s)	E_1 (eV)	E_2 (eV)
3887	3886.28	4 Fe	0.63	0.05	3.23
	3887.05	20 Fe	4.2	0.91	4.09
3902	3899.71	4 Fe	0.21	0.09	3.25
	3905.53	3 Si	0.86	1.90	5.06
3910	3909.84	364 Fe		2.83	5.99
3934	3933.67	1 Ca II	0.91	0.00	3.14
3968	3968.47	1 Ca II	0.45	0.00	3.11
4046	4045.82	43 Fe	22	1.48	4.53
4065	4063.60	43 Fe	9.9	1.55	4.59
4070	4071.74	43 Fe	9.1	1.60	4.63
4110	4107.49	354 Fe	5.6	2.82	5.82
4130	4132.06	43 Fe	2.7	1.60	4.59
4145	4143.87	43 Fe	2.9	1.55	4.53
4175	4175.64	354 Fe	4.7	2.83	5.79
4185	4184.90	355 Fe	3.9	2.82	5.77
	4187.80	152 Fe	6.5	2.41	5.36
4203	4202.03	42 Fe	2.0	1.48	4.42
4216	4216.19	3 Fe	0.0031	0.00	2.93
	4219.36	800 Fe	27	3.56	6.48
4227	4226.73	2 Ca	1.0	0.00	2.92
	4227.43	693 Fe	38	3.32	6.24
4255	4254.35	2 Cr	2.0	0.00	2.90
4273	4271.76	42 Fe	5.2	1.48	4.37
4292	4289.72	1 Cr	0.95	0.00	2.88
	4294.13	41 Fe	0.71	1.48	4.35
4307	4307.91	42 Fe	5.9	1.55	4.42
4325	4325.76	42 Fe	6.1	1.60	4.45
4378	4375.93	2 Fe	0.0094	0.00	2.82
	4384.55	41 Fe	7.7	1.48	4.29
4403	4404.75	41 Fe	4.4	1.55	4.35
4426	4427.31	2 Fe	0.0099	0.05	2.84
4460	4461.65	2 Fe	0.0052	0.09	2.85
4481	4481.13	4 Mg II		8.83	11.58
	4481.33	4 Mg II		8.83	11.38
	4482.17	2 Fe	0.0053	0.11	2.86
4571	4571.10	1 Mg		0.00	2.70
4585	4583.83	38 Fe II		2.79	5.49
4650	4649.14	1 O II		22.90	25.55
	4650.84	1 O II		22.87	25.52
4675	4673.75	1 O II		22.88	25.52
	4676.23	1 O II		22.90	25.53
4919	4919.00	318 Fe	2.9	2.85	5.36
	4920.50	318 Fe	6.5	2.82	5.33
4955	4957.31	318 Fe	2.2	2.84	5.33
	4957.61	318 Fe	6.4	2.80	5.29
5005	5006.13	318 Fe	1.3	2.82	5.29
5019	5018.78	13 O		10.69	13.15
	5019.34	13 O		10.69	13.15
	5020.13	13 O		10.69	13.15
5041	5041.06	5 Si II	0.473	10.02	12.47
5055	5056.02	5 Si II	0.380	10.03	12.47
	5056.35	5 Si II		10.03	12.47
5110	5110.41	1 Fe	0.0014	0.00	2.41

TABLE 4.—*Wavelength Identifications of Perseid Meteor*—Continued

λ measured (Å)	λ identified (Å)	Multiplet no.	gA ($\times 10^8$/s)	E_1 (eV)	E_2 (eV)
5142	5139.26	383 Fe	1.6	2.99	5.39
	5139.48	383 Fe	2.0	2.93	5.33
	5142.93	16 Fe		0.95	3.35
5170	5166.29	1 Fe		0.00	2.41
	5167.34	2 Mg	1.2	2.70	5.09
	5167.49	37 Fe	0.26	1.48	3.87
	5168.90	1 Fe		0.05	2.44
	5171.60	36 Fe	0.12	1.48	3.86
	5172.70	2 Mg	3.5	2.70	5.09
5184	5183.62	2 Mg	6.4	2.70	5.09
5226	5226.88	383 Fe	2.0	3.03	5.39
	5227.19	37 Fe	0.27	1.55	3.91
5269	5269.54	15 Fe	0.098	0.86	3.20
	5270.36	37 Fe	0.20	1.60	3.94
5328	5328.05	15 Fe	0.087	0.91	3.23
	5328.53	37 Fe	0.052	1.55	3.87
	5328.98	12 O		10.69	13.01
	5329.59	12 O		10.69	13.01
	5330.66	12 O		10.69	13.01
5343	5341.03	37 Fe	0.042	1.60	3.91
5370	5371.49	15 Fe	0.062	0.95	3.25
5428	5429.70	15 Fe	0.039	0.95	3.23
5453	5455.61	15 Fe	0.022	1.01	3.27
5525	5528.46	9 Mg	1.6	4.33	6.56
5570	5569.62	686 Fe	2.4	3.40	5.62
	5572.85	686 Fe	3.4	3.38	5.60
5586	5586.76	686 Fe	4.2	3.35	5.56
	5588.75	21 Ca	5.4	2.51	4.72
5775	5772.26	17 Si		5.06	7.20
5800	5797.91	9 Si		4.93	7.09
5893	5889.95	1 Na	1.8	0.00	2.10
	5895.92	1 Na	0.90	0.00	2.09
5960	5957.61	4 Si II	0.356	10.02	12.09
5980	5978.97	4 Si II	0.527	10.03	12.09
6000	5999.47	16 N		11.55	13.61
6123	6122.22	3 Ca	1.2	1.88	3.89
6155	6154.23	5 Na		2.09	4.70
	6155.99	10 O		10.69	12.70
	6156.78	10 O		10.69	12.70
	6158.20	10 O		10.69	12.70
6348	6347.09	2 Si II	0.31	8.09	10.03
6371	6371.36	2 Si II	0.387	8.09	10.02
6440	6439	18 Ca	3.2	2.51	4.43
6456	6453.64	9 O		10.69	12.61
	6454.48	9 O		10.69	12.61
	6456.01	9 O		10.69	12.61
6483	6481.73	21 N	0.0662	11.70	13.61
	6482.74	21 N		11.70	13.61
	6483.75	21 N		11.70	13.61
	6484.88	21 N	0.2725	11.70	13.61
6562	6562.82	1 H		10.15	12.04

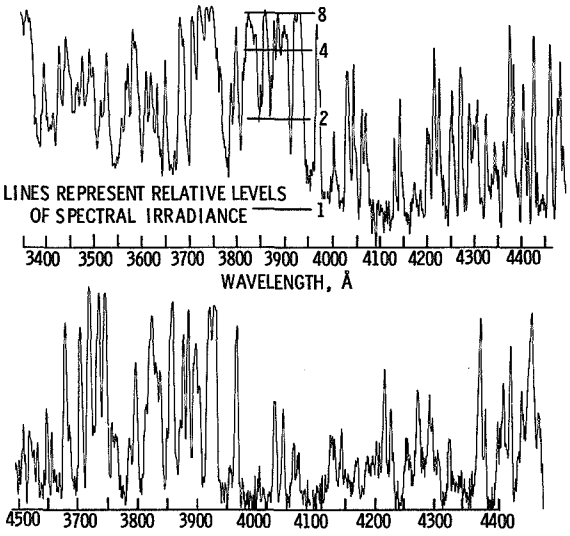

FIGURE 5.—Spectral irradiance from sporadic meteor.

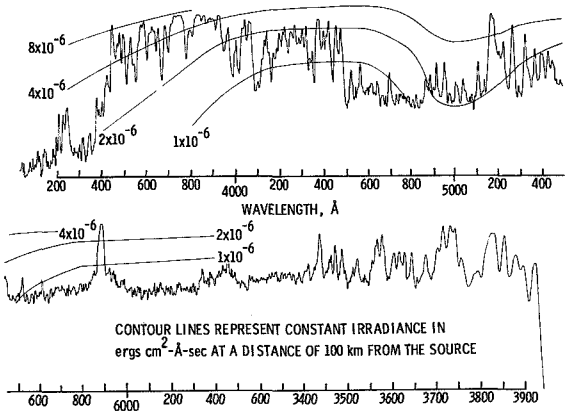

FIGURE 6.—Spectral irradiance from Taurid meteor.

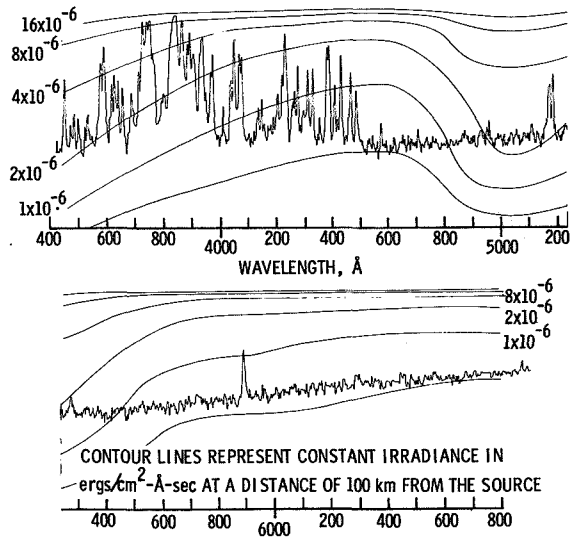

FIGURE 7.—Spectral irradiance from Geminid meteor.

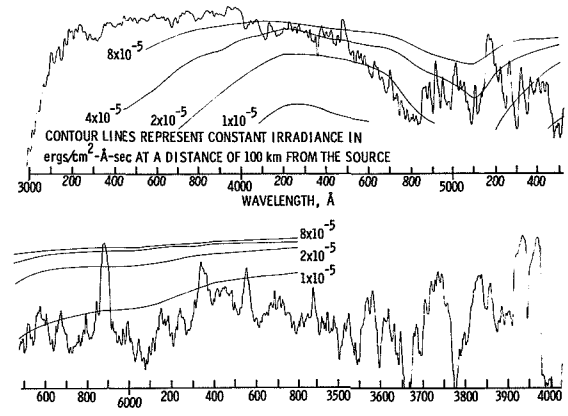

FIGURE 8.—Spectral irradiance from Perseid meteor.

several different energy levels is taken to be indicative that the excited state populations follow a Boltzmann distribution. In particular, the relative populations of the neutral excited states in the energy range of 2 to 6 eV are obtained. This is the energy region in which the number of lines in a good meteor spectrum allows one to measure the populations. Iron, because of the large number of lines of different energy levels, is a convenient reference element for these measurements.

As has been shown by Ceplecha (1964, 1967), Harvey (1970) and Millman (1932, 1935), the population distribution in this range is similar to that of a Boltzmann distribution. Especially for the fainter meteors, we can assume that all of the states are underpopulated relative to a gas in local thermodynamic equilibrium since the observed states are depopulated by radiative transfers (which occur quickly, compared to time between collisions). We can also assume that the very high (>6 eV) energy states are overpopulated relative to the lower energy states in local thermodynamic equilibrium (LTE) because of the high initial relative velocities of the ablated meteor atoms. However, as the underpopulation

due to radiative transfer affects all the atoms and little radiation is observed from very high energy states (excluding ionic radiation), we can ignore these effects if we restrict ourselves to working on a relative basis and in a limited energy range.

The analysis, then, simply consists of selecting pairs of lines within the 2 to 6 eV energy range and computing an "effective meteor radiation temperature" T^*. Thus, T^* is calculated from

$$\frac{I_{in}}{I_{jl}}=\frac{h\nu_{in}N_iA_{in}}{h\nu_{jl}N_jA_{jl}}=\frac{h\nu_{in}g_iA_{in}}{h\nu_{jl}g_jA_{jl}}e^{-(E_i-E_j)/kT^*}$$

where I_{in} is the intensity of radiation for the transition from the ith to the nth atomic state, I_{jl} is the intensity of radiation for the transition from the jth to the lth atomic state, N_i is the number of particles in the ith atomic state with energy E_i above the ground state, h is Planck's constant, ν_{in} is the frequency of observed radiation for the transition from the ith to the nth state, g_i is the statistical weight of the ith state, A_{in} is the Einstein probability coefficient for the transition from the ith to the nth state, and k is the Boltzmann constant. The results of the calculations are shown in tables 5 to 8 for the sporadic, the Taurid, the Geminid, and the Perseid meteors, respectively. Excitation energies comparable to temperatures of hundreds of thousands of degrees are available in the initial meteor atomic collisions. General agreement in the range of T^* calculated from different pairs of lines indicates that the first atomic collisions do not dominate the meteor radiation process.

In general, table 5 reflects the advantage of high spectral resolution and its resultant effect

TABLE 5.—*Sporadic "Effective Meteor Radiation Temperature"*

Element	Lines (Å)	Temperature (° K)
Fe I	4384, 4376	2280
Fe I	3570, 3491	2453
Fe I	3648, 3680	2880
Fe I	4144, 4216	2540
Fe I	4404, 4427	2565
Fe I	av	2544±197 standard error

TABLE 6.—*Taurid "Effective Meteor Radiation Temperature"*

Element	Lines (Å)	Temperature (° K)
Fe I	4384, 4376	2490
Fe I	3570, 3441	3880
Fe I	3648, 3680	3360
Fe I	4405, 4427	2740
Fe I	4046, 4427	2570
Fe I	3631, 3707	3640
Fe I	3758, 3719	3870
Fe I	3581. 3719	3950
Fe I	4216, 4046	2260
	av	3196±640 standard error

TABLE 7.—*Geminid "Effective Meteor Radiation Temperature"*

Element	Lines (Å)	Temperature (° K)
Fe I	4384, 4376	2560
Fe I	3648, 3680	3680
Fe I	4405, 4427	2745
Fe I	4046, 4427	2800
Fe I	3631, 3707	4680
Fe I	3581, 3719	4150
Fe I	4046, 4216	2500
	av	3302±776 standard error

TABLE 8.—*Perseid "Effective Meteor Radiation Temperature"*

Element	Lines (Å)	Temperature (° K)
Fe I	4384, 4376	2780
Fe I	4405, 4427	2790
Fe I	4046, 4427	2670
Fe I	4046, 4216	2500
Fe I	5139, 5110	3970
	av	2942±525 standard error
Na I	5153, 5893	10,770
Ca I	6439, 4226	4470
Mg I	5528, 5184	12,810

on "effective radiation temperature" measurements. The Taurid measurements are compromised somewhat by overexposure. The Geminid measurements are relatively clean, while the Perseid measurements are poor because of bad imagery.

The abundances of elements relative to iron were computed by using the "effective radiation temperatures." That is, the atomic ratio of element a to element b, where element "b" is always iron, was obtained from

$$\frac{N_a}{N_b}=\frac{I_{ina}}{I_{jlb}}\frac{B(T)_a}{B(T)_b}\frac{g_{jb}A_{jlb}\nu_{jlb}}{g_{ia}A_{ina}\nu_{ina}}e^{-(E_{jb}-E_{ia})/kT^*} \quad (2)$$

where N_a is the number of atoms of element a, N_b is the number of atoms of iron, $B(T)_a$ is the partition function of element a, and $B(T)_b$ is the partition function of iron. Partition functions from Corliss (1962) were used. Iron was used as the reference element its prevalence in neutral spectra, and because of the large number of lines suitable for spectral measurements.

The ratios of the peak intensities of the relevant lines were used. The radiation of the element in question was compared to that of an iron line in the same spectral region, of similar energy level, and of comparable line strength where possible. The silicon determinations are highly uncertain because of the weakness of the 3905 Å line and the blending of other lines in this region of the spectrum. The element ratios calculated from the spectral measurements of the four meteors are presented in tables 9 to 12. "Derived compositions" based on the element ratios and typical meteorite oxygen abundances are also listed in the tables.

A dc arc was used as an empirical tool for data analysis. Some difficulty has been experienced in obtaining arc temperatures as low as some of the "equivalent radiation temperatures" of the meteors. Nevertheless, there is good general qualitative agreement between a dc arc and neutral meteor spectra. The arc studies indicate that the individual "equivalent radiation temperatures" obtained by this type of method are uncertain to several hundred degrees Kelvin for favorable line intensity measurements. The studies also show that reasonable silicon abundance measurements are possible with the 3905 Å line with high resolution and good plate quality.

TABLE 9.—*Element Ratios and "Derived Composition" of Sporadic Meteor*

Element ratios (atomic)	Derived composition (percent by weight)
$\frac{Ni}{Fe}=0.15$	Fe—68
	Ni—10
	Ca—0.0058
$\frac{Ca}{Fe}=5.9\times10^{-5}$	Mn—0.13
	Cr—0.015
	Mg—0.19
$\frac{Mn}{Fe}=1.8\times10^{-3}$	Si—9.8
	O—11
$\frac{Cr}{Fe}=2.2\times10^{-4}$	
$\frac{Mg}{Fe}=1.16\times10^{-3}$	
$\frac{Si}{Fe}=0.13$	

RADIATION

Four meteor spectra, each of more than 100 lines, have been reduced and analyzed. These four spectra of a sporadic, a Taurid, a Geminid, and a Perseid meteor may be taken as generally representative of bright meteor spectra in the optical range. The analyses of these spectra have shown a surprising simplicity and consistency of the radiation process for the neutral radiation.

The populations of the neutral excited states in the 2 to 6 eV energy range have been found to be consistent with that of a Boltzmann distribution within the experimental error. This may be taken as an indication that this type of radiation is produced by a gas that is near equilibrium. A physical concept that can be correlated with these measured results is as follows: meteoric gas is initially energized by the passage and ablation of a meteoroid. The following "relaxation and mixing" of this energized gas probably involves hundreds of collisions within milliseconds. The relaxation and mixing can be considered in terms of the downward velocity cascade of meteoric atoms (and impacted atmospheric molecules) through a series of collisions with atmospheric molecules. For a simple elastic hard sphere

TABLE 10.—*Element Ratios and "Derived Composition" of Taurid Meteor*

Element ratios (atomic)	Derived composition (percent by weight)
$\frac{Ni}{Fe}=0.106$	Fe—13
$\frac{Ca}{Fe}=1.5\times10^{-4}$	Ni—1.6
$\frac{Mn}{Fe}=3.2\times10^{-4}$	Ca—0.0015
$\frac{Cr}{Fe}=5.1\times10^{-4}$	Mn—0.0043
$\frac{Mg}{Fe}=1.8$	Cr—0.0068
$\frac{Si}{Fe}=4.6$	Mg—10
$\frac{Na}{Fe}=8.1\times10^{-5}$	Si—30
$\frac{Al}{Fe}=1.7\times10^{-2}$	Na—0.00045
	Al—0.11
	O—44

TABLE 11.—*Element Ratios and "Derived Composition" of Geminid Meteor*

Element ratios (atomic)	Derived composition (percent by weight)
$\frac{Ni}{Fe}=0.114$	Fe—13
$\frac{Ca}{Fe}=2.0\times10^{-3}$	Ni—1.7
$\frac{Mn}{Fe}=4.0\times10^{-4}$	Ca—0.02
$\frac{Cr}{Fe}=5.1\times10^{-4}$	Mn—0.0055
$\frac{Mg}{Fe}=2.06$	Cr—0.0068
$\frac{Si}{Fe}=4.2$	Mg—12
$\frac{Na}{Fe}=1.0\times10^{-4}$	Si—27
$\frac{Al}{Fe}=1.9\times10^{-2}$	Na—0.00057
	Al—0.13
	O—45

model, the most probable energy transfer from an incident atom to a target atom has been calculated to be of the order of 25 percent of the incident atom energy. For a simple series of collisions with atmospheric molecules at rest, more than 20 collisions are required for a typical meteoric atom of 30 km/s initial velocity to "cool" to a velocity of 1.26 km/s (which corresponds to a 4000° K gas velocity). This simple cascade is a minimum case, as both a more realistic atomic scattering potential and collision-increased atmospheric-molecule velocity will decrease the most probable energy transfer to less than 25 percent of the incident atom energy. However, even the minimum number of collisions is sufficient for the velocity distribution to approach that of an equilibrium gas. In some cases, a Boltzmann distribution has been shown to be closely approached after only three collisions per particle (Kittel, 1958).

Some complication is introduced because the radiation that is photographed with a streak camera or spectrograph is a composite of the radiation from the series of collisions. That is, this radiation results initially from a few very high energy collisions, from many more collisions of moderate energy at a longer and later instant when the gas is approaching equilibrium, of many, many more collisions of moderately low energy at a still later time when the gas is very close to an equilibrium velocity distribution, and, finally, of still more collisions when the gas is practically in equilibrium, but still cooling and radiating as the meteor wake. This interpretation is in general agreement with radiation times and energy levels observed in wake and flare radiation (Harvey, 1971b).

It appears, from the time-integrated spectral measurements, that superposition of radiation from all of the radiation times results in a spectrum that is similar to that of a gas near equilibrium. This probably results from the initial collisions being too few and having too broad a spectrum (many energy levels can be excited) to dominate the radiation, and the later wake radiation being too energy-limited to dominate

TABLE 12.—*Element Ratios and "Derived Composition" of Perseid Meteor*

Element ratios (atomic)	Derived composition (percent by weight)
$\frac{Ca}{Fe}=3.9\times10^{-4}$	Fe—13
$\frac{Mn}{Fe}=4.9\times10^{-4}$	Ca—0.0037
$\frac{Cr}{Fe}=1.1\times10^{-3}$	Mn—0.0064
$\frac{Mg}{Fe}=0.68$	Cr—0.014
$\frac{Si}{Fe}=5.6$	Mg—3.9
$\frac{Na}{Fe}=5.2\times10^{-5}$	Si—36
	Na—0.00028
	O—45
	H—?

the spectrum. Thus, an intermediate case must dominate. The relatively few initial high energy collisions will tend to average the many inefficient low energy collisions to an intermediate case.

However, this does not mean that all meteor radiation is simple or straightforward. Resonance or nonequilibrium effects are observed in all detailed studies of radiation sources, be they flames, arcs, stellar atmospheres, or other sources. This obviously is the case with the strong ionic emissions in bright, fast meteors. This is evidenced by the absence of such radiation in faint meteors, and the absence of normally expected ionic lines. Several articles concerning *H* and *K* radiation are in the literature (Harvey, 1971b; Hoffman, 1971; Hoffman and Longmire, 1968; Rajchl, 1963). The observed Mg II and Si II radiation is even more anomalous because of its higher energy levels and the absence of many normally strong ion lines.

As significant as the general agreement in "effective radiation temperatures," shown in tables 5 to 8, is the fact that there is no identified neutral iron radiation that is not in general agreement with a Boltzmann distribution. The same is true of other neutral spectra where there are enough suitable lines to make a meaningful measurement. Thus, all of the neutral line radiation appears well behaved, the expected lines are present and are at the expected intensity, unexpected lines are not present.

We may conclude, then, that optical meteor radiation does not result from just the initial collisions of meteoric atoms with atmospheric molecules, but by a complete energy-cascade-via-collisions process. Since this involves at least tens to hundreds of collisions, it is basically a statistical process, and can be treated in terms of equilibrium distributions (over limited ranges) and deviations from equilibrium. The radiation can also be treated in terms of individual atomic cross sections but this requires even more detailed knowledge of the meteor conditions.

COMPOSITION

The measurement of composition need not be strongly dependent upon the assumption that the excited state populations are given by a Boltzmann distribution. The composition measurements require only that the meteor radiation processes of the relevant spectral lines be basically the same. That is, the population distribution of excited states of different atoms need to be similar. The distribution does not even need to be known very well, if the energy levels of the excited states chosen for measurement are close together.

If the meteoric excitation process is selective with respect to one atom over another, then problems may arise. However, since optical meteor excitation is basically collisional, that is, no radiative coupling occurs, it is unlikely that neutral radiation excitation is significantly selective in light of the consistency of the "effective radiation temperature measurements." Selectivity does, of course, show up in the ionic radiation and renders these lines unstable for abundance measurements. This need not prevent the use of neutral radiation for composition measurements.

Perhaps the most notable result of the measurement of the four meteors is that they are indicative of nickel-iron or stony meteorite composition. However, it should be noted that the sodium and calcium abundances are very low compared to cosmic or meteorite abundances. No effects such as neutral atom depletion by ionization, incomplete dissociation, or self absorp-

tion in the meteor plasma have been considered in these preliminary abundance values. Such effects will be considered in a subsequent paper.

The significant elements which have not been obtained from the analysis are oxygen, carbon, and hydrogen (silicon has already been discussed). Reasonable values for the abundances of oxygen can be obtained from those elements with which it is combined in meteorites. Carbon is not expected in major abundances, but is important for studies of meteorite origin and evolution. The best hope for measured carbon abundances is probably the very difficult one of measuring carbon band systems. Needless to say, observational difficulties for these measurements are extreme. A somewhat unexpected result is the strength of Hα in bright, fast meteor spectra. Little hydrogen would generally be expected after repeated passes of a meteoroid at distances of less than 1 AU from the Sun. Both the high energy level of the excited state and the low atomic weight (and hence low kinetic energy) are significant aspects of the hydrogen radiation which will require serious consideration.

CONCLUDING REMARKS

Four spectra, which are believed to be generally representative of the spectra of brighter meteors obtained by the Faint Meteor Spectra Patrol, have been reduced and analyzed. The neutral line radiation from these meteors was determined to be similar to that of a gas in equilibrium at a relatively low temperature. These results demonstrate that the powerful concept of local thermodynamic equilibrium can be fruitfully applied to meteor spectroscopy. In the past, poor quality of spectral data and the dominance of anomalous ionic radiation in much of the better spectra have served as deterrents to detailed quantitative analysis of meteor spectra. Thus, it is hoped that the present results will hasten the transition of meteor spectroscopy from primarily qualitative studies which have characterized it in the past to detailed quantitative studies which improved data now warrant.

The "derived composition" of the slow sporadic meteor appears to be generally similar to that of a typical nickel-iron meteorite. The "derived compositions" of the three shower meteors appear to be similar to and seem to indicate stony meteorite composition. These "derived compositions," although presently the most comprehensive direct data on meteor composition, are early results that are expected to be rapidly supplemented by additional data of even greater quality and quantity.

REFERENCES

Ayers, W. G., McCrosky, R. E., and Shao, C. -Y., 1970. Photographic observations of 10 artificial meteors, *Smithson. Astrophys. Obs. Spec. Rept.* No. 317, 1–40.

Ceplecha, Z., 1964. Study of a bright meteor flare by means of emission curve of growth, *Bull. Astron. Inst. Czech.*, **15**, 102–112.

——, 1965. Complete data on bright meteor 32281, B*ull. Astron. Inst. Czech.*, **16**, 88–101.

——, 1967. Spectroscopic analysis of iron meteoroid radiation, *Bull. Astron. Inst. Czech.*, **18**, 303–310.

Cook, A. F., Jacchia, L. G., and McCrosky, R. E., 1963. Luminous efficiency of iron and stone asteroidal meteors, *Smithson. Contrib. Astrophys.*, **7**, 209–220.

Corliss, C. H., 1962. Ionization in the plasma of a copper arc, *J. Res. Nat. Bur. Standards*, **66A**, 169–175.

Corliss, C. H., and Bozman, W. R., 1962. *Experimental transition probabilities for spectral lines of seventy elements*, NBS Monograph **53**, U.S. Dept. of Commerce, Washington.

D'Aiutolo, C. T., Kinard, W. H., and Nauman, R. J., 1967. Recent NASA meteoroid penetration results from satellites, *Smithson. Contrib. Astrophys.*, **11**, 239–251.

Elterman, L., 1964. Atmospheric attenuation model, 1964, in the ultraviolet, visible, and infrared regions for altitudes to 50 km, *U.S. Air Force Environ. Res. Papers* No. 46 (AFCRL–64–740), Sept. 1964, 1–40.

Griem, H. R., 1964. *Plasma Spectroscopy*, McGraw-Hill Book Co., New York, 580 pp.

GRYGAR, J., KOHOUTEK, L., AND PLAVCOVÁ, Z., 1968. Simultaneous radar and optical observation of meteors at Ondřejov in 1962, in *Physics and Dynamics of Meteors*, edited by L. Kresák and P. M. Millman, D. Reidel Publ. Co., Dordrecht, Holland, 63–69.

HALLIDAY, I., 1961. A study of spectral line identifications in Perseid meteor spectra, *Publ. Dominion Obs.*, **25**, 1–16.

——, 1969. A study of ultraviolet meteor spectra, *Publ. Dominion Obs.*, **25**, 315–322.

HARVEY, G. A., 1967a. Photometry of spectrograms of three artificial meteors, *NASA Tech. Note* **D-3930**, 1–30.

——, 1967b. A method of slitless absolute spectral photometry, *NASA Tech. Note* **D-3765**, 1–20.

——, 1970. Spectra of faint optical meteors, unpublished.

——, 1971a. The NASA LRC faint meteor spectra patrol, *NASA Tech. Note* **D-6298**, 1–25.

——, 1971b. The calcium *H*- and *K*-line anomaly in meteor spectra, *Astrophys. J.*, **165**, 669–671.

HOFFMAN, H. S., 1971. Ionic spectra of meteors, *Astrophys. J.*, **163**, 393–403.

HOFFMAN, H. S., AND LONGMIRE, M. S., 1968. Meteor ion spectra, *Nature*, **218**, 858–859.

JACCHIA, L. G., VERNIANI, F., AND BRIGGS, E., 1967. An analysis of the atmospheric trajectories of 413 precisely reduced photographic meteors, *Smithson. Contrib. Astrophys.*, **10**, 1–139.

KITTEL, C., 1958. *Elementary Statistical Physics*, J. Wiley and Sons, New York, 228 pp.

LINDBLAD, B. A., 1963. The relation between visual magnitudes and the durations of radar echoes, *Smithson. Contrib. Astrophys.*, **7**, 27–39.

MILLMAN, P. M., 1932. An analysis of meteor spectra, *Harvard College Obs. Ann.*, **82**, 113–146.

——, 1935. An analysis of meteor spectra: second paper, *Harvard College Obs. Ann.*, **82**, 149–177.

——, 1967. Some characteristics of the major meteor showers, *Smithson. Contrib. Astrophys.*, **11**, 105–108.

MOORE, C. E., 1945. A multiplet table of astrophysical interest, *Contrib. Princeton Univ. Obs*, No. 20.

RAJCHL, J., 1963. A short note on meteor spectra with low dispersion, *Smithson. Contrib. Astrophys.*, **7**, 155–156.

Page intentionally left blank

10. NASA–LRC Faint Meteor Spectra

GALE A. HARVEY
Langley Research Center, NASA
Hampton, Virginia

A brief description is given of the instrumentation, the facilities, and the patrol technique used by the NASA Langley Research Center Faint Meteor Spectra Patrol. A classification of 500 meteor spectra obtained in the first 2-½ years of the patrol is given. The general characteristics of "typical" spectra are discussed and preliminary conclusions drawn. Examples of unusual spectra are briefly described.

THE NASA LANGLEY RESEARCH CENTER (LRC) has established a meteor spectra patrol in the south-central part of New Mexico. This patrol, the NASA-LRC Faint Meteor Spectra Patrol, is operated by Smithsonian Astrophysical Observatory personnel under contract to LRC. The patrol direction, spectral data reduction, and analysis are performed at the Langley Research Center.

The primary spectrographs of the patrol are 15-cm aperture, $f/1.3$ Maksutov slitless spectrographs equipped with photomultiplier-actuated shutter systems. Twenty Maksutov spectrographs are assigned to the patrol. The first meteor spectrum was recorded on August 20, 1968. The patrol is now yielding spectra at the rate of several hundred per year.

The NASA-LRC Faint Meteor Spectra Patrol was initially established as part of the NASA meteoroid hazard research. The patrol was the primary data source for LRC meteor spectral studies. The primary objective of these studies was to relate the well determined luminous efficiency of low-velocity iron and nickel artificial meteors to natural meteors. However, by the time the patrol became operational, this had been done, on a statistical basis with the luminous efficiency study of iron and stone meteors by Cook, Jacchia, and McCrosky (1963), and the luminous-efficiency velocity-dependence study by Verniani (1967). At the same time, detailed understanding of meteor radiation processes was lacking, and the heterogeneous nature of the meteoroid environment was becoming more and more apparent (Grygar et al., 1968; Lindblad, 1963; Millman, 1967). Accordingly, the LRC meteor spectral studies were redirected toward study of meteor radiation and composition measurements.

The purpose of this paper is to describe briefly the NASA-LRC Faint Meteor Spectra Patrol and the first 500 spectra obtained by the patrol. Statistical conclusions are given and examples of meteor spectra are presented and discussed.

INSTRUMENTATION AND PATROL TECHNIQUE

The Langley Research Center developed fast, extended wavelength- range spectrographs (Harvey, 1967) to obtain spectra of the artificial meteors of the Meteor Simulation Program (Ayers et al., 1970). Subsequently, several models of Maksutov slitless spectrographs with high near-ultraviolet transmission have been fabricated for the Faint Meteor Spectra Patrol. The primary spectrographs of the Faint Meteor Spec-

tra Patrol are eleven 15-cm aperture, $f/1.3$ spectrographs with first-order inverse dispersions of 165 Å/mm, or 123 Å/mm. Nine other Maksutov spectrographs of different designs and with inverse dispersions of 450 and 1300 Å/mm are also assigned to the patrol. The circular field of view of most of the spectrographs is 21° in diameter.

Since very high-speed film (ASA~8000) is used in the spectrographs, continuous exposure of the spectrographs to the night sky requires a prohibitive amount of plate changing and film processing. To alleviate this problem, a photoelectric meteor detection-shutter system has been developed for the spectrographs. This shutter system effects a 2-s exposure when a meteor occurs in the field of view of the spectrograph. With the exception of an extreme sensitivity to lightning, the photoelectric shutter systems have proven efficient and well matched to the spectrographs.

Until December 1970, no ballistic data were available for sporadic meteors obtained by the patrol, and complete reductions were limited to major shower meteors. Since December 1970, a two-station ballistic system has been in operation, and it is expected that approximately 10 percent of the sporadic meteor spectra will have ballistic data after this time.

The Faint Meteor Spectra Patrol is operated on a routine nightly basis with highly skilled master observer Roy Proctor and observer Norbert Roth having alternate nights on. Special emphasis is placed on optimum operation during major meteor showers. The patrol is generally operated when cloud cover is less than 50 percent. A more complete description of the NASA-LRC Faint Meteor Spectra Patrol is given by Harvey (1971).

STATISTICS OF SPECTRA

Most of the spectra obtained by the Faint Meteor Spectra Patrol are in the brightness interval +1 to −3 absolute photographic meteor magnitude. This deduction was made by comparing these spectra with several absolutely reduced spectra, and from limited visual observations. The first meteor spectrum was obtained during the night of August 20, 1968. The 500th spectrum was obtained during the night of February 28, 1971. The most spectra obtained in one night, 26, were obtained on the night of December 13, 1969. Of the first 500 spectra, 345 have 1 to 9 spectral features, 86 have 10 to 19 features, 51 have 20 to 49 features, and 18 have more than 49 features. These groups correspond to Millman's d, c, b, and a class spectra respectively (Millman, 1963), and are based on examination with a visual comparator.

Typical examples of "d" spectra are shown in figure 1. Figure 1(a) is a reproduction of spectrum 374 and was recorded on an $f/0.83$, 150-mm aperture spectrograph of 500 Å/mm inverse dispersion. Figure 1(b) is a reproduction of spectrum 322 and was recorded on an $f/1.3$, 150-mm aperture spectrograph of 165 Å/mm inverse dispersion. This spectrograph was equipped with a rotating shutter which produced 20 occultations per second. The strongest features in these spectra are multiplets 4, 5, and 20 of neutral iron.

Typical examples of "c" spectra are shown in figure 2. Figure 2(a) is a reproduction of spectrum 454 and was recorded on an $f/0.83$, 150-mm aperture spectrograph of 500 Å/mm inverse dispersion. Figure 2(b) is a reproduction of spectrum 13 and was recorded on an $f/1.3$, 150-mm aperture spectrograph of 165 Å/mm inverse dispersion. Again, the strongest features in the spectra are multiplets 4, 5, and 20 of iron.

Typical examples of "b" spectra are shown in figure 3. Figure 3(a) is a reproduction of spectrum 244 and was recorded on an $f/1.3$, 150-mm aperture spectrograph of 165 Å/mm inverse dispersion. Although the green magnesium triplet and the sodium D lines are quite strong in this spectrum, multiplets 4, 5, and 20 are still the strongest features in the spectrum. Figure 3(b) is a reproduction of spectrum 246 and was recorded on an $f/1.3$, 150-mm aperture spectrograph of 123 Å/mm inverse dispersion. Forty-three features were counted by visual examination; however, a microdensitometer tracing would easily allow more than 50 features to be identified. Although the sodium D lines are strong, multiplets, 4, 5, and 20 of iron are again the strongest features.

Typical examples of "a" spectra are shown in figure 4. Figure 4(a) is a reproduction of spec-

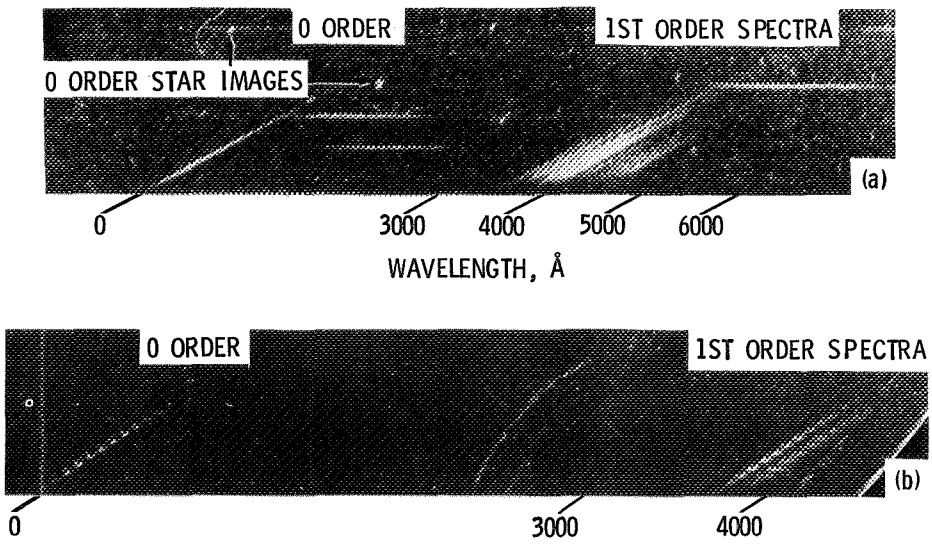

FIGURE 1.—Meteor spectra with one to nine features ("d" spectra). (a) Spectrum No. 374. (b) Spectrum No. 322.

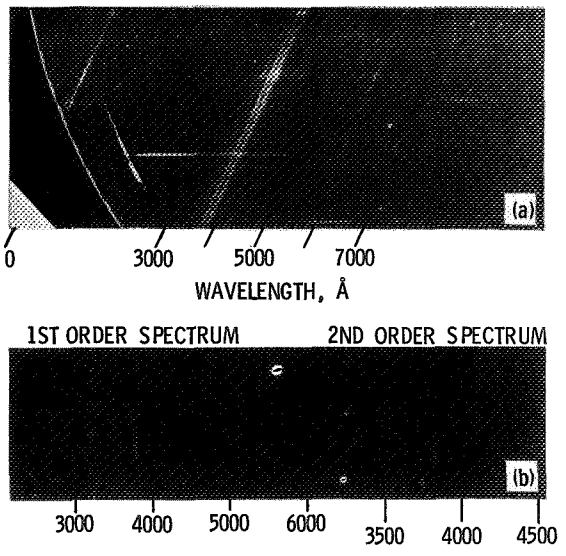

FIGURE 2.—Meteor spectra with 10 to 19 features ("c" spectra). (a) Spectrum No. 454. (b) Spectrum No. 13.

trum 166 and was recorded on an $f/1.3$, 150-mm aperture spectrograph of 123 Å/mm inverse dispersion. This spectrum is of a Geminid meteor and has been analyzed in a companion paper (Harvey, 1972). Multiplets 4, 5, and 20 of iron are again the strongest features in the spectrum. Figure 4(b) is a reproduction of spectrum 67(a) and was recorded on an $f/1.3$, 150-mm aperture spectrograph of 123 Å/mm inverse dispersion. This spectrum is of a Perseid meteor. The strongest lines are from multiplet 1 of ionized calcium, multiplets 4, 5, and 20 of iron, and the sodium D lines.

In figures 1 to 4, multiplets 4, 5, and 20 of neutral iron are the dominant radiation in most of the spectra. Of the first 500 meteor spectra from the Faint Meteor Spectra Patrol, approximately 60 percent have multiplets 4, 5, and 20 of iron as the dominant radiation and hence are Millman's (1963) type Z spectra. Twenty-five percent of the spectra have magnesium or sodium as the strongest radiation and thus are type X spectra, while 8 percent have neutral calcium or oxygen as the strongest radiation, and 7 percent are of indeterminant class. Only about 2 percent of the spectra have the H and K lines of calcium as the strongest radiation and hence are type Y spectra. One to 2 percent of the first group are nearly pure iron spectra, expected of nickel-iron type meteoroids. As will be discussed later, a small percentage of the second group are essentially iron-free spectra. Except for these iron-rich and iron-poor spectra, both of the first two groups are generally consistent with compositions similar to typical stony meteorites.

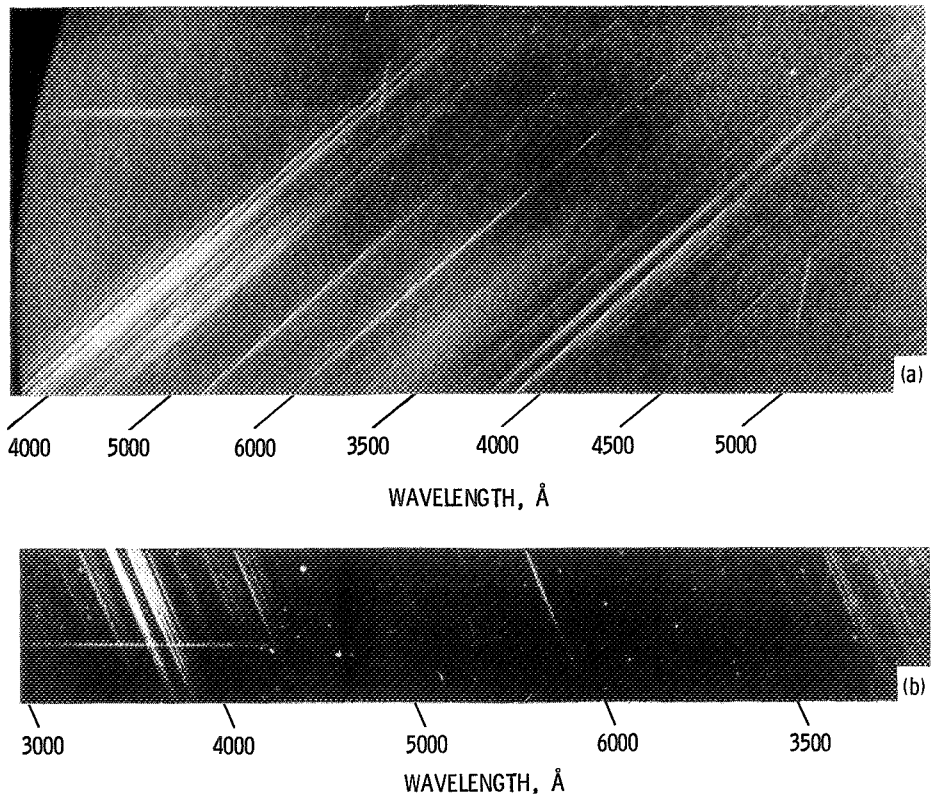

FIGURE 3.—Meteor spectra with 20 to 49 features ("b" spectra). (a) Spectrum No. 244. (b) Spectrum No. 246.

These statistics of meteor radiation are important observational results, because they offer strong support for the most vulnerable assumptions used in the optical meteor mass determinations. These assumptions are that the iron in slow meteors is the dominant radiator in the Super-Schmidt blue region of the spectrum, and that most meteors are of composition similar to typical stony meteorites. Thus, the photometric meteor mass determinations are statistically valid. However, this does not mean that all individual photometric meteor mass determinations are accurate.

NONREPRESENTATIVE SPECTRA

As seen in the previous section, iron is the dominant radiation species in most faint meteor spectra. However, iron deficient spectra have been obtained. Examples of extremely iron-deficient or iron-free meteors are shown in figure 5. Figure 5(a) is reproduced from spectrum 401 and was recorded on an $f/1.3$, 150-mm aperture spectrograph of 123 Å/mm inverse dispersion. Figure 5(b) is reproduced from spectrum 299 and was recorded on a similar spectrograph. The strongest feature in these spectra is the multiplet 3 of neutral magnesium. The other strong lines are multiplet 1 of ionized calcium, multiplet 2 of neutral calcium, and multiplet 2 of neutral magnesium. Multiplets 4 and 5 of iron are present, but very weak. Two similar spectra were among 39 prismatic spectra obtained from Super-Schmidt spectral patrols in 1966 to 1968. These were two of the better spectra, and at that time it was thought that this type of meteor might be fairly common. However, on the basis of classification of 500 spectra, only about 1 percent of all meteors have this type of spectrum.

A similar type of spectrum is shown in figure

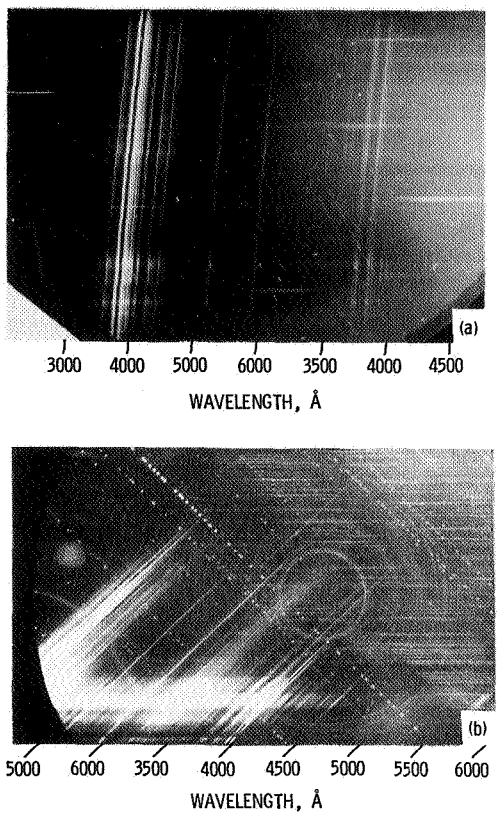

FIGURE 4.—Meteor spectra with more than 49 features ("a" spectra). (a) Spectrum No. 166. (b) Spectrum No. 67a.

6. Figure 6(a) is reproduced from spectrum 228 and figure 6(b) is reproduced from spectrum 95. Both are 123 Å/mm inverse dispersion spectra. They are two-line spectra with multiplet 3 of neutral magnesium being strong and multiplet 2 of neutral calcium being weak. They appear to be slow meteors of similar composition to the meteors of 5(a) and 5(b). About 1 percent of the spectra are of this type.

On several meteor spectra, what appears to be a persistent feature near 3840 Å has been observed. It is shown in figure 7. This radiation is present at the bottom of the first-order spectrum in figure 7(a) and most strongly at the top of the second-order spectrum in figure 7(b). The abrupt beginning of the meteor is due to the opening of the shutter. The persistence of the 3840 Å feature is denoted by its higher position along the trailed spectrum. This radiation appears to be present in several percent of the spectra. It is suspected that this feature is band radiation because it seems to occur in low dispersion spectra more often than in high dispersion spectra. It seems that in many meteor spectra, this is the strongest initial feature which fades as the usual iron and magnesium lines intensify. This radiation is difficult to analyze because it is in the region of multiplets 4 and 20 of neutral iron and 3 of neutral magnesium. Halliday

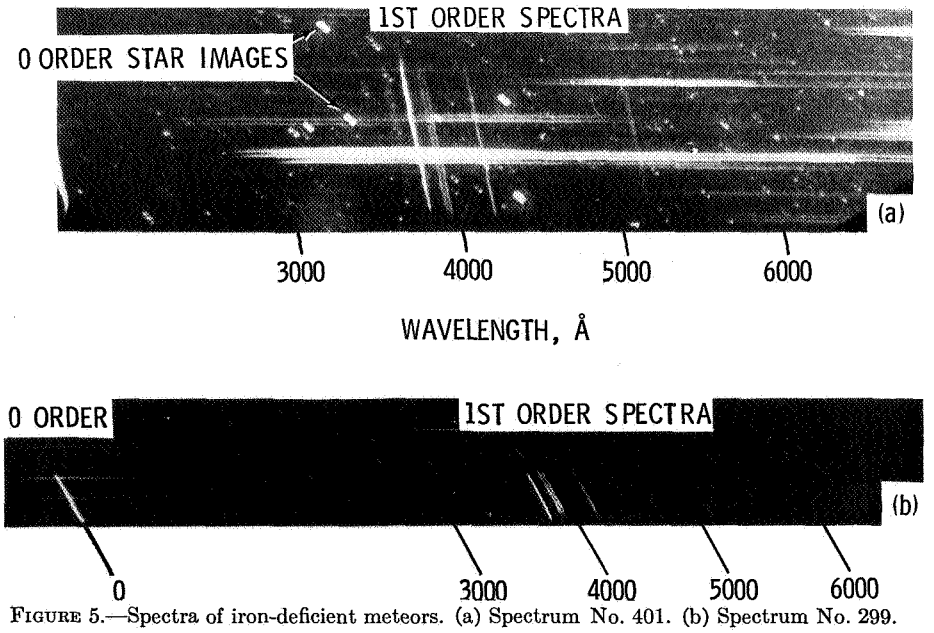

FIGURE 5.—Spectra of iron-deficient meteors. (a) Spectrum No. 401. (b) Spectrum No. 299.

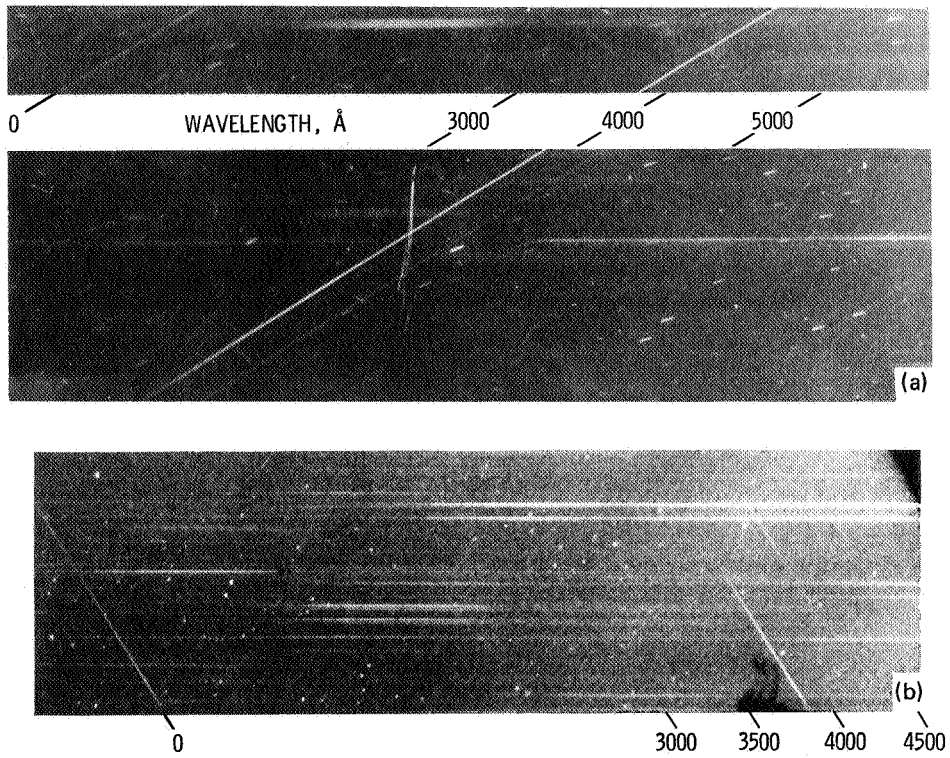

FIGURE 6.—Spectra of iron-deficient meteors. (a) Spectrum 228. (b) Spectrum No. 95.

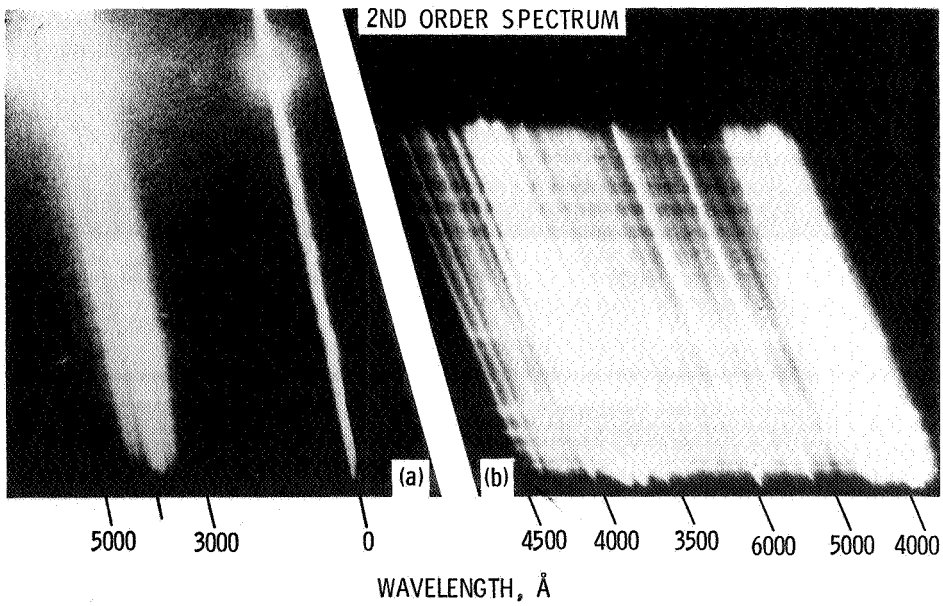

FIGURE 7.—Meteor spectra with persistent UV radiation. (a) Spectrum No. 24. (b) Spectrum No. 251.

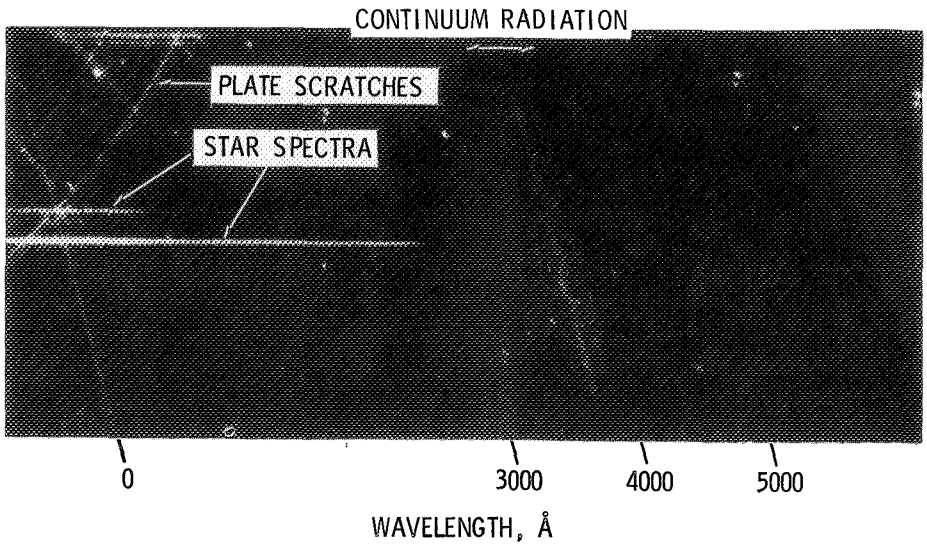

FIGURE 8.—Spectrum of faint, continuum radiation meteor (Spectrum No. 6).

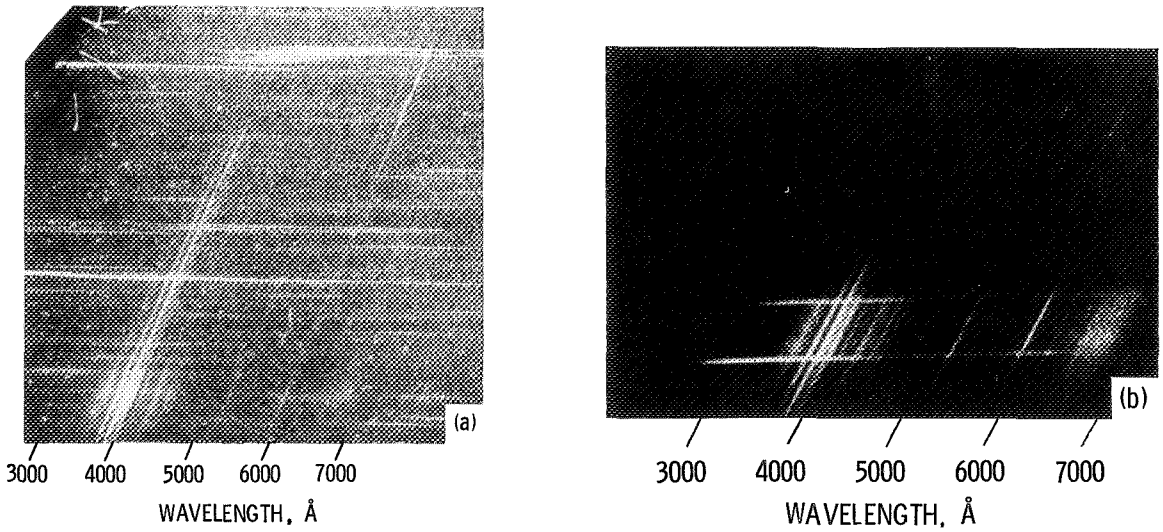

FIGURE 9.—Spectra of faint Perseid and Leonid meteors. (a) Spectrum No. 56, Perseid meteor. (b) Spectrum No. 8, Leonid meteor.

(1969) discusses a similar, if not the same, feature in his UV Lyrid spectrum.

Almost all of the radiation of the 500 meteors recorded by the patrol is atomic line radiation. The most general exception is a low level of unresolved radiation in the 6000 Å to 7000 Å region. However, one meteor was recorded in which no atomic line radiation appears. This spectrum is shown in figure 8. This figure is reproduced from spectrum 6 and was recorded on an $f/0.83$, 150-mm aperture spectrograph of 500 Å/mm inverse dispersion. The faint continuum extends from 3600 Å to 4000 Å, with a stronger feature near 3800 Å. This is the only spectrum of this type obtained by the patrol to date.

Fast, bright meteors are characterized by extreme dominance of the radiation from multiplet 1 of ionized calcium, multiplet 4 of ionized magnesium, and multiplet 2 of ionized silicon. Figure 9 shows spectra of faint Perseid and Leonid meteors in which the ionic radiation is absent, or at low levels relative to the neutral spectrum. The low strength of ionic radiation relative to neutral radiation, and the virtual absence of other multiplets of ionized calcium, magnesium, and silicon confirm that the observed ionic radiation in bright, fast meteors is anomalous.

Sodium abundances may be indicative of lifetimes and origins of meteoroids. The two spectra shown in figure 10 are indicative of the range of sodium abundances in meteoroids. Figure 10(a) is reproduced from spectrum 430. Figure 10(b) is reproduced from spectrum 432. The spectra were obtained on the same $f/1.3$, 150-mm aperture spectrograph of 123 Å/mm inverse dispersion on consecutive nights. In figure 10(a) sodium is the dominant radiating element, in figure 10(b) no sodium radiation is recorded. Both spectra have more than 50 features as determined from an examination with a visual comparator.

Preliminary conclusions which can be drawn from the NASA-LRC Faint Meteor Spectra are:

(1) Approximately 60 percent of optical meteors have similar spectra in which multiplets 4, 5, and 20 of iron are the dominant radiation. Thus, the optical meteor mass determinations, that are based on the assumption that the predominant radiation from slow meteors in the blue region of the spectrum is iron radiation, are statistically valid.

(2) A small percentage of meteoroids are essentially iron free.

(3) Persistent radiation near 3840 Å occurs in faint meteors.

(4) A few (<0.5 percent) faint meteors are not predominantly atomic line radiators.

(5) Ionic radiation in bright, fast meteors is anomalous.

(6) Sodium abundances in meteors vary widely.

ACKNOWLEDGMENTS

The author wishes to acknowledge the contribution of the patrol personnel; Roy Proctor, master observer and station manager, and Norbert Roth, observer. Their skill and dedication in implementing and operating a new observing system in a different mode of operation are responsible in large measure for the results of the subject patrol.

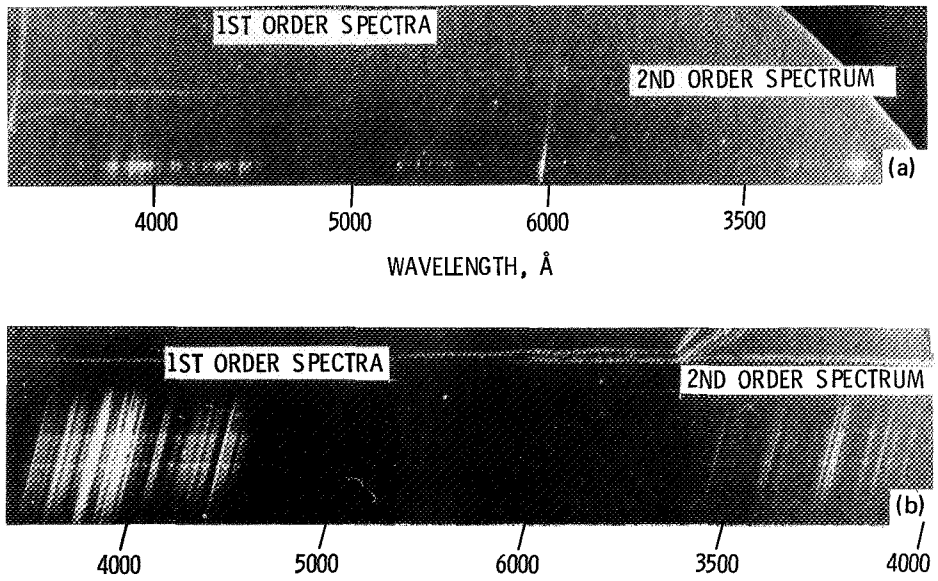

FIGURE 10.—Spectra of sodium rich and sodium-deficient meteors. (a) Spectrum No. 430, sodium-rich meteor. (b) Spectrum No. 432, sodium-deficient meteor.

REFERENCES

AYERS, W. G., MCCROSKY, R. E., AND SHAO, C. -Y., 1970. Photographic observations of 10 artificial meteors, *Smithson. Astrophys. Obs. Spec. Rept.*, No. 317, 1–40.

COOK, A. F., JACCHIA, L. G., AND MCCROSKY, R. E., 1963. Luminous efficiency of iron and stone asteroidal meteors, *Smithson. Contrib. Astrophys.*, **7**, 209–220.

GRYGAR, J., KOHOUTEK, L., AND PLAVCOVÁ, Z., 1968. Simultaneous radar and optical observations of meteors at Ondřejov in 1962, in *Physics and Dynamics of Meteors*, edited by Ľ. Kresák and P. M. Millman, D. Reidel Publ. Co., Dordrecht, Holland, 63–69.

HALLIDAY, I., 1969. A study of ultraviolet meteor spectra, *Publ. Dominion Obs.*, **25**, 315–322.

HARVEY, G. A., 1967. A description of four fast slitless spectrographs, *NASA Tech. Note* **D–4145**, 1–38.

——, 1971. The NASA LRC faint meteor spectra patrol, *NASA Tech. Note* **D–6298**, 1–25.

——, 1972. Spectral analysis of four meteors, see Paper No. 9, this volume.

LINDBLAD, B. A., 1963. The relation between visual magnitudes and the durations of radar echoes, *Smithson. Contrib. Astrophys.*, **7**, 27–39.

MILLMAN, P. M., 1963. A general survey of meteor spectra, *Smithson. Contrib. Astrophys.*, **7**, 119–127.

——, 1967. Some characteristics of the major meteor showers, *Smithson. Contrib. Astrophys.*, **11**, 105–108.

VERNIANI, F., 1967. Meteor masses and luminosity, *Smithson. Contrib. Astrophys.*, **10**, 181–195.

Page intentionally left blank

11. The Auroral Green Line in Perseid Spectra Near Sunspot Maximum

JOHN A. RUSSELL
University of Southern California
Los Angeles, California

Thirty-one spectra photographed during the Perseid showers of 1969 and 1970 are found to exhibit greater ionization and stronger, more frequent appearance of the forbidden oxygen line at 5577 Å than Perseid spectra obtained with the same instrument in 1961. Data from 13 Perseid showers indicate a relationship between the frequency of occurrence of the oxygen line and solar activity. In 1969–70, near sunspot maximum, the strength of this so-called auroral green line is greatest near shower maximum, as though the nature of the meteoroids were a function of their distance from the core of the stream, or, alternatively, the strength of the green line were a function of the altitude of the radiant.

SINCE 1948, A SPECTROGRAPHIC STUDY of the annual Perseid meteors has been conducted by the University of Southern California, generally at an observing site in the Sierra-Nevada range in northern California (Russell, 1959). An earlier summary of the results of this project showed the shower of 1961, during which 10 spectra were obtained with one prism spectrograph, to be the most productive of spectra of any shower observed by U.S.C. through 1963 (Russell, 1964). In 1969 and 1970, 31 spectra were recorded with the same instrument used in 1961. The distribution in time of the spectra from the 1969 shower has already been discussed (Russell, 1969). In this paper the spectral features will be considered.

The spectra from the 1961 shower were classified into four groups on the basis of the presence of certain spectral lines as follows:

Group 1—The *H* and *K* lines of ionized calcium

Group 2—The magnesium triplet at 5175 Å, the auroral green line of neutral oxygen at 5577 Å, the *D* line of sodium, and a calcium-iron blend near 6170 Å

Group 3—Only the *D* line of sodium and the blend at 6170 Å

Group 4—Only the *D* line of sodium

In 1961 these four categories sufficed, as the green line was present in or absent from all spectra in a given category. For the spectra of 1969 and 1970 this was not the case, and all groups except number four were bifurcated, a prime following the group number indicating the presence of 5577 Å. The results are shown in table 1. It will be noted that in 1969 and 1970, compared to 1961:

(a) The *H* and *K* lines appeared almost four times as often.

(b) Lone occurrences of the *D* line were $\frac{1}{12}$ as frequent.

(c) The green line appeared with nearly twice the frequency.

It is clearly evident from item (a) that the level of ionization of calcium was higher in the

TABLE 1.—*Number of Spectra in Defined Groups for 3 Perseid Showers*

Group	1	1′	2	2′	3	3′	4	Total	Percent with *H* and *K*	Percent with *D* only	Percent with 5577 Å
1961	0	1	0	2	3	0	4	10	10	40	30
1969	3	4	1	4	5	4	0	21	33	0	57
1970	2	2	0	3	1	1	1	10	40	10	60

1969–70 spectra than in those of 1961. Item (b) indicates indirectly that the same was true for silicon. The observation in 1969–70 of only one questionable spectrum in group 4 may be attributed to the nearly equal densities of the *D* line and the blend at 6170 Å, whereas in 1961 the *D* line was distinctly the stronger of the two, and in very faint spectra could be seen alone. Compare figures 1 (a) and (b). The two features were also closer together in 1961 as indicated in table 2.

The blend to the red of the *D* line in the 1961 spectra was attributed principally to neutral calcium. Figure 1(c) shows the one 1969 spectrum, recorded at the plate edge where the focus is better in the red, in which the feature is resolved into what are probably the calcium blend at 6170 Å and the SiII doublet at 6360 Å. The increased strength and greater wavelength of this blend in 1969–70 may be attributed to a stronger SiII component. This interpretation is supported by the observation of Hirose and his co-workers (1968) that where the plate sensitivity is favorable, the SiII lines are the strongest lines to be found in Perseid spectra. It is interesting to note that this near equality in the density of the *D* line and the red blend is so consistent in the 1969–70 Perseid spectra that the meteor in figure 1(d), whose path missed the Perseid radiant by 8°, was easily judged to be sporadic because of the additional evidence provided by the weakness of the red blend.

The added strength of the SiII feature appears unrelated to plate sensitivity. The same emulsion was used all three years, and no difference in the location of the red cutoff could be observed by comparing spectra of the same stars recorded in 1961 and in 1969–70. As the SiII component in the resolved 1969 spectrum in figure 1(c) is stronger than the calcium component, the lower photographic density in 1961, the result of less efficient development, would suppress the calcium component and make the blend farther from the *D* line than in 1969. The reverse of this is observed. Hence the increased strength of SiII in 1969–70 is believed to be real.

Millman, Cook, and Hemenway (1971) using an image orthicon tube in place of a photographic emulsion, observed the auroral green line in all 14 of the 1969 Perseid spectra studied. With our more conventional techniques, the line at 5577 Å is totally absent from some spectra whereas in others it is the most prominent feature. The irregularities of appearance of the green line have been well covered. Halliday (1960) was the first to suggest that the velocity of the meteor and the extent of solar activity were likely contributing factors. Velocity differences cannot be invoked to explain differences in spectra from the same shower, but there is evidence in these data that the sunspot cycle is involved. In figure 2, the percentage of spectra showing the green line is plotted for 13 Perseid showers from 1948 through 1970. The 13 points are joined by the dashed line. Through each point is a vertical line, the length of which is inversely proportional to the square root of the number of spectra represented by the point. The longest lines indicate single spectra; the shortest line, 21 spectra. Average daily sunspot numbers, plotted by the year, are joined by the solid line. If the numbers on the percentage scale are multiplied by two, they serve as sunspot numbers. Despite the absence of data for several showers, the correlation is clearly evident.

Lindblad (1968) found several meteor parameters to be correlated with solar activity, explaining the correlation as the result of the Earth's atmosphere, at the critical height, having a maximum density at solar minimum and vice

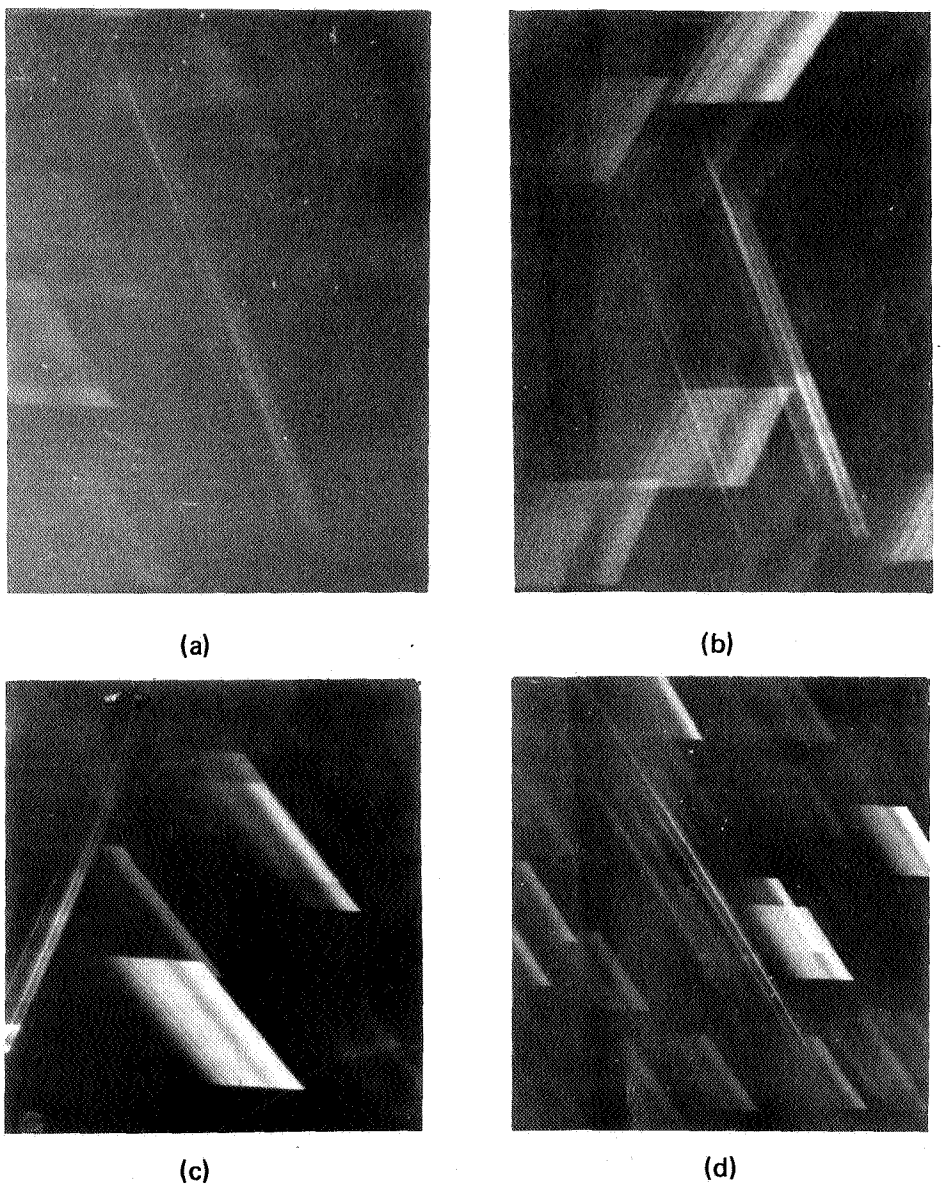

FIGURE 1.—The *D* line of sodium is the marked line. Violet is to the left throughout. (a) 1961 Perseid spectrum showing strong *D* line. (b) 1969 Perseid spectrum showing the *D* line and blend at 6170 Å of nearly equal density. (c) 1969 Perseid spectrum showing resolution of the blend to the red of the *D* line. (d) Sporadic spectrum showing very weak radiation to the red of the *D* line.

versa. Increased ionization and green line strength in Perseids near sunspot maximum may both be fostered by this density effect. It is well known that ionized lines are enhanced in the spectra of giant stars whose atmospheres are of lower density than those of stars on the main sequence. The low density may also favor the oxygen atom's remaining in the excited state until the forbidden line is emitted.

The appearances of the auroral green line in figure 2 were recorded without taking account of the strength of the line. In figure 3, the relative

TABLE 2.—*Linear Separation of the* D *Line and the Feature to the Red thereof for Different Years*

Year	Separation (cm)	Probable error (cm)
1961	0.0234	±0.00076
1969	0.0264	±0.00030
1970	0.0257	±0.00062

density of the line, on a scale of 5, is plotted against the time of appearance for the spectra of 1961, 1969, and 1970, using circles, dots, and triangles respectively. The ordinates are defined as follows:

0. No oxygen green line observable
1. Green line present but very faint
2. Green line easily seen but well below *D* line density
3. Green line approximately as dense as the *D* line
4. Green line is the densest feature in the spectrum.

The consistent strength of the oxygen line on the night of 1969 August 11–12 until 1^h PST is not likely a statistical fluctuation. The line was generally weak the balance of the night as well as on the previous and following nights. The single strong oxygen line observed on the night of 1969 August 10–11 is in the spectrum of a sporadic meteor, another example of the consistently similar appearance of Perseid spectra compared to those of sporadic meteors.

The *Monthly Bulletin of the American Association of Variable Star Observers* for August 1969, shows sunspot activity in a state of decline during the shower and quite unrelated to the behavior of the green line. The planetary magnetic 3-hr range indices of the International Union of Geodesy and Geophysics, published by the Institut für Geophysik in Göttingen, Germany, look more promising. The night of August 11–12 activity was consistently three times what it was the previous night and twice what it was on the following night. However, unless rapid and significant variations in geomagnetic activity are masked by the three-hour means, solar activity provides no explanation for the strong green line August 10–11, for the sudden change in the

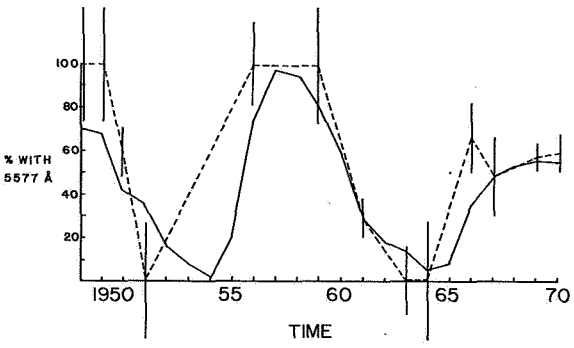

FIGURE 2.—Percentage of spectra from each of 13 Perseid showers showing the forbidden oxygen line at 5577 Å. The solid line delineates sunspot numbers for the same period.

middle of the second night, or for the presence in a weak Perseid spectrum of the green line with greater intensity than it possessed in a stronger spectrum obtained four minutes later on the same film. Moreover, the magnetic range indices seem uncorrelated with the green line activity in 1970!

Figure 3 indicates that all of the green lines in Perseid spectra with strength rated 3 or 4 appeared on the night of maximum both in 1969 and in 1970. If the strength of the green line is in any way related to the position of the Earth in the meteor stream, the peak of green line activity would be expected about 6 hr later from year to year. Maximum in 1969 occurred about 11 p.m. PST on August 11. In 1970 it occurred about 5 a.m. PST August 12. In 1969 the green line activity was clearly on the decline during the night, whereas in 1970 it was increasing, as one would expect if the position of the Earth in the stream were a factor. Also, the three green line spectra of 1961 behave much like those of 1969, as they should, since two 4-yr calendrical cycles intervene, resulting in maxima on the same day and nearly the same hour.

Variations in the density of meteoroids in the same or different streams have been discussed by Ceplecha (1967), Jacchia (1963), Kresák (1968), Russell (1964), and Verniani (1967), but I am aware of no evidence of variations in a given stream that are a function of distance from the stream center.

Millman (1968) points out that when a shower

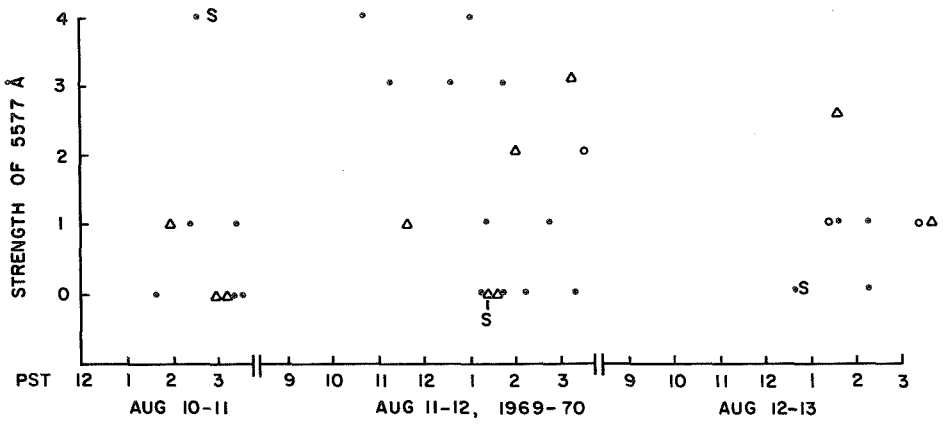

FIGURE 3.—Strength of the forbidden oxygen line relative to the sodium *D* line. Spectra from 1961, 1969, 1970 are plotted as circles, dots, and triangles, respectively. Sporadic spectra are marked *S*.

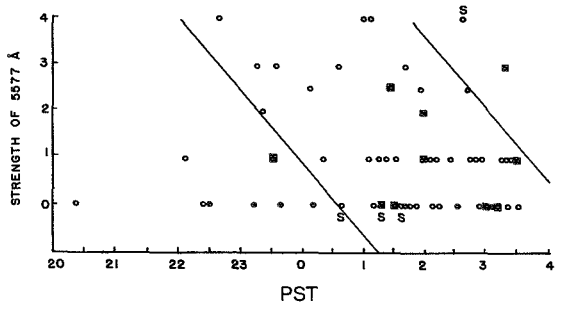

FIGURE 4.—Green-line strength as a function of local time for the Perseid showers in figure 2. The 1970 data are shown as squares. See text for other details.

radiant is at low elevation, bright meteors observed by radar may have a range spread of over 100 km, as they remain in the meteor echo height zone for several seconds. This suggests, as an alternative explanation for the concentration of strong green lines in 1969, that a low radiant could likewise allow a meteor to remain in the green-line producing zone for a longer period. During the Perseid shower, the radiant is rising throughout the hours of darkness, the value of cosec Z at 21^h being about twice what it is at midnight and three times its value at $2^h\ 30^m$. Thus the strong green lines in 1969 were occurring when the radiant was lowest as well as at shower maximum, since the two events were nearly simultaneous.

Figure 4 shows the green line data for all showers included in figure 2 in which at least one green line appearance was noted, plotted against the PST of appearance of the meteor. The 1970 data are plotted as squares, while 1961 spectra in groups 3 and 4 are plotted as filled circles. Sporadics are marked *S*. The decline in green line strength after shower maximum, or with decreasing zenith distance, in 1969 and the increase toward shower maximum in 1970 are muddied by the inclusion of all of the data. If one is willing to eliminate sporadic meteors, meteors observed in 1970, the single-line group 4 meteors of 1961, a spectrum consisting of only the *H* and *K* lines in terminal burst, and a meteor that was barely in the camera field, only the meteor plotted at $22^h\ 25^m$ lies outside the arbitrarily drawn diagonal lines, and those remaining within indicate a tendency for green line strength to decline with increase in the altitude of the radiant during the night. The contrary behavior of the 1970 data may be related to an effect noted by Hajduk (1968) who showed that whereas for Orionids, long duration echoes decrease in frequency with decreasing zenith distance of the radiant, for Geminids the reverse is true. Possibly an anomalous variation in 1970 of the height of the layer producing the green line resulted in the same type of reversal that Hajduk observed for different showers in a layer presumed to be at a fixed altitude.

It is a pleasure to acknowledge the contribution of Cecelia L. Snyder to the reduction of the 1970 data.

REFERENCES

CEPLECHA, Z., 1967. Classification of meteor orbits, *Smithson. Contrib. Astrophys.*, **11**, 35–60.

HAJDUK, A., 1968. Factors affecting radar-meteor echo durations, in *Physics and Dynamics of Meteors*, edited by Ľ. Kresák and P. M. Millman, D. Reidel Publ. Co., Dordrecht, Holland, 45–49.

HALLIDAY, I., 1960. Auroral green line in meteor wakes, *Astrophys. J.*, **131**, 25–33.

HIROSE, H., NAGASAWA, K., AND TOMITA, K., 1968. Spectral studies of meteors at the Tokyo Astronomical Observatory, in *Physics and Dynamics of Meteors*, edited by Ľ. Kresák and P. M. Millman, D. Reidel Publ. Co., Dordrecht, Holland, 105–118.

JACCHIA, L. G., 1963. Meteors, meteorites and comets: Interrelations, in *The Moon, Meteorites and Comets*, edited by B. M. Middlehurst and G. P. Kuiper, Univ. of Chicago Press, 774–798.

KRESÁK, Ľ., 1968. The relations between orbits and physical characteristics of meteors, in *Physics and Dynamics of Meteors*, edited by Ľ. Kresák and P. M. Millman, D. Reidel Publ. Co., Dordrecht, Holland, 217–235.

LINDBLAD, B. -A., 1968. Long-term variations in meteor radar rates, meteor heights and radar-echo amplitudes, in *Physics and Dynamics of Meteors*, edited by Ľ. Kresák and P. M. Millman, D. Reidel Publ. Co., Dordrecht, Holland, 50–62.

MILLMAN, P. M., 1968. The radar meteor echo, in *Physics and Dynamics of Meteors*, edited by Ľ. Kresák and P. M. Millman, D. Reidel Publ. Co., Dordrecht, Holland, 3–13.

MILLMAN, P. M., COOK, A. F., AND HEMENWAY, C. L., 1971. Spectroscopy of Perseid meteors with an image orthicon, *Can. J. Phys.*, **49**, 1365–1373.

Russell, J. A., 1959. Some Perseid meteor spectra of the past decade, *Sky Telesc.*, **18**, 549–551.

——, 1964. The spectra of faint Perseids, *Meteoritics*, **2**, 117–125.

——, 1969. Perseid meteor spectra photographed in 1969, *Sky Telesc.*, **38**, 424–425.

VERNIANI, F., 1967. Meteor masses and luminosity, *Smithson. Contrib. Astrophys.*, **10**, 181–195.

12. Image-Orthicon Spectra of Geminids in 1969

P. M. MILLMAN
National Research Council of Canada
Ottawa, Ontario

A. F. COOK
Smithsonian Astrophysical Observatory
Cambridge, Massachusetts

AND

C. L. HEMENWAY
State University of New York at Albany and Dudley Observatory
Albany, New York

The spectra of 25 meteors, recorded with an image-orthicon technique in December 1969, are studied in relation to similar records made in August of the same year. Of 19 Geminid meteors in the absolute visual magnitude range 0 to +2, only one showed any evidence of the forbidden line of oxygen at 5577 Å, while all Perseid meteors recorded in August exhibited the oxygen line, a result of the large difference in geocentric velocity between the two showers. Atoms identified in faint Geminid meteors include neutral iron, magnesium, calcium and sodium. The molecular bands of nitrogen are also observed.

THE PROGRAM OF IMAGE-ORTHICON METEOR SPECTROSCOPY, operated at the Springhill Meteor Observatory (lat 45°12′ N, long. 75°28′ W, elev 101.5 m) in conjunction with meteor radar, photographic and visual programs, was commenced in August 1969. A report on the 1969 Perseid meteors observed by the image-orthicon technique was made by Millman, Cook, and Hemenway (1971). This present paper gives some preliminary results from observations of the Geminid meteor shower, made in December 1969. The observing equipment used has been described previously by Hemenway, Swider and Bowman (1971).

OBSERVATIONAL DATA

The combined observational program was carried out at Springhill on two nights, December 12/13 and 13/14, 1969. In 7^h41^m observing time with the image-orthicon equipment some 41 meteors were recorded. Of these records 16 were unsuitable for detailed study, showing only one feature or being too faint for analysis. The remaining 25 orthicon spectra were divided into four groups on the basis of the detail shown and apparent shower affiliation.

Observational parameters for the 25 meteors studied are listed in table 1. An identifying serial number was assigned in chronological order to all 41 orthicon records and these numbers appear in the first column. The next four columns list the Universal Time of each meteor by day, hour, minute and second respectively. The type of radar echo recorded on the range-time display of the high-power (3 MW) equipment at Springhill is listed in the original terminology

TABLE 1.—*Observational Parameters for 25 Meteors, December 1969*

Serial no.	Universal time d	h	m	s	Radar echo type	Radar echo duration (s)	Orthicon record Motion (frames)	Orthicon record Duration (frames)	Height Begin (km)	Height End (km)	Spectrum features	Apparent visual magnitude
Group I (Geminids)												
13	13	09	55	10	Ahe2	27	8	11	95	78	16	
1	13	05	05	18	E3	49	7	14	93	77	14	2
18	13	10	29	13	Ahe3	42	5	>14	(95)	78	14	
3	13	05	19	01	(F)	(22)	11	19	(95)	87	13	0 (tr 1s)
41	14	11	00	06	Af	20	6	9	93	80	12	
6	13	06	00	10	F	19	4	2	(102)	95	12	1½
16	13	10	14	14	Af	21	6	5	93	79	10	
37	14	10	24	45	Af	18	7	12	92	79	10	
Group II (Geminids)												
32	14	09	35	21	Af	29	>5	>7	92	(77)	8	
17	13	10	22	07	Ahe2	32	6	7	(103)	(76)	7	
21	13	11	04	43	Ahf	1.8	5	3	82	73	6	
29	14	09	26	11	Ahf	1.3	4	(15)	107	94	[a]6	
28	14	09	18	11	Ahf	17	3	4	90	83	5	
34	14	09	55	07	Ahe2	17	2	2	95	84	5	
Group III (Geminids)												
36	14	10	10	58	Ahf	14	2	2	93	84	4	
38	14	10	27	27	Af	12	2	8	92	82	3	
33	14	09	37	31	Ah	0.2	2	6	(93)	87	3	
23	14	08	18	52	Dhbe2	29	2	0	92	82	3	
26	14	08	48	49	Ahe2	13	4	2	96	91	2	
Group IV (Non-shower)												
9	13	08	04	57	—	—	0	(17)	—	—	[a]7	3
27	14	09	17	23	Af	12	6	5	97	88	7	
24	14	08	39	55	E2	1.0	>5	>5	92	(76)	>5	
30	14	09	28	36	F	21	2	7	95	(90)	6	
8	13	06	07	27	F	14	2	0	90	87	2	1½
2	13	05	18	09	—	—	3	0	—	—	2	3

[a] Showing 5577 Å of O I.

developed by McKinley and Millman (1949), followed by the maximum duration of the echo on this radar. For meteor 9 there was no radar echo and for meteors 2 and 3 the high-power radar was off for a film change. Meteor 3 was recorded on the low-power (20 kw) equipment and the observed duration, indicated by brackets, must be multiplied by an empirical factor of 1.65 to convert to high-power duration.

The image-orthicon record frames were recorded at a frequency of 15/s. In columns 8 and 9 the duration of observed motion of the meteor image, and the maximum observed duration for the brightest feature in the spectrum, are recorded in units of frames. The field covered by the image orthicon was centered at an elevation of 45° and due east, true azimuth 090°. Using the zero-order star images as calibration points the elevation and azimuth were read off for the beginning and end of each meteor trail. These

were then combined with the radar ranges to give the tabulated heights. It should be noted that the heights given in table 1 were determined without the assistance of photographic records which were available in the case of some heights listed previously for the Perseids. Individual values of Geminid heights could have errors of 2 or 3 km, or more in uncertain cases. Where the height is somewhat uncertain due to incompleteness of data the number is given in brackets. In the last two columns are listed the number of different spectral features observed and the visual magnitudes. It is unfortunate that there was not more of an overlap between the visual and the orthicon records.

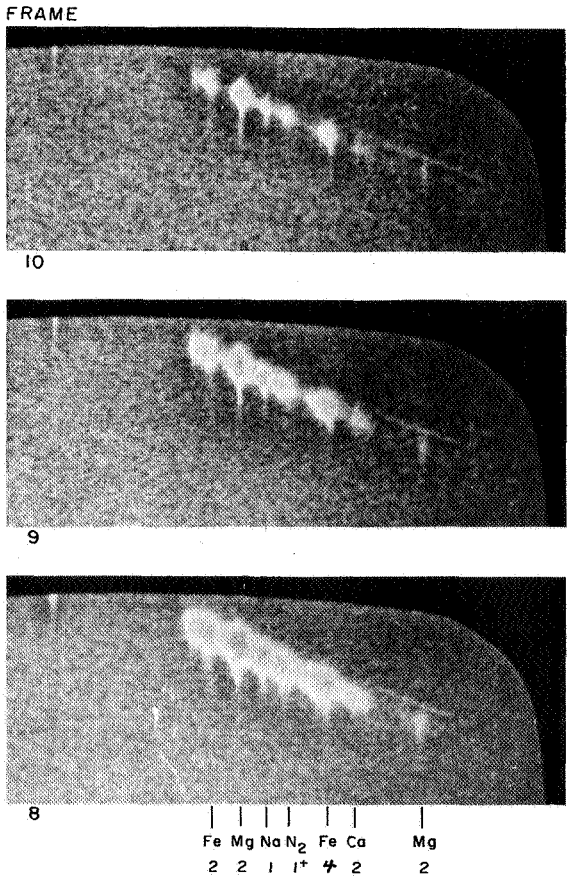

FIGURE 1.—Three successive frames from the record of meteor no. 1 in Group I. The apparent visual magnitude of this meteor was 2, absolute visual magnitude +1.1, and 14 different spectral features were measured.

SPECTROSCOPIC IDENTIFICATIONS

The study of the spectra was carried out by identifying the features in the records of Group I, and then using these identifications to extrapolate for the fainter, less-detailed spectra in the other groups. A general knowledge of the nature of Geminid meteor spectra was also available from previous photographic programs. Typical spectra from Group I are reproduced in figures 1 and 2. The definition was not good enough for more than a very approximate wavelength determination but the identity of various features could easily be followed from the strong spectra down to the weakest examples. A complete list of the features identified in all the spectra is given by wavelength in table 2. The chief contributors to these features are listed by multiplet in the second column of the table. The last five columns give the number of times each feature was identified in the various groups. No photometry of the spectra was attempted but the intensity of each

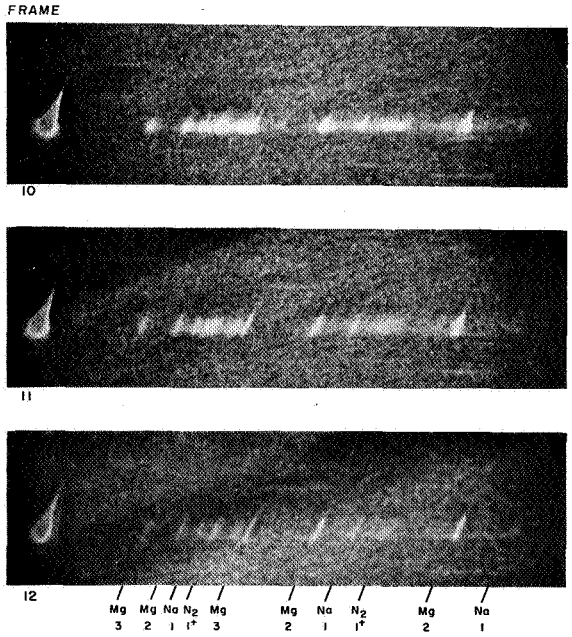

FIGURE 2.—Three successive frames from the record of meteor no. 3 in Group I. This meteor had a visual train of 1-s duration and the observed apparent visual magnitude was 0, giving an absolute visual magnitude of −0.2. Note the difference in appearance between the nitrogen bands and the magnesium lines.

TABLE 2.—*Spectroscopic Features Identified*

Approximate wavelength (Å)	Dominant contributing multiplets (Moore, 1945)	Frequency of identification				
		Group I	Group II	Group III	Group IV	All
3450	Fe I (6)	3	0	0	0	3
3580	Fe I (23) (24)	6	1	0	1	8
3730	Fe I (5)(21)	8	3	0	3	14
3880	Fe I (4) (20), Mg I (3)	8	6	2	5	21
4070	Fe I (43)	5	0	0	0	5
4230	Fe I (3), Ca I (2)	7	5	0	4	16
4380	Fe I (2) (41)	7	5	2	5	19
4700	Mg I (11)	2	0	0	0	2
4900	Fe I (318)	3	0	0	0	3
5180	Fe I (1), Mg I (2)	8	6	5	6	25
5350	Fe I (15)	2	0	0	0	2
5580	O I (3F)	0	1	0	1	2
5890	Na I (1)	8	5	5	6	24
6170	Ca I (3) (20)	2	0	0	0	2
6300 6500 6700	N_2 1st$^+$	8	6	3	5	22

feature is closely correlated with the number of times it is identified.

These spectra exhibit normal characteristics for Geminid meteors. The Mg green multiplet is generally strongest, followed closely by the Na yellow lines. Then we have low level Fe multiplets in the blue and violet and the N_2 molecular bands in the red. The image orthicon durations listed in table 1 correspond to the tube memory, except for the two cases where the O I line at 5577 Å was identified. These durations, indicated by brackets, are out of line with the others and represent real durations of the green-line luminosity. They correspond to the durations for the same feature found in image-orthicon Perseid spectra (Millman et al., 1971). However, in contrast to the Perseids, where all spectra studied exhibited the oxygen green line, only one Geminid spectrum, No. 29, showed this feature. There is always the possibility that this was not a Geminid meteor, even though the trail seemed to agree with the mean radiant position. The duration of motion was too short to check the shower affiliation through a measure of angular velocity.

DISCUSSION

The mean values, by group, of various observational parameters are listed in table 3. In columns 4 and 5 the mean logs of peak amplitude are given for the head echoes (h) and the long enduring echoes (e), using arbitrary units. The three groups of Geminid spectra, selected by numbers of features, represent successively fainter groups of meteors. This is indicated by the successively shorter mean durations of the radar echoes, and a similar sequence for the orthicon motion durations and image durations. A good estimate of the luminosity of the meteors in the three groups is difficult because of the small number of visual records, but using the values of table 3, and comparing with similar results in the previous study of the Perseid shower (Millman et al., 1971), we can conclude that the mean absolute visual magnitude of Group I is about +0.5, with the meteors in Groups II and III being some half to one magnitude fainter. The height of the oxygen line in Meteor 29 was omitted in calculating the mean heights listed in

TABLE 3.—*Mean Values of Observational Parameters by Group*

Group	Spectrum features	Radar echo			Interval, radar echo to orthicon record (s)	Orthicon record		Height	
		Duration (s)	*h* ampl. (log)	*e* ampl. (log)		Motion duration (s)	Image duration (s)	Begin (km)	End (km)
I	13	27	0.16	1.95	0.4	0.45	0.61	94	82
II	6	9.3	0.12	1.37	0.9	0.30	0.28	91	82
III	3	6.6	0.04	1.53	0.7	0.16	0.17	93	85
IV	5	7.8	—	1.53	0.8	0.27	0.21	94	86

table 3. The orthicon heights for the Geminid spectra average about 14 km lower than for the Perseid spectra, a somewhat greater differential than would have been expected on the basis of the relative geocentric velocities of the two showers, 35:60 km/s.

In summary we see that the spectra of the shower Geminid meteors in the visual absolute magnitude range from 0 to +2 show little or no evidence of the oxygen line at 5577 Å while the orthicon spectra of the faster Perseid meteors in the same luminosity class all exhibit this feature. The early continuum at the upper end of the meteor trails, observed so prominently in the Perseid spectra, seems much fainter or absent in these Geminid spectra, though there is still an indication of very faint band structure. This point requires further study.

REFERENCES

HEMENWAY, C. L., SWIDER, A., AND BOWMAN, C., 1971. Meteor spectroscopy using an image orthicon, *Can. J. Phys.*, **49**, 1361–1364.

MCKINLEY, D. W. R., AND MILLMAN, P. M., 1949. A phenomenological theory of radar echoes from meteors, *Proc. Inst. Radio Eng.*, **37**, 364–375.

MILLMAN, P. M., COOK, A. F., AND HEMENWAY, C. L., 1971. Spectroscopy of Perseid meteors with an image orthicon, *Can. J. Phys.*, **49**, 1365–1373.

MOORE, C. E., 1945. A multiplet table of astrophysical interest, *Contrib. Princeton Univ. Obs.*, No. 20, parts 1, 2.

Page intentionally left blank

13. An Unusual Meteor Spectrum

A. F. Cook
Smithsonian Astrophysical Observatory
and Harvard College Observatory
Cambridge, Massachusetts

C. L. Hemenway
State University of New York at Albany
and Dudley Observatory
Albany, New York

P. M. Millman
National Research Council of Canada
Ottawa, Ontario

AND

A. Swider
State University of New York at Albany
and Dudley Observatory
Albany, New York

An extraordinary spectrum of a meteor at a velocity of about 18.5±1.0 km s^{-1} (approximate uncertainty) was observed from the Springhill Meteor Observatory with an image-orthicon camera at 1970 August 10 ^{d} 2^h 48^m 51^s UT. The radiant of the meteor was at an altitude of about 49°. It was first seen showing a yellow-red continuous spectrum alone at a height of 137±8 km (estimated uncertainty) which we ascribe to the first positive group of nitrogen bands. At 1.60^s after its initial appearance the meteor had descended to 116±6 km above sea-level when it brightened rapidly from its previous threshold brighness into a uniform continuum. After a further 0.73^s at a height of 106±6 km the D*-line of neutral sodium appeared and 0.14^s later (height 105±5 km) all the other lines of the spectrum also appeared. The continuum remained dominant to the end 0.40^s later (height 87±5 km) or 3.87^s after initial appearance.*

Water of hydration and entrained carbon flakes of characteristic dimension about 0.2 micron or less are proposed as constituents of the meteoroid to explain these phenomena.

THE METEOR DISCUSSED in this paper was observed on the cooperative program of meteor observation commenced in 1969 at the Springhill Meteor Observatory. This program involves the use of an image-orthicon tube, backed up by auxiliary information from meteor radars and spectrographs, and a visual observing team (Millman et al., 1971).

TRAJECTORY

The meteor was observed by the G.E. image-orthicon camera model 4TE17A1 containing a specially selected GL 7967 image-orthicon tube with an S–20 photocathode and fitted with a 50 mm camera lens at $f/0.95$ and a Bausch and Lomb replica transmission grating (300 lines mm^{-1}, blazed at 17°27′) described by Hemenway et al. (1971). The observation was made from the Springhill Meteor Observatory at Springhill, Ontario (latitude 45°12′ N, longitude $5^h1.9^m$ W, elevation 102 m). The meteor radars and spectrographs, and the visual team were not operating at the time of the meteor's appearance. The meteor appeared at 1970 August $10^d2^h48^m51^s$ UT. The output of the image-orthicon tube was recorded on an Ampex 7000 video tape recorder along with time signals from CHU. The video tape was played back through a television monitor which was photographed on 16 mm motion picture film with a Bolex H–16 camera at a rate of 15 frames s^{-1} with individual exposures of about $\frac{1}{30}$ s. The film was projected on the back side of a ground glass screen for tracing, measurement and analysis. Further details of this equipment are given by Hemenway et al. (1971). A star field was also observed with the grating removed at $2^h0^m0^s$ UT.

The star field was traced and used to establish a grid of right ascension and declination for the equinox of 1855 by use of the *Atlas des nördlichen gestirnten Himmels* (Schönfeld and Krüger, 1899). The positions of the meteor spectrum together with the zero order, when available, and the sodium *D*-line in all available orders (out to the third in some frames) were also plotted. Also the zero orders of α and β Cassiopeiae were marked.

The nominal coordinates read off were right ascension and declination for the equinox of 1855 fitted to the star field at $2^h0^m0^s$ UT. These were precessed forward for 116 years to the equinox of 1971. They were next transformed to local hour angle and declination at Springhill and then to azimuth and altitude at Springhill. As expected the "observed" values for the zero orders of α and β Cassiopeiae did not match their computed directions at $2^h48^m51^s$ UT. The dispersion of the grating was parallel to the horizon at the centre of the field so that we expected a shift in azimuth only unless the camera had been moved when the grating was attached. This evidently did happen so that our final azimuths and altitudes were reached by transforming from our zenith without the grating to a new zenith at azimuth 45° E of N, altitude 89.0° and shifting these azimuths by a correction of −3.9°.

A final shift to a system of coordinates along the trail with pole at the pole of the trail was made, longitude along the trail being reckoned from the point of the trail's highest declination on the 1855 coordinate system. On this system the curvature of the 1st and 2nd orders was evident; the latitudes covered the ranges 6.9° to 6.0° and 14.2° to 14.0° respectively. The 3rd order was seen on only a few frames at latitude 22.5°. Reductions in longitude in the sense zero order minus order were found as follows: 1st order +4.6°, 2nd +10.4°, 3rd +16.2°. The adopted longitudes of the zeroth order were the mean from all observed

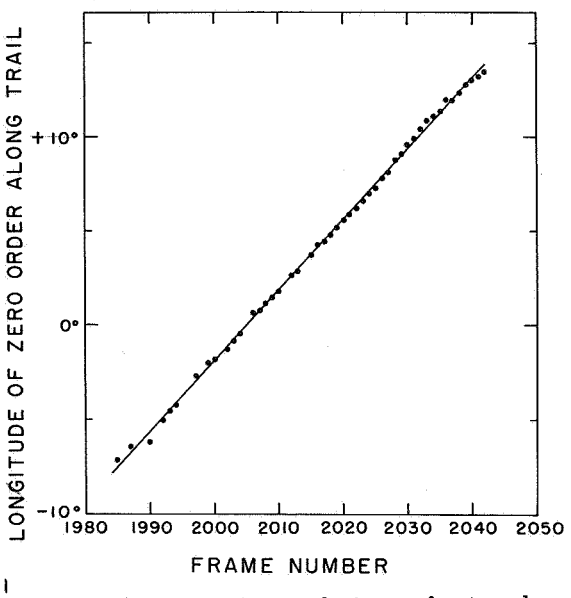

FIGURE 1.—Longitude of zero order image of meteor along trail as a function of kinescoped frame number.

orders for each frame. Figure 1 exhibits the resulting plot of longitude along the trail versus frame number (linear with time) and the adopted fit which appears to be a straight line.

If we read off from the fit of figure 1 three longitudes at equal intervals of frame number (and thus also of time) we may construct the plane triangles exhibited in figure 2. Let L denote longitude along the trail, the subscript 2 the middle epoch and the subscripts 1 and 3 the initial and final epochs respectively. Then the angular distances from the initial epoch to the middle epoch and from the middle epoch to the final epoch are α_1, α_2 respectively and the distances travelled along the trajectory are

$$D_1 \equiv D_2 \equiv D \equiv V(t_2 - t_1) \equiv V(t_3 - t_2) \qquad (1)$$

where V is the velocity of the meteor, t_1 is the initial epoch, t_2 is the middle epoch and t_3 the final epoch. The corresponding ranges are R_1, R_2 and R_3. By the law of sines we have

$$\frac{\sin\alpha_1}{D} = \frac{\sin\theta_1}{R_1} = \frac{\sin(\pi-\alpha_1-\theta_1)}{R_2} = \frac{\sin(\alpha_1+\theta_1)}{R_2}$$

$$\frac{\sin\alpha_2}{D} = \frac{\sin\theta_2}{R_3} = \frac{\sin(\pi-\alpha_2-\theta_2)}{R_2} = \frac{\sin(\alpha_2+\theta_2)}{R_2} \qquad (2)$$

where the angles θ_1, θ_2 are indicated in figure 2. Evidently we have

$$\theta_1 + \theta_2 \equiv \pi \qquad (3)$$

and θ_2 is the angular distance from the radiant at the middle epoch. Elimination of θ_1 from equations (2) and (3) yields

$$\frac{\sin\alpha_2}{\sin\alpha_1} = \frac{\sin(\theta_2+\alpha_2)}{\sin(\theta_2-\alpha_1)} \qquad (4)$$

a transcendental equation to be solved for θ_2. In the present case we have from figure 1, $L_1 = -7.5°$, $L_2 = +3.15°$, $L_3 = +13.8°$ and $\alpha_1 = \alpha_2 = 10.65°$ both estimated as uncertain by $\pm 0.10°$. The result is plainly $\theta_1 = \theta_2 = 90.0°$ and the uncertainty can be shown by differentiation of equation (4) to be $\Delta\theta_2 = \pm 2.8°$. This is the internal uncertainty of the position of the radiant along the trail. The internal uncertainty normal to the trail is $\pm 0.6°$. We estimate the corresponding external uncertainty due to paucity of stars here and there in the field of view at about $\pm 10°$ and $\pm 2°$ respectively.

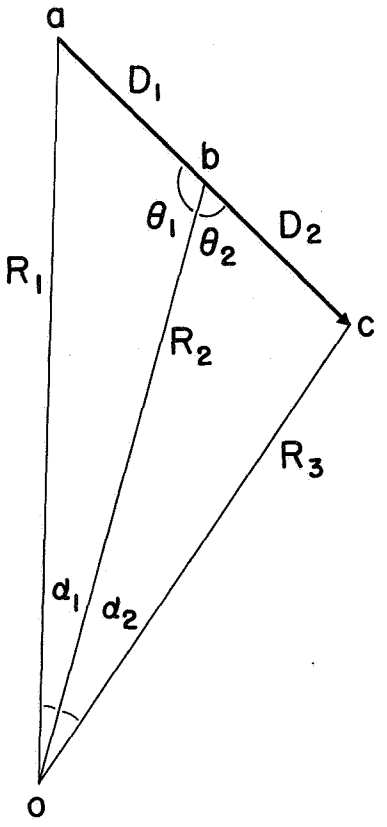

FIGURE 2.—Plane triangles formed by the meteor's trajectory and the observing station. The meteor was at a, b, and c at epochs 1, 2, and 3 respectively and at ranges R_1, R_2, and R_3, respectively. The observed angular lengths of the corresponding segments of the trail are α_1 and α_2.

The adopted longitude of the radiant along the trail is $-86.8°$. This transforms to azimuth 172.5°, altitude 48.6°, local hour angle $-4.8°$, declination $+4.0°$, right ascension 289.7° (1971) and finally to celestial longitude 292.0°, latitude $+26.2°$. The meteoric apex was calculated by a formula from Olivier (1925) to be at celestial longitude 47.8°. The elongation from the meteoric apex was 103.1°.

We then turned to figure 5, p. 12 of Jacchia and Whipple (1961) which exhibits the geocentric velocity, V_G, as a function of elongation of the geocentric radiant from the meteoric apex for 413

meteors. At 103° from the apex there is a principal maximum of population over the range $15 < V_G < 19$ km s^{-1} which corresponds to $19 < V_\infty < 23$ km s^{-1} where V_∞ denotes the velocity outside the atmosphere. A secondary concentration occurs just under the parabolic limit at $V_G = 24$ km s^{-1}. Occasional stragglers appear at lower velocities. The length of the trail is so long even for the part which shows the spectrum of vapours of meteoritic material that evidently we were looking at a meteor of Ceplecha's (1968) Class C. We sought that velocity which best fits the expected end height from his figure 27, p. 42. The procedure commenced with a succession of trial values of $V_\infty \simeq V$ which then allowed us to compute corresponding values of D and of the ranges, which from equations (2) and (3) are

$$R_1 = D\frac{\sin\theta_2}{\sin\alpha_1}, \quad R_2 = D\frac{\sin(\theta_2+\alpha_2)}{\sin\alpha_2}, \quad R_3 = D\frac{\sin\theta_2}{\sin\alpha_2} \tag{5}$$

then heights above sea-level were read off from a graph of isolines of constant height with range as abscissa and altitude as ordinate (used in routine reductions of meteors observed at Springhill). An extract from these calculations appears in table 1. We adopted 18 km s^{-1} as the best fit.

The best overall compromise appears to lie at the mean of the lower edge of the principal maximum of Jacchia and Whipple's (1961) distribution and the best fit to the end height for Ceplecha's (1968) Class C. Thus we finally adopted a velocity of 18.5 ± 1.0 km s^{-1} (estimated uncertainty).

TABLE 1.—*End Heights Computed for Various Velocities Compared with Those Expected for Ceplecha's (1968) Class C*

Velocity, V (km s^{-1})	Corresponding end height, H_e (km)	End height, H_e for Ceplecha's Class C (km)	Difference (km)
16	74	82	−8
17	79	82	−3
18	84	83	+1
19	90	83	+7

At this point diurnal aberration was removed followed by zenith attraction both for the radiant and the velocity. The geocentric radiant and velocity were then transformed to the heliocentric radiant and velocity and an orbit determined. The assembled results appear in table 2.

THE SPECTRUM

The most convenient way to describe the spectrum is in the form of a chronology, table 3.

TABLE 2.—*Circumstances of the Meteor*[a,b]

Frame no.	Epoch (s)	Description	1971 R.A. (deg)	1971 Decl. (deg)	Azimuth E from N (deg)	Altitude (deg)	Range (km)	Height (km)
1985	0.00	Beginning	2.7	+67.8	31.9	45.6	190±10	137±8
2013.5	1.90	Middle epoch	30.1	+68.5	26.1	36.2	187±10	112±6
2042	3.80	Final epoch	55.1	+64.5	21.7	26.3	190±10	87±5
2043	3.87	End						87±5
		App. radiant			172.5	48.6		
		Geoc. radiant	288.5	−0.7				

[a] The meteor appeared at 1970 August $10^d\ 2^h\ 48^m\ 51^s$ UT.

[b] Velocity outside the atmosphere is approximately equal to velocity in the atmosphere, i.e., 18.5 ± 1.0 km s^{-1}; geocentric velicity is 14.7 km s^{-1}. Geocentric radiant from celestial longitude is 289.8°, latitude +21.4° (1971). Elongation from meteoric apex is 106.8°. Orbital elements: $a = 2.5$ AU, $e = 0.66$, $\omega = 236°$, $i = 9°$, $\Omega = 137°$, $P = 3.9$ y, $q = 0.84$ AU, $Q = 4.1$ AU, $\pi = 13°$.

Details of the spectrographic identifications are listed in table 4.

PROPOSED EXPLANATION

We attempt a very tentative explanation of the foregoing sequence of events. We note that the radiations of molecular nitrogen remained approximately constant during a descent through 21 km in height. This implies that the surface area being struck by air molecules decreased with height in such a way as to nearly cancel the rise in atmospheric density. This may be explained if most of the exposed surface belonged to fragments shed from the meteoroid. In that case the fragments must have been so small as to have been stopped locally and must have been shed at a rate decreasing so as to cancel the rise in density of the atmosphere.

A frontal surface element must have radiated in an environment somewhere between the two extremes of radiation from a flat surface into a hemisphere with perfect insulation in the other hemisphere and isotopic radiation into the entire sphere. At an accommodation coefficient of unity for a very rough surface (Öpik 1958, pp. 52–54) and for radiation with emissivity unity (Öpik 1958, p. 55) into a hemisphere oriented in the direction of flight, the temperature of the surface in radiative equilibrium with the heat flux from the air stream at the beginning of the meteor was 500°±70° K (U.S. Committee, etc. 1962). For isotropic radiation over a sphere it was 350°±50° K. We may adopt as a rough estimate 430°±100° K. Such a temperature suggests release of water of hydration. It is common for such a release to break down the affected substance into a powder. In this way we account for the initial appearance of the meteor.

Fresh surface would have been exposed by this process and while it would have continued it is entirely reasonable to expect that more and more of the exposed area would have been resistant to

TABLE 3.—*Chronology of Events*

Epoch (s)	Height (km)	Event
0.00	137±8	At this initial appearance only a yellow-red continuum can be seen which we ascribe to the 1st positive group of N_2 by analogy with other spectra (Millman et al. 1971). Next the 2nd positive group appeared in the blue-violet and near UV. Both features remained near threshold until the next epoch.
1.60	116±6	A general brightening occurred into a uniform continuum.
1.90	112±6	This is the middle frame of the measured path.
2.33	106±6	The *D*-line of Na appeared.
2.47	105±5	Other lines of the spectrum appeared.
3.80	87±5	This is the last measured frame.
3.87	87±5	Here the meteor ended abruptly, the *D*-line having brightened very roughly in proportion to atmospheric density all the way with the continuum remaining dominant right to the end. Maximum absolute photographic magnitude of the meteor was very approximately zero. Identifications of spectral features are listed in table 4. Frames of the spectrum near the end are exhibited in figure 3.

TABLE 4.—*Spectral Features*[a]

Wavelength Å	Order	Intensity	Element and multiplet or molecule and group
3500	2	Weak	Fe (6)
3600	2	Weak	Fe (23)
3725	2	Medium	Fe (5), (21)
3835	2	Strong	Mg (3)
3890	2	Medium	Fe (4), (20)
4050	2	Weak	Fe (43)
4227	2	Medium	Ca (2)
4571	2	Weak	Mg (1)
4900	2	Medium	Fe (318)
5177	1, 2	Strong	Mg (2)
5300–5400	1, 2	Medium	Fe (15)
5520	1, 2	Medium	
5892	1, 2 3	Very Strong	Na (1)
6130	1	Weak	[b] N_2, 1^+
6450–6650	1	Weak	[b] N_2, 1^+

[a] The numbers of the multiplets are those assigned by Moore (1945).

[b] The entry N_2, 1^+ refers to molecular nitrogen, first positive group.

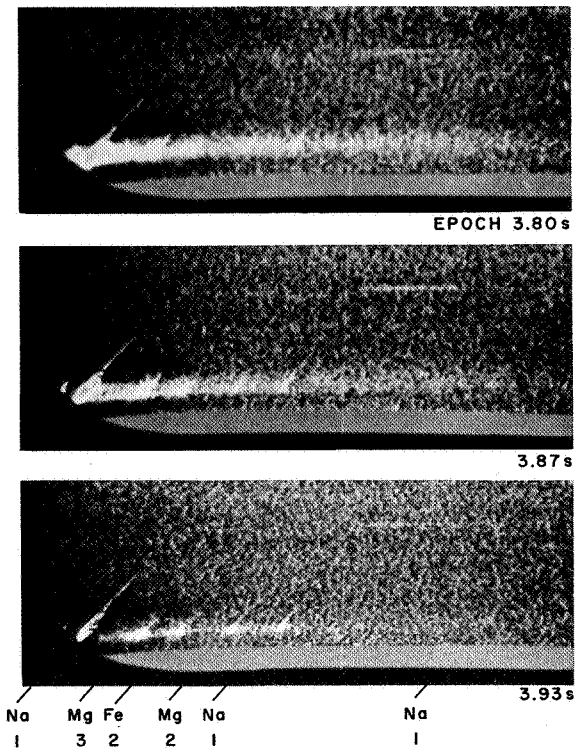

FIGURE 3.—Three kinescoped frames of the spectrum near the epoch of disappearance of the meteor.

complete collapse as the water of hydration was baked away. In that way we account for the failure of the meteor to brighten until 1.60^s after the appearance and through a descent of 21 km.

The sudden brightening at 1.60^s occurred when the two limiting temperatures in radiative equilibrium had reached 1400°±130° K and 1000°±90° K. We may estimate 1200°±150° K. At this temperature we postulate the onset of melting of baked out portions of the surface and their spinning off in droplets by rotation of the meteoroid to explain the brightening. This melting would have had the character of surface tension overcoming viscosity (Cook, 1968, p. 153), perhaps pulling together adjacent elements. Sizes up to the limit set by the critical Bond number (Cook, 1968, p. 154) would have been possible for the stone droplets. An explanation of the continuum is required. Here we tentatively suggest entrained carbon flakes which were not hydrated and were small compared with the wavelengths radiated, i.e., of characteristic radii of a few tenths of a micron. Their small emissivities would have sent their temperatures up possibly to that appropriate to loss of heat largely by vaporization. The high temperature of vaporization of a refractory substance like carbon combines with the expected decrease of emissivity with increasing wavelength for very small particles to produce a relatively bluish continuous radiation.

The appearance of vaporized sodium at 2.33^s signaled the rise of the spun off droplets of stone to the temperature required to release sodium. Then general vaporization corresponding to the usual beginning of a meteor began at epoch 2.47^s. All the foregoing implies ablation as small fragments of stone, later as fragments of some refractory substance such as carbon and droplets of stone, and finally as vaporizing fragments of carbon and droplets of stone.

It is an evident consequence of these ideas that after the onset of melting and spraying new surfaces still loaded with water of hydration would have been exposed so that crumbling would have occurred followed by melting and spraying. Random phasing of these successive processes across the surface of the meteoroid would have rapidly developed.

While all the foregoing is plausible if not subject to proof, the final feature—the steady rise to an abrupt end without a flare—is more difficult. Only an extremely tentative triad of assumptions has occurred to us. Since the area subject to vaporization was apparently roughly constant during this interval we assume that (1) the cloud of stone droplets and refractory (carbon) flakes was steadily replenished at the required rate. The abrupt ending requires then that (2) the final breakup of the meteoroid was into droplets similar in size to those still travelling in the cloud and further that (3) their size was small enough to allow abrupt exhaustion of the droplets and thus of the meteor.

CONCLUDING REMARKS

This paper reports an entirely new behavior of meteoric spectra. Only an instrument as sensitive as the television system used, or one still more sensitive, can detect these very faint phenomena, and more observations are urgently required to pass beyond the speculations presented above to a more satisfactory understanding of the faint early portions of meteor spectra dominated by bands and continua.

REFERENCES

ANON., 1962. U.S. Standard Atmosphere, 1962, U.S. Committee on Extension of the Standard Atmosphere, Supt. of Documents, Washington.

CEPLECHA, Z., 1968. Discrete levels of meteor beginning height, *Smithson. Astrophys. Obs., Spec. Rept.* No. 279.

COOK, A. F., 1968. The physical theory of meteors, *Physics and Dynamics of Meteors*, ed. by Ľ. Kresák and P. M. Millman, D. Reidel Publ. Co., Dordrecht, Holland, 149–160.

HEMENWAY, C. L., SWIDER, A., AND BOWMAN, C., 1971. Meteor spectroscopy using an image orthicon, *Can. J. Phys.*, **49**, 1361–1364.

JACCHIA, L. G., AND WHIPPLE, F. L., 1961. Precision orbits of 413 photographic meteors, *Smithson. Contrib. Astrophys.*, **4**, 97–129.

MILLMAN, P. M., COOK, A. F., AND HEMENWAY, C. L., 1971. Spectroscopy of Perseid meteors with an image orthicon, *Can. J. Phys.*, **49**, 1365–1373.

MOORE, C. E., 1945. A multiplet table of astrophysical interest, *Contrib. Princeton Univ. Obs.* No. 20.

OLIVIER, C. P., 1925. *Meteors*, Williams and Wilkins, Baltimore, 173.

ÖPIK, E. J., 1958. *Physics of Meteor Flight in the Atmosphere*, Interscience, New York.

SCHÖNFELD, E. AND KRÜGER, A., 1899. *Atlas des nördlichen gesternten Himmels*, 2nd. ed., edited and corrected by F. Küstner, Marcus and Weber, Bonn.

Page intentionally left blank

14. Spectroscopy of Project Fire I, April 14, 1964

PETER M. MILLMAN
National Research Council of Canada
Ottawa, Ontario

The Fire I test, April 14, 1964, was designed to study the heating of an Apollo-type reentry vehicle. The total reentry complex weighed approximately 230 kg and entered the upper atmosphere at a velocity of 11.5 km/s. The spectrum of the reentry complex has been studied in the wavelength range 3700 to 8800 Å, where 102 multiplets of 21 atoms and the band systems of 5 diatomic molecules have been identified. Comparisons with meteor spectra are made.

THE WRITER OF THIS PAPER served as a part-time consultant at the Avco Everett Research Laboratory during the period 1962 to 1967 (Millman, 1968). The work at Avco involved the study of the spectra of various reentry objects resulting from the tests made in the space-research program of the United States. One of the tests that has recently been declassified is Project Fire I, the high-speed reentry of a scaled-down model of the Apollo Command Module. This was launched from Kennedy Space Center, Florida, at $21^h\,42^m\,25^s$ UT, April 14, 1964. The reentry was sighted at $22^h\,10^m\,02.5^s$ UT over a point at lat. 08.8° S, long. 14.9° W, height 92 km, just southwest of Ascension Island. Photographic coverage by Avco was carried out from three aircraft flying to the northeast of the reentry track at heights between 2.5 and 4.3 km. This experiment produced what were, in effect, a number of very brilliant artificial fireballs, and it is of interest to study the spectrum of the luminosity in relation to comparable studies of bright meteors.

OBSERVATIONAL DATA

The complete reentry event of Project Fire I involved the reentries of the main rocket body, the Apollo model (termed the reentry package, R/P), an Antares II–A5 rocket motor with housing (termed the velocity package, V/P), and several other unidentified pieces of hardware. The R/P was in the form of a blunt-faced vehicle 64.5 cm in diameter with a conical after-body 53.6 cm long, and weighed 86.6 kg. The V/P was cylindrical in form, approximately 356 cm long and 76 cm in diameter, with a spent weight of 143.8 kg. Most of the data given here concerning the R/P, the V/P, and their reentry trajectory are taken from Popper et al. (1965). For more detailed information concerning the mechanical construction, including the chemical elements involved, see McKee (1966). Over most of the trajectory covered by the spectrographs, that is, above 50 km, the R/P and V/P were too close together to be separated on the record and the spectrum photographed is a composite of the two bodies. For convenience these will be referred to as the Fire Reentry Complex, FR/C.

The R/P was designed to study the heating of a blunt, high-speed reentry vehicle and the radiation emitted by it. It was equipped with six heat shields on its forward surface and these were ejected at various heights, measured by both telemetry and photography. Details concerning the heat shields are listed in table 1. The weight of the R/P was 40 percent heat shields, 40 percent electronics and 20 percent structure.

TABLE 1.—*Heat Shields on Fire I Reentry Package*

No., counting from the outside	Material	Thickness (cm)	Approximate ejection height (km)
1	Beryllium calorimeter	0.25	70—66
2	Phenolic heat shield	0.50	58—56
3	Beryllium calorimeter	0.50	50—46
4	Phenolic heat shield	0.50	43—40
5	Beryllium calorimeter	0.25	36—32
6	Phenolic heat shield	1.00	

TABLE 2.—*Observed Velocity of Fire I Reentry Complex*

Height (km)	Velocity (km/s)
90	11.5
75	11.5
65	11.3
55	10.6
50	9.9
45	8.8
40	7.0

The observed velocity of the FR/C is given in table 2. The trajectory was inclined at 13.3° to the horizontal and the visible portion extended for over 220 km in length from a height of 92 km down to 41 km above sea level. Several isolated bursts were observed still lower. The projection of the trajectory on the ocean surface had an angle of 122° from true north through east, taken in the direction of motion.

Photometry of the visible radiation in the range 4000 to 6500 Å gave results consistent among three independent recordings taken from two aircraft. For comparison with meteor observations these data, expressed in watts per steradian (Popper et al., 1965), have been reduced to absolute panchromatic magnitude, M_{pan}, by multiplying by 4π and assuming a total radiation of 0.126 W as equivalent to $M_{pan}=0$. A summary of the photometry is listed in table 3. The first part of the table refers to the complete FR/C. The four brightest bursts, well off scale for the photometric record, were due to the breakup of the V/P. From 56 km down, the magnitudes refer to the R/P only. Comparison with table 1 will show maxima in luminosity at the heights where the heat shields were rejected.

Spectrograms of the FR/C for Project Fire I were obtained with four K–24 cameras, mounted on a DC–6 aircraft flying at 3.65 km altitude. The lenses were of 17.8 cm focal length, aperture ratio $f/2.5$, and were fitted with objective transmission gratings, 300 lines/mm, giving a dispersion of 187 Å/mm in the first order at the center of the field. Three spectrographs were run with Eastman Royal-X Pan film, the fourth with Eastman Aero IR film, and a K2 filter. Exposures of 2 s each were made continuously and the data acquisition period was 28 s for one of the spectrographs loaded with panchromatic film and about 20 s for the other three spectrographs. The distance from the aircraft to the FR/C varied between 175 and 120 km during the period of data acquisition.

SPECTROGRAPHIC IDENTIFICATIONS

The general identification of the atomic and molecular features appearing in the Fire I spectra were made by a group, which included the writer, at the Avco Everett Laboratory under the direction of Charles C. Petty and Richard M. Carbone. Many of these identifications have been illustrated in Popper et al. (1965). However, the present writer is responsible for the selection of the data and the height analysis given here. In general, measurement of the spectra was carried out using enlarged photographic prints (about 16×) and the original films were only used for identification of fine detail, or for examination of the very faint features.

The typical appearance of Fire I spectra is illustrated in figures 1 and 2, where many of the more prominent molecular bands and atomic-line multiplets are marked for identification. In the case of the atomic lines the multiplet numbers used are from Moore (1945), while for the molecules the vibrational band sequences only have been indicated, with Pearse and Gaydon (1963) as the primary reference. Heights in kilometers are placed at the left of the corresponding levels in the spectra, which are oriented in the figures with motion downward. The last spectra shown, under 50 km height, are primarily of the R/P only while the remainder are for the FR/C.

TABLE 3.—*Photometry of Fire I Reentry Complex, April 14, 1964*

UT $22^h\ 10^m$ +	Height (km)	M_{pan}	Remarks
02.5 s	91.6	−13.1	Photometric threshold
02.8	91.2	−14.2	Luminosity Max.
03.3	89.9	−13.1	Min.
03.8	88.6	−14.6	Max.
04.1	87.6	−13.6	Min.
04.5	86.6	−14.8	Max.
05.0	84.9	−13.2	Min.
05.8	83.2	−14.4	Max.
06.1	82.1	−14.0	Min.
06.5	81.2	−14.5	Max.
07.1	79.5	−13.6	Min.
07.9	77.5	−14.6	Max.
08.2	76.7	−14.2	Min.
08.7	75.3	−15.1	Max.
09.1	74.2	−14.6	Min.
09.9	72.4	−16.7	Shelf in light curve
10.5	70.5	−18.8	Max.
11.2	68.7	−16.4	Min.
11.8	67.3	−20.5	Luminosity increasing rapidly and record goes off scale
13.0	64	<−21	Brilliant burst
13.5	63	<−21	Very brilliant burst
15.2	59	<−21	Very brilliant burst
15.8	57	<−21	Most brilliant burst
16.2	56.4	−17.7	Record begins again
16.5	55.5	−18.3	Rapid oscillations
16.8	54.9	−19.4	Max.
17.4 18.9	53.5 50.0	−13.5 to −17.0	Rapid oscillations
19.4	48.8	−17.9	Max.
20.0 20.5	47.5 46.5	−16.5 to −17.5	Rapid oscillations
20.5	46.2	−19.9	Max.
20.8 22.0	45.5 42.5	−14.5 to −15.5	Rapid oscillations
22.2	42.1	−19.1	Max.
22.5	41.4	−15.8	Luminosity decreasing and oscillating
23.1	40.1	−13.2	Final spectrographic record
	35.6	−17.1	Max.
	32.6	−19.1	Max.

Vibration of the cameras in the aircraft is evident in many of the spectra as wavy lines. These are more marked for some cameras and for the features where the luminosity is of short duration. Evidence for a wake of Na and AlO luminosity, and possibly CaCl, is seen at the beginning of the overexposed frame at 64½ km in figure 2.

HEIGHTS OF SPECTROGRAPHIC FEATURES

Heights for the various spectrographic exposures are available from the trajectory analysis, carried out by Avco using direct photographs. The first feature visible on the spectrograms is

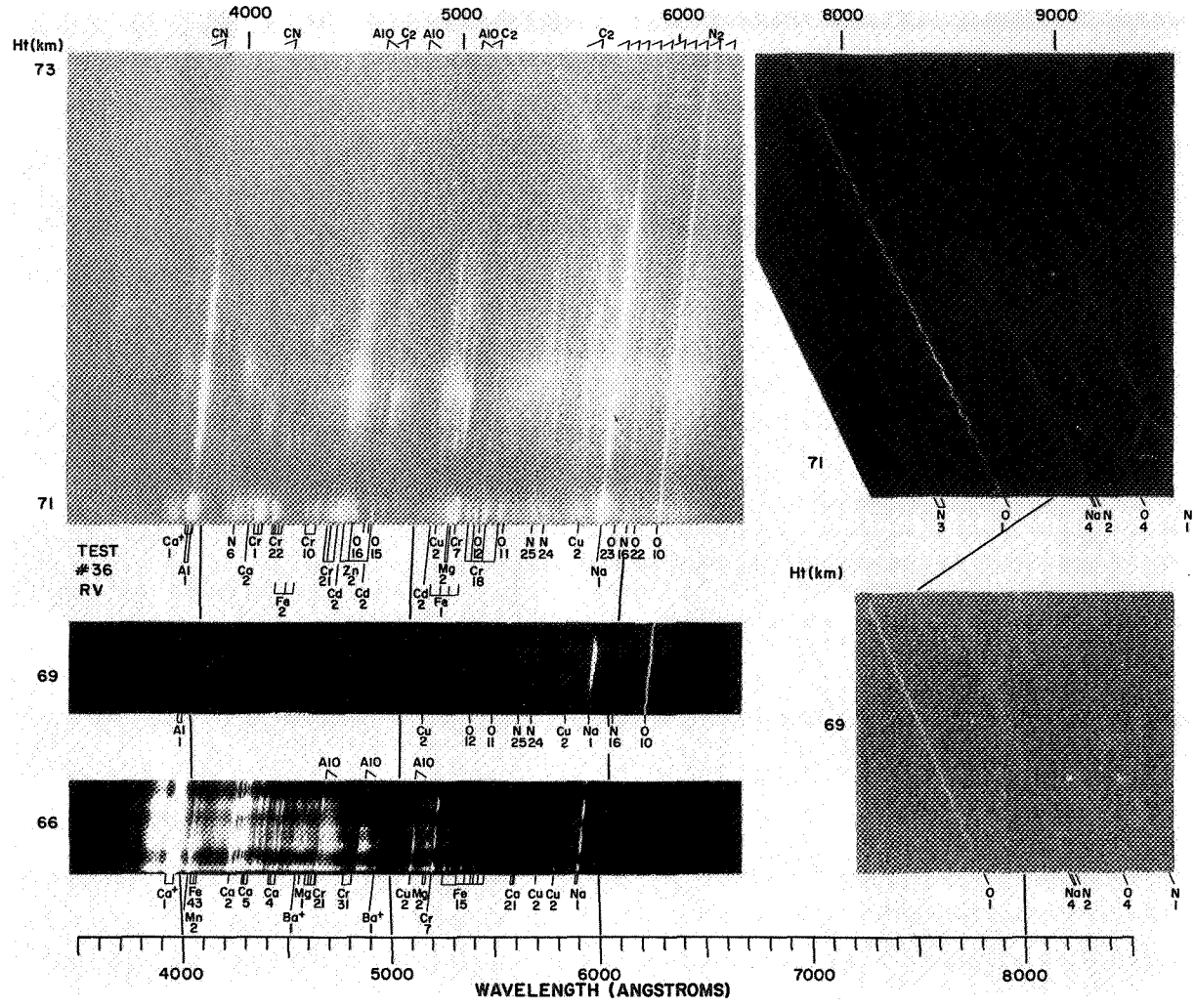

FIGURE 1.—Examples of spectra of the Fire I Reentry Complex from the upper part of the trajectory. Multiplet numbers are from Moore, 1945. The spectrum at 66 km is reproduced from the second order as the first order was overexposed.

the cyanogen band system in the violet, which appears at a height of 88.5 km. This is quickly followed by the first positive band system of nitrogen in the red at 87.5 km and the violet lines of neutral aluminum at 84.5 km. A listing of the heights of first appearance for all features identified is given in table 4. This table includes 102 multiplets of 18 neutral atoms and 3 singly ionized atoms, and the band systems of 5 diatomic molecules. These atoms and molecules are:

H, Li, Be, N, O, Na, Mg, Al, K, Ca, Ca^+,

Ti, Cr, Mn, Fe, Cu, Zn, Sr^+, Cd, Ba, Ba^+,

BeO, C_2, CN, N_2, AlO.

This is not claimed to be a complete list but it does include most of the easily seen features.

The height of disappearance is difficult to determine in many cases owing to the rapidly varying luminosity and to the overexposure in the bursts. Most of the atomic lines fade out between 55 and 50 km, after the breakup of the V/P. Some multiplets of Mg, Ca, Cr, Cu, Zn,

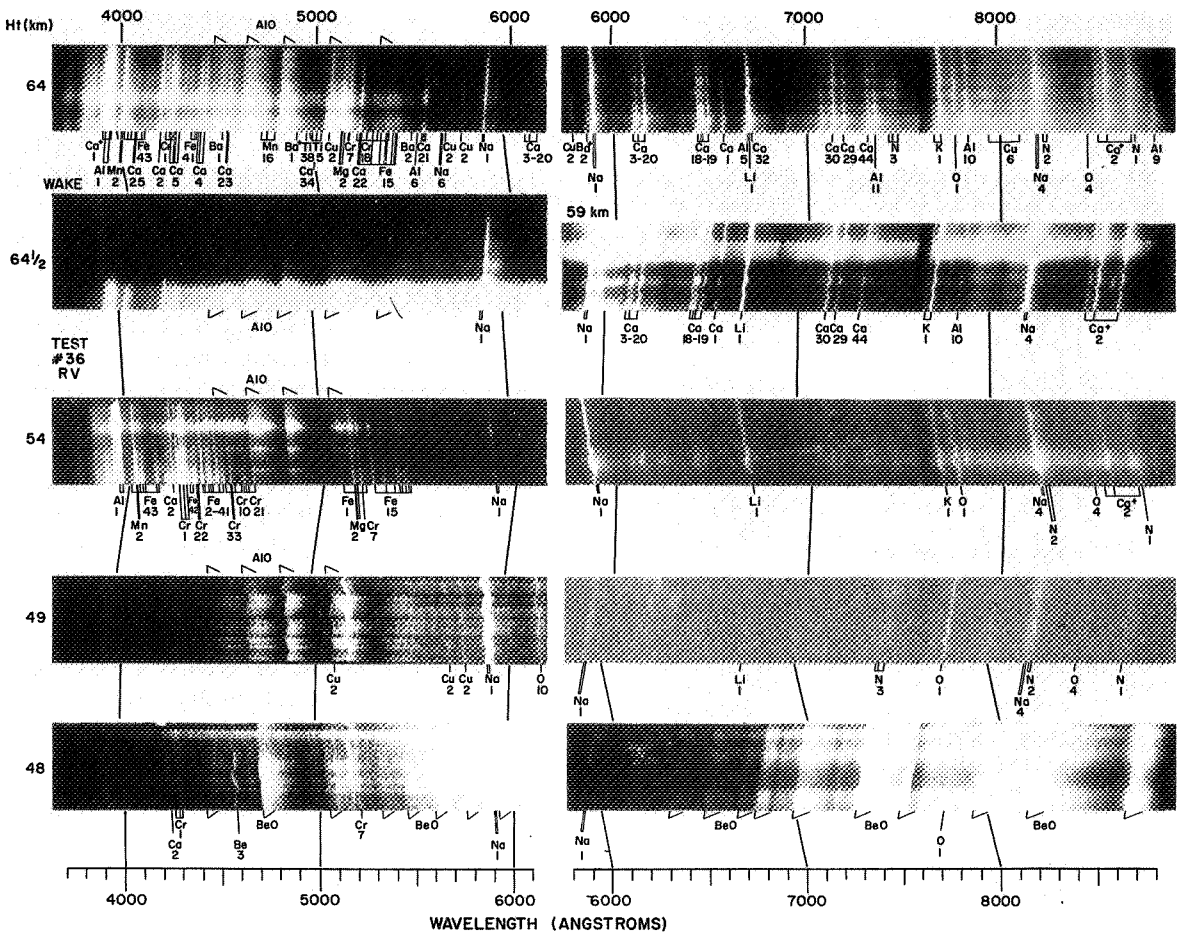

FIGURE 2.—Examples of spectra of the Fire I Reentry Complex from the lower part of the trajectory. Multiplet numbers are from Moore, 1945. The panchromatic spectra at 64 and 54 km are reproduced from the second order as the first order was overexposed.

and Cd are visible a little below 50 km, while Na and K remain down to the end of the spectrographic record near 40 km height. Bands of CN and N_2 disappear near 70 km, but C_2 is recorded down to 65 km and AlO to just below 50 km. It is possible that, in addition to the molecules listed, bands of CaCl and CaF are present in the 65 to 55 km range. The rejection of the beryllium heat shields produces a strong Be and BeO spectrum starting just below 50 km. Some 20 or more BeO band sequences have been identified (Pearse and Gaydon, 1963; Herzberg, 1933; Lagerquist, 1948) in the blue-green and the red systems. These remain visible down to the end of the spectrographic record.

DISCUSSION

The general range of heights observed in the Fire I spectrum is similar to the range for spectra of slow fireballs (Millman, 1971) extended to somewhat greater heights of appearance. The early appearance of the CN and N_2 bands is of interest in relation to the faint band structure observed with image-orthicon equipment at the beginning of meteor trajectories (Millman et al.,

TABLE 4.—*Heights of the Initial Appearance of Features in the Fire I Reentry-Complex Spectrum*

Height (km)	Multiplet numbers (Moore, 1945) and molecular band sequences[a]
88.5	CN (3883, 4216)$_b$
87.5	N_2 (first positive)$_c$
84.5	Al I (1)$_b$
79.0	O I (1)$_b$
78.0	O I (10)$_b$
77.0	N I (2)$_e$
74.0	O I (4)$_e$
73.5	N I (1)$_d$ (16)$_d$, O I (40?)$_g$
73.0	N I (24)$_e$ (25)$_e$, O I (12)$_e$, Na I (1)$_a$ (4)$_b$, C_2 (4737, 5165, 5636)$_c$
72.0	N I (3)$_e$ (6)$_e$ (10)$_f$, O I (11)$_g$ (22)$_f$ (23)$_g$, Ca I (2)$_b$, Ca II (1)$_b$, Cr I (1)$_b$ (7)$_b$ (21)$_d$, Cu I (2)$_c$, AlO (4648, 4842, 5079)$_b$
71.5	O I (15)$_e$ (16)$_f$ (17)$_e$ (18)$_f$, Mg I (2)$_c$, Cr I (10)$_e$ (18)$_b$ (22)$_c$, Mn I (2)$_b$, Fe I (1)$_f$ (2)$_f$ (3)$_g$, Cd I (2)$_e$
71.0	Zn I (2)$_e$
68.0	Mg I (1)$_d$, Ca I (3)$_c$ (4)$_c$ (5)$_c$ (18)$_c$ (19)$_c$ (20)$_c$ (21)$_c$ (22)$_c$ (23)$_c$ (25)$_f$, Cr I (6)$_g$ (8)$_f$ (31)$_f$ (60)$_f$ (145)$_f$ (185?)$_g$, Fe I (15)$_c$ (41)$_f$ (42)$_f$ (43)$_f$, Sr II (1)$_g$, Ba I (2)$_e$, Ba II (1)$_d$ (2)$_e$
65.0	H I (1)$_f$, Li I (1)$_b$, N I (8)$_g$, Na I (5)$_d$ (6)$_e$ Al I (5)$_e$ (6)$_f$ (9)$_d$ (10)$_d$ (11)$_d$, K I (1)$_c$, Ca I (1)$_d$ (29)$_d$ (30)$_d$ (31)$_g$ (32)$_e$ (34)$_g$ (41)$_g$ (44)$_d$ (47)$_d$ (48)$_g$ (49)$_g$, Ca II (2)$_c$, Ti I (4?)$_g$ (5)$_c$ (6)$_c$ (38)$_d$ (42)$_e$ (44)$_e$ (106)$_c$, Mn I (16)$_d$, Cu I (6)$_g$, AlO (4470, 5337)$_e$
55.0	Mg I (3)$_d$, Fe I (4)$_e$ (16)$_g$ (20)$_f$ (37)$_g$ (68)$_f$
48.0	Be I (3)$_e$, BeO (>20 band sequences, 4180–8712)$_a$, AlO (4307)$_g$

[a] The subscripts a, b, c, d, e, f, g, in this table form a qualitative scale which indicates the degree of prominence of each feature in a descending sequence of values.

1971; Papers 12 and 13, this volume). As in the case of the faster cometary meteors (Millman, 1971) the atomic lines of O and N appear in Fire I relatively high compared to the rest of the spectrum. They remain visible to heights below 50 km, which is lower than normally observed in meteors. In contrast to most meteor spectra, where the input of atoms from the meteoroid has a fairly constant composition along the trail, reentry spectra exhibit a nonhomogeneous structure resulting from a diversity of atomic input into the radiating vapor. A good example is the spot appearances of Cu, Cr and Fe at different heights between 73 and 71 km, figure 1. It has also been found that trace elements in a reentry vehicle may appear in the spectrum with unexpected prominence. This warns us against a superficial estimate of the chemical composition of an unknown body, based only on the qualitative appearance of its spectrum. The greater mass and low velocity of reentry vehicles result in the greater prominence of molecular bands in their spectra when compared to meteor spectra. A great variety in the chemical composition of different components in the reentry objects produces considerable diversity in the observed band systems. As noted by Millman (1968), 54 band systems of 27 different molecules were identified in a study of 41 reentries that took place in the period 1960 to 1964.

In any general treatment of the physics of solid objects moving at high speed through the Earth's upper atmosphere the reentry data give us an important extrapolation of the meteor data toward more massive objects and lower velocities. It is hoped that, in the future, a photometric analysis of these spectrographic records will become available.

ACKNOWLEDGMENTS

It is a pleasure to acknowledge useful discussions with Marilyn L. Bankoff, Richard M. Carbone and Charles C. Petty at the Avco Everett Laboratory, Everett, Mass., and with the late Luise Herzberg at the Defence Research Board, Ottawa, Ont.

REFERENCES

HERZBERG, L., 1933. Über ein neues bandensystem des berylliumoxyds und die struktur des BeO-moleküls, *Z. Physik*, **84**, 571–592.

LAGERQUIST, A., 1948. Investigations of the band-spectrum of beryllium oxide, inaugural dissertation for Ph.D., Univ. Stockholm, Almquist and Wiksells Boktryckeri Ab., Uppsala, 1–98.

MCKEE, C. W., 1966. Project Fire photographic summary and record of reentry phenomena at hyperbolic velocities, *NASA Tech. Note* **D-3571**, 1–68.

MILLMAN, P. M., 1968. A brief survey of upper-air spectra, in *Physics and Dynamics of Meteors*, edited by L. Kresák and P. M. Millman, D. Reidel Publ. Co., Dordrecht, Holland, 84–90.

——, 1971. Heights of meteor spectra, *J. Roy. Astron. Soc. Can.*, **65**, 37–38.

MILLMAN, P. M., COOK, A. F., AND HEMENWAY, C. L., 1971. Spectroscopy of Perseid meteors with an image orthicon, *Can. J. Phys.*, **49**, 1365–1373.

MOORE, C. E., 1945. A multiplet table of astrophysical interest, *Contrib. Princeton Univ. Obs.*, No. 20.

PEARSE, R. W. B., AND GAYDON, A. G., 1963. The identification of molecular spectra, Chapman and Hall, London, 1–347.

POPPER, L. A., MAHONEY, P. A., PLAYDON, R. T., BANKOFF, M. L., AND STAAL, J. V., 1965. Re-entry data report Project Fire (14 April 1964) ETR #225 Atlas Missile 263D, *Avco Everett Research Lab., Res. Note* No. 503, 1–52.

Page intentionally left blank

15. Motion of a Fragment in Disturbed Air Behind a Meteor Body

V. PADEVĚT
Astronomical Institute of Czechoslovak Academy of Sciences
Ondřejov, Czechoslovakia

EVEN IF WE USE the classical physical theory of meteors, there may still be some possibility for agreement between observations and theory. The effect of disturbed air behind the main body on the motion and ablation of fragments has not yet been considered. This effect may have important consequences, observed partly as the difference between the photometrically and the dynamically determined masses of the meteor body. By use of extreme mathematical conditions, this difference can be made to reach orders of magnitude during the latter part of the trajectory. However, the physical interpretation is considered only roughly in this paper, and the computed model needs further improvement. But the main purpose here—finding an important effect for the explanation of the discrepancy between the dynamic and the photometric masses, especially for large bodies—has been achieved.

ASSUMPTIONS

The mathematical model used here contains the following simplifications: If a single meteor body with velocity v and radius R deposits its mass only in small fragments of radius R_f, the ablation of a spherical stony parent body is given by the following equations:

$$\frac{dR}{dt} = \frac{-\Lambda(t)\rho v^3}{8Q\rho_m} \tag{1}$$

$$\frac{dv}{dt} = \frac{-3\Gamma\rho v^2}{4R\rho_m} \tag{2}$$

$$\frac{d\rho}{dt} = b\rho v \cos z_R \tag{3}$$

and

$$\Lambda(t) = A_0 + A_1 \cdot t + A_2 \cdot t^2 \tag{4}$$

where $Q = c \cdot \tau_c$, Λ is the heat-transfer coefficient, ρ is the density of the free atmosphere, ρ_m is the density of the meteoroids, c is the specific heat of the meteoroid, b is the reciprocal of the density scale height of the atmosphere, and the temperature of the meteoroid outside the atmosphere is taken as zero. Equation (4) is simply an approximate polynomial expansion of second degree in time for the heat-transfer coefficient.

The following idealized history of each small fragment is assumed. The fragment leaves the parent body with temperature τ_c. Starting with this temperature, the fragment is heated to the evaporation temperature, cooling by radiation being taken into account. Isothermal heating is assumed for such small fragments, and the following equations are thus valid for the first part of the trajectory:

$$\frac{c \cdot \rho_m R_f}{3}\frac{dT}{dt} + \sigma_R(T^4 - T_0^4) = \frac{\Lambda_f \rho_f v^3}{8} \tag{5}$$

$$\frac{dv}{dt} = \frac{-3\Gamma\rho_f v^2}{4R_f\rho_m} \tag{6}$$

$$\frac{dH}{dt} = -v \cos z_R \tag{7}$$

and

$$\rho_f = \rho - F(H_0 - H) \tag{8}$$

Here, σ_R is the Stefan-Boltzmann constant, Λ_f the heat-transfer coefficient for fragments, and Γ the drag coefficient.

We deal with a very simplified case in this paper, the air density at height H being the only disturbed entity; the density in the wake is denoted by ρ_f. In equation (8), F describes this disturbance. The function F also depends on the height of fragment separation, H_0; it has two extreme values: $F=0$ if the atmosphere behind the parent body is not disturbed, and $F=\rho$ if there is a vacuum behind.

After being heated to the evaporation temperature, the fragment starts the second part of its trajectory. The temperature is determined by radiation, vaporization, and aerodynamic heating. Mass loss and luminosity occur until the energy flux is balanced by radiation. The second part of the fragment's trajectory can be described by the following equation:

$$\frac{dR_f}{dt} = -\frac{\Lambda_f \rho_f v^3 - 4\sigma_R(T^4 - T_0^4)}{8Q_f \rho_m} \qquad (9)$$

and by equations (6), (7), and (8). Here, Q_f is the heat of ablation of vapors from the fragment. Visual radiated luminosity I_f belonging to one fragment is then described in terms of the luminous efficiency coefficient τ_0 by

$$I_f = \tfrac{1}{2} A (\tfrac{4}{3}\pi\rho_m)^{2/3} \tau_0 v^3 R_f^{2}{}_{(H_0)} \times \left[\sigma_f \Gamma \rho_f v^3 - \frac{4\sigma_R(T^4 - T_0^4)}{Q_f}\right] \times \exp\left[-\frac{\sigma_f}{3}(v_{H_0}^2 - v^2)\right] \qquad (10)$$

where

$$\sigma_f \equiv \frac{\Lambda_f}{2\Gamma Q_f}$$

Also, A denotes the shape factor.

PROCEDURE USED

The total light intensity at a given height H_m is the sum of all the partial intensities from all the fragments that separated from the parent body at heights $H \geq H_m$. It is clear that the fragments that separated within heights $H_1 > H \geq H_m$ are not shining, because they are not yet heated enough. The beginning of the light curve is taken at the height corresponding to the air density ρ_B computed for the ending of the preheating period according to the formula by Ceplecha and Padevět (1961):

$$\rho_B = \frac{8\lambda\tau(R)}{a v_\infty^3 R}\left(WR\frac{e^{WR}+e^{-WR}}{e^{WR}-e^{-WR}} - 1\right) \qquad (11)$$

where $W = (b \cos z_R \cdot v_\infty)^{1/2}/\beta$, β^2 is the thermal diffusivity, λ is the thermal conductivity of the meteoroid, τ is the temperature at which structural failure occurs, and a is the accommodation coefficient. The end of the light curve is defined to be at the height where the velocity has decreased to 5 km/s.

The dynamic and photometric masses can now be computed and compared by means of the same procedures as for observed meteors. Equations (1) to (4) are used to find the radius and thus the mass of the body, and the conventional luminous equation

$$m_p(t) = \frac{2}{\tau_0}\int_t^{t_{\text{end}}} \frac{I(t')}{v^3}\,dt' + m_{\text{end}} \qquad (12)$$

is used to determine the photometric mass. Here, v is the velocity of the parent body and I is the instantaneous intensity. The integration constant m_{end} was taken as the dynamically determined mass at the terminal point.

The change of air density behind the parent body might alter the computed photometric masses, but there is no need to attain higher values than those in the paper by McCrosky and Ceplecha (1970). However, if, for example, a constant factor for decreasing the density behind the main body is used, this undesired effect happens. But such a simple model for the function F does not correspond even to a primitive physical guess. We would expect a decrease of the disturbance farther behind the meteor body, terminating with the density of the undisturbed atmosphere. It seems that each realistic model of the disturbance will result in a decrease of luminosity originating from one fragment. In an attempt to increase the photometric mass, we should find a model of the disturbance that would decrease the level of the photometric mass as little as possible and we should look for another

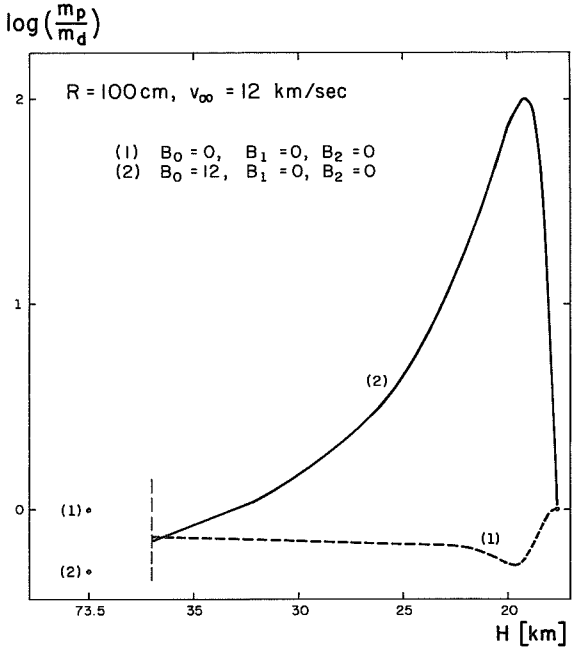

FIGURE 1.—Logarithm of the ratio of the photometric mass m_p to the dynamical mass m_d for an initial radius $R_\infty = 100$ cm and an initial velocity $v_\infty = 12$ km/s.

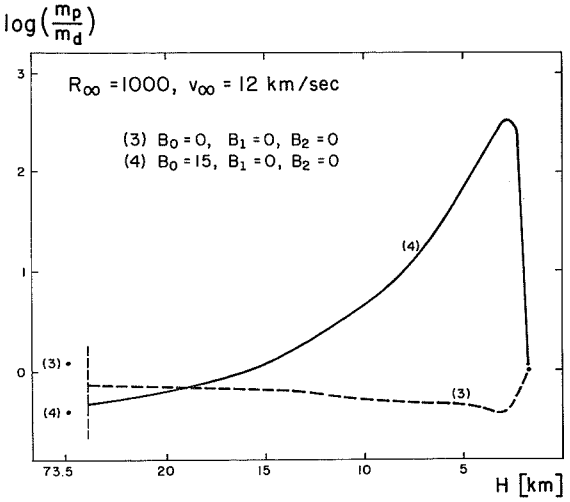

FIGURE 2.—Logarithm of the ratio of the photometric mass m_p to the dynamical mass m_d for an initial radius $R_\infty = 1000$ cm and an initial velocity $v_\infty = 12$ km/s.

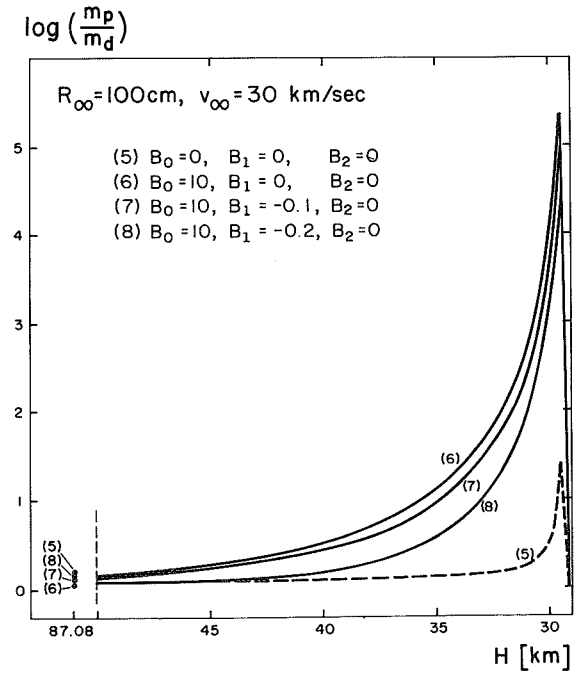

FIGURE 3.—Logarithm of the ratio of the photometric mass m_p to the dynamical mass m_d for an initial radius $R_\infty = 100$ cm and an initial velocity $v_\infty = 30$ km/s.

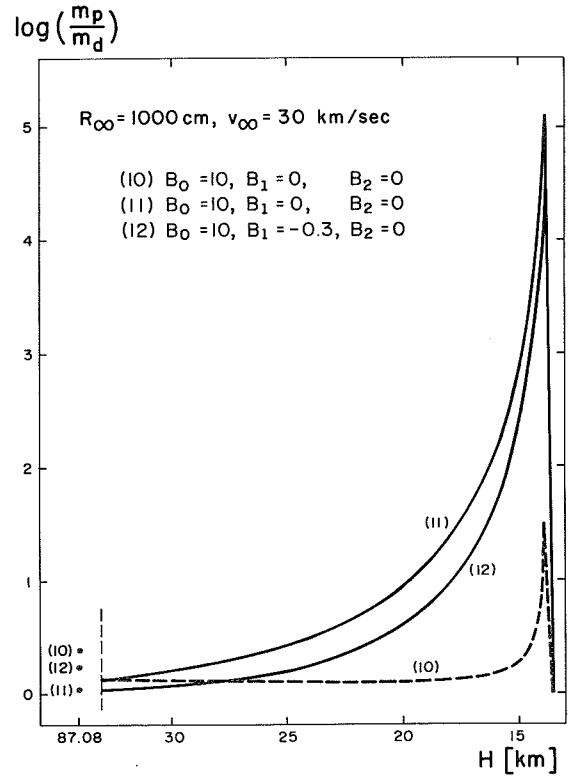

FIGURE 4.—Logarithm of the ratio of the photometric mass m_p to the dynamical mass m_d for an initial radius $R_\infty = 1000$ cm and an initial velocity $v_\infty = 30$ km/s.

effect strong enough to increase the level. The first condition may be met by a rather extreme and simple function—the discontinuous function $F=\rho$ for an interval of $H_0>H>H_2$, and $F=0$ for an interval of $H_2\geqq H\geqq H_m$. The fragments begin by moving in vacuum but cannot move ahead of the decelerating parent body. As an extreme case, we can imagine that the fragments are moving in a trap close behind the body, departing at height H_2. This extreme choice of the function F serves the computations well as the first approximation of some more realistic model. The real function should start from a value very close to the air density (almost vacuum), followed by a steep change that is represented here by the discontinuous jump to zero. All our preliminary computations used this discontinuous function.

An additional parameter now is the number of fragments crossing the discontinuity in the air density at a given height H_m. If the discontinuous function F is as above, only one change results: The height of the separation of the corresponding fragment will be higher than in the case without any disturbance. But we are interested in differences of orders of magnitude, and this is not possible with the above model with Λ constant. On the other hand, if we assume that Λ decreases with time, a steep decrease of the main-body mass results during the second part of the trajectory. Generally speaking, the decrease of Λ with time can be expected from the physical point of view.

RESULTS

Until now, only a limited number of cases have been computed. The numerical choice of parameters was made rather arbitrarily, with only great differences between the computed photometric and the computed dynamic masses being accepted. We can guess that the differences will be less after more physical factors are included, but the computed examples illustrate the general situation well.

Using the above model, we can explain the great difference between the dynamic and the photometric mass during the second part of the trajectory, if we assume chondritic densities for the body. As a function of time, the difference between the two masses is less in the first part of the trajectory and becomes greater at the end (see figs. 1 to 4).

COMMENTS

$D=B_0+B_1\cdot H_2+B_2\cdot H_2^2$ is the difference in height in kilometers between the fragment separation (H_0) and that of departure from the trap (H_2).

Numerical parameters used for computation of the values in tables 1 to 4 (cgs) are as follows:

a	$=1$
A	$=1.21$
b	$=1.6\times10^{-6}$ cm^{-1}
c	$=10^7$ cm^2 s^{-2} deg^{-1}
Q_f	$=8\times10^{10}$ cm^2 s^{-2}
initial R_f	$=0.01$ cm
T_0	$=0°$ K
T_B	$=2580°$ K
cos z_R	$=1$
Γ	$=0.5$
λ	$=3\times10^5$ g cm s^{-3} deg^{-1}
ρ_m	$=3.5$ g cm^{-3}
σ_f	$=\dfrac{\Lambda_f}{2\Gamma Q_f}=2\times10^{-12}$ cm^{-2} s^{-2}
τ_c	$=600°$ C

The results do not depend on the value τ_0.

REFERENCES

Ceplecha, Z., and Padevět, V., 1961. The beginning of rapid evaporation of meteors of different dimensions, *Bull. Astron. Inst. Czech.*, **12**, 191–195.

McCrosky, R. E., and Ceplecha, Z., 1970. Fireballs and the physical theory of meteors, *Bull. Astron. Inst. Czech.*, **21**, 271–296.

TABLE 1.—*Meteoroid With Initial Velocity* $v_\infty = 12$ *km/s and Radius* $R_\infty = 100$ *cm*

Velocity v (km/s)	Dynamical mass m_d (g)	Height H (km)	Epoch t (s)	Assumed heat-transfer coefficient Λ
5.000	6.0967×10^{2}	17.654	4.2592	0.00224
5.692	6.4917×10^{2}	17.999	4.1959	0.01734
6.446	7.8346×10^{2}	18.363	4.1370	0.03138
7.225	1.0994×10^{3}	18.750	4.0816	0.04458
7.980	1.7900×10^{3}	19.161	4.0286	0.05720
8.669	3.2799×10^{3}	19.601	3.9768	0.06952
9.268	6.4496×10^{3}	20.072	3.9253	0.08178
9.772	1.3035×10^{4}	20.570	3.8728	0.09426
10.191	2.6252×10^{4}	21.111	3.8184	0.10719
10.536	5.1745×10^{4}	21.706	3.7610	0.12082
10.822	9.9022×10^{4}	22.365	3.6994	0.13545
11.058	1.8352×10^{5}	23.104	3.6322	0.15140
11.255	3.2981×10^{5}	23.945	3.5576	0.16911
11.421	5.7708×10^{5}	24.920	3.4727	0.18922
11.561	9.8699×10^{5}	26.079	3.3737	0.21267
11.680	1.6587×10^{6}	27.506	3.2540	0.24100
11.780	2.7585×10^{6}	29.358	3.1011	0.27714
11.866	4.5839×10^{6}	31.994	2.8875	0.32754
11.939	7.7595×10^{6}	36.419	2.5258	0.41270
12.000	1.4661×10^{7}	73.536	0.0000	1.00000

TABLE 2.—*Meteoroid With Initial Velocity* $v_\infty = 12$ *km/s and Radius* $R_\infty = 1000$ *cm*

Velocity v (km/s)	Dynamical mass m_d (g)	Height H (km)	Epoch t (s)	Assumed heat-transfer coefficient Λ
5.000	4.3224×10^{4}	1.7160	5.2882	0.05170
6.281	8.8988×10^{4}	2.2542	5.2282	0.06718
7.454	2.4031×10^{5}	2.8161	5.1762	0.08050
8.408	7.1522×10^{5}	3.4026	5.1285	0.09263
9.145	2.0631×10^{6}	4.0220	5.0826	0.10425
9.708	5.4479×10^{6}	4.6686	5.0370	0.11574
10.144	1.3075×10^{7}	5.3541	4.9903	0.12742
10.487	2.8694×10^{7}	6.0834	4.9419	0.13949
10.762	5.8364×10^{7}	6.8585	4.8907	0.15215
10.987	1.1141×10^{8}	7.6891	4.8360	0.16561
11.174	2.0175×10^{8}	8.5869	4.7766	0.18011
11.330	3.4984×10^{8}	9.5653	4.7112	0.19596
11.463	5.8537×10^{8}	10.643	4.6380	0.21355
11.576	9.5153×10^{8}	11.699	4.5544	0.23343
11.674	1.5114×10^{9}	12.860	4.4564	0.25647
11.759	2.3604×10^{9}	14.281	4.3374	0.28406
11.832	3.6457×10^{9}	16.114	4.1851	0.31878
11.896	5.6144×10^{9}	18.698	3.9716	0.36624
11.952	8.7454×10^{9}	23.053	3.6087	0.44380
12.000	1.4661×10^{10}	73.532	0.0000	1.00000

TABLE 3.—*Meteoroid With Initial Velocity* $v_\infty = 30$ *km/s and Radius* $R_\infty = 100$ *cm*

Velocity v (km/s)	Dynamical mass m_d (g)	Height H (km)	Epoch t (s)	Assumed heat-transfer coefficient Λ
5.000	3.2649×10^{-5}	29.104	1.7436	0.01609
23.680	7.7116×10^{-1}	29.455	1.7215	0.02887
26.363	2.8707×10^{1}	29.826	1.7074	0.03705
27.493	2.2584×10^{2}	30.220	1.6934	0.04514
28.144	9.9065×10^{2}	30.641	1.6789	0.05352
28.571	3.1699×10^{3}	31.091	1.6637	0.06230
28.874	8.3382×10^{3}	31.576	1.6476	0.07159
29.101	1.9233×10^{4}	32.096	1.6303	0.08154
29.276	4.0281×10^{4}	32.646	1.6117	0.09226
29.416	7.8608×10^{4}	33.250	1.5914	0.10396
29.530	1.4512×10^{5}	33.919	1.5691	0.11683
29.623	2.5621×10^{5}	34.675	1.5442	0.13114
29.701	4.3758×10^{5}	35.540	1.5161	0.14733
29.766	7.2682×10^{5}	36.548	1.4837	0.16591
29.822	1.1836×10^{6}	37.757	1.4455	0.18784
29.870	1.9020×10^{6}	39.260	1.3988	0.21462
29.910	3.0356×10^{6}	41.235	1.3387	0.24899
29.945	4.8632×10^{6}	44.094	1.2542	0.29726
29.975	7.9709×10^{6}	49.320	1.1101	0.37931
30.000	1.4661×10^{7}	87.079	0.0000	1.00000

TABLE 4.—*Meteoroid With Initial Velocity* $v_\infty = 30$ *km/s and Radius* $R_\infty = 1000$ *cm*

Velicity v (km/s)	Dynamical mass m_d (g)	Height H (km)	Epoch t (s)	Assumed heat-transfer coefficient Λ
5.000	8.6440×10^{-3}	13.510	2.2721	0.01375
24.240	2.6803×10^{3}	13.855	2.2333	0.03189
26.458	6.9058×10^{4}	14.219	2.2193	0.03842
27.473	4.5678×10^{5}	14.605	2.2052	0.04498
28.083	1.7743×10^{6}	15.016	2.1907	0.05173
28.496	5.1904×10^{6}	15.455	2.1755	0.05881
28.799	1.2789×10^{7}	15.928	2.1593	0.06634
29.030	2.7879×10^{7}	16.438	2.1420	0.07438
29.211	5.5661×10^{7}	16.993	2.1234	0.08303
29.358	1.0420×10^{8}	17.600	2.1030	0.09246
29.479	1.8520×10^{8}	18.272	2.0807	0.10280
29.579	3.1676×10^{8}	19.024	2.0557	0.11433
29.664	5.2456×10^{8}	19.875	2.0276	0.12732
29.736	8.4820×10^{8}	20.838	1.9951	0.14225
29.798	1.3466×10^{9}	21.976	1.9568	0.15984
29.851	2.1108×10^{9}	23.377	1.9101	0.18126
29.897	3.2897×10^{9}	25.198	1.8499	0.20871
29.937	5.1470×10^{9}	27.790	1.7652	0.24718
29.971	8.2266×10^{9}	32.286	1.6207	0.31234
30.000	1.4661×10^{10}	87.077	0.0000	1.00000

16. The Distribution of $1/a$ in Photographic Meteor Orbits

B. A. LINDBLAD
Lund Observatory
Lund, Sweden

A study is made of the distribution of reciprocal semi-major axis in photographic meteor orbits. A detailed classification of the orbits is made according to quality. The distribution of 1/a in precise orbits is multimodal with two broad maxima approximately centered on 0.05 and 0.40 $(AU)^{-1}$. Minima in the distribution appear near 0.20 and 0.66 $(AU)^{-1}$ corresponding to Jupiter's and Mars' position in the 1/a diagram. Considerable fine structure appears in the 1/a distribution. Resonance gaps corresponding to commensurabilities with Jupiter are detected. The gaps are similar to the well studied Kirkwood gaps in the asteroid belt.

DURING THE LAST 20 TO 30 YEARS photographic double-station programs have provided detailed information about radiants and orbits of individual meteors. The number of individual orbits listed in the photographic catalogues is about 3600, or if only precisely reduced orbits are considered about 1800. The number of precisely reduced photographic meteor orbits is thus now comparable to the number of asteroid and comet orbits.

The purpose of the present investigation is to study the frequency distribution of the reciprocal of the semi-major axis of precisely reduced meteor orbits and in particular to look for fine structure in the distribution.

OBSERVATION MATERIAL

The study includes the majority of precisely reduced photographic two station orbits published to date. In all 1822 meteor orbits, comprising 1218 meteors recorded in the Harvard meteor program and 604 recorded in the Dushanbe and Odessa programs, are used.

The methods used in the Harvard program for obtaining the meteor path, velocity and orbit from the segmented trials on the photographic plates, are described in detail in Whipple and Jacchia (1957) and Hawkins (1957). Descriptions of the Dushanbe reductional program are given by Katasev (1957) and Babadjanov and Kramer (1963).

The survey included 139 small-camera meteor orbits published by Whipple (1954), 413 Super-Schmidt meteor orbits listed by Jacchia and Whipple (1961), 313 Super-Schmidt meteor orbits listed by Hawkins and Southworth (1961) and 352 Super-Schmidt meteor orbits listed by Posen and McCrosky (1967). Of the published 144 small-camera orbits, five were excluded because of incomplete data. Of the 360 orbits in the Hawkins and Southworth random samples of Super-Schmidt meteors 47 are excluded since they are already in the 413 orbits listed by Jacchia and Whipple. The total number of Harvard orbits used in the analysis was 1218. The fireball orbits published by McCrosky (1967), were not used in this study, since the fireball data represent a selection of extremely bright objects and their orbits (semi-major axis) are

probably influenced by observational bias (Kresák, 1970).

The survey further included 73 small-camera orbits listed by Katasev (1957), 225 orbits recorded at Odessa and listed by Babadjanov and Kramer (1963, 1967) and 330 orbits recorded at Dushanbe and published by Babadjanov and Kramer (1963, 1967) and Babadjanov et al. (1969). Of the 73 meteors published by Katasev 24 are excluded because of incomplete data. The total number of USSR orbits available in the study was 604.

The data sample used in the present investigation differs from that of a previous study (Lindblad, 1971a) in the following minor respects: (1) a few hyperbolic meteors which were omitted in the first study have now been included; (2) an additional 77 Dushanbe orbits have been included in the analysis; (3) a total of 100 fireball orbits have been excluded.

DATA CLASSIFICATION AND PREPARATION

Classification on the Basis of Quality

Because of the necessity to select orbits of very high precision we have assigned to each meteor orbit a degree of reliability. This index of orbital accuracy was obtained as follows.

Whipple (1954) and Jacchia and Whipple (1961) assign to each individual orbit a quality class. Whipple classified the small-camera meteor orbits as of quality A, A−, B and C. Only orbits marked A and A− were assigned by us to the high accuracy group. Jacchia and Whipple list the Super-Schmidt orbits as of quality 1.0, 1.5, . . ., 4.0. Classes 1.0, 1.5 and 2.0 were assigned to the high accuracy group. Hawkins and Southworth (1961) do not give a quality index but in Hawkins and Southworth (1958) they list the standard deviation Δv_∞ of the extrapolated extra-atmosphere velocity v_∞. This quantity is directly related to the observational error in $1/a$, and was therefore used by us as a quality index. Only orbits for which $\Delta v_\infty \leqslant 0.1$ km/s were assigned to the high precision group. Posen and McCrosky (1967) do not give a quality index but list the number of segments measured on each individual meteor trail. Trails with 20 or more measured segments were assigned by us to the high precision group.

In the Odessa and Dushanbe catalogues no direct quality index is given. The catalogues, however, list the quantity sin Q, where Q is the angle between the apparent great circles of motions as seen from the two observing stations. Only orbits with sin $Q \geq 0.40$ were assigned by us to the high accuracy group. This index of quality is particularly appropriate for the Dushanbe orbits, since a number of these were collected using a very short base line between the two observing stations (Stohl, 1970).

The number of orbits assigned to the high and low accuracy groups are 755 and 1067, respectively. Thus slightly less than half of the data sample (41 percent) falls into the high accuracy group.

Computer Program

Orbital elements and other relevant data for each meteor were available on cards. The reciprocal of the semi-major axis, $1/a$, was computed to 0.0001 $(AU)^{-1}$. The program prepared histograms of $1/a$, in class intervals of 0.0050 $(AU)^{-1}$. The program further prepared a smoothed distribution of the data and then compared this distribution with the observed one in order to obtain a chi-square test of significance.

DISTRIBUTION OF RECIPROCAL SEMI-MAJOR AXIS

The frequency distribution of reciprocal semi-major axis $1/a$ of the high accuracy and low accuracy samples are compared in figure 1. Shower meteors, representing about 50 percent of the data, are included in both diagrams. No correction for observational selection (cosmic weight) has been applied to the data.

Figure 1 shows for the more accurate orbits a multimodal distribution. Two broad maxima, corresponding to the long period and short period orbits, respectively, are approximately centered on 0.05 and 0.40 $(AU)^{-1}$, while a third, less pronounced maximum is centered on about 0.71 $(AU)^{-1}$. The paucity of orbits near $1/a = 0.20$ is clearly related to Jupiter's position in the diagram. We note that this minimum is not very pronounced in the low accuracy sample, indicating that precision orbits are necessary in order to resolve details of the $1/a$ distribution.

The main maximum in the distribution of $1/a$

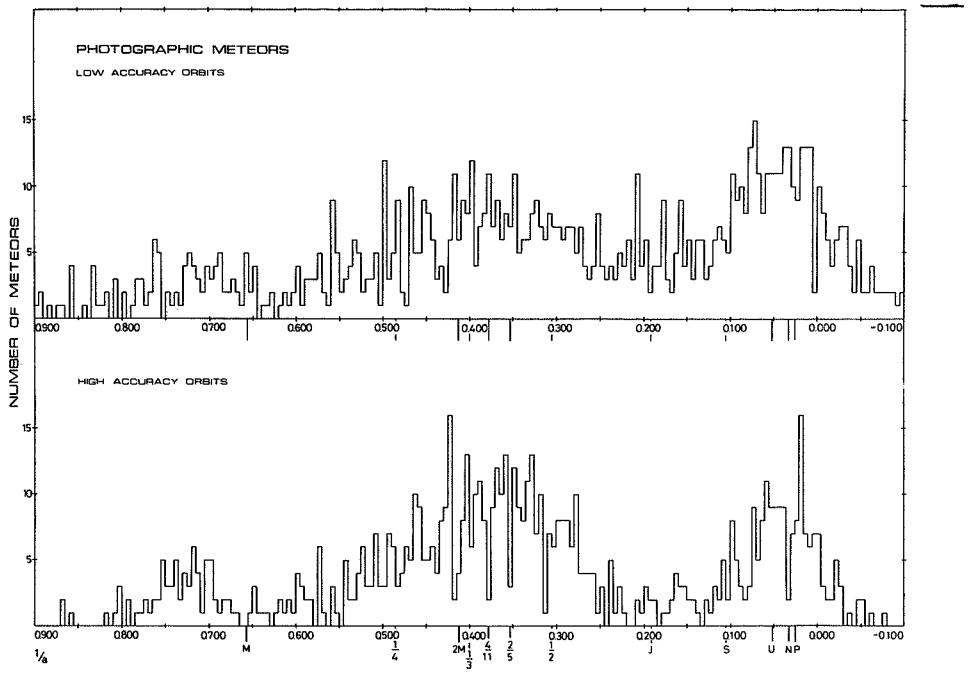

FIGURE 1.—Distribution of photographic meteor orbits in reciprocal semi-major axis in intervals of 0.0050 AU^{-1}.

coincides rather closely with the corresponding distribution for asteroids. If only accurate orbits in the interval 0.20–0.55 $(AU)^{-1}$ are considered the mean reciprocal semi-major axis of short period meteor orbits is 0.404 $(AU)^{-1}$. This value is surprisingly similar to the corresponding value 0.366 $(AU)^{-1}$ deduced from the numbered asteroid population. We interpret this result as indicating that the orbital distribution of minor objects in the solar system is to a large extent determined by the perturbational effects of Jupiter.

The second maximum, corresponding to long period meteor orbits, includes a number of stream meteors in retrograde orbits (Perseids, Orionids, etc.). It, however, also includes a surprisingly large number of sporadic meteors in both direct and retrograde orbits.

About 5 percent of the accurate orbits are hyperbolic. The number of hyperbolic orbits in the accurate Harvard and USSR samples, are 16 and 19 respectively. As may be seen from figure 1 most of these orbits are very near to the hyperbolic limit. In the less accurate data sample 14 percent of the orbits are hyperbolic. (A number of hyperbolic orbits are outside the range of the diagram.) The larger percentage of hyperbolic orbits in the low accuracy sample is evidence that the majority of hyperbolic orbits are the result of measuring errors.

Stream Orbits vs Sporadic Orbits

The above data analysis has been performed regardless of the stream—or sporadic—character of the individual meteor orbits. In a further study the sample was subdivided into a stream and a sporadic component using the D-criterion proposed by Southworth and Hawkins (1963). This computer method provides an impersonal means of separating sporadic and shower meteors. It is known to give very reliable results in photographic data samples (Lindblad, 1971b). The computer search was undertaken at the rejection level $D_s = 0.13$.

The $1/a$ distribution for stream and sporadic meteors, respectively, are compared in figure 2. Only accurate orbits are included in the diagram.

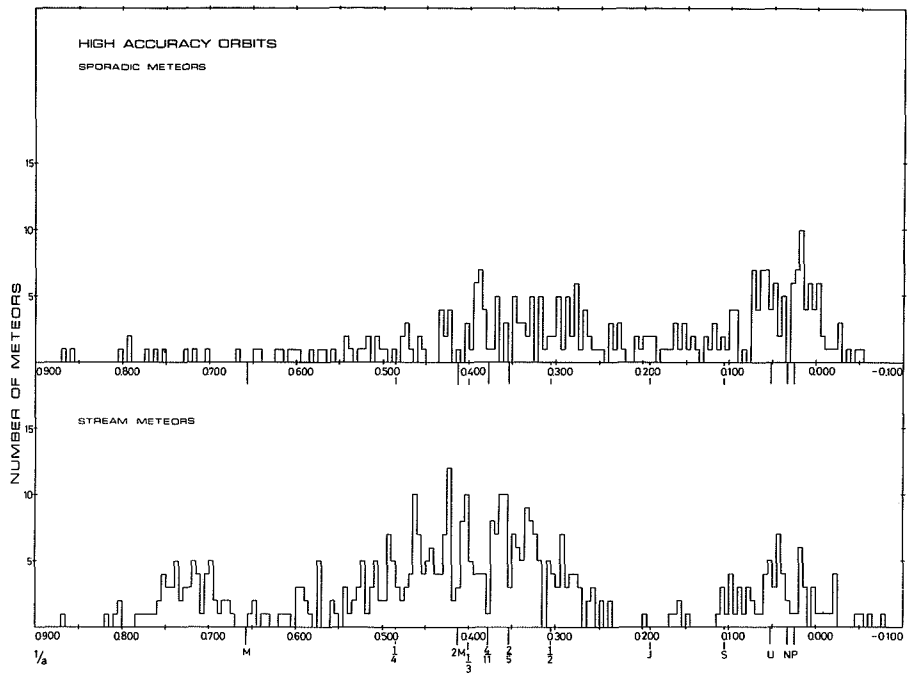

FIGURE 2.—Distribution of meteor orbits in reciprocal semi-major axis in intervals of 0.0050 AU^{-1}. Accurate orbits only.

Noticeable differences exist between the two distributions. It is observed that the separation between short period and long period orbits is more pronounced in the stream component. The grouping of orbits between 0.67 and 0.77 $(AU)^{-1}$ in the stream sample is missing in the sporadic sample. Inspection of the data showed that this maximum was ascribable to the Geminid stream. It should hence not be considered as an intrinsic property of the $1/a$-distribution.

It is interesting to speculate on the different $1/a$ distributions for stream and sporadic meteors. If the Geminids are excluded one could perhaps consider the sporadic meteor histogram as an error-dispersed version of the stream histogram. The sporadic meteors may be of greater age and are thus more gravitationally perturbed than stream meteors. It is, however, difficult to understand how any meteors can exist for any length of time in an orbit with an $1/a$ value near to Jupiter's value.

The large number of long period sporadic orbits could be indicative of a reservoir of non-stream meteors in the outer parts of the solar system. A significant fraction of the sporadic meteors may be of considerable age and may have an evolutionary history different from that of the stream meteors. This question deserves further detailed study.

Direct vs Retrograde Orbits

Direct and retrograde orbits of stream meteors are compared in figure 3. Again, only accurate orbits are included. Inspection of the diagram indicates that two types of stream meteors are predominant in the data samples; stream meteors having $1/a > 0.20$ and moving in direct orbits, stream meteors having $1/a < 0.20$ and moving in retrograde orbits. It is observed that there are practically no stream meteors moving in short period, retrograde orbits, and only very few moving in long-period, direct orbits.

A similar study of the non-stream meteor group, figure 4, indicated a somewhat more dispersed system. The two groups mentioned above are present in the diagram but in addition

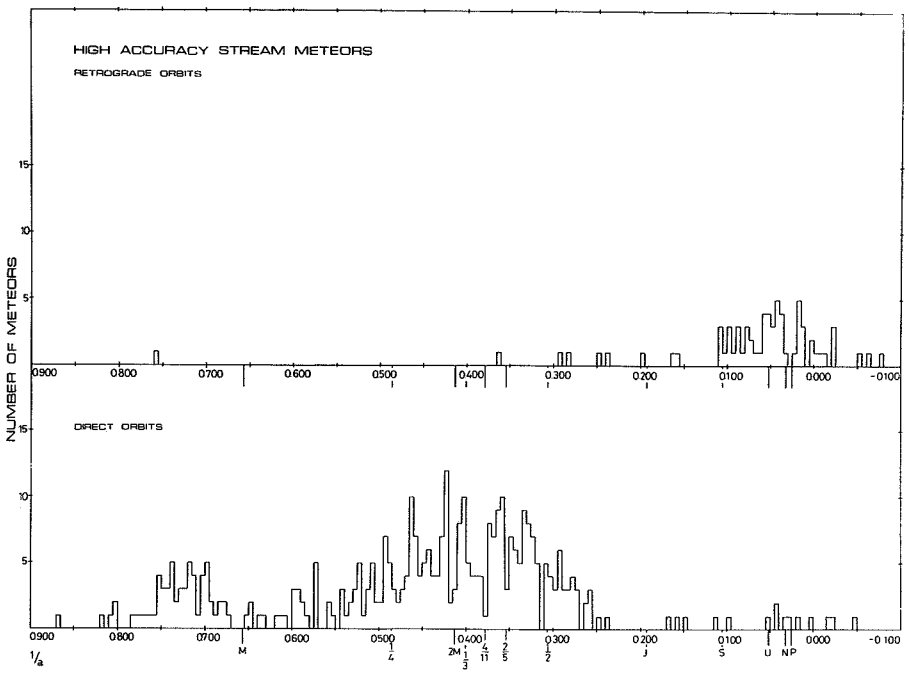

FIGURE 3.—Distribution of meteor orbits in reciprocal semi-major axis in intervals of 0.0050 AU^{-1}. Accurate stream orbits only.

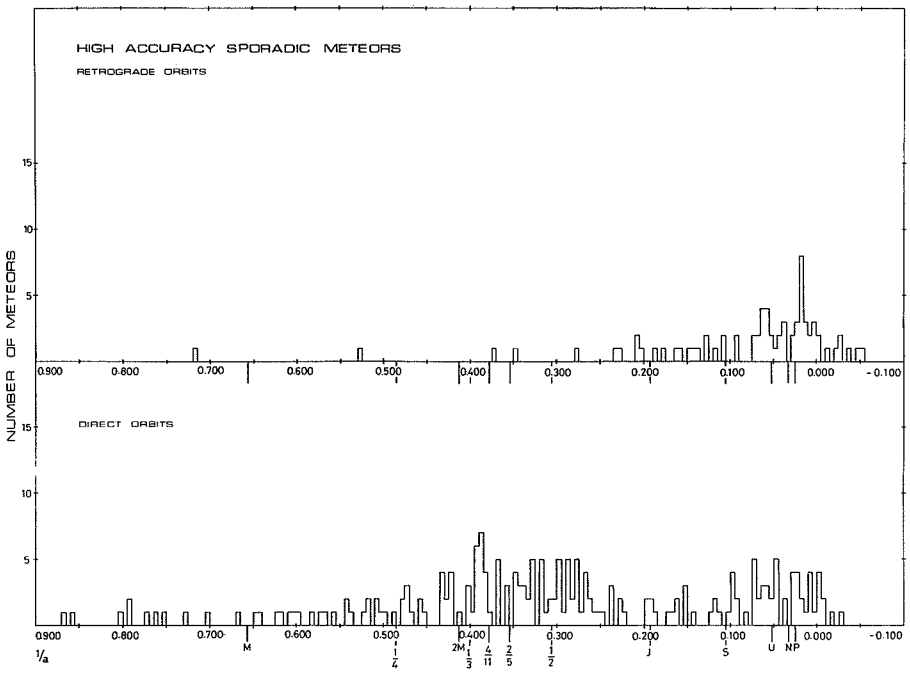

FIGURE 4.—Distribution of meteor orbits in reciprocal semi-major axis in intervals of 0.0050 AU^{-1}. Accurate sporadic orbits only.

a number of sporadic meteors moving in long period, direct orbits are observed.

If it is assumed that stream meteors are the disintegration products of comets, the two types of stream meteors (fig. 3) can be explained as associated with short period comets in direct orbits and long period comets in retrograde orbits, respectively. The reason why very few stream meteors are observed in direct, long-period orbits is, however, not at all clear. In this category we find streams such as the Lyrids, Ursids, and Monocerotids, all associated with well known comets moving in long-period, direct orbits. It is possible, but not very likely, that these particular streams may be under-represented in the data sample studied.

FINE STRUCTURE OF $1/a$-DISTRIBUTION

The histograms, figures 1 to 4, depict the frequency distribution of reciprocal semi-major axis $1/a$ in intervals of 0.0050 $(AU)^{-1}$. It will be noticed that there is considerable fine structure in the distributions. The question naturally arises whether this structure is accidental, or if it is found to be significant, what is the cause of this structure.

Kirkwood Gaps

In the $1/a$-distribution of accurate orbits, figure 1, deep minima or gaps are located at 0.305 to 0.315, 0.350 to 0.355, 0.375 to 0.380 and 0.395 to 0.400. These minima correspond to orbital periods of $\frac{1}{2}$, $\frac{2}{5}$, $\frac{4}{11}$ and $\frac{1}{3}$ respectively of Jupiter's orbital period. The $\frac{1}{2}$ gap appears to be slightly displaced. A minimum at 0.410–0.420 corresponds to twice the orbital period of Mars. Additional, but less pronounced minima occur at 0.320 to 0.325, 0.335 to 0.340 and 0.360 to 0.365 corresponding to $\frac{5}{11}$, $\frac{3}{7}$ and $\frac{5}{13}$ of Jupiter's orbital period. Knees at 0.270 to 0.275 and 0.425 to 0.430 could indicate the $\frac{3}{5}$ and $\frac{3}{10}$ resonance gaps.

The observed fine structure is thus related to the orbital period of Jupiter, with few meteors having values of $1/a$ corresponding to commensurabilities with Jupiter. The phenomena is thus of a similar nature as the Kirkwood gaps in the asteroidal belt. The discovery of Kirkwood gaps in the meteor population indicates that the time scale necessary to produce resonance effects of this type in the solar system is very short.

The question arises whether the observed gap structure could be produced by several well defined meteor streams of small scatter in $1/a$. An investigation of the major meteor streams in our sample showed that the standard deviation of $1/a$ in a stream is of the order of 0.10 $(AU)^{-1}$. Hence, the internal scatter within a stream is almost an order of magnitude larger than the spacing between the observed maxima and minima. That corresponding minima exist also in the sporadic meteor background may be inferred by direct inspection. From figure 2 it is seen that the $\frac{1}{2}$, $\frac{2}{5}$, $\frac{4}{11}$, $\frac{1}{3}$ and $2\times$ Mars minima may be easily identified.

Tests of Statistical Significance

The statistical significance of the observed fine structure was tested with the chi-square test. Histograms of $1/a$ in class intervals of 0.0050 $(AU)^{-1}$ were taken as the observed distributions. A smoothed distribution was next constructed by using a running mean of 11 class intervals. This distribution was considered as the hypothetical or "true" distribution. For various parts of the observed distribution the probability that the observed gaps could have occurred by chance was calculated with the help of the chi-square test.

For the interval 0.30 to 0.40 $(AU)^{-1}$ the chi-square test gives a 10 percent probability that the observed gap structure is accidental. This interval includes the $\frac{1}{2}$, $\frac{2}{5}$, $\frac{4}{11}$ and $\frac{1}{3}$ Jupiter resonance minima. In the interval 0.40 to 0.45 $(AU)^{-1}$ the probability of an accidental occurrence was less than 1 percent. For the entire range 0.30 to 0.45 the probability of an accidental occurrence of the gaps is about 0.5 percent.

It should, however, be observed that the significance problem answered by the chi-square test is one of testing if an observed series of maxima and minima are significant, without regard to the actual positioning of the maxima and minima. In the present problem the positions of the minima may be specified in advance to certain multiples of the orbital period of Jupiter (and Mars). The detection of a series of gaps at the

predicted positions is thus of higher statistical significance than indicated by the chi-square test.

Velocity Errors

In order to obtain $1/a$ with an accuracy of 0.005 $(AU)^{-1}$ meteor orbits with an accuracy in heliocentric velocity of 0.06 km/s or about 0.16 percent (for $v_H = 38$ km/s) are needed. This corresponds to an error of about 0.3 percent in semi-major axis. The 1218 Harvard orbits, on which this study is mainly based, are given to 0.01 km/s in geocentric and heliocentric velocity and to 0.001 AU in semi-major axis a. It is evident that the real errors are somewhat larger. For the better half of the data sample the velocity error is probably 0.04–0.05 km/s. The velocity errors are thus just at the limit of what is acceptable for the purpose of the present study.

Sampling Procedure

For about 15 percent of the accurate orbits the semi-major axis a is only given to three digits, in which case spurious gaps in the 1/a-distribution could appear because of the smallness of the sampling interval. A series of computer runs in synthetic distributions showed that this effect was negligible.

As a further check on the consistency of the data the mean motions μ were computed for all meteors, and histograms of μ were plotted. The same gaps as above were detected and tested for statistical significance. Very nearly the same chi-square probabilities were derived.

REFERENCES

Babadjanov, P. B., Getman, T. I., Zauseyev, A. F., and Karaselnikova, S. A., 1969. Orbits of 77 photographic meteors, *Bull. Inst. Astrofys. Akad. Nauk Tadjikistan*, Dushanbe, no. 49, 3–12.

Babadjanov, P. B., and Kramer, E. N., 1963. Methods and some results of photographic researches of meteors. *Results of Researches on the Program of the International Geophysical Year, Ionosphere and Meteors*, No. 12, Moscow, Publ. House, Academy of Sciences, USSR.

Babadjanov, P. B., and Kramer, E. N., 1967. Orbits of bright photographic meteors, *Smithson. Contrib. Astrophys.*, **11**, 67–80.

Hawkins, G. S., 1957. The method of reduction of short-trail meteors, *Smithson. Contrib. Astrophys.*, **1**, 207–214.

Hawkins, G. S., and Southworth, R. B., 1958. Statistics of meteors in the Earth's atmosphere, *Smithson. Contrib. Astrophys.*, **2**, 349–364.

——, 1961. Orbital elements of meteors, *Smithson. Contrib. Astrophys.*, **4**, 85–95.

Jacchia, L. G., and Whipple, F. L., 1961. Precision orbits of 413 photographic meteors, *Smithson. Contrib. Astrophys.*, **4**, 97–129.

Katasev, L. A., 1957. *Photographic methods in meteor astronomy*, Moscow, State Publ. House of Technical Literature (Engl. trans. Monson Press, Jerusalem, 1964).

Kresák, Ľ., 1970. On the orbits of bright fireballs, *Bull. Astron. Inst. Czech.*, **21**, 1–9.

Lindblad, B. -A., 1971a. Meteor streams, in *Space Research XI*, 287–297.

——, 1971b. A computer stream search among 2401 photographic meteor orbits, *Smithson. Contrib. Astrophys.*, **12**, 14–24.

McCrosky, R. E., 1967. Orbits of photographic meteors, *Smithson. Astrophys. Obs. Spec. Rept.* No. 252.

Posen, A., and McCrosky, R. E., 1967. Private communication.

Southworth, R. B., and Hawkins, G. S., 1963. Statistics of meteor streams, *Smithson. Contrib. Astrophys.*, **7**, 261–285.

Stohl, J., 1970. On the problem of hyperbolic meteors, *Bull. Astron. Inst. Czech.*, **21**, 10–17.

Whipple, F. L., 1954. Photographic meteor orbits and their distribution in space, *Astron. J.*, **59**, 201–217.

Whipple, F. L., and Jacchia, L. G., 1957. Reduction methods for photographic meteor trails, *Smithson. Contrib. Astrophys.*, **1**, 183–206.

Page intentionally left blank

17. A Working List of Meteor Streams

ALLAN F. COOK
Smithsonian Astrophysical Observatory
Cambridge, Massachusetts

THIS WORKING LIST which starts on the next page has been compiled from the following sources:

(1) A selection by myself (Cook, 1973) from a list by Lindblad (1971a), which he found from a computer search among 2401 orbits of meteors photographed by the Harvard Super-Schmidt cameras in New Mexico (McCrosky and Posen, 1961)

(2) Five additional radiants found by McCrosky and Posen (1959) by a visual search among the radiants and velocities of the same 2401 meteors

(3) A further visual search among these radiants and velocities by Cook, Lindblad, Marsden, McCrosky, and Posen (1973)

(4) A computer search by Lindblad (1971b) among 1827 precisely reduced photographed meteors from all available sources

(5) Visual radiants reported by Hoffmeister (1948)

(6) A report on the Phoenicid shower of December 5, 1956, by Ridley (1962)

(7) A list of visual radiants by McIntosh (1935)

(8) A report on the June Lyrids by Hindley (1969)

(9) Two papers on radar radiants in the southern sky by Weiss (1960a, b)

(10) A paper on radar radiants in the southern hemisphere by Nilsson (1964)

(11) Several compilations of visual, photographic, and radar radiants by Whipple and Hawkins (1959), McKinley (1961), Millman and McKinley (1963), and Jacchia (1963)

This list is restricted to streams that the author is convinced do exist. It is perhaps still too comprehensive in that there are six streams with activity near the threshold of detection by photography not related to any known comet and not shown to be active for as long as a decade. Unless activity can be confirmed in earlier or later years or unless an associated comet appears, these streams should probably be dropped from a later version of this list. The author will be much more receptive to suggestions for deletions from this list than he will be to suggestions for additions to it. Clear evidence that the threshold for visual detection of a stream has been passed (as in the case of the June Lyrids) should qualify it for permanent inclusion.

A comment on the matching sets of orbits is in order. It is the directions of perihelion that should match, a condition clearly met in most cases:

(1) April Lyrids and Comet 1861 I Thatcher
(2) η Aquarids, Orionids, and P/Comet Halley
(3) τ Herculids and Comet 1930 VI Schwassmann-Wachmann 3
(4) Daytime β Taurids, Southern Taurids, Northern Taurids, and P/Comet Encke
(5) June Boötids and P/Comet Pons-Winnecke 1915 III
(6) o Draconids and Comet 1919 V Metcalf
(7) Southern and Northern ι Aquarids
(8) Perseids and Comet 1862 III Swift-Tuttle
(9) Aurigids and Comet 1911 II Kiess
(10) Daytime Sextantids and Geminids
(11) Annual Andromedids and the predicted orbit of P/Comet Biela for 1972
(12) Andromedids and P/Comet Biela 1852 III

I.—*Working List of Meteor Streams*

Name	Dates[a]	Max.	Longitude of Sun (1950)					Geocentric radiant			
			Beginning (deg)	Half max. (deg)	Max. (deg)	Half max. (deg)	End (deg)	R.A. 1950 (deg)	Decl. 1950 (deg)	Velocity (km s^{-1})	Sun (deg)
Quadrantids	Jan. 1–4	Jan. 3	280.8	282.5	282.7	282.9	283.4	230.1	+48.5	41.5	282.7
δ Cancrids	Jan. 13–21	Jan. 16	293		296		301	126	+20	28	296
Virginids	Feb. 3–Apr. 15		314				25	186	0	35	350
δ Leonids	Feb. 5–Mar. 19	Feb. 26	316		338		359	159	+19	23	338
Camelopardalids	Mar. 14–Apr. 7		353				17	118.7	+68.3	6.8	359.0
σ Leonids	Mar. 21–May 13	Apr. 17	1		27		52	195	− 5	20	28
δ Draconids	Mar. 28–Apr. 17		7				27	281	+68	26.7	14
κ Serpentids	Apr. 1–7		11				17	230	+18	45	14
μ Virginids	Apr. 1–May 12	Apr. 25	12		35		51	221	− 5	29	35
α Scorpiids	Apr. 11–May 12	May 3	21		42		51	240	−22	35	42
α Boötids	Apr. 14–May 12	Apr. 28	24		36		51	218	+19	20	36
φ Boötids	Apr. 16–May 12	May 1	26		40		51	240	+51	12	40
April Lyrids	Apr. 20–23	Apr. 22	30.7	31.2	31.7	32.2	32.7	271.4	+33.6	47.6	31.7
η Aquarids	Apr. 21–May 12	May 3	30	39	42.4	45	51	335.6	− 1.9	65.5	42.4
τ Herculids	May 19–June 14	June 3	58		72		83	228	+39	15	72
χ Scorpiids	May 27–June 20	June 5	65		74		89	247	−13	21	74
Daytime Arietids	May 29–June 19	June 7	67	71	76	83	88	44	+23	37	77
Daytime ζ Perseids	June 1–17	June 7	70	72	76	83	86	62	+23	27	78
Librids	June 8–9, 1937	June 8	77.6		78.2		78.4+	227.2	−28.3	16±2	78.2
Sagittariids	June 8–16, 1957–8	June 11	77		80		82	304	−35	52	80
θ Ophiuchids	June 8–16	June 13	77		82		85	267	−28	26.7	82
June Lyrids	June 11–21, 1969	June 16	79	81	84.5	87.5	90	278	+35	31±3	84.5
Daytime β Taurids	June 24–July 6	June 29	91	93	96	99	103	86	+19	30	96
Corvids	June 25–30, 1937	June 26	94.8	94.9	95.2	97.6	97.9	191.9	−19.1	10±2	95.9
June Boötids	June 28, 1916	June 28	97.5		97.6		97.7	219	+49	13.9	98
July Phoenicids	July 3–18	July 14	101		112		116	31.1	−47.9	47±3	109.6
o Draconids	July 7–24	July 16	104				121	271	+59	23.6	113
Northern δ Aquarids	July 14–Aug. 25	Aug. 12	111		139		152	339	− 5	42.3	139
Southern δ Aquarids	July 21–Aug. 29	July 29	118	121	125	129	155	333.1	−16.5	41.4	125.0
α Capricornids	July 15–Aug. 10	July 30	123		126		138	307	−10	22.8	127
Southern ι Aquarids	July 15–Aug. 25	Aug. 5	112		131		151	333.3	−14.7	33.8	131.0
Northern ι Aquarids	July 15–Sept. 20	Aug. 20	112		147		177	327	− 6	31.2	147
Perseids	July 23–Aug. 23	Aug. 12	120	138	139	141	150	46.2	+57.4	59.4	139.0
κ Cygnids	Aug. 9–Oct. 6	Aug. 18	136		145		193	286	+59	24.8	145
Southern Piscids	Aug. 31–Nov. 2	Sept. 20	158		177		219	6	0	26.3	177
Northern Piscids	Sept. 25–Oct. 19	Oct. 12	182		199		206	26	+14	29	199
Aurigids	Sept. 1, 1935	Sept. 1			157.9			84.6	+42.0	66.3	157.9
κ Aquarids	Sept. 11–28	Sept. 21	168		178		184	338	− 5	16.0	178
Southern Taurids	Sept. 15–Nov. 26	Nov. 3	172		220		244	50.5	+13.6	27.0	220.0

I.—*Working List of Meteor Streams*—Continued

Name	Dates[a]	Max.	Longitude of Sun (1950)					Geocentric radiant			
			Beginning (deg)	Half max. (deg)	Max. (deg)	Half max. (deg)	End (deg)	R.A. 1950 (deg)	Decl. 1950 (deg)	Velocity (km s^{-1})	Sun (deg)
Northern Taurids	Sept. 19–Dec. 1	Nov. 13	176	206	230	240	249	58.3	+22.3	29.2	230.0
Daytime Sextantids	Sept. 24–Oct. 5	Sept. 29	179		184		190	152	0	32.2	183.6
Annual Andromedids	Sept. 25–Nov. 12	Oct. 3	182	184	190	195	230	5	+ 8	23.2	190
								20	+34	18.2	228
Andromedids	Nov. 27, 1885	Nov. 27	246.6	246.65	246.7	246.75	246.8	25	+44	16.5	247
Orionids	Oct. 2–Nov. 7	Oct. 21	189	206.7	207.7	208.3	225	94.5	+15.8	66.4	208.0
October Draconids	Oct. 9	Oct. 9	196.25		196.3		196.35	262.1	+54.1	20.43	196.3
ϵ Geminids	Oct. 14–27	Oct. 19	201		206		214	104	+27	69.4	209
Leo Minorids	Oct. 22–24	Oct. 24	209		211		211	162	+37	61.8	211
Pegasids	Oct. 29–Nov. 12	Nov. 12	215		230		230	335	+21	11.2	230
Leonids	Nov. 14–20	Nov. 17	231	234.447	234.462	234.477	237	152.3	+22.2	70.7	234.5
Monocerotids	Nov. 27–Dec. 17	Dec. 10	245		258		265	99.8	+14.0	42.4	257.6
σ Hydrids	Dec. 3–15	Dec. 11	251		259		263	126.6	+ 1.6	58.4	259.0
Northern χ Orionids	Dec. 4–15	Dec. 10	252		258		261	84	+26	25.2	258
Southern χ Orionids	Dec. 7–14	Dec. 11	255		259		262	85	+16	25.5	259
Geminids	Dec. 4–16	Dec. 14	252	260.6	261.7	262.1	264.2	112.3	+32.5	34.4	261.0
December Phoenicids	Dec. 5, 1956	Dec. 5	253.18	253.45	253.55	253.65	253.70	15	−55	21.7	253
								15	−45	11.7	254
δ Arietids	Dec. 8–14		256				262	52	+22	13.2	257.6
Coma Berenicids	Dec. 12–Jan. 23		260				303	175	+25	65	282
Ursids	Dec. 17–24	Dec. 22	265	269	270	271	272	217.06	+75.85	33.4	270.66

[a] Unless otherwise indicated, all calendar dates are for the year 1950.

II.—*Working List of Meteor Streams*

Name	Daily motion of radiant		Number in sample of McCrosky and Posen (1961)	Maximum visual zenithal rate (hr^{-1})	Maximum radar echo rate (hr^{-1})
	R.A. (deg)	Decl. (deg)			
Quadrantids			17	140	
δ Cancrids			7		
Virginids	+0.81	−0.33	6		
δ Leonids	+0.75	−0.50	24		
Camelopardalids	+1.35	+0.51	4		
σ Leonids	+0.44	+0.11	19		
δ Draconids			4		

Name	Daily motion of radiant		Number in sample of McCrosky and Posen (1961)	Maximum visual zenithal rate (hr^{-1})	Maximum radar echo rate (hr^{-1})
	R.A. (deg)	Decl. (deg)			
κ Serpentids			4		
μ Virginids	+0.53	−0.30	7		
α Scorpiids	+0.50	−0.19	5		
α Boötids	+0.7	+0.2	8		
ϕ Boötids			6		
April Lyrids	+1.1	0.0	5	12 96(1922)	
η Aquarids	+0.9	+0.4	7	30	
τ Herculids	−0.1	+0.9	14		
χ Scorpiids	+0.9	+0.5	11		
Daytime Arietids	+0.7	+0.6			60
Daytime ζ Perseids	+1.1	+0.4			40
Librids				10(1937)	
Sagittariids					30
θ Ophiuchids			4	2	
June Lyrids				9	
Daytime β Taurids	+0.8	+0.4			30
Corvids				13(1937)	
June Boötids				100(1916)	
July Phoenicids	+1.04	+0.53			30
o Draconids			3		
Northern δ Aquarids	+1.0	+0.2	9	20	
Southern δ Aquarids	+0.80	+0.18	13	30	
α Capricornids	+0.9	+0.3	21	30	
Southern ι Aquarids	+1.07	+0.18	12	15	
Northern ι Aquarids	+1.03	+0.13	3	15	
Perseids	+1.35	+0.12	45	70	
κ Cygnids	0.0	0.0	8	5	
Southern Piscids			14		
Northern Piscids			9		
Aurigids				30	
κ Aquarids			5		
Southern Taurids	+0.79	+0.15	46	7	
Northern Taurids	+0.76	+0.10	45	<7	
Daytime Sextantids					30
Annual Andromedids	+0.38	+0.66	23		
Andromedids				13 000(1885)	
Orionids	+1.23	+0.13		30	
October Draconids			2	30 000(1933)	
ϵ Geminids	+0.7	0.0	7		
Leo Minorids			3		
Pegasids			6		
Leonids	+0.70	−0.42	5	14 000(1833)	
Monocerotids			3		
σ Hydrids	+0.7	−0.2	8		
Northern χ Orionids			4		
Southern χ Orionids			8		
Geminids	+1.02	−0.07	77	70	
December Phoenicids				100	20
δ Arietids			7		
Coma Berenicids	+0.88	−0.45	11		
Ursids				20 110(1945)	

III.—*Working List of Meteor Streams*

Name	Orbital elements						
	a	e	q	ω (deg)	Ω (deg)	ι (deg)	π (deg)
Quadrantids	3.08	0.683	0.977	170.0	282.7	72.5	92.8
δ Cancrids	2.3	0.80	0.45	283	296	0	219
Virginids	2.63	0.90	0.26	304	350	3	294
δ Leonids	2.62	0.75	0.64	259	338	6	237
Camelopardalids	1.534	0.352	0.974	185.0	359.0	8.2	184.0
σ Leonids	2.35	0.66	0.75	248	28	1	276
δ Draconids	2.770	0.640	0.996	171.1	13.7	37.5	184.8
κ Serpentids	∞	1.00	0.45	275	14	64	289
μ Virginids	3.12	0.83	0.48	280	35	10	315
α Scorpiids	2.15	0.90	0.21	134	222	3	356
α Boötids	2.65	0.71	0.75	247	36	18	283
ϕ Boötids	1.25	0.24	0.95	226	40	19	266
April Lyrids	28	0.968	0.919	214.3	31.7	79.0	246.0
Comet 1861 I	55.7	0.983	0.921	213.4	31.2	79.8	244.6
η Aquarids	13	0.958	0.560	95.2	42.4	163.5	137.6
Orionids	15.1	0.962	0.571	82.5	28.0	163.9	110.5
P/Comet Halley 1835 III	18.0	0.967	0.587	110.7	56.8	162.3	167.5
τ Herculids	2.70	0.63	0.97	204	72	19	276
Comet 1930 VI	3.09	0.673	1.011	192.3	77.1	17.4	269.4
χ Scorpiids	3.11	0.77	0.68	257	74	6	331
Daytime Arietids	1.6	0.94	0.09	29	77	21	106
Northern δ Aquarids	2.62	0.97	0.07	332	139	20	111
Southern δ Aquarids	2.86	0.976	0.069	152.8	305.0	27.2	97.8
Daytime ζ Perseids	1.6	0.79	0.34	59	78	0	137
Southern Piscids	2.33	0.82	0.42	107	357	2	104
Northern Piscids	2.06	0.80	0.40	291	199	3	130
Librids	2.5/10	0.65/0.92	0.88/0.85	46/49	258.2	4/5	305/308
Sagittariids	∞	1.00	0.10	142	260	99	42
θ Ophiuchids	2.90	0.84	0.46	101	262	4	4
June Lyrids	2.5/10	0.67/0.92	0.83/0.84	237/231	84.5	44/50	321/315
Daytime β Taurids	2.2	0.85	0.34	246	276.4	6	162
Southern Taurids	1.93	0.806	0.375	113.2	40.0	5.2	153.2
Northern Taurids	2.59	0.861	0.359	292.3	230.0	2.4	162.3
P/Comet Encke 1970*l*	2.217	0.847	0.339	185.9	334.2	12.0	160.1
Corvids	2.5/10	0.60/0.90	1.013/1.012	7.6/7.9	274.9	3/4	282.5/282.8
June Boötids	3.27	0.69	1.02	180	98	18	278
P/Comet Pons-Winnecke 1915 III	3.261	0.702	0.971	172.4	99.8	18.3	272.2
July Phoenicids	2.5/∞	0.62/1.00	0.96/0.97	31/24	289.6	82/87	321/313
o Draconids	∞	1.00	1.01	190	113	43	303
Comet 1919 V	∞	1.000	1.115	185.7	121.4	46.4	307.2
α Capricornids	2.53	0.77	0.59	269	127	7	36
Southern ι Aquarids	2.36	0.912	0.208	131.8	311.0	6.9	82.8
Northern ι Aquarids	1.75	0.84	0.26	308	147	5	95
Perseids	28	0.965	0.953	151.5	139.0	113.8	290.5
Comet 1862 III	24.3	0.960	0.963	152.8	138.7	113.6	291.5
κ Cygnids	3.09	0.68	0.99	194	145	38	339
Aurigids	∞	1.000	0.802	121.5	157.9	146.4	279.4
Comet 1911 II	153	0.996	0.684	110.3	158.0	148.4	268.3
κ Aquarids	3.20	0.74	0.81	236	178	2	54

III.—*Working List of Meteor Streams*—Concluded

Name	Orbital elements						
	a	e	q	ω (deg)	Ω (deg)	ι (deg)	π (deg)
Daytime Sextantids	1.25	0.87	0.16	213	3.6	22	217
Geminids	1.36	0.896	0.142	324.3	261.0	23.6	225.3
Annual Andromedids	3.22	0.82	0.58	267	190	4	97
	3.29	0.76	0.79	238	228	12	106
P/Comet Biela (1972)	3.54	0.77	0.82	255	213	8	108
Andromedids	3.53	0.76	0.86	222	247	13	109
P/Comet Biela 1852 III	3.52	0.756	0.861	223.2	247.3	12.6	110.4
October Draconids	3.51	0.717	0.996	171.8	196.3	30.7	8.1
P/Comet Giacobini-Zinner 1946 V	3.51	0.717	0.996	171.8	196.3	30.7	8.1
ϵ Geminids	26.77	0.97	0.77	237	209	173	86
Leo Minorids	58.6	0.99	0.65	106	211	124	317
Comet 1739	∞	1.00	0.674	104.8	210.3	124.3	315.1
Pegasids	3.86	0.75	0.97	196	230	8	65
December Phoenicids	2.96	0.68	0.98	0	73	16	74
	2.96	0.67	0.99	359	74	13	72
Comet 1819 IV	2.96	0.699	0.892	350.2	79.2	9.1	69.4
Leonids	11.5	0.915	0.985	172.5	234.5	162.6	47.0
P/Comet Tempel-Tuttle 1965 IV	10.27	0.904	0.982	172.6	232.4	162.7	45.7
Monocerotids	42	0.997	0.14	135.8	77.6	24.8	213.4
Comet 1917 I	27.65	0.993	0.190	121.3	88.0	32.7	209.6
σ Hydrids	30.0	0.992	0.244	120.7	79.0	125.5	199.8
Northern χ Orionids	2.22	0.79	0.47	281	258	2	179
Southern χ Orionids	2.18	0.78	0.47	101	79	7	180
δ Arietids	2.13	0.605	0.838	232.8	257.6	1.8	130.4
Coma Berenicids	∞	1.00	0.58	258	282	134	180
Ursids	5.70	0.85	0.9389	205.85	270.66	53.6	116.51
P/Comet Tuttle 1939 X	5.70	0.821	1.023	207.0	269.8	54.6	116.8

(13) October Draconids and P/Comet Giacobini-Zinner 1946 V

(14) Leo Minorids and Comet 1739 Zanotti

(15) Pegasids, December Phoenicids, and Comet 1819 IV Blanplain

(16) Leonids and P/Comet Tempel-Tuttle 1965 IV

(17) Monocerotids and Comet 1917 I Mellish

(18) Northern and Southern χ Orionids

(19) Ursids and P/Comet Tuttle

In the case of the Sextantids and the Geminids, the temporary character of the Sextantids and the concentration and strength of the Geminids suggest two parent bodies for the streams. The similarities in the directions of perihelion, distances at perihelion, and semimajor axes then imply that these two parent bodies separated from a common body at an earlier time. In the case of the Pegasids, December Phoenicids, and Comet 1819 IV Blanplain, the strength, concentration, and single apparition of the December Phoenicids suggest that a small comet still exists; the presence of meteors in the orbital plane of the Pegasids suggests that another comet separated long ago from Comet 1819 IV. If we were in the presence of a broad distribution of meteoroids, there would be continuous activity from northern and southern radiants in October, November, and December.

In two cases some serious failure to match occurs. Among the Daytime Arietids, Northern δ Aquarids, and Southern δ Aquarids, it is clear

that the Northern δ Aquarids do not fit and are dubious members of the system; and in the case of the Daytime ζ Perseids, Southern Piscids, and Northern Piscids, it is clear that the Southern Piscids do not fit and are dubious members of the system. The traditional association between the α Capricornids and P/Comet Honda-Mrkos-Pajdušáková is rejected, as the directions of perihelia diverge by nearly 30°.

Of the 57 entries in the list, two are additional radiants associated with P/Comet Encke and six more are associated with another radiant, each in the sense that they appear to come from the same parent body. One of these pairs is the η Aquarids and Orionids associated with P/Comet Halley. Another is the pair of Andromedid radiants, one that of the great showers, the other that of the current weak annual stream matching the current predicted orbit of P/Comet Biela. The remaining four pairs are not associated with a comet; two are pairs of daylight and night showers—the Daytime Arietids with the Southern δ Aquarids and the Daytime ζ Perseids with the Northern Piscids. The remaining two are merely northern and southern branches of the same streams; these two cases are the ι Aquarids and the χ Orionids. Thus, we deal here with 49 separate streams. Two additional pairings appear to be at the level of parent meteoroid-shedding bodies having separated from a larger body at an earlier time. These pairings are the Daytime Sextantids with the Geminids and the Pegasids with the December Phoenicids, which in turn apparently came from Comet 1819 IV Blanplain. It appears that 47 initial parent bodies are required to explain the present list of streams. Some 15 of the 49 currently required parent bodies have been observed as Comets. Two are lost, and P/Comet Biela is perhaps the best target for an effort at recovery. Small asteroids might be searched for along the orbits of the Geminids and Sextantids, and comets might be searched for along the orbits of the highly concentrated Quadrantids, Librids, and Corvids. The other 29 parent objects are associated with weak or diffuse stream systems, so a search for them would be tantamount to a general search of the sky.

The author is grateful for access to B. G. Marsden's (1972) catalog of orbits of comets in advance of publication, and also for the predicted orbit of P/Comet Biela in 1972. This work was supported in part by contract NGR 09–015–033 from the National Aeronautics and Space Administration.

NOTES ON INDIVIDUAL STREAMS

Virginids, σ Leonids, and μ Virginids	These streams are contributors to Hoffmeister's (1948) visual Virginids.
α Scorpiids	This stream is a contributor to Hoffmeister's (1948) Scorpius-Sagittarius system.
April Lyrids	This stream is a weak annual one at the threshold of detection for visual observers but has given stronger displays in 1884 (22 hr^{-1}), 1922 (96 hr^{-1}), and 1948 (20 hr^{-1}).
η Aquarids and Orionids	At this inclination, $\Omega-\omega$ should be compared between orbits, not π. The three values are 307.4°, 305.5°, and 306.2° for the η Aquarids, the Orionids, and P/Comet Halley, respectively.
τ Herculids	Some evidence exists that this stream was detected visually, its radiant being regarded as early activity of the June Boötids (Olivier, 1916; Smith, 1932).
χ Scorpiids	This stream is a contributor to Hoffmeister's (1948) Scorpius-Sagitarrius system.
Librids	This shower was observed only in 1937. Two sets of elements are given to present likely extremes.
Sagittariids	This shower was observed only by radar and only in 1958. It was absent in the years 1952 to 1956.
θ Ophiuchids	This stream is the maximum of Hoffmeister's (1948) Scorpius - Sagittarius system.

June Lyrids	This weak visual stream has appeared only from 1966 onward (Hindley, 1969). Two sets of elements are given to present likely extremes.
Corvids	This shower was observed only in 1937. Two sets of elements are given to present likely extremes. Hoffmeister's Orbit I (1948, p. 122) for $a=2.5$ is incorrect.
June Boötids	This shower was strong only in 1916 (100 hr^{-1}) and showed 6 hr^{-1} in 1921 (Hoffmeister, 1921).
July Phoenicids	This shower was observed only by radar from 1953 through 1958. It does not appear in visual lists, although it should if it is not a recent arrival at the Earth's orbit. Two sets of elements are given to present likely extremes.
α Capricornids	These are Weiss' (1960b) Capricornids. They are not resolvable visually from the Southern δ Aquarids.
Southern ι Aquarids	These are Weiss' (1960b) Piscis Austrinids. They are not resolvable visually from the Southern δ Aquarids.
Northern ι Aquarids	Early on, this shower is not resolvable visually from the Southern δ Aquarids, and in its feeble late stages, it contributes to Hoffmeister's (1948) visual Piscids.
Southern Piscids and Northern Piscids	These streams contribute to Hoffmeister's (1948) visual Piscids.
Aurigids	This shower was strong for 1 hr before morning twilight on one night only.
Southern Taurids and Northern Taurids	These streams cannot be resolved from one another visually.
Annual Andromedids	This stream begins its activity by contributing to Hoffmeister's (1948) visual Piscids and then moves northward toward the radiant of the famous Andromedid showers. Two radiants and sets of elements are given to display the changes during the Earth's passage through the stream.
Andromedids	Strong showers occurred on December 5, 1741; December 7, 1798 (~400 hr^{-1}); December 7, 1830; December 6, 1838 (~100 hr^{-1}); December 6, 1847 (~150 hr^{-1}); November 30, 1867; November 27, 1872; November 27, 1885 (~13,000 hr^{-1}); November 23, 1892 (~300 hr^{-1}); November 24, 1899 (~100 hr^{-1}); November 21, 1904 (~20 hr^{-1}); and November 15, 1940 (~30 hr^{-1}).
October Draconids	Strong showers occurred in 1927 (17 hr^{-1}), 1933 (30 000 hr^{-1}), 1946 (10 000 hr^{-1}), and 1952 (200 hr^{-1}).
Leonids	Strong showers occurred in 1799, 1832, 1833, 1834, 1839, 1866, 1867, 1868, 1898, 1901, 1903, 1961, 1965, 1966, and 1969. In other years, activity was very feeble.
December Phoenicids	This shower appeared only in 1965. The northern radiant is visual; the southern is from radar observations.
Coma Berenicids	The December portion of this stream is called the December Leo Minorids by Cook et al. (1972), but Lindblad (1971b) found bridging meteors that connect the December Leo Minorids to Coma Berenicids in January.

REFERENCES

COOK, A. F., 1973. Discrete levels of beginning height of meteors in streams, *Smithson. Contrib. Astrophys.*, in press.

COOK, A. F., LINDBLAD, B. A., MARSDEN, B. G., MCCROSKY, R. E., AND POSEN, A., 1973. Yet another stream search among 2401 photographic meteors, *Smithson. Contrib. Astrophys.*, in press.

HINDLEY, K. B., 1969. The June Lyrid meteor stream in 1969, *J. Brit. Astron. Assoc.*, **79**, 480–484.

HOFFMEISTER, C., 1921. Die Beobachtung von Meteoren des Winneckeschen Kometen, *Astron. Nachr.*, **215**, 455–466.

——, 1948. *Meteorströme*, Johann Ambrosius Barth, Leipzig.

JACCHIA, L. G., 1963. Meteors, meteorites, and comets: Interrelations, in *The Moon, Meteorites and Comets*, edited by B. M. Middlehurst and G. P. Kuiper, Univ. of Chicago Press, Chicago, 774–798.

LINDBLAD, B. -A., 1971a. A computerized stream search among 2401 photographic meteor orbits, *Smithson. Contrib. Astrophys.*, **12**, 14–24.

——, 1971b. Meteor streams, in *Space Research XI*, 287–297.

MARSDEN, B. G., 1972. *Catalogue of Cometary Orbits*, Smithson. Astrophys. Obs., Cambridge, Mass., 1–70.

MCCROSKY, R. E., AND POSEN, A., 1959. New photographic meteor showers, *Astron. J.*, **64**, 25–27.

MCCROSKY, R. E., AND POSEN, A., 1961. Orbital elements of photographic meteors, *Smithson. Contrib. Astrophys.*, **4**, 15–84.

MCINTOSH, R. A., 1935. An index to southern meteor showers, *Mon. Not. Roy. Astron. Soc.*, **95**, 709–718.

MCKINLEY, D. W. R., 1961. *Meteor Science and Engineering*, McGraw-Hill Book Co., New York, 145–157.

MILLMAN, P. M., AND MCKINLEY, D. W. R., 1963. Meteors, in *The Moon, Meteorites and Comets*, edited by B. M. Middlehurst and G. P. Kuiper, Univ. of Chicago Press, Chicago, 674–773.

NILSSON, C., 1964. A southern hemisphere radio survey of meteor streams, *Australian J. Phys.*, **17**, 205–256.

OLIVIER, C. P., 1916. The meteor system of Pons-Winnecke's comet, *Mon. Not. Roy. Astron. Soc.*, **77**, 71–75.

RIDLEY, H. B., 1962. The Phoenicid meteor shower of 1956 December 5, *J. Brit. Astron. Assoc.*, **72**, 266–272.

SMITH, F. W., 1932. A discussion of meteor orbits connecting with the Pons-Winnecke comet, *Mon. Not. Roy. Astron. Soc.*, **93**, 156–158.

WEISS, A. A., 1960a. Radio-echo observations of southern hemisphere meteor shower activity from 1956 December to 1958 August, *Mon. Not. Roy. Astron. Soc.*, **120**, 387–403.

——, 1960b. Southern hemisphere meteor activity in July and August, *Australian J. Phys.*, **13**, 522–531.

WHIPPLE, F. L., AND HAWKINS, G. S., 1959. Meteors, in *Handbuch der Physik*, Springer-Verlag, Berlin, **52**, 519–564.

Page intentionally left blank

18. Origin and Evolution of Recent Leonid Meteor Showers*

BRUCE A. MCINTOSH
National Research Council of Canada
Ottawa, Ontario

The four most prominent returns of the Leonid shower in the past decade fall into two broad classes. The 1966 and 1969 showers were of short duration, had a high proportion of small particles, and occurred with the longest apparent delay after the perihelion passage of the parent comet Temple-Tuttle. By contrast, the 1961 and 1965 returns were of long duration, and had more large particles. The 1961 return preceded the comet.

There are three major influences on particle orbits: ejection velocity, radiation pressure, and close encounters with planets. The observations are explainable in a qualitative way on the basis of the first two. But some speculation concerning the results of planetary perturbations must be invoked.

RADAR OBSERVATIONS of the Leonid meteor shower during the 13-year period from 1957 to 1969 have been described previously (McIntosh and Millman, 1970; McIntosh, 1970). Detailed examination of these data along with the orbital parameters of the supposed parent comet P/Temple-Tuttle (1965 IV) (Marsden, 1968) allow some speculation about the evolution of this shower in recent times. Its past history in terms of planetary perturbations has been discussed by Kazimirčak-Polonskaja et al. (1968).

OBSERVATIONAL EVIDENCE

The four most prominent returns of the shower in the past decade fall into two broad classes. The 1966 and 1969 showers were of short duration, had a high proportion of small particles, and occurred with the longest apparent delay after the perihelion passage of the comet. In contrast, the 1961 and 1965 returns were of long duration, and had more large particles. The 1961 return appeared to precede the comet. Quantitative values are shown in table 1. Here ΔT is the delay after the comet passed the descending node and s is determined from the assumption of a mass-distribution model such that the number of particles having masses between m and $m+dm$ is given by

$$dN \propto m^{-s}\, dm$$

The uncertainty in shower duration for 1965 results from the fact that the radiant was below the horizon at Ottawa near the peak of the shower. Hence the duration to ¼ strength is the result of a somewhat uncertain extrapolation. For 1961, the uncertainty is due to equipment failure for a period of time.

Figure 1 shows the positions of the comet in its orbit at the times of the returns listed in the table. It is apparent that there are large spacings between the comet and those points along the orbit where there were significant showers.

Figure 2 shows in more detail the geometry as

* The author has discovered an error in his calculations that modifies the results as presented at the symposium. This paper is a revised version.

TABLE 1.—*Observational Data on the Four Major Leonid Showers in the 1960's*

Year	ΔT (days)	Mass index s	Duration to ¼ strength (hr)
1961	−1266	1.9	(~24)
1965	+195	1.6	~36
1966	560	2.2	1.2
1969	+1656	~2.4	1.3

the Earth passes through the plane of the comet's orbit. We show the distance and angle from the comet orbit to the Earth in a series of planes perpendicular to the comet's orbit. The planes are two hours of Earth motion apart. The distance of closest approach is 0.003 AU or 4.5×10^5 km. The 1965, 1966, and 1969 returns are shown in position with respect to the node. The spreading out of the 1965 concentration of particles and the lack of any very definite peak is in distinct contrast to the narrow, sharply peaked concentrations of 1966 and 1969. The reader is reminded that observations of this shower have a finite sampling period with dead-time intervals when the radiant is below the horizon. These are shown by McIntosh and Millman (1970), their figure 2.

ORIGIN OF THE PARTICLE CONCENTRATIONS AND THEIR DIFFERENT CHARACTERISTICS

There are three major influences on particle orbits: ejection velocity, radiation pressure, and close encounters with planets. According to Whipple's icy conglomerate model for comets, (Whipple, 1951) particles will be ejected from a comet with velocities, v, varying as

$$v \propto r^{-q/8}(b\rho)^{-1/2}$$

where r is the distance from the sun

b is particle radius

and ρ its density.

Particles are presumed to be emitted initially on the surface facing the Sun but their final motion is complicated by two factors: possible rotation of the comet and the fact that the final motion of the escaping gases, which provide the momentum

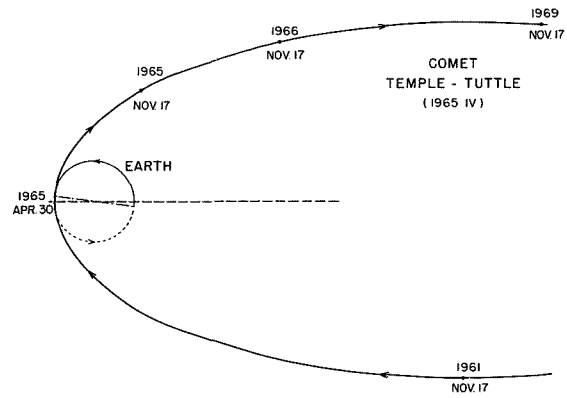

FIGURE 1.—Positions of the comet P/Temple-Tuttle (1965 IV) at the times when the Earth encountered major concentrations of Leonid meteors in the 1960's. Comet perihelion was April 30, 1965, and the line of nodes is 7.4° from the major axis.

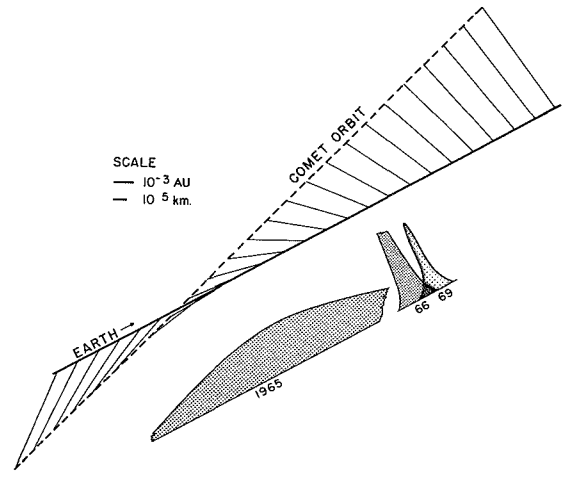

FIGURE 2.—Detail of the Earth passing close to the comet's orbit. Lines from comet orbit to Earth orbit are at 2-hr intervals of the Earth's motion and represent angles and distances in planes perpendicular to the comet's orbit. Rate curves are in correct position with respect to the node but are otherwise only pictorial.

transfer for carrying off the particles, is predominantly in the antisolar direction. Figure 3 indicates some of the parameters necessary for a quantitative discussion of the effect of ejection velocity on orbital parameters. Particles are ejected at a position where the radius vector is r and makes an angle ν with perihelion. Ejection velocity is resolved into components v_r in the

radial direction and v_b perpendicular to the radius in the plane of the orbit.

Radiation pressure is usually taken into account by expressing it as a fraction, β say, of the gravitational force. The orbital speed V of the particles is then given by

$$V^2=\mu(1-\beta)\left(\frac{2}{r}-\frac{1}{a}\right)$$

where μ is the solar gravitational constant and a the semimajor axis. The ratio β depends on particle size as,

$$\beta \propto \frac{1}{\rho b}$$

It is now of interest to determine when the particle will again reach the node and what the value of the radius vector will be. These parameters may be assessed by determining the perturbations to the original orbit. The delay with which the particle follows the comet is determined by the change in orbital period resulting from the change in semi-major axis, a. For the radius vector, since the nodal passage is within a few degrees of perihelion, it is sufficient to consider changes in the perihelion distance q. These perturbations (exclusive of any planetary effects) are

$$\frac{da}{a}=\frac{1}{1-e}\left[\beta\frac{1+e^2+2e\cos\nu_0}{1+e}+2e\sin\nu_0\frac{v_r}{V_q}+(1+e\cos\nu_0)\frac{v_b}{V_q}\right]$$

$$\frac{dq}{q}=\beta\frac{1-\cos\nu_0}{1+e}-\sin\nu_0\frac{v_r}{V_q}+\frac{(1-\cos\nu_0)(2+e+e\cos\nu_0)}{1+e\cos\nu_0}\frac{v_b}{V_q}$$

where e is the eccentricity and V_q is the comet velocity at perihelion. Note that the perturbation in semi-major axis is strongly influenced by the factor $1/(1-e)$ which is about 10 in the case of the Leonids. The magnitude of the perturbations is illustrated by the values in table 2 which have been calculated for a comet of 1 km radius at 1 AU and particles of density 1 g/cm³. It is apparent that the perturbations due to radiation pressure are of roughly equal magnitude to those due to ejection velocity.

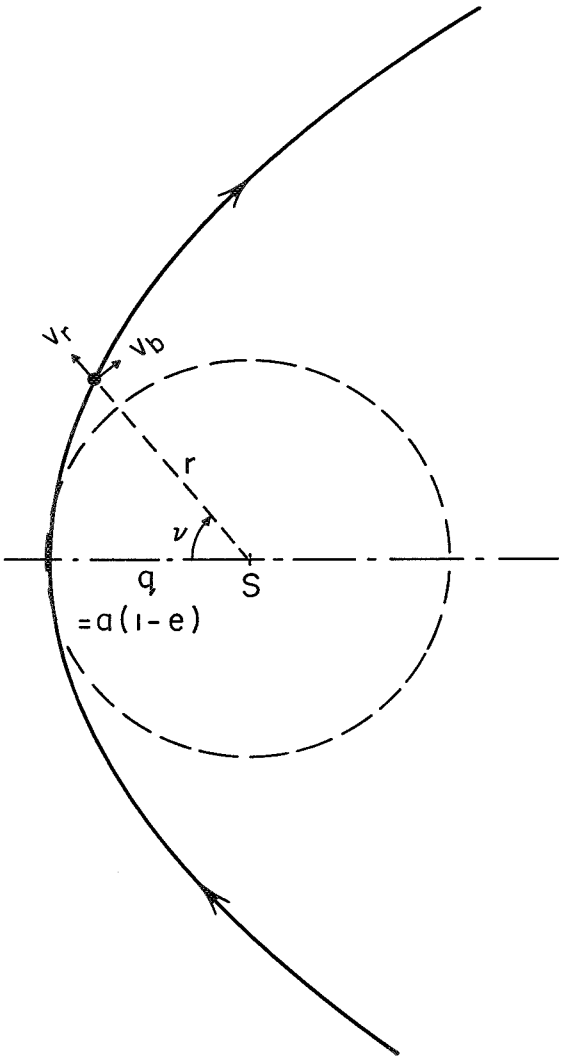

FIGURE 3.—Necessary parameters for considering ejection from the comet of particles with velocities v_r, v_b.

Calculations have been made on a model with particles of density 1 g/cm³ ejected in four directions $\pm v_r$, $\pm v_b$. Release of particles from the comet has been followed from $r=2$ AU through perihelion and out to 2 AU. Particles in three mass classes at 1 g, 0.1 g, and 0.01 g are emitted in numbers and velocities according to the foregoing theory.

The resultant positions of the particles in terms of Δq and ΔT are shown in figure 4. The values of delay are for one period of revolution of the comet. The distributions for each particle

TABLE 2.—*Typical values of ejection velocity and radiation pressure parameter for particles of density 1 g/cm³ released from a comet of radius 1 km at 1 AU*

Particle mass	Ejection		Radiation β
	v	v/V_q	
1g	8 m/s	2×10^{-4}	1×10^{-4}
0.01g	18 m/s	4.5×10^{-4}	4×10^{-4}

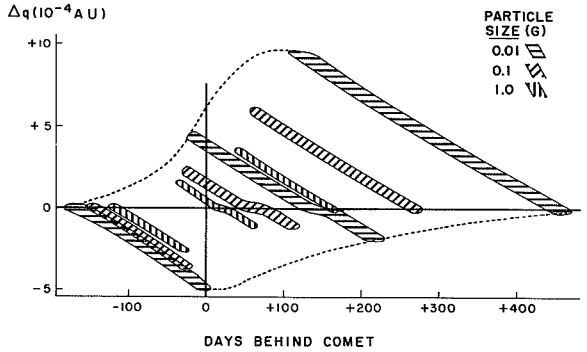

FIGURE 4.—Perturbed position of particles after one orbit for ejection in four directions ($\pm v_r$, $\pm v_b$), for three particle size classes. The dotted outline encloses the region of Δq, ΔT values for isotropic ejection of 0.01-g particles.

size class are essentially similar in form. In each case there are three branches, the outer two resulting from ejection in the ($\pm$) direction of the orbital motion. The one with the greatest delay and lying outside the original orbit results from the $+v_b$ component, and the branch preceding the comet and inside the orbit is associated with $-v_b$. The central branch which has a kink where it crosses the orbit results from ejection in the plus or minus radial direction. Either direction ($\pm v_r$) exclusively will produce this branch because of the change of sign of the sin ν factor.

If particles are emitted isotopically, the distribution in Δq, ΔT becomes that shown by the dotted outline in figure 4, for 0.01 g particles. There will be a further smearing of this distribution in the orbital plane since in reality there will be a range of particle sizes with a distribution of velocities in each size class. Thus there will be a smeared-out, thin plane of particles, the larger ones tending to be more concentrated close to the comet while the smaller ones will achieve positions mostly outside the original orbit and very quickly lagging behind the comet. The thinness of the layer becomes apparent when one notes that in 1966 and 1969 the width to ¼ strength was about 3 Earth diameters. There were significant concentration changes in distances less than one Earth diameter. It is possible that this effect is due to concentrations in the direction within the orbital plane, but because of the rapid spreading of particles in the plane it seems more plausible that the concentration is that of a thin plane.

The distance of closest approach between the Earth and the comet orbit at this recent passage was 0.003 AU some 3 times the maximum Δq perturbation indicated in figure 4. Only very small particles could have achieved orbits at this distance for the uniform ejection model described here. From this point on then, one must speculate as to the mechanism which allows particle orbits at this distance from the comet orbit. Irregular ejection at higher velocities—an explosion-type of event, is a possibility. One can retain the uniform ejection model by noting that planetary encounters perturb the perihelion distance (see fig. 2 of Kazimirčak-Polonskaja et al., 1968). Once the particles begin to diverge from the comet, gravitational perturbations will be different for the particles than for the comet itself. This is essentially the problem that the Russian authors have attempted, that of following a particular swarm of particles through the gravitational perturbations of many revolutions. The results are only as good as the initial conditions which in most cases are not known to sufficient precision.

Thus, assuming that the particles have been moved out to an Earth-encounter position by planetary perturbations, we can examine figure 4 in the light of the observations in table 1. The 1969 return consisted mainly of smaller particles at a delay of 1600 days behind the comet. If we place greatest emphasis on particles emitted close to perihelion, figure 4 indicates a delay of 200 to 400 days per revolution, for small particles only (0.01 g). These particles were probably ejected about five revolutions ago or are between 100 and 200 years old.

Moving back toward the comet in figure 4, one finds particles of all three size classes at a delay of about 100 days per orbit. Hence for the return of

1966 at a total delay of 560 days, an age of five or six orbital revolutions is again indicated. There arises now the interesting question: Are the 1966 and 1969 returns associated with the same ejection event?

If one visualizes the form of figure 4 going over to a continuous distribution of particle sizes and with a distribution of velocities for each size increment, it seems doubtful that there will remain concentrations sufficient to explain the high rates of 1966 without there being significantly high rates in 1967 and 1968. This question cannot be resolved with our own data, since at Ottawa the radiant was below the horizon at the time of passage through the orbital plane in 1968 and was poorly placed in 1967. Rate information for these years is lacking. It is, of course, possible that the particles observed in 1966 resulted from a large outburst at a particular point on the orbit.

In 1965, the shower width to ¼ strength was about 36 hours with indication of some activity over 4 days. This indicates more than an order of magnitude increase in the thickness of the particle belt as compared with 1966 and 1969. As well as this difference, we note that the 1965 return comprised mostly large particles.

Kazimirčak-Polonskaja et al. (1968) have shown that the longitude of the node has undergone large perturbations, particularly due to close approaches to Jupiter (see also Guth, 1968). However, the spread in nodal perturbations as indicated by the width of the 1965 return is of the same order as the total shift over the past 200 years. Thus the spread in the 1965 return must have resulted from planetary perturbations over many centuries. The unusual feature of the 1965 event is that although probably the oldest, it was closest to the present position of the comet with ΔT of only 195 days. A glance at figure 4 shows two possible explanations. There is the possibility of very small delays, a few days per revolution, leading to a very indefinite age of perhaps 20 to 100 revolutions. The alternative is to choose the greater interval of one of the outer branches, say ± 100 days, and allow it to exist for so long that the total delay or advance is an entire period. This requires some 150 to 200 revolutions or 6000 years roughly. The 1961 shower was closer in nature to the 1965 event than to the others, having roughly the same duration but a slightly higher content of intermediate sized particles. This may represent either an advance of 1266 days or a delay of one period minus 1266 days.

PROBLEMS AND CONCLUSIONS

The difference in age between the two basic types of shower seems a necessary conclusion. To put actual values on the ages is more difficult. That the particles very quickly become distributed around the orbit is apparent from figure 4. One would expect that in the older showers, such as the 1965 return, the Earth would encounter fewer particles, because of the dispersion along the orbit. From the observational evidence (McIntosh and Millman, 1970) the Earth encountered as many large particles (echoes ≥ 1 s duration) in 1965 as in the shower of 1966. The ages of the showers are in the ratio of about 30:1. If the original concentrations were the same (there is in fact no reason why this should be so) the particle density along the orbit should be reduced by $\frac{1}{30}$ in the 1965 return. But because of the nodal broadening, the Earth is immersed in the stream some 30 times longer in 1965 than in 1966 and is therefore sampling the same integrated concentration in both cases.

One of the major problems with the evolution of the Leonids is whether ejection of particles from the comet has taken place uniformly as the comet swings around the Sun, or whether only as discrete ejection at a single position along the orbit. Figure 4 indicates that uniform ejection would form a wide belt which in a few tens of revolutions would be spread around the orbit. The lack of any degree of shower activity except within a few years of perihelion passage argues against uniform ejection at repeated passages.

REFERENCES

GUTH, V., 1968. Perturbations of the line of nodes of the Leonids during the years 1866–1966, in *Physics and Dynamics of Meteors*, edited by Ľ. Kresák and P. M. Millman, D. Reidel Publ. Co., Dordrecht, Holland, 476–480.

KAZIMIRČAK-POLONSKAJA, E. I., BELJAEV, N. A., ASTAPOVIČ, I. S., AND TERENTEVA, A. K., 1968. Investigation of perturbed motion of the Leonid meteor stream, in *Physics and Dynamics of Meteors*, edited by Ľ. Kresák and P. M. Millman, D. Reidel Publ. Co., Dordrecht, Holland, 449–475.

MARSDEN, B. G., 1968. Reports on the progress of astronomy, Comets, *Quart. J. Roy. Astron. Soc.*, **9**, 304–321.

MCINTOSH, B. A., 1970. Radar observations of the 1969 Leonid meteor shower, *Bull. Radio and Elect. Eng. Div., N.R.C. Can.*, **20**, No. 2, 30–33.

MCINTOSH, B. A., AND MILLMAN, P. M., 1970. The Leonids by radar—1957 to 1968, *Meteoritics*, **5**, 1–18.

WHIPPLE, F. L., 1951. A comet model. II. Physical relations for comets and meteors, *Astrophys. J.*, **113**, 464–474.

19. New Evidence for Interplanetary Boulders?

ZDENEK SEKANINA
Smithsonian Astrophysical Observatory
Cambridge, Massachusetts

The present paper critically discusses the method of detection, the magnitude and the rate of occurrence of sudden disturbances in the motions of some short-period comets. The disturbances have recently been suggested as potential indicators of collisions between the comets and interplanetary boulders—minor objects whose existence was predicted by M. Harwit in 1967. The character of explosive phenomena, caused by an impact of such a boulder on a comet's nuclear surface, depends significantly on the surface texture of the target body. To advance our understanding of the impact mechanism, a method is suggested which would supply a good deal of the missing information about the structure and optical properties of nuclear surfaces from precise photometric observations of cometary nuclei at large solar distances.

THE IMPACT HYPOTHESIS

RECENT EXTENSIVE DYNAMICAL STUDIES of a number of short-period comets by Marsden (1969, 1970), by Yeomans (1972), and by Marsden and Sekanina (1971) resulted in a discovery of easily detectable disturbances in the motions of the comets we call 'erratic': P/Biela, P/Brorsen, P/Giacobini-Zinner, P/Perrine-Mrkos, P/Schaumasse, possibly also P/Forbes and P/Honda-Mrkos-Pajdušáková. The disturbances differ from the regular nongravitational effects and seem to take form of sudden impulses of about 1 m/s, perhaps preferably at larger solar distances. Their interpretations in terms of processes stimulated by internal cometary sources of energy have been discarded on various grounds. In contrast, hypervelocity impacts of small objects seem to be consistent with empirical evidence. The existence of interplanetary boulders has been predicted by Harwit (1967), of spatial density as high as 10^{-18} g/cm^3. Application of the mechanism of crater formation at hypervelocity impacts suggests that the observed disturbances can be generated by collisions of the boulders with low density comet nuclei, if the comet-to-boulder mass ratio is about 10^6. As a result of such an impact the comet would lose as much as 10 percent of its mass. Repeated impacts can easily result in a splitting of the nucleus, or its complete disintegration in a relatively short period of time. With Harwit's space mass density of boulders the proposed hypothesis predicts an average rate of some five impacts per 100 revolutions for a comet 1 km in diameter. To produce an impulse of 1 m/s the average boulder should be 10^8 g in mass, or 3 to 10 m in diameter, depending on its mass density; the comet would be 10^{14} g in mass, and 0.2 g/cm^3 in density. Such a nucleus can be composed of snows mixed with highly porous dust grains. Impacts of the same boulders would not measurably affect motions of the comets with heavy compact cores like P/Encke.

These have been some of the main conclusions formulated by Marsden and Sekanina (1971) from their extensive study of the motions of the

'erratic' comets. In the present paper we discuss numerical values of some of the fundamental constants of the problem in greater detail. We will refer to the above paper as to Paper 1.

RADIAL AND TRANSVERSE COMPONENTS OF THE NONGRAVITATIONAL EFFECTS IN THE DAILY MEAN MOTION

An acceleration, the radial component of which is Z_1 (positive outward from the Sun) and transverse component Z_2 (perpendicular to Z_1 in the orbit plane, positive in the direction of motion), applied at a solar distance r generates an instantaneous rate of change in the daily mean motion

$$\dot{\mu} = -\frac{3e \sin v}{a(1-e^2)^{1/2}} Z_1 - \frac{3(1-e^2)^{1/2}}{r} Z_2 \qquad (1)$$

where v is the true anomaly, a and e are the semi-major axis and eccentricity of the orbit. We accept that the nongravitational acceleration varies with the solar distance r,

$$Z_i = A_i f(r)$$
$$f(1\ \mathrm{AU}) = 1 \qquad (2)$$
$$i = 1, 2, 3$$

where A_i are the acceleration components at 1 AU in units of the solar gravitational acceleration at 1 AU. Upon integrating over a revolution period, and writing

$$I_j = \int_{-\pi}^{\pi} f(r) r^j \, dv \qquad (3)$$

we obtain the change in the daily mean motion per revolution:

$$\Delta\mu = -3A_2 k I_1 a^{-1/2} \qquad (4)$$

There is no contribution from the periodic variations in the radial component of the acceleration. However, there is a secular effect from Z_1 because of its contribution to the "effective" gravitational constant. On the one hand we have

$$\Delta\left(\int_0^P \frac{k^2}{r^2}\, dt\right) = 2\pi p^{-1/2}\, \Delta k = 2\pi p^{-1/2} a^{3/2} (\Delta\mu)_r \qquad (5)$$

where $p = a(1-e^2)$ and $(\Delta\mu)_r$ is the change, per revolution, in the daily mean motion due to the change in the Gaussian constant k. On the other hand, from equation (2),

$$\Delta\left(\int_0^P \frac{k^2}{r^2}\, dt\right) = -A_1 k I_2 p^{-1/2} \qquad (6)$$

so that

$$(\Delta\mu)_r = -(2\pi)^{-1} A_1 k I_2 a^{-3/2} \qquad (7)$$

It is convenient to convert $\Delta\mu$ of equation (4) to ΔT_2 and $(\Delta\mu)_r$ of equation (7) to ΔT_1, the effective rates of delay ($\Delta T_i > 0$) or advance ($\Delta T_i < 0$) in the perihelion passage per revolution due to, respectively, the transverse and radial components of the acceleration of equation (2). Expressing ΔT_i in days per revolution per revolution we find

$$\Delta T_1 = 58 A_1 I_2 a^{3/2} \qquad (8)$$
$$\Delta T_2 = 1096 A_2 I_1 a^{5/2}$$

The integrals I_1 and I_2 are of the same order of magnitude. For a typical short-period comet ratio $\Delta T_2/\Delta T_1$ is about 10, even when the radial component is almost an order of magnitude larger than the transverse component.

DYNAMICAL DISTURBANCES

The computer programs used by the authors, mentioned earlier for calculating the orbital elements and nongravitational parameters from comet observations, are designed to search for smoothly, continuously varying deviations from the gravitational law. If a disturbance is detected by the program in a comet's motion, contradicting the above assumption, the integration procedure does not necessarily fail. What does happen depends much on the number of the comet's apparitions linked. A solution may be found, which gives quite an acceptable distribution of residuals, but the nongravitational parameters are inconsistent with those computed from the comet's adjacent apparitions not including the dynamical anomaly. Figure 1 shows an example of such a forced solution. The regular nongravitational effects shape the continuous background SABEFZ. Between t_B and t_E a disturbance BCTDE is superposed on the quiescent phase BE. If an attempt is made to link apparitions between t_A and t_Z, and the nongravitational effects are allowed to vary exponentially with time,

$$A \sim \exp(-Bt) \qquad (9)$$

the empirical fit yields the curve A'CDFZ' such

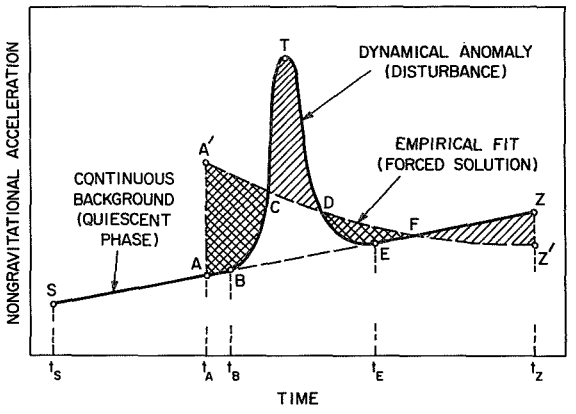

FIGURE 1.—Sudden dynamical anomaly, or disturbance, interferes with continuous, quiescent-phase nongravitational effects in a comet's motion. The disturbance can be detected by means of a 'forced' solution: the cross-shaded areas compensate the one-way shaded areas.

that

$$\text{area(AA'CBA)} + \text{area(DFED)} = \text{area(CTDC)} + \text{area(FZZ'F)} \quad (10)$$

The coefficient B of the secular variations—negative in the quiescent phase in figure 1—suddenly becomes positive due to the disturbance.

Thus, figure 1 is a very obvious demonstration that whenever a disturbance is involved, B comes out fictitious. It is easy to understand that the sign and magnitude of B depends not only on the disturbance-to-background ratio, but also on the selected span of time. For example, B would be strongly negative, if we tried to link apparitions between t_S and t_E. Moreover, the forces generating the quiescent-phase and disturbance effects may work in opposite directions, and we may fail to find a satisfactory solution of the form of equation (9) and must accept another empirical form. If only three apparitions are linked it is always possible to find a satisfactory solution with constant A. Figure 1 corresponding to this case would have a staircase shape, and the general rule, equation (10), would again be in power. In practice, however, the validity of equation (10) is only approximate. The reason comes from the difference between the real orbit (with the unknown profile of the disturbance) and the fictitious orbit found by the forced continuous solution. The differential perturbations, predominantly due to Jupiter, along the two orbits should be taken into account in equation (10). In practice, the perturbations are very small unless the comet makes a close approach to Jupiter during the critical period of time. Unfortunately, these encounters are fairly frequent and often limit our results in accuracy.

SUDDEN IMPULSES

We do not—and practically cannot—have direct evidence of the character of the dynamical disturbances affecting the 'erratic' comets. We guess that they take form of discrete discontinuities (see Paper 1), because so far it has always been found that observations from only the minimum number of apparitions, necessary for the least-squares procedure to work, can satisfactorily be fitted whenever a disturbance is involved. Outside that span the forced solution completely fails. Typically, there are long intervals of quiescent phase before such a disturbance (P/Giacobini-Zinner), or after it (P/Biela), or both before and after (P/Schaumasse).

If we take the disturbance in the form of a sudden impulse ($t_B \to t_E$ in fig. 1) and are able to estimate the quiescent-phase background, we can determine the impulsive increment in the orbital velocity, ΔV_v, associated with the discontinuity, from the difference between the disturbed and quiescent nongravitational parameters. The impulse corresponds to the area BCTDEB in figure 1.

The component of the nongravitational acceleration along the orbital velocity vector, Z_v, is given by

$$Z_v = (Z_1 V_1 + Z_2 V_2)\, V^{-1} \quad (11)$$

where Z_1, Z_2 are identical with those of equation (2), V is the orbital velocity, V_1 and V_2 its radial and transverse components respectively. Integrating over the revolution period, we have from equation (11)

$$\psi = \int_0^P Z_v\, dt = \kappa A_2 \int_{-\pi}^{\pi} f(r) r \left\{\frac{2}{r} - \frac{1}{a}\right\}^{-1/2} dv \quad (12)$$

where v is the true anomaly; $\kappa = 29.8 \times 10^3$, if ψ is to be given in meters per second. The expression, equation (12), is independent of Z_1 for the reasons discussed above.

Let ψ_{quiesc} and ψ_{distrb} be ψ for the quiescent phase

and the disturbed period, respectively. The impulsive increment in the orbital velocity associated with the disturbance is then

$$\Delta V_v = (\psi_{\text{distrb}} - \psi_{\text{quiesc}})\nu + (\text{effect of differential perturbations}) \quad (13)$$

where ν is the number of revolutions covered by the forced fit. The positive ΔV_v means the comet is effectively decelerated, the negative means accelerated. If A_2 has been allowed to be subject to secular variations, its effective value during the period of time covered by the forced fit must be used in equation (12).

The total impulsive velocity, ΔV, associated with the disturbance cannot be derived from its component along the orbital velocity vector, because the angle between the impulse and the orbit tangent is not known. Assuming that the discontinuity in motion is due to a collision with a small object moving in a circular orbit around the Sun in the comet's orbital plane, we have derived in Paper 1 the following formula for the mean quadratic relative velocity between the two colliding bodies, averaged by integration over a revolution period:

$$w = (\overline{w^2})^{1/2} = \kappa a^{-1/2}\left[2 - \frac{4}{\pi}(1-e)^{1/2}K\{(2e)^{1/2}(1+e)^{-1/2}\}\right]^{1/2} \quad (14)$$

where $K\{m\}$ is the complete elliptic integral of the first kind with modulus m. Similarly we can calculate the mean quadratic component of the relative collision velocity in the direction of the comet's motion:

$$w_v = (\overline{w_v^2})^{1/2} = \kappa a^{-1/2}\left[1 + (1-e^2)^{1/2} - \frac{4}{\pi}(1-e)^{1/2} \cdot K\{(2e)^{1/2}(1+e)^{-1/2}\}\right]^{1/2} \quad (15)$$

Relating the direction of the impulsive velocity to that of the relative collision velocity we now can find ΔV averaged over a revolution period:

$$\overline{\Delta V} = \Delta V_v \times \left[1 - \frac{1-(1-e^2)^{1/2}}{2 - \frac{4}{\pi}(1-e)^{1/2}K\{(2e)^{1/2}(1+e)^{-1/2}\}}\right]^{-1/2} \quad (16)$$

The ratio $\overline{\Delta V}/\Delta V_v$ is listed in table 1 as a function of the eccentricity.

TABLE 1.—*Ratio* $\overline{\Delta V}/\Delta V_v$ *vs Eccentricity*, e

e	$\overline{\Delta V}/\Delta V_v$
0.1	2.24
0.2	2.22
0.3	2.19
0.4	2.15
0.5	2.10
0.6	2.04
0.7	1.96
0.8	1.87
0.9	1.75

IMPULSIVE VELOCITIES ASSOCIATED WITH THE DISTURBANCES OBSERVED IN MOTIONS OF THE 'ERRATIC' COMETS

The method described in the preceding section can give a reasonable estimate of the impulsive velocity, particularly if there is no close approach to Jupiter involved. Table 2 lists ΔV_v and $\overline{\Delta V}$ obtained in this way for the 'erratic' comets and compares them with the values derived by Marsden for P/Schaumasse, P/Perrine-Mrkos and P/Biela, and by Yeomans for P/Giacobini-Zinner, who have used a different approach. These authors have computed what we call ΔV_v from the difference between the observed time of perihelion passage and that extrapolated from a quiescent phase.

The fundamental difference between the two methods is that the one we suggest tends to smooth the disturbance out and represents therefore a lower limit of the most probable impulsive velocity. On the other hand, the method applied by Marsden and by Yeomans extrapolates, and therefore tends to exaggerate the effect of the disturbance. Indeed, table 2 clearly shows that our values of the impulsive velocity are systematically smaller. In any case, the table suggests that 1 m/s, which was accepted in Paper 1 for the

TABLE 2.—*'Erratic' Comets: Impulsive Velocities Associated With Dynamical Disturbances*

Comet[a]	Disturbance between—	ΔV_v from eq. (13) (m/s)	$\overline{\Delta V}$ from eq. (16) (m/s)	ΔV_v derived otherwise[b] (m/s)	Comet's mean motion effectively[c]	
					In quiescent phase	By disturbance
P/Biela	1772/1805	0.8	1.5		*A*	*D*
	[d] 1842/43	0.1	0.2	[e] 1 M_2	*A*	*D*
P/Brorsen	[f] 1846/73	(0.3)	(0.5)		*A*	?
	1873/79	1.6	3.0		*A*	*D*
P/Schaumasse	1927/43	0.2	0.5	1.9 M_1	*A*	*A*
P/Perrine-Mrkos	1955/68	1.5	3.0	3.5 M_1	*A*	*A*
P/Giacobini-Zinner	1959/65	0.6	1.1	1.4 *Y*	*D*	*D*

[a] Data on P/Honda-Mrkos-Pajdušáková and P/Forbes are inconclusive.
[b] M_1 = Marsden (1970); M_2 = Marsden (1971) [also in Marsden, Sekanina (1971)]; *Y* = Yeomans (1971).
[c] *A* = accelerated; *D* = decelerated.
[d] Satellite nucleus at splitting.
[e] Velocity of separation essentially in sunward direction.
[f] Impulsive velocity rather uncertain.

typical impulsive velocity, seems indeed to be a representative value for the 'erratic' comets.

RATE OF DISTURBANCES

The rate of dynamical disturbances is another critical quantity for the impact hypothesis. Table 3 lists the number of observed disturbances, $\mathfrak{N}$, for the 'erratic' comets; the length, ℓ, of their trajectories swept out between the first and last observed apparitions of each of the comets; and the disturbance rate, Γ, defined as the number of disturbances per 100 AU:

$$\Gamma = 100\mathfrak{N}/\ell \qquad (17)$$

For the known 'erratic' comets the average *observed* rate is about one disturbance per 100 AU (see column 6 of table 3), a value about four times as high as the one predicted from the impact hypothesis in Paper 1. However, it is easy to show that the data of table 3 are strongly affected by observational selection.

The number of boulder impacts on a cometary nucleus is statistically proportional to the volume of space swept out by the comet. The volume is given as a product of the comet's collisional cross-section and the length of its trajectory. Ideally, $\mathfrak{N}$ should depend linearly on ℓ in figure 2. However, since we deal with observed lengths of trajectories that are very short compared to the rate of presumed impacts, statistical dispersion is significant and the observed disturbance rates for individual comets differ widely from each other. We identify only the best observed 'erratic' comets. It is therefore logical that the upper left corner of figure 2, the area of the highest disturbance rates, is populated most, whereas the strongest bias takes place along $\mathfrak{N}=0$. Observational selection is also responsible for a factor of three between the mean least-square rate $\mathfrak{N}/\ell$ (dot-and-dashed line) and the differential rate $d\mathfrak{N}/d\ell$ (dashed line). It is the latter that should more properly match the unbiased disturbance rate. Indeed, the rate predicted from the impact hypothesis (solid line) agrees with the slope $d\mathfrak{N}/d\ell$.

For the above reasons it is convenient to write the number of the 'erratic' comets with disturbance rates between Γ and $\Gamma+d\Gamma$ in the form

$$dN_c(\Gamma) = N_c\phi(\Gamma)\,d\Gamma, \int_0^\infty \phi(\Gamma)\,d\Gamma = 1 \qquad (18)$$

and to see how the total number, N_c, of the 'erratic' comets among known short-period comets and

TABLE 3.—*'Erratic' Comets: Observed Rates of Dynamical Disturbances*

Comet	First/last apparition	Number of revolutions covered	Length of swept-out trajectory (AU)	Number of detected disturbances	Disturbance rate (per 100 AU)
P/Biela	1772/1852	12	226	2	0.88
P/Brorsen	1846/79	6	95	2	2.10
P/Schaumasse	1911/60	6	131	1	0.76
P/Perrine-Mrkos	1896/1968	11	210	1	0.48
P/Giacobini-Zinner	1900/66	10	187	1	0.53
P/Honda-Mrkos-Pajdušáková	1948/69	4	61	1?	[a] 1.23
P/Forbes	1929/61	5	100	1?	[a] 0.75

[a] The disturbance rate of this comet is weighted by a factor of ¾ to allow for the uncertainty as to whether the disturbance indeed occurred.

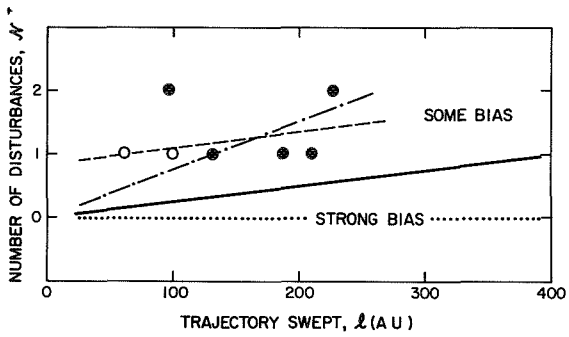

FIGURE 2.—Observed dynamical disturbances. Solid circles: definite 'erratic' comets. Open circles: probable 'erratic' comets. Solid line: disturbance rate predicted from the impact hypothesis (see Paper 1). Dot-and-dashed line: least-square solution to the mean observed disturbance rate, $\mathfrak{N}/\ell$. Dashed line: least-square solution to the mean-differential disturbance rate, $d\mathfrak{N}/d\ell$.

the characteristic disturbance rate, Γ_c, given by

$$\int_0^{\Gamma_c} \phi(\Gamma)\, d\Gamma = \int_{\Gamma_c}^{\infty} \phi(\Gamma)\, d\Gamma \qquad (19)$$

depend on the choice of the distribution function $\phi(\Gamma)$. The number of comets with disturbance rates higher than Γ,

$$N_c^+(\Gamma) = N_c \int_{\Gamma}^{\infty} \phi(\gamma)\, d\gamma \qquad (20)$$

proves the most useful quantity for practical trials, because our statistics of disturbances is relatively complete for very high values of Γ.

Approximating $\phi(\Gamma)$ first by the Maxwellian velocity distribution function, with Γ_m being the most frequent Γ,

$$\phi(\Gamma)\, d\Gamma = 4\pi^{-1/2}\Gamma^2\Gamma_m^{-3} \exp[-(\Gamma/\Gamma_m)^2]\, d\Gamma \qquad (21)$$

we find

$$N_c^+(\Gamma) = N_c\{2\pi^{-1/2}\Gamma\Gamma_m^{-1} \times \exp[-(\Gamma/\Gamma_m)^2] + \mathrm{erfc}(\Gamma/\Gamma_m)\} \qquad (22)$$

where

$$\mathrm{erfc}(x) = 1 - 2\pi^{-1/2}\int_0^x \exp(-x^2)\, dx \qquad (23)$$

The characteristic rate is

$$\Gamma_c = 1.087\Gamma_m \qquad (24)$$

The fit to the empirical data is, however, unsatisfactory.

Alternatively, we can assume that $\phi(\Gamma)$ has the form of a two-dimensional Maxwellian velocity distribution. This assumption seems to be more plausible in view of presumably low obliquities between orbital planes of the short-period comets and interplanetary boulders. Then

$$\phi(\Gamma)\, d\Gamma = \Gamma\Gamma_m^{-2} \exp[-\Gamma^2/2\Gamma_m^2]\, d\Gamma \qquad (25)$$

$$N_c^+(\Gamma) = N_c \exp[-\Gamma^2/2\Gamma_m^2] \qquad (26)$$

and

$$\Gamma_c = \Gamma_m(\log_e 4)^{1/2} \qquad (27)$$

There is an improvement upon equation (22) in matching the data of table 3, but the fit is still poor for $N_c^+ < 3$.

Let us next accept an exponentially decreasing distribution

$$\phi(\Gamma)\, d\Gamma = \beta^{-1} \exp[-\Gamma/\beta]\, d\Gamma \qquad (28)$$

so that

$$N_c^+(\Gamma) = N_c \exp[-\Gamma/\beta] \qquad (29)$$

and

$$\Gamma_c = \beta \cdot \log_e 2 \qquad (30)$$

The fit is now good except for $N_c^+ = 1$.

Finally, if we take

$$\phi(\Gamma)\, d\Gamma = (2\zeta)^{-1}\Gamma^{-1/2} \exp[-\Gamma^{1/2}/\zeta]\, d\Gamma \qquad (31)$$

$$N_c^+(\Gamma) = N_c \exp[-\Gamma^{1/2}/\zeta] \qquad (32)$$

$$\Gamma_c = (\zeta \cdot \log_e 2)^2 \qquad (33)$$

we get a very good fit to all the seven data.

Unfortunately, the testing data are too scanty to resolve the ambiguity in $\phi(\Gamma)$ unequivocally, and the best fit does not necessarily mean the best solution. Indeed, a fit at least as good as that by equation (32) is obtained from

$$N_c^+(\Gamma) = 2.7\Gamma^{-1.4} \qquad (34)$$

which gives no prediction for N_c whatsoever.

Table 4 lists the characteristic rate Γ_c and the extrapolated N_c for the four applied $\phi(\Gamma)$. The dependence of the two parameters on the character of $\phi(\Gamma)$ is significant. The mean rate of disturbances computed in Paper 1 from equations of the impact hypothesis, certain physical assumptions and dynamical evidence comes out 0.25 per 100 AU (solid line in fig. 3 of paper 1), which is in order-of-magnitude agreement with the data of table 4.

PHASE EFFECT AND ALBEDO OF COMETARY NUCLEI

The dimensions and mass of an average 'erratic' comet are important for the impact hypothesis for two reasons:

(1) The impact rate is proportional to the collisional cross-section of the comet's nucleus.

(2) If the impulsive velocity is known, the mass of the nucleus determines the magnitude of the impulse exerted by a boulder impact, which equals the momentum gained by the material expelled from the nucleus. The momentum, in turn, determines the mass of the boulder.

An upper limit for a cometary radius can be derived from dynamical considerations of a cometary splitting. For P/Biela (classed as an 'erratic' comet) the requirement that the separation velocity be higher than the velocity of escape from the surface of the nucleus of radius R and mean density ρ gives a condition

$$R\rho^{1/2} < 1.3 \text{ km} (\text{g cm}^{-3})^{1/2} \qquad (35)$$

For $\rho \simeq 0.2$ g cm^{-3} we find $R < 3$ km. If we require that the separation velocity exceeds the escape velocity from the sphere of action of the nucleus we must use another formula (Sekanina, 1968) and get for P/Biela

$$R\rho^{1/3} < 12 \text{ km} (\text{g cm}^{-3})^{1/3} \qquad (36)$$

or $R < 20$ km for a low-density snowball. These estimates are too crude to be used for the calculation of an 'erratic' comet's mass.

The photometry of faint cometary images at large solar distances appears to be more fruitful

TABLE 4.—*'Erratic' Comets: Total Number and Characteristic Disturbance Rate as a Function of the Disturbance Frequency Distribution*

Distribution $\phi(\Gamma)$ assumed	Characteristic disturbance rate Γ_c (per 100 AU)	Total of expected 'erratic' comets N_c	Data fit
Three dimensional Maxwellian	0.77	8	poor
Two dimensional Maxwellian	0.70	10	good for $N_c^+ > 2$
Damped exponential in Γ	0.50	15	good for $N_c^+ > 1$
Damped exponential in $\sqrt{\Gamma}$	0.06	50	good

for analyzing the dimensions of cometary nuclei. However, the practical solution of the problem is very delicate not only because of the obvious observational difficulties (very faint images; coma contamination must be reduced as much as possible), but also because of an ambiguity in interpretation.

Disregarding the sources of periodic or quasi-periodic variations in brightness (such as the shape of the nucleus), we shall deal with the geometrical albedo and phase law, the two quantities that are determined by the optical properties of the nuclear surface and enter the reduction photometric formula, from which the nuclear diameter is computed.

There is no chance to obtain direct information about the nuclear reflectivity from ground-based observations. However, it might be possible to determine the phase law from very accurate photometric observations.

The two candidates for the surface texture to be considered in reference to the impact hypothesis proposed in Paper 1, namely snow of H_2O and asteroid-like compact but porous material, differ considerably from each other in both the reflectivity and the phase variations (Sekanina, 1971). A smooth surface of unpacked H_2O snow has a geometrical albedo 0.5, a phase coefficient $\beta \simeq 0.002$ mag deg^{-1} for small phase angles and generally resembles a Lambert surface (Veverka, 1970). On the other hand, a typical geometrical albedo for asteroids is about 0.15, and the phase coefficient is characteristically $\beta \simeq 0.03$ mag deg^{-1}. For Icarus, this law is still correct at phase angles as large as 100° (Gehrels et al., 1970).

Incorporation of the significant phase effect into the photometric formula brings the absolute brightness up by 0.5^m at phase angle 18°, by 1^m at 42°, and by more than 1^m everywhere between 42° and 127°, as compared to the Lambert law. Because a strong phase effect also implies a lower albedo, hence a larger cross section, an average asteroid-like nucleus would be larger in diameter than a snow covered nucleus by a factor 2.5, 3 and 3.5, while both nuclei have equal apparent magnitudes under equal geometrical conditions at phase angles 25°, 48° and 75°, respectively.

Obviously, the discrimination of cometary nuclei by the phase effect can significantly improve the accuracy of the photometric determinations of cometary radii, and thus bring down the uncertainty in the mass of individual comets by at least one order of magnitude.

Unfortunately, nuclear magnitudes of the quality required by the suggested phase-discrimination method are not available. To illustrate the difficulties encountered in an attempt to detect phase variations in published sets of magnitudes we have compiled table 5 from the homogeneous series of photographic magnitudes of comets at large solar distances, obtained by Roemer and her collaborators (Roemer, 1965, 1967, 1968; Roemer and Lloyd, 1966; Roemer et al., 1966). The table lists a sample of more extensively observed comets of the two types considered in Paper 1 ('erratic' and core-mantle). The type identification based on the dynamical evidence is given in column 2, the degree of consistency with the phase-law evidence is commented on in the last column. Two phase laws have been tested in terms of the dispersion in the absolute magnitude, H_0: $\beta = 0.00$ mag deg^{-1}, an approximation good for a smooth snow surface and therefore presumably suitable for the 'erratic' comets; and $\beta = 0.03$ mag deg^{-1}, which is assumed to work reasonably well for the core comets. The absolute magnitudes have been computed from apparent magnitudes, applying the inverse square reduction law. Only magnitudes from solar distances larger than 1.2 AU have been made use of, so that phase angles have been conveniently kept within 50°. Table 5 reveals that except for P/Arend-Rigaux and perhaps P/Encke, the dispersion in H_0 is rather high and the results therefore inconclusive. A particularly bothering trouble is a systematic difference between the absolute magnitudes at successive apparitions of the same comet. This effect is most noticeable in the case of P/Giacobini-Zinner.

For the sake of comparison we have also calculated the quantities of columns 3 to 5 of table 5 for two minor planets of the Apollo type. For Adonis, using photographic magnitudes by six observers, we obtain respectively $+0.7^m$, $\pm 0.47^m$ and $\pm 0.39^m$ (the minimum being $\pm 0.36^m$ for $\beta = 0.06$ mag deg^{-1}). For 1960 UA, Object Giclas, we have used photographic magnitudes by Roemer (1965) and photoelectric B magnitudes (reduced to the photographic system) by Rakos (1960), and found, respectively, $+0.5^m$, $\pm 0.37^m$ and

TABLE 5.—*Phase effect [β = Phase Coefficient (mag/deg)]*

Comet	Interpretation of dynamical evidence[a]	Average effect of phase in absolute magnitude: $H_0(\beta = 0.00) - H_0(\beta = 0.03)$ (mag)	Dispersion in H_0		Agreement: phase effect vs dynamics
			$\beta = 0.00$ (mag)	$\beta = 0.03$ (mag)	
P/Encke	core	+0.5	±0.47	±0.29	yes
P/Giacobini-Zinner	erratic	[b] 0.8	[c] 0.70	[c] 0.75	yes?
P/Schaumasse	erratic	0.8	0.41	0.54	yes
P/Tempel 2	core	0.7	0.45	0.60	no
P/Arend-Rigaux	core	0.6	0.39	0.15	yes
P/Forbes	erratic?	0.7	0.76	0.65	no?
P/Schwassmann-Wachmann 2	core?	0.5	0.49	0.59	no?
P/Whipple	——	+0.5	0.36	0.40	——

[a] See: Sekanina (1971), Marsden and Sekanina (1971).
[b] Equals to +0.8^m before perihelion in 1959; and +0.7^m after perihelion in 1959 and in 1965.
[c] Equals to ±0.40^m and ±0.57^m, respectively, before perihelion in 1959; and to ±0.34^m and ±0.40^m, respectively, after perihelion in 1959 and in 1965.

±0.26^m. This may suggest that a difference of 0.1^m in the H_0 dispersion between the two phase laws might already be a meaningful discrimination level, if the dispersion itself is within, say, ±0.5^m. To obtain more convincing results precise photometry must be applied.

FINAL REMARKS

We conclude that the hypothesis of fairly frequent collisions of interplanetary boulders with cometary nuclei, suggested in Paper 1 and examined from specific viewpoints in the present paper, looks reasonably consistent with the limited information available on the character and rate of disturbances observed in the motions of the 'erratic' short-period comets. Precise photometry of cometary nuclei, if conducted in the future, is believed to improve significantly our knowledge of the amount of mass and energy involved in the sort of collisions under consideration. We do not exclude a possibility of a different interpretation of the observed phenomena, but we do not see any at present that could compete with the impact hypothesis. We also feel that collisional processes involving fairly large objects of the solar system should be subjected to extensive investigations rather than rejected as *ad hoc* assumptions without seriously considering the chances, effects and characteristics of the collisional mechanism itself.

ACKNOWLEDGMENTS

The writer's thanks are due to B. G. Marsden for providing ephemerides of the comets and asteroids studied above, and to J. F. Veverka for discussing photometry problems.

NOTE

Since the time of the IAU Colloquium #13 our understanding of the problems discussed in this paper has further advanced. We know of two more "erratic" comets, P/Finley and P/Comas Solá (Marsden, B. G., Sekanina, Z., and Yeomans, D. K., 1973 Comets and Nongravitational Forces. V. Astron. J. **78**, 211–225).

REFERENCES

GEHRELS, T., ROEMER, E., TAYLOR, R. C., AND ZELLNER, B. H., 1970. Minor planets and related objects. IV. Asteroid (1566) Icarus, *Astron. J.*, **75**, 186–195.

HARWIT, M., 1967. The cloud of interplanetary boulders, in *The Zodiacal Light and the Interplanetary Medium*, edited by J. L. Weinberg, *NASA* **SP–150**, Supt. of Documents, U.S. Govt. Printing Office, Washington, 307–313.

MARSDEN, B. G., 1969. Comets and nongravitational forces II, *Astron. J.*, **74**, 720–734.

——, 1970. Comets and nongravitational forces III, *Astron. J.*, **75**, 75–84.

——, 1971. The motion, splitting and present condition of Biela's comet, *Bull. American Astron. Soc.*, **3**, 269.

MARSDEN, B. G., AND SEKANINA, Z., 1971. Comets and nongravitational forces IV, *Astron. J.*, **76**, 1135–1151.

RAKOS, K. D., 1960. Light variations of the fast moving minor planet discovered on October 22, 1960, by H. L. Giclas, *Lowell Obs. Bull.*, **5**, 28–29.

ROEMER, E., 1965. Observations of comets and minor planets, *Astron. J.*, **70**, 397–402.

——, 1967. Comet notes, *Publ. Astron. Soc. Pacific*, **79**, 272–273, 372–374, 503–505, 632–634.

——, 1968. Comet notes, *Publ. Astron. Soc. Pacific*, **80**, 106–108, 345–347.

ROEMER, E., AND LLOYD, R. E., 1966. Observations of comets, minor planets, and satellites, *Astron. J.*, **71**, 443–457.

ROEMER, E., THOMAS, M., AND LLOYD, R. E., 1966. Observations of comets, minor planets, and Jupiter VIII, *Astron. J.*, **71**, 592–601.

SEKANINA, Z., 1968. Motion, splitting and photometry of Comet Wirtanen 1957 VI, *Bull. Astron. Inst. Czech.*, **19**, 153–170.

——, 1971. A core-mantle model for cometary nuclei and asteroids of possible cometary origin, in *Physical Studies of Minor Planets*, edited by T. Gehrels, *NASA* **SP–267**, Supt. of Documents, U.S. Govt. Printing Office, Washington, 423–428.

VEVERKA, J. F., 1970. Photometric and polarimetric studies of minor planets and satellites, PhD. dissertation, Harvard Univ., 97–107.

YEOMANS, D. K., 1972. Nongravitational forces in comet Giacobini-Zinner, in *The Motion, Evaluation of Orbits and Origins of Comets*, edited by G. A. Chebotarev, E. I. Kazimirchak-Polonskaya and B. G. Marsden, D. Reidel Publ. Co., Dordrecht, Holland, 181–186.

20. Cosmic Dust in the Atmosphere and in the Interplanetary Space at 1 AU Today and in the Early Solar System

H. FECHTIG
Max-Planck-Institut für Kernphysik
Heidelberg, Germany

Reliable measurements of cosmic dust abundances have been obtained by ionization detectors during particle impact and by collectors controlled either by inflight shadowing or by penetration-hole identification. A description of the techniques used is given.

Crater-number densities observed on the lunar surface and on lunar samples represent an important source of information on cosmic dust fluxes. The related results from the Apollo 11 and 12 missions are reviewed. The overall knowledge gained from these measurements leads to the following flux model: The cumulative flux Φ *vs mass* m *follows the extrapolation from larger meteoroid-size range (Watson's Law) and can be described by*

$$\Phi = 10^{-14.6} \mathrm{m}^{-1} \qquad [m^{-2}\, s^{-1}]$$

The Pioneer 8 dust experiment and lunar samples indicate a depletion of the flux at approximately 10^{-8} *g. However, cosmic dust particles exist in interplanetary space at least down to 0.3* μ *diameter. They are interpreted as nonmetallic particles in the solar system.*

The atmosphere shows an enhancement in particles of about one order of magnitude compared to the flux in interplanetary space at 1 AU. No depletion or cutoff could be detected. These particles are interpreted as lunar debris or as disintegrated products from fireballs.

The numbers of large lunar craters (>140 m diameter) in Mare Tranquillitatis and in Oceanus Procellarum are compared with the meteoroid flux. These comparisons lead to a time-variable flux of $\Phi \cdot e^{-Bt}$, *with* $B = 2.6$ *and* $t =$ *time in* 10^9 *yr. Thus, the meteoroid flux at the formation of the lunar maria was approximately 4 orders of magnitude higher than today.*

THE RESULTS OF COSMIC DUST RESEARCH are reviewed in this paper. A description of a detector based on ionization during particle impact and of a controlled collection technique is given. Meteoroid fluxes today and in the early solar system are formulated from the distribution of craters in various areas of the Moon. Finally, the fluxes in interplanetary space, near the Earth, and in the upper atmosphere are discussed.

DETECTORS AND COLLECTORS

Experience has shown that detectors based on ionization during particle impact can achieve reliable results. Figure 1 shows a schematic diagram of the detector designed for the HEOS A2 satellite (Hoffmann, 1971). A particle hitting the hemispherical gold or tungsten target produces a plasma cloud during impact around the impact

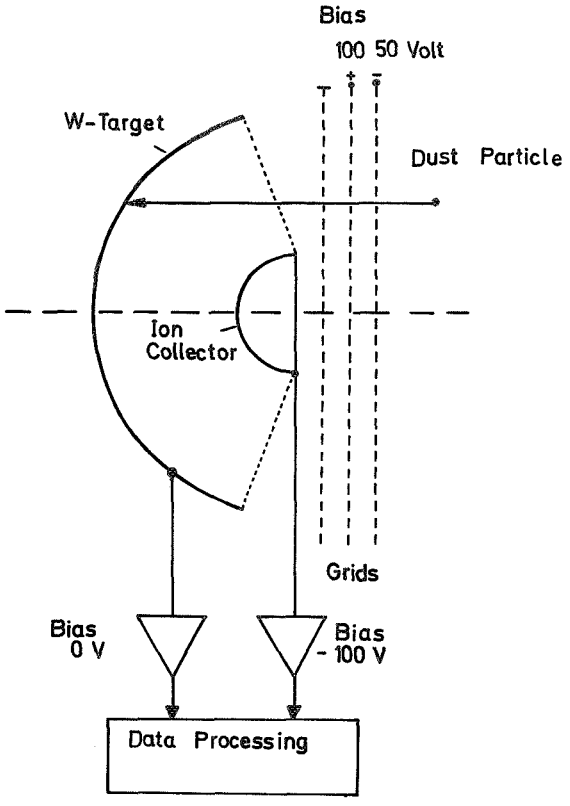

FIGURE 1.—HEOS dust-detector schematic diagram.

point. This plasma cloud expands radially. A concentrically mounted and negatively biased ion collector records the ions from this plasma cloud as the electrons are collected at the hemisphere. From one impact, the hemispherical target and ion collector sense pulses that are identical in pulse height, but different in polarity. From these coincident pulses one can derive mass and velocity of the impacted particle.

Figure 2 shows schematically the detector for the Helios probe (Grün, 1970). The target consists of inclined strips of gold or tungsten. Electrically biased grids in front of and behind the target separate the electrons and positive ions and produce coincident pulses on the grids. The ions are accelerated into a time-of-flight tube. At the end of the tube the ions are recorded as a function of flight time using a particle multiplier. Thus, a mass spectrum of the ion pulse is obtained. From these measurements information concerning chemical composition of the projectiles can be determined.

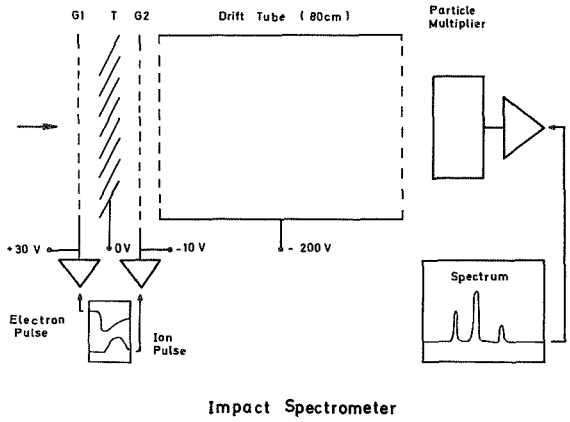

FIGURE 2.—Helios dust-detector schematic diagram.

These detectors have been calibrated using a 2-MV high voltage Van de Graaff electrostatic accelerator. Figure 3 shows the calibration of the detector in the mass range between 10^{-14} and 10^{-9} g for iron, aluminum, and carbon projectiles in the velocity range between 1 and 40 km/s (Hoffmann, 1971). For these ranges of measurements the following relationship holds:

$$C \sim m \cdot v^{3.5} \qquad (1)$$

where C = charge-pulse height
m = projectile mass
v = impact velocity

As shown by Auer and Sitte (1968), Grün (1970), and Hoffmann (1971), the rise time of the charge pulse—a function of the expansion velocity of the plasma—depends on the impact velocity of the projectile, i.e., on the plasma temperature. In figure 3 the rise time of the charge pulse is plotted as a function of impact velocity. Further experiments showed that rise time is independent of projectile mass.

Thus, particle mass m and impact velocity v can be determined from the knowledge of pulse height and rise time of the ion or electron pulse.

Ions are produced according to the relationship expressed in equation (1), a function of the impact velocity. Not only the intensity of the ion pulse, but also the composition of the ion pulse, i.e., the mass spectrum, depend strongly on the impact velocity as shown by Friichtenicht (1964), Grün (1970), and Dietzel (1971). Figure 4 shows an example of the spectra for various impact veloci-

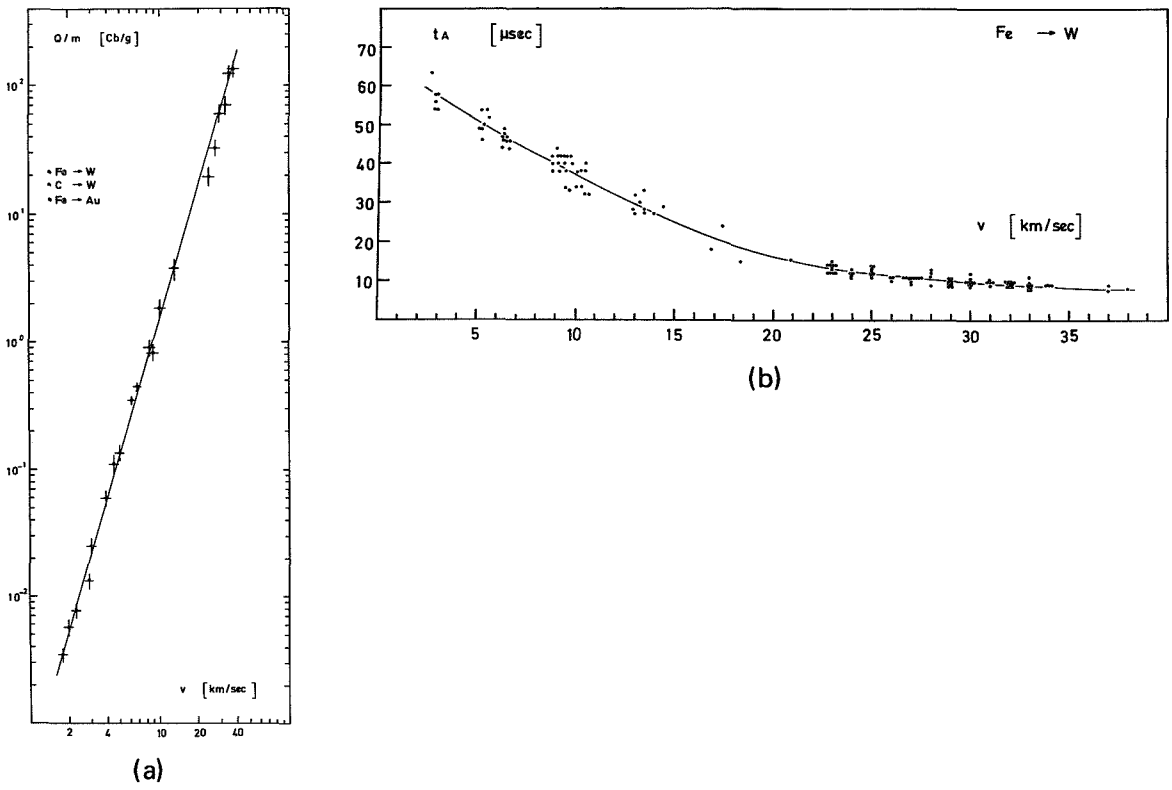

FIGURE 3.—Calibration characteristics of dust detectors. (a) Charge pulse per projectile mass vs impact velocity. (b) Rise time t_A vs impact velocity v.

ties of Al projectiles impacted on an Li-coated tungsten target. For low-impact velocities readily ionized alkalis can be detected that are present in the projectile or are impurities in the target material. Therefore, the Li ions are much more abundant than the Al ions because of different ionization potentials. At higher impact velocities (5 km/s) Al ions are as frequent as Li ions. At hypervelocity impacts (8 km/s) the Al line exceeds that of the Li line considerably (Dietzel, 1971).

The first version of the described detectors has been flown several times successfully aboard a rocket payload to detect cosmic dust in the upper atmosphere (Fechtig, Feuerstein, and Rauser, 1971; Rauser and Fechtig, 1972). Detectors based on the same technique are in Earth orbit on OGO III and in lunar orbit on Lunar Orbiter 35 (Alexander et al., 1971, 1972). Also, Berg and coworkers (Berg and Gerloff, 1971; Gerloff and Berg, 1971) have flown a similar detector aboard the Pioneer 8 and 9 deep-space probes. For the velocity measurements both groups use thin films in front of the detectors at the beginning of a time-of-flight tube. A first pulse is produced by a particle penetrating the film. The second pulse is obtained by particle impact on the solid target at the end of the time-of-flight tube. Thus, the impact velocity is measured. However, there may be undesired effects such as particle fragmentation (Grün and Rauser, 1969) during penetration or instrument cutoffs, especially for low-density projectiles at low relative impact-velocities.

The collectors of the first generation experiments (Hemenway and Soberman, 1962) applied the low-angle shadowing technique in the laboratory shortly before and after flight to mark contaminants by respective shadows. However, it appeared that the contamination problem was not solved by this technique. The last mounting

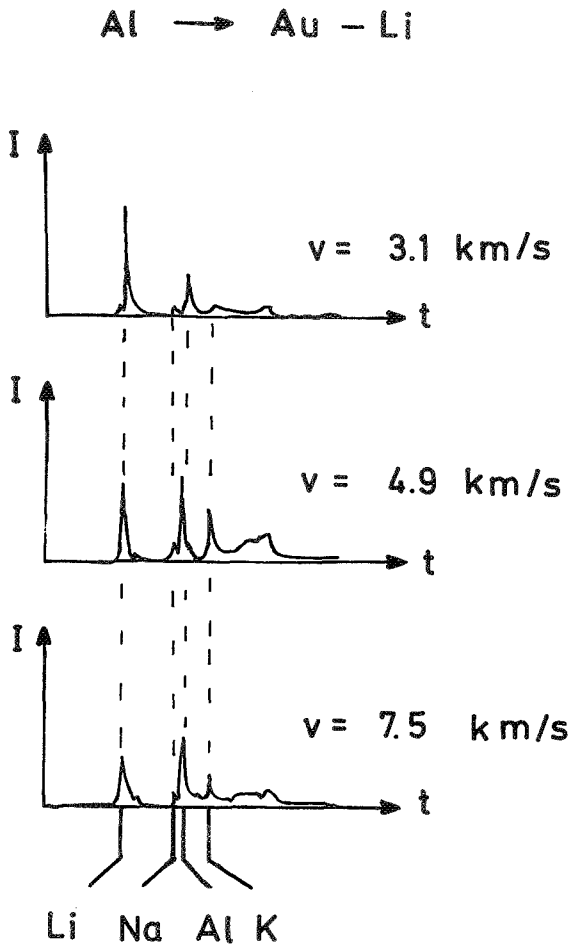

FIGURE 4.—Ion-pulse mass spectra. Projectiles: Al particles. Targets: Li-coated Au targets.

before flight and the first after flight were done before the correct shadows could identify the contaminants. For example, most round particles were produced by the evaporation process itself.

Recent collection experiments therefore apply an *in situ* shadowing technique, the so-called "inflight shadowing" (Skrivanek et al., 1970; Hemenway and Hallgren, 1970). By this technique the collection surface is shadowed several times during flight in different directions. Therefore, by different shadows one can discriminate in altitude and also exclude pre- and post-flight contaminants. Particles that may be produced by the inflight shadowing device can be identified chemically.

Another control technique is based on the penetration-hole identification first proposed by Yaniv and Shafir (1967), and, in another version, applied by our group (Auer et al., 1970): Particles must penetrate a thin nitrocellulose film before impacting on a solid target. Figure 5 shows the collector (metal plates) with a thin film mounted in front. Figure 5 also shows a penetration hole with a particle-strewn field beneath. The particle obviously was a low-density one that fragmentated as it penetrated the foil.

The inflight shadowing technique has the advantage of collecting very small particles (0.1-μ-diameter range) at low relative velocities. However, the collection area is comparatively small ($\sim$100 mm^2). The penetration-hole identification method is applicable for large surfaces ($\sim$100 cm^2), implying a cutoff because of limited penetrability of micron-sized particles at low relative velocities.

LUNAR CRATER DISTRIBUTIONS AND EARLY METEOROID FLUXES

The distribution of craters in various lunar areas is an important source of information concerning the distribution of meteoroids in the interplanetary space at 1 AU. Figure 6 shows the distribution of lunar impact craters as a function of crater diameters for the Mare Tranquillitatis (MT) and the Oceanus Procellarum (OP) as published by Shoemaker et al. (1970). The large craters on the production curve (>140 m diameter in MT and >50 m diameter in OP) follow a $D^{-2.9}$ distribution law which corresponds well with the overall m^{-1} distribution of the meteoroids (D = crater diameter, m = meteoroid mass). The deviation from -3 is explained by a variable D/d ratio of crater diameters to projectile diameters. Therefore, these crater numbers are considered as the time-integral of impacts since the existence of these lunar areas. Since MT is older than OP, MT has more large craters than OP. MT averages 2.4 times as many large craters as OP (Shoemaker et al., 1970), although MT is only 10 percent older than OP according to dating results of the related lunar samples (Albee et al., 1970).

A similar relation exists between the number of large craters in the Lunar Highlands compared to the related number in MT or OP. According to

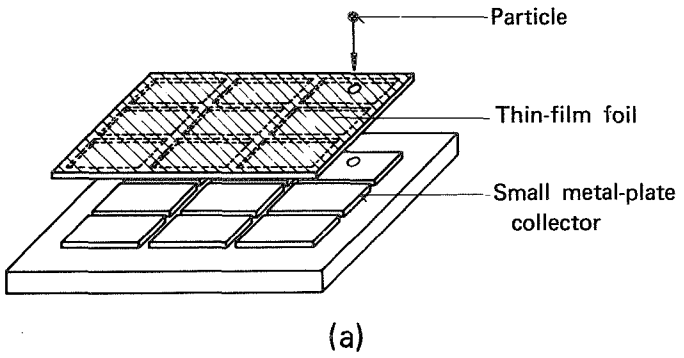

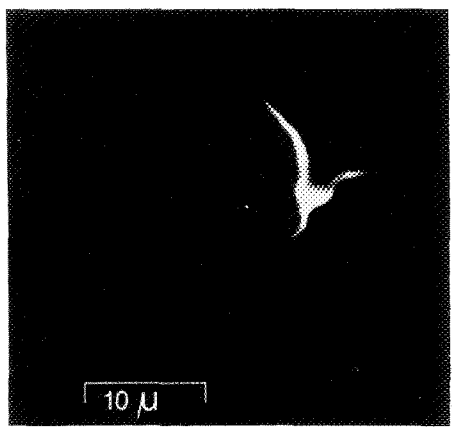

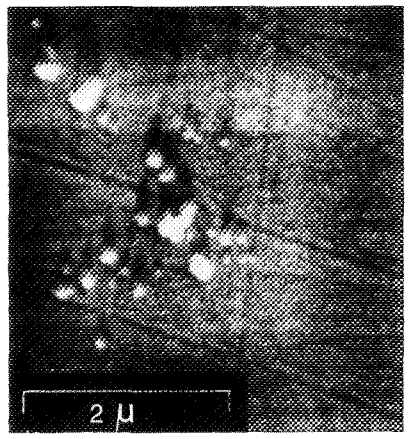

FIGURE 5.—(a) Controlled collector by hole identification. (b) Hole-fragmented particle.

Hartmann (1966) the number of large craters in the Southern Lunar Highland is as much as 30 to 50 times higher than in MT.

These crater-number densities cannot be interpreted on the basis of a time-constant meteoroid influx. Baldwin (1969, 1970, 1971) and Hartmann (1970) have plotted the crater-number densities of various maria as a function of age normalized by the known ages of MT and OP. We tried to combine these observations with meteoroid fluxes known from direct measurements (Bloch et al., 1971).

Let us first assume a general flux function $\varphi(m)$ in differential form or

$$\Phi(m) = \int_{m_0}^{\infty} \varphi(m)\, dm$$

in integral form known from direct observations. If one assumes that the decrease of meteoroids in the past is only given by impacts on planets and their moons, one can write:

$$-\frac{dN}{dt} \sim N \qquad (2)$$

Therefore, the time dependence is

$$N = N_0 e^{-Bt}$$

an exponential function. For the meteoroid flux in the past one can define a flux function $f(m, t)$ in differential form or $F(m, t)$ in integral form as follows:

$$\begin{aligned} f(m, t) &= \varphi(m) \cdot e^{-Bt} \\ F(m, t) &= \Phi(m) \cdot e^{-Bt} \end{aligned} \qquad (3)$$

For today $t=0$. The flux functions are $f(m, 0) = \varphi(m)$ and $F(m, 0) = \Phi(m)$. To determine B one can compare the numbers of craters in MT and OP in relation to the related ages:

$$\int_{-3.6}^{0} \int_{m_0}^{\infty} \varphi(m) \cdot e^{-Bt}\, dm\, dt = R \cdot \int_{-3.3}^{0} \int_{m_0}^{\infty} \varphi(m) \cdot e^{-Bt}\, dm\, dt \qquad (4)$$

with $R=2.4$, the average ratio of large craters in MT to OP. From these determinations one finds

$$B = 2.6 \qquad (5)$$

The time variable flux function therefore reads:

$$\begin{aligned} f(m, t) &= \varphi(m) \cdot e^{-2.6t} \\ F(m, t) &= \Phi(m) \cdot e^{-2.6t} \end{aligned} \qquad (6)$$

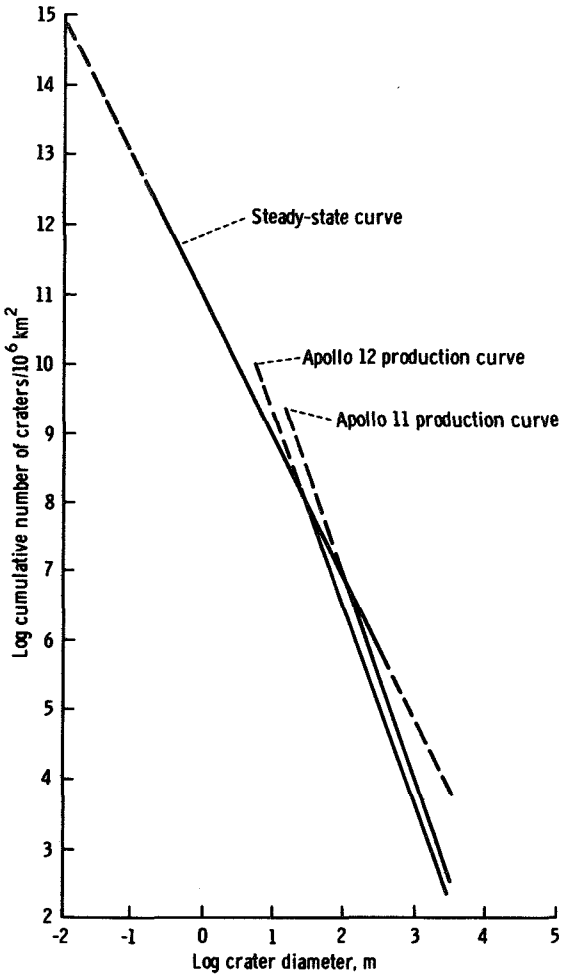

FIGURE 6.—Size frequency distribution of lunar craters at the Apollo 11 and 12 landing sites according to Shoemaker et al. (1970).

If one applies this formalism to the model age of the Lunar Highlands (LH) of $4.6 \cdot 10^9$ yr, the Lunar Highlands would show 12 times as many large craters as MT and therefore the production curve would begin at about 3-km diameter. Table 1 shows the enhancement of the meteoroid flux at the formation of MT, OP and LH by 4 to 5 orders of magnitude.

So far no special flux function $\Phi(m)$ for the present meteoroid flux has been used. Gault (1970) tried to compare the densities of large craters in MT with flux rates based on a time-constant influx. He used fluxes according to Naumann (1966) and Hawkins (1963) and

TABLE 1.—*Meteoroid Fluxes at the Formation of OP, MT, and LH*

Area	Age (10^9 *yr*)	$F(m, t)$
OP	3.3	$5.3 \times 10^3\ \Phi$
MT	3.65	$1.3 \times 10^4\ \Phi$
LH	4.6	$1.6 \times 10^5\ \Phi$

according to Shoemaker (Gault, 1970). Gault's conclusion, assuming a time-constant influx, was consistent with the crater distributions in MT. However, a time-constant influx cannot explain crater distribution in the Lunar Highlands or explain the difference in distributions between MT and OP related to their absolute formation ages. But these can be explained if one accepts the flux to be

$$\Phi = 10^{-14.6}\, m^{-1} \qquad [m^{-2}\, s^{-1}] \qquad (7)$$

This flux function, equation (7), is lower than the one given by Naumann, Hawkins, and Shoemaker. But equation (7) does agree with the flux given by Watson (1956) and will be discussed in the next section of this paper with respect to other flux data.

If one accepts, for the moment, this flux function to be valid for today, the time-variable flux is

$$F(m, t) = 10^{-14.6} m^{-1} e^{-2.6t} \qquad (8)$$

The comparison with the crater-number densities in MT and OP works if one further accepts the D/d values for large craters to be on the order of 10. This value is quite low, but the corresponding value of 2 for μ-sized craters is experimentally known (Bloch et al., 1971; Mandeville and Vedder, 1971). This information suggests that the flux assumed is still too high for the large-crater range (km diameters). The fact that the meteoroids show a d^{-3} distribution and the craters show a $D^{-2.9}$ distribution is interpreted in the variability of the D/d values of 2 for μ-sized craters at 20 km/s impact velocity and increasing with increasing meteoroid diameters.

The distribution of smaller craters (<140 m diameter in MT and <50 m diameter in OP) in the diagram of figure 6 shows a D^{-2} distribution for MT and OP. As interpreted by Shoemaker

et al. (1970) and experimentally shown by Gault (1970), small craters are lacking because of meteoroid impacts (for example, from erosive effects of ejecta material), solar wind (from sputtering effects), and possibly thermal gradient influences. This distribution could be verified down to crater diameters of about 50 μ as shown by Hörz, Hartung, and Gault (1971) and by Neukum (1971).

The time-variable formalism can be applied to crater sizes in the equilibrium status and mean crater lifetimes t can be calculated by the formula

$$\Phi(m) \int_{-t}^{0} e^{-2.6t}\, dt = \frac{N}{F}$$

where

N/F = cumulative number of craters on the equilibrium curve

$\Phi(m)$ = cumulative flux of the corresponding meteoroids.

For 0.3 mm diameter craters (observable on small lunar surface samples) the mean crater lifetime is approximately 10^7 yr. For 1-m diameter craters the lifetime is 10^8 to 10^9 yr which is consistent with cosmic-ray-exposure age determinations for the Apollo 12 soil of 350 million yr (Kirsten, Steinbrunn, and Zähringer, 1971).

The latest progress has been gained by scanning smooth-crater glass linings of sample No. 12063.106, glass-coated sample No. 12024.8.1, and a glass ellipsoid from sample No. 14257 (Fechtig, Mehl, Neukum, and Schneider, 1972). It was possible to discover and count craters down to about 0.3μ diameters with a $D^{-0.8}$ size distribution. The crater number density for craters $\geq 1\mu$ diameter is found to be 10^3 craters per cm^2. The conversion into fluxes according to Neukum and Dietzel (1971) results in a $m^{-0.6}$ distribution down to 0.15μ diameter particles (fig. 7).

The overall meteoroid flux distribution as derived from the distribution of lunar craters is shown in the flux diagram of figure 8. The general slope in the mass distribution is -1 according to equation (7). The distribution shows a depletion at about 30μ-diameter particle size. There, the slope changes to -0.6 down to meteoroid masses of about 10^{-15} g. These submicron-sized craters are considered as an important observation concerning the existence of submicron-sized solid particles in the interplanetary space. The lower slope in the mass distribution may be interpreted by a variable cutoff for small particles due to the Poynting-Robertson effect. This variability is caused mainly by different eccentricities of the particle orbits (Dohnanyi, 1969) and a variability of the chemical composition of the particles. According to Shapiro et al. (1966) metallic particles show a much higher cross section for the influence of the solar electromagnetic interaction than nonconductive particles. Therefore, the smallest particles would be the nonmetallic particles since the metallic component cannot survive as close as 1 AU to the Sun.

THE PRESENT METEOROID FLUX

Figure 9 shows the flux of cosmic dust cumulatively plotted as a function of mass. The results are discussed in four groups:

(a) Results from lunar crater distributions

(b) Results obtained in interplanetary deep space (including zodiacal light measurements)

(c) Spacecraft results (between Earth and Moon and from Lunar Orbiter)

(d) Results from dust collectors and detectors in the atmosphere (rocket- and balloon-borne experiments).

Lunar Craters

The general mass distribution derived from lunar-crater statistics have been discussed in the previous section. The results are labeled "MOON" in figure 9. The slope for larger particles ($>30\mu$ diameter) is -1, for smaller particles ($<30\mu$ diameter), -0.6.

Interplanetary Deep Space

Measurements were reported by Alexander et al. (1971) from the Mariner IV dust experiment and by Berg and Gerloff (1971) from the Pioneer 8 and 9 experiments. Leinert (1971) has calculated fluxes from earlier zodiacal-light measurements by Elsässer (1958), Ingham (1961) and Weinberg (1964).

From the Pioneer dust experiment a cutoff was

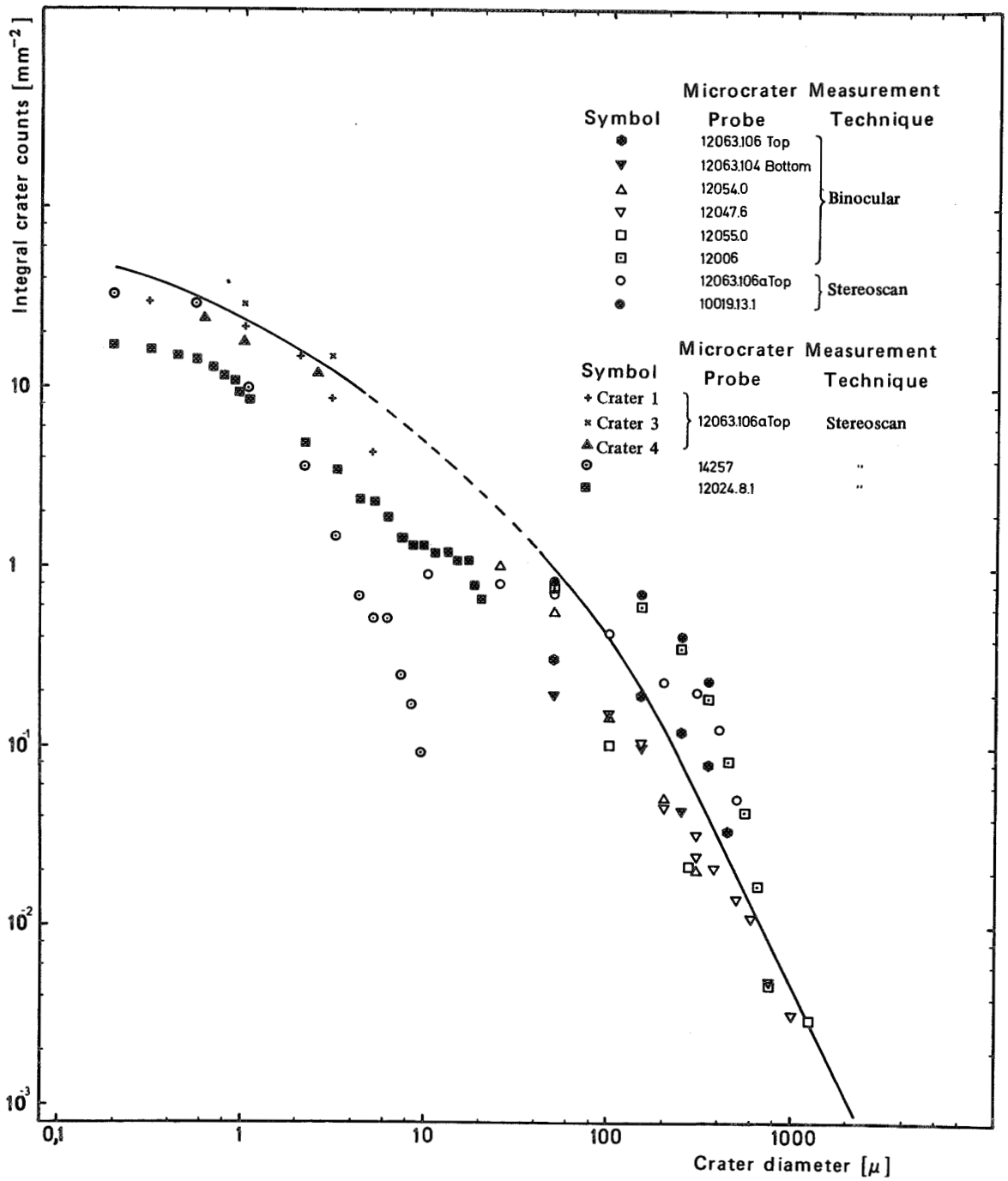

FIGURE 7.—Microcrater distribution on various lunar samples.

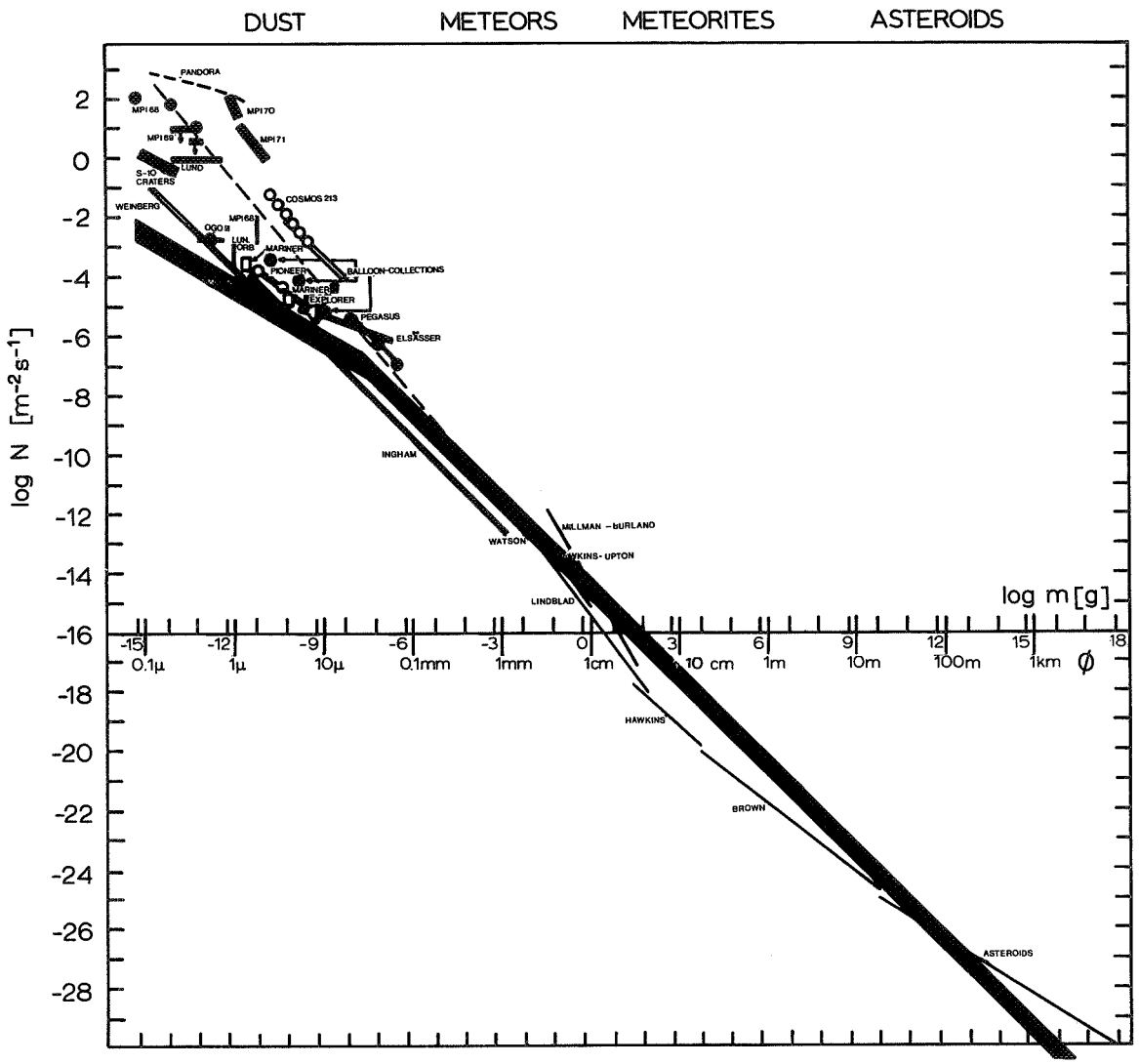

FIGURE 8.—Cumulative meteoroid fluxes as a function of mass.

reported (Berg and Gerloff, 1971; Gerloff and Berg, 1971) at about 10^{-11} g and interpreted with orbit elements according to Dohnanyi (1969). Generally, the *in situ* results and the indirect measurements of the zodiacal light are very similar. The cutoff from the zodiacal-light measurements is a question of interpretation.

A comparison of these results with the results from lunar-crater statistics leads one to question the Pioneer detection cutoff of particles at 10^{-11} g. On the contrary, submicron-sized lunar craters have been found, thus indicating the existence of submicron-sized particles in the interplanetary space. Two possible explanations of this apparent discrepancy are as follows:

(a) If a variable particle-size cutoff exists because of chemical composition, the smallest particles are nonmetallics (silicates, quartz). The general lack of metals for the smallest particles influences heavily the ion production of the impact detectors used in the Pioneer mission as discussed in a previous section of this paper.

(b) The Pioneer dust experiment with a quasi-circular orbit around the Sun cannot detect

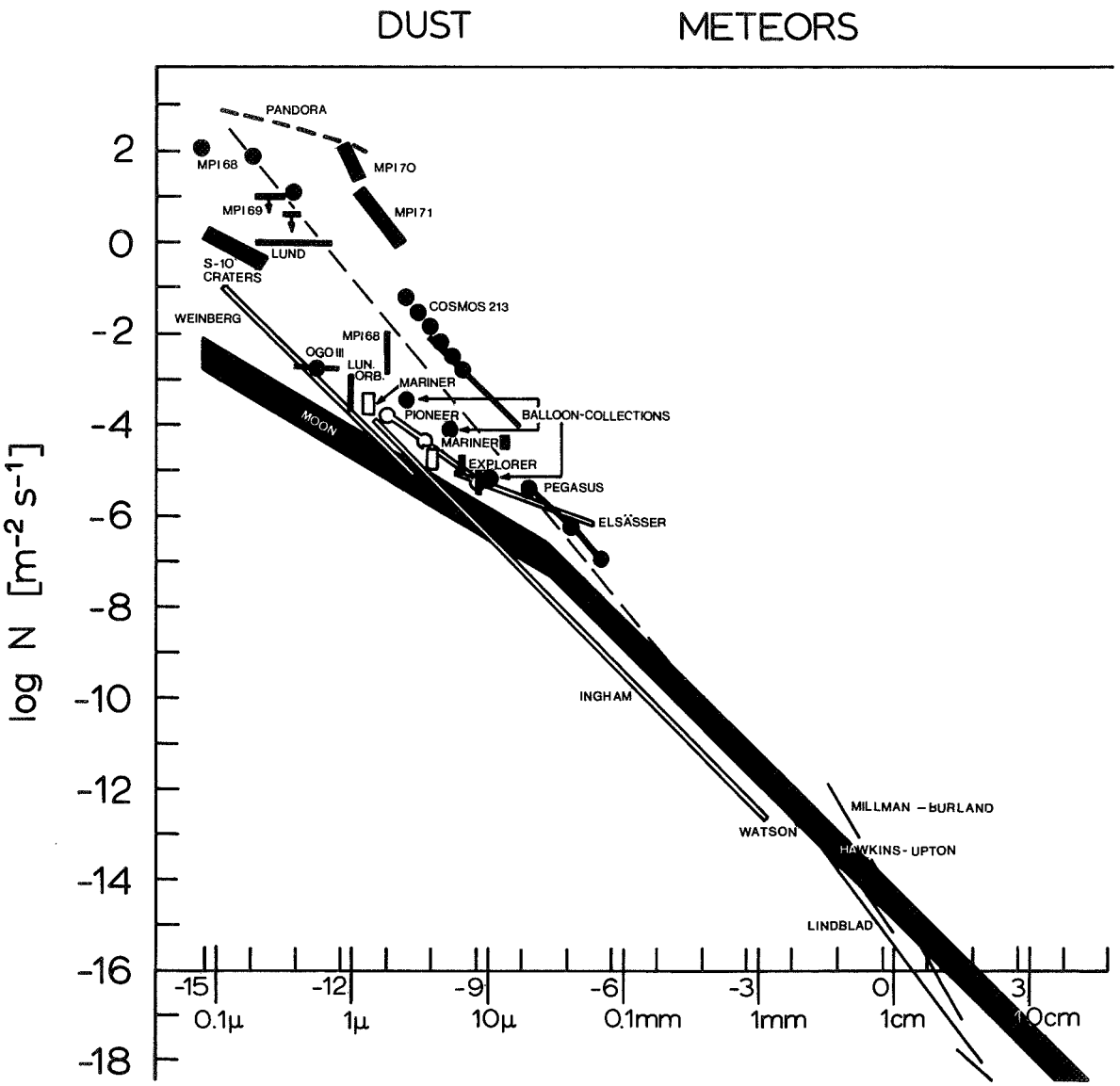

FIGURE 9.—Cumulative cosmic dust fluxes as a function of mass.

circularly orbiting particles, since the relative velocity is not high enough for small particles to penetrate the thin foil in front of the detector and produce enough ions to be recorded. (The lowest relative velocity must exceed 0.7 km/s to be detected.)

Spacecraft Results

Higher fluxes have been measured by Earth and Moon satellites. Using different techniques, results were reported from the following experiments: capacitive detectors on Pegasus (Anon., 1966, 1967), penetration-experiment on Explorer XXIII (Naumann, 1966), microphones on Cosmos 213 (Nazarova and Rybakov, 1971), ionization detector on OGO III (Alexander, Arthur, and Bohn, 1971), ionization detector on Lunar Orbiter 35 (Alexander et al., 1971), and the S 10- S 12-craters (Hemenway et al., 1968). Two possible explanations for these higher near-Earth fluxes are:

(a) Temporarily higher influxes of lunar debris are produced both by impacts of meteor streams and sporadic dust particles on the lunar surface. This origin was discussed by Alexander et al. (1971). Gault et al. (1963) and Colombo et al. (1966) have also discussed this problem.

(b) Fireballs that might be of low-density material (Dubin, 1971) form disintegrated products.

Atmospheric Dust

The highest flux numbers are reported from experiments in the atmosphere using rocket and balloon-borne dust collectors and detectors. Based on the Pandora and the balloon-top collections by Hemenway et al. (1971), the balloon collections of Brownlee et al. (1971), the MPI 68, 69, 70 collections (Auer et al., 1970; Fechtig and Feuerstein, 1970; Fechtig, Feuerstein, and Rauser, 1971), the LUSTER 68 flight through a NLC display (Farlow et al., 1970), and the detector results of "Lund" (Lindblad et al., 1970), MPI 70, 71 (Fechtig, Feuerstein, and Rauser, 1971; Rauser and Fechtig, 1972), one can state the following items:

(a) No cutoff down to masses of about 10^{-15} g could be found.

(b) Easily fragile particles are evident and support Jacchia's (1955) and Verniani's (1969) observations of low-density material.

(c) Large variations probably due to meteor shower activities and Noctilucent Cloud displays are observed for the fluxes.

(d) Still not sufficiently known is the influence of the upper atmosphere on the dynamics of small particles. In 1970 we (Rauser and Fechtig, 1972) measured a velocity profile of micron-sized particles between 70 and 110 km altitude.

The measured velocities are lower than expected at 110 km altitude which suggests that the particles are of a fluffy low-density material. However, the measured velocities are about 2 orders of magnitudes higher than expected (Kornblum, 1969) at 70 to 80 km altitudes. The existence of a temperature minimum at about 85 km altitude leads one to expect a diameter and/or density increase of particles by absorption of condensable material like water or CO_2. This mechanism might also explain the Noctilucent Clouds. A layering effect can be calculated from the detailed data.

Finally, total influx rates can be calculated from the flux curve. One calculates a total daily influx of interplanetary material on the Earth of about 25 tons. This number is consistent with investigations by Keays et al. (1970). These authors have investigated lunar samples for meteoritic components. Although the investigations were carried out in a completely different scientific field, the results show an agreement.

SUMMARY

This paper contains a description of techniques used in recent experiments to detect and analyze cosmic dust and micrometeorites. Furthermore, the results both from the study of lunar crater statistics and from *in situ* measurements have been reviewed.

Ionization detectors and controlled collectors represent important progress in the techniques used in the research field of cosmic dust.

The results from lunar crater statistics show an agreement with the results obtained from *in situ* measurements in interplanetary space and derived from zodiacal-light measurements. The near-Earth results show an enhancement in the flux numbers. This can be caused either by secondary lunar debris or by disintegration of low-density fireballs in the outer atmosphere.

For future experiments *in situ* measurements are needed in interplanetary space. The question of the chemical composition of particles is important with respect to the origin of cosmic dust.

REFERENCES

ANON., 1966. The meteoroid satellite project Pegasus, first summary report, *NASA Tech. Note* **D-3505.**

ANON., 1967. Scientific results of project Pegasus, interim report, *NASA* **X-53629.**

ALBEE, A. L., ET AL., 1970. Ages, irradiation history, and chemical composition of lunar rocks from the Sea of Tranquillity, *Science*, **167**, 463–466.

ALEXANDER, W. M., ARTHUR, C. W., AND BOHN, J. L., 1971. Lunar Explorer 35 and OGO III: dust particle measurements in selenocentric and cislunar space from 1967 to 1969, *Space Research XI*, 279–285.

ALEXANDER, W. M., ARTHUR, C. W., BOHN, J. L., JOHNSON, J. H., AND FARMER, B. J., 1972. Lunar Explorer 35: 1970 dust particle data and shower related picogram ejecta orbits, *Space Research XII*, 349–355.

AUER, S., FECHTIG, H., FEUERSTEIN, M., GERLOFF, U., RAUSER, P., WEIHRAUCH, J., AND LINDBLAD, B. A., 1970. Rocket experiments using extremely sensitive detectors for cosmic dust particles, *Space Research X*, 287–294.

AUER, S., AND SITTE, K., 1968. Detection technique for micrometeoroids using impact ionization, *Earth Planetary Sci. Letters*, **4**, 178–183.

BALDWIN, R. B., 1969. Absolute ages of the lunar maria and large craters, *Icarus*, **11**, 320–331.

——, 1970. Absolute ages of the lunar maria and large craters, II. The viscosity of the Moon's outer layers, *Icarus*, **13**, 215–225.

——, 1971. On the history of lunar impact cratering: the absolute time scale and the origin of planetesimals, *Icarus*, **14**, 36–52.

BERG, O. E., AND GERLOFF, U., 1971. More than two years of micrometeorite data from two Pioneer satellites, *Space Research XI*, 225–235.

BLOCH, M. R., FECHTIG, H., GENTNER, W., NEUKUM, G., AND SCHNEIDER, E., 1971. Meteorite impact craters, crater simulations and the meteoroid flux in the early solar system, *Proc. Second Lunar Sci. Conf., Geochim. Cosmochim. Acta, Suppl.*, **2**, 2639–2652.

BROWNLEE, D., HODGE, P., AND BUCHER, W., 1971. Extraterrestrial dust in the stratosphere, unpublished.

COLOMBO, G., SHAPIRO, I. I., AND LAUTMAN, D. A., 1966. The Earth's dust belt: fact or fiction? 3. Lunar ejecta, *J. Geophys. Res.*, **71**, 5719–5731.

DIETZEL, H., 1971. Univ. Heidelberg.

DOHNANYI, J. S., 1969. On the origin and distribution of Meteoroids, *Bellcomm. Inc.*, **TR 69-105-3-2.**

DUBIN, M., 1971. Introduction, presented at COSPAR Meeting, Seattle, 1971.

ELSÄSSER, H., 1958. Interplanetare materie, *Mitt. Astr. Inst. Tübingen*, **35**, 73.

FARLOW, N. H., FERRY, G. V., AND BLANCHARD, M. B., 1970. Examination of surfaces exposed to a noctilucent cloud, August 1, 1968, *J. Geophys. Res.*, **75**, 6736–6750.

FECHTIG, H., AND FEUERSTEIN, M., 1970. Particle collection results from a rocket flight on August 1, 1968, *J. Geophys. Res.*, **75**, 6751–6757.

FECHTIG, H., FEUERSTEIN, M., AND RAUSER, P., 1971. Simultaneous collection and detection experiment for cosmic dust, *Space Research XI*, 335–346.

FECHTIG, H., MEHL, A., NEUKUM, G., AND SCHNEIDER, E., 1972. Meteoroid fluxes as derived from lunar crater number densities, unpublished.

FRIICHTENICHT, J. F., 1964. Micrometeoroid simulation using nuclear accelerator techniques, *Nucl. Instr. Methods*, **28**, 70–78.

GAULT, D. E., 1970. Saturation and equilibrium conditions for impact cratering on the lunar surface: criteria and implications, *Radio Sci.*, **5**, 273–291.

GAULT, D. E., SHOEMAKER, E. M., AND MOORE, H. J., 1963. Spray ejected from the lunar surface by meteoroid impact, *NASA Tech. Note* **D-1767**, Washington.

GERLOFF, U., AND BERG, O., 1971. A model for predicting the results of in situ meteoroid experiments: Pioneer 8 and 9 results and phenomenological evidence, *Space Research XI*, 397–413.

GRÜN, E., 1970. Massenspektrometrische Analysen von Ionen beim Aufschlag schneller Staubteilchen, thesis, Univ. Heidelberg.

GRÜN, E., AND RAUSER, P., 1969. Penetration studies of iron dust particles in thin foils, *Space Research IX*, 147–154.

HARTMANN, W. K., 1966. Martian cratering, *Commun. Lunar Planet. Lab.*, Univ. Ariz., **4**, part 4, No. 65, 121–131.

——, 1970. Lunar cratering chronology, *Icarus*, **13**, 299–301.

HAWKINS, G. S., 1963. Impacts on the Earth and Moon, *Nature*, **197**, 781.

HEMENWAY, C. L., AND HALLGREN, D. S., 1970. Time variation of the altitude distribution of the cosmic dust layer in the upper atmosphere, *Space Research X*, 272–280.

HEMENWAY, C. L., HALLGREN, D. S., AND KERRIDGE, J. F., 1968. Results from the Gemini S–10 and S–12 micrometeorite experiments, *Space Research VIII*, 521–535.

HEMENWAY, C. L., HALLGREN, D. S., LANDATE, A. T., PATASHNICK, H., RENZEMA, T. S., AND GRIFFITH, O. K., 1971. A new high altitude balloon-top cosmic dust collection technique, *Space Research XI*, 393–395.

HEMENWAY, C. L., AND SOBERMAN, R. K., 1962. Studies of micrometeorites obtained from a recoverable sounding rocket, *Astron. J.*, **67**, 256–266.

HOFFMANN, H. J., 1971. Entwicklung eines Detektors zur Massen und Geschwindigkeitsanalyse von kosmischen Staubteilchen, thesis, Univ. Heidelberg.

HÖRZ, F., HARTUNG, J. B., AND GAULT, D. E., 1971. Micrometeorite craters and related features on lunar rock surfaces, *Earth Planet. Sci. Letters*, **10**, 381–386.

INGHAM, M. F., 1961. Observations of the zodiacal light from a very high altitude station, *Mon. Not. Roy. Astron. Soc.*, **122**, 157–176.

JACCHIA, L. G., 1955. The physical theory of meteors, 8, fragmentation as cause of the faint meteor anomaly, *Astrophys. J.*, **121**, 521–527.

KEAYS, R. R., GANAPATHY, R., LAUL, J. C., ANDERS, E., HERZOG, G. F., AND JEFFERY, P. M., 1970. Trace elements and radioactivity in lunar rocks: implications for meteorite infall, solar wind flux, and formation conditions of Moon, *Science*, **167**, 490–493.

KIRSTEN, T., STEINBRUNN, F., AND ZÄHRINGER, J., 1971. Location and variation of trapped rare gases in Apollo 12 lumar samples, *Proc. Second Lunar Sci. Conf., Geochim. Cosmochim. Acta, Suppl.*, **2**, 2639–2652.

KORNBLUM, J. J., 1969. Concentration and collection of meteoric dust in the atmosphere, *J. Geophys. Res.*, **74**, 1908–1919.

LEINERT, C., 1971. The zodiacal light lines in the particle flux diagram, *Space Research XI*, 249–253.

LINDBLAD, B. A., ARINDER, G., AND WIESEL, T., 1970. Rocket observations of micrometeorites, *Space Research X*, 295–304.

MANDEVILLE, J. -C., AND VEDDER, J. F., 1971. Microcraters formed in glass by low density projectiles, *Earth Planet. Sci. Lett.*, **11**, 297–306.

NAUMANN, R. J., 1966. The near-earth meteoroid environment, *NASA Tech. Note* **D–3717**, Washington.

NAZAROVA, T. N., AND RYBAKOV, A. K., 1971. Meteor particle studies from space vehicles, *Space Research XI*, 357–361.

NEUKUM, G., 1971. thesis, Univ. Heidelberg.

NEUKUM, G., AND DIETZEL, H., 1971. On the development of the crater population on the Moon with time under meteoroid and solar wind bombardment, *Earth Planet. Sci. Lett.*, **12**, 59–66.

RAUSER, P., AND FECHTIG, H., 1972. Combined dust collection and detection experiment during a noctilucent cloud display above Kiruna, Sweden, *Space Research XII*, 391–402.

SHAPIRO, I. I., LAUTMAN, D. A., AND COLOMBO, G., 1966. The Earth's dust belt: fact or fiction? 1. Forces perturbing dust particle motion, *J. Geophys. Res.*, **71**, 5695–5704.

SHOEMAKER, E. M., BATSON, R. M., BEAN, A. L., CONRAD, C., JR., DAHLEM, D. H., GODDARD, E. N., HART, M. H., LARSON, K. B., SCHOBER, G. G., SCHLEICHER, D. L., SUTTON, R. L., SWANN, G. A., AND WATERS, A. C., 1970. Preliminary geologic investigation of the Apollo 12 landing site, Part A: geology of the Apollo 12 landing site, *Apollo 12 Preliminary Science Report, NASA*, **SP–235**.

SHOEMAKER, E. M., HAIT, M. H., SWANN, G. A., SCHLEICHER, D. L., DAHLEM, D. H., SCHOBER, G. G., AND SUTTON, R. C., 1970. Lunar regolith at tranquillity base, *Science*, **167**, 452–455.

SKRIVANEK, R. A., CARNEVALE, R. F., AND SARKISIAN, R. D., 1970. Results of in-flight shadowing performed on the ESRO rocket flight of 7 June 1968, *Space Research X*, 281–286.

VERNIANI, F., 1969. Structure and fragmentation of meteoroids, *Space Sci. Rev.*, **10**, 230–261.

WATSON, F. G., 1956. *Between the planets*, Harvard Univ. Press, Cambridge, Mass.

WEINBERG, J., 1964. The zodiacal light at 5300 Å, *Ann. d'Astrophys.*, **27**, 718–738.

YANIV, A., AND SHAFIR, U., 1967. Preliminary results of a micrometeoroid collection experiment in the Luster program, *Space Research VII*, 1403–1411.

Page intentionally left blank

21. Dust Storms in Space?

ROBERT G. ROOSEN AND OTTO E. BERG
Goddard Space Flight Center, NASA
Greenbelt, Maryland

AND

NEIL H. FARLOW
Ames Research Center, NASA
Moffett Field, California

Silverberg (1970) has explained the "dust storms" observed by the early satellite-borne microphone detectors by postulating that the orbital planes of short-period, low-inclination comets are filled with micrometeoroids. We report here on three separate approaches to test the validity of this hypothesis.

(1) Optical scans of the Gegenschein brightness can yield no useful information on the nearly isotropic sheets of dust predicted by Silverberg.

(2) An attempt to directly collect dust particles during a predicted high flux period by means of a sounding rocket yielded negative results.

(3) Over three years of particle impact data from extremely sensitive detectors flown aboard Pioneers 8 and 9 show no observable dust storms.

Hence Silverberg's hypothesis appears untenable.

However, we should not rule out the possibility that observable showers of very small particles can be blown directly off the nuclei of some comets passing between the Earth and the Sun.

VARIOUS INVESTIGATORS (e.g., Silverberg, 1970; Poultney, 1972; McCracken, Alexander, and Dubin, 1967) have suggested that there are dust streams in interplanetary space in which the flux of micrometeoritic (i.e., mass $<10^{-8}$ gm) particles is enhanced by factors of up to 100 or more over the sporadic background. We discuss here several recent investigations of this possibility.

IN SITU MEASUREMENTS

It has been suggested (Silverberg and Poultney, 1969; Silverberg, 1970) that the periods of apparently enhanced micrometeoritic flux reported by various investigators using satellite-borne microphone detectors can be explained by postulating that small, low density particles are produced in sufficient quantities from debris in the orbits of short period, low-inclination comets to produce dust storms when the satellites pass through the comets' orbital planes. Silverberg (1970) further points out: "In general, there appears to be no dust event seen by the satellites [carrying microphone detectors] which was not near the plane of a periodic comet. Furthermore, no satellite passed through the plane of a low-inclination comet without registering a flux increase."

Several years of observational results now available from the Pioneer 8 and 9 interplanetary dust detectors (Berg and Gerloff, 1970, 1972) make it possible to test the validity of this suggestion.

Table 1 summarizes the characteristics of the five largest dust showers discussed by Silverberg and Poultney (1969). The last column of Table 1 lists the number of counts that would be expected to be observed by the Pioneer 8 and 9 detectors in the same showers (The effective cross section of the Pioneer 8 and 9 detectors for a unidirectional flux near the ecliptic plane is about 0.005 m^2).

Figure 1 shows all counts registered on the front film as a function of time for the Pioneer 8 and 9 detectors during the periods when complete telemetry was available. The count rates are shown separately depending on whether or not the Sun was within the 120° field of view of the detectors.

The times at which cometary enhancements are predicted are also shown, and it is apparent that no dust showers are seen then—indeed no detectable showers appear anywhere in the data. Hence the Pioneer observations are completely at odds with the early microphone observations. In particular we can make the following points:

(1) No comet-associated dust storms were detected to a limit at least a factor of 100 more sensitive than the previously reported highest rates.

(2) The previously reported events were for particles in the mass range 10^{-8} to 10^{-9} gm, whereas the events shown in figure 1 are due to particles smaller than 10^{-11} gm. Indeed, the largest particle observed by the Pioneer detectors in more than three years of operation is 10^{-10} gm (Berg and Gerloff, 1971). Hence the particles presumed to cause these dust storms are much too rare to even have been observed with a total cross section (so far) of 3×10^5 m s, much less cause dust storms involving hundreds of impacts per day.

(3) It is no good to suppose that these storms occur only occasionally, since Silverberg's claim is that they were invariably observed whenever a satellite-borne detector passed through the orbital plane of any short period, low inclination comet whose perihelion distance was less than 1 AU.

Figure 1 also shows the positions of ten of the most active meteor streams (Porter, 1952). In view of the perturbing effects of solar wind and radiation pressure on the orbits of picogram-sized dust particles it is not surprising that no dust storms are observed connected with meteor streams (Millman, 1970; Mazets, 1971).

Figure 2 shows the corrected monthly sums for the three years of available data.

As an example of the limits that can be set on the flux of any possible stream (with low orbital inclination) let us assume a typical duration of 10 hr (3.6×10^4 s), and further assume that three hits in that period define a stream. Then any stream must have a flux of less than 0.02 particle m^{-2} sec^{-1}

COMET ENCKE

In addition to the Pioneer results, a number of other investigations were carried out during the

TABLE 1.—*Five Largest Dust Showers Discussed by Silverberg (1970) and Silverberg and Poultney (1969)*[a]

Satellite	Date(s) of "storm"	Associated comet	Count rate (m^{-2} s^{-1})	Duration of storm (hours)	Predicted no. of counts for a Pioneer-type detector
Vanguard 3	Nov. 16–18, 1959	Honda-Mrkos-Pajdusakova	0.2	70	250
Explorer 1	Feb. 3, 1958	Brorsen-Metcalf	0.2	15	55
Electron 2	Jan. 30–31, 1964	Brorsen-Metcalf	0.11	15	30
Sputnik 3	May 15, 1958	Halley	7	5	630
Electron 2	Feb. 23–25, 1964	Encke	0.0058	44.4	5

[a] Count rates shown are those expected for a Pioneer-type detector exposed to similar storms. The data in the first four columns are from Dubin and McCracken (1962), McCracken et al. (1965), and Nazarova (1968).

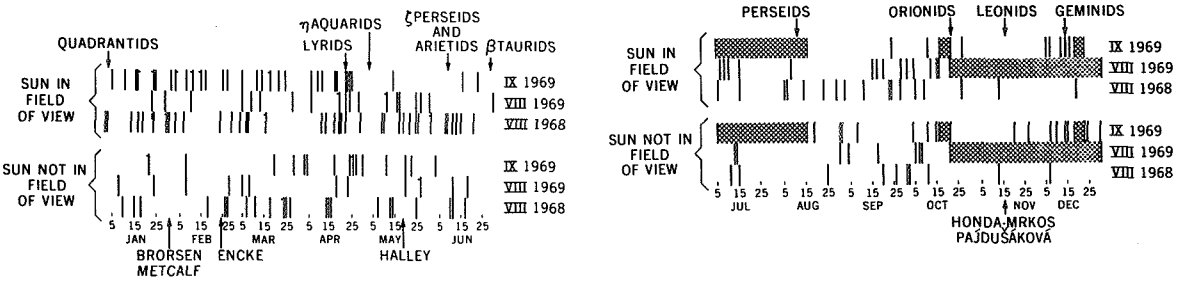

FIGURE 1.—All events registered by the front films of the Pioneer 8 and 9 detectors during 1968 and 1969. The abscissa is satellite longitude. The crosshatched regions indicate periods when daily telemetry was not available. Horizontal tic marks indicate numbers of events greater than one observed on the same day.

favorable opportunity of February 1971, when the Earth passed through Encke's node only six weeks after the comet itself, and a shower of dust particles blown directly off the comet's nucleus was predicted (Roosen, 1970; Poultney, 1972).

Optical Observations

Roosen (1969, 1970) reported on an anomalous shadow observed in the center of the Gegenschein on February 21, 1969, two days before the Earth passed through the node of Comet Encke. It was for a time believed that this observation might support Silverberg's hypothesis. An attempt was made to reproduce the observation in February 1971. Although observations were planned from four separate observing sites in the continental U.S., clouds prevented observations on February 23 and February 24, but observations on the other nights showed no evidence for a shadow. In particular, observations on February 21, 1971, did not reproduce the event observed February 21, 1969.

Indeed, optical scans of the Gegenschein brightness would not be expected to be very efficient in testing the Silverberg hypothesis. Silverberg predicts an almost isotropic sheet of dust stretching some several astronomical units past the Earth. As pointed out by Roosen, the shadow expected for such a collection of dust is only slightly greater than 1 percent deep. Hence the dust could not be detected by the shadow technique unless enough was present to increase the Gegenschein brightness by a factor of three or more. Further, the shadow reported by Roosen was much wider than that

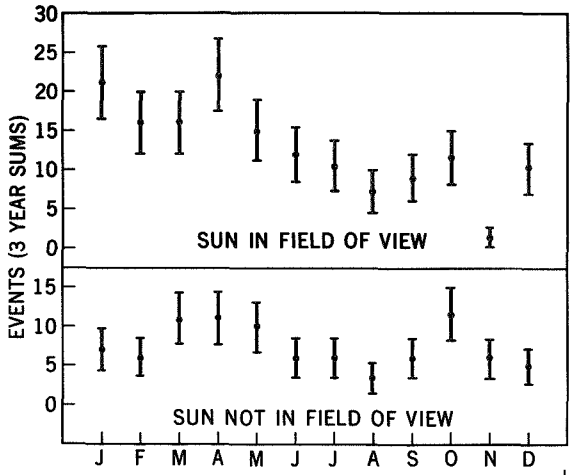

FIGURE 2.—Monthly sums of the 3 years of available data corrected for periods when telemetry was unavailable. The error bars represent probable errors in the number of observed events, assuming Poisson statistics.

predicted for Silverberg's isotropic sheet, and can only be interpreted as due to a relatively small cloud whose center was only about 60 Earth radii from the Earth. Also, since the estimated time of passage of the Earth through the dust sheet is only 5 hours (Poultney, 1970), observations of the antisolar region on days other than February 24 could not include the dust predicted by Silverberg.

Dust in the Upper Atmosphere

One of us (NHF) launched a Luster rocket at 1440 GMT on February 24, 1971, from White Sands Missile Range. The techniques used have been described by Farlow and Ferry (1972) and

Ferry and Farlow (1972). In the range of 80 to 118 km altitude, no increase was observed over the normal contamination background. A very slight enhancement found in the 70 to 80 km interval was also observed on 2 Luster flights from Churchill, Canada in April and May 1970. Hence no increase in mesospheric dust was detected.

Lidar observations by G. S. Kent (1971) in Jamaica also indicate no major enhancement in atmospheric dust on February 24 or on following days, although an enhancement was observed at the time of the Earth's passage through the orbital plane of Comet Bennett in May 1970 (Kent et al., 1971). [It is not surprising that no increase in event rates connected with this comet was observed by the Pioneer detectors, since its orbital inclination was so high (~90°) that any dust would be out of their field of view.]

Hence any dust blown directly off the nucleus of Comet Encke at the favorable 1971 apparition seems to have been indetectable.

CONCLUSIONS

Primarily from the Pioneer 8 and 9 results we can conclude that the flux of picogram sized dust particles near the Earth's orbit has been constant to within the observational limits over three years of observation. In particular, since dust streams are not observed, they cannot explain the microphone-detected events discussed by Silverberg (1970) and Silverberg and Poultney (1969). However, the possibility of rare events due to dust blown directly off a cometary nucleus (such as that reported for Comet Bennett by Kent et al., 1971, and discussed by Silverberg, 1970, and Poultney, 1971) cannot be completely ruled out.

REFERENCES

Berg, O. E., and Gerloff, U., 1970. Orbital elements of micrometeorites derived from Pioneer 8 measurements, *J. Geophys. Res.*, **75**, 6932–6939.

Berg, O. E., and Gerloff, U., 1971. More than two years of micrometeorite data from two Pioneer satellites, *Space Research XI*, 225–235.

Dubin, M., and McCracken, C. W., 1962. Measurements of distribution of interplanetary dust, *Astron. J.*, **67**, 248–256. Also *NASA* **RP 103**.

Farlow, N. H., and Ferry, G. V., 1972. Cosmic dust in the mesosphere, *Space Research XII*, 369–380.

Ferry, G. V., and Farlow, N. H., 1972. Upper atmospheric dust concentrations in polar regions, *Space Research XII*, 381–390.

Kent, G. S., Sandford, M. C. W., and Keenliside, W., 1971. Laser radar observations of dust from Comet Bennett, *J. Atmos. Terr. Phys.*, **33**, 1257–1262.

McCracken, C. W., Alexander, W. M., and Dubin, M., 1967. Direct measurements of the mass distribution and time variations in the flux of small dust particles, in *Meteor Orbits and Dust*, edited by G. S. Hawkins, *NASA* **SP-135**, 259–270. Also *Smithson. Contrib. Astrophys.*, **11**, 259–270.

Mazets, E. P., 1971. Cosmic dust and meteor showers, *Space Research, XI*, 363–369.

Millman, P. M., 1970. Meteor showers and interplanetary dust. *Space Research, X*, 260–265.

Nazarova, T. N., 1968. Solid component of interplanetary matter from vehicle observations, *Space Sci. Rev.*, **8**, 455–466.

Porter, J. G., 1952. *Comets and meteor streams*, J. Wiley and Sons, New York, 123 pp.

Poultney, S. K., 1970. Circular letter to observers.

——, 1972. Laser radar studies of upper atmosphere dust layers and the relation of temporary increases in dust to cometary micrometeoroid streams, *Space Research XII*, 403–421.

Roosen, R. G., 1969. The Gegenschein, Ph.D. dissertation, Univ. of Texas.

——, 1970. The Gegenschein and interplanetary dust outside the Earth's orbit, *Icarus*, **13**, 184–201.

Silverberg, E. C., 1970. Interplanetary dust streams. Observation by satellites and lidar. dissertation, Univ. Maryland, Dept. of Phys. and Astron., Tech. Rept. **70-066**.

Silverberg, E., and Poultney, S. K., 1969. Cometary interpretation of the micrometeorite enhancements observed by satellites, Univ. Maryland, Dept. of Phys. and Astronomy, Tech. Rept. **69-965**.

22. Lunar Rocks as Meteoroid Detectors

JACK B. HARTUNG AND FRIEDRICH HÖRZ
Manned Spacecraft Center, NASA
Houston, Texas

AND

DONALD E. GAULT
Ames Research Center, NASA
Moffett Field, California

About 5000 microcraters on seven lunar rocks recovered during the Apollo 12 mission have been systematically studied using a stereomicroscope. Based on comparisons with laboratory cratering experiments, at least 95 percent of all millimeter-sized craters observed were formed by impacts in which the impact velocity exceeded 10 km/s. The dynamics of particle motion near the Moon and the distribution of microcraters on the rocks require an extralunar origin for these impacting particles.

The microcrater population on at least one side of all rocks studied was in equilibrium for millimeter-sized craters; i.e., statistically, craters a few millimeters in diameter and smaller were being removed by the superposition of new craters at the same rate new craters were being formed. Selected surfaces of some rocks, particularly those with glass coatings, are not in equilibrium. For every particle incident upon these "production" surfaces, there remains for observation a corresponding crater; thus the population of craters on such a surface is directly related to the total population of particles impacting that surface.

Crater size-distribution data from production surfaces, together with an experimentally determined relationship between the crater size and the physical parameters of the impacting particle, yield the mass distribution of the interplanetary dust at 1 AU. Based on assumptions corresponding to an impact velocity of about 20 km/s and a particle density of 3 g/cm³, the cumulative particle flux versus mass distribution relationship is

$$\log \mathrm{N} = -0.5 \log \mathrm{m} + \mathrm{C} \qquad \text{for } 10^{-8} < \mathrm{m} < 10^{-6} \text{ g}$$

where N *is the number of particles of mass* m *in grams, and larger, and* C *depends on the time-area product, which is, for the present, unknown. For particles smaller than 10^{-8} g, our observations indicate a sharper decrease in the absolute value of the slope of the flux versus mass curve than is indicated by satellite-borne-experiment data. This result may be due to a genuine relative decrease in the number or kinetic energy of smaller particles, or it may be due to our inability to observe quantitatively the smallest microcraters. For particles larger than 10^{-6} g, the slope of the flux versus mass curve increases smoothly to an absolute value greater than one.*

THE STUDY OF TINY SOLID PARTICLES moving within the solar system—meteoroids—has a long and interesting history. Initially, analysis of visible light streaks in the night sky by astronomers provided the basis for most of what was known about meteoroids. More recently, radio electromagnetic radiation reflected from ionized particles produced during entry of a meteoroid into the atmosphere has been studied using radar techniques. Photometric analysis of the zodiacal light has led to some information about the population of interplanetary particles. With the artificial satellite came a more direct means of detecting meteoroids, and now, very sophisticated electronic devices are used for these studies. The objectives of these efforts have been to determine the mass, velocity, composition, and number density or flux of the particles.

Our purpose in this paper is to discuss a new method that may be applied to the study of meteoroids. That method is the use of exposed lunar rock surfaces as meteoroid detectors. The approach is similar to that of other workers who have studied craters on the actual surface of the Moon that were formed by much larger interplanetary bodies (Shoemaker et al., 1970; Gault, 1970; Hartmann, 1970).

The operation of a lunar rock meteoroid detector is quite simple. A lunar rock surface exposed to space will suffer the impact of interplanetary particles. Each impact produces a small crater on the rock surface. Each crater may be considered a geologic signal, which corresponds to an electronic signal from a satellite detector or to a visible light signal on a photographic plate. Although the operation of a lunar rock as an instrument is simple, as in other experimental methods, its calibration and the analysis and interpretation of data obtained are difficult.

At least one breakthrough has been made in connection with the development of the lunar rock meteoroid detector. In satellite detectors, considerable effort has been expended to maximize the number of events detected. In other words, a large time-area product for the instrument was considered desirable. An estimate of a typical time-area product for a lunar rock meteoroid detector is made in the following manner. The surface area of an exposed face of a lunar rock may be taken to be 100 cm^2 or 10^{-2} m^2. Cosmic-ray exposure times for whole lunar rocks from 3×10^7 to 5×10^8 yr based on measurements of spallation rare gases have been determined by several workers and summarized by Bogard et al. (1971). Exposure times of 10^5 to 5×10^7 yr have been determined by Crozaz et al. (1970), Fleischer et al. (1970), Lal et al. (1970), and Price and O'Sullivan (1970) based on measurements of energetic nuclear particle track densities. Also, exposure times of 10^5 to 10^6 yr have been inferred for rock 10017 by Shedlovsky et al. (1970) based on the analysis of the radioactive nuclides Al^{26} and Mn^{53}, which are produced by the interaction of energetic solar flare particles with certain stable nuclides in lunar rocks. For the purposes of this example, a relatively low exposure time of 10^6 years may be taken. This results in a time-area product for the lunar rock meteoroid detector of about 10^4 m^2-yr, which is several orders of magnitude greater than the value for artificial satellite-borne instruments.

Unfortunately, this relatively low time-area product for typical lunar rocks is still far greater than the optimum for this experiment. The problem is one of retaining a record of only a portion of all events actually occurring on a rock surface, because after a sufficient exposure time, from a statistical viewpoint, the addition of new craters causes the destruction of an equal number of previously existing craters. Most surfaces have reached this state of maturity with respect to cratering and thus are termed "equilibrium" surfaces. A typical crystalline lunar rock with an equilibrium crater population is shown in figure 1.

It is possible to avoid this problem by carefully selecting a lunar rock surface which has not reached equilibrium, that is, a "production" surface, or one upon which there exists essentially one crater or signal corresponding to each particle that impacted the surface. Rocks with such surfaces do exist among those so far returned from the Moon, but they are rare and not easily obtained for analysis. An example of a production surface is the glass-coated surface of rock 12054, a portion of which is shown in figure 2.

MICROCRATER DESCRIPTION

Observations of lunar rock meteoroid detector surfaces were made using an optical stereoscopic microscope with an available range of magnifica-

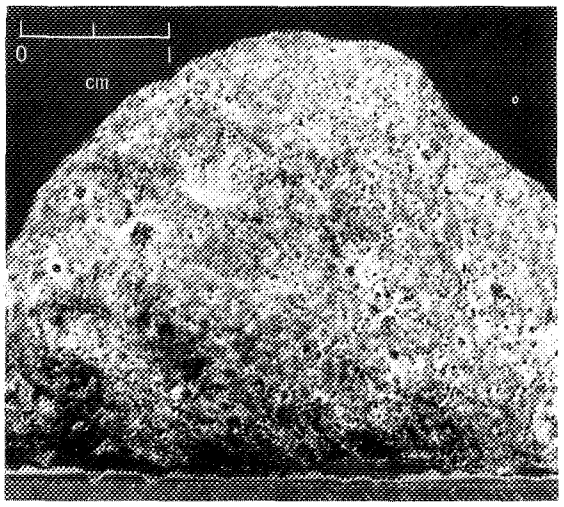

FIGURE 1.—The surface of rock 12017, shown here, has a typical microcrater density of 10 to 20 microcraters with pits larger than 0.2 mm/cm². This surface is in equilibrium with respect to the microcratering process. The largest craters may be recognized by the dark-colored dots (glass-lined pits) surrounded by light-colored areas (halo material). Most of the craters are too small to be recognized on the scale of this photograph. (NASA MSC photograph 70–45307)

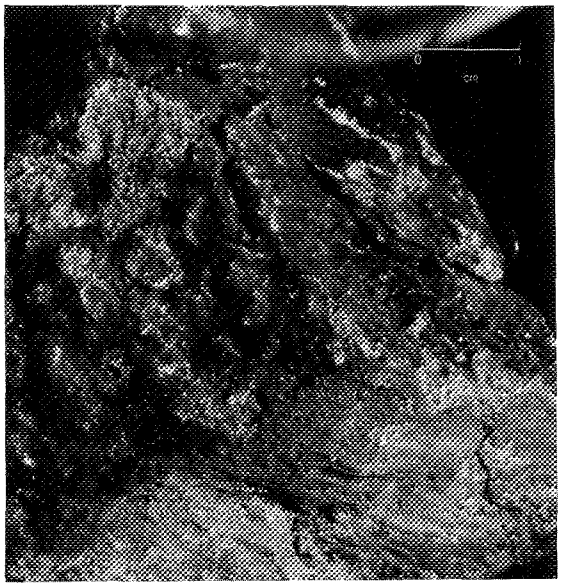

FIGURE 2.—A portion of the glass-coated surface of rock 12054 is shown here. The glass coating shows the effects of a relatively short period of meteoroid bombardment. The surface has not yet reached equilibrium with respect to microcratering; otherwise, the glass coating would have been removed. The largest cratering events penetrate the glass coating and cause the spalling away of the entire thickness of the coating, thus exposing the light-colored underlying rock. The smaller craters do not penetrate the glass and can be observed as light dots with diameters as small as the resolution limit of the photograph; however, the presence of dust particles on the rock surface makes positive identification difficult at this scale. (NASA MSC photograph 70–22995)

tion of from 3.2× to 200×. Essentially all observations were made while working at magnifications of between 10× and 100×. The observational procedure used consisted of first performing a reconnaissance study of the entire rock to gain familiarity with the interesting features and problems related to a particular rock. Then more detailed observations were made. Quantitative data were taken by selecting a field of view of known size which was judged to be representative of the surface and then measuring the important parameters defined by Hörz et al. (1971b) for each crater observed in that field of view. The location of each field of view was indicated on a whole-rock photograph or model. Following this, a completely new field of view was selected and the process repeated until each face of a rock had been thoroughly studied. Faces of rocks were distinguished, based largely on the geometry of the rock.

Microcraters on lunar rocks have been described by LSPET (1969), Neukum et al. (1970), Hörz et al. (1971a, 1971b), and Bloch et al. (1971a). These features may be described in terms of three major elements: a central glass-lined pit, a surrounding halo zone consisting of intensely microfractured crystalline material, and a roughly concentric spall zone. The stereoscopic photographs of figure 3 show a portion of an exceptionally large and fresh microcrater which illustrates the typical relationship between these three elements. The diameter of the halo zone is usually from 2 to 2.5 times that of the glass-lined pit. The diameter of the spall area is most often 2.5 to 5 times that of the pit. The ratio of spall diameter to pit diameter decreases as pit size decreases for small craters in glass. For example, on the glass coating of rock 12054 the average spall to pit diameter ratio was about 3 for 200-micron-diameter pits. For 50-micron-diameter pits, this ratio

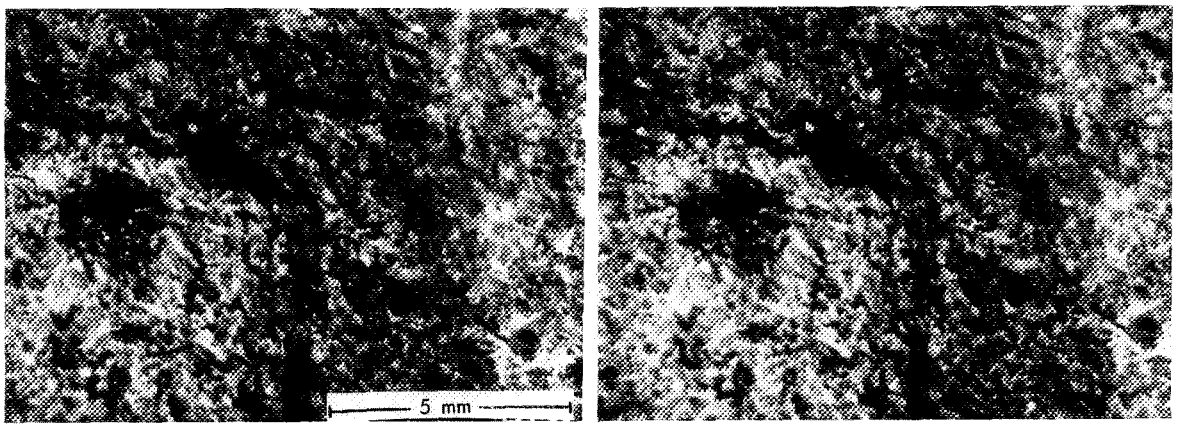

FIGURE 3.—A portion of an exceptionally large and fresh microcrater is shown in this stereoscopic view. The dark glass-lined pit is surrounded and underlain by lighter crystalline or "halo" material which is thoroughly microfractured. The spall area is delineated by a scarp surrounding the pit and halo. Radially outward, a portion of a concentric ring of darker material is shown, and beyond that is the normal rock surface which displays numerous smaller craters, two of which are easily recognized at the lower right of the photograph. The darker ring is attributed to a very thin layer of condensed silicate vapor produced during the impact event which formed the large microcrater. (NASA MSC photographs 70–29946 and 70–29947).

averaged about 2.5. Pit depths are quite variable but are normally one-fifth to one-half the pit diameter.

A scanning electron micrograph of a single typical small microcrater on a glass fragment is shown in figure 4. On equilibrium rock surfaces, the spall areas are relatively larger, and those areas for adjacent craters overlap and tend to destroy one another. On such surfaces, only the most recent craters have easily identifiable spall areas.

The glass that lines most pits appears to be derived from the melting of the host rock, based on the usual similarity in the color of the host minerals and the color of the glass linings, especially for the smaller craters. In general, the glass that lines larger pits appears darker. These observations do not rule out the possibility that melted material from the impacting particle has been incorporated in the glass linings.

Recently, Carter and McKay (1971) have produced glass-lined pits by impact at velocities of 7 km/s in laboratory experiments by raising the temperature of the target material. Bloch et al. (1971b) and Mandeville and Vedder (1971) have produced similar, but much smaller (micron-sized), pits using Van de Graaff microparticle accelerators. For all these experiments, the impact velocity required to produce glass-lined pits is much greater than the 2-km/s escape velocity for the Moon. Therefore, we have concluded that, in general, such pits were formed by the impact of extralunar or interplanetary micrometeoroids.

Although the great majority, over 95 percent, of the impact features observed on lunar rock surfaces are of the glass-lined-pit type described previously, other types of features do exist and represent sources of possible spurious signals. The production of most glass-lined pits is a process of mass removal from the rock surface. Occasionally, a similar appearing feature is observed which is clearly the result of a mass-addition process. In these cases, a dark glass mass has evidently been deposited on the surface. These features are more irregular in outline and are found in greater numbers near the soil line on a rock. We attribute these features to the secondary "splashing on" of liquid ejecta produced during small impacts in the soil near the rock.

On certain rocks, particularly fine-grained crystalline rocks, a relatively large number of clearly identifiable impact craters are observed which do not possess a central glass-lined pit. These craters are recognized by the existence of a depression lined with thoroughly microfractured halo material and occasionally surrounded by an

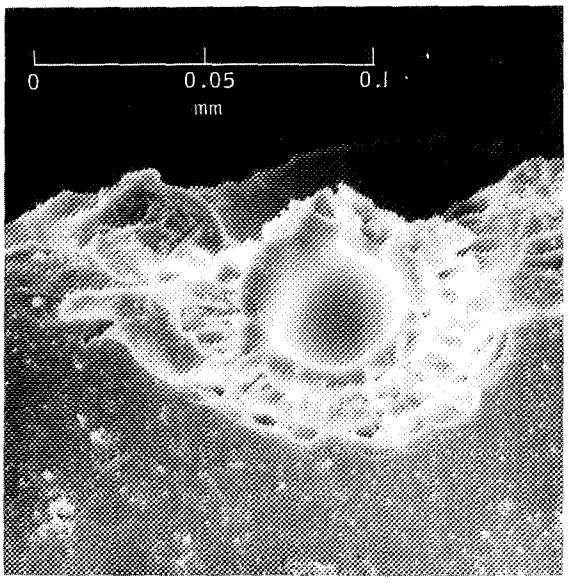

FIGURE 4.—A scanning electron micrograph of a small microcrater. The glass-lined pit and the spall area are nicely illustrated, but the microfractured halo zone is essentially invisible because the scanning electron microscope technique produces an image of the topography only and does not record any albedo differences present on the surface under study. In this case, the host rock is a millimeter-sized glass fragment from the lunar soil collected during the Apollo 11 mission. (Scanning electron micrograph courtesy of D. S. McKay, NASA MSC photograph 70–40177)

observable spall area. Craters in this group appear on the average larger than the coexisting glass-lined-pit-type craters in the same area. We are working on the hypothesis that these pitless craters are produced by the impact of slightly larger meteoroids; and, because of somewhat different mechanical properties of the host rock, the pits are destroyed in the cratering process, while similar impacts on a different rock would not cause destruction of the larger pits. Alternatively, these craters may be the product of impacts by solid particles, either secondary or primary, moving at somewhat lower relative velocities at impact.

In addition to the difficulty in distinguishing between impact craters produced by primary interplanetary particles and secondary particles originating on the Moon, other problems exist that serve to degrade the quality of the statistical data obtained. These problems, taken as a group, compose the overall recognition problem. An example is that the glass lining a small pit occurring in single-mineral grain is often the same color as the host grain, thus making recognition difficult. Small craters in the halo zones of larger craters are not easily observed because the halo of the small crater does not contrast with its surroundings. Microcrater halos are also not well developed on already strongly microfractured whole rocks or on the extremely fine-grained breccias. The highly irregular surface on the microscopic scale of essentially all rocks also contributes to the recognition problem. Finally, lunar rocks are partially coated by "welded dust" (Hörz et al., 1971a), loose dust particles, and other material while resting on the lunar surface and by lunar soil during the collection and processing of the rocks. Rocks are generally cleaned of loosely adhering material, using a gas jet arrangement before our observations are made, but often, dust-filled depressions or a scattering of fine dust remains on the surface after cleaning. Our procedures do not at present include additional cleaning of whole rock surfaces.

Fortunately, the recognition problem may be avoided or at least reduced greatly by the very careful selection of the lunar sample surface to be used as a meteoroid detector. We have found that craters with diameters as low as a few tens of microns are readily recognizable on the glass coatings of certain lunar rocks. Both from the standpoint of obtaining a production population of microcraters and of minimizing the recognition problems, a glass coating on a rock surface is by far the best meteoroid detector.

MICROCRATER POPULATION DATA

The basic quantitative data obtained in the course of this study to date consist of the areal density and size distribution of microcraters. Because of the way our microcraters, or geologic signals, are analyzed, there is a tendency to underestimate the actual number of events detected. We do not count a crater, or receive a signal, unless it is recognized and identified as corresponding to a definite impact event. In contrast to some meteoroid detection experiments, if an error exists for our experiment, it is on the side of failing to observe an event rather than observing too many events. Consequently, our

data represent minimum values for the actual number of events recorded.

Shown in figure 5 is a log-log graph of the cumulative areal number density of craters versus crater size as indicated by the diameter of the glass-lined pit for eight different rocks. For each rock, several faces were analyzed, but only the data for the faces yielding the highest crater densities are plotted on this summary plot for the reasons indicated previously. A more detailed presentation of the data for all these rocks except 12054 has been given by Hörz et al. (1971b).

Several points related to the data presented in figure 5 are important. First, the maximum crater densities for all rocks except 12054 are essentially the same, within a factor of 2, for pit diameters near 0.2 to 0.4 mm. When an appropriate spall area for each crater is considered, this value for crater density is about 10 percent of saturation (as defined by Gault, 1970). This level of saturation is higher than that for most regolith-covered areas on the lunar surface which have been studied on a larger scale and shown to be equilibrium surfaces with respect to cratering (Shoemaker et al., 1970; Gault, 1970).

The probable reason a higher level of saturation exists on rock surfaces than on the regolith is that craters on rock surfaces are removed only by superposition of new craters, while craters on the regolith are, in addition, filled in by the sedimentation of ejecta material from nearby, but not necessarily superimposing, cratering events (Soderblom, 1970). However, in general, these considerations lead to the view that the most densely cratered surfaces of all rocks studied so far, except 12054, are in equilibrium with respect to cratering. The cratering on the thin glass coating of rock 12054 has obviously not yet reached equilibrium; otherwise, the delicate glass coating itself would be completely ruptured and destroyed.

The curves in figure 5 for all rocks except 12054 begin to flatten, that is, the absolute value of the slope decreases, for craters with pit diameters below about 0.2 mm. The curve for rock 12054 remains relatively steep down to a pit diameter of

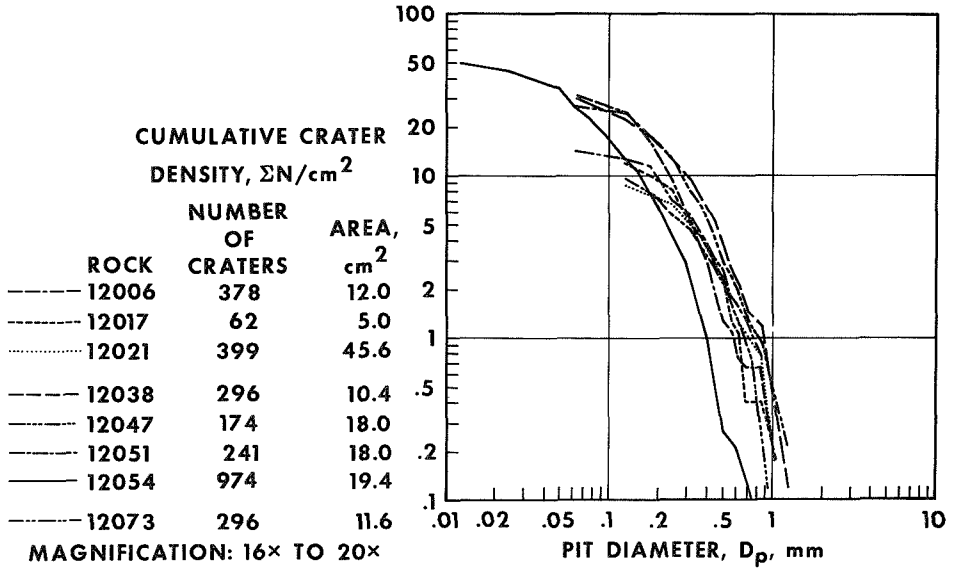

FIGURE 5.—The cumulative areal crater density versus crater size is shown for several lunar rocks. For each rock, the face having the maximum crater density is shown. Similar maximum crater densities for all rocks except 12054 suggest these rock surfaces have reached equilibrium with respect to the cratering process. The flattening of the curves for all rocks except 12054 at smaller crater sizes illustrates the recognition problem that exists for most rocks. The curve for rock 12054 extends to smaller crater sizes, indicating the superior "sensing" qualities of glass-coated surfaces.

0.05 mm. This comparison illustrates the recognition problem relative to the smaller craters on crystalline rock and breccia surfaces. The presence of a relatively large number of 0.05-mm pits on rock 12054 indicates that a similar relative number of smaller events must have occurred on the other rocks, but that the craters formed have simply not been recognized.

The curves in figure 5 appear to steepen as larger crater sizes are approached. Unfortunately, the number of large events observed is insufficient to permit a definite conclusion based on these data. Several possible explanations are considered by Hörz et al. (1971b).

Of particular interest is the flattening of the curve at smaller crater sizes for rock 12054. This flattening may, with no further consideration, be attributed to the recognition problem, which, for a glass-coated surface, simply shifts the flattening to smaller crater sizes, where the observational problems again become dominant. However, we believe, based only on qualitative data obtained during microscopic study of rock 12054, that the flattening of this curve is, at least in part, attributable to a genuine relative decrease in the number or energy of smaller particles impacting the surface of the rock. It will be shown later that the particle size at which this tendency toward fewer events occurs agrees generally with results obtained independently by other investigators of meteoroids.

The data obtained for rock 12054 are presented in detail in figure 6. The data corresponding to two independent investigators working at magnifications of 20×, 40×, and 100× are indicated. The procedure for viewing at different magnifications was to select a field of view at 20×, take data at that magnification, increase the magnification to 40× without moving the sample, take data at 40×, increase the magnification to 100× also without moving the sample, and take data at 100×. Occasionally, the 100× field of view would

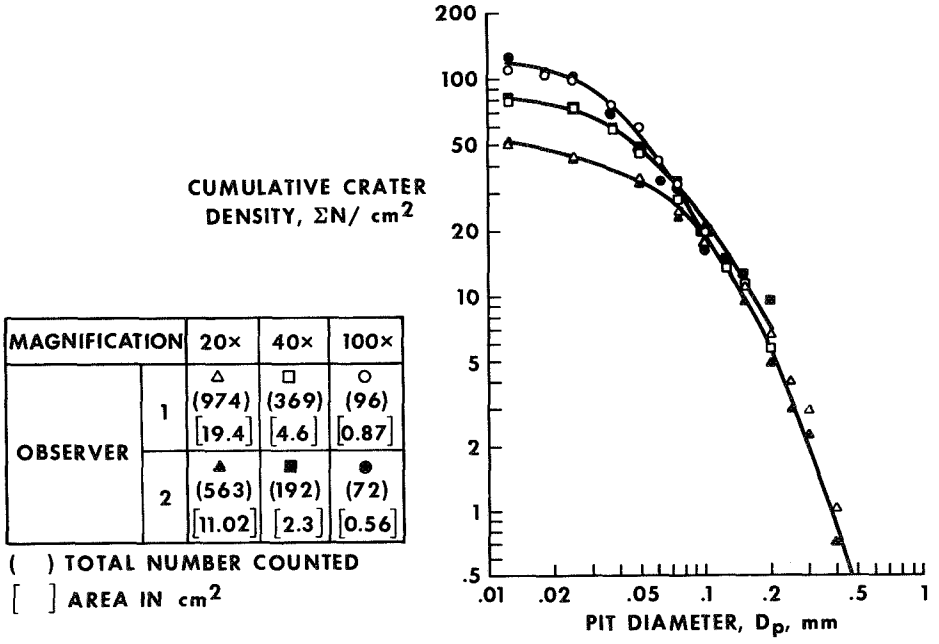

FIGURE 6.—Microcrater density and size data are shown for rock 12054. Results of independent study by two observers at three different magnifications are indicated. The recognition problem is further illustrated by the successively greater densities of smaller craters observed at successively higher magnifications. However, based on qualitative observations, the flattening of the envelope of the curves shown may be in part due to a genuine relative decrease in the number or energy of the smaller interplanetary particles. The curve shown here for a magnification of 20× is the same as the one shown for rock 12054 in figure 5.

be rejected because it fell in an area of extremely poor viewing conditions or in the spall area of a single larger crater. Therefore, the data for 100× magnification may be considered to be "selected" to obtain the maximum crater densities present.

Fields of view counted by one observer were not intentionally duplicated by the other observer. Agreement between the two different workers is within the limits of probable error at essentially all magnifications. This shows a lack of bias on the part of the observers and a uniformity of the crater population over different parts of the surface studied.

The recognition problem also exists for glass surfaces, as is well illustrated by the different positions at which flattening of the curves occurs. The flattening begins at larger crater sizes when lower magnification is used The crater diameter at which flattening occurs is well above the resolution limit of the microscope. We conclude that where the curves at successive magnifications agree, the data are accurate and free from the recognition problem. The recognition problems experienced in our microscopic studies are similar to those experienced in the evaluation of lunar surface photography at various levels of resolution (Shoemaker et al., 1970).

However, we argue that the flattening of the curve for a magnification of 100× is, at least in part, an effect due to a genuine decrease in the relative number or energy of micrometeoroids making the smallest craters (less than 0.05-mm pit diameter), based on the following evidence. When a glass surface is viewed at a magnification of 20×, for example, a number of minute features exist which may or may not be impact craters. A judgment is required to decide whether these features should be considered craters. At a magnification of 100×, when observing conditions are good, the abundance of such features is significantly reduced. The curves, of course, reflect this depletion, but the appearance is the same as would exist if the recognition problem were the entire explanation for the flattening of the curve for a magnification of 100×. The uncertainty described here will be eliminated when observations can be made on an especially prepared surface of rock 12054, using both an optical and a scanning electron microscope.

DETECTOR CALIBRATION STUDIES

To relate quantitatively the geologic signals or microcraters described so far to meteoroids or interplanetary dust requires a sizable ground-based calibration effort. In spite of all the hypervelocity impact experiments that have been undertaken, the development of a well-calibrated lunar rock meteoroid detector is just beginning. The objectives of such a calibration are the determination of the mass, velocity, shape, and composition of individual meteoroids.

Laboratory experiments by Vedder (1971), Bloch et al. (1971b), and Mandeville and Vedder (1971) using Van de Graaff microparticle accelerators provide at present the basis for such a calibration. In these experiments, particles with masses in the range 5×10^{-13} to 5×10^{-9} g were accelerated to velocities as high as 30 km/s, though most of the data were obtained for impact velocities below 10 km/s. Various glasses, crystalline materials, and rock materials were used as targets. Projectiles were polystyrene, density = 1.08 g/cm^3, and iron, density = 7.87 g/cm^3. These projectile and target materials represent fairly well the boundary conditions anticipated for lunar rock meteoroid detectors on the lunar surface. However, at present, experimental limitations do not permit simulation of the range of particle masses and/or sizes necessary to evaluate quantitatively the lunar microcraters under study. The experimental projectiles, 0.1 to 6 microns in diameter, produced craters only a few microns in diameter, whereas the craters of interest on lunar rocks are tens to hundreds of microns in diameter. We must, therefore, extrapolate the experimental parameters over several orders of magnitude.

The fundamental problem consists of relating measurable parameters associated with the crater to the important characteristics of the impacting projectile, which are as follows:

(1) Size
(2) Density } (If any two are known, the third may be determined.)
(3) Mass
(4) Shape
(5) Velocity (magnitude and direction)

Because all experiments have so far used spherical projectiles, we will assume spherical projectile geometry. Mandeville and Vedder (1971) indicate that for oblique impacts, the crater depth

and threshold for spallation are determined by the normal component of velocity, while the asymmetry of the crater is controlled by the tangential component. Because the effect of the velocity *direction* on the size of the glass-lined pit has not yet been clearly determined, we may assume the velocity parameter to be either the normal component or the total impact velocity.

Two approaches to the calibration of the lunar rock meteoroid detector have been suggested. The first relies on the result of both sets of experiments that over the projectile mass range studied for a constant projectile density, the ratio of the glass-lined pit diameter, D_p, to the projectile diameter, d, is very nearly independent of the projectile size or mass, m. This ratio, D_p/d, does, however, vary with the projectile impact velocity (Mandeville and Vedder, 1971; Bloch et al., 1971b). This variation for both groups of experiments is shown in figure 7. Thus, using these curves for a given impact velocity and a given projectile density, ρ we may estimate a single value of D_p/d and calculate the mass, m, of a projectile which formed a pit of diameter, D_p, by use of the equation

$$m=\frac{\pi\rho}{6}\left(\frac{D_p}{D_p/d}\right)^3 \qquad (1)$$

where m is in grams, ρ is in g/cm^3, and D_p is in centimeters.

The second possible approach is based on the relationship that exists between the kinetic energy of the impacting projectile and the mass of the target material displaced during the cratering event. With this approach, the mass of the projectile would be determined by measuring the volume of the crater, finding the required kinetic energy through use of the experimentally derived relationship, and assuming some average impact velocity.

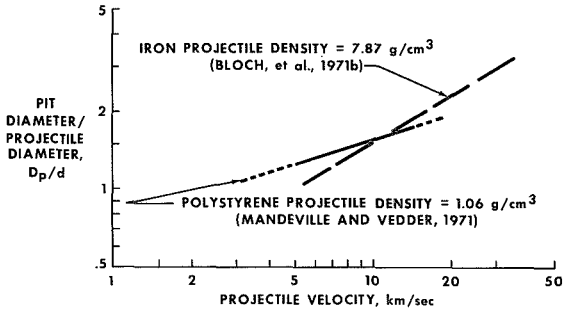

FIGURE 7.—A summary of available experimental cratering data is shown. In this study, 0.1- to 6-micron iron or polystyrene particles were accelerated, using Van de Graaff microparticle accelerators. Target materials were silicate glass or crystalline material with densities of about 2.5 g/cm^3.

An essential difference between these two approaches is that the first requires a pit diameter measurement and the second requires a pit volume measurement or estimate based on a model crater geometry. The advantage of the first approach is that no pit geometry model is required as long as the pit diameter is a well-defined parameter. The second approach offers the possible advantage of permitting a D_p/d which is not necessarily constant for all sizes of particles. Because neither accurate measurements of pit volumes nor careful crater geometry determinations have been made, for the purposes of this paper we have chosen the first approach to solve the calibration problem.

METEOROID POPULATION DATA

Using equation (1), we have converted the crater size distribution data corresponding to the envelope of the curves in figure 6 to particle mass distribution curves which are shown in figure 8(a). Because the D_p/d ratio varies with projectile velocity and density, as indicated in figure 7, curves are presented for several different values of that ratio. This method of presentation also allows visualization of mass distribution curves that would represent the situation where D_p/d did in fact increase with increasing projectile size, other parameters being held constant. An increase of D_p/d with increasing projectile kinetic energy is suggested from crater scaling laws (Moore et al., 1964). However, at present, no quantitative data on the actual magnitude of D_p/d variations are available.

Unfortunately, the data presented in figure 8(a) do not yield an independent determination of the absolute flux of meteoroids impacting the lunar rock meteoroid detector because, as yet, no appropriate exposure time data have been obtained for this rock surface. However, we can

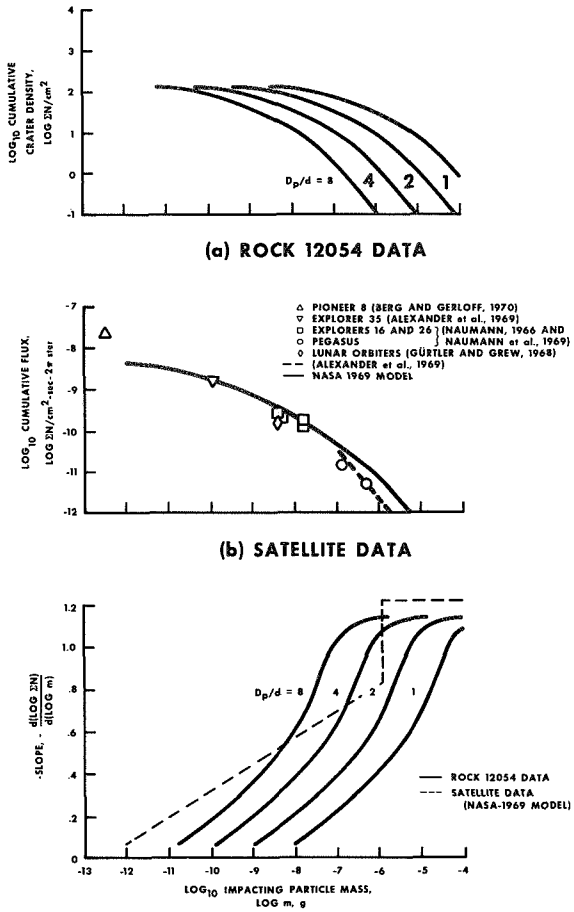

FIGURE 8.—Meteoroid crater density data derived from the study of rock 12054 for a range of possible D_p/d ratios shown in (a) are compared with similar flux data based on satellite-borne experiments, shown in (b). A direct comparison cannot be made because the exposure time of the lunar rock surface is not yet known. Comparison of the slopes of the curves for the two sets of data is meaningful because the slopes indicate the relative numbers of particles without regard for absolute values for areas, times, or exposure angles. Such a comparison (c) shows agreement that there are, relatively, increasingly fewer particles with masses below about 10^{-6} g. Lunar rock data suggest a somewhat higher minimum or cut-off particle size than the satellite data show. The angularity of the satellite data curve is artificial and due only to the equations selected to represent the data.

learn something about the mass distribution of micrometeoroids by comparing our data derived from rock 12054 with data obtained from artificial-satellite-borne detection experiments. Figure 8(b) is a log-log plot of cumulative particle flux versus particle mass, showing data from satellite-borne experiments where redundant detection devices were operating and also showing a curve representing an integrated summary of these and other data available in 1969 (Cour-Palais, 1969).

The first derivatives (slopes) of the curves in figures 8(a) and 8 (b) expressed as a function of log m may be compared directly and are plotted in figure 8(c). Assuming a constant D_p/d value between 2 and 4 for particles with masses greater than 10^{-6} gram, the absolute value of the slope greater than one indicates a successively greater increase in the total number of particles for each incremental decrease in the value of log m. A marked relative depletion of particles with masses below 10^{-6} g is clearly shown by the decreasing slope for these smaller particles. These results are in good agreement with those based on satellite-borne experiments, as is shown in figure 8(c). However, at even smaller particle sizes, the curves diverge beyond what might be considered experimental error. Our lunar rock data suggest a cut-off or almost total absence of particle smaller than 10^{-10} to 10^{-11} gram. This result disagrees somewhat with the NASA 1969 model (fig. 8(c)) and seriously with the result of Berg and Gerloff (1970), who show a considerable number of particles in this size range and smaller (fig. 8(b)).

This sharper decrease in the absolute value of the slope for the lunar rock data is probably in part due to the recognition problem discussed previously. However, we suggest that even after this effect is fully accounted for, the cut-off may still occur at a higher mass than that indicated by the satellite data. Our results are based on optical microscope observations. Scanning electron microscope studies are required to evaluate the population of extremely small micrometeoroids and thus to establish a more reliable value for the cut-off or minimum meteoroid size.

METEOROID COMPOSITION

The investigation of lunar microcraters may also yield information concerning the chemical composition of micrometeoroids. The impact-

melted glass linings of pits may be analyzed for traces of the projectile material. Though extensive data are lacking, Bloch et al. (1971b) and Chao et al. (1970) noted no enhancement of iron or nickel relative to the surrounding host rocks, with the possible exception of one crater (Bloch et al., 1971b). Thus, it may be concluded that most of the craters are produced by projectiles of nonmetallic composition. This is in agreement with independent studies of "meteoritic contamination" of the total lunar regolith as well as selected glass coatings for which carbonaceous chondrite compositions of the projectiles were suggested by Ganapathy et al. (1970) and Morgan et al. (1971).

These results can be substantiated in a qualitative way by our microscopic observations. If we consider only craters with smaller diameters than the average grain size of the host crystalline rock, or if we limit ourselves to craters which are confined to single feldspar crystals, we observe that most of these craters possess clear or transparent glass linings. Only a very small proportion have dark glass linings. If projectiles of metallic composition were abundant, we should see many more craters with dark glass linings.

This deficiency of metallic (opaque) particles may be explained by considering the Poynting-Robertson effect. It has been shown that the Poynting-Robertson effect is important in causing particles to be removed from the solar system and that the efficiency of the Poynting-Robertson effect is a direct function of the opacity of the orbiting particle. In other words, a clear particle should stay longer at a given distance from the Sun than a dark or opaque particle of the same size and density. Therefore, the number of small, clear particles should be relatively greater than the number of small, dark particles, which are under the influence of the Poynting-Robertson effect. We suggest that this effect may explain the relative excess of small clear-glass-type pits on lunar rocks.

SUMMARY OF RESULTS AND FUTURE RESEARCH

Just as we have learned about meteoroids by observing the interaction of these particles with the Earth, so we may expect to learn more about meteoroids by observing the effects of their interaction with the Moon. We have shown that the effects of single meteoroids are recorded on lunar rocks in the form of microcraters. Study of these microcraters has already produced estimates of the mass distribution of meteoroids and may be expected to produce velocity, composition, and flux information related to solid interplanetary particles.

Further experimental work is required to improve the calibration of the lunar rock meteoroid detector. Additional study of especially selected and carefully prepared lunar rock surfaces is planned to extend in either direction the range of meteoroid masses detected with confidence. Chemical analysis of pit glass from a lunar rock has been reported by Chao et al. (1970), but a much more extensive effort will be required to determine what can and cannot be learned about meteoroid composition using this approach. Finally, a successful measurement of the time of exposure of a lunar rock surface or the time since the formation of a single microcrater is of prime importance. The demonstration and application of such capabilities will lead to an independent measure of the flux of meteoroids averaged over about 10^6 years.

REFERENCES

ALEXANDER, W. M., CORBIN, J. D., ARTHUR, C. W., AND BOHN, J. L., 1970. Picogram dust particle flux: 1967–1968 measurements in selenocentric, cislunar and interplanetary space, *Space Research X*, 252–259.

ANON., 1969. Preliminary examination of lunar samples from Apollo 11, *Science*, Lunar Sample Preliminary Examination Team (LSPET), **165**, 1211–1227.

BERG, O. E., AND GERLOFF, U., 1970. Orbital elements of micrometeorites derived from Pioneer 8 measurements, *J. Geophys. Res.*, **75**, 6932–6939.

BLOCH, R., FECHTIG, H., GENTNER, W., NEUKUM, G., SCHNEIDER, E., AND WIRTH, H., 1971a. *Natural and simulated impact phenomena—a photo-documentation*, Max-Planck-Institut für Kernphysik, Heidelberg, MPI H–1971 VI.

BLOCH, R., FECHTIG, H., GENTNER, W., NEUKUM, G., AND SCHNEIDER, E., 1971b. Meteorite impact craters, crater simulations and the meteoroid flux in the early solar system, *Proc. Second Lunar Sci. Conf., Geochim. Cosmochim. Acta, Suppl.*, **2**, 2639–2652.

BOGARD, D. D., FUNKHOUSER, J. G., SCHAEFFER, O. A., AND ZAHRINGER, J., 1971. Noble gas abundances in lunar materials—cosmic ray spallation products and radiation ages from the Sea of Tranquility and the Ocean of Storms, *J. Geophys. Res.*, **76**, 2757–2779.

CARTER, J. L., AND MCKAY, D. S., 1971. Influence of target temperature or crater morphology and implications on the origin of craters on lunar glass spheres, *Proc. Second Lunar Sci. Conf., Geochim. Cosmochim. Acta, Suppl.*, **2**, 2653–2670.

CHAO, E. C. T., BORMAN, J. A., MINKIN, J. A., JAMES, O. B., AND DESBOROUGH, G. A., 1970. Lunar glasses of impact origin: physical and chemical characteristics and geologic implications, *J. Geophys. Res.*, **75**, 7445–7479.

COUR-PALAIS, B. G., 1969. Meteoroid Environment Model—1969 (near Earth to lunar surface), *NASA* **SP-8013**.

CROZAZ, G., HAACK, U., HAIR, M., MAURETTE, M., WALKER, R., AND WOOLUM, D., 1970. Nuclear track studies of ancient solar radiations and dynamic lunar surface processes, in *Proc. Apollo 11 Lunar Science Conf.*, edited by A. A. Levinson, **3**, 2051–2080.

FLEISCHER, R. L., HAINES, E. L., HART, H. R., JR., WOODS, R. T., AND COMSTOCK, G. M., 1970. The particle track record of the Sea of Tranquility, *Proc. Apollo 11 Lunar Sci. Conf., Geochim. Cosmochim. Acta, Suppl.*, **1**, 2103–2120.

GANAPATHY, R., KEAYS, R. R., LAUL, J. C., AND ANDERS, E., 1970. Trace elements in Apollo 11 lunar rocks: implications for meteorite influx and origin of the Moon, *Proc. Apollo 11 Lunar Science Conf.*, edited by A. A. Levinson, **2**, 1117–1142.

GAULT, D. E., 1970. Saturation and equilibrium conditions for impact cratering on the lunar surface: criteria and implications, *Radio Sci.*, **5**, 273–291.

GÜRTLER, C. A., AND GREW, G. W., 1968. Meteoroid hazard near the Moon, *Science*, **161**, 462.

HARTMANN, W. K., 1970. Preliminary note on lunar cratering rates and absolute time scales, *Icarus*, **12**, 131–133.

HÖRZ, F., HARTUNG, J. B., AND GAULT, D. E., 1971a. Micrometeorite craters and related features on lunar rock surfaces, *Earth and Planet. Sci. Lett.*, **10**, 381–386.

——, HARTUNG, J. B., AND GAULT, D. E., 1971b. Micrometeorite craters on lunar rock surfaces, *J. Geophys. Res.*, **76**, 5770–5798.

LAL, D., MACDOUGALL, D., WILKENING, L., AND ARRHENIUS, G., 1970. Mixing of the lunar regolith and cosmic ray spectra: evidence from particle-track studies, *Proc. Apollo 11 Lunar Science Conf.*, edited by A. A. Levinson, **3**, 2295–2304.

MANDEVILLE, J. -C., AND VEDDER, J. F., 1971. Microcraters found in glass by low density projectiles, *Earth and Planet. Sci. Lett.*, **11**, 297–306.

MOORE, H. J., GAULT, D. E., AND HEITOWIT, E. D., 1964. Change of effective target strength with increasing size of hypervelocity impact craters, presented to the 7th Hypervelocity Impact Symposium, Tampa, Florida.

MORGAN, J. W., LAUL, J. C., GANAPATHY, R., AND ANDERS, E., 1971. Glazed lunar rocks: origin by impact, *Science*, **172**, 556–558.

NAUMANN, R. J., 1966. The near Earth meteoroid environment, *NASA* **TN D-3717**.

——, JEX, D. W., AND JOHNSON, C. L., 1969. Calibration of Pegasus and Explorer XXIII detector panels, *NASA* **TR R-321**.

NEUKUM, G., MEHL, A., FECHTIG, H., AND ZÄHRINGER, J., 1970. Impact phenomena of micrometeorites on lunar surface materials, *Earth and Planet. Sci. Lett.*, **8**, 31–35.

PRICE, P. B., AND O'SULLIVAN, D., 1970. Lunar erosion rate and solar flare paleontology, *Proc. Apollo 11 Lunar Science Conf.*, edited by A. A. Levinson, **3**, 2351–2360.

SHOEMAKER, E. M., HAIT, M. H., SWANN, G. A., SCHLEICHER, D. L., SCHABER, G. G., SUTTON, R. L., DAHLEM, D. H., GODDARD, E. N., AND WATERS, A. C., 1970. Origin of the lunar regolith at Tranquility Base, *Proc. Apollo 11 Lunar Sci. Conf., Geochim. Cosmochim. Acta, Suppl.*, **1**, 2399–2412.

SHEDLOVSKY, J. P., HONDA, M., REEDY, R. C., EVANS, J. C., JR., LAL, D., LINDSTROM, R. M., DELANY, A. C., ARNOLD, J. R., LOOSLI, H. H., FRUCHTER, J. S., AND FINKEL, R. C., 1970. Pattern of bombardment-produced radionuclides in rock 10017 and in lunar soil, *Proc. Apollo 11 Lunar Sci. Conf., Geochim. Cosmochim. Acta, Suppl.*, **1**, 1502–1532.

SODERBLOM, L. A., 1970. A model for small-impact erosion applied to the lunar surface, *J. Geophys. Res.*, **75**, 2655–2661.

VEDDER, J. F., 1971. Microcraters in glass and minerals, *Earth and Planet. Sci. Lett.*, **11**, 291–296.

Page intentionally left blank

23. Artificial Meteor Ablation Studies

MAXWELL B. BLANCHARD
Ames Research Center, NASA
Moffett Field, California

Artificial meteor ablation was performed on natural minerals, composed predominately of magnetite and hematite, using an arc-heated plasma stream of air. Analysis of the ablated debris indicates most was composed of two or more minerals. Wustite, a metastable mineral, was found to occur as a common product. The "magnetite" model, whose content was 80 percent magnetite, 14 percent hematite, 4 percent apatite, and 2 percent quartz, yielded ablated products consisting of over 12 different minerals. Magnetite occurred in 91 percent of all specimens examined, hematite in 16 percent, and wustite in 39 percent. The "hematite" model, whose content was 96 percent hematite and 3 percent quartz, yielded ablated products consisting of over 13 different minerals. Hematite occurred in 47 percent of all specimens examined, magnetite in 60 percent, and wustite in 28 percent. The more volatile elements (Si, P, and Cl) were depleted by a reduction of about 50 percent in the amounts present. Also, the relative abundance of Fe increased as a result of both volatile depletion (loss of Si, P, Cl, and Ca) and a reduction in its oxidation state. Hematite was converted to magnetite in the ablation zone along the model's front face. Also, quartz and apatite minerals were converted to an Fe-rich glass consisting of varying amounts of Si, P, Cl, and Ca, depending upon the accessory minerals available at the time of melting. These glass phases occurred as unusual myrmekiticlike intergrowths, which are unique textural indicators of the environment through which the material has survived. The chemistry and mineralogy of these phases remains the only trace of the original minerals. This study has shown that artificially created ablation products from iron oxides exhibit unique properties that can be used for their identification. These properties depend on the composition of the original material and the environmental conditions of formation. In addition to the accepted elemental criteria, these properties are morphologic characteristics, textural parameters, and the existence of metastable minerals.

OVER THE PAST FEW YEARS many investigators have searched for cosmic dust. They have examined particles from sediments (Marvin and Einaudi, 1967), glacial ice (Hodge et al., 1967), and the atmosphere. Atmospheric particles have been collected using aircraft (Carr, 1970), balloons (Brownlee and Hodge, 1969), and rockets (Farlow et al., 1970). In some instances, particle collections have been so sparse that long and involved analytical methods have had to be used to demonstrate even the existence of any specimens (Ferry et al., 1970, and Blanchard et al., 1968). In other instances, the abundance of particles has been overwhelming (Hemenway and Soberman, 1962). In either case, however, the basic problem was to identify the cosmic dust particles and separate them from the artificial and naturally occurring terrestrial contaminants.

Investigators have had only limited success at making positive identifications. Elemental evidence has been the main requisite to substantiate cosmic origin. The most common approach has been to examine the collection for a group of particles containing Ni. Usually occurrence of Ni in sufficient quantity to correlate with Ni-Fe meteorites, or more simply cosmic abundance, allows a case for cosmic origin to be made. Of course, possible contaminants must be ruled out first. Indeed, certain investigations (Blanchard and Farlow, 1966; Blanchard et al., 1967) have shown this latter need quite effectively. However, the relative abundance of Ni-rich particles has been small when compared with the total population. For example, less than 3 percent of spherules collected from Greenland ice contained Ni (Hodge et al., 1967). The remaining particle types are often characterized by a similar assemblage of elements but without Ni. More recently, the occurrence of Ti has been proposed to indicate a volcanic origin for Fe-rich spherules (El Goresy, 1967). Early investigations suggested the occurrence of Mn to indicate a terrestrial origin, but recent studies (El Goresy, 1967) indicate Mn has no genetic importance. At any rate, firmer criteria for identifying particles of cosmic origin are needed.

The most recent results obtained by the Smithsonian's short-lived phenomena program (Anonymous, 1970), indicate large quantities of cosmic material are reaching Earth. Results of the Prairie Network (McCrosky, 1968) have shown a frequency of fireballs perhaps two orders of magnitude greater than earlier studies. Even though large amounts of cosmic dust are reaching the Earth's surface, very little is being positively identified because Ni abundance is not an adequate criterion. More emphasis on chemistry and mineralogy is required for firm cosmic identification.

Meteors, fireballs, and micrometeoroids have one property in common: they ablate while entering the Earth's atmosphere. Micrometeoroid interaction with the atmosphere has been examined theoretically (Kornblum, 1969) and results indicate only submicron-size particles may pass through the atmosphere unaltered. Moreover, those particles in the micron size range would be nearly, if not entirely, ablated away. Larger bodies experience vaporization and fragmentation during entry. That destructive action on these larger bodies may be severe has been shown by experiments designed to study drag, ablation, and radiation effects using a constricted-arc supersonic jet to simulate meteor entry to the Earth's atmosphere (Shepard et al., 1967).

Using this unique experimental facility, it has been possible to simulate meteor ablation under controlled conditions. Initial studies (Blanchard, 1969) showed that mineral fractionation played a key role in determining the form and type of products formed. These products showed a resemblance to the parent body (Blanchard, 1970a and b) but also exhibited features characteristic of this unique environment.

Therefore, a new series of experimental studies in artificial meteor ablation has been initiated for the purpose of learning more about the reactions and products resulting from the ablation environment. This paper is the first of several that will present results of artificial ablation experiments performed on synthetic and natural materials designed to determine those features occurring in naturally ablated products characteristic (or nearly so) of the ablation environment.

PROCEDURE

The models used for these experiments were "magnetite" and "hematite," each with accessory minerals. The facility used for these artificial meteor ablation experiments was a constricted-arc supersonic jet (fig. 1). Operation of the arc jet requires a potential difference of about 1 kV between the tungsten cathode and multiple anode; a current of about 100 A is used. A plasma is generated that flows from the cathode toward the anode, consisting of: electrons, a small amount of argon used to bathe the cathode to reduce its oxidation rate, and high-pressure air ionized to simulate the Earth's atmosphere through which the artificial meteor is traveling. By matching the chamber pressure and the nozzle exit pressure the plasma stream is focused into a near-parallel shaped beam. Facility conditions established for these experiments simulate a low velocity meteor traveling about 12 km/s at an altitude of 70 km.

A pan-shaped copper collector, with a water-cooled jacket to prevent melting, was precleaned and placed inside the chamber. The model to be

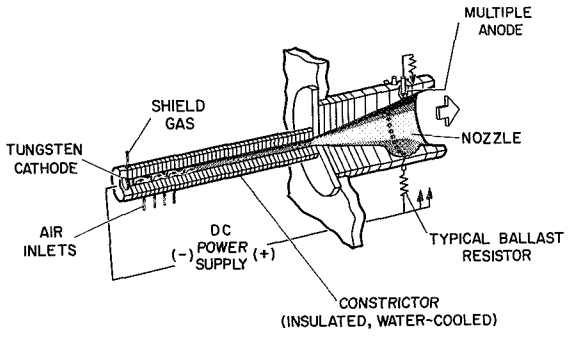

FIGURE 1.—Schematic drawing of a constricted-arc supersonic jet.

ablated was mounted facing the arc jet on a hollow rod cooled by water circulating within it. The model was moved by a servomechanism into the plasma beam after the beam was focused. The entire period of ablation usually lasted no more than 30 s. Generally, about 90 percent of the ablated material was recovered on the collector and chamber floor. The remaining material, distributed throughout the tunnel, was too contaminated for analytical use.

Material recovered from the chamber floor was sorted from any obvious contaminants. Despite attempts to minimize contamination by precleaning the chamber with a vacuum cleaner and repeated washings with distilled water and absorbent paper towels, small chips from screws, bolts, and other sources were occasionally found. However, all material on the collector was contaminant free. This latter material was immediately recovered after the experiment and returned to a cleanroom where the debris was removed from the collector using a brush and a strong pressure rinse with trifluorotrichloroethane. The material was flushed into filtering apparatus and finally recovered on a membrane filter. This procedure prevented contamination in the particle size range below 1 mm.

Optical microscopy studies were performed using the stereo microscope by subdividing the material into groups based on particle morphology. Each group was weighed and counted. Representative numbers of particles from each group were selected for analysis. Analyses were performed using a metallurgical microscope, x-ray diffraction/fluorescence and an electron microprobe. For all analyses, the original model, the ablated front face, and the debris collected were compared. Metallurgical microscopy studies consisted of viewing polished specimens with bright- and dark-field incident light to examine textures and identify phases. Only a few samples of each particle group were examined in this manner. X-ray fluorescence studies consisted of determining relative abundance of the principal elemental constituents in the models for making comparisons with the collected debris. Bulk samples were examined to detect changes in abundance of volatile elements.

The principal analytical method for identifying the many iron oxide phases was x-ray diffraction which easily and reliably separates all of the iron oxide minerals. Over 1000 individual particles ranging from 10 μ to 700 μ were analyzed. Specimens were mounted on this glass rods and positioned inside 57.3-mm-diameter Debye-Scherrer cameras. Exposure periods ranged from 12 to 24 hr using Ilford-G film. All cameras were purged with helium gas during the exposure period to minimize background from air scatter. Identifications were made using film overlays similar to that shown in figure 2. Data for all suspected minerals were taken from ASTM cards and converted into Debye-Scherrer film format on a stable base drafting medium. Phototransparencies were then made with six separate patterns on each transparent overlay. Most of the particles contained two or more minerals; these particles were identified by visually subtracting the diffraction pattern for each major constituent in the film, leaving the most intense lines from minerals remaining to be matched again.

Electron microprobe studies using the MAC Model 400 were performed on the original model and on the ablation zone along the model's front face. Over 100 individual grains of each mineral present in the model were qualitatively analyzed with an energy dispersive, silicon detector and a multichannel pulse height analyzer. Grains in the model and those in the ablated zone along the frontal face were then compared for elemental homogeneity.

Quantitative analyses were performed with spectrometers having either a sealed proportional detector using a LiF crystal, or a flow proportional detector using an ADP or PET crystal depending on the wavelength and peak-to-background ratio

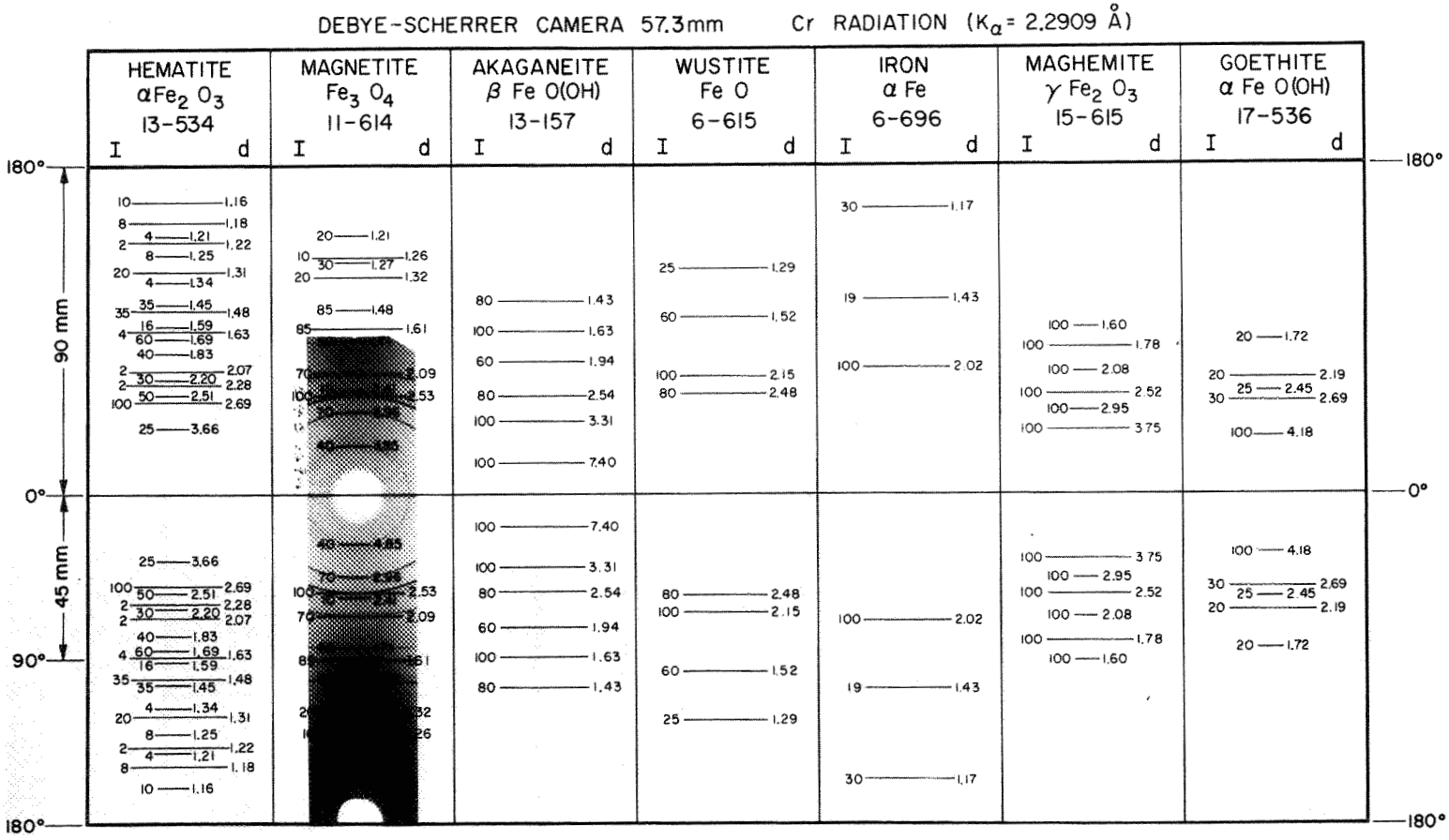

FIGURE 2.—X-ray diffraction film overlay.

required. All analyses were conducted with an accelerating potential of 25 kV. Specimen current for qualitative analysis using the energy-dispersive detector was usually 0.0100 μA. For quantitative analysis using the crystal spectrometers it ranged between 0.0050 and 0.0100 μA, depending on the nature of the grain to be analyzed. Corrections for drift, background, and detector dead time were applied to all data. Absorption corrections were made using the method outlined by Adler and Goldstein (1965). Heinrich's (1966) mass absorption values were used in this procedure. X-ray fluorescence corrections were made using Colby's (1966) procedure. Atomic number corrections were made according to Thomas's (1964) procedure.

RESULTS AND DISCUSSION

Optical Studies

Particles found on the collector were subdivided into groups on the basis of their morphology. Figure 3 illustrates the particle groups; their descriptions are given in table 1. Groups C and D represent those particles not readily exhibiting characteristics of melted products and substantiate that at least a certain part of the ablated debris does not look like melted products. For these experiments, this portion of the debris represented 20 percent by weight of all collected products. A histogram of the collected debris from the "magnetite" ablation experiment showing its weight percent and the quantity of particles in each group is shown in figure 4. The distribution of particle groups and their relative amounts compares favorably for both "hematite" and "magnetite" models even though the amount of "hematite" ablated was less than 10 percent of the amount of "magnetite" ablated. A frequency size distribution was made for the group X particles (fig. 5). This positively skewed distribution indicates the bulk of the small particle debris centers about a median value of 354 μ. However, there is a sizable quantity of debris generated by the ablation process in the size range down to 2 or 3 μ. Smaller particles probably exist but are not collected because they remain in the plasma beam and are evenly dispersed throughout the chamber. A quantity of particles in the 1 to 100 μ size range were recovered on membrane filters and showed a great diversity of colors, e.g., yellow, red, orange, clear, milky. Because many of these also appear in particle collections taken with the plasma beam operating but without a model ablating, most are probably contaminants from the facility. However, many molten particles as small as a few microns in size struck larger bodies already solidified on the collector leaving splatter marks on the surface of the larger bodies (fig. 6).

X-Ray Diffraction Studies

X-ray diffraction analysis of approximately 1000 individual ablated specimens was performed. Particle sizes ranged from 10 to 700 μ. Selected specimens from each morphologic group were examined in numbers proportional to the amount present in each group. Those selected were judged to be most typical for that group, although an unusual specimen was almost always examined. Because most of the specimens analyzed contained two or more minerals the diffraction patterns were complex. Development of the film overlay technique, using actual ASTM file data converting d values into measurements drawn on transparent films, allowed rapid identifications for most of the diffraction patterns. Table 2 shows the magnetite data compiled from 614 patterns, of which 59 percent contained two or more minerals. The "magnetite" mineral model was composed of 80 percent magnetite, 14 percent hematite, 4 percent apatite, and 2 percent quartz. The hematite occurred interstitially between euhedral magnetite grains. Over 12 different minerals were recognized in the ablation products. Note that the frequency of occurrence given cannot be compared with percent abundance. Magnetite, for example, will be somewhat less in abundance than the 91 percent frequency of occurrence suggests because it occurred alone, as a major constituent mixed with other minerals, and occasionally as a minor constituent. Hematite and wustite will be considerably less in abundance than the 16 percent and 39 percent listed because they occurred almost exclusively as minor constituents. Hematite occurred alone only occasionally and wustite only rarely. Nearly all the wustite identified was based on the four most intense d spacings; only two patterns had five (all that can be recorded on film using Cr radiation) of the eight lines listed on the ASTM card. All of

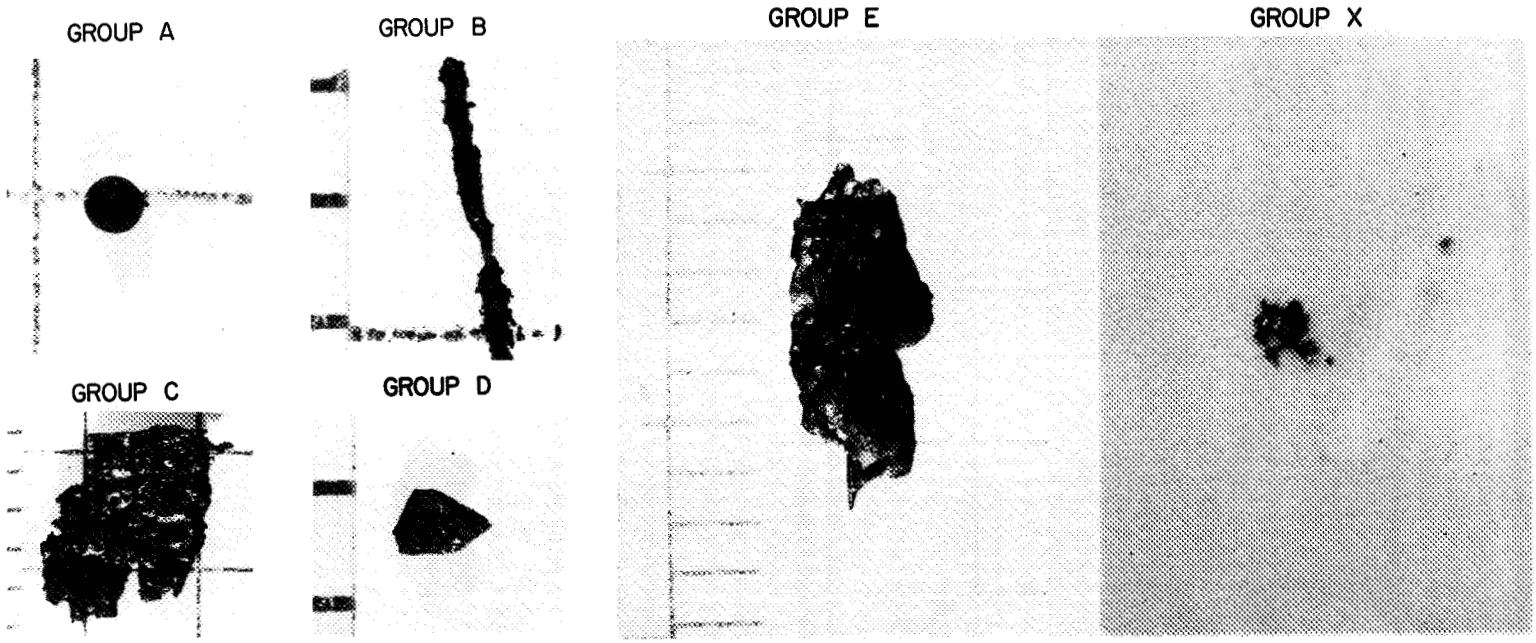

FIGURE 3.—Illustration of particle groups collected from ablation experiment.

TABLE 1.—*Characteristics of Particle Groups Collected From Ablation Experiment*

Group	Shape	Color	Texture
A	Spheres, spheroids, flattened spheroids; many have protuberances.	*Fresh*—silver *Oxidized*—red brown, brown, copper, gold, blue, purple, gray, black	Dull lusterless finish on red brown and gray particles; metallic colors have shiny surface but are not often smooth; general surface appears grainy, some are rough and scaley; many show voids; some are hollow.
B	Flattened droplets and elongated pieces; length-to-width-ratio >5.	*Fresh*—silver *Oxidized*—red brown, brown, copper, blue, gold, gray, black	Dull lusterless finish on red brown and gray particles; metallic colors have shiny surface but are not often smooth; surface appears grainy; some particles are very rough and show discrete octahedrons; many voids at surface.
C	Platelike, very thin flat chips generally equant or rectangular outlines.	*Fresh*—silver *Oxidized*—red brown, brown, copper, blue, gray, black	Dull lusterless on red brown and gray particles; metallic colors have a shiny surface but are not smooth; some show discrete octahedrons; many have very small (<10 μ) flattened droplets on the top surface.
D	Pyramidal, tabular, equant blocks and granules; no more than one side shows melted surface; most easily distinguished by angular edges and broken sides; collector shaped surface and melted surfaces are not readily recognized.	Almost all have fresh surfaces that yield a shiny silver and black color; only occasionally are oxidized surfaces found.	Characterized by freshly broken edges and sides; all particles have angular appearance; voids occur.
E	Irregular or ropy bodies; shape controlled by collector; melted surfaces immediately recognized; length-to-width ratio >2 or 3; some have octahedral crystals at surface.	Fresh edges are shiny silver or black, collector shaped sides are shiny gray, sometimes blue or gold; melted surface ranges in color from dull red brown to shiny gold, silver, or gray.	Sharp pointed edges and grainy surface features; voids are dominant; octahedral crystals are common.
X	Pyramidal, tabular, granular, platelike chips, flattened droplets, and spherules; all particles smaller than 1 mm.	Yellow, red, orange, clear, milky, amber, gray, black, silver.	Ranges from freshly broken edges and sides to shiny smooth surfaces.

the hematite identified had four or more of the most intense lines. Most of the time eight or more lines were present. Magnetite's identification was almost always based on the presence of 12 or more lines in the diffraction pattern. Patterns that were not identified usually could be divided into about five separate mineral groups based on pattern similarities.

An attempt was made to correlate mineral content of the particles with earlier recognized morphologic groups (fig. 3 and table 1). Results are shown in table 3 for the "magnetite" model. Note that all groups (even those not readily exhibiting signs of having been melted) reflect about the same frequency of occurrence for magnetite, hematite, and wustite. This characteristic suggests that mineralogical trends can be established from a smaller quantity of samples and even by restricting the specimens to one particle group. Lepidocrocite appears only in irregular-shaped particles, whereas goethite appears only in particles resembling thin platelike chips. Perhaps this association can be best explained by the uniqueness of the particle groups in that they both

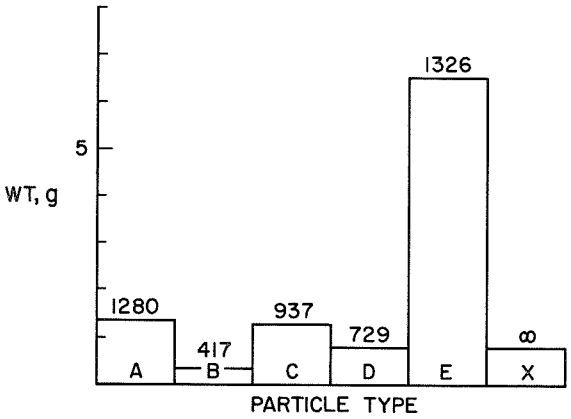

FIGURE 4.—Collected debris from magnetite model.

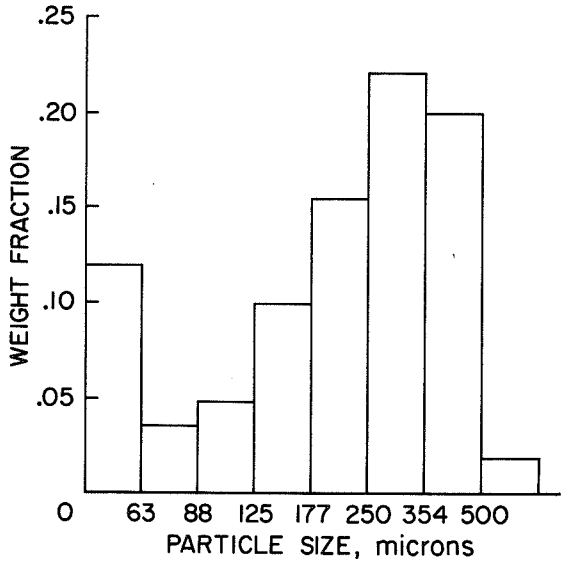

FIGURE 5.—Frequency size distribution of group *X* particles.

have an unusually high ratio of surface area to volume, which favors the formation of alteration products.

With the foregoing results in mind, an examination of hematite ablation products was performed. However, a lower quantity of specimens was examined: 181 particles were analyzed, of which 56 percent contained two or more minerals. Table 4 gives data from the hematite analysis. The model was composed of 96 percent hematite, 3 percent quartz with some magnetite. Magnetite occurred

FIGURE 6.—Flattened droplet with micron size splatter drops.

as a few small individual octahedral crystals in a porous matrix of hematite. Over 13 different minerals were recognized in the ablation products. These minerals were identified in a manner similar to that for the "magnetite" model. The most significant difference noted was the reduction in the amount of hematite present and, at the same time, a dramatic increase in the amount of magnetite and wustite present in the products. As before, the existence of unidentified patterns suggest about five minerals may be represented. The occurrence of akaganeite, lepidocrocite, and goethite are believed to be post ablation alteration products probably from magnetite. Copper particles encountered came from the collector or facility chamber parts. Aluminum particles originated from a pan used to cover the collector during transit.

X-Ray Fluorescence

Analyses were conducted on bulk powdered samples from the model and ablated products. These studies were performed to correlate the "be-

TABLE 2.—*X-Ray Diffraction Analysis of Ablation Products From "Magnetite" Model*

Mineral	Occurrence[a]		Percent frequency of occurrence
	Major constituent	Minor constituent	
Magnetite	549	12	91
Hematite	5	94	16
Wustite	2	236	39
Lepidocrocite	2		<1
Goethite	1		<1
Unknown (≈5 different patterns)	20	1	3
Copper contaminant	15		2
Aluminum contaminant	2		<1

[a] Total number of particles analyzed: 614.
41% patterns with one mineral
59% patterns with two or more minerals

TABLE 4.—*X-Ray Diffraction Analysis of Ablation Products From "Hematite" Model*

Mineral	Occurrence[a]		Percent frequency of occurrence
	Major constituent	Minor constituent	
Hematite	67	18	47
Magnetite	84	25	60
Wustite	2	49	28
Akaganeite	3	4	4
Lepidocrocite	1	1	1
Goethite	2	1	1
Unknown (≈5 different patterns)	9	1	6
Copper contaminant	3	4	4
Aluminum contaminant	10	1	6

[a] Total number of particles analyzed: 181.
44% patterns with one mineral
56% patterns with two or more minerals

TABLE 3.—*Comparison of Particle Shape With Mineral Content of Ablated Products From "Magnetite" Model*

Shape	Number analyzed	Percent frequency of occurrence					
		Magnetite	Hematite	Wustite	Lepidocrocite	Goethite	Unknown
Spherules	142	98	24	37			1
Flattened particles	87	96	17	36			3
Thin plate-like chips	13	85	15	38		8	
Granules	168	99	11	43			3
Irregular bodies	173	96	13	45	1		6
Total	583						

fore" and "after" chemistry. Earlier experiments (Walters and Giutronich, 1967) have demonstrated that vapor fractionation can seriously affect the end products by depleting certain more volatile elements. The role of vapor fractionation in the formation of the ablation products was indicated by analysis of powdered samples of the model and products. As shown in table 5 the elements Si, P, and Cl show strong evidence of volatile depletion by about 50 percent reduction in amounts present. The element Ca shows an apparent depletion of 20 percent of the amount present. An increase in the relative abundance of Fe is a result of both volatile depletion and a reduction in its oxidation state. This last feature is discussed in more detail later.

Electron Microprobe Analysis

Electron microprobe analyses were performed on the "magnetite" and "hematite" models and along the ablated portion on their front faces. Figure 7 is a photomicrograph of a polished surface for these models. In the "magnetite" model, magnetite occurs as euhedral grains with hematite occurring principally at grain boundaries. Sub-

TABLE 5.—*X-Ray Fluorescence Analyses*

Sample	Principal elemental constituents (weight percent)				
	Si	P	Cl	Ca	Fe
Magnetite model "B"	2.4±0.5	1.1±0.2	0.3±0.1	1.6±0.3	61.0±2.0
Magnetite ablated "B"	1.2±0.1	0.5±0.1	0.1±0.1	1.3±0.2	77.5±1.0
Hematite model	1.8±0.3				63.7±1.6
Hematite ablated	1.6±0.1				68.5±0.6

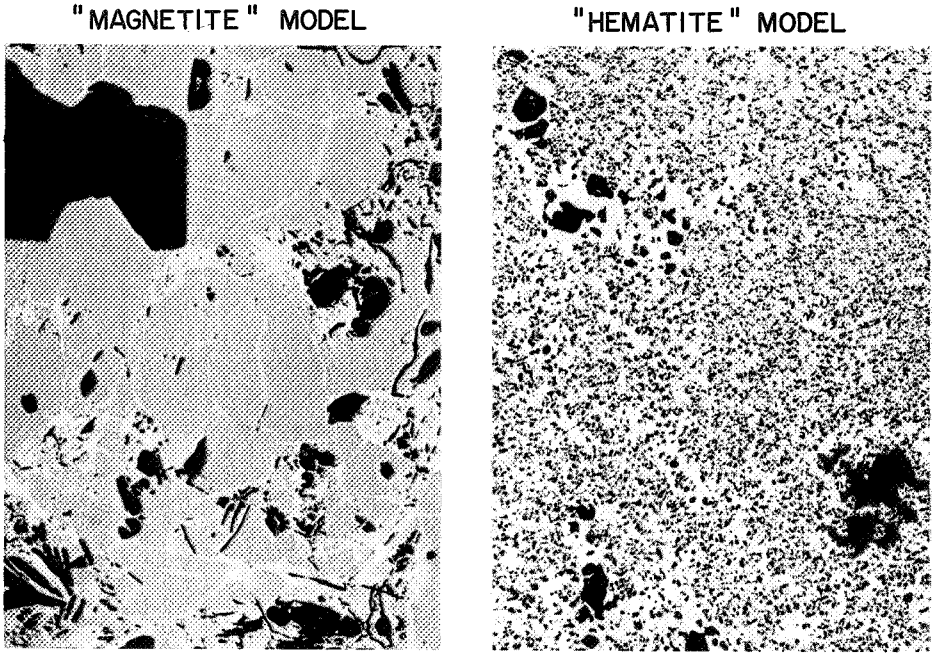

FIGURE 7.—Polished sections of "magnetite" and "hematite" models.

hedral grains of apatite and anhedral grains of quartz are encountered occasionally. For the "hematite" model, magnetite occurs as very few euhedral grains isolated in a porous groundmass of microcrystalline hematite. Occasionally anhedral grains of quartz are encountered. Table 6 reports results of the analysis for the principal elements in each mineral. For these analyses, over 10 different grains of each mineral were analyzed quantitatively for the elements listed. Many more grains were analyzed using an energy dispersive detector to ensure the homogeneity of each mineral.

Analyses of the ablated zone on the front face of the "magnetite" model revealed several features; among them is the apparent conversion of all hematite to magnetite in this zone and in a melt zone extending a few hundred microns deep beneath this surface. New products here are the result of chemical reactions occurring in the gas cap on the front face of the model. These newly formed products from the "magnetite" model are illustrated in figure 8. In the upper left-hand corner the original minerals are seen; magnetite, hematite at the grain boundaries, and one rather large grain of apatite are evident. In the central portion of the figure the hematite has been converted to magnetite, which is the only conspicuous difference. Obviously, this zone reached a molten

TABLE 6.—*Electron Microprobe Analysis of Mineral Grains in Hematite and Magnetite Models and Their Ablated Products*

Sample	Principal elemental constituents (weight percent)				
	Si	P	Cl	Ca	Fe
Magnetite model					
Magnetite	0.3±0.1	0.0	0.0	0.0	71.5±0.4
Hematite	0.0	0.0	0.0	0.0	70.0±0.3
Apatite	0.2±0.1	19.4±0.3	1.5±0.4	39.4±0.4	0.0
Quartz	46.2±0.3				0.4±0.1
Magnetite ablated zone					
Magnetite	0.0	0.0	0.0	0.0	72.2±0.3
Intergrowths	12.4 to 14.8±0.2	1.8 to 2.0±0.2	0.0 to 0.3±0.2	4.8 to 7.7±0.2	34.3 to 44.6±1.4
Hematite model					
Hematite	0.2±0.1				70.1±0.3
Quartz	47.4±0.4				0.4±0.2
Hematite ablated zone					
Magnetite	0.0				72.6±0.2
Intergrowths	15.0 to 16.04±0.5				49.4 to 53.1±1.9

state and in a reducing environment which explains the absence of hematite. In the right-hand portion magnetite occurs with unusual myrmekiticlike intergrowths, which exhibit planar features running generally parallel to the original orientation of the model's front face. Often the intergrowths themselves are aligned parallel with one another but perpendicular to the planar features. Electron probe studies have shown these intergrowths consist of the same elements but in different proportions. More quantitative studies showed the composition range to be 12.4 to 14.8 percent Si, 1.8 to 2.0 percent P, 0.0 to 0.3 percent Cl, 4.8 to 7.7 percent Ca, 34.3 to 44.6 percent Fe, and 33.2 to 41.4 percent O. Oxygen content was determined by subtracting the sum of all components from 100 percent. The Si, P, Cl, and Ca for this new phase came from quartz and apatite minerals occurring in the "magnetite" model. Local differences in the overall abundance of apatite and quartz from place-to-place within the model yielded compositions which vary in abundance of Si, P, Cl, and Ca.

An illustration of newly formed products from the "hematite" model is shown in figure 9. In the upper left-hand side, the original mineral hematite is seen. In the central section, the hematite has been converted to magnetite. However, original surface textures are generally preserved from the hematite through this zone of magnetite. Obviously, this zone has reached a molten state and in a reducing environment, which explains the absence of any hematite. In the right-hand portion, magnetite again occurs with myrmekiticlike intergrowths similar to those of the "magnetite" model. However, electron probe studies revealed a different composition: 15.1 to 16.4 percent Si, 49.4 to 53.1 percent Fe, and 31.9 to 34.2 percent O. This change in content results from the presence of quartz (and the lack of apatite) in the "hematite" model. Silicon for this phase came from the quartz.

X-ray diffraction Debye-Scherrer powder patterns were taken of several pieces of this intergrowth material chipped from the edge of a polished specimen, and yielded no pattern, suggesting the material was amorphous. This phase is considered to be an Fe-rich glass with varying amounts of Si, P, Cl, and Ca depending on the availability of accessory minerals in the model at the time of melting. Clearly, these intergrowths are a unique textural indicator of the environment through which the material has survived, and the chemistry and mineralogy of these phases remains the only trace of the original minerals.

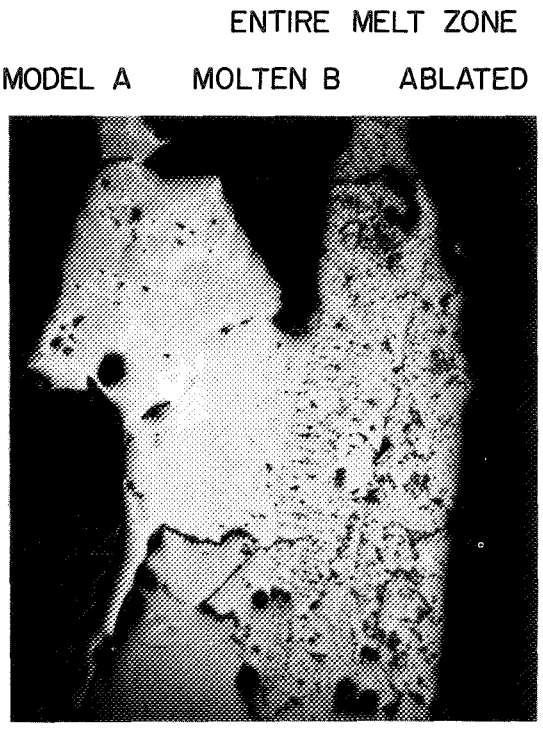

FIGURE 8.—Magnetite ablated model.

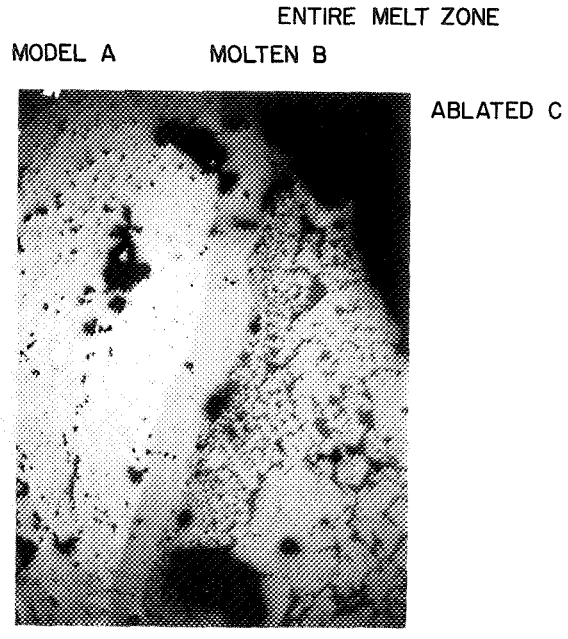

FIGURE 9.—Hematite ablated model.

CONCLUDING REMARKS

This study has shown that artificially created ablation products from iron oxides exhibit unique properties that can be used for identification. These properties depend on the composition of the original material and the environmental conditions of formation. In addition to the accepted elemental criteria, these properties are: morphologic characteristics, textural parameters, and the existence of metastable minerals.

Elemental criteria have been effectively used in a recent investigation of debris collected by aircraft from the Revelstoke and Allende events (Carr, 1970). However, the largest particle size of this material was less than the minimum size examined in this study so application of the proposed properties will have to await further collections.

Morphological characteristics recognized in this study included spherules, flattened droplets, elongated particles, and irregular or ropy bodies with vesicular features. A considerable portion of the debris found in this study was so fragile that many pieces less than 1000 μ in size did not even appear as melted products, yet x-ray diffraction studies clearly showed that all were indeed melted products.

Textural parameters recognized in this study are the existence of myrmekiticlike intergrowths

indicative of the ablation environment. Moreover, the elemental content of these glassy intergrowths offers the only real clues to the initial mineral content of the original body. Serious problems exist in extrapolating back to original mineral content using these phases because certain more volatile elements have been depleted.

Formation of a metastable mineral, wustite, occurred in this study. Wustite was only found in particles less than 1000 μ in size. Particles in this size range radiate heat sufficiently fast to produce a quenching condition, which is responsible for preserving the wustite.

The ablation facility simulated a meteor traveling approximately 12 km/s at an altitude of 70 km. At this altitude, the oxygen partial pressure is about 10^{-2} mm. In contrast, the partial pressure of oxygen at sea level is about 160 mm. Indications are the oxygen partial pressure may reach a maximum as high as 16 mm but only for a short time in the gas cap on the model's front face. While this environment oxidizes metallic iron, it reduces Fe_2O_3. Therefore, an upper limit is clearly indicated for the oxygen available to produce a reaction with the ablating material. Moreover, there is evidence that molecular bound oxygen is lost from the hematite as revealed by mass spectrometry measurements (Ferry, 1970). This loss of oxygen together with rapid cooling explains the formation of wustite from both "magnetite" and "hematite" models. Loss of oxygen is also responsible for formation of magnetite from the "hematite" model. A temperature composition diagram for the iron-oxygen system (Darken and Gurry, 1946) shows that α iron and magnetite would be the normal expected products if wustite was not preserved by rapid cooling (fig. 10).

Formation of wustite during meteor ablation, and akaganeite, lepidocrocite, and goethite during later alteration, has been recognized for some time in meteorite fusion crusts. Wustite and akaganeite were also found in the fusion crust of the Sputnik IV fragment (Marvin, 1963). Spherules of wustite have also been found associated with other material of suspected extraterrestrial origin (high nickel/iron ratio) from ancient (Marvin and Einaudi, 1968) and marine (Millard and Finkelman, 1970) sediments. Assuming industrial contaminants have been ruled out, it appears the existence of wustite and its association with other iron oxides can be used as firm criteria in identifying debris ablated from meteors and fireballs.

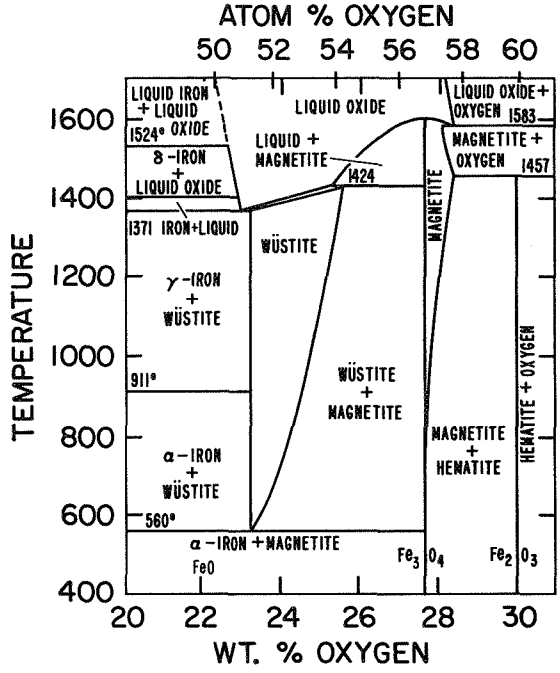

FIGURE 10.—Iron-oxygen system at a total oxygen pressure of one atmosphere; temperature-composition phase diagram. From Darken and Gurry, 1946. Iron-oxygen equilibria involving liquid oxide, *J. Amer. Chem. Soc.*, **68**: 799.

ACKNOWLEDGMENTS

The author wishes to express his gratitude for assistance rendered by the following individuals: Richard Ferguson, electron probe microanalysis; Gary Cunningham, x-ray fluorescence; Thomas Palmer, x-ray diffraction; and Francis Hughes, microparticle manipulation. During the analysis, invaluable suggestions were rendered by H. D. Shade, G. V. Ferry, and N. H. Farlow. Sincerest appreciation is expressed to W. C. A. Carlson and C. E. Shepard of the Ames High Enthalpy Research Branch for their interest in the ablation project and their assistance in making the supersonic arc jet facility available for these experiments.

REFERENCES

ADLER, I., AND GOLDSTEIN, J., 1965. Absorption tables for electron probe microanalysis, *NASA Tech. Note* **D-2984**, 267.

ANON., 1970. Annual report, 1969: Smithsonian Institution—center for short lived phenomena, Cambridge, Mass., 246 pp.

BLANCHARD, M. B., 1970a. Artificial meteor ablation studies of iron oxide minerals, *EOS–Trans. Amer. Geophys. Union*, **51**, 831.

——, 1970b. Wustite—a common occurrence in artificial meteor ablation products, *Meteoritics*, **5**, 181.

——, 1969. Preliminary results of artificial meteor ablation (abstract), *Meteoritics*, **4**, 261.

BLANCHARD, M. B., FERRY, G. V., AND FARLOW, N. H., 1968. Analyses of particles on surfaces exposed to the 1965 Leonid meteor shower by the Luster sounding rocket. *J. Geophys. Res.*, **73**, 6347–6360.

BLANCHARD, M. B., FARLOW, N. H., FERRY, G. V., AND SHADE, H. D., 1967. Contaminants vs micrometeorites from the 1965 Leonid meteor shower, *Proc. Amer. Assoc. Contam. Contr.*, 139–145.

BLANCHARD, M. B., AND FARLOW, N. H., 1966. Contamination control during designing, fabrication, test, and launch of an upper atmosphere rocket payload, *J. Contam. Contr.*, **5**, 22–25.

BROWNLEE, D. E., AND HODGE, P. W., 1969. Results of a large volume micrometeorite collection at an altitude of 115,000 feet (abstract), *Meteoritics*, **4**, 264.

CARR, M. H., 1970. Atmospheric collection of debris from the Revelstoke and Allende fireballs, *Geochim. Cosmochim. Acta*, **64**, 689–700.

COLBY, J. W., 1966. The applicability of theoretically calculated intensity corrections in microprobe analysis, in *The Electron Microprobe*, edited by McKinley, Heinrich, and Wittry, J. Wiley and Sons, 95–188.

DARKEN, L. S., AND GURRY, R. W., 1946. The system iron-oxygen, II equilibrium and thermodynamics of liquid oxide and other phases, *J. Amer. Chem. Soc.*, **68**, 748–816.

EL GORESY, A., 1967. Electron microprobe analysis and microscopic study of polished surfaces of magnetic spherules and grains collected from the Greenland Ice, *Smithson. Astrophys. Obs., Spec. Rept.* No. 251.

FARLOW, N. H., FERRY, G. V., AND BLANCHARD, M. B., 1970. Examination of surfaces exposed to a noctilucent cloud, Aug. 1, 1968, *J. Geophys. Res.*, **75**, 6736–6750.

FERRY, G. V., BLANCHARD, M. B., AND FARLOW, N. H., 1970. Microparticle collection experiments during the 1966 Orionid and Leonid meteor showers, *J. Geophys. Res.*, **75**, 859–870.

FERRY, G. V., 1970. Preliminary interpretation of mass spectra from artificial meteor ablation, *Meteoritics*, **5**, 196–197.

HEINRICH, K. F. J., 1966. X-ray absorption uncertainty, in *The Electron Microprobe* edited by McKinely, Heinrich and Wittry, J. Wiley and Sons, 296–377.

HEMENWAY, C. L., AND SOBERMAN, R. K., 1962. Studies of micrometeorites obtained from a recoverable sounding rocket, *Astron. J.*, **67**, 256–266.

HODGE, P. W., WRIGHT, F. W., AND LANGWAY, C. C., 1967. Studies of particles for extraterrestrial origin 5, compositions of the interiors of spherules from Arctic and Antarctic ice deposits, *J. Geophys. Res.*, **72**, 1404–1406.

KORNBLUM, J. J., 1969. Micrometeoroid interactions with the atmosphere, *J. Geophys. Res.*, **74**, 1893–1970.

MARVIN, U. B., 1963. Mineralogy of the oxidation products of the Sputnik 4 fragment and of iron meteorites, *J. Geophys. Res.*, **68**, 5059–5068.

MARVIN, U. B., and EINAUDI, M. T., 1967. Black, magnetic spherules from Pleistocene and recent beach sands, *Geochim. Cosmochim. Acta*, **31**, 1871–1884.

MCCROSKY, R. E., 1968. The distribution of magnitudes, masses, and energies of large meteoritic bodies, *Smithson. Astrophys. Obs. Spec. Rept.* No. 280.

MILLARD, H. T., AND FINKELMAN, R. B., 1970. Chemical and mineralogical compositions of cosmic and terrestrial spherules from a marine sediment, *J. Geophys. Res.*, **75**, 2125–2135.

SHEPARD, C. E., VORREITER, J. W., STINE, H. A., AND WINOVICH, W., 1967. A study of artificial meteors as ablators, *NASA Tech. Note* **D-3740**.

THOMAS, P. M., 1964. A method for correcting for atomic number effects in electron-probe microanalysis, *United Kingdom Atomic Energy Authority, Res. Group Rept.* No. AERE–R4593.

WALTERS, L. S., AND GIUTRONICH, J. E., 1967. Vapor fractionation of silicate melts at high temperatures and atmospheric pressures, *Solar Energy*, **XI**, 163–169.

24. Possible Evidence of Ablation on Cosmic Dust Particles

CURTIS L. HEMENWAY
Dudley Observatory and
State University of New York at Albany
Albany, New York

ÖPIK (1937) AND WHIPPLE (1950) have predicted that small dust particles should be able to enter the Earth's atmosphere without reaching their melting temperature and thus retain their original shape prior to entry. They have shown that the critical size is a strong function of velocity as well as the physical parameters of the dust particle. A number of investigators have collected particles at high altitude believed to be of this type (Hemenway and Soberman, 1962; Wright and Hodge, 1964; Thomsen, 1963). This brief paper presents possible evidence of the existence of small bodies collected with our Sesame collector (Hemenway et al., 1967; Hemenway et al., 1971) which apparently were sufficiently large to experience surface ablation and melting.

Figure 1 shows a scanning electron micrograph of a 19 μ diameter, irregular particle col-

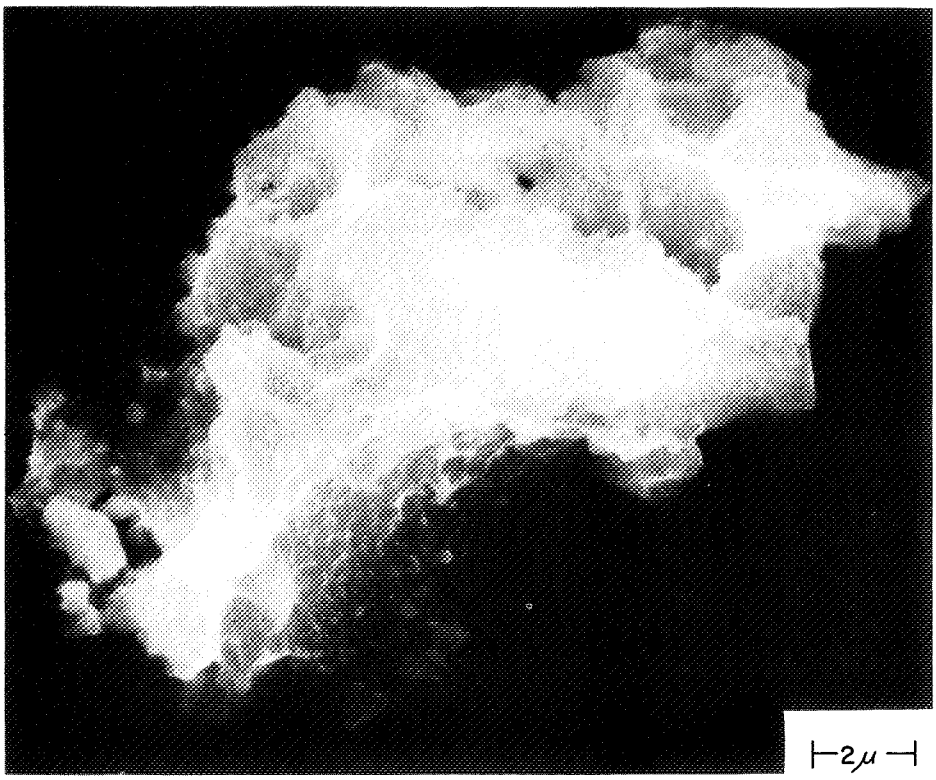

FIGURE 1.—Ablated particle with reentrant cavities.

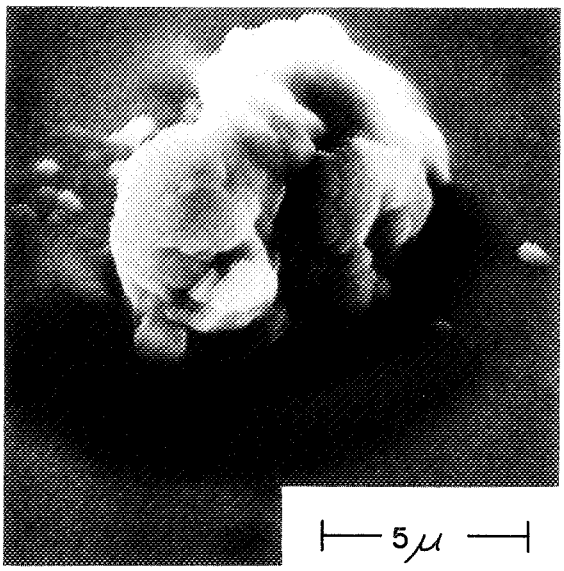

FIGURE 2.—Ablated particle with rounded nodules.

lected August 13, 1970. This particle has reentrant cavities over much of its surface and appears to have surface characteristics somewhat similar to those of much larger meteoritic bodies. This particle has a number of small melted nodules over much of its surface.

Figure 2 shows a scanning micrograph of a 14 μ diameter irregular particle collected November 18, 1967, having numerous rounded nodules. This particle (fig. 2) is similar to that published in Space Research XI (Hemenway et al., 1971). Both of these particles were collected shortly after the Leonid meteor shower.

Figure 3 shows a 63 μ diameter irregular particle collected August 14, 1966, and may have been stably oriented during entry such that only one side experienced significant ablation. Parallel flow marks can be seen on this particle.

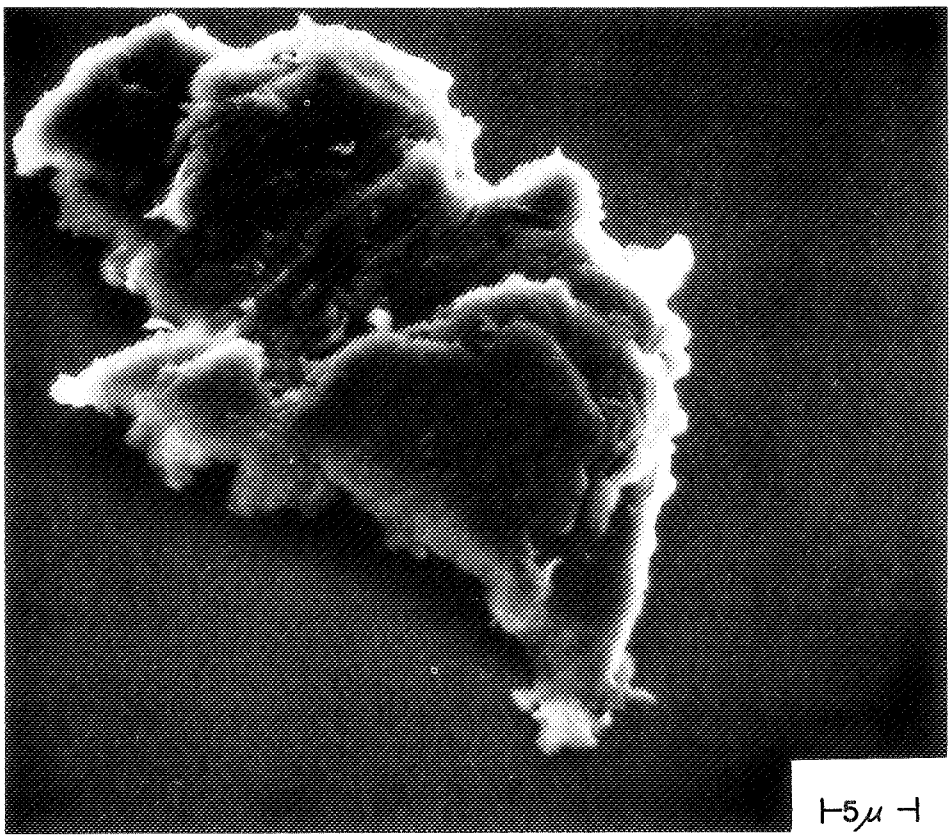

FIGURE 3.—Particle showing parallel flow marks.

Only about 5 percent of our Sesame balloon particles show evidence of surface ablation and less than 0.5 percent of the collected particles are spheres. The absence of ablation signatures on most of our balloon particles is evidence that the balloon particles are for the most part fragile fragments which have crumbled from larger meteoric bodies and have been partially shielded during reentry. This conclusion is supported by the observed enhancement in the apparent balloon flux at times of meteor shower activity (Hemenway et al., 1967).

REFERENCES

HEMENWAY, C. L., HALLGREN, D. S., AND COON, R. E., 1967. High altitude balloon-top collections of cosmic dust, *Space Research VII*, 1423–1431.

HEMENWAY, C. L., HALLGREN, D. S., LAUDATE, A. T., PATASHNICK, H., RENZEMA, T. S., AND GRIFFITH, O. K., 1971. A new high altitude balloon-top cosmic dust collection technique, *Space Research XI*, 393–395.

HEMENWAY, C. L., AND SOBERMAN, R. K., 1962. Studies of micrometeorites obtained from a recoverable sounding rocket, *Astron. J.*, **67**, 256–266.

ÖPIK, E., 1937. Basis of the physical theory of meteor phenomena, *Pub. Ast. Obs. Tartu*, **29**, 1–67.

THOMSEN, W. J., 1953. The annual deposit of meteoritic dust, *Sky Telesc.*, **12**, 147–148.

WHIPPLE, F. L., 1950. Theory of micro-meteorites Part I, in an isothermal atmosphere, *Proc. Nat. Acad. Sci.*, **36**, 687–695.

WRIGHT, F. W., AND HODGE, P. W., 1964. Composition studies of extra terrestrial particles, *Annals of N.Y. Acad. of Sci.*, **119**, 287–297.

Page intentionally left blank

25. Ablation in Meteors

V. N. LEBEDINETS
Astronomical Council, Academy of Sciences
Moscow, U.S.S.R.

PHOTOGRAPHIC AND RADAR OBSERVATIONS of meteors reveal essential discrepancies from the simplest physical theory of meteors. The simplest theory (Whipple, 1943; Herlofson, 1948; Kascheev et al., 1967) proceeds from the following suppositions: (1) the meteoroid is a dense nonfragmenting body; (2) the sole ablation mechanism is evaporation; and (3) the whole energy transferred to a body by colliding air molecules is spent on evaporation. In addition, the simplest theory of radiowave reflection from meteor trails that does not take into account diffusive and thermodiffusive expansion of a meteor trail and change of the electron line density along the trail is used for the interpretation of the results of radar observations.

The discrepancy of the observational data versus the simplest theory of meteors is usually ascribed to fragmentation of meteoroids, only one fragmentation mechanism being considered: that of a friable body of low density under the action of aerodynamical pressure. Nevertheless, at present, any detailed theory of ablation of very friable bodies free from intrinsic contradictions is absent. It is believed that the reference to friability and fragmentation automatically explains all peculiarities of meteors.

In a number of our works (Lebedinets, 1963, 1966; Lebedinets and Portnyagin, 1966a, 1967; Lebedinets et al., 1969; Lebedinets and Shushkova, 1968), a more precise theory of the ablation of dense meteoroids, as well as the theory of radar-meteor reflection and radar-meteor detectability, was devised (Lebedinets, 1963, 1966; Lebedinets and Sosnova, 1968, 1969). Comparison of the more precise theory with the observational data permits some conclusions on the mechanism of meteoroid ablation.

RADAR-METEOR FRAGMENTATION SYMPTOMS

Verniani and Hawkins (1965) and Verniani (1966) have published the parameters of 320 radar meteors $+7^m$ to $+9^m$. Analyzing these data, Verniani (1969) concludes:

> The degree of fragmentation of meteors with a mass of 10^{-4} grams appears to be even more severe than that of the average faint photographic meteors having a mass of the order of 1 gram. As a matter of fact, the discrepancy between the theory and observations is greater for radio meteors: the average length in the studied sample is very short, only 40 percent of its theoretical value.

Since the accuracy of radar measurements of individual meteor parameters is relatively small, the average values are more interesting. Table 1 lists mean parameters obtained for 320 meteors.

The density of each meteoroid was calculated according to deceleration. The shape factor was assumed to be $A=1.5$ (corresponding to a randomly oriented cube) and the drag coefficient $\Gamma=1.1$ (as "The radio meteors of the present sample are so small that, without any doubt, they have experienced free molecular flow; therefore, we shall use $\Gamma=1.1$" (Verniani and Hawkins, 1965)). Assuming $A=1.5$ and density $\delta=0.8$ g/cm^3, Verniani and Hawkins suppose that the body does not melt entirely in the process of ablation.

Let us compare mean parameters of radar meteors (table 1) with the simplest theory.

TABLE 1.—*Mean Parameters of 320 Radar Meteors*

No-atmosphere velocity	v_0 =34.45 km/s
Photographic magnitude	M_{pm} =+8.05
Zenith angle	cos z =0.798
Beginning height	h_b =95.0 km
End height	h_e =86.9 km
Maximum ionization height	h_m =90.8 km
Initial mass	m_0 =1.4×10^{-4} g
Maximum electron line density	log α_m =8.54 (cm^{-1})
Ablation coefficient	log σ =−11.75 (cm^2/s^2)
Meteoroid density (median value)	δ =0.8 g/cm^3

According to Herlofson (1948), the atmospheric densities ρ_m at the height of maximum ionization h_m and ρ_e at the height of the trail end h_e are

$$\rho_m = \frac{2Qm_0^{1/3}\delta^{2/3}\cos z}{\Lambda A H v_0^2} \qquad \rho_e = 3\rho_m \qquad (1)$$

where Q is the evaporation energy of 1 g of meteor substance, Λ is the heat-transfer coefficient, m_0 is the initial mass, H is the atmospheric scale height, and v_0 is the initial velocity.

Under the conditions of free molecular flow, $\Lambda \approx 1$. According to Lebedinets and Portnyagin (1967) and Öpik (1958a), $Q=8\times10^{10}$ ergs/g for stone and iron meteoroids. Substituting values of m_0, δ, z, A, and v_0 from table 1 into equation (1) and using the Tables of the Standard Atmosphere (1964), we find $h_m=99.4$ and $h_e=93.3$ km. The theoretical values of h_m and h_e are correspondingly 7.6 and 6.5 km greater than the observational ones. Practically the whole observed trail is situated lower than the theoretical height of the trail end. If a meteoroid breaks up, its evaporation height increases independently from the mechanism of fragmentation, and the discrepancy between observed and theoretical heights becomes even more.

Thus, the very small mean density of radar meteors, 0.8 g/cm^3, assumed by Verniani (1966, 1969) is incompatible with the observed heights of radar meteors for any ablation mechanism. This result stands to reason, for stone and iron meteoroids of any density and structure with $m_0=1.4\times10^{-4}$ g and $v_0=34.45$ km/s moving under the conditions of free molecular flow cannot reach the height of 80 km without melting (or evaporating) completely. After complete melting, such a small body gathers in a spherical droplet (if it does not break up in the process of heating) that is stable under the action of the forces of surface tension and aerodynamical pressure (Lebedinets and Portnyagin, 1967). Assuming a mean chemical composition the same as the most widely distributed type of stone meteorites, i.e., chondrites (Lebedinets, 1966; Vinogradov, 1965), we obtain the droplet density $\delta=3.5$ g/cm^3. For a sphere, $A=1.21$. At such a δ and A from equation (1), we find $h_m=93$ and $h_e=87$ km. The theoretical height of the trail end practically coincides with the observational one, and the height of maximum ionization is larger by 2.2 km than the observational height. It will be shown below that this small discrepancy is explained by the selectivity of radar observations.

Comparing the observational meteor height with the theoretical one, Verniani (1966) utilizes, instead of the simple formula, equation (1), a more complex one obtained from the combination of the equations of evaporation and deceleration, in which he includes the ablation parameter σ. For a nonfragmenting body, we have

$$\sigma = \frac{\Lambda}{2\Gamma Q} \qquad (2)$$

At $\Lambda=1$, $\Gamma=1.1$, and $Q=8\times10^{10}$ ergs/g, we obtain $\sigma=5.6\times10^{-12}$ s^2/cm^2.

Values of σ can be calculated according to the observational data if the deceleration and electron line density at a given point of the trail, as well as the whole ionization curve, are measured. Verniani and Hawkins' radar observations did not allow measurement of the meteor deceleration; they gave only 3 to 4 values of velocity v at different moments t. Verniani and Hawkins approximated the dependence $v(t)$ by a straight line, and according to the inclination of this line, a mean deceleration related to the mean meteor height was determined. Thus, the mean value of $\sigma=1.8\times10^{-12}$ shown in table 1 was obtained.

The value of $\sigma=1.8\times10^{-12}$ obtained by Verniani and Hawkins turns out to be three times as small as the value of $\sigma=5.6\times10^{-12}$ obtained from equation (1) at $\Lambda=1$, $\Gamma=1.1$, and $Q=8\times10^{10}$ ergs/g.

For very small meteoroids that are heated through and that are moving under the condition of free molecular flow, the values of A and Γ cannot differ essentially from 1. Thus, the single parameter that may be changed in equation (1) is the energy of ablation Q. At $\sigma = 1.8 \times 10^{-12}$, $A = 1$, and $\Gamma = 1.1$ from equation (1), we have $Q = 2.5 \times 10^{11}$ ergs/g. There is no widely distributed substance with such a high evaporation energy in nature. If there is another ablation mechanism, such as blowing-off of the melted layer, separation of dust particles from a very friable body, and so on, then the ablation energy can only be lower than at evaporation.

Thus, the value of $\sigma = 1.8 \times 10^{-12}$ erg/g obtained by Verniani and Hawkins for nonfragmenting radar meteors cannot be correct at those heights where they were observed. In the case when measured deceleration is related not to the whole body but to a swarm of very small fragments, Verniani and Hawkins' procedure leads to an underestimate of the meteoroid density by $N^{1/3}$. However, the essential fragmentation assumption is incompatible with the observed radar-meteor heights. Therefore, we can conclude that the mean deceleration obtained by Verniani and Hawkins is overestimated.

The main cause of such an overestimate apparently is the influence of radar-observation selectivity. As shown in a number of works (Lebedinets, 1963, 1966; Öpik, 1958b; Greenhow, 1963), the upper parts of faint meteor trails are not registered in radar observations, owing to the influence of the initial radius of meteor trails on the amplitude of the radar echo. This effect grows with increasing radar power and decreasing wavelength, and consequently it is especially large for the equipment of the Harvard Radio Meteor Project (Hawkins, 1963). Since deceleration grows exponentially with time, we will overestimate the mean meteor deceleration when throwing away the initial part of the meteor. There are a number of causes of overstating the mean meteor deceleration of Verniani and Hawkins. The precision of radar-meteor velocity measurements is comparatively low (appreciably lower than assumed by Verniani, 1966), and negative deceleration (acceleration) is obtained for 39 meteors as a result. The authors did not take these meteors into account. Besides accidental errors in velocity, there are two systematic ones due to the diffusion effect and the rapid change of the effective electron line density along the trails of faint meteors (Kascheev et al., 1967; Lebedinets and Sosnova, 1969). The first error leads to underestimation of mean velocity, and the second, to overestimation of mean meteor deceleration.

THE PHYSICAL THEORY OF FAINT METEORS

The physical theory of radar meteors includes three main sections: (1) the ablation theory, (2) the theory of ionization and meteor-trail formation, and (3) the theory of radiowave reflection from meteor trails and detectability of radar meteors. The first systematic statement of all main aspects of the physical theory of radar meteors was made by the author in 1963 (Lebedinets), and a more detailed one, in 1966 (Lebedinets). However, numerical calculations in those articles were preliminary to a certain degree, as only approximate solutions of the problem of radiowave reflection from meteor trails and evaporation of small meteoroids were used. These calculations can now be made more precisely.

The Ablation of Small Meteoroids

The overwhelming majority of radar meteors registered by highly sensitive equipment are produced by small meteoroids with masses less than 10^{-3} g. Such small particles have completely melted at the beginning of intensive evaporation, regardless of their initial structure and density. If the particle does not break up in the process of heating, then it gathers after melting in a droplet that is steady under the forces of surface tension and aerodynamical pressure (Lebedinets and Portnyagin, 1967). Hence, in the process of evaporation (only during this time can a meteor be observed), small meteoroids can be considered as spherical bodies with the density of stone or iron.

With provisions for the expenditure of energy on thermal radiation from the surface of a body, heating, evaporation, and deceleration of small nonfragmenting meteoroids are described by the

series of equations (Lebedinets and Shushkova, 1968):

$$\frac{\Lambda}{8}\rho v^3 = \sigma T^4 + C_1 Q T^{-1/2} \times \exp(-C_2 T) + \frac{C\delta^{2/3} m^{1/3} \rho v \cos z}{4AH}\frac{dT}{d\rho} \quad (3)$$

$$\frac{dm}{d\rho} = -\frac{4AHm^{2/3}}{\rho v \delta^{2/3}\cos z} C_1 T^{-1/2}\exp(-C_2 T) \quad (4)$$

and

$$\frac{dv}{d\rho} = -\frac{\Gamma A H v}{m^{1/3}\delta^{2/3}\cos z} \quad (5)$$

Here, ρ is the atmospheric density, σ is the Stefan-Boltzmann constant, C is the heat capacity, and C_1 and C_2 are constants that characterize the dependence of the meteoroid evaporation rate on the temperature T (Lebedinets and Portnyagin, 1967).

The system of equations (3) to (5) was integrated by Lebedinets and Shushkova (1968), and the ionization curves of meteors produced by meteoroids with different m_0 and v_0 were obtained.

Ionization and the Initial Radius of the Trail

Kascheev et al. (1967) and Lebedinets (1966) determined the values of the ionization probability of meteors, β, proceeding from the available data on the diffusion and the ionizing effective cross sections at collisions of different pairs of atoms and molecules. In the interval $20 \leq v \leq 70$ km/s, the following dependence was obtained:

$$\beta = 4\times 10^{-25} v^{3.5} \quad (6)$$

where v is in centimeters per second. The average atomic weight is accepted to be $\mu = 23$. At $v < 20$ km/s, β must diminish rapidly with a decrease in v. The dependence $\beta(v)$ accepted by us is shown in figure 1.

An analogous calculation of β was carried out by Sida (1969), who obtained a stronger dependence for $\beta(v)$ and smaller values of β at mean meteor velocities (dotted curve in fig. 1). For example, he finds β (40 km/s) = 0.03, but from equation (6), $\beta = 0.05$. Values of β determined by Sida are slightly underestimated, as he did not take into account that the effective cross sections of ionization Q for Na, K, Ca, Fe, Si, and Mg are underestimated in Bydin and Buchteev's works (Lebedinets and Portnyagin, 1966b); in their model, the atoms deviating from the initial direction of motion by more than 1°20′ were not recorded. Moreover, the dependence obtained by Bydin and Buchteev for a sufficiently wide velocity interval is weaker than that accepted by Sida, $Q_i \sim (v - v_i)^2$, where v_i is the minimum velocity corresponding to the ionization threshold. For Ca, Fe, Si, and Mg, the measurements of Q_i were carried out at velocities greater than or equal to 60, 80, 120, and 125 km/s, respectively. Extrapolating values of Q_i toward small velocities following such a strong dependence Q_i on v, Sida underestimated Q_i at small and mean meteor velocities. At higher meteor velocities, 50 to 70 km/s, the values of β by Sida practically agree with ours.

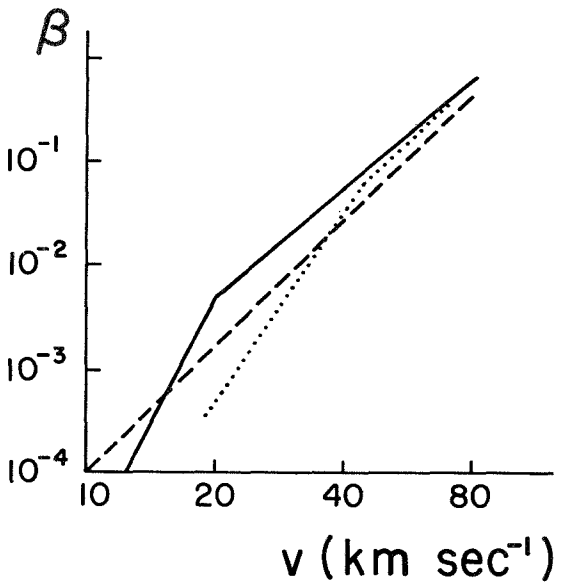

FIGURE 1.—The dependence of the probability of ionization on velocity $\beta(v)$. Solid line—dependence computed in this paper. Dashed line—dependence used by Verniani and Hawkins (1965). Dotted line—dependence computed by Sida (1969).

Verniani and Hawkins (1965) adopt the following dependence of β on v in the whole meteor velocity interval:

$$\beta = 10^{-28} v^4 \quad (7)$$

(dashed line in fig. 1). It seems rather unlikely that the same dependence of $\beta(v)$ applies over the

whole interval of meteor velocities, if only because ionization of oxygen (which makes up 50 percent of meteoritic matter) becomes impossible at $v<16$ km/s.

Initial expansion of the ionized meteor trail was considered in detail by Lebedinets (1963, 1966) and Lebedinets and Portnyagin (1966b). We assumed that the initial radius of the ionized trail $r_0 \sim v\rho^{-1}$ and that at the height of 96 km and at $v=40$ km/s, $r_0=1$ m.

The Detectability of Radar Meteors

It was shown by Lebedinets (1963) and Davies and Gill (1960) that detectability of radar meteors can be represented as a product of the geometrical factor P_1^{-1}, which characterizes the relative detectability of meteors with different radiant coordinates, and the physical factor P_2^{-1}, which characterizes the relative detectability of meteors with different velocities. The calculation of P_1 is comparatively simple; it is enough to know the antenna directional pattern.

The calculation of the physical factor is more complicated. The sensitivity of a meteor radar is usually characterized by the minimum value α_{ef}^{min} of the effective electron line density α_{ef} of meteor trails that can be recorded. The value of α_{ef} is that of the electron line density α obtained according to the power of the radio echo P_r, with the help of the formula of Lovell and Clegg (1948):

$$P_r = \frac{P_t G_t G_r \lambda^3 \alpha_{ef}^2}{32\pi^2 R^3} \left(\frac{e^2}{m_e c^2}\right)^2 \qquad (8)$$

Here, P_t is the transmitter power, G_t and G_r are the directivities of the transmitting and the receiving antennas, λ is the wavelength, R is the range, e and m_e are the electron charge and mass, and c is the velocity of light.

The precise formula for the power of the radar echo is

$$P_r = \frac{P_t G_t G_r \lambda^3}{128\pi^4 R^3} \left| \int_{-\infty}^{x_0} g(x) \exp\left(-i\frac{\pi}{2}x^2\right) dx \right|^2 \qquad (9)$$

$$x_0 = \frac{2vt}{\sqrt{R\lambda}}$$

where t is the time counted from the moment of the meteor passing across the point of specular reflection from the trail, and $g(x)$ is the reflection coefficient at the given point in the moment t.

From equations (8) and (9), we note that

$$\alpha_{ef} = \frac{m_e c^2}{2\pi e^2} \left| \int_{-\infty}^{x_0^m} g(x) \exp\left(-i\frac{\pi}{2}x^2\right) dx \right| \qquad (10)$$

where x_0^m is the value of x_0 at which α_{ef} is largest.

With provision for a random position of the specular reflection point on the trail, the probability of detection of the trail produced by the meteoroid with given m_0, v_0, and z is proportional to the length of the trail section $\ell(m_0, v_0, z, \lambda, \alpha_{ef}^{min})$ at which $\alpha_{ef} > \alpha_{ef}^{min}$. Then, for the relative detectability of meteors with different velocities, we can write

$$\frac{1}{P_2} = \int_0^\infty \ell(m_0, v_0, z, \lambda, \alpha_{ef}^{min}) n(m_0)\, dm_0 \qquad (11)$$

where $n(m_0)$ is the meteor mass distribution, usually presented as a power function

$$n(m_0) \sim m_0^{-S} \qquad (12)$$

where we have assumed that $S=2$.

In equation (10), $g(x)$ is a complex function of α, λ, and r_0. The calculation of $g(x)$ for various values of α, λ, and r_0 was carried out by digital computer on the basis of the precise solution of the problem of radiowave reflection from meteor trails obtained previously by Lebedinets and Sosnova (1968, 1969).

Figure 2(a) shows the curves of P_2^{-1} as a function of v_0 for the radar at $\lambda=7.5$ m with different sensitivities α_{ef}^{min}: (1) 3.16×10^8/cm, (2) 10^9/cm, (3) 3.16×10^9/cm, (4) 10^{10}/cm, (5) 5×10^{10}/cm, (6) 10^{11}/cm, and (7) 2×10^{11}/cm. We assumed that $\cos z = \frac{2}{3}$ and adopted $P_2=1$ for all curves at $v_0=40$ km/s. Analogous data for the radar at $\lambda=12$ m are shown in figure 2(b).

Radar-Meteor Deceleration

One of the most complicated problems of radar-meteor investigations is the transition from a measured meteor velocity to a no-atmosphere one. Radar observations do not allow the determination of the location of the reflection point on the trail, so we must use the same mean correction for deceleration $\overline{\Delta v}(v_0)$ for all meteors with a given velocity.

For a meteor with given m_0, v_0, and z, the mean

correction for deceleration to the observations with the given radar is

$$\overline{\Delta v}(v_0, m_0, z, \lambda, \alpha_{ef}^{min}) = \frac{\int_{he}^{hb} [v_0 - v(h, m_0, v_0, z)]\, dh}{\ell(m_0, v_0, z, \lambda, \alpha_{ef}^{min}) \cos z} \tag{13}$$

where $v(h, m_0, v_0, z)$ is the meteor velocity at the altitude h; integration is over that part of the trail where $\alpha_{ef} \geq \alpha_{ef}^{min}$. The mean correction for deceleration for all meteors of a given velocity is

$$\Delta v(v_0, \lambda, \alpha_{ef}^{min}) = \frac{\int_0^{\infty}\int_0^{\pi/2} \overline{\Delta v}(m_0, v_0, z, \lambda, \alpha_{ef}^{min})\, \ell(m_0, v_0, z, \lambda, \alpha_{ef}^{min}) n(m_0) f(z)\, dm_0\, dz}{\int_0^{\infty}\int_0^{\pi/2} \ell(m_0, v_0, z, \lambda, \alpha_{ef}^{min}) n(m_0) f(z)\, dm_0\, dz} \tag{14}$$

where $f(z)$ is the meteor distribution in z.

The function $v(h, v_0, m_0, z)$ was found by numerical integration of equations (3) to (5). There is some uncertainty in the choice of Γ. We can write $\Gamma = 1 + k(v_a/2Q)v$ (where v_a is the thermal velocity of evaporating molecules) for small meteoroids moving under the conditions of free molecular flow including the reactive impulse of evaporating molecules. Assuming that at $T \approx 2000°$ K, $v_a = 1.5 \times 10^5$ cm/s and $Q = 6 \times 10^{10}$ ergs/g, we obtain

$$\Gamma = 1 + 1.25 \times 10^{-6}\, kv \tag{15}$$

k is equal to $4/9$ in the case of a large, nonrotating spherical meteoroid that evaporates from the frontal surface only; k is equal to 0 in the case of an infinitely small or an infinitely rapidly rotating body when the evaporation rates from both the frontal and the rear surface are the same. In the case of real bodies of finite size rotating with the finite rate velocity of evaporation from the frontal surface somewhat larger than that from the rear, the value of k is not equal to 0.

Numerical integration of equations (3) to (5) was carried out for a number of values of k from 0 to $4/9$; the value of k that leads to the best agreement between no-atmosphere velocities of radar meteors of streams and Super-Schmidt

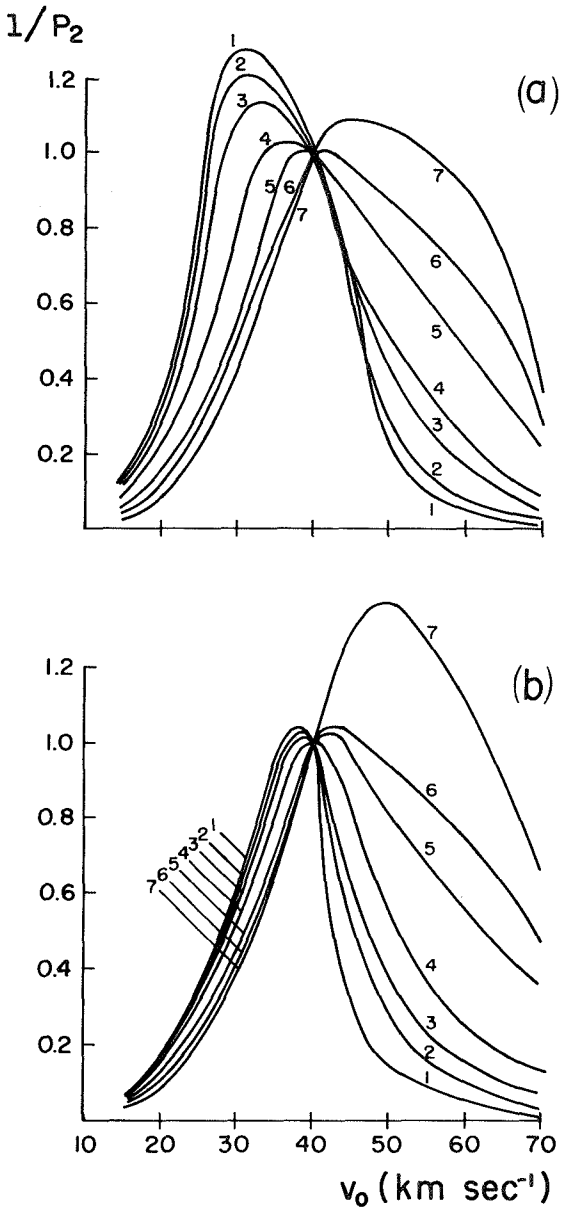

FIGURE 2.—Relative detectability of radar meteors with different velocities by radar. At (a) $\lambda = 7.5$ m and (b) $\lambda = 12$ m with different sensitivities α_{ef}^{min}: (1) 3.16×10^8/cm, (2) 10^9/cm, (3) 3.16×10^9/cm, (4) 10^{10}/cm, (5) 5×10^{10}/cm, (6) 10^{11}/cm, and (7) 2×10^{11}/cm.

meteors was chosen from comparison with radar-meteor observational data. We found $k = 0.094$ for observations at $\lambda = 12$ m with $\alpha_{ef}^{min} = 3 \times 10^{10}$/cm (Korpusov, 1970; Korpusov and Lebedinets, 1970). For four active meteor streams, table 2 gives N, the number of the recorded radar meteors

TABLE 2.—*Mean Velocities (in the Atmosphere and No Atmosphere) for Four Meteor Streams*[a]

Stream	N	$\bar{V}$ (km/s)	$\bar{V}_0$ (km/s)	$\bar{V}_{01}$ (km/s)	$\bar{V}_{02}$ (km/s)
Geminids	344	35.4	36.4	36.2	36.2
Quadrantids	163	41.6	42.6	42.9	42.6
Orionids	86	66.6	67.6	67.5	67.6
Southern Taurids	43	28.7	29.8	29.6	30.3

[a] The first three columns of data are taken from Korpusov and Lebedinets (1970); the fourth column is taken from Jacchia and Whipple (1961); and the last, from Hawkins and Southworth (1961).

of the stream; $\bar{v}$, the mean measured velocity; $\bar{v}_0$, the mean no-atmosphere velocity obtained at $k=0.094$; and $\bar{v}_{01}$ and $\bar{v}_{02}$, the mean no-atmosphere velocities of Super-Schmidt meteors of the stream according to Jacchia and Whipple (1961) and Hawkins and Southworth (1961), respectively.

It is seen from table 2 that mean no-atmosphere meteor-stream velocities obtained from radar observations are in agreement with photographic observational data no worse than is the agreement of the data of the most precise photographic observations among themselves. Thus, radar observations at $\lambda=12$ m (Korpusov and Lebedinets, 1970) do not reveal any deceleration that would surpass the theoretical deceleration at the meteoroid density $\delta=3.5$ g/cm^3. The dependence of the mean correction for deceleration $\overline{\Delta v}$ on $\alpha_{ef}{}^{min}$ for the radar at $\lambda=7.5$ m at values of v_0 of 15, 20, 30, 40, 50, and 70 km/s is shown in figure 3(a) in curves (1) through (6), respectively. It is assumed that $k=0.094$ and $\cos z=\frac{2}{3}$. The same data for $\lambda=12$ m are presented in figure 3(b).

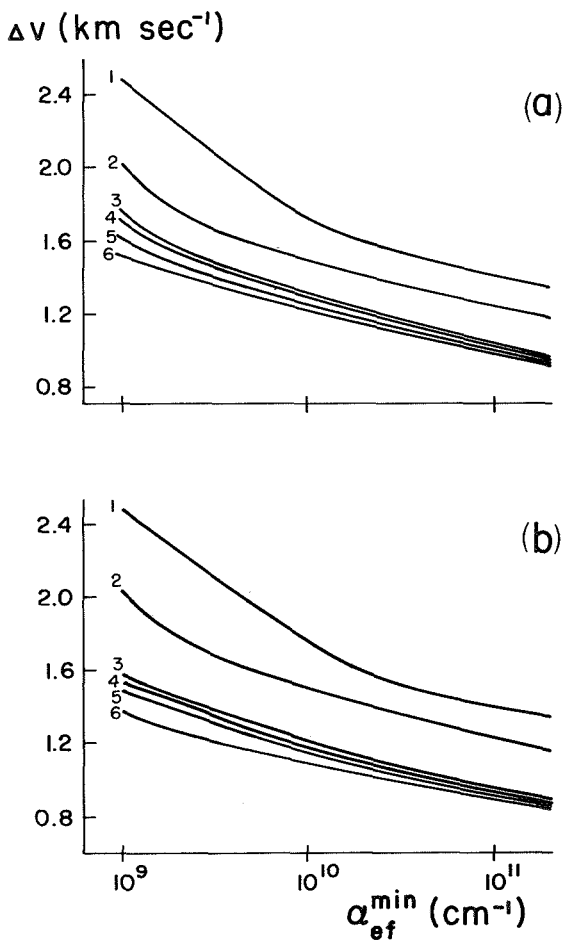

FIGURE 3.—Mean corrections for deceleration as a function of radar sensitivity $\alpha_{ef}{}^{min}$. For (a) $\lambda=7.5$ m and (b) $\lambda=12$ m for different velocities: (1) 15 km/s, (2) 20 km/s, (3) 30 km/s, (4) 40 km/s, (5) 50 km/s, and (6) 70 km/s.

Radar-Meteor Heights

Ionization curves $\alpha(h, m_0, v_0, z)$ of meteors with different m_0, v_0, and z were obtained by Lebedinets and Shushkova (1968). Curves of the effective electron line density $\alpha_{ef}(h, m_0, v_0, z, \lambda)$ for $\lambda=7.5$ and 12 m were found by them with the help of equation (10). Using these curves, we can find the theoretical height distributions of radar meteors with given v_0 and z for the observations at given λ and $\alpha_{ef}{}^{min}$, with allowance for a random

position of the reflection point on the trail:

$$N_0(h, v_0, \lambda, \alpha_{ef}^{min}) = \int_{m_{01}}^{m_{02}} n(m_0)\, dm_0 \quad (16)$$

Here, m_{01} and m_{02} are two roots of the equation

$$\alpha_{ef}(h, m_0, v_0, z, \lambda) = \alpha_{ef}^{min} \quad (17)$$

which is solved by a numerical method.

Comparison of the theoretical distribution of radar-meteor heights with observed ones requires that account be taken of the low precision of radar-meteor height measurements. Besides that, both the variety of meteoroid physical properties and the meteor-radiant zenith distance influence the dispersion of the observed radar-meteor heights. If we assume that all factors leading to the height dispersion follow a Gaussian distribution with the dispersion σ_h, it is necessary to transform equation (16) by the law

$$N(h, v_0, \lambda, \alpha_{ef}^{min}) = \frac{\sqrt{2}}{\sqrt{\pi}\sigma_h} \int_0^{\infty} N_0(h_0) \times \exp\left[-\frac{(h-h_0)^2}{2\sigma_h^2}\right] dh_0 \quad (18)$$

COMPARISON WITH OBSERVATIONS

It is seen from figure 2 that radar observations have great selectivity with respect to meteor velocities: Slow meteors are poorly observed, owing to the strong dependence of ionization probability on velocity; and fast meteors, owing to the effect of the initial trail radius on the radar echo amplitude. In this connection, it is interesting to consider the results of meteor-velocity measurements from the Harvard Radio Meteor Project (Hawkins, 1963) with a radar system of very high sensitivity, $\alpha_{ef}^{min} = 3 \times 10^9$/cm, at the short wavelength $\lambda = 7.3$ m. The histogram of the observed velocity distribution of 320 radar meteors (Verniani and Hawkins, 1965) is shown in figure 4(a), and that of 2500 Super-Schmidt meteors (McCrosky and Posen, 1961), in figure 4(b).

Radar meteors with low and high velocities are almost absent: For example, about 20 percent of the photographic meteors and less than 1 percent of the radar meteors have a velocity $v_0 > 55$ km/s. Hawkins et al. (1964) take into account the effect of the dependence of β on v alone for the calculation of the physical factor, assuming $\beta \sim v^4$ (dashed line in fig. 4, normalized on the total number of meteors, 320). For the photographic method, the detectability is proportional to v^n, where n varies from 2 to 3, based on evaluations by different authors (Öpik, 1958a; Jacchia, 1949; Whipple, 1954). Thus, an increase in the relative number of radar meteors at high velocities compared with photographic meteors would be expected without allowance for the influence of r_0; the picture is inverse in reality. The solid curve in figure 1, which defines the relative detectability of radar meteors with different velocities according to our calculations, is plotted in figure 4(a) as a continuous line (the curve is normalized to 320 meteors); the curve satisfactorily describes the observed radar-meteor distribution. Thus, the observed radar-meteor distribution characterizes radar selectivity much better than it does the real distribution of meteoroid velocities; this is due to both the influence of the dependence of β on v (at low v_0) and the influence of r_0 (at high v_0). It is seen from the theoretical calculations (fig. 3) and from the above comparison of velocities of radar-meteor streams obtained in Obninsk with

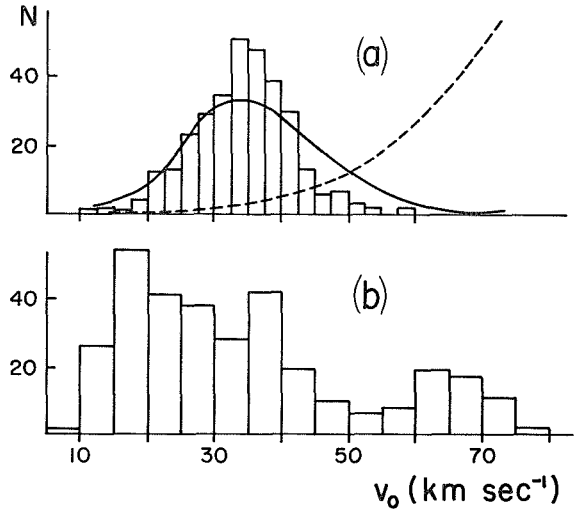

FIGURE 4.—(a) Histogram of the velocity distribution of 320 radio meteors (Verniani and Hawkins, 1965). The continuous line is the relative detectability of meteors with different velocities (curve 3 in fig. 2); the dashed line $N \sim v_0^4$. Both lines are normalized to the total number of meteors, 320. (b) Velocity distribution of 2500 Super-Schmidt meteors (McCrosky and Posen, 1961).

photographic observational data (table 2) that mean velocity corrections of radar meteors for the transition from a measured velocity to a no-atmosphere one are comparatively small. This contradicts the results of velocity measurements of the Harvard Radio Meteor Project (Hawkins et al., 1964; Southworth, 1962), which found that the mean measured velocities of radar-meteor streams are about 2 to 3 km/s less than those found from photographic observational data. For example, for the Geminids, the mean velocity is 33.7 km/s, which is about 2.5 km/s less than that obtained from photographic observations (see table 2). This discrepancy cannot be explained by radar-meteor deceleration; it is a consequence of the imperfection of the method of velocity measurements. The positions of the first three maxima of the diffraction picture, including the first, are usually used for velocity measurements (Hawkins et al., 1964). It was theoretically and experimentally shown (Kascheev et al., 1967; Lebedinets, 1966) that use of the first maximum of the diffraction pattern of the radar echo leads to an understatement of the velocity by some kilometers per second for velocity measurements in the case of underdense trails. The same result was obtained for observations at $\lambda = 12$ m in Obninsk (Korpusov, 1970; Korpusov and Lebedinets, 1970). For example, for the Orionids, the mean measured velocity of radar echoes from underdense trails with the first maximum included is 65.3 km/s, and with it excluded is 66.5 km/s. This effect must be much stronger in the Harvard measurements, where the radar had higher power and a shorter wavelength. This conclusion is in good agreement with Evans' (1966) velocity determinations made by measuring the radial velocity of head echoes: For the Geminids, the mean velocity was found to be 35.98 km/s, and for the Quadrantids, 42.25 km/s; from a comparison with the data in table 2, we see that the correction for deceleration turns out to be small (approximately 0.5 km/s).

It is necessary to point out another source of error in the radar-meteor velocity determinations. Curves of $\alpha_{ef}(h)$ for faint meteors have very steep slopes at both ends, which leads to some overstatement of the radar-meteor velocity near the point of appearance and to an understatement near the point of disappearance; consequently, the deceleration is overstated (if the first maximum of the diffraction pattern of the radar echo is used in velocity measurements).

Measured height distributions of 320 radar meteors (Verniani and Hawkins, 1965) for velocity intervals of 15 to 25, 25 to 35, and 35 to 45 km/s are shown in figure 5(a). Theoretical height distributions for velocities of 20, 30, and 40 km/s at values of σ_h of 5 and 7 km are shown in figures 5(b) and 5(c). It is seen that the theoretical distributions of radar-meteor heights are in good agreement with observed ones.

CONCLUSIONS

(1) A comparison of theoretical calculations with the results of radar-meteor observations shows that the theory of radio meteors devised by Lebedinets (1963, 1966), Lebedinets and Portnyagin (1966a, 1967), Lebedinets et al. (1969), Lebedinets and Shushkova (1968), and Lebedinets and Sosnova (1968, 1969) satisfactorily represents observational data.

(2) The results of radar-meteor observations are incompatible with the idea of low density for small meteoroids in the ablation process.

(3) Fragmentation plays no essential role in the ablation of radar meteors.

(4) The main mechanism of radar-meteor ablation is evaporation. During intensive evaporation, small meteoroids have a density close to that of usual stone meteorites.

(5) Considerable shortness of observed trails of radar meteors compared with predictions of the simplest theory of meteors is explained by two reasons: (a) The simplest theory of meteors is imperfect (a more precise theory gives shorter trails); (b) the upper parts of meteor trails are not observed in radar observations, owing to the effect of the initial trail radius on the amplitude of the radar echo.

(6) Available data from radar-meteor observations do not permit a solution of the problem of the structure and density of small meteoroids before they begin their intensive evaporation (i.e., before complete melting).

(7) Large decelerations of radar meteors obtained in a number of works are apparently the consequence of an imperfection in the method of velocity measurements.

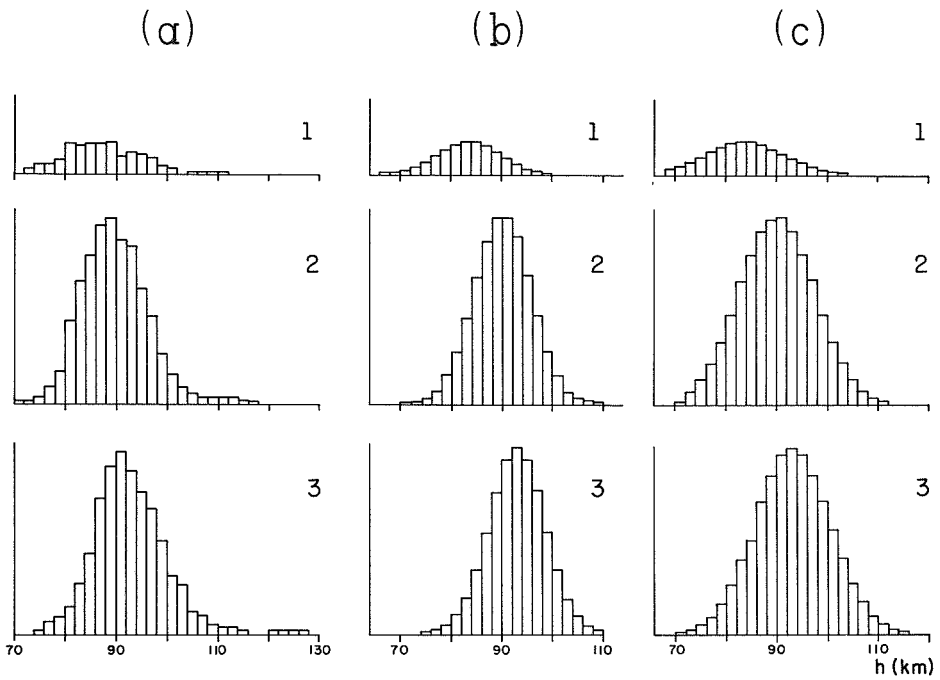

FIGURE 5.—(a) Observed height distribution of radio meteors (Verniani and Hawkins, 1965) for three velocity intervals: (1) 15 to 25 km/s, (2) 25 to 35 km/s, and (3) 35 to 45 km/s. (b, c) Theoretical height distribution for the same velocity intervals as in figure 5(a). At dispersion of height (b) $\sigma_h = 5$ km and (c) $\sigma_h = 7$ km.

REFERENCES

ANON., 1964. *Tables of Standard Atmosphere,* Moscow Publ. House of Standards.

DAVIES, J. G., AND GILL, J. C., 1960. Radio echo measurements of the orbits of faint sporadic meteors, *Mon. Not. Roy. Astron. Soc.*, **121**, 437–462.

EVANS, J. V., 1966. Radar observations of meteor decelerations, *J. Geophys. Res.*, **71**, 171–188.

GREENHOW, J. S., 1963. Limitations of radar techniques for the study of meteors, *Smithson. Contrib. Astrophys.*, **7**, 5–17.

HAWKINS, G. S., 1963. The Harvard radio meteor project, *Smithson. Contrib. Astrophys.*, **7**, 53–62.

HAWKINS, G. S., AND SOUTHWORTH, R. B., 1961. Orbital elements of meteors, *Smithson. Contrib. Astrophys.*, **4**, 85–95.

HAWKINS, G. S., SOUTHWORTH, R. B., AND ROSENTHAL, S., 1964. Preliminary analysis of meteor radiants and orbits, *Harvard College Obs., Smithson. Astrophys. Obs., Radio Meteor Project,* Res. Rept. No. 7, 32 pp.

HERLOFSON, N., 1948. The theory of meteor ionization, *Rept. Progr. Phys.*, **11**, 444–454.

JACCHIA, L. G., 1949. Photographic meteor phenomena and theory, *Harvard College Obs. and Center of Analysis, Mass. Inst. Tech.*, Tech. Rept., No. 3, 36 pp.

JACCHIA, L. G., AND WHIPPLE, F. L., 1961. Precision orbits of 413 photographic meteors, *Smithson. Contrib. Astrophys.*, **4**, 97–129.

KASCHEEV, B. L., LEBEDINETS, V. N., AND LAGUTIN, M. F., 1967. *Meteoric Phenomena in the Earth's Atmosphere,* Moscow, Publ. House Nauka.

KORPUSOV, V. N., 1970. Measurement of meteor velocities and radiants at a wavelength of 12 m, *Trans. Inst. Experimental Meteorology,* No. 16, pp. 88–99, Moscow.

KORPUSOV, V. N., AND LEBEDINETS, V. N., 1970. Orbits of radio meteors, *Astron. Vestnik, USSR,* **4**, 102–107 (*Solar System Res.*, **4**, 82–88).

LEBEDINETS, V. N., 1963. Density of meteoric matter in the vicinity of the Earth's orbit, *Astron. Zh.*, **40**, 719–732 (1964, *Soviet Astr. AJ*, **7**, 549–558).

——, 1966. *Physical Meteor Theory and Meteor Matter in the Earth's Orbit's Vicinity from Radar Observation Results*, A Doctor's Degree, Obninsk, USSR.

LEBEDINETS, V. N., AND PORTNYAGIN, Y. I., 1966a. The mechanism of the fragmentation of small meteoric bodies in the atmosphere, *Dokl. Akad. Nauk. USSR*, **168**, 543–546.

LEBEDINETS, V. N., AND PORTNYAGIN, Y. I., 1966b. The initial radius of an ionized meteoric trail, *Geomagnetizm i Aeronomiya*, **6**, 712–716 (*Geomagn. and Aeronom.*, **6**, 544–547).

LEBEDINETS, V. N., AND PORTNYAGIN, Y. I., 1967. Fragmentation of dense meteoroids in the atmosphere, *Astron. Zh.*, **44**, 874–888 (1968, *Soviet Astr. AJ*, **11**, 700–711).

LEBEDINETS, V. N., PORTNYAGIN, Y. I., AND SOSNOVA, A. K., 1969. Drag and heat transfer coefficients of meteorites. I. Weak shielding conditions, *Astron. Vestnik, USSR*, **3**, 223–229 (*Solar System Res.*, **3**, 187–191).

LEBEDINETS, V. N., AND SHUSHKOVA, V. B., 1968. Evaporation and acceleration of small meteoroids, in *Physics and Dynamics of Meteors*, IAU Symp. No. 33, edited by Ľ. Kresák and P. M. Millman, Dordrecht, Holland, D. Reidel Publ. Co., 193–204.

LEBEDINETS, V. N., AND SOSNOVA, A. K., 1968. Radio reflections from meteor trails, in *Physics and Dynamics of Meteors*, IAU Symp. No. 33, edited by Ľ. Kresák and P. M. Millman, Dordrecht, Holland, D. Reidel Publ. Co., 27–44.

LEBEDINETS, V. N., AND SOSNOVA, A. K., 1969. Radiowave reflection from meteor trains. II. Diffraction pictures, *Geomagnetizm i Aeronomiya*, **9**, 680–688 (*Geomagn. and Aeronom.*, **9**, 550–556).

LOVELL, A. C. B., AND CLEGG, J. A., 1948. Characteristics of radio echoes from meteor trails: I. The intensity of the radio reflections and electron density in the trails, *Proc. Phys. Soc.*, **60**, 491–498.

MCCROSKY, R. E., AND POSEN, A., 1961. Orbital elements of photographic meteors, *Smithson. Contrib. Astrophys.*, **4**, 15–84.

ÖPIK, E. J., 1958a. *Physics of meteor flight in the atmosphere*, Interscience. New York.

——, 1958b. Problems in the physics of meteors, *Amer. J. Phys.*, **26**, 70–80.

SIDA, D. W., 1969. The production of ions and electrons by meteoritic processes, *Mon. Not. Roy. Astron. Soc.*, **143**, 37–47.

SOUTHWORTH, R. B., 1962. Deceleration of radio meteors (abstract, *Amer. Astron. Soc.*), *Astron. J.*, **67**, 283.

VERNIANI, F., 1966. Physical characteristics of 320 faint radio meteors, *J. Geophys. Res.*, **71**, 2749–2762.

VERNIANI, F., 1969. Structure and fragmentation of meteoroids, *Space Sci. Rev.*, **10**, 230–261.

VERNIANI, F., AND HAWKINS, G. S., 1965. Masses, magnitudes, and densities of 320 radio meteors, *Harvard College Obs., Smithson. Astrophys. Obs., Radio Meteor Project*, Research Rept. No. 12, 35 pp.

VINOGRADOV, A. P., 1965. The composition of meteorites, *Geokhimiya*, **8**, 1275–1312.

WHIPPLE, F. L., 1943. Meteors and the Earth's upper atmosphere, *Rev. Mod. Phys.*, **15**, 246–264.

WHIPPLE, F. L., 1954. Photographic meteor orbits and their distribution in space, *Astron. J.*, **59**, 201–217.

Page intentionally left blank

26. A Possible Mechanism for the Capture of Microparticles by the Earth and Other Planets of the Solar System

F. Di Benedetto
Rome University
Rome, Italy

By application of Lyttleton's theory for the formation of comets, it is shown that a possible mechanism for the origin and formation of a concentration of cosmic particles around the Earth and the other planets of the solar system exists.

In the vicinity of the neutral point, where the velocity of colliding particles is not greater than 6 km/s, it is found that if the solid particles after collision must remain in a solid state, there can be no possibility of accretion for Mercury, Mars, and the Moon, where the maximum value of the "closing-in parameter" p *(distance of the center of the planet to the asymptotic trajectory) is less than the radius of the planet.*

On the other hand, the capture radii of microparticles in solid form varies from a minimum of 2.95 planetary radii for Venus and 3.47 for the Earth, to about 986 for Jupiter.

In this paper, we shall apply Lyttleton's theory on the formation of comets to explain a possible mechanism concerning the origin and formation of a concentration of cosmic microparticles around the Earth and the other planets of our solar system.

This process of formation and concentration of particles can be conceived as bringing about an increment of particles along an axis, i.e., along a certain direction, deriving from, say, a meteor swarm of cometary origin, under the action of the most important force that is believed to act upon these particles—the planetary gravitational force.

MECHANISM FOR THE POSSIBLE INCREASE OF PARTICLES

Suppose that a cloud of meteor particles encounters a planet from any arbitrary direction and that, in the limited time in which this phenomenon occurs, the planet's trajectory can be considered a straight line. The single particles forming the cloud, on the other hand, can all be considered to have the same (vector) velocity **V**.

Then we take the x axis through the center of the planet parallel to the direction from which the single particles of the swarm are approaching the planet from outside the gravitational field of influence of that planet.

We now follow the movement of a single meteor particle. We can assume that, starting from the surface of the planetary gravitational field of attraction, which we consider to be finite, the trajectory of this particle with respect to the center of the planet is hyperbolic.

The basic consequence, then, is that all the hyperbolic trajectories described by the single meteor particles belonging to the cloud must intersect the x axis at points on that part on the opposite side of the planet.

The action of the planet is evidently that of a convergent lens: Particles that form a meteor

cloud with an initial density are obliged to converge toward the x axis.

This process is similar to that indicated by Lyttleton (1953) for the formation of comets under the gravitational attraction of the Sun.

Let us now see what happens to all particles found on the surface of a hyperboloid. In this case, it is sufficient to consider a cross section of the hyperboloid with a plane passing through the x axis. We then obtain two hyperbolic trajectories of two particles of the meteor cloud, which are symmetrical with respect to the x axis, contained in a plane passing through the center T of the planet (fig. 1). It is immediately evident that two such particles are on "collision trajectories." The collision point C is situated on the x axis at a distance $\ell/2$ from the center T of the planet.

Before dealing with this subject mathematically, we shall give a brief description of the physics of the impact phenomena. Just before impact at point C, the two particles A and B have the same radial velocity $\mathbf{V}$ (along the x axis); the transverse components of $\mathbf{V}$ of both particles previously in A and B, perpendicular to the x axis, have the same magnitude but opposite directions. These two components at point C make possible a relative collision velocity of both particles.

By this process, the action of planetary gravity comes into play and leads to a change of the relative velocity of particle A with respect to the velocity of B. The relative velocity goes from zero at points A and B, nearly on the surface of the planetary sphere of attraction, to finite values. These relative values assume a certain magnitude at point C and increase toward the planet; they decrease rapidly immediately outward from point C, since the action of the planetary sphere of attraction is practically nil for moving particles arriving at a distance greater than the radius of this sphere.

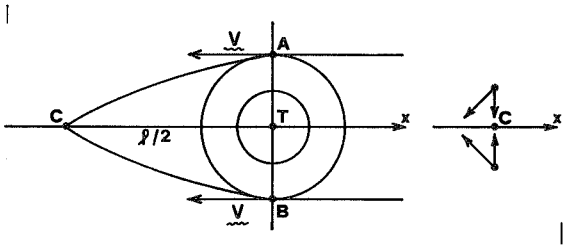

FIGURE 1.—Dynamics of the impact phenomena of a planet with center at T.

If the masses of two opposite particles are equal and if the collision of the particles is inelastic, the total relative kinetic energy would be lost. The velocity of a particle thus formed after the collision would obviously be equal to the radial component, whose direction is along the negative part of the x axis.

On the other hand, the velocity component normal to the x axis before the collision takes place is not negligible. Therefore, such a collision, by eliminating transverse motion, is capable of reducing the energy of the cosmic particle, originally in a hyperbolic orbit, to values of energy that *may* correspond to an elliptic orbit. Cosmic particles can thus be captured by the planet after collision.

We therefore have available in the solar system a mechanism that can possibly change hyperbolic velocities of particles to elliptic velocities and bring about the capture of these particles by a planet.

The above qualitative description of the capture mechanism is also valid even when the two particles that collide have neither the same velocity nor the same mass.

The essential part of the concept is to admit that this process exists, which would permit dust particles to be accumulated along a certain portion of the x axis.

At the beginning of the process, the presence of meteoroid material along the x axis greatly enhances the probability of repetition of particle collisions that follow the first, in the initial phase.

It should be noted that not all particles are captured by the planet. Those particles that are located farther away from the center, before and after collision, may have a radial component of velocity that is greater than the escape velocity. In this case, the particles can never be captured by the planet.

On the other hand, particles that cross the x axis nearer the planet can, after collision, have a radial velocity that is less than the escape velocity and, therefore, can be captured.

We can thus admit that along the x axis there is a portion characterized by the latter. This part can be called the "concentration segment," whose farther end from the planet defines the so-called "neutral point," introduced by Lyttleton for

comets. This point represents the separation point; i.e., for distances from the center of the planet greater than that determined by the neutral point, all particles that arrive along the x axis will continue with velocities greater than the appropriate escape velocity, while for distances less than that of the neutral point, all particles lying on the concentration segment will definitely be captured by the planet.

THEORETICAL DETERMINATION OF THE NEUTRAL POINT

The position of the neutral point along the x axis can be determined by the following considerations, due mainly to Lyttleton.

With reference to figure 1, let **V** represent the (vector) velocity of one of the many particles of a cloud. This vector is parallel to the x axis; the trajectory of the particle is therefore parallel to the x axis and is at a distance p from the x axis.

Owing to the gravitational attraction of the planet, all particles with velocity **V** describe hyperbolic trajectories until point C, on the x axis, is reached.

In polar coordinates r, θ, with the center of the coordinate system coincident with the center of the planet, the equation of the trajectory, which is hyperbolic, is given by

$$r=\frac{\ell}{e\cos\theta+1} \tag{1}$$

where $e=c/a=\sqrt{a^2+b^2}/a$ is the eccentricity ($e>1$), $\ell/2$ is the distance of point C from the center T of the planet (origin) along the transverse axis, and ib is the semi-minor axis (imaginary for a hyperbola). The distance CT, which corresponds to $e\cos\theta=1$, is related to the parameter ℓ by

$$2CT=\ell \tag{2}$$

By applying the area integral to the motion of the particle, which is subject only to a central force, we have

$$r^2\dot{\theta}=\text{constant}=h \tag{3}$$

Therefore,

$$r^2\,d\theta=h\,dt \tag{4}$$

where $h=\sqrt{\mu l}=V_\infty p$ (moment of momentum per unit mass). The quantity $\mu=GM$, with G the gravitational constant and M the mass of the planet; V_∞ is the velocity of the particle at infinity, i.e., before it reaches the sphere of attraction of the planet. We then have

$$\tfrac{1}{2}r^2\,d\theta=\tfrac{1}{2}p\,ds \tag{5}$$

where ds is the differential of the arc of the hyperbolic trajectory of the particle. Therefore,

$$\tfrac{1}{2}p\,ds=\tfrac{1}{2}h\,dt \tag{6}$$

and

$$p\frac{ds}{dt}=pV_\infty=h \tag{7}$$

From equation (7), we have

$$V_\infty=\frac{h}{p} \tag{8}$$

On the other hand, it can be shown that the radial component of velocity dr/dt at point C on the x axis is equal to the velocity at infinity V_∞. Furthermore, we know that the velocity of a particle on a parabolic trajectory around the planet is given by

$$V_p^2=\frac{2GM}{r} \tag{9}$$

so that, if after collision of two conjugate particles A and B, $V\leq V_p$ at $r=\ell/2$, then the two particles involved in the collision will be captured by the planet. This relationship leads to

$$V_\infty^2\leq\frac{2GM}{p} \tag{10}$$

i.e.,

$$p\leq\frac{2GM}{V_\infty^2} \tag{11}$$

The parameter p, therefore, depends on the mass M of the planet and the velocity V_∞ of the particle outside the sphere of influence of the planet itself. It is obvious that p must be greater than the radius R of the planet, so that

$$R\leq p\leq\frac{2GM}{V_\infty^2} \tag{12}$$

An analysis carried out by Lyttleton shows that particles can remain in solid form if the kinetic energy converted into heat by the collision does not cause complete evaporation of the colliding particles.

TABLE 1.—*Maximum Values of* p *for the Planets and the Moon*

Planet	M ($g \times 10^{27}$)	R ($cm \times 10^{5}$)	p ($cm \times 10^{6}$)	Accretion
Mercury	0.328	2420	121.52	no
Venus	4.871	6100	1804.97	yes
Earth	5.977	6378	2214.72	yes
Mars	0.645	3380	239	no
Jupiter	1899.5	71350	703870	yes
Saturn	569.01	60400	210849.5	yes
Uranus	86.666	23800	32114	yes
Neptune	202.804	2200	75150	yes
Pluto	4.786	3000	1773.47	yes
Moon	0.074	1738	27.421	no

In the vicinity of the neutral point, V_∞ must not be greater than about 6 km/s. By taking this approximate value for V_∞, we can roughly determine the radius p of capture of the planets, provided that equation (12) is valid. We adopt cgs units so that $G = 6.67 \times 10^{-8}$ and $V_\infty = 10^5 V$, where V is the radial velocity at point C expressed in kilometers per second. The values of p and other important parameters are listed in table 1.

CONCLUSIONS

The planets for which accretion of solid particles is possible are those indicated in the last column of table. 1. The capture radii for these planets are listed in table 2.

As the value of p must be greater than the radius R of the related planet, we reach the very important conclusion that not all the planets of the solar system can accrete dust by collision processes that conserve dust in a solid state.

TABLE 2.—*Capture Radii of Microparticles in Solid Form*

Planet	Radii (× radius of the planet)
Venus	2.95
Earth	3.47
Jupiter	985.8
Saturn	34.9
Uranus	13.5
Neptune	341.1
Pluto	5.9

REFERENCE

LYTTLETON, R. A., 1953. *The Comets and Their Origin*, Cambridge Univ. Press.

27. On the Influence of the Atmospheric Dust on the Zodiacal Light Polarization

N. B. Divari and S. N. Krylova
Odessa Polytechnic Institute
Odessa, U.S.S.R.

Three-color observations of the nightglow brightness and polarization were made at the Majaky Observatory in October 1969 to determine the brightness of zodiacal light at the ecliptic pole. On the assumption that the degree of polarization of zodiacal light is 0.20 at the ecliptic pole, the corresponding brightnesses are found to be 68, 70, and 96 G2 stars of the 10th magnitude per square deg. at 0.37, 0.53, and 0.58μ.

The large diurnal variations in observed intensity and direction of polarization are attributed to the effects of dust in the Earth's atmosphere.

For investigation of the zodiacal light component in the brightness of the night sky at the ecliptic pole, photoelectric observations of the night sky light were made at the observatory Majaky near Odessa (USSR) in autumn 1969. The observation was carried out with interference filters $\lambda=0.37$, 0.53, and 0.58 μ and a Polaroid which allows measurement of intensity, degree and angle of polarization by Fessenkov's (1935) method. At the time of these observations the zenith distance of the North ecliptic pole varied from 26° to 65°. The observed brightnesses were expressed in units of the stars G2, of the 10th magnitude per square deg.

Figure 1 shows for the North ecliptic pole the observed brightness I_{obs}, the degree of polarization P (in percent) and the angle φ of polarization measured from the meridian of the ecliptic pole in a counterclockwise direction. The dashed line shows the angle $\beta_\odot$ between the meridian of the ecliptic pole and the direction from the ecliptic pole to the Sun.

The measured degree of polarization is equal to 2 to 3 percent. The degrees of polarization averaged over all the nights of observation are equal to 0.020 for $\lambda=0.37$ μ, 0.031 for $\lambda=0.53$ μ and 0.026 for $\lambda=0.58$ μ.

The observed intensity of polarized component of light $(I_{obs})_p$ is determined by the formula

$$(I_{obs})_p=I_{obs}P \qquad (1)$$

where I_{obs} is the observed intensity of light, P is the observed degree of polarization. The intensity of the polarized component I_p outside the atmosphere may be calculated by the formula

$$I_p=(I_{obs})_p p^{-\sec z} \qquad (2)$$

where p is the transmission coefficient of the atmosphere and z is the zenith distance of the ecliptic pole.

The values I_p averaged over every night of observation are listed in table 1. The figures in parentheses give the intensity averaged over the measurements made when the zenith distance of the ecliptic pole was lower than 60°.

In table 2 our values are compared with the data obtained by other authors quoted in the references.

If all the polarization was caused only by the scattering of sunlight by the zodiacal cloud, the

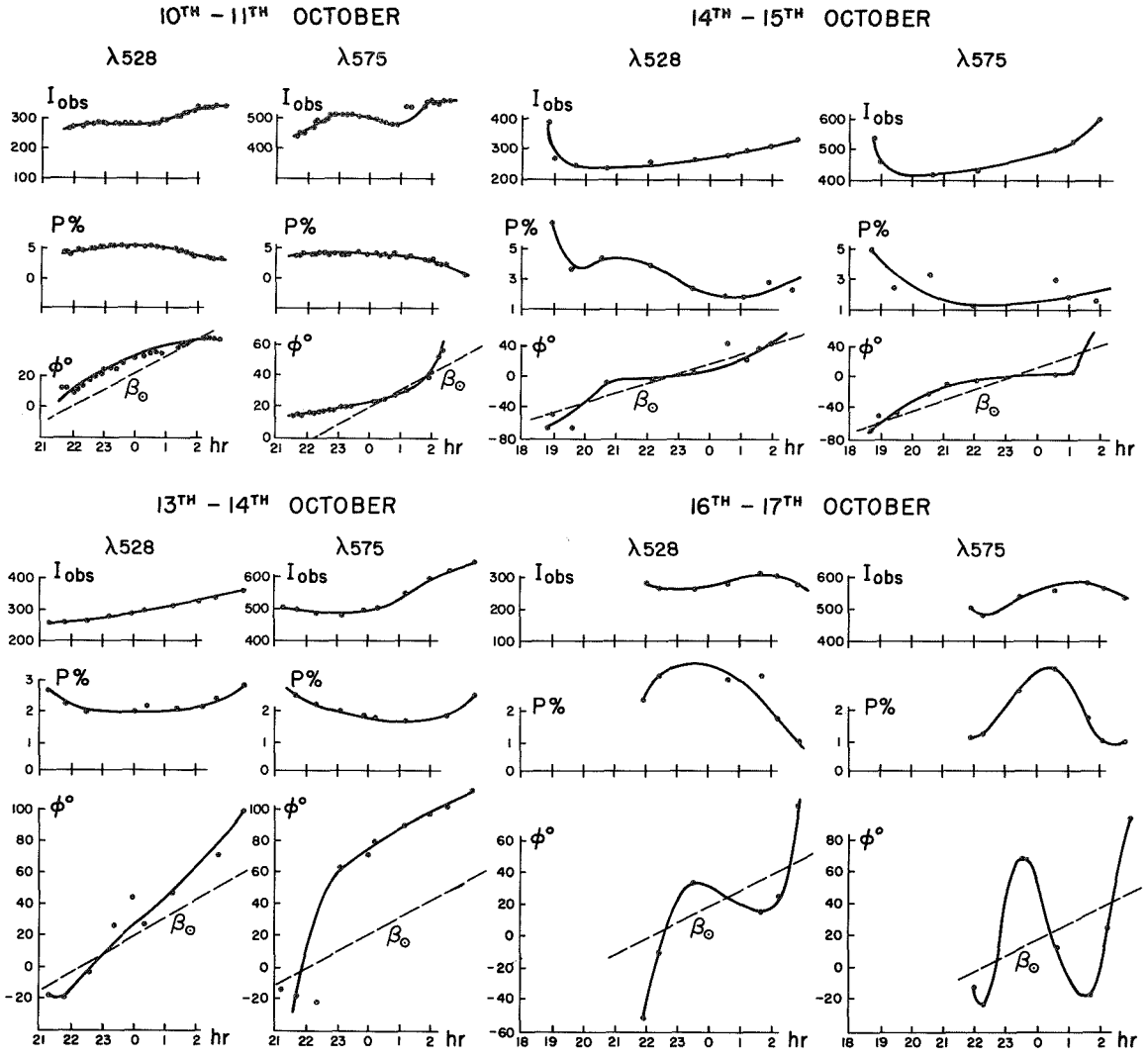

FIGURE 1.—Measured intensity I_{obs}, observed degree P (in percent) and observed angle ϕ of polarization in the North ecliptic pole.

intensity of zodiacal light I_{ZL} at the ecliptic pole would be determined from the values I_p and P_{ZL} by the formula

$$I_{ZL}=I_p/P_{ZL} \tag{3}$$

If, according to Weinberg (1964), we adopt $P_{ZL}=0.20$, we get from our values of I_p the following intensity of zodiacal light at the ecliptic pole:

$I_{ZL}=71$ for $\lambda 0.53\mu$ and $I_{ZL}=103$ for $\lambda 0.58\,\mu$

But the observed polarization is not induced by the zodiacal light only, because the direction of the measured polarization does not coincide with the direction to the Sun. As may be seen in figure 1, the angle φ differs considerably from the angle $\beta_\odot$. The deviation of the polarization angle from the scattering angle was observed in the zodiacal light by J. L. Weinberg (1964) in the light of the day sky (the sunlight scattered by the atmosphere) by E. V. Pyaskovskaya-Fessenkova (1958) and in the twilight by G. V. Rosenberg (1942). A qualitative explanation of this phenomenon as the result of multiple scattering and reflection from the Earth surface may be found in

TABLE 1.—*The Averaged Values of* I_p *in Units of the Stars G2 of the 10th Magnitude per Square Deg*

Night	$\lambda=0.53\ \mu$	$\lambda=0.58\ \mu$
Oct. 10–11, 1969	18.8 (19.3)	26.1 (27.5)
Oct. 13–14, 1969	12.0 (9.3)	17.8 (16.0)
Oct. 14–15, 1969	11.3 (11.0)	22.1 (17.0)
Oct. 16–17, 1969	15.0 (16.0)	16.3 (18.0)
Average values	14.3 (13.9)	20.6 (19.6)

TABLE 2.—*Values of* I_p *Resulting From Different Investigations*

Reference	I_p
Weinberg (1963)	18.5
Beggs et al. (1964)	35
Dumont (1965)	12.6
Dumont and Sanchez (1966)	9.7
Gillet (1967)	11.5
Wolstencroft and Rose (1967)	26.5
Sparrow and Ney (1968)	10.5
Ingham and Jameson (1968)	10.7
Present study	14.3
" "	20.6

the paper of H. C. van de Hulst (1948). In a paper by Divari (1968), it was pointed out that scattering of light in the Earth's atmosphere (the tropospheric component) may have an influence on the degree and on the angle of observed polarization.

To estimate this influence, we have analyzed our observations at the ecliptic pole. The reduction of the observations was made by the method of successive approximations. Let us suppose that measured intensity I_{obs} consists of five components, that is

$$I_{obs}=I_{ZL}p^{\sec z}+I_S p^{\sec z}+I_N+I'_{ZL}+I'_S \quad (4)$$

where I_{ZL} and I_S are the intensities of the zodiacal light and all the stars outside the atmosphere, I_N is the intensity of the light of the night sky, I'_{ZL} and I'_S are the intensity of the zodiacal light I_{ZL} and the starlight I_S scattered by the atmosphere. The intensity of tropospheric components I'_{ZL} and I'_S, the degrees of polarization P'_{ZL} and P'_S and the angles of polarization β'_{ZL} and β'_S of these tropospheric components may be computed by the formulae given in Divari's (1968) paper.

As a first approximation we have adopted two models of the zodiacal light: one according to Megill and Roach (1961) with intensity at the ecliptic pole equal to 110 stars, and the other according to Divari (1968) with intensity at the ecliptic pole equal to zero. For these two models we have computed the tropospheric components I'_{ZL} and I'_S by the formulae given by Divari (1968). The tropospheric brightnesses I'_{ZL} and I'_S obtained in such a way were small as compared to the observed brightness for the two models. Taking these computed quantities I_S, I'_S and I_{ZL}, I'_{ZL} (for the two models) and subtracting them from I_{obs}, we obtained the intensity I_N of the light of the night sky (atmospheric component). We have used this intensity I_N as a first approximation for the reduction of the measured brightnesses I_1, I_2 and I_3 at three positions of the Polaroid. Subtracting I_N, I_S, I'_S, I'_{ZL} from the measured brightnesses I_1, I_2, I_3 we can obtain the intensity $(I_{ZL})_1$, $(I_{ZL})_2$ and $(I_{ZL})_3$ of the zodiacal light by only three positions of the Polaroid, turned by steps of 60°. These reduced values of $(I_{ZL})_1$, $(I_{ZL})_2$, $(I_{ZL})_3$ were used for determining the degree and angle of the observed zodiacal light.

The averaged values of the degree of polarization for three wavelengths and two models of the zodiacal light are listed in table 3.

TABLE 3.—*The Averaged Degree of Polarization* P_{ZL} *at the Ecliptic Pole*

	First model of the zodiacal light			Second model of the zodiacal light		
λ, μ	0.37	0.53	0.58	0.37	0.53	0.58
P_{ZL}	0.075	0.08	0.11	0.31	0.475	0.057

One can see that for the first model the degree of polarization at the ecliptic pole is very low ($\sim$0.10) and for the second model it is very high ($\sim$0.45). This shows that the brightness I_N of atmospheric component found in the first approximation does not provide the required degree of polarization for the zodiacal light ($\sim$0.20) at the ecliptic pole. To have that value of the degree of polarization, we have to choose such a value of the intensity I_N of the atmospheric component that, being subtracted from the measured intensity I_1, I_2, I_3, it would provide a degree of polarization

TABLE 4.—*The Averaged Brightnesses of the Zodiacal Light at the Ecliptic Pole (for $z \leq 60°$ and $P_{ZL}=0.20$) Outside the Atmosphere in Units of Stars G2 10th Magnitude per Square Deg.*

Night	$\lambda=0.37\ \mu$	$\lambda=0.53\ \mu$	$\lambda=0.58\ \mu$
Oct. 10–11, 1969	70	95	127
Oct. 13–14, 1969	—	55	84
Oct. 14–15, 1969	80	53	84
Oct. 16–17, 1969	54	78	90
Averaged over all the nights	68	70	96

equal to 0.20. The intensity I_N found in such a manner together with I_S, I'_S and I'_{ZL} found above were used for the determination of the intensity I_{ZL} of the zodiacal light according to formula (4). The values obtained for the brightness of the zodiacal light at the ecliptic pole are listed in table 4.

As is seen from that table, the intensity of the zodiacal light at the ecliptic pole increases with the increase of the wavelength λ.

As the observed direction of polarization does not coincide with the reference plane, we have computed the intensity and angle of polarization of the unknown component which turns the polarization vector out from this plane. To achieve this, we have taken for the polarized component of the zodiacal light the following values: $(I_p)\lambda_{0.53}=70\times0.20=14$ and $(I_p)\lambda_{0.58}=96\times0.20=19$ stars G2 of the 10th magnitude per square deg.

In figure 2 three vectors are shown, representing three components of the light of the night sky at the ecliptic pole: $(I_{ZL})_p$ is the zodiacal light component directed to the Sun and $(I_{obs})_p$ is the observed polarized intensity (observed angle φ) and an unknown component $(I_2)_p$ with an unknown angle ψ.

Projecting the vectors on the direction forming an angle of 45° with the vector $(I_2)_p$ and taking into account the necessity to double the angles,

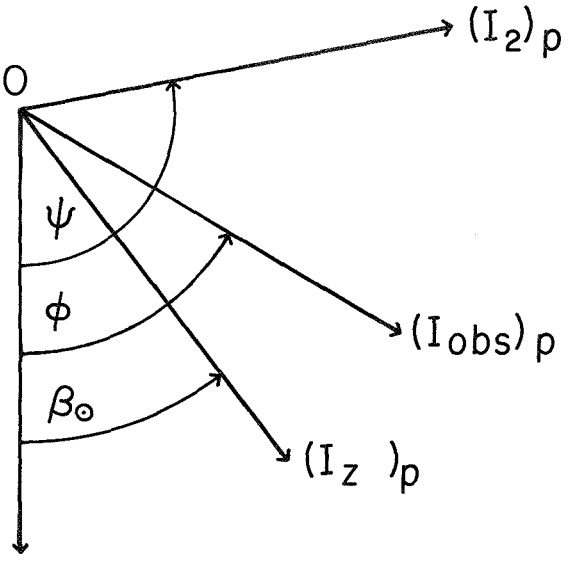

FIGURE 2.—Diagram of the vectors of polarization: $(I_{obs})_p$ is the observed vector of polarization with angle; $(I_{ZL})_p$ is the vector of the zodiacal light polarization with angle; $(I_2)_p$ is the polarization vector of an unknown component.

we have

$$\tan 2\psi = \frac{(I_{obs})_p \sin 2\varphi - (I_{ZL})_p \sin 2\beta_\odot}{(I_{obs})_p \cos 2\varphi - (I_{ZL})_p \cos 2\beta_\odot} \qquad (5)$$

If we project the three vectors on the direction forming 45° with vector $(I_{ZL})_p$, we have

$$(I_2)_p = (I_{obs})_p \frac{\sin 2(\varphi-\beta_\odot)}{\sin 2(\psi-\beta_\odot)} \qquad (6)$$

We have computed $(I_2)_p$ and ψ according to formulae (5) and (6). Figure 3 shows these two quantities. As may be seen from this figure, the intensity and angle of polarization of the unknown component vary through the night in a wide range. These results show that Stokes parameters of the zodiacal light are very much disturbed by the Earth's atmosphere and their determination is possible only in very good atmospheric conditions.

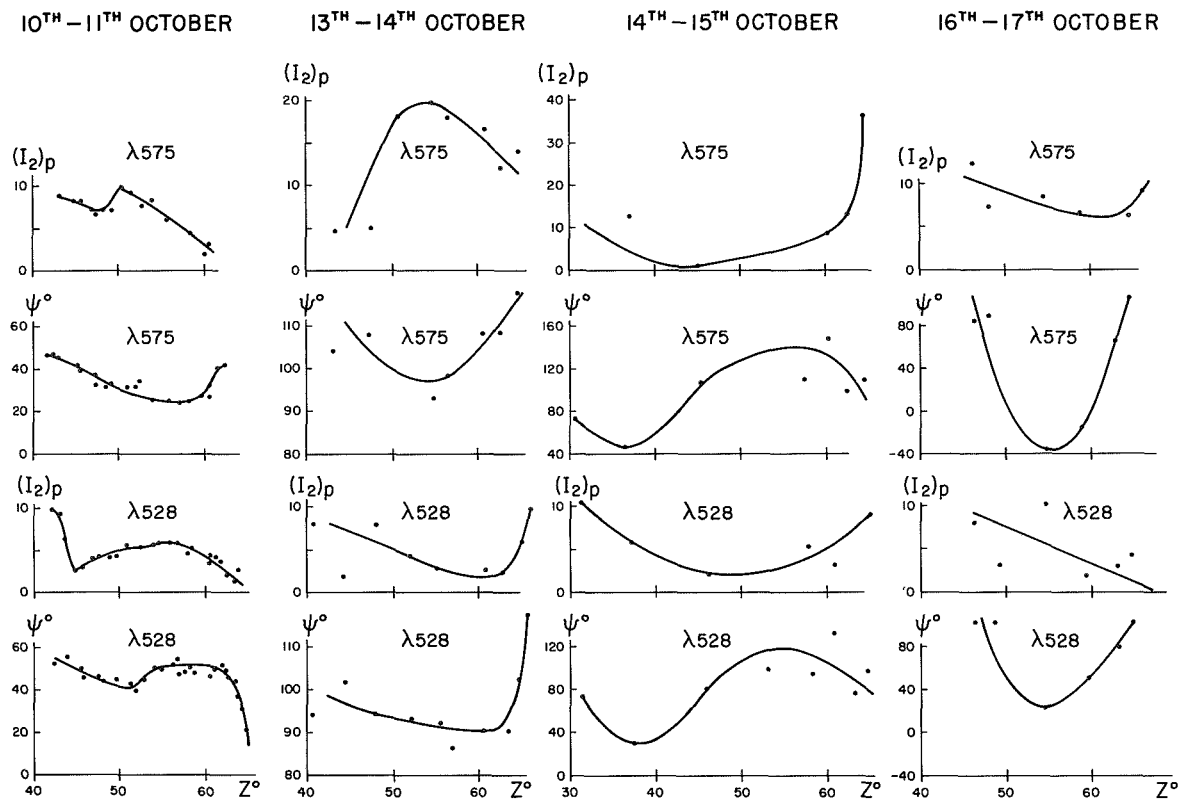

FIGURE 3.—The intensity $(I_2)_p$ and the angle ψ of the polarized unknown component.

REFERENCES

BEGGS, D. W., BLACKWELL, D. E., DEWHIRST, D. W., AND WOLSTENCROFT, R. D., 1964. Further observations of the zodiacal light from a high altitude station and investigation of the interplanetary plasma. III. Photoelectric measurements of polarization, *Monthly Notices Roy. Astron. Soc.*, **128,** 419–430.

DIVARI, N. B., On the polarization of light scattered by the troposphere of several components of the night sky, *Astron. Zhurn. Akad. Nauk.*, SSSR, **45,** 634–644.

DUMONT, R., 1965. Separation des composantes atmospherique, interplanetaire et stellaire du ciel nocturne a 5000 Å. Application a la photometrie de la lumiere zodiacale et du gegenschein, *Ann. d'Astrophys.*, **28,** 265–320. Translation in NASA TT F–11, Dec. 1967, 164.

DUMONT, R., AND SANCHEZ, M. F., 1966. Polarisation du ciel et polarisation de la lumiere zodiacale vers 5000 Å, sur l'ensemble de la sphere celeste, *Ann. d'Astrophys.*, **29,** 113–118.

FESSENKOV, V. G., 1935. Determination de la polarisation de la couronne solaire, *Astron. Zhurn. Akad. Nauk.*, SSSR, **12,** 309–321.

GILLET, F. C., 1967. Measurement of the brightness and polarization of zodiacal light from balloons and satellites, in *The Zodiacal Light and Interplanetary Medium*, edited by J. L. Weinberg, *NASA* **SP–150,** Supt. of Documents, U.S. Govt. Printing Office, Washington.

INGHAM, M. F., AND JAMESON, R. F., 1968. Observations of the polarization of the night sky and a model of the zodiacal cloud normal to the ecliptic plane, *Mon. Not. Roy. Astron. Soc.*, **140,** 473–482.

MEGILL, L. R., AND ROACH, F. E., 1961. The integrated starlight over the sky, *National Bureau of Standards Tech. Note* No. 106.

PYASKOVSKAYA-FESSENKOVA, E. V., 1958. Scattering and polarization of light by the atmosphere in the Libyan Desert, *Akademii Nauk. Doklady*, SSSR, **123,** 269–271.

ROSENBERG, G. V., 1942. On a new phenomenon in the scattered light of a twilight sky, *Akademii Nauk. Doklady*. SSSR, **36**, 270–274.

SPARROW, J. G., AND NEY, E. P., 1968. OSO–B2 satellite observations of zodiacal light, *Astrophys. J.*, **154**, 783–787.

VAN DE HULST, H. C., 1948. *The Atmospheres of the Earth and Planets*, edited by G. P. Kuiper, Chicago.

WEINBERG, J. L., 1963. *Photoelectric Polarimetry of the Zodiacal Light at* λ5300, thesis, Colorado.

——, 1964. The zodiacal light at 5300 Å, *Ann. d'Astrophys.*, **27**, 718–738.

WOLSTENCROFT, R. D., AND ROSE, L. J., 1967. Observations of the zodiacal light from a sounding rocket, *Astrophys. J.*, **147**, 271–292.

28. Optical Properties of Atmospheric Dust From Twilight Observations

N. B. Divari, Y. I. Zaginayilo,
and L. V. Kovalchuk
Odessa Polytechnic Institute
Odessa, U.S.S.R.

Three methods of approximation are described and are used to separate the primary twilight brightness from the observed brightness. Photoelectric observations obtained at the Majaky Observatory in 1968–69 (Zaginayilo) are combined with observations from a balloon and from Pic-du-Midi Observatory (Link et al., 1967) to derive the atmospheric scattering phase functions at 0.37 μ and 0.58 μ as a function of height.

Comparison of these data with data for a Rayleigh atmosphere provide information on the optical properties of dust in the upper atmosphere.

The observed brightness B_{obs} of the twilight sky may be considered as the sum of the primary brightness B_1 and the secondary one B_2:

$$B_{obs}=B_1+B_2 \qquad (1)$$

For investigation of the optical properties of the Earth's atmosphere it is necessary to separate the primary brightness B_1 from the observed brightness B_{obs}. It is a difficult problem. As there is no widely adopted method now for separating the primary brightness, we have determined this brightness by using three approximation methods.

The first method was proposed by V. G. Fessenkov (1968a) and utilizes observations in two points of the solar meridian with zenith distances $z=70°$. By this method the brightness of the secondary twilight in the observation point is determined from observations in the other point (the base point) lying in the Earth's shadow and having the zenith distance $z=70°$.

This method may be extended to points of the sky with zenith distances different from $z=70°$. Values of coefficient k are listed in table 1. The coefficient k is used for computations of the secondary brightness $B_2(z)$ in the observation point from the secondary brightness $B_2'(70°)$ in the base point $z=70°$, $A=180°$ by the formula $B_2(z)=kB_2'(70°)$.

In the second method, proposed by Divari (1971), we use another coefficient k_1 which is defined by the ratio $B_1(B_1+B_2)=k_1$. This coefficient k_1 may also be found from the computations for the standard atmosphere. Values of this coefficient are listed in table 2.

These values found according to the data of Divari and Plotnikova (1965), for corresponding wavelengths and atmospheric transmission coefficients may be considered only as a first approximation.

The third method for the determination of the primary brightness is V. G. Fessenkov's method of observations of the point of the sky with zenith distance $z=80°$ and azimuth $A=30°$ (from the Sun azimuth). This method requires measurement of intensity, degree and angle of polarization of the light of the twilight sky in the quoted point (Fessenkov, 1968b).

TABLE 1.—*Values of Coefficient* $k = B_2(z)/B_2'(70°)$ *used for* $A = 0°$ *at Wavelengths* $\lambda = 0.37\ \mu$ *and* $\lambda = 0.58\ \mu$ *With Corresponding Atmospheric Transmission Coefficients* $p = 0.59$ *and* $p = 0.89$ *(Base Point* $z = 70°$, $A = 180°$)

g / z	λ=0.37 μ, p=0.59				λ=0.58 μ, p=0.89			
	4°	6°	10°	14°	4°	6°	10°	14°
80°	1.31	1.46	1.51	1.54	2.12	2.55	2.63	2.73
70	0.891	1.47	1.37	1.37	1.10	2.00	2.11	2.17
60	0.809	1.30	1.25	1.25	0.673	1.19	1.24	1.26
40	0.583	0.897	0.846	0.842	0.337	0.574	0.579	0.580
20	0.451	0.650	0.592	0.585	0.222	0.368	0.366	0.363
0	0.385	0.535	0.503	0.496	0.185	0.304	0.303	0.300
−20	0.388	0.535	0.557	0.555	0.195	0.324	0.328	0.323
−40	0.458	0.650	0.746	0.749	0.254	0.427	0.438	0.436
−60	0.600	0.873	0.988	0.998	0.403	0.684	0.711	0.710

TABLE 2.—*Values of Coefficient* $K_1 = B_1/(B_1+B_2)$ *Used for the Wavelengths* $\lambda = 0.37$ *and* $\lambda = 0.58\ \mu$ *(Transmission Coefficients* $p = 0.59$ *and* $p = 0.89$*) and Computed According to the Data of Divari and Plotnikova (1965) for* $A = 0°$

g / z	λ=0.37 μ, p=0.59				λ=0.58 μ, p=0.89			
	4°	6°	10°	14°	4°	6°	10°	14°
80°	0.70	0.79	0.66	0.43	0.80	0.76	0.52	0.49
70	0.75	0.74	0.24	0.16	0.75	0.62	0.22	0.22
60	0.73	0.68	0.10	$8.0\ 10^{-2}$	0.72	0.55	0.12	0.12
40	0.69	0.59	$3.4\ 10^{-2}$	$3.4\ 10^{-2}$	0.69	0.46	$5.6\ 10^{-2}$	$5.6\ 10^{-2}$
20	0.65	0.52	$2.3\ 10^{-2}$	$2.2\ 10^{-2}$	0.66	0.40	$3.7\ 10^{-2}$	$3.5\ 10^{-2}$
0	0.63	0.47	$1.6\ 10^{-2}$	$1.5\ 10^{-2}$	0.65	0.36	$2.7\ 10^{-2}$	$2.3\ 10^{-2}$
−20	0.63	0.44	$9.4\ 10^{-3}$	$8.0\ 10^{-3}$	0.64	0.33	$1.6\ 10^{-2}$	$1.2\ 10^{-2}$
−40	0.62	0.35	$4.1\ 10^{-3}$	$2.7\ 10^{-3}$	0.63	0.27	$7.6\ 10^{-3}$	$4.3\ 10^{-3}$
−60	0.51	0.13	$7.9\ 10^{-4}$	$2.7\ 10^{-4}$	0.56	0.14	$1.4\ 10^{-3}$	$3.0\ 10^{-4}$

Having the primary brightness B_1 as the function of the Sun depression g ($g = z - 90°$, where z is the zenith distance of the Sun) or of the effective height of the twilight ray h, it is possible to determine the scattering coefficient $\sigma(\theta, h)$ of the atmosphere as a function of the scattering angle θ and the height h above the surface of the Earth. This procedure is described by Divari (1971).

Knowing $\sigma(\theta, h)$, we can find the volume scattering coefficient $\Sigma(h)$ (or extinction coefficient) according to

$$\Sigma(h) = \int \sigma(\theta, h)\, d\omega \qquad (2)$$

where $d\omega$ is an element of solid angle and integration is over all the angles.

For the purpose of comparing the three foregoing methods of separating primary brightness B_1 and determining the scattering coefficients, we have used the photoelectric observations of twilight sky made by Y. I. Zaginayilo in 1968–

1969 at the observatory Majaky near Odessa (USSR).

Figure 1 shows the observed brightness B_{obs} in the solar meridian at the points $z=70°$ and $z=-60°$ (the minus sign indicates that the observed point is on the antisolar side of the Sun meridian) and the primary brightnesses $B_1^{(1)}$ and $B_1^{(2)}$ found by the two methods above. As may be seen, the $B_1^{(1)}$ and $B_1^{(2)}$ at the point $z=70°$ are nearly equal in the interval 2° to 8° of the Sun depression. For $g>8°$, the second method leads to lower values than the first one ($B_1^{(2)}<B_1^{(1)}$). At the point $z=-60°$ the deviation of $B_1^{(2)}$ from $B_1^{(1)}$ begins earlier, approximately at $g=4°$.

Figure 2 shows the primary brightnesses $B_1^{(1)}$ and $B_1^{(2)}$ at the wavelength $\lambda=0.58\,\mu$ obtained from the observed brightness B_{obs} at the point $z=30°$ of the Sun meridian. In the same figure we have shown the brightness $B_1(25)$ ($\lambda=0.53\,\mu$) which was obtained by F. Link, L. Neuzil, and I. Zacharov (1967) by means of balloon observations at the height of 25 km above the Earth's surface. By crosses we have shown the observed brightnesses, obtained by Link et al. (1967) from the observation (at the wavelength $\lambda=0.53\,\mu$) at the Pic-du-Midi observatory ($H=2.9$ km). It seems from comparing the data presented in figure 2 that $B_1^{(2)}$ gives a more realistic approximation of primary brightnesses than $B_1^{(1)}$.

In figure 3 we have shown the phase functions $\sigma(\theta)$ for $\lambda 0.37\,\mu$ and $\lambda 0.58\,\mu$ obtained from the $\sigma(\theta, h)$ by averaging in the height interval 30 to 130 km. The vertical bars indicate the standard errors. The same figure shows the Rayleigh scattering function $\sim 1+\cos^2\theta$. As seen from figure 3, the intensity of scattered light increases

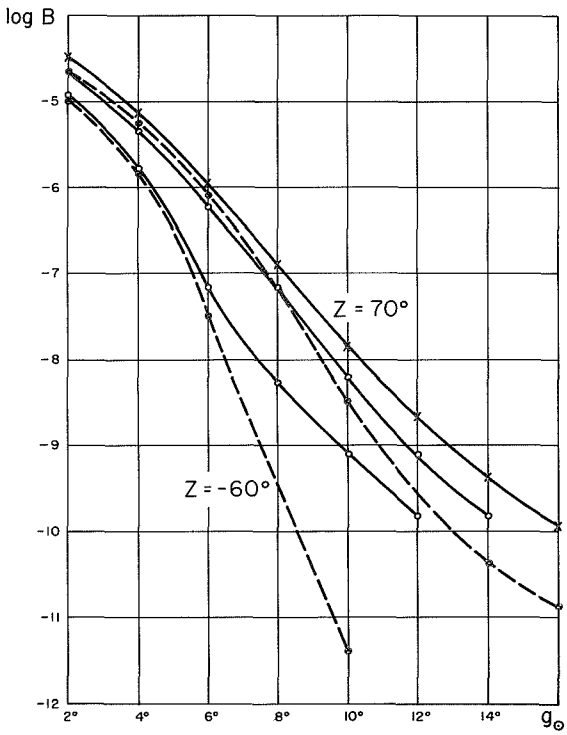

FIGURE 1.—Log of the observed brightness B_{obs} at the points $Z=70°$ (crosses) and $Z=-60°$ of the solar meridian and primary brightnesses $B_1^{(1)}$ (open circles) and $B_1^{(2)}$ (black dots) for the same point of the sky, plotted against $g_\odot$, the solar depression angle.

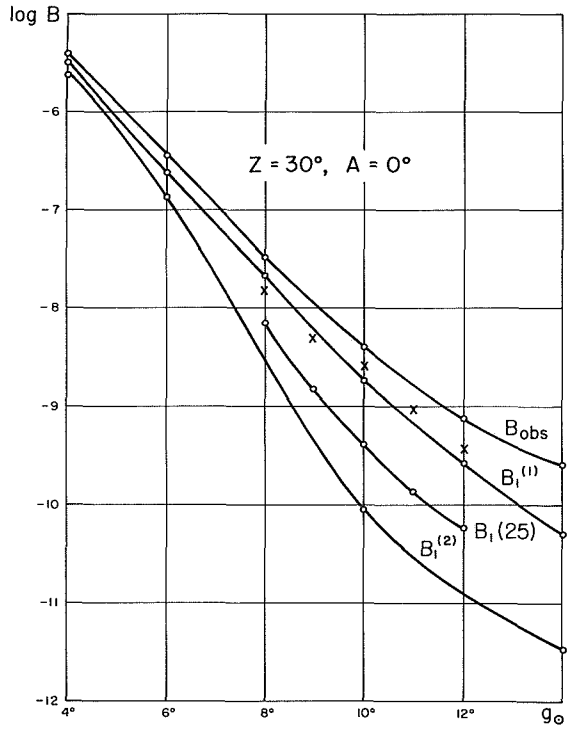

FIGURE 2.—Log of the observed brightness B_{obs} and primary brightnesses $B_1^{(1)}$ and $B_1^{(2)}$ at wavelengths λ 0.58 μ from observations at the point $Z=30°$ of the sun meridian. $B_1(25)$ is primary brightness according to Link et al. (1967) from balloon observation. Crosses are their observations of brightness at the Pic-du-Midi. Abscissae are solar depression angles $g_\odot$.

with the decrease of angle θ steeper than for Rayleigh scattering. It seems that it is the manifestation of the influence of aerosols on the optical properties of atmosphere. It may be pointed out that the increase of scattering intensity with the decrease of the scattering angle θ is flatter at $\lambda 0.37\ \mu$ than at $\lambda 0.58\ \mu$.

Figure 3 also shows the aerosol phase function $\sigma_a(\theta)$ obtained from the atmospheric scattering coefficient $\sigma(\theta)$ by subtracting the Rayleigh scattering coefficient $\sigma_R(\theta)$, calculated for standard atmosphere CIRA, 1965. In the same figure we show the aerosol phase function obtained by E. V. Pyaskovskaya-Fessenkova (1970) from observations of the day skylight. As may be seen, there is a good agreement between the phase functions obtained from twilight and daytime observations.

The scattering coefficient $\sigma(\theta)$ was defined from observations in the sun meridian for the interval of scattering angles $\theta=25°$ to 155°. Since for the determination of the extinction coefficient Σ it is necessary to integrate $\sigma(\theta)$ over the interval θ from $\theta=0°$ to $\theta=180°$, we extrapolate this function from $\theta=25°$ to $\theta=0°$ and from $\theta=155°$ to $\theta=180°$. The extrapolation from $\theta=25°$ to $\theta=0°$ was made by taking into account the results found by G. Newkirk and J. A. Eddy (1963) for the small angles from the stratospheric coronagraph observations. The extrapolation in the angle interval 160° to 180° is made with sufficient certainty and the error of this extrapolation according to our estimations can reach a few percent of the value of Σ.

Figure 4 shows the extinction coefficients $\Sigma^{(1)}$, $\Sigma^{(2)}$ and $\Sigma^{(3)}$ obtained for the primary

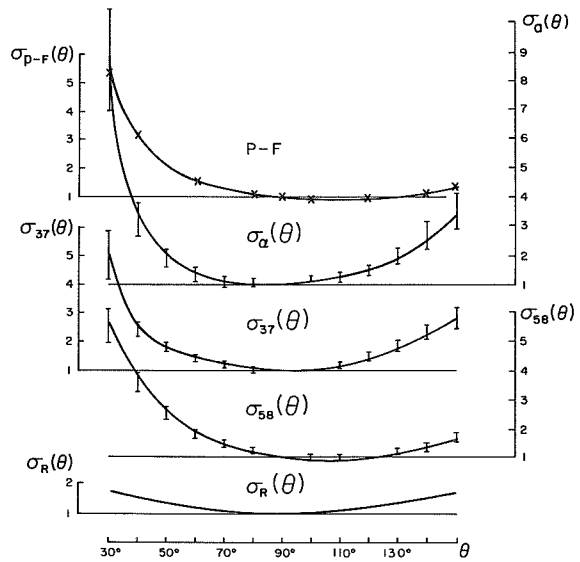

FIGURE 3.—Atmospheric phase function $\sigma_{37}(\theta)$ for λ 0.37 μ and $\sigma_{58}(\theta)$ for λ 0.58 μ and aerosol phase function $\sigma_a(\theta)$ for λ 0.37 μ. *P–F* is aerosol phase function according to Pyaskovskaya-Fessenkova (1970) for λ 0.546 μ. $\sigma_R(\theta)$ is Rayleigh phase function for λ 0.37 μ.

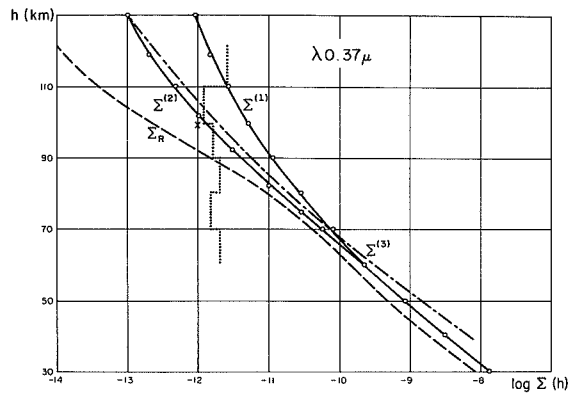

FIGURE 4.—Extinction coefficient $\Sigma^{(1)}$, $\Sigma^{(2)}$ and $\Sigma^{(3)}$ obtained from the primary brightnesses $B_1^{(1)}$, $B_1^{(2)}$ and $B_1^{(3)}$ at the wavelength λ 0.37 μ. Point X is the value according to Mikirov (1963). Dotted line portrays extinction coefficient according to Fiocco and Columbo (1964).

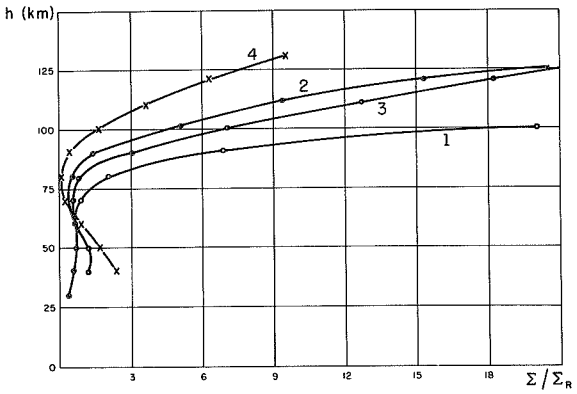

FIGURE 5.—Ratios Σ/Σ_R. Curve 1 is ratio obtained from $B_1^{(1)}$ in the Sun meridian. Curve 2 is ratio obtained from $B_1^{(2)}$ in the Sun meridian. Curve 3 is ratio obtained from $B_1^{(2)}$ at the point $Z=80°$, $A=30°$. Curve 4 is ratio obtained from $B_1^{(3)}$ at the point $Z=80°$, $A=30°$.

brightnesses $B^{(1)}$, $B^{(2)}$ and $B^{(3)}$ at wavelength $\lambda 0.37\ \mu$, computed by the three foregoing methods. In the same figure there is the Rayleigh extinction coefficient Σ_R computed for atmosphere model CIRA 1965. The dotted line indicates the extinction coefficient found for the heights 60 to 120 km by G. Fiocco and G. Colombo (1964) by means of laser observations. The cross indicates the extinction coefficient found by A. E. Mikirov (1963) by means of rocket measurements.

To present the importance of the aerosols in the atmospheric scattering, we have computed the ratio Σ/Σ_R for different heights from 30 to 125 km. As is seen from figure 5, the values of this ratio are near unity in the height interval 30 to 80 km and rapidly increase above 80 km. It seems that this phenomenon is the result of the light scattered by dust which penetrates into the Earth's atmosphere from the interplanetary space or arises from meteor ablation.

The presented data and the results of comparing the twilight data with data obtained by other methods permit the conclusion that the twilight method offers good possibilities for investigation of the optical properties of the upper atmosphere and can be used for monitoring the dust concentration in the upper atmosphere.

REFERENCES

Divari, N. B., 1971. The results of investigation of dust in the upper atmosphere by the twilight method, *Space Research XI*, 351–355.

Divari, N. B., and Plotnikova, L. I., 1965. Computed brightness of the twilight sky, *Astron. Zhurn. Akad. Nauk.*, SSSR, **42**, 1090–1103.

Fessenkov, V. G., 1968a. *Atmosfernaya optika*, Nauka Press, Moscow, 96. Translated and published by Plenum Publ. Corp., New York, "Atmospheric optics," edited by N. B. Divari, 1970, 90.

——, 1968b. *Atmosfernaya optika*, Nauka Press, Moscow, **175**.

Fiocco, G., and Colombo, G., 1964. Optical radar results and meteoric fragmentation, *J. Geophys. Res.*, **69**, 1795–1805.

Link, F., Neusil, L., and Zacharov, I., 1967. Mesures simultanees du ciel crepusculaire in ballon et au sol, *Ann. Geophys.*, **23**, 207–216.

Mikirov, A. E., 1963. Aerosol scattering coefficient measurements at 80–100 km, *Space Research III*, 155–161.

Newkirk, G., Jr., and Eddy, J. A., 1963. Influx of meteor particles in the upper atmosphere of the Earth as determined from stratospheric coronagraph observations, *Space Research III*, 143–154.

Pyaskovskaya-Fessenkova, E. V., 1970. *Atmosfernaya optika*, Nauka Press, Moscow, **94** (to be translated by Plenum Publ. Corp.).

Page intentionally left blank

29. Unusual Chemical Compositions of Noctilucent-Cloud Particle Nuclei

CURTIS L. HEMENWAY
Dudley Observatory and
State University of New York at Albany
Albany, New York

On August 8, 1970, two Pandora sounding rocket payloads were launched from the ESRO range in Kiruna, Sweden during a noctilucent cloud display. Large numbers of sub-micron particles were collected, most of which appear to be made up of a high-density material coated with a low-density material. Typical electron micrographs are shown. Particle chemical compositions have been measured by use of dispersive x-ray analysis equipment attached to a Philips EM 300 electron microscope and have revealed that most of the high-density particle nuclei have atomic weights greater than iron.

ON AUGUST 8, 1970 at 1:48 and at 3:54 local time, two Nike Apache sounding rockets containing Pandora micrometeorite collectors were launched into a noctilucent cloud display above Esrange in Kiruna, Sweden. The visual observation of the noctilucent clouds was carried out by Nathan Wilhelm of Meteorological Institute of Stockholm University and Ralph Carnevale (AFCRL) who were stationed at Sundsvall, 600 km south of Esrange. Figure 1 shows a photograph of the noctilucent cloud over Esrange into which the rockets were launched as seen from Sundsvall.

The sampling surfaces as in past Pandora flights (Hemenway and Hallgren, 1970; Hallgren and Hemenway, 1970) consisted of thin nitrocellulose films supported on copper grids. Since in-flight shadowing was used, the grids were

FIGURE 1.—Photograph of the noctilucent cloud sampled.

seeded with tungsten oxide particles to act as a monitor of the quality of the shadows.

All payload functions performed as planned but unfortunately the trajectory of each payload was about 10 km lower than planned, with the result that the shadowing for the first two sampling increments from each payload took place at an altitude where the ambient pressure was too high for producing sharp shadows. For Pandora N, the first payload launched, the altitudes sampled were 82 to 94 km and 94 to 124 km and for Pandora M the altitudes were 85 to 96 km and 97 to 133 km.

Figure 2 shows examples of an unusual type of particle found in large numbers on Pandora N and to a lesser extent on Pandora M. The particles generally consist of high-density material surrounded by a round-to-elliptical, droplet-like

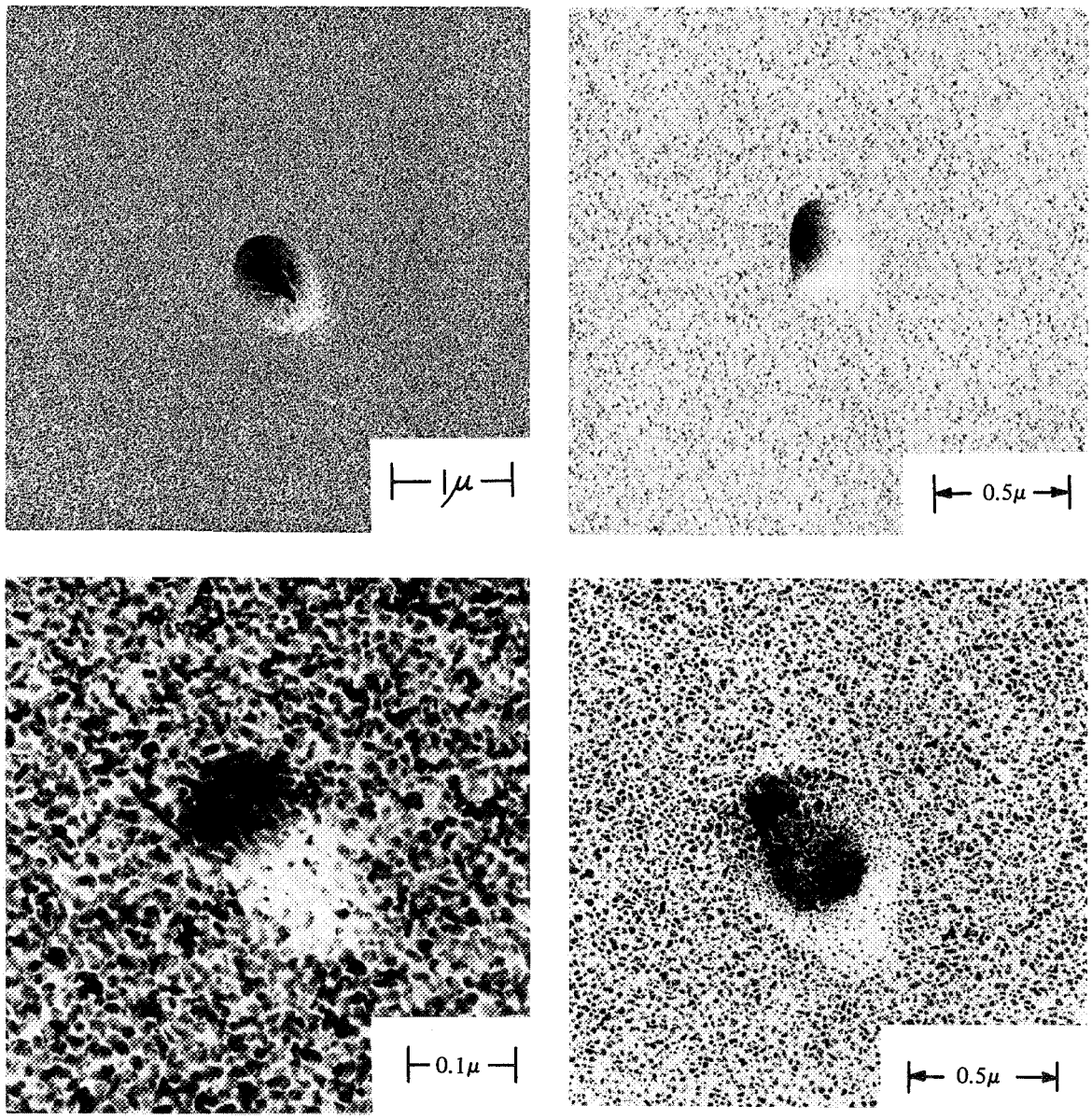

FIGURE 2.—Electron micrographs of noctilucent cloud particles collected.

coating of low electron optical density. Approximately 70 percent of the collected particles were of this unusual type. Somewhat similar two-component particles were collected during a noctilucent cloud display in 1962 (Hemenway et al., 1962).

By using an x-ray spectrometer attached to our Phillips 300 electron microscope, it has been possible to obtain qualitative chemical analyses from a study of the characteristic x-ray emission from some of the collected particles. Figure 3 shows an example of x-ray spectra of a particle and the nearby background in which the lanthanum lines located at 47.2° and 48.5° associated with a noctilucent cloud particle are clear. The remaining lines of tungsten and gold are noted on the left sides of the spectra. Figure 4 shows an additional example of x-ray spectra of a particle and nearby background in which a silicon peak at 42.0° associated with the particle and other peaks of uncertain origin can clearly be seen.

The presence of high atomic number elements is consistent with the high electron-optical density of the nuclei of the coated particles. Tentatively, the following elements have been identified as associated with the haloed particles: lanthanum, silicon, thulium, praseodymium, osmium, ytterbium, and tantalum. There are a number of weak lines which have not been identified and other marginal identifications which have not been included even though they

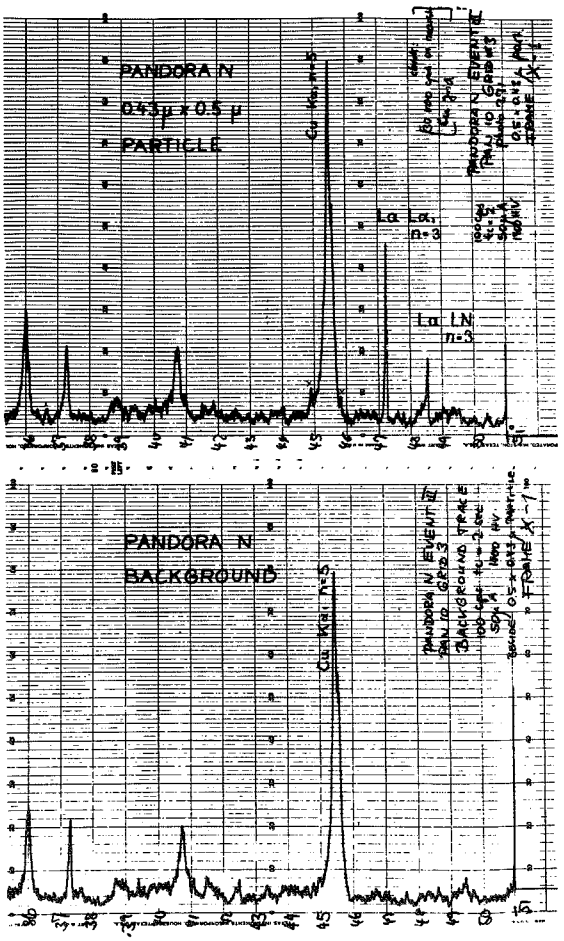

FIGURE 3.—X-ray spectra of a particle and nearby background.

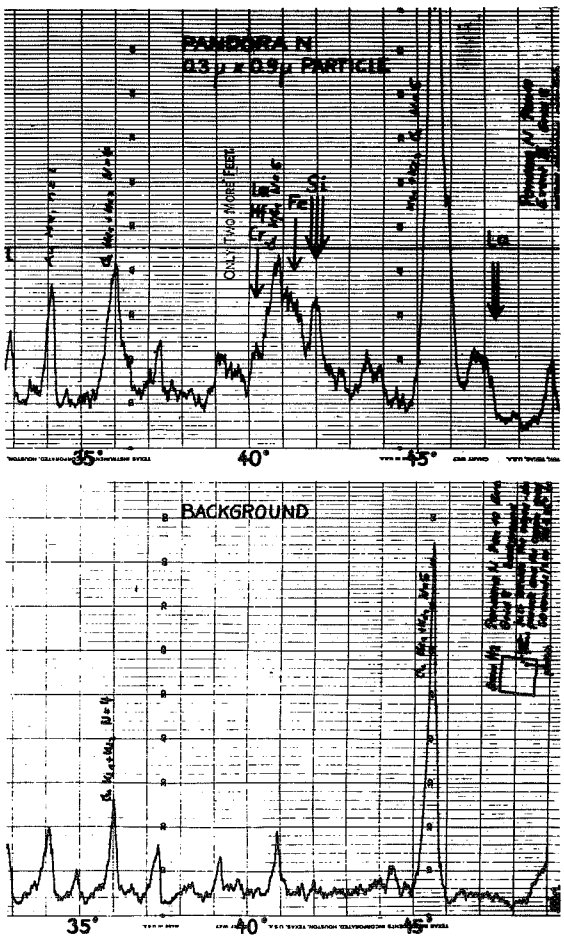

FIGURE 4.—X-ray spectra of a particle and nearby background.

seem to be mostly high z elements. The one observation which is clear is that the observed x-ray lines from these particles appear for the most part to be restricted to elements of atomic number greater than iron.

The possibility that the particles are fallout from atomic bomb testing has been considered and has difficulties. For example, if atomic bomb debris can be carried upward through the stratosphere to an altitude of 85 km then the wide variety of terrestrial spores, salt particles, bits of mica, etc., found in the troposphere should also be elevated. Such is not the case. Furthermore, Rauser and Fechtig (1972) have shown that noctilucent cloud particles measured at Kiruna, Sweden two days after our collection flight were entering the mesopause from above and falling downward through it. In addition, it has been many years since any known space tests of atomic devices have been carried out and furthermore such an origin would appear to require too large a mass of fissioned material and a high efficiency mechanism for concentrating particles into the Polar regions.

The possibility that supernova particulate remnants have been encountered has also been suggested and appears to have even more severe difficulties although Greenberg (1969) has suggested that an interstellar component of dust might exist in the solar system. Additional measurements and flight collections will be necessary before the origin of these intriguing and unexpected particles can be identified.

The author expresses his thanks to Douglas Hallgren, Anthony Laudate, David Wachtel, Helga Schroeder, Gail Heylmun, Richard Schwarz and William Radigan for many hours of sample scanning and analysis. My thanks go also to James Lease of Goddard Space Flight Center. I wish to thank George Witt and Nathan Wilhelm of MISU and Ralph Carnevale of AFCRL and the Swedish Space Technology groups for their support in Sweden.

REFERENCES

GREENBERG, J. M., 1969. A possible inter-relation between interstellar and interplanetary cosmic dust, *Space Research IX*, 111–115.

HALLGREN, D. S., AND HEMENWAY, C. L., 1970. Sounding rocket samplings of cosmic dust, *Space Research XI*, 377–381.

HEMENWAY, C. L., AND HALLGREN, D. S., 1970. Time variation of the altitude distribution of the cosmic dust layer in the upper atmosphere, *Space Research X*, 272–280.

HEMENWAY, C. L., SOBERMAN, R. K., AND WITT, G., 1964. Sampling of noctilucent cloud particles, *Tellus*, **16**, 84–88.

RAUSER, P., AND FECHTIG, H., 1972. Combined dust collection and detection experiment during a noctilucent cloud display above Kiruna, Sweden, *Space Research XII*, 391–402.

30. The Physical Nature of Interplanetary Dust as Inferred by Particles Collected at 35 km

DONALD E. BROWNLEE
PAUL W. HODGE
AND
WILLIAM BUCHER
University of Washington
Seattle, Washington

Particles were collected at an altitude of 35 km by two flights of a volume-sampling micrometeorite collector. The collection scheme is very sensitive and is capable of collecting a significant number of particles. Many of the particles collected have chemical compositions similar to solar or to iron meteorites. Morphology of collected particles indicates that both true micrometeorites and ablation products were collected.

A BALLOON-BORNE MICROMETEORITE COLLECTOR has been built which is sensitive enough to collect significant numbers of true micrometeorites even if the actual particle flux is an order of magnitude less than that indicated by penetration detectors mounted on spacecraft. Collections are made at 35-km altitude, a level where under normal conditions the probability of finding terrestrial aerosols larger than 3μ is exceedingly small (Junge, 1961). The collector is a volume-sampling device and is orders of magnitude more sensitive than other collection devices, primarily because it takes advantage of the tremendous spatial concentration of extraterrestrial dust particles in the stratosphere.

COLLECTOR DESIGN

The collector consists basically of an air pump which pulls air through an array of cylindrical collection rods. Particles are collected on the oil-coated rods by inertial deposition. The collection rods are 0.25-in. diameter $\times$ 2.25-in. long and are nearly 100 percent efficient for collecting particles (larger than 2μ) from the 350-ft s^{-1} moving air stream. The design of the collector is shown schematically in figure 1. The pump is an air ejector system similar in principle to the one described by Wood et al. (1966). The driving gas for the pump is derived from the catalytic decomposition of hydrazene. The collector's fuel tanks carry 150 lb of hydrazene and the pump is capable of sampling over 10^6 ft^3 of ambient air at 35 km during a 5-hr period. The pump draws air through the horn-shaped air inlet and the collection-rod assembly. The 22 collection rods are mounted normal to the air flow in a slide-gate mechanism that seals the collection rods from contamination before and after the collection phase of the flight. A cover over the end of the horn and a butterfly valve just behind the collection-rod assembly prevent contamination of the air channel upstream and downstream of the collection rods before collection. The rod-holding assembly and the interior portions of the butterfly valve and inlet horn are critically cleaned in our class-100 cleanroom in Seattle, coated with silicone oil and sealed from

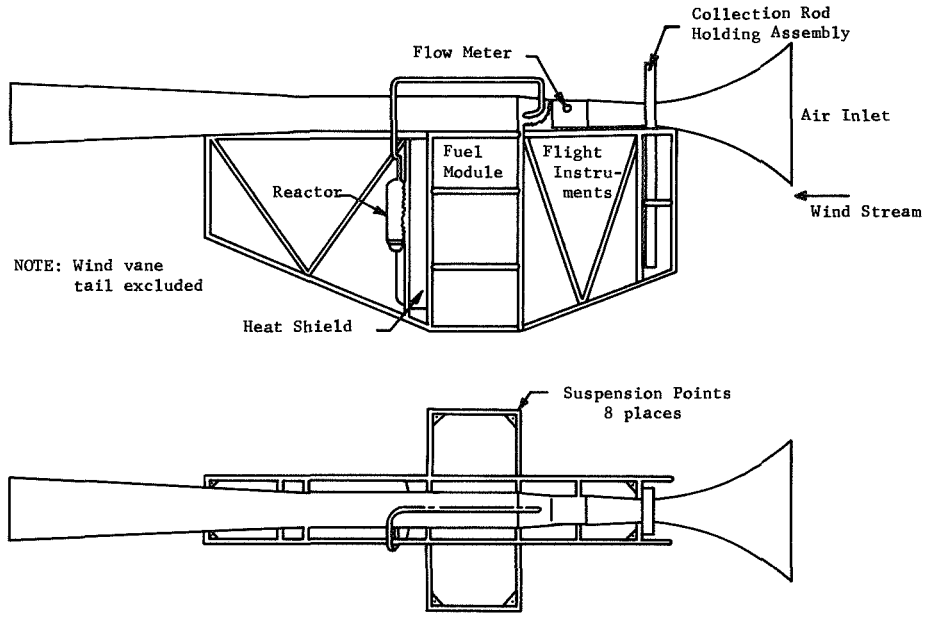

FIGURE 1.—Collector schematic diagram.

contamination until the collector begins to function 35 km over Texas.

To prevent contamination from the balloon, rigging, and exterior portions of the gondola, the collector is suspended 3000 ft below the balloon on a nylon line. The wind-velocity gradient in the stratosphere typically produces a wind against the collector of 5 ft s^{-1}. This wind completely isolates the collector from particulate matter emitted by the balloon and is used to isolate the collector's air inlet from dust generated by the gondola and pump exhaust. A 30-ft boom (see fig. 2) is attached to the exhaust end of the collector. At altitude, 400 ft^3 of sail area is deployed at the end of the tail which gives the collector the aerodynamic characteristics of a wind vane. The wind acting on the tail orients the gondola so that the air inlet horn is at all times upwind of all other parts of the system. The environment is exactly analogous to a laminar-flow cleanroom. The orientation of the collector is monitored both with a flux gate magnetometer and with a sequence camera.

Because of the orientation of the cylindrical collection rods relative to the airstream, particles can only be collected on one half of each rod. For each rod the upstream half is considered a collection surface and the downstream half is considered a control. Both halves of each rod go through exactly the same cleaning and handling procedures so that the control technique is nearly ideal.

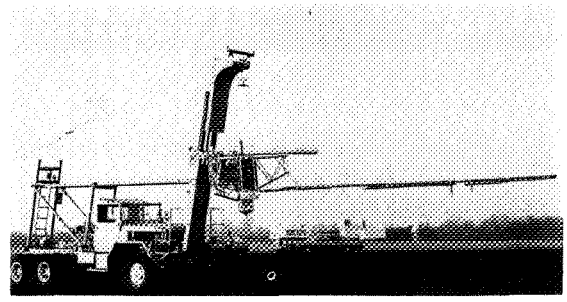

FIGURE 2.—Collector just prior to launch.

COLLECTION FLIGHTS

The collector, the Vacuum Monster (VM), has now had two collection flights, one on April 21, 1970 and one on May 2, 1971. The ambient-air volume actually sampled by the collection rods on the first and second flights was 171 000 ft^3 and 200 000 ft^3 respectively. On the first flight the microscopic rod scanning techniques were 100 percent effective for only particles 10μ and larger.

On this flight 12 particles ($\geq 10\mu$) were found on the upwind sides of the collection rods and seven on the downwind sides. This is not a good signal-to-noise ratio but morphological analysis with a scanning electron microscope (SEM) and chemical analysis with a microprobe indicates that at least two of the particles are very probably extraterrestrial. One is a 12-μ opaque spherule (fig. 3) and the other is a $10\mu \times 30\mu$ cellular particle (fig. 4). Microprobe analysis indicates that the major constituents of the sphere are Fe and Mg (Si could not be detected because of interference from the substrate) and the minor constituents are Ni, Ti, Cr. The Fe content of the sphere is $\sim$15 percent and the Mg content is roughly similar. The composition of the cellular particle is Si, Mg, S, and Fe in order of abundance.

On the second collection flight, techniques were improved so that the scanning process was 100 percent efficient for particles $\geq 5\mu$ and about 25 percent efficient for 3-μ particles. The scanning process detected 306 particles ($\geq 3\mu$) (fig. 5) on the upwind sides of the rods and none on the downstream sides. This is an excellent signal-to-noise ratio and indicates that all the particles on the rods came in through the horn during the collection phase of the flight. The largest particle collected was a 12-μ transparent spherule with chondritic composition. The number of large particles collected on this flight is in agreement with the number on the first flight if one subtracts the background contamination. The size distribution of the second collection is very steep and most of the particles are 2μ to 3μ in size. Over 80 percent of all the particles collected are spheres. Ninety percent of the spheres are transparent. Of the irregular particles many are highly irregular with a very low density structure. Microprobe analysis of 50 of the particles indicates that a little over 10 percent of the collection has meteoritic composition. Most of the transparent spheres are aluminum oxide. It seems unlikely that these could be extraterrestrial and at this point we are not sure whether the transparent spheres came from the pump exhaust or the atmosphere. Neither source seems reasonable and at present the Al_2O_3 spheres are a real mystery. All of the nontransparent spheres analyzed to date have meteoritic compositions. Some are Fe, Ni (Fe/Ni $\approx$ 20) and others are Fe, Ni, S. Of the irregular particles analyzed, few contained detectable elements. This is possibly due to the difficulty in microprobing small low-density particles. One of the irregular particles did, however, contain Si, Mg, S, Fe and Ni.

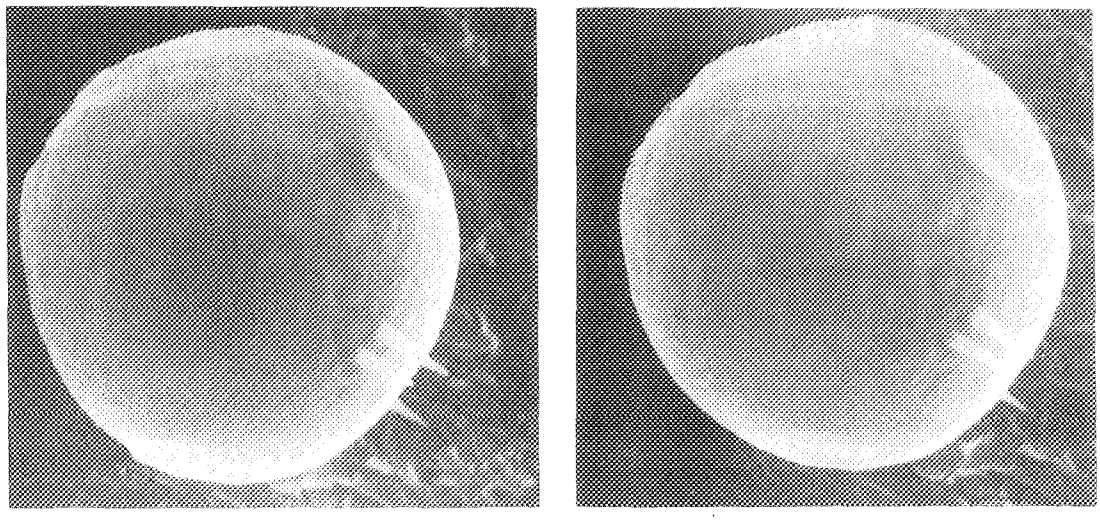

FIGURE 3.—A 12-μ spherule with chondritic composition. (A stereographic pair of photographs.)

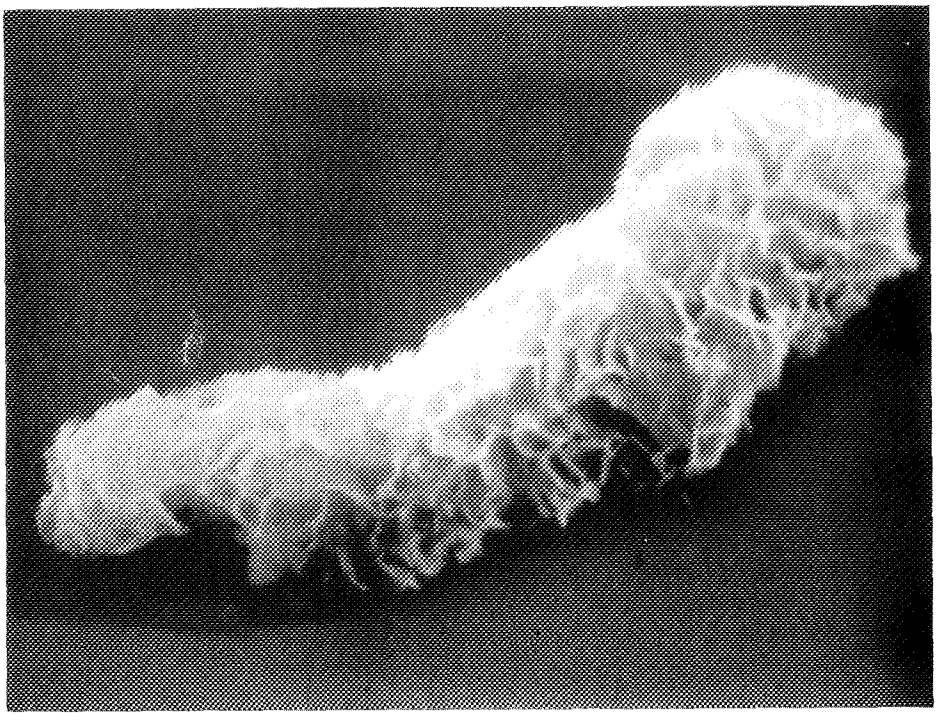

FIGURE 4.—A 30 × 10 μ cellular particle.

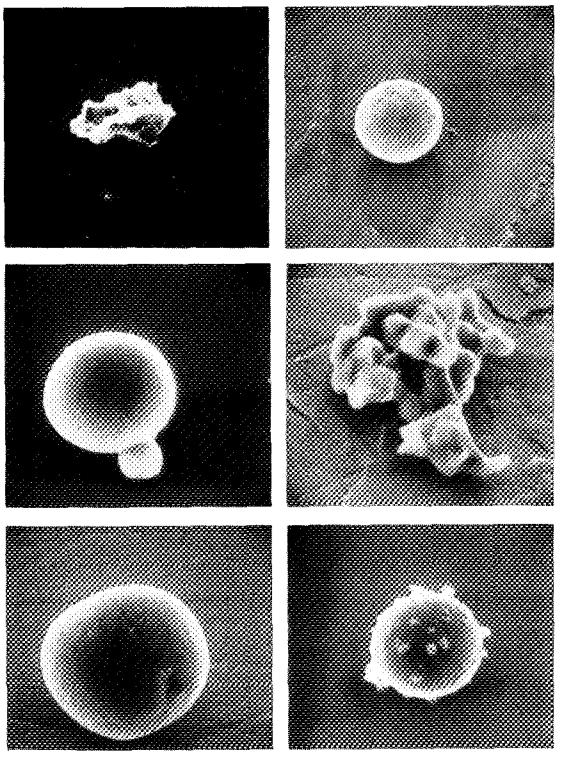

FIGURE 5.—Particles of 3 to 4 μ diameter from the second collection flight.

CONCLUSION

Both of the VM flights sampled large quantities of air and the time-area-products (TAP) of the collections is quite large. For the last flight the TAP for 3-μ spheres (density = 3 g cm^{-3}) was 7 × 10^5 m^{2}s. This is a very large TAP and it is predicted that the collection should contain approximately 30 true micrometeorites ($\geq 3\mu$) on the basis of the flux model of Kerridge (1970). Our analysis so far indicates that the micrometeorite flux in the stratosphere is certainly not higher than that predicted from the Kerridge model and is probably in reasonable agreement with it.

On the basis of chemical and morphological considerations we feel that we have collected extraterrestrial particulate matter from the stratosphere both in the form of micrometeorites and ablation products. The cellular particle from the first flight probably could not be an ablation product because of its complicated porous structure.

The low-density structure and primitive near-solar composition of this particle is strongly suggestive of a cometary origin. The spherule from the first flight has a similar composition to the cellular particle with the exception of the sulfur content. The sphere has an ordinary chondritic composition and we feel that it is most probably an ablation product of a larger body. Of the particles analyzed from the second flight most of those with meteoritic compositions are spheres and are probably also ablation products. Excluding the Al_2O_3 spheres, the spheres seem to fall into three compositional groups: chondritic, nickel-iron and nickel-iron-sulfur. The irregular particles that contain detectable elements have compositions compatible with carbonaceous chondrites.

We plan to do extensive quantitative analysis on the meteoritic particles from the balloon collections for accurate comparison with the compositions of the standard source of interplanetary matter, meteorites. At this point in the analysis it seems that the composition of most of the meteoritic particles is similar to the most primitive meteorite types. This is consistent with the studies of trace elements in the lunar soil by Ganapathy et al. (1970) that indicate that the mean composition of micrometeorites is similar to that of the Type I carbonaceous chondrite meteorites. The structure of some of the irregular particles is very low density which is consistent both with comet models and meteor studies. The structure and compositions of these particles will be studied with the goal of determining the physical nature, origin, and space density of interplanetary dust grains.

ACKNOWLEDGMENT

We gratefully acknowledge the partial support of the National Aeronautics and Space Administration through Grant NGR 48-002-033.

REFERENCES

GANAPATHY, R., REID, R., KEAYS, J., LAUL, J., AND ANDERS, E., 1970. Trace elements in Apollo 11 lunar rocks: Implications for meteorite influx and origin of moon, *Proc. Apollo 11 Lunar Sci. Conf., Geochim. Cosmochim. Acta, Suppl.*, **1**, 1117–1142.

JUNGE, C. E., 1961. Stratospheric aerosol studies, *J. Geophys. Res.*, **66**, 2163–2182.

KERRIDGE, J. F., 1970. Micrometeorite environment at the Earth's orbit, *Nature*, **288**, 616–619.

WOOD, R., ZELLER, H., OLSON, R., DEETER, R., MAFFITT, K., AND ANDERSON, H., 1966. Studies of extraterrestrial dust at 40 km, *Applied Sci. Div., Litton Systems, Inc.*, Rept. No. 3063.

Page intentionally left blank

31. On the Manganese Content of Cosmic Flakes From Deep-Sea Sediments

KARL UTECH
Gesellschaft für Weltraumforschung
Bonn-Bad Godesberg, West Germany

Cosmic flakes belong to the category of cosmic microparticles. They occur together with cosmic spherules in sediments (Utech, 1965). These flakes appear to represent ablation products of iron meteorites burnt away during the passage of a meteorite through the atmosphere by friction against air molecules. Microprobe analyses of flakes from deep-sea deposits proved the particles to consist of magnetite which in most cases had been altered into maghemite in the outer zones. This is in agreement with the assumption that they represent fragments of fusion crust of iron meteorites. Most of the flakes, however, contained a small percentage of manganese. This element is not a common constituent of iron meteorites. The author attempts to explain the presence of manganese in flakes and its absence in cosmic spherules.

MAGNETITE FLAKES of deep-sea sediments were known to most investigators for a long time but little attention was paid to these particles until a relationship was found to exist in the frequency of the occurrence between flakes and cosmic spherules on occasion of an investigation of Permian rock salt, sampled from a pit in the vicinity of Wolfenbüttel, northern Germany.

Rock salt is formed in shallow basins which have become cut off from the open ocean. Thus the water is allowed to evaporate and salt is precipitated. The rate of salt formation is high and consequently the concentration of cosmic spherules therein contained is low. During the work on the rock salt samples it was noticed that the concentration of flakes was also low in contrast to deep-sea deposits where spherules and flakes are plentiful. This was the first hint that the flakes might be of cosmic origin.

As judged by their magnetic properties and confirmed by microprobe and Debye-Scherrer analyses, the flakes consist of magnetite. Most of those extracted from deep-sea sediment cores were weathered and more highly oxidized in the outer zones to maghemite. Microprobe analyses showed however the flakes from deep-sea sediments contained some manganese of the order of magnitude from 0.5 to 2.0 percent. Manganese is not a common constituent of iron meteorites of which the flakes were assumed to be ablation products, but is present in deep-sea deposits.

A check on cosmic spherules from the same sediments confirmed previous analyses that spherules did not contain manganese, at least not in their internal parts. Now the question arose if the flakes could be of cosmic origin and be ablation products of iron meteorites as the spherules are, if they contained manganese and the spherules did not. To solve this question the following investigations were carried out.

Thin sections of flakes were studied under high magnification. They showed the same magnetite skeletons as cosmic spherules. Apparently during their genesis they must have been in a ± liquid

state and then rapidly chilled, as cosmic spherules too. However the mechanics of origin of flakes appear to differ from those of spherules. Flakes, or fusion crust respectively, are practically burnt off a meteorite whereas spherules are detached from the surface of fusion crust. Some flakes showed a certain flow structure at the surface as sometimes can also be observed on fusion crust of iron meteorites. One flake was found with an almost perfectly developed spherule at its surface. Apparently this flake was torn from the meteorite prior to the detachment of the spherule from the fusion crust. These observations are in agreement with the assumption that the flakes are of cosmic origin.

In order to find out how manganese could penetrate the flakes and not the spherules, some flakes from deep-sea deposits were cut into two pieces and embedded upside down for analyses with the microprobe analyzer. Then the electron beam was moved slowly across the flake to determine whether the manganese contents varied within an individual flake. This assumption could however not definitely be proved, although several of these analyses had been carried out.

The same test was repeated on a flake from a rock-salt sample. It did not contain manganese and consisted of high-grade magnetite only.

As previously mentioned, rock salt is formed in shallow basins which have become separated from the open sea. In contrast to deep-sea deposits, shallow waters do not contain manganese in any appreciable amount. As a consequence, flakes which fell into these basins cannot be contaminated with manganese as seems to be the case with those which fell into the deep ocean and became embedded in sediments containing this element.

Flakes which in most cases are only a few microns thick are exposed with all sides to the manganese of the sediment, thus offering this element the possibility to penetrate the flakes from all directions in the course of time.

Cosmic spherules, on the other hand, offer the manganese only their external sides. Furthermore, the shells of the spherules are often thicker than the flakes. For these reasons manganese is prevented from penetrating spherule magnetite thoroughly. The flakes and spherules worked with had been extracted from deep-sea sediments of Quaternary age. Perhaps spherules embedded in older deep-sea sediments may also contain some manganese as the time factor cannot be overlooked in the process of manganese penetration, but this is an unproved assumption as such sediments had not been available.

CONCLUSIONS

Flakes and spherules are of the same composition when extracted from sediments which do not contain manganese. If manganese is present in the sediment, it penetrates the thin flakes in the course of time. This penetration takes place from all sides of the flakes, in contrast to cosmic spherules which offer the manganese only their external sides. As the shells of spherules are also thicker than flakes, manganese cannot penetrate the magnetite of spherules thoroughly, but may only be detected at the surface of uncleaned species.

These conclusions should not be extended at the present time to cosmic spherules embedded in deep-sea sediments of an age older than Quaternary.

REFERENCE

UTECH, KARL, 1965. Kosmische Magnetitflitter in Sedimenten, *N. Jb. Geol. Paläont. Mh.* **3**, 164–166.

32. The Cosmic Dust Analyzer: Experimental Evaluation of an Impact Ionization Model

J. F. Friichtenicht, N. L. Roy,
and D. G. Becker
TRW Systems
Redondo Beach, California

Determination of the elemental composition of cosmic dust particles by means of an impact ionization time-of-flight mass spectrometer has been investigated at several institutions. In most configurations, the instrument supplies the identity of ion groups of both target and particle materials extracted from the impact plasma and the number of ions contained in each group. Experiments have shown that the fractional ionization of a given species is not constant with impact velocity nor is the fractional ionization the same for different kinds of atoms. A model of the impact ionization effect developed at TRW involves an equilibrium plasma condition with the consequence that the fractional ionization for an arbitrary atomic species can be specified by the Saha equation if the plasma volume (V) *and temperature* (T) *are known. It follows that* T *can be determined by taking the ratio of the Saha equations for two elements present in the target in known concentration. (Taking the ratio negates the requirement of knowing* V.) *Given* T, *the procedure can be reversed to yield the relative abundance of elements contained in the impacting particle. To test the model, a* $PbZrO_3$-$PbTiO_3$ *target was bombarded with high velocity Fe, MoB, and NiAl particles and the number of Pb, Ti, and Zr ions was determined in a time-of-flight mass spectrometer. For each event, the relative abundance of Ti to Pb was taken as known (from electron microprobe analysis) and* T *was determined from the Ti-Pb measurement. The Zr to Pb ratio was found to be in good agreement with the microprobe analysis (0.38 calculated mean value compared to 0.34 actual). The result was valid for all particle materials and for a velocity range* $17 < v < 47$ *km/s.* T *ranged from 3300 to 11 500° K and was only mildly velocity dependent.*

The cosmic dust analyzer under development at TRW may be described as an impact ionization time-of-flight mass spectrometer. As implied by this description, the instrument utilizes ion time-of-flight techniques to separate the microplasma formed by the impact of a high velocity particle upon a solid surface into its constituent parts. The plasma contains ions of both particle and target material, which may be extracted from the impact plasma by the application of an electric field to the impact surface. This is most easily accomplished by placing a potential difference between the impact surface and a high transmittance grid located in close proximity to the surface and parallel to it. All singly ionized atoms reach the plane of the grid with the same kinetic energy (given by the product of the unit electronic charge and the applied voltage); however, the velocity of a particular ion at this point depends upon its mass. Thus, the atomic mass of

the ions may be determined by measuring their transit time from the grid to an ion collector located some distance away.

First, the formation of the plasma and the extraction of ions from it may be considered instantaneous, with the consequence that all ions of a given mass reach the collector at the same time. Actually, it has been observed that the ions may possess an appreciable thermal (random) velocity which adds to the electrically imparted velocity. This causes a small spread in arrival times of ions of a given charge-to-mass ratio. Nevertheless, by proper selection of accelerating voltage and drift distance, the ions can be segregated into distinct groups according to their mass. With the accelerating voltage and flight distance specified, measurement of the transit time is sufficient to determine the mass of each ion group. Determination of the atomic mass identifies the corresponding element.

The foregoing defines the basic instrumental requirements of the cosmic dust analyzer. The key measurements to be made are the transit time of the various ion groups from the impact surface to the ion collector and the total charge contained within each group. The instant of impact is signaled by the emission of positive charge from the impact (target) surface, resulting in a negative signal. This signal may be used to initiate the ion time-of-flight measurement. A convenient means of measuring the total charge within each ion group is to integrate the ion current at the collector. In this case the ion collector signal has a stairstep appearance; the position in time of a step corresponds to the time of arrival of a given ion group and its amplitude is proportional to the charge contained within the ion group. The number of ions in each group is obtained by dividing the total charge by the unit electron charge.

According to its description, the instrument supplies direct measurements of the number of ions in each group reaching the collector and provides the timing information necessary to identify the species of the ions. These data alone would be extremely useful in evaluating the gross characteristics of cosmic dust particles. However, a more sophisticated objective is that of quantitatively determining the relative abundances of the neutral elements contained in the particles. As might be expected intuitively and as has been verified experimentally, the fractional degree of ionization of all atomic species is not the same. Moreover, the relative ionizing efficiencies change with impact velocity. Hence, additional information is needed in order to process the raw data to obtain the desired final result. A method has been conceived to obtain that information; this paper will report the results of laboratory experiments which indicate that the method is a valid approach to the problem.

At the heart of the method is a theoretical model of the impact ionization process that was originally developed because it successfully explained various phenomena observed in earlier impact experiments. Briefly, the model assumes that the impact produces a plasma in thermal equilibrium. If this is the case and if the plasma temperature and volume can be found, the degree of ionization of any atomic species in the plasma can be computed provided that the species has a known ionization potential. The requirement to specify the plasma volume can be shown to disappear if we are content to determine relative abundances, leaving only the plasma temperature to be measured. If the impact target contains two elements in known concentration, the model provides equations by which measurement of the relative ion signals of these two elements can be reduced to plasma temperature. Given the temperature, the model supplies further theoretical relationships for processing the data to yield the relative atomic abundances of the elemental constituents in the impacting particle.

This model of impact ionization and the theoretical relationships derived therefrom should be experimentally verified. The best approach to this task appears to be to employ test particles and an impact target that are each composed of two elements in known relative concentrations, utilizing the theory to be described in the section of this paper on the impact ionization model to independently determine the plasma temperature from each of the two-element combinations. If the two values of plasma temperature so determined should agree for each hypervelocity impact event, then the model may be considered to have been verified. Unfortunately, we have been unable to locate a source of particles with sufficiently homogeneous properties to successfully complete this type of experiment.

We have therefore developed an alternative approach that seems to be almost as satisfactory. The alternate involves the use of a target material containing three major elements with known relative abundances. Two of these are treated as control elements, and the relative ion abundances of the control species are observed and used to compute the plasma temperature as previously described. This plasma temperature and the magnitude of the ion signal from the third element are then combined to compute the relative atomic abundance of the latter. The computed value can of course be compared directly to the known abundance of the third material; good agreement indicates that the model is essentially correct. In comparison with the postulated "best" approach, the alternate suffers by not directly involving the properties of the impacting particle in the calculations, and the verification provided thereby assumes that the target and particle materials become intimately mixed in the impact plasma. This assumption requires its own experimental test. Even in the absence of such a test, however, any agreement found from the alternate experiment is strong evidence that the model is a reasonably good representation of the impact ionization phenomenon.

We will describe herein an experiment in which the alternative approach was employed and in which data were acquired for a number of impact events involving different particle compositions. As we hope to show, these data appear to possess a sufficiently good agreement with the known target composition that the desired verification can be said to have been achieved.

IMPACT IONIZATION MODEL

It was first shown experimentally by Friichtenicht and Slattery (1963) that free electric charge, both positive and negative, is produced at the point of impact of a high velocity microparticle on a solid surface. More recent experiments reported by Hansen (1968) and by Auer and Sitte (1968) have shown that the positive charge consists of ions of both the impacting particle and target materials and that the negative charge carriers are electrons. Unpublished data obtained at TRW have demonstrated this effect in considerable detail for a large number of particle-target material combinations. For low impact velocities, both Hansen and Auer and Sitte found that easily ionized impurities (sodium and potassium) accounted for the majority of the emitted positive charge even though the impacting particles were ~98 percent iron. At higher impact velocities, however, iron became the dominant ionic species, and ions of other high ionization potential elements made an appearance. Particularly significant was the detection of ions from refractory metal targets.

Based on these observations, Hansen (1968) advanced a theoretical model to describe the impact ionization effect. In this model, it is assumed that a small, high density plasma is formed in the immediate vicinity of the impact site. The plasma expands due to its internal pressure; however, the collision frequency of atoms and electrons within the plasma is very high (on the order of 10^{14} per second initially), with the consequence that the plasma temperature is spatially uniform (i.e., that the plasma temperature is nearly the same throughout the plasma volume) but decreases as the plasma expands. At some point the plasma becomes collisionless as the density decreases. To the extent that the plasma may be considered to be in thermal equilibrium immediately prior to becoming collisionless, the Hansen model described in the following paragraphs should apply.

When a plasma in thermal equilibrium at absolute temperature T contains several species of atoms and ions, the degree of ionization of each species s whose ionization energy is E_I^s is related to T according to Saha's equation (cf. Sutton and Sherman, 1965):

$$n_e n_i^s / n_n^s = C T^{3/2} u_{i,n}^s \exp(-E_I^s/kT) \qquad (1)$$

where n_e, n_i^s, and n_n^s are the numbers per unit volume of electrons, ions of species s, and neutral atoms of species s, respectively; C is a constant; $u_{i,n}^s$ is the ratio u_i^s/u_n^s, in which u_i^s and u_n^s are respectively the internal partition functions of ions and neutrals of species s; and k is Boltzmann's constant. The Saha equation shows that the fractional ionization of a given species of atom depends on the ratio of the ionization energy of that species to the mean thermal energy of the plasma. For reasonably low plasma temperatures, only a small fraction of the atoms are ionized

(except for those with very low ionization potentials). In order to use the impact ionization effect to reliably determine the relative abundance of the elements in cosmic dust and meteoroids, a measure of the plasma temperature must be obtained.

It would at first appear that the number density of ions, electrons, and atoms must be specified. However, from the argument given above, the plasma rapidly expands to a collisionless state. Thus, the total number of ions is constant at later times during the expansion process. Since all of the ions regardless of species are extracted from the same volume, a direct measurement of n_e, $n_n{}^s$, and $n_i{}^s$ is not required to determine the relative abundance of the different kinds of atoms. If N_e, $N_n{}^s$, and $N_i{}^s$ are, respectively, the total numbers of electrons, atoms, and ions in the plasma, and if V is the volume of the plasma at any time prior to its expansion to a collisionless state, then $n_e=N_e/V$, $n_n{}^s=N_n{}^s/V$, and $n_i{}^s=N_i{}^s/V$. Clearly, $n_e n_i{}^s/n_n{}^s$ can be replaced in equation (1) by $N_e N_i{}^s/N_n{}^s V$. As we will shortly see, V can be ignored in the type of experiment that we perform. Our experimental techniques provide a direct measurement of $N_i{}^s$ for each s and of N_e. (If all $N_i{}^s$ are measured, N_e can be obtained as $\Sigma_s N_i{}^s$, since the total number of electrons is equal to that of ions; however, an independent measurement of N_e is readily obtained and serves as a useful check of the data.) The quantity of principal interest to be extracted from the experiments is $N_n{}^s$.

Consider first an idealized case in which the plasma contains two species from the target and one from the particle; let these species be denoted by superscripts (1), (2), and (3), and assume that the identities of (1) and (2), their ionization energies $E_I{}^{(1)}$ and $E_I{}^{(2)}$, and their partition function ratios $u_{i,n}{}^{(1)}$ and $u_{i,n}{}^{(2)}$ are all known. If equation (1) is written for species (1) and for species (2) and if the former result is divided by the latter, one finds that

$$(N_i{}^{(1)}/N_i{}^{(2)})\,(N_n{}^{(2)}/N_n{}^{(1)}) = f'(T)\exp\left[(E_I{}^{(2)}-E_I{}^{(1)})/kT\right] \quad (2)$$

in which $f'(T)\equiv u_{i,n}{}^{(1)}/u_{i,n}{}^{(2)}$. (The partition functions are functions of temperature; the functional dependence is assumed to be known.) It is almost always true that $N_n{}^s \gg N_i{}^s$, and then the ratio $N_n{}^{(1)}/N_n{}^{(2)}$ is approximately equal to the relative concentration of the two kinds of atoms in the target material. Let A denote this ratio, whose value is known. Now, suppose that species (1) and (2) have been selected such that $E_I{}^{(2)} \neq E_I{}^{(1)}$. Writing $E_I{}^{(2)}=E_I{}^{(1)}+\Delta E_I{}^{(1,2)}$ and substituting into equation (2), we obtain

$$N_i{}^{(1)}/N_i{}^{(2)} = f'(T)A\exp(-\Delta E_I{}^{(1,2)}/kT) \quad (3)$$

from which

$$kT=\Delta E_I{}^{(1,2)}\{\ln\left[f'(T)A\,(N_i{}^{(2)}/N_i{}^{(1)})\right]\}^{-1} \quad (4)$$

According to equation (4), the plasma temperature can be found from a measurement of the number of ions of the two control elements in the target. (Remember that $f'(T)$ is a known function.) If, as often happens, $f'(T)$ is essentially constant over a range of temperatures, the computation of T from the $N_i{}^{(2)}/N_i{}^{(1)}$ measurement is quite simple; if $f'(T)$ is not constant, iterative solutions can be employed.

It follows at once that the procedure employed to derive equation (2) can be applied for species (1) and (3), with the result:

$$N_n{}^{(3)}/N_n{}^{(1)} = g'(T)\,(N_i{}^{(3)}/N_i{}^{(1)}) \times\exp\left[(E_I{}^{(3)}-E_I{}^{(1)})/kT\right] \quad (5)$$

where $g'(T)\equiv u_{i,n}{}^{(1)}/u_{i,n}{}^{(3)}$. Thus, if $N_i{}^{(3)}/N_i{}^{(1)}$ has also been measured, the relative abundance $N_n{}^{(3)}/N_n{}^{(1)}$ can be computed. The procedure is readily generalized to a situation in which the particle contains a multiplicity of elements and the relative abundance of each is computed in turn from measurements of the corresponding ion ratios. This is the way in which it is intended to reduce data from the actual cosmic dust analyzer experiment.

We saw that one way of checking the validity of these equations in this application would be to employ not only a target containing two control species (1) and (2), but also a test particle containing two other species whose relative concentrations in the particle are known; these are species (3) and (4). If the impact ionization model is valid, an equation similar to equation (4) can be written for the latter species, replacing $N_i{}^{(2)}/N_i{}^{(1)}$ by $N_i{}^{(4)}/N_i{}^{(3)}$, $f'(T)$ by $h'(T)\equiv u_{i,n}{}^{(3)}/u_{i,n}{}^{(4)}$, and $\Delta E_I{}^{(1,2)}$ by $\Delta E_I{}^{(3,4)}$. Then a measurement of $N_i{}^{(4)}/N_i{}^{(3)}$ would give an independent determination of T that could be compared with that found from $N_i{}^{(2)}/N_i{}^{(1)}$; agree-

ment would strongly imply that the predictions of the model are correct.

The alternative check, used as the basis of our experiment for the reasons stated earlier, consists of employing a three-constituent target, with the relative abundances of all constituents known. We argue that the equilibrium plasma model implies a thorough mixing of the plasma constituents and that, as a result, target and particle constituents are interchangeable in the equations. Denoting the target species by (1), (2), and (3), we treat (1) and (2) as "knowns," using a $N_i^{(1)}/N_i^{(2)}$ measurement to compute T according to equation (4), and (3) as the "unknown," computing $N_n^{(3)}/N_n^{(1)}$ from the temperature calculation and equation (5). Of course, the actual value of $N_n^{(3)}/N_n^{(1)}$ is known; this known value can be compared to that computed from equation (5), and good agreement is evidence for the validity of the model. We noted that the evidence is not quite so strong as in the first approach, because now the particle properties do not directly enter into the calculations and hence the assumption of mixing, which is central to this work, remains an assumption.

In spite of the above limitation, it is important to observe that the state of knowledge of the impact ionization effect with respect to basic theoretical considerations is sufficiently primitive at the present time that *any* direct evidence for the validity of a proposed theoretical model of the process would represent a major advance. This was an important consideration in our decision to perform the experiment to be described.

EXPERIMENTAL APPARATUS AND TECHNIQUES

All of the experimental data on the impact ionization effect were acquired with the TRW electrostatic microparticle accelerator described by Friichtenicht (1962). This device is a two million volt Van de Graaff generator in which the high voltage terminal has been modified to accept microparticle charging and injection equipment. It is capable of charging and accelerating a variety of micron size range particulate materials to high velocities. The final velocity obtained is dependent upon the size of the particular particle, the material used, and the accelerating potential. Particle velocities range down to about 1 km/s for all materials. The upper velocity limit is, for practical purposes, dependent upon the electronics used for particle detection. For carbonyl iron particles, the maximum detectable velocity is about 50 km/s; for lower density materials, the maximum velocity is much higher. Particles may be accelerated either continually or in single bursts.

Particles from the accelerator pass through a particle charge-velocity detector which consists of a cylindrical drift tube of known length and capacitance and an associated amplifier. The rectangular pulse derived from this detector as the charged particle traverses its length provides the necessary data for computing particle mass and velocity. The details have been described elsewhere (Shelton et al., 1960; Hansen and Roy, 1966).

The charged particle "beam" from the accelerator has a broad distribution due to particle size variation. For experimental convenience the beam is further conditioned by means of particle velocity (i.e., transit time) selection equipment (Roy and Becker, 1971) which may be set to limit the particles reaching the experimental area to only those having a velocity lying within a narrow velocity range. All others are electrically deflected.

A detailed block diagram of the experimental apparatus including a schematic representation of the target and collector assemblies is shown in figure 1. The target and collector assemblies are housed in a cylindrical vacuum enclosure about 45 cm in diameter by 125 cm long. Particles from the accelerator traverse a velocity selection system (not shown in the figure) and then a charged particle detector prior to entry into the main experimental volume. The particles pass through an aperture in the ion collector and proceed onward to impact on the target assembly.

The target assembly is mounted at the downstream end of the system (most distant from the accelerator) such that simulated micrometeoroids produced by the accelerator will impact near the center of the target and normal to its surface. Since particles from the accelerator are confined to a 6.3 mm diameter circle, a 5 cm diameter target was considered ample for these tests. The target is mounted inside a shielded housing as

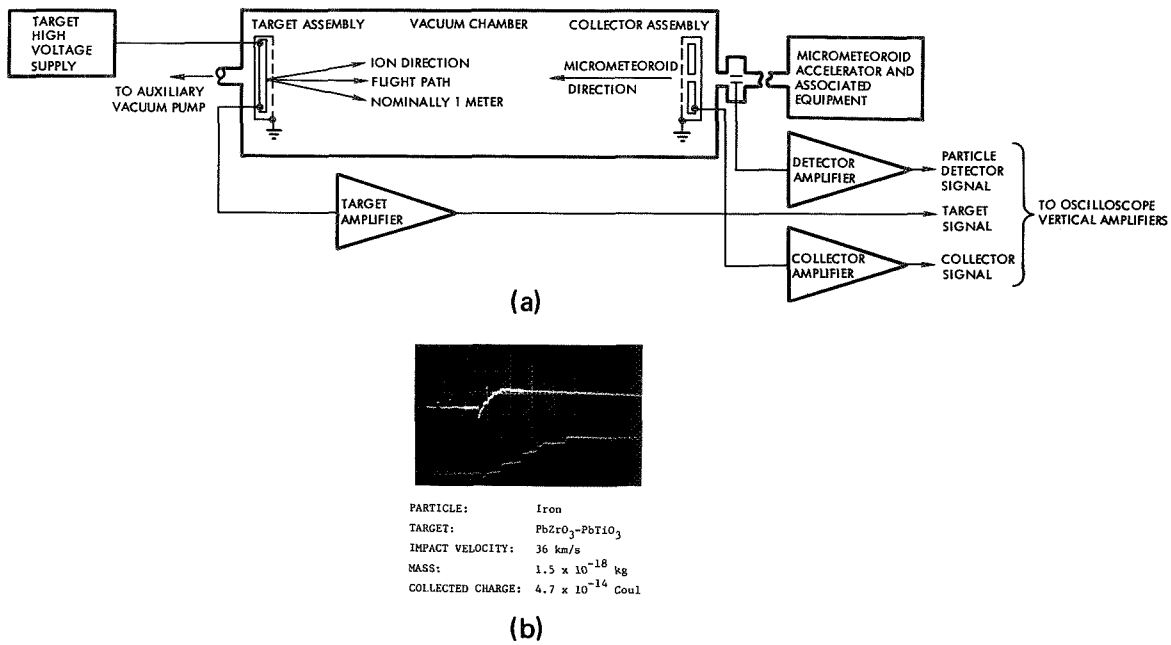

FIGURE 1.—Detailed block diagram of the experimental configuration, with the internal target and collector assemblies depicted schematically. Signal outputs from the experiment are illustrated in (b); the upper trace is the sum of particle detector, target, and collector signals with sweep speed set at 20 μsec/div; lower trace, target and collector signals at 5 μsec/div.

shown in the figure, with the extraction and acceleration grid mounted approximately 1 cm from the target surface. Cable connectors with hermetic seals provide means for introducing the target bias voltage (+3000 V) and withdrawing the target signal from the vacuum chamber.

The ion collector mechanical assembly is mounted at the opposite (upstream) end of the vacuum chamber at a distance of approximately 1 m from the target. The collector plate is about 30 cm in diameter and is centered on the axis of the particle beam. The entire assembly has a small hole (about 1.25 cm) at the center which allows the particles to pass. The collector plate is surrounded by a grounded shield. In order to maintain electrical shielding while permitting ions to enter, the side of the shield which faces the target is made from screening cloth of reasonably high transmittance. The large diameter collector plate is required to collect a substantial fraction of the ions originating at the target, due to expansion of the beam as a result of the initial thermal energy of the ions. Again, a hermetically sealed cable connector allows the collector signal to be extracted from the vacuum enclosure.

The photographic record of a typical event is shown in figure 1(b). This particular oscillogram records the data from the impact of an iron particle on a $PbZrO_3$-$PbTiO_3$ target at 36 km/s. The sequence of events begins when a particle from the accelerator is found by the time interval selection equipment to have a transit time within the preselected transit time (velocity) boundaries. This event causes the bias voltage on a particle deflector to be removed, thereby allowing the selected particle to enter the experimental region. Just prior to arrival of the particle at the particle detector depicted schematically in figure 1, a proportional delay generator produces an output pulse to initiate an oscilloscope sweep that will present the signal amplitude and transit time information produced by the particle as it passes through the detector (upper trace on the oscillogram). This information allows the particle parameters (velocity, mass, and radius) to be calculated for each impacting particle. The particle then passes through the collector aperture

enroute to the target. Just prior to arrival of the particle at the target, a second sweep is initiated which will present the target impact signal and the ion charge and transit time information (lower trace of the oscillogram). The signal obtained from the target is essentially a step function for impacts above about 10 km/s, while that from the collector rises in staircase fashion. Either or both waveforms may be differentiated to produce sharp pulses at impact and/or upon arrival of each ion group at the collector.

In Figure 1(b), the lower trace is the sum of the target and collector signals at a sweep speed of 5 μsec/division. The initial negative step represents charge leaving the target, while the following positive-going steps represent the same charge arriving at the collector, now separated into individual charge "packets" distinguishable as ions of the constituent elements of particle and target material. The upper trace is the sum of the signals from the particle detector, the target, and the collector. The upper trace is presented at a slower sweep speed (20 μsec/division), insuring that the waveform being measured is due to the impact of the detected particle.

A total of 33 separate impact events on a lead titanate-lead zirconate target were recorded using the apparatus shown in figure 1. Of these, 12 particles were nickel-aluminide, seven were molybdenum boride, and the remainder were iron. The impact velocity range extended from 16.8 to 46.8 km/s. For each event the total number of lead, zirconium, and titanium ions reaching the collector was measured.

DATA ANALYSIS

All data from impacts of Fe, MoB, and NiAl particles onto the $PbZrO_3/PbTiO_3$ target sample were analyzed in accordance with the equilibrium plasma model discussed in the section on the impact model. There we saw that two of the target elements were to be treated as knowns and used to compute the relative abundances of the third element treated as an unknown. The ionization energies of Pb, Ti, and Zr are, respectively, 7.42 eV, 6.82 eV, and 6.84 eV. Examination of equation (3) shows that the two control species (1) and (2) must have an appreciable difference $\Delta E_1^{(1,2)}$ in ionization energy in order for this equation to yield meaningful results. This clearly required that Pb be one of the control elements. Ti was arbitrarily selected as the second control element, meaning that Zr became the "unknown."

The appropriate partition functions for all three elements were available in the literature (Aller, 1963) at four fixed temperatures: 3600, 5700, 8000, and 10 000° K. Using these values and the ionization energies of the elements, we were able to compute values of the functions

$$f(T) \equiv f'(T) \exp(-\Delta E_I^{(1,2)}/kT) \tag{6a}$$

and

$$g(T) \equiv g'(T) \exp\left[(E_I^{(3)} - E_I^{(1)})/kT\right] \tag{6b}$$

where superscripts (1), (2), and (3) now signify Pb, Ti, and Zr, at the four given temperatures. On the assumption that the partition function ratios are smooth, well-behaved functions, we used the computations to plot $f(T)$ and $g(T)$ vs T. Equations (3) and (5) can be rewritten

$$N_i^{(1)}/N_i^{(2)} = Af(T) \tag{7a}$$

and

$$N_n^{(3)}/N_n^{(1)} = (N_i^{(3)}/N_i^{(1)})g(T) \tag{7b}$$

The experiment gave measured values of $N_i(\mathrm{Pb})/N_i(\mathrm{Ti})$, which equals $N_i^{(1)}/N_i^{(2)}$, and $N_i(\mathrm{Zr})/N_i(\mathrm{Pb})$, which equals $N_i^{(3)}/N_i^{(1)}$. Since A is given by $N_n(\mathrm{Pb})/N_n(\mathrm{Ti})$ and is known, the former value could be used to compute $f(T)$. From the plots, T and then $g(T)$ were found, after which $N_n(\mathrm{Zr})/N_n(\mathrm{Pb})$ could be evaluated.

The "true" relative abundances of Pb, Ti, and Zr in the target sample were determined by electron microprobe analyses. To check for inhomogeneities, readings were taken at four separate points on the impact surface using an incident electron beam diameter on the order of one micron, with an analyzed depth also on the order of 1 micron. The composition found for the four points (table 1) indicates good homogeneity. The mean composition of the crystal was found to be as follows:

Pb = 58.62±.55 atomic percent
Ti = 21.17±.16 atomic percent
Zr = 19.73±.67 atomic percent

where all quoted error values are 2σ limits. In

terms of relative abundances,

$$N_n(\mathrm{Ti})/N_n(\mathrm{Pb}) = 0.361 \pm .006 \qquad (8a)$$

and

$$N_n(\mathrm{Zr})/N_n(\mathrm{Pb}) = 0.337 \pm .015 \qquad (8b)$$

The mechanics of data reduction to $N_n(\mathrm{Zr})/N_n(\mathrm{Pb})$ were straightforward and should be obvious in the light of the preceding discussion. The graphical method by which $f(T)$ values were used to obtain $g(T)$ naturally contains a number of approximations whose effects on the accuracy of the experiment are difficult to determine. Existing theory is sufficiently complete to permit the use of a high-speed digital computer to separately evaluate the partition functions u_i and u_n for almost any material at any temperature. Ideally, such a computation could have been performed for a large number of temperatures, after which the computer could have evaluated $f(T)$ and $g(T)$ at these temperatures. Interpolations necessary to obtain the functions at any temperature could also have been included in the program. Such techniques will actually be employed to reduce cosmic dust analyzer in the space experiment, but they did not appear justified in the present context due to time and cost factors. After examining all aspects of the current experiment, we conclude that our graphical approxi-

TABLE 1.—*Electron Microprobe Analysis of Target Sample*

Element	Point 1	Point 2	Point 3	Point 4
Pb (atomic percent)	59.08	57.90	59.00	58.48
Ti (atomic percent)	21.24	21.19	21.99	20.95
Zr (atomic percent)	19.68	18.93	19.72	20.57

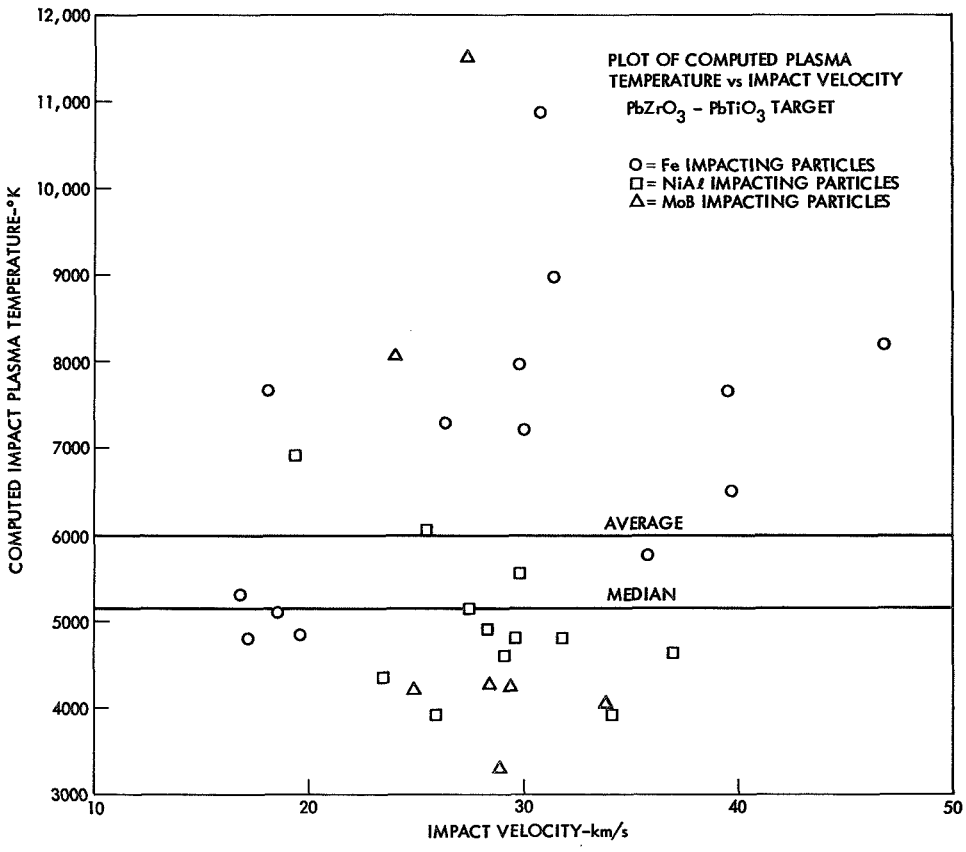

FIGURE 2.—Computed impact plasma temperature vs particle impact velocity: various particles, $PbZrO_3$-$PbTiO_3$ target. Data points shown are the computed result using the known relative abundance of two target elements together with the impact ionization model. Computed average and median impact temperatures as indicated.

mation has not materially affected its significance or validity.

Figure 2 is a plot of the impact plasma temperature computed from equations (7a) and (4) as a function of impact velocity. The data scatter widely and there is no observable trend with increasing velocity; NiAl impacts appear to produce lower plasma temperatures on the average than do Fe impacts. (The model would predict such a trend due to the lower ionization potential of aluminum.) These results are similar to what has been observed with all other particle/target combinations employed during this program, and they tend to confirm that mechanical details of the materials at the impact sites (yield strengths, angle of impact, hardness, etc.), all of which are essentially random variables in the size range of the particles impacted, are more important in determining the amount of energy available for material vaporization and ionization than is the total energy of impact.

Remember, however, that the equilibrium plasma model says nothing at all regarding the relationship, if any, between impact velocity and plasma temperature. In fact, when the seemingly scattered data are analyzed further to compute $N_n(\mathrm{Zr})/N_n(\mathrm{Pb})$ according to equation (7b), surprisingly good agreement is found from one point to the next. Table 2 summarizes the velocity, plasma temperature, and relative Zr abundance $N_n(\mathrm{Zr})/N_n(\mathrm{Pb})$ for all of the data; the average Zr abundance is

$$<N_n(\mathrm{Zr})/N_n(\mathrm{Pb})>=0.38\pm.12 \qquad (9)$$

where the error value is a 2σ limit. Comparison with equation (8b) shows very good agreement, and the value of the standard deviation ($\sigma=0.06$) for the 33 points is reasonably small. In addition, no one data point deviates more than about 40 percent from the average, which is rather remarkable given the fact that the data were acquired over a considerable period of time with three different particle materials and the method of analysis was rather crude in several aspects, as we have noted.

The sensitivity of this system for predicting elemental relative abundances from ion ratio measurements is illustrated in figure 3, where we have plotted the Zr/Pb ion ratio as a function of the Ti/Pb ion ratio. The three curves have been computed for different assumed compositions of the target material, using the four fixed temperatures at which the partition functions were available; the middle curve corresponds to the *actual* composition given by the microprobe analysis, the upper curve to a 50 percent higher Zr content, and the lower curve to a 50 percent lower Zr content. (In both cases, the Ti content has been altered in inverse proportion.) The measured ion ratios are seen to cluster quite closely to the middle curve, and there is little difficulty in determining that the Zr content of the substance is much closer to 20 percent than to either 10 or 30 percent.

Figure 4 is a plot of the computed Zr/Pb ratio as a function of impact velocity. It is included as one possible check on the validity of the model and the method of analysis, since if both are correct the ratio $N_n(\mathrm{Zr})/N_n(\mathrm{Pb})$ should be independent of v. The plot shows this to be the case.

CONCLUSIONS

The results presented in the preceding section provide fairly convincing proof that the use of an assumed thermal equilibrium plasma model can be used to process data from an impact ionization time-of-flight mass spectrometer in order to convert the raw ion data to relative abundances of the elemental constituents of cosmic dust particles. We do not wish to imply that the equilibrium condition is actually met; even intuitive arguments would suggest that a plasma cannot be in thermal equilibrium shortly before the plasma becomes collisionless, because the collision frequency must approach zero in some asymptotic fashion. However, a "quasi-equilibrium" plasma is conceivable, and the analysis would then yield an "effective" plasma temperature. On the basis of the data presented in figure 3, the model appears to be relatively sensitive in computing relative abundances. Considering the application and the precision requirements that can sensibly be placed on this kind of flight experiment, the rudimentary model appears to be quite satisfactory.

As mentioned earlier, a remaining question is verification that the particle material becomes thoroughly mixed with the target material, which is a requirement if a common plasma temperature is to be assigned to both materials. Our search for

TABLE 2.—*Summary of Experimental Data*

Date and particle material	Temperature (° K)	Velocity (km/s)	$N_n(Zr)/N_n(Pb)$	Squared deviation
9/17/70	4480	29.4	0.255	0.01440
MoB particles	4200	24.8	0.354	0.00044
	11 500	27.3	0.374	0.00000
	8050	24.0	0.408	0.00109
	4050	33.8	0.375	0.00000
	3300	28.9	0.250	0.01562
	4270	28.4	0.265	0.01210
9/22/70	5550	29.8	0.423	0.00230
NiAl particles	4350	23.4	0.295	0.00640
	6900	19.4	0.239	0.01850
	5150	27.5	0.419	0.00194
	3925	34.1	0.371	0.00002
	4600	29.3	0.393	0.00032
	4800	31.8	0.403	0.00078
	4630	37.0	0.374	0.00000
	4800	29.6	0.444	0.00476
	6050	25.5	0.323	0.00270
	4900	28.3	0.384	0.00008
	3920	25.9	0.357	0.00032
1/16/71	4850	19.6	0.314	0.00372
Fe particles	5100	18.5	0.373	0.00000
	7650	18.1	0.419	0.00194
	5300	16.8	0.375	0.00000
	4800	17.2	0.391	0.00026
3/4/71	7650	39.5	0.534	0.02528
Fe particles	7280	26.3	0.401	0.00068
	8180	46.8	0.394	0.00036
	7950	29.8	0.391	0.00026
	6470	29.7	0.367	0.00006
	7200	30.0	0.432	0.00325
	8970	31.4	0.449	0.00548
	10 870	30.7	0.430	0.00302
	5750	35.7	0.406	0.00096
			Av = 0.375	Sum = 0.12705

FIGURE 4.—Computed zirconium/lead relative abundance $N_n(Zr)/N_n(Pb)$ vs particle impact velocity. Zirconium/lead relative abundance is computed using measured experimental values and the impact ionization model. Each computed value for relative abundance is plotted against the particle impact velocity from which the experimental values were obtained. Target surface analysis, as determined by electron microprobe, is as indicated to the right of the figure.

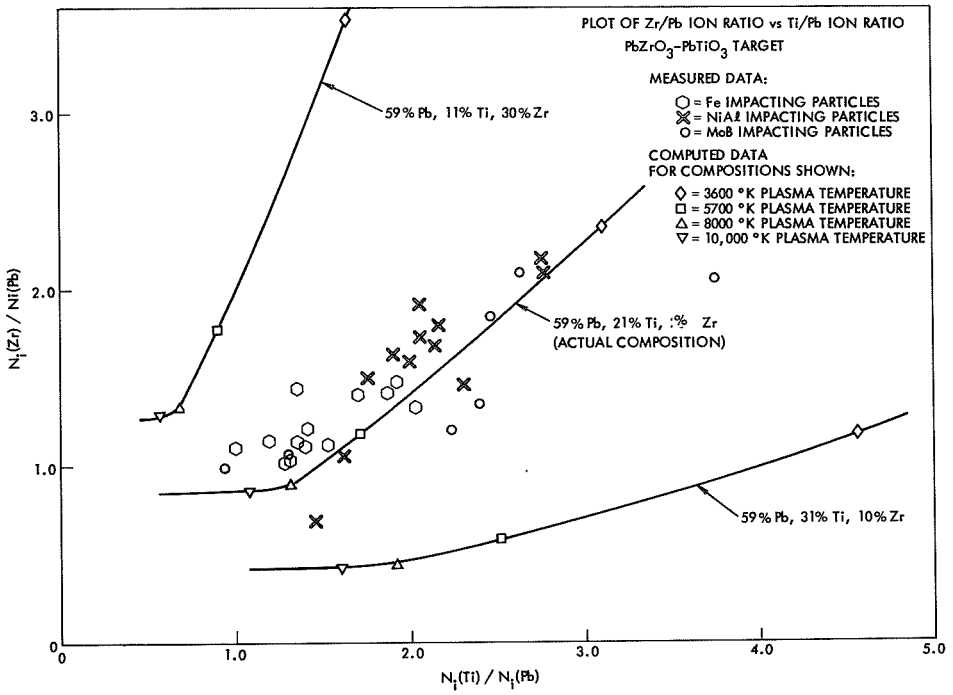

FIGURE 3.—Zirconium/lead ion ratio $N_i(\mathrm{Zr})/N_i(\mathrm{Pb})$ vs titanium/lead ion ratio $N_i(\mathrm{Ti})/N_i(\mathrm{Pb})$. Data points are derived from the ratio of the indicated ion groups, the amplitudes of which are measured from the collector waveform. Each point represents a single impact event. The curves shown are computed using the indicated target composition for each and the equations which characterize the impact ionization model. Bending of the curve is caused by the temperature dependence of the partition functions for ions and neutrals of each of the subject elements.

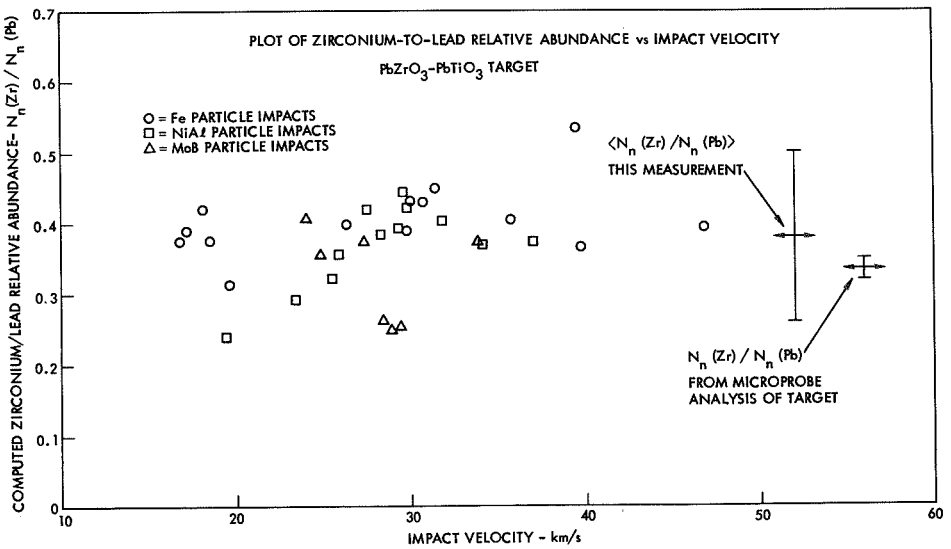

satisfactory two-element particle materials will continue in an effort to answer this question.

Another practical task that must be accomplished is the selection of the control elements in the target. The control elements can, in principle, take several forms; a substrate can by some means be impregnated with the two control elements, a binary compound material can be used, or vapor (or electrolytically) deposited films can be employed. Whatever the form, homogeneity of the materials on a microscopic scale is a necessary condition. Several other factors must also be considered:

(1) The ionization potentials of the two elements must differ by about one electron volt in order to obtain a substantial change in the ratio of the ion signals from the control elements as the plasma temperature changes.

(2) The ionization potentials must be low enough to ensure a sufficient degree of ionization to obtain detectable signals.

(3) The mass of the atoms should lie outside of the mass range of elements expected from the cosmic dust particles.

(4) The materials must be stable when exposed to the space environment.

In conclusion we would suggest that laboratory experimentation for the purposes of further verification (and possible improvement) of the model and selection and test of target materials be continued. An early flight test of even a simplified version of a cosmic dust analyzer would be a highly desirable undertaking. Such a flight test would provide a measure of the signal magnitudes from naturally occurring cosmic dust particles and could crudely identify the major elemental constituents.

REFERENCES

ALLER, L. H., 1963. *Astrophysics—The Atmosphere of the Sun and Stars*, second edition, The Ronald Press Co., New York, 115–117.

AUER, S., AND SITTE, K., 1968. Detection technique for micrometeoroids using impact ionization, *Earth Planet. Sci. Letters*, **4**, 178–183.

FRIICHTENICHT, J. F., 1962. Two-million-volt electrostatic accelerator for hypervelocity research, *Rev. Sci. Instr.*, **33**, 209–212.

FRIICHTENICHT J. F., AND SLATTERY, J. C., 1963. Ionization associated with hypervelocity impact, *NASA Tech. Note* **D–2091**.

HANSEN, D. O., 1968. Mass analysis of ions produced by hypervelocity impact, *Appl. Phys. Letters*, **13**, 89–91.

HANSEN, D. O., AND ROY, N. L., 1966. A solid-state low-noise preamplifier, *Nucl. Instr. Methods*, **40**, 209–212.

ROY, N. L., AND BECKER, D. G., 1971. A time interval selector and proportional delay generator, *Rev. Sci. Instr.*, **42**, 204–209.

SHELTON, H., HENDRICKS, C. D., JR., AND WUERKER, R. F., 1960. Electrostatic acceleration of microparticles to hypervelocities, *J. Appl. Phys.*, **31**, 1243–1246.

SUTTON, G. W., AND SHERMAN, A., 1965. *Engineering Magnetohydrodynamics*, McGraw-Hill Book Co., New York, 225.

33. On the Primordial Condensation and Accretion Environment and the Remanent Magnetization of Meteorites

AVIVA BRECHER
University of California, San Diego
La Jolla, California

Attention is drawn to the fact that neither astronomical observations, nor laboratory data can, as yet, sufficiently constrain models of the origin and evolution of the solar system. But, if correctly approached and interpreted, the magnetic remanence of meteorites could help in constructing a self-consistent model.

In the context of various models for the early evolution of a solar nebula, the possible roles assigned to ambient magnetic fields and the paleointensities required to establish the stable natural remanent magnetization (NRM in range 10^{-4} to 10^{-1} cgsm) observed in meteorites, are discussed. It is suggested that the record of paleofields present during condensation, growth, and accumulation of grains is likely to have been preserved as chemical (CRM) or thermochemical (TCRM) remanence in unaltered meteoritic material. This interpretation of the meteoritic NRM is made plausible by experimental and theoretical results from the contiguous fields of rock magnetism, magnetic materials, interstellar grains, etc. Several arguments (such as the anisotropy of susceptibility in chondrites, suggesting alignment of elongated ferromagnetic grains, or the characteristic sizes and morphology of carrier phases of remanence, etc.) as well as general evidence from meteoritics (cooling rates, chemical and mineralogical data) can be used to challenge the interpretation of NRM as thermo-remanence (TRM) acquired on a "planetary" parent body during cooling of magnetic mineral phases through the Curie point in fields of 0.2 to 0.9 Oe.

Fine-particle theories appear adequate for treating meteoritic remanence, if models based on corresponding types of permanent magnet materials, e.g., powder-ferrites for chondrites; diffusion hardened alloys for iron meteorites, are adopted, as suggested here.

Finally, a potentially fruitful sequence of experiments is suggested for separating the useful component of NRM in determining the paleofield intensity and its time evolution.

IT HAS BECOME APPARENT IN RECENT YEARS that the record of the physico-chemical condensation environment in the circumsolar region may have been at least partly preserved in meteorites. (See Anders, 1971a, for an up-to-date review.)

Recent systematic attempts to use the chemical evidence derived from the study of meteorites in order to constrain models of the origin and evolution of the solar system material have led to the emergence of several alternative interpretations of the same body of chemical and mineralogical evidence. If indeed, as is widely held, meteorites

originated in several small, asteroidal (Levin, 1969; Anders, 1971b) or cometary (Öpik, 1968; Wetherill, 1971) bodies, which accreted (Alfvén and Arrhenius, 1970) in the region between the terrestrial and the giant planets (2 to 5 AU) or beyond, they should reflect this transition zone paleo-environment. The wide spectrum of physical and chemical properties, from the dense ($\rho \sim 8$ g/cm^3), coarsely crystalline and chemically reduced iron meteorites to the fluffy ($\rho \sim 2$ g/cm^3), more oxidized and fine-grained disordered phases of carbonaceous chondrites (Kerridge, 1967), must be explained by a single parametrized model of condensation and accretion. In Section 1, some aspects of the condensation of solid grains in several representative models will be high-lighted. The characteristic size and composition spectrum of unaltered grains in meteorites appears not to be incompatible with most models. Moreover, it appears that astronomical observations of circumstellar condensation, or available laboratory data cannot, at this stage, help rule out or drastically constrain these models. In Section 2, the interaction of magnetic fields in space with the grains, as well as their role in fractionation and aggregation processes in the solar system, will be discussed. The duration and importance of the grain stage in the preaggregation lifetime of meteoritic material, and the likelihood of grains having acquired early a stable chemical remanent magnetization (CRM), if growing in magnetic fields, will be discussed. In Section 3, the possible evidence for the presence of a magnetic field during grain growth and agglomeration, as expressed in the shape anisotropy and apparent alignment of magnetic grains in chondrites, will be reviewed, and placed into the framework of the natural remanent magnetization (NRM) of meteorites, tektites and lunar materials. It can be expected that the stable natural remanent magnetization found in all the types of meteorites will provide information on the ambient magnetic fields in the circumsolar region at the time of condensation and agglomeration of grains into solid bodies. The possible origins, modes of acquisition, and carrier phases of this fossil magnetism will also be discussed in the context of relevant data from rock-magnetism and magnetic materials, in Section 3.

The importance of meteoritic paleomagnetism in further constraining theories of primordial condensation might be decisive, if integrated with the chemical, mineralogical and thermal history picture for various classes of meteorites. Therefore, in Section 4 an experimental approach for selecting the useful components of NRM and its carrier phases, and retrieving information on the paleointensity, will be outlined. Several potentially useful directions for future experimental and theoretical research in meteoritic magnetism will be indicated and tests of consistency with extant theories will be sketchily described.

1. CONDENSATION MODELS AND OBSERVED PROPERTIES OF COSMIC GRAINS

Among the several condensation models attempting to account for chemical fractionation patterns in meteoritic material are those of Larimer and Anders (1967) and Larimer (1970) based on molecular equilibria in the "cosmic" gas, be it rapidly or slowly cooled; of Blander and Katz (1967) and Blander and Abdel-Gawad (1969), in which nucleation of solid grains is retarded until the cooling gas has become supersaturated; or of Arrhenius and Alfvén (1971), where condensation proceeds at manifest thermochemical non-equilibrium as "cool" grains grow in a "hot" plasma-gas medium. These models must (partially) overlap with theories which approached the problem of planetary cosmogony from the physical-dynamical point of view, attempting to explain mostly the observed, large-scale, rather than fine structure, fractionation in the solar system. Examples are the magneto-hydrodynamical models (Alfvén, 1954; Hoyle, 1963) in which the magnetic fields required to arrive at the observed angular momentum distribution in the solar system, could also afford chemical fractionation in an ionization-controlled sequence of condensation of elements (Jokipii, 1964; Arrhenius and Alfvén, 1971). In a hydrodynamical model proposed by Cameron (1969, 1973) no magnetic fields are explicitly considered, the observed chemical and dynamical features being attributed to gravitational settling and thermally driven convection and turbulence in a solar nebula. Pressure and temperature parameters borrowed from this model were incorporated into the "chemical" model of Larimer and Anders (1967) and Larimer (1970).

Astronomical Observations

To what extent could astronomical observations of circumstellar gas-dust envelopes be used to further select between these models? Recent infrared observations of young T-Tauri stars like R-Monocerotis (which, having spectral type G and close to solar mass, is similar to our Sun), or of later-type cool stars like T-Tauri (K-type) or VY Canis Majoris (M-type) (Low and Smith, 1966; Low et al., 1970; Herbig, 1970), revealed the presence of envelopes of dust at temperatures of 500 to 900° K, in which grain sizes of submicron and a few microns appear to be present. Such objects have been tentatively interpreted as pre-planetary systems, and parameters such as temperature and molecular distributions for a disk-nebula model (Herbig, 1970) appeared to be in reasonable agreement with those expected for a solar nebula in most models. The rapid mass loss rates ($\lesssim 10^{-7}\ M_\odot$/yr) inferred by Kuhi (1964) for T-Tauri protostars of $M \gtrsim M_\odot$ seemed to be characteristic of this highly luminous, late phase of contraction along the Hayashi track along which our Sun presumably evolved (Cameron, 1963) and to suggest that both matter and angular momentum transfer to the nebula from the central star is occurring (Low and Smith, 1966; Schwartz and Schubert, 1969). Such a T-Tauri stage, with a time scale (10^6 to 10^7 yr, or shorter) compatible with observations, was in fact incorporated into the evolutionary history of the Sun in both hydrodynamical (Cameron, 1969) and hydromagnetic (Hoyle and Wickramasinghe, 1968) models of the formation of a solar nebula. Moreover, the enhanced solar winds associated with T-Tauri activity and the magnetic fields presumed to be dragged out with solar plasma and "wound up" have been further incorporated into theories of early heating of asteroidal bodies, thus accounting for apparent metamorphism in some meteorites (Sonett et al., 1970; Sonett, 1971). The high opacity of T-Tauri dust envelopes and the average grain temperature of $T \sim 600°$ K inferred, agree with the fairly high ($\sim 500°$ K) "hohlraum" temperatures needed in Sonett's model of asteroid melting; in Hoyle's model also, the opacity becomes very large when $T \sim 500°$ K. In Cameron's model, submicron iron grains, within the size range observed in the so-called "primitive" meteorites (Anders, 1971a; Wood, 1967), give the main contribution to the high nebular opacity leading to convection, mixing, and, finally, to accretion of solids. Moreover, the accretion temperatures for chondritic material were estimated to be within a 100° K interval centered about 500° K (Anders, 1971a). If gas temperatures across a disk nebula range from $\sim 1500°$ K in the inner region to $\sim 350°$ K at the edges, as inferred for VY CMa from molecular emission (Herbig, 1970), one could perhaps recover both the fast aggregation of metal and silicate grains in the higher temperature region and the finer "smoke" fraction condensed in cooler regions proposed in various models (Wood, 1967; Hoyle and Wickramasinghe, 1968). A similar range for grain temperatures is provided for, if iron grains are to grow in a plasma-gas medium of densities $n \sim 10^7$ to 10^{17} cm^{-3}, at 1 AU (Lehnert, 1970; Arrhenius and Alfvén, 1971); the ionization might be maintained by the violent T-Tauri activity. Thus observations of T-Tauri stars do not appear to specifically rule out any of the proposed models, which all seem to be flexible enough to accommodate such an evolutionary stage.

Other recent observations of both hotter, early (A to F spectral type) pre-main sequence stars (Strom et al., 1971; Woolf et al., 1970) and of late supergiants and variable stars (Gillett et al., 1970) have revealed extensive circumstellar obscuration by gas and dust, either in shell or in disk configurations, to be a general phenomenon. But dust is also widely associated with the generally lower density plasma-gas environments of interstellar clouds ($n \lesssim 10^4$ cm^{-3}), where grains at temperatures inferred to range from 10 to $< 10^{3°}$ K are imbedded in generally hotter gas ($T \sim 10^{2°}$ K to $10^{4°}$ K) (Harper and Low, 1971; Greenberg, 1968) so that $T_{gr}/T_{gas} \lesssim 0.1$. Such thermal disequilibrium is an essential feature in the Arrhenius and Alfvén (1971) model, with temperature and plasma-gas density regimes for growth of grains defined in Lehnert (1970). It thus appears that most primordial condensation models are at least partially consistent with astronomical observations.

Grain Characteristics

Grain sizes, such as those observed in the matrix of carbonaceous meteorites (0.01 to 1μ and $> 5\mu$),

are not too helpful in determining place of origin; submicron grains are known to be present both in interstellar clouds (Greenberg, 1968) and in envelopes of T-Tauri stars, where larger grains are also present (Low et al., 1970). Only grains larger than a few microns seem to have survived close to the hotter (A-F) stars (Strom et al., 1971), as smaller grains may have been sputter-evaporated in hot stellar winds (Meyer, 1971), or blown out by radiation pressure. In our own solar system, solid grains of $\sim 1\mu$ sizes have been identified as a plausible source of the infrared continuum of comets (KrishnaSwamy and Donn, 1968), and analyses of zodiacal light indicated grain sizes in the 0.1 to 10μ range (Greenberg, 1967). A similar size spectrum is observed for laboratory quenched condensation of metallic (Fe, Co, Ni, etc.) and other (C, SiO_2, SiC) grains of refractory materials (Kimoto et al.; 1963, Kimoto and Nishida, 1967; Lefèvre, 1970) expected to be amongst the earliest condensates (Gilman, 1969; Hoyle and Wickramasinghe, 1968; Arrhenius and Alfvén, 1971 and others). These range from polyhedral to deformed subhedral crystals, showing twinning and stacking faults, to hexagonal plates, to spherulitic silica, to be compared to other expected or observed crystal growth habits (Donn and Sears, 1963; Meyer, 1971).

The observed forms of aggregation for these submicron grains in laboratory condensation may be highly significant: Ferromagnetic metals (Fe, Ni, Co) were generally observed to collect into chains which, if deposited in the presence of a magnetic field, aligned themselves parallel to it. This tendency to shape anisotropy (Kimoto and Nishida, 1967; Lefèvre, 1970; Donn and Sears, 1963) insures stable magnetic moments for ferromagnetic grains (single-domain behavior) over a wide range of sizes (see Sec. 2). The magnetic energy of cohesion for submicron iron grains was measured and found to be an order of magnitude larger than for microscopic Fe crystals (Tanaka and Tamagawa, 1967). This supports the feasibility of proposed fast aggregation and size fractionation mechanisms for magnetic grains in the solar system (Wood, 1962; Harris and Tozer, 1967), discussed below. The clusters of $\sim 10^3$ to 10^4 submicron magnetite grains observed in carbonaceous chondrites (Kerridge, 1970) might be attributed to magnetic interactions.

But nonferromagnetic silica grains of similar diameters (0.02–0.04μ; 0.05–0.08μ) also formed chains and floccules. For silicate grains of similar size ($\sim 0.02\mu$) in the matrix fraction of some primitive carbonaceous chondrites (such as Renazzo) Wood (1962) had proposed flocculation due to the likely electric charging of such grains. An interesting result from studies of growth kinetics (Sutherland, 1970) is that flocculation and chain formation is likely even in the absence of directional mechanisms. In any case, the likelihood of shape anisotropy for submicron grains or assemblies of grains has observational consequences not only in the case of interstellar polarization of starlight due to grain alignment in weak magnetic fields (Greenberg, 1968), but also in the case of the magnetic properties of meteorites (see Sec. 3).

The observationally inferred compositions of cosmic grains also agree well with some meteoritic materials and with the predictions of most condensation models. Silicates have been identified in the infrared in both interstellar and circumstellar dust (Hackwell et al., 1970; Gillett et al., 1970), while in the solar system their presence may be surmised in the zodiacal dust (MacQueen, 1968), in comets (Maas et al., 1970), and on asteroids (McCord et al., 1970). Iron grains are also likely to be present in interstellar space (Wickramasinghe and Nandy, 1970); in some circumstellar envelopes (Gillett et al., 1970) (where possible infrared excess at 3μ and 5μ might be attributed to hot iron grains, at 900° K and $\lesssim 500°$ K) and in comets as submicron grains (Liller, 1960). In Professor Arrhenius' laboratory, meteoritic crystalline silicates were grown directly from the vapor in plasma-sputtering experiments (Meyer, 1971), and Ni-Fe phases similarly produced are being studied by the present author.

2. GRAINS AND MAGNETIC FIELDS

Individual Grains in Space

The existence and duration of the preaggregation grain stage, in the lifetime of meteoritic material can sometimes be inferred for primitive grains in chondrites; for example, it was found that the (H, He) gas content in small ($<50\mu$) pyroxene grains is concentrated in the outer (0.5μ) skin and correlates inversely with grain size (Eberhardt et al., 1965). The solar wind implantation

of these gases into surfaces of small ($\sim 10\mu$) individual silicate grains was studied (Lord, 1969) and was shown to be an efficient mechanism; the high proton contents (4×10^{19} to 2×10^{20}/g) of several chondrites (Chatelain et al., 1970) implies exposure of grains to the present 1 AU solar wind flux ($\sim 2\times10^{8}$ cm^{-2} s^{-1}) for $\sim 10^{4}$ equivalent years. A similar equivalent exposure age (10^{3} to 10^{4} yr) was inferred for isotropically irradiated individual crystallites in primitive meteorites (Lal and Rajan, 1969; Pellas et al., 1969). Heating to $\sim 500°$ K cannot have occurred during or after the agglomeration of grains and chondrules, or else irradiation damage would have been annealed (see also Green et al., 1971). These and the implanted noble gas component found in the magnetic grains of the unaltered carbonaceous chondrite Orgueil (Jeffery and Anders, 1970), imply that grains must have been individually suspended and exposed to cosmic irradiation in space, post-condensation and prior to agglomeration, during $\lesssim 10^{4}$ yr. This might well have occurred during a "jet stream" stage (Alfvén and Arrhenius, 1970) or during the $\sim 5\times10^{3}$ yr estimated for the completion of angular momentum and matter transfer to the outer nebula (Hoyle and Wickramasinghe, 1968), and is not incompatible with most condensation models.

Magnetic Fields and Grain Alignment

In several studies (Spitzer and Tukey, 1949; Jones and Spitzer, 1967) attempting to explain the polarization of starlight by a partial alignment of elongated ferromagnetic or ferrite interstellar grains in weak magnetic fields, it has been shown that fields of 5×10^{-5} to 5×10^{-8} gauss would effectively align both single domain (~ 0.01 to 1μ) and larger, multi-domain grains, as well as "superparamagnetic" clusters of fine ferromagnetic particles imbedded in the nonmagnetic matrix of a host grain. Alignment of dia- or para-magnetic grains would require higher fields of lower grain temperatures (Greenberg, 1968). It was confirmed by a study (Purcell, 1969) on the efficiency of various alignment mechanisms that the degree of shape anisotropy and the temperature ratio $T_{\text{grain}}/T_{\text{gas}}$ are crucial parameters. A low $T_{\text{gr}}/T_{\text{gas}}$ ratio is required, such as the observationally inferred values ($\lesssim 0.1$) for "dense" HI, and HII interstellar clouds (Harper and Low, 1971) and such as featured in the "cool grains-hot gas" non-equilibrium plasma-condensation model of Arrhenius and Alfvén (1971) and in the laboratory condensation work on which it is based. Moreover, in a partially ionized protoplanetary nebula in which the ionization controlled sequential condensation of species takes place with simultaneous fractionation, the parameters derived by Jokipii (1964) to account for the observed noble gases abundance pattern determine the magnetic field value at 1 AU to be $B \gtrsim 5\times10^{-5}$ gauss, similar to the present observed interplanetary field value in our neighborhood.

Could this field value partially align anisotropic ferromagnetic grains? Consider the additional requirements $\delta = \tau_{\text{coll}}/\tau_{\text{mag}} \lesssim 1$ for partial alignment of grains (Purcell, 1969), where $\delta \propto B^2/a\rho_{\text{gas}}v_{\text{gas}}$, is the ratio of collisional to magnetic relaxation times. If, for a given value of the parameter δ, only the number density of atoms, n is allowed to increase from interstellar values, then a field of $\sim 10^{-5}$ gauss at $n \sim 10^{7}$ cm^{-3} may align ferromagnetic and ferritic grains as effectively as $\sim 10^{-8}$ gauss at $n \sim 10$ cm^{-3}. But, if $n \sim 10^{17}$ cm^{-3}, as required for growth of iron grains in hydrogen (Lehnert, 1970), a field of ~ 1 gauss will be needed to achieve a comparable degree of alignment. If the distributed density in the asteroid belt was indeed five orders of magnitude lower than in the terrestrial and jovian region during accretion, as it is today (Alfvén and Arrhenius, 1970), then partial grain alignment could have been achieved even by $\sim 10^{-5}$ gauss interplanetary fields. Varying degrees of anisotropy of the magnetic susceptibility were found in chondrites (Stacey et al., 1961; Weaving, 1962) testifying to partial alignment of elongated Fe/Ni grains in the stony matrix by some orienting agency, very likely by both magnetic fields and by enhanced solar winds (Greenberg, 1967, 1970). This evidence will be discussed below in the context of similar occurrences in terrestrial rock-magnetism (Sec. 3).

The role possibly played by the magnetic fields in the early solar system consists not only in transferring material and angular momentum to the periphery of the condensing disk and helping establish the large scale physico-chemical distribution observed, but also in leading to fine-structure chemical fractionation, as a result of ambipolar diffusion (Arrhenius and Alfvén, 1971).

Moreover, as pointed out by Spitzer (1963), not only is ambipolar diffusion helped by grains, but submicron grains help maintain the magnetic field and slow down its decay, by supporting a current system as they become partially charged in the plasma. Such small grains, with large surface-to-volume ratio, could perhaps flocculate by interacting electrostatically (Wood, 1962) and form chondritic matrix-like aggregates.

On the other hand, magnetic fields are not explicitly integrated into the "chemical" models (Anders, 1971a) although it is generally conceded that the ferromagnetism of meteoritic Ni/Fe grains, as they cooled below their Curie temperature ($T_c \lesssim 900°$ K), triggered the metal-silicate fractionation which lead to loss of metal from the iron-rich material of Cl and H-chondrites. Harris and Tozer (1967) suggested that magnetic interactions might enhance the capture cross-section of 1 to 10μ ferromagnetic grains by a factor of $\sim 10^4$, leading to rapid aggregation into clusters of 10^3 to 10^4 grains. This type of clusters of grains was indeed observed for magnetite spherules of (0.1 to 1μ) in the "primitive" carbonaceous chondrite Orgueil (Kerridge, 1970). This process might have, in turn, led to a size fractionation process in a protoplanetary nebula whereby large aggregates of ferromagnetic grains could have been preferentially retained in the inner regions, while single domain-size grains (0.03 to 0.05μ) could have been carried outward by a violent solar wind during a T-Tauri stage (Sonett et al., 1970). Let us examine the modes of acquisition of remanence for a growing grain, immersed in an ambient field.

Magnetization of Grains

The quantity determining the stability of a grain's magnetization M is a relaxation time (Irving, 1964), $\tau \propto \exp v\Delta E/kT$ (where v is the volume of magnetic material, ΔE is an energy barrier to magnetization reversal proportional to the coercivity H_c, and T is the grain temperature). This connects clearly the stability of a grain's magnetization to a critical volume at a given T, or to blocking temperature for a given grain size. Below a critical size d_B, the grain is superparamagnetic, its magnetic moment being rendered unstable by thermal fluctuations, and no remanence is acquired. Doubling the grain volume at constant T may increase τ by ten orders of magnitude (see fig. 1). Above d_B, stable single domain behavior is exhibited, up to a critical size for multi-domain configuration of lower remanence and stability. The transition from the superparamagnetic to single- to multi-domain regime of magnetization is illustrated in figure 2 for magnetite, at several temperature values (Strangway et al., 1968). Note that critical diameters for single domain behavior are $d \gtrsim 0.03\mu$ and 0.05μ for Fe and Ni respectively, but at elongation $\ell/d \sim 10$, the critical sizes increase to above 0.12μ and 0.21μ, and to generally larger sizes for ferrites (Jones and Spitzer, 1967) as illustrated in figures 1 and 2. Thus, the stability of the remanent magnetization acquired depends on the ratio v/T. If, at constant T, the magnetization becomes "blocked" as the growing grain reaches the critical size d_B, the stable moment is a CRM. If, at constant v, the temperature of the cooling grains reaches the blocking value (within $\sim 100°$ C below the Curie point T_c), a TRM is acquired. If the cooling and growth processes are simultaneous, a more complex TCRM is established. Both TRM and CRM have similar stability characteristics, figure 3(a), (Kobayashi, 1959), but CRM is an order of magnitude lower than a TRM acquired in very weak fields $\lesssim 1$ Oe. Moreover TRM $\propto H$ holds for $H \lesssim 2$ Oe and saturation can

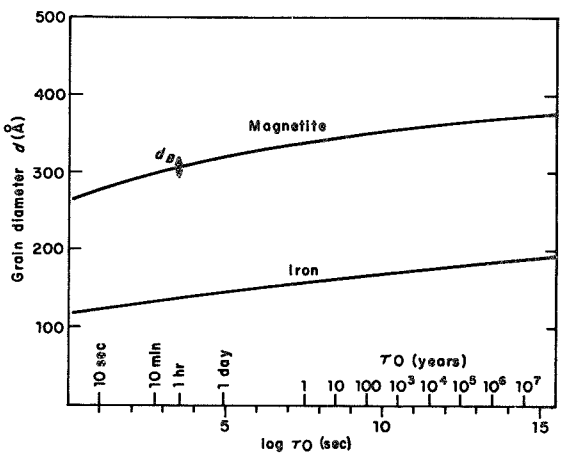

FIGURE 1.—The dependence of the relaxation time τ_0 on grain diameter, at room temperature, for iron and magnetite. (Reproduced from Irving, 1964.)

set in, but CRM $\propto H$ up to 50 Oe. Both have identical values in ~30 Oe fields, and become even harder to distinguish (Banerjee, 1970). Not only shape anisotropy (Strangway et al., 1968), but also ferromagnetic impurities in a less magnetic grain (Jones and Spitzer, 1967) as well as dislocations and defects in crystals (Verhoogen, 1959) may increase the critical size for single domain behavior and stabilize the remanence in large, multi-domain grains (pseudo-single domain grains of magnetite may reach ~40μ size). As the small magnetic grains accrete into a rock complex, they may acquire depositional remanence (DRM) and remain partially aligned in the matrix. If the complex "sets" from high temperatures in the presence of a field, a high coercivity remanence will result from the alignment of anisotropic grains (Stacey, 1960a, b). The effect of interactions between magnetic grains in a matrix is to also increase the critical size but to reduce the coercivity (fig. 4 and Haigh, 1958) and the small field TRM (Dunlop and West, 1969). The CRM is not decreased by interactions, so that the only difference between TRM and CRM, namely their relatively low field intensity, may be erased for interacting grains in a meteorite or rock. In a rock, even a small fraction of single domain grains will dominate the magnetic properties, as it will have preserved the stablest remanence. The presence of such grain fraction had been known to exist in tektites (Senftle et al., 1964; Thorpe and Senftle, 1964), has been established for car-

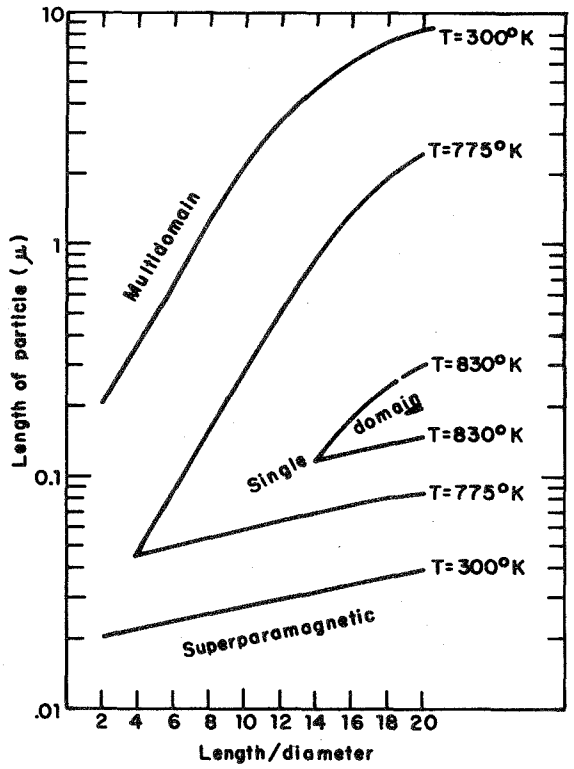

FIGURE 2.—The range of grain sizes for single domain behavior in magnetite, as a function of shape anisotropy and temperature. (Reproduced from Strangway et al., 1968.)

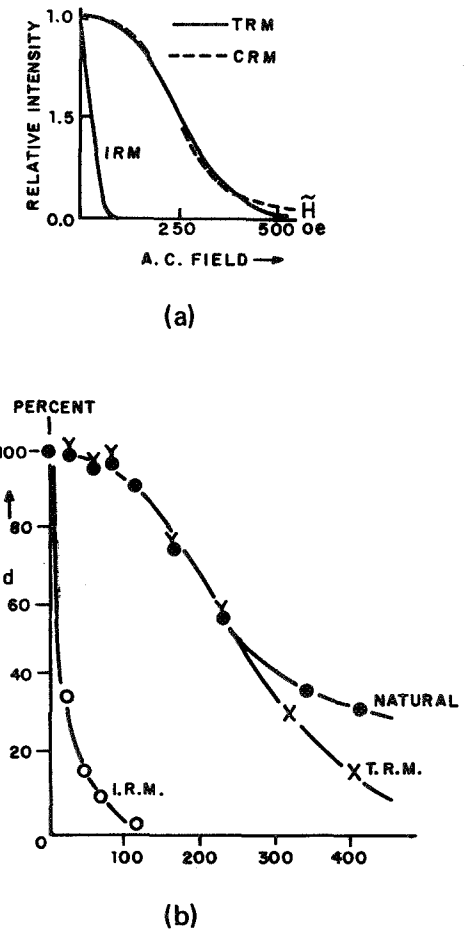

FIGURE 3.—(a) Characteristic behavior of IRM and weak field TRM and CRM in AF demagnetization (after Banerjee, 1970). (b) Stability of NRM vs artificial TRM and IRM in the Brewster chondrite (from Weaving, 1962). By comparing with (a), the NRM appears to be a CRM.

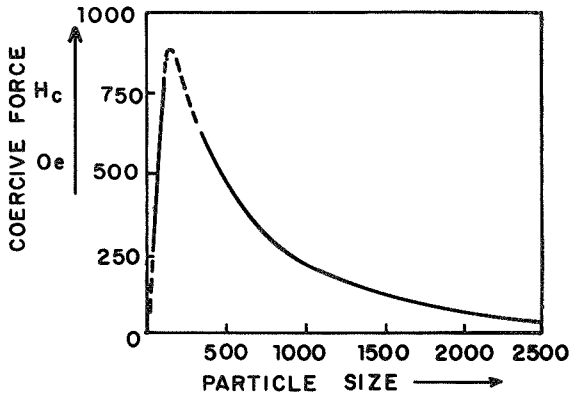

FIGURE 4.—Coercivity dependence on grain diameter, for iron (from Haigh, 1958).

bonaceous chondrites (Kerridge, 1970) and only very recently, for terrestrial igneous rocks (Evans and Wayman, 1971). If chemical and crystalline phase changes continue to occur after the accretion of grains into a rock-like complex, CRM's will ensue (Kobayashi, 1959; Haigh, 1958). If cooling below the Curie points of various materials (see table 1) takes place after accretion, a TRM will be acquired. If the grain, such as Ni/Fe meteoritic grains, crystallized or grew directly from the vapor phase below T_c (Arrhenius and Alfvén, 1971), and continued to cool, a partial thermoremanence (P)TRM could compound the initial CRM. A complex NRM of this type may also be expected for iron meteorites, where the crystalline ordering observed is attributed to diffusional changes during slow prolonged cooling (Goldstein, 1969). At constant temperature, in a steady field an isothermal remanence (IRM) may be acquired, which in general, is the less intense and the least stable among remanence types (Irving, 1964).

3. THE MAGNETIC PROPERTIES OF METEORITES AND THEIR INTERPRETATION, WITH REFERENCES TO ROCK MAGNETISM

Paleomagnetic Methods

The most widely used methods of paleomagnetic analysis are:

(a) Thermal demagnetization, which removes remanence components unstable above a certain temperature and reveals the carrier phases as the changes in NRM occur close to the Curie points (T_c) (see table 1). This method is marred by chemical and crystal phase changes upon heating and cooling.

(b) Alternating-field (AF) demagnetization, which removes the NRM components with a coercivity lower than a selected peak amplitude H_{AF}. It may introduce artificial anisotropies, and anhysteretic secondary remanence (ARM). (For a full discussion of subtleties involved, see Irving, 1964; Schwartz, 1969; Doell and Smith, 1969.)

(c) Demagnetization by steady fields (dc), which determines the coercivity H_c of the NRM, or the field value needed to erase the NRM. The value of the destructive field depends on the fraction of grains with a given coercivity. In general, a rock may be described as an assemblage of ferromagnetic or ferritic (see table 1) grains imbedded in an inert or less magnetic matrix. A spectrum of grain sizes, will lead to a spectrum of microcoercivities, and blocking temperatures in demagnetization studies. The bulk coercivity H_c is a qualitative guide to stability, or "hardness" of remanence only. A high value for H_c does indicate high stability (bulk "hardness"), but a low H_c value implies only that a large fraction of grains has low coercivity ("soft") though a small, highly stable grain fraction may exist.

The remanent properties of a rock are expressed in its NRM intensity (M_n, the magnetization, is given in gauss; or as specific intensity per unit density M_n/ρ; or as volume intensity M_n/v) and in its susceptibility χ, usually expressed as the induced moment in unit field per cm^3 or per gram in cgsm. For terrestrial rocks, M_n is in the range $\sim 10^{-4}$ to 10^{-2} emu/cm^3 for igneous rocks, but 10^{-6} to 10^{-8} emu/cm^3 for the sedimentary type.

Remanence in Meteorites, Tektites and Moon Samples, Its Character and Possible Origins

The most recent and complete survey of the magnetic properties of meteorites is that of Guskova and Pochtarev (1969), some of whose earlier results are reproduced in figure 5 and table 2. To summarize: For stony meteorites, a direct dependence of the specific susceptibility χ on the Ni/Fe content was found increasing from 10 to

TABLE 1.—*Some Characteristics of Magnetic Phases in Meteorites*

Phase	Type	T_C or T_N	M_S(emu/g)
Ni-Fe: α(kamacite)	Ferromagnetic	~750° C	iron meteorites 90–140
$\alpha+\gamma$(plessite)	Ferromagnetic	400–600° C	iron meteorites 180–220
γ(taenite)	(Paramagnetic)	0–600° C	
Fe	Ferromagnetic	770° C	~218
Ni	Ferromagnetic	358° C	~54.4
Fe_3O_4 (magnetite)	Ferrimagnetic	580° C	92
$NiFe_2O_4$ (trevorite)	Ferrimagnetic	585° C	51
$MnFe_2O_4$	Ferrimagnetic	300° C	84
$MgFe_2O_4$	Ferrimagnetic	440° C	24.5
FeS_{1+x} ($0<x<0.15$) (pyrrhotite)	Ferrimagnetic	320° C	<19.5
$(Fe, Ni)_3P$		$\leq$420° C	
$(Fe, Ni)_3C$		$\leq$215° C	
FeS (troilite)	Antiferromagnetic	320° C	
Fe_2SiO_4 (fayalite)	Antiferromagnetic	126° K	
$FeSiO_3$ (pyroxene)	Antiferromagnetic	40° K	

20×10^{-3} cgsm for the L- (low iron ~7 to 12 percent Ni/Fe) to ~50 to 60×10^{-3} cgsm for the H- (high iron) subgroup (Guskova, 1963), with the lowest values of 0.2 to 3.5×10^{-3} cgsm for the Ni/Fe poor (2 to 3 percent wt.) achondrites (Pochtarev and Guskova, 1962). The range for M_n is 0.5 to 40×10^{-3} cgsm. For stony-irons, with a volumetric fraction of Ni/Fe of ~50 percent, M_n~5 to 70×10^{-3} cgsm and χ is up to 0.2 to 1 cgsm. For iron meteorites an inverse correlation between the volume susceptibility and the Ga-Ge content was found (table 2), χ and M_n increasing from group I to IV. The range for χ is 0.8 to 4 cgsm, and for M_n~10 to 300×10^{-3} cgsm, with the finest structured octahedrites exhibiting the highest remanence. The range of coercivity is from a low H_c~0.5 to 1.5 Oe for iron meteorites to values of ~5 to 20 Oe for chondrites. It was thought (Pochtarev, 1967; Stacey et al., 1961) that these low H_c values (to be compared to H_c~60 to 220 Oe for terrestrial igneous rocks) confirm that the coarsely crystalline structure of the metal Ni/Fe phases in meteorites (Wood, 1967; Goldstein, 1969), is magnetically "soft," and cannot have preserved useful paleomagnetic information. This belief was shown to be erroneous by the finding (Guskova, 1963) of a "hard" NRM component in chondrites, stable to H_{AF}~300 Oe and T~800° C, i.e., of TRM stability type. Even though stony and stony-iron meteorites showed both a "soft" and a "hard" remanence to be present (Guskova and Pochtarev, 1967; Stacey and Lovering, 1959; Stacey et al., 1961), only a "hard" component was found in iron meteorites. It was realized that this "hard" NRM could be either a CRM or a TRM (Stacey and Lovering, 1959), or more likely, a TCRM acquired as the high temperature γ-Ni/Fe phase transformed to the strongly ferromagnetic α-Ni/Fe phase, which further cooled in an external field in the neighborhood of T_c, the equilibration between the alloy phases proceeding down to T~400° C. Nevertheless, the stable NRM components were simplistically treated as pure TRM's acquired during cooling in a dipole field like the Earth's (with values of H~0.15 Oe experienced for the stony fraction and H~0.6 Oe for the iron core, on a parent planet differentiated by zonal melting (Guskova and Pochtarev, 1967; Pochtarev, 1967).

The more subtle fact is that, in this planetary model for the parent body, the iron meteorites which derived from its core should not have shown any NRM because the field would have decayed already above $T_c\lesssim$770° C at the time of their solidification (Stacey et al., 1961). It can be argued on several grounds that an interpretation of the "hard" NRM as a CRM is more plausible. In fact it was found (Pochtarev, 1967) that a best fit of chondritic remanence to theoretical TRM

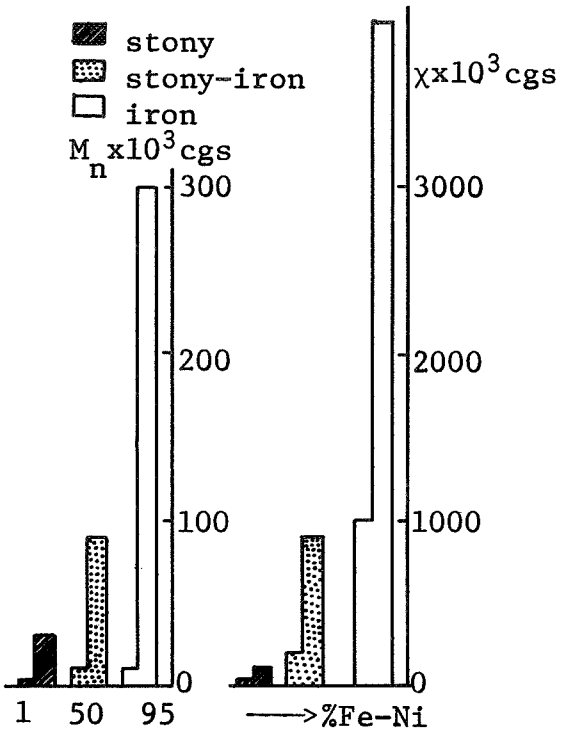

FIGURE 5.—The intensity of NRM (M_n) and the susceptibility (χ) of meteorites, correlated with Ni/Fe content (from Guskova and Pochtarev, 1967).

models requires a value for the parameter σ_{RT}/σ_{BT} (ratio of spontaneous magnetization at room vs blocking temperature) of 1.5 to 2, compared to values of $\sim$3 for normal TRM, and to values $\gtrsim$1 expected for CRM (Stacey et al., 1961), thus suggesting that a CRM component is present. Moreover, CRM's had repeatedly been mistaken for TRM's in terrestrial rock magnetism, because of their identical stability to AF demagnetization (Banerjee, 1970). A comparison of figure 3(a) with figure 3(b) suggests that the NRM of the chondrite Brewster (Weaving, 1962) does appear to behave more like CRM than TRM.

There have been many, varied arguments advanced against a theory of an origin of meteorites in a single planetary parent body in general, and against an origin of iron meteorites in the core of one or a few large differentiated bodies, in particular (Levin, 1969; Anders, 1971b; Goldstein, 1969; Buseck and Goldstein, 1968; Fricker et al., 1970). The arguments will not be repeated here, but they further weaken the case for a simple TRM acquired in the field of a terrestrial type planet (Pochtarev, 1967; Guskova and Pochtarev, 1967), and make the various estimates of paleointensity of H$\lesssim$1 Oe, rather doubtful. Furthermore, in iron meteorites, a considerable thermal

TABLE 2.—*The Anticorrelation of Ga-Ge Content and the Magnetic Susceptibility for Iron Meteorites*

From Guskova and Pochtarev (1969)

Ga-Ge group	Mn ($\times 10^3$ cgsm)	χ ($\times 10^3$ cgsm)
I	30	1500
IIIa	60	1600
IIIb	70	1700
IVa	120	1100

From Guskova (1963)

Group	Ga, ppm	Ge, ppm	Mn ($\times 10^3$ cgsm)	χ ($\times 10^3$ cgsm)
I	80–100	300–420	26	580
II	40–65	130–230	33	660
III	8–24	15–80	300	670
IV	1–3	<1	300	1000

hysteresis—due to crystal phase transformations ($\alpha \rightleftarrows \gamma$) particularly in the plessitic, fine grained ($<1\mu$) fraction of Ni/Fe, and to oxidation or decomposition of secondary magnetic phases such as sulfides, phosphides, carbides—would preclude a reliable estimate of the paleointensity being made from thermomagnetic analyses. Some experiments for testing the suitability of meteoritic samples for paleointensity determinations are suggested in Section 4. An important observation suggesting the continued presence of a magnetic field from the condensation and growth of grains through the aggregation stage (see Sec. 2) is that of the anisotropic susceptibility in chondrites, and, perhaps of the unusual type of crystalline anisotropy found in iron meteorites (Stacey et al., 1961; Weaving, 1961). The various degrees of anisotropy ($\chi_{max}/\chi_{min} \sim 1.4$ to 2.1) in chondrites were concluded to be due to partial alignment of elongated metal grains along the direction of maximum χ, reminiscent of "stringing" observed in artificial powder samples of Fe, Ni, Fe_3O_4, set in a magnetic field (Stacey, 1960a, b). Moreover, the orienting action of streaming solar winds (Greenberg, 1967, 1970), especially if a T-Tauri type activity did take place, should also contribute to the alignment of elongated grains inferred from magnetic anisotropy. Such a grain fraction, even though of large physical sizes (Wood, 1967) (10 to 100μ), could carry stable remanence (Strangway et al., 1968; Dunlop and West, 1969). Pseudo-single domain behavior of large irregularly shaped, or anisotropic (lamellar, acicular) grains could be attributed to slip dislocations (Bozorth, 1951), to inclusions (such as phosphides, sulfides and carbides in the Ni/Fe), or to any other structural and compositional inhomogeneities, such as the Ni concentration in the Ni-Fe alloy. Magnetic "hardening" of grains could result also from cosmic irradiation during growth which may cause surface damage in the growing grain and implant nonmagnetic impurities, such as protons (Sec. 2). Annealing in hydrogen is known to improve the magnetic susceptibility of Ni/Fe alloys (Bozorth, 1951), and electrolytically implanted hydrogen can cause magnetic "hardening" of iron grains. Thus, if growing in a hydrogen-rich gas and/or being exposed to solar winds (Sec. 1), even large grains may have preserved a stable remanence. All such assemblies of irregularly shaped grains could be reduced to equivalent ellipsoids (Brown, 1960) and treated by "fine-particles" or "inclusion" theories (Kneller, 1969) devised for ferrite permanent-magnet materials. For tektites (Senftle et al., 1964; Thorpe and Senftle, 1964), stable remanence was found to reside in submicroscopic spherules of Ni/Fe with $\sim$23 percent Ni; an alloy in this composition range has the highest possible coercivity (Bozorth, 1951). In lunar microbreccia and rocks, a very stable, high coercivity ($H_c \sim 100$ to 200 Oe) remanence was found to reside in either native or meteoritic iron grains (Strangway et al., 1970; Doell et al., 1970; Nagata et al., 1970). Weak field susceptibilities of $\sim 10^{-3}$ emu/g, similar to chondritic values, were found for tektites and lunar samples, the intensity of remanence correlating with the iron content. It appears likely that for all these types of materials, fine particle models could be used to account for observed magnetic properties.

In the case of iron meteorites, the "hard" remanence found is perhaps more difficult to understand, given the macroscopic bandwidths of the ferromagnetic kamacite (α—Ni/Fe with $T_c \lesssim 770°$ C, depending on Ni content) ranging from <0.2 mm in the finest octahedrites to >2.5 mm in the coarsest; the kamacite bands are separated by Ni-rich, paramagnetic taenite (γ—Ni/Fe) bands of $\lesssim 100\mu$ widths (Goldstein, 1969). But in hexahedrites, Neumann slip bands separating thin (1 to 10μ) kamacite lamellae; in octahedrites, inclusions and precipitations, often as oriented lamellae (phosphates and sulfides), as well as compositional inhomogeneities attributed to diffusional equilibration of Ni in the cooling alloy phases; and in the Ni-rich ataxites the spindles of 10 to 100μ of kamacite separated by taenite lamellae—all could contribute to the "hard" component of NRM. A relevant example (Irving, 1964) from rock magnetism is the high stability of the CRM found for hematite-rich macroscopic lamellae (1 to 10 mm long, 5 to 20μ thick) evolved from an ilmenite ground mass.

Or, the "hard" component may originate in the crystalline ordering of the $\alpha-\gamma$ Ni/Fe phases. A "memory" effect (see Sec. 4) was found (Stacey et al., 1961) for the high temperatures ($T \approx 630$ to 800° C) component of the NRM, which reappeared with the same intensity and direction upon cooling under T_c, after repeated demagnetizations. These suggest another class of

permanent magnet materials, namely the diffusion—or dispersion-hardened alloys (Kneller, 1969). They consist of two crystalline phases, one being strongly ferromagnetic (like $\alpha-$Ni/Fe) and the other weakly—or nonmagnetic (like $\gamma-$Ni/Fe); the ferromagnetic phase is dispersed either as "islands" or as plates separated by nonmagnetic layers, with the highly oriented structure being established by cooling in a magnetic field. In many magnetically annealed anisotropic materials, some crystal axes are preferentially aligned. The crystalline anisotropy which gives rise to the "memory" effect for the high-T remanence in iron meteorites, may have led to the highly oriented $\alpha-\gamma$ ordering (the Widmannstätten pattern). The NRM could have, of course, been established as a TCRM, as cooling and phase-changes occurred simultaneously in the Ni/Fe alloy (Goldstein, 1969), but an interesting possibility, now being experimentally explored by our group, is the simultaneous condensation of α and γ phase (Arrhenius and Alfvén, 1971) from the vapor, below T_c, in the presence of a magnetic field. If the growth takes place in the film-configuration, demonstrated "contact" control and "remote" control of the magnetization by the earliest deposit exceeding critical thickness, could establish the direction of the CRM throughout the growing solid. Maurain's (1901) pioneering study of CRM acquired during controlled growth of Fe films in magnetic fields, demonstrated that the critical single domain thickness for films deposited in an ambient magnetic field was $\sim 200\mu$ for Ni and $\sim 85\mu$ for Fe, more than two orders of magnitude larger than for layers deposited in the absence of field. It is thus possible that an extremely stable CRM was recorded in the thick ordered layers of Ni/Fe growing in the $\alpha+\gamma$ duplex field of temperature. It can therefore be surmised that a stable CRM could have been acquired, already in the early stages of growth of magnetic solid grains in space, and that field information on this condensation environment could be retrieved, if approached experimentally in a suitable way.

Fields and Remanence in Various Models

Keeping in mind the field values (0.1 to 1 gauss) required to establish the NRM of meteorites, if it were a TRM, what values of ambient fields might one expect in various models? The strong magnetic field (of $H\sim 100$ gauss) at the Sun's surface for an expanded radius $R_0 \gtrsim 3\times 10^{12}$ cm (implying $H\sim 10^{-2}$ gauss at 1 AU for a dipole $\sim 1/R^3$ fall-off, or ~ 4 gauss if a solar wind $\sim 1/R^2$ fall-off is assumed), required to complete the angular momentum transfer in $\tau\sim 5\times 10^3$ yr in Hoyle's model, could have decayed to the present interplanetary value of $\gtrsim 5\ \gamma = 5\times 10^{-5}$ gauss required by Jokipii (1964) to account for noble gas fractionation by ambipolar diffusion, at 1 AU, by the end of the Helmholtz contraction time of $\sim 10^7$ yr (Hoyle and Wickramasinghe, 1968; Cameron, 1969). Thus, at least for a short time interval, field values of a few tenths of a gauss could have been attained in the asteroid belt region, (perhaps with simultaneous cooling below T_c) and TRM's were acquired. In another scheme, Sonett et al. (1970) and Sonett (1971) proposed a disturbance field of ~ 0.3 gauss at 3 AU in order to achieve short lived ($<10^6$ yr) heating of asteroids, during a T-Tauri phase. For a maximum allowed field at Sun's surface of ~ 20 gauss (with a decay time of ~ 2.2 billion yr) steady fields at 1 AU may reach values of 50 γ for $\sim 1/R^2$ fall off. But the early rapid spin of the Sun is supposed to lead to field amplification by $\times 10^3$ due to "winding-up" of field lines. The values then may become ~ 0.5 gauss at 1 AU, and lower by one magnitude at 3 AU. It thus appears that, in this case also, partial thermoremanence might have been acquired by meteoritic material, depending on the size of the parent body and location within it, which determine the degree and duration of the heating episode. Many other parameters (Sonett, 1971) must be guessed at, before values of induction fields and (P)TRM's can be evaluated in this model. Chemical changes, and therefore CRM's, are also likely to occur in reheated material; or, if only mildly reheated, earlier remanence of either type acquired prior to accretion into parent bodies may have survived. In general, the Thellier method of inferring the paleofield from $H_{\text{ancient}} = H_{\text{known}}(\text{NRM/TRM})$, by comparing NRM with an artificial TRM (acquired by first heating the sample above T_c, then allowing it to cool in a known field), may not be warranted. Unfortunately, little is known about field intensities needed to establish CRM at growth and crystal-

lization of solids, as experiments in this area are lacking.

4. SUGGESTIONS FOR EXPERIMENTAL WORK IN METEORITIC PALEOMAGNETISM

A most important recent development in meteoritic magnetism is the finding of a sizeable stable, high-coercivity NRM of $\sim 10^{-3}$ to 10^{-5} gauss cm^3/g in several "primitive" carbonaceous chondrites (Types I, II) (Banerjee and Hargraves, 1971). The authors realized that this stable NRM could be used to infer on the paleointensity of magnetic fields in the solar nebula. They were also aware that the NRM could be either a CRM, acquired during the growth of Ni/Fe grains in a magnetic field; or a TCRM, acquired when and if Ni/Fe grains were oxidized into magnetite (Fe_3O_4) and trevorite ($NiFe_2O_4$), and subsequently cooled; or perhaps a (P)TRM acquired during cooling in the field of their parent body. Unfortunately, the authors stopped short of determining the intensity of the ancient fields and ascertaining the type of remanence, because the British Museum did not allow heating bulk samples to the minimum of 400° C intended in order to induce an artificial TRM.

Even though estimated grain temperatures at accretion of carbonaceous chondrite materials are in the range 300° K to 450° K (Anders, 1971a), the authors heated powder samples of Orgueil up to 600 to 800° C, risking to incur drastic chemical changes and thus to irreversibly blur the fossil field record. Nor could they have discriminated, based solely on the stability of NRM to AF demagnetization, between a CRM and a TRM (Banerjee, 1970), though the mode of acquisition of the NRM is as revealing of the physical environment as the paleointensity itself.

The several experiments suggested below could insure the retrieval of precious information on paleofields; they are based on recent techniques developed in rock magnetism, which do not run the risk of irreversible alterations.

First Suggested Experiment

First, in order to determine the intensity of ambient fields at condensation, one could exploit the "memory effect" exhibited by magnetic materials such as magnetite, hematite, nickel and cobalt (Ozima et al., 1964; Kobayashi and Fuller, 1968; Nagata et al., 1961). When thermally cycled through the so-called isotropic point T_K of minimum magnetocrystalline anisotropy, after demagnetization, a remarkable recovery of the initial NRM, within a fraction of its initial value, is observed. For magnetite, $T_K = -145°$ C, so that cooling from rather than heating above, room temperature through T_K, in known fields, may yield within a fraction the desired paleointensity. The "memory" of the initial fields is associated with the hardest fraction of grains, with high microcoercivities. Appreciable soft remanence can be acquired without "memory" loss, being erased after a single cooling cycle in field-free space. Nor does repeated thermal cycling change the stability of "memory" to ac field demagnetization. The amplitude of the recovered fraction of NRM after the first cycle may also reveal its mode of acquisition: low field TRM's ($H \lesssim 2$ Oe) have the highest rate of recovery of various artificial IRM's and TRM's, and the lowest relative amplitude loss after several cooling-heating cycles (Nagata et al., 1961).

Second Suggested Experiment

Since the size distribution of magnetite grains in Orgueil had been studied (Kerridge, 1970) and found to peak in the submicron range for clustered grains, but have a lower cutoff at $\sim 5\mu$ for single grains, it could be verified whether the large magnetic grains can exhibit single domain behavior, as suggested by the finding that physical sizes of 0.5 to 50μ for magnetite grains in a natural basalt corresponded to effective sizes of 0.03 to 0.08μ (Dunlop and West, 1969). This could be achieved by combining AF demagnetization with low-temperature cycling (Merrill, 1970). As the former affects remanence of a given coercivity regardless of its carriers, but the latter affects mainly multi-domain grains, the relative intensities of NRM components residing in each grain size-fraction could be appraised. This would reveal whether useful stable remanence is carried by large, multi-domain grains, and would be of great significance in qualifying the magnetically useful grain fraction in most chondrites. For example,

although kamacite (Ni/Fe) grains in chondrites are generally $<50\mu$, they may reach mm sizes, as found in the Renazzo (carbonaceous type II) meteorite (Wood, 1967).

Third Suggested Experiment

It is important to ascertain the reliability of paleointensity estimates for chondrites, which are based on the assumption that the entire NRM is a simple TRM (Stacey et al., 1961). For carbonaceous chondrites in particular, some questions of possible importance are: If a secondary CRM was acquired upon the oxidation of small ($<10\mu$) Ni/Fe grains as they cooled into the range $T \lesssim 450°$ K where the oxide is stable (Wood, 1967; Anders, 1971a), would the original information have been lost? And if a primary CRM was established upon growth of magnetite plaques and spherules directly from a vapor phase (Arrhenius and Alfvén, 1971), and compounded into (P)TCRM's subsequently, would the components be resolvable? Significant recent work (Kellogg et al., 1970; Marshall and Cox, 1971) investigating this aspect, showed that, as long as oxidation occurs during the initial cooling of the nebular material, both the original (P)TRM (of the Ni/Fe grains) and the TCRM (acquired by further cooling after oxidation of Ni/Fe into magnetite) are proportional to the ambient field, with the same proportionality constant. In general, the proportionality TRM $\propto H$ holds in low ($H \lesssim 2$ Oe) fields (Everitt, 1961), and will hold for (P)TRM's and (P)TCRM's.

But if the NRM, prior to an oxidation of Ni/Fe grains, was not a simple TRM as was assumed for meteorites, the presence of an earlier CRM, (due to recrystallization, diffusional phase changes, etc.) superposed on the TRM could be detected. The procedure involves comparing the spectra of blocking temperatures and microcoercivity of the NRM with those of an artificial TRM (Schwartz, 1969; Schwartz and Symons, 1970), and requiring that the plot of NRM vs TRM after partial thermal and AF demagnetizations, be linear and intercept the origin. If the reliability criteria are not met, the estimate for paleointensity based on laboratory TRM must be rejected. Thus, before estimated values of 0.15 to 0.9 Oe for the ancient field in which chondrites acquired their NRM (Stacey et al., 1961); or of 0.15 Oe for stony, but 0.6 Oe for iron meteorites in a "planetary" body (Guskova and Pochtarev, 1967, 1969) as TRM are to be accepted, they must fulfill the reliability criteria formulated in Schwartz (1969).

Fourth Suggested Experiment

A procedure was developed (Doell and Smith, 1969) to improve the linearity of NRM vs induced TRM, which is indicative of the reliability of paleofield intensity derived (Schwartz, 1969). It involves the use of AF and thermal "cleaning" in tandem. For example, using low AF field demagnetization, prior to thermomagnetic analysis for carbonaceous chondrites, will erase low temperature PTRM's (possibly, acquired by postoxidation cooling of the magnetite grains) which are known (Everitt, 1961) to reside in a low coercivity grain fraction.

Fifth Suggested Experiment

Finally, a method for directly determining the effective size distribution of magnetic grains was described by Dunlop and West (1969). This involves analyzing experimental AF demagnetization curves for suites of PTRM's induced over consecutive, narrow temperature intervals. It yields the same information as the second experiment above, though more laborious, but is applicable to any type of magnetic grains. If undertaken for chondrites and iron meteorites, this procedure could indicate whether indeed they behave as assemblies of high coercivity single- or multi-domain grains and whether the general theoretical models proposed above (Sec. 3), apply.

Sixth Suggested Experiment

In order to confirm the conclusion of several authors (Stacey et al., 1961; Weaving, 1962), that the anisotropic susceptibility of chondrites is due to a general alignment of elongated metal grains, the particles size and elongation spectrum could be simply determined by ferromagnetic resonance techniques (Brown, 1960). The resonance frequency for iron oxide powders is in the microwave region, and is a function of the shape de-

magnetization factor $(N_b - N_a)$, indicative of the elongation (b/a) of ellipsoidal grains. A spectrum of resonant frequencies may yield directly the relative volume fractions of grains of a given elongation.

Other Suggested Experiments

More narrowly directed experiments, able to confirm or disprove certain aspects of meteoritic genesis, could also be conceived. For example:

(a) The suggestion (Whipple, 1966; Cameron, 1966) that chondrules formed in electrical ("lightning") discharges, from the remelting of the dust found in the matrix of chondrites (Wood, 1967), could be verified as follows. It is known that, where struck by lightning, terrestrial rocks acquire a very large secondary IRM, which constitutes magnetic "noise" (Irving, 1964). The presence of such a large, but "soft" IRM component in the NRM of individual chondrules, could be ascertained simply by comparing the stability type of the NRM in AF demagnetization to that of artificial TRM's and IRM's. Chondrules of diverse types and metal content, such as those found in the carbonaceous type II chondrite Renazzo, should exhibit a common "soft"-type component, when compared to the NRM of the fine grained unaltered matrix.

Similarly, if the class C2 of carbonaceous chondrites experienced lower peak temperatures than C3 and C4, as proposed (Anders, 1971a), an increasingly prominent soft, IRM component should be found in the bulk NRM. This was perhaps already seen (Stacey et al., 1961) for Mokoia (recrystallized type III), where only an unstable NRM was found, erased upon heating to only $\sim$200° C. It is also interesting that, for the Brewster ordinary chondrite, the NRM was seen to symmetrically increase from center to the outer surface by a factor of $\sim$60, and change its stability type from TRM at center to IRM at edges. If it is an IRM, the high remanence ($\sim 3 \times 10^{-1}$ emu/g), implies exposure to fields as high as 450 Oe (Weaving, 1962), perhaps experienced during the meteorite fall through the atmosphere, across electrical discharge fields.

(b) The magnetic properties could be used to validate or invalidate the case for cogenetic groups of meteorites. For instance, it should be determined whether the hypersthene chondrites (which are often presumed to derive from a single parent body shattered in a collision with the parent of Ga-Ge group III irons, Jain and Lipschutz, 1969) have similar remanence. It is known that shock (Hargraves and Perkins, 1969) or stress (Stott and Stacey, 1960; Kern, 1961a, b, c) only decreases the intensity of the NRM by affecting its least stable carriers, so that the original information is still recoverable from shocked meteorites. For example, Farmington, a "shocked," apparently severely reheated chondrite (Wood, 1967) had an NRM less stable under thermal demagnetization (disappearing at 500° C) than an artificial TRM. This implies that no reheating above 500° C occurred since the event which caused the shock degassing of Farmington, and that the NRM must be either a (P)TRM acquired upon cooling below 500° C, or a CTRM if the shock event caused the characteristic "light-dark" phases and veins. Indeed, to account for the large ($\sim$70 percent) "soft" component of chondritic NRM (demagnetized in $H_{AF} \sim 5$ to 10 Oe or at 250° C), Guskova (1963) suggested that it may have been acquired anhysteretically at the breakup of the parent body. In that case, only the hard component of NRM, surviving in $H_{AF} \sim 300$ Oe, contains the information on the parent body environment.

(c) If the iron meteorites in Ga-Ge groups IIIa and IIIb do derive from different "raisins" (Levin, 1969) in the same parent body ($R \sim 200$ km), the former being nearer to the surface as indicated by cooling rates data (Goldstein, 1969) ($\gtrsim 5°$ C/10^6 yr for IIIa, $<2°$ C/10^6 yr for IIIb), the assumption that their NRM is a TRM acquired in a dipole field of a planetary parent body (Pochtarev, 1967) would allow the dipole moment of the parent body ($a \sim HR^3$) to be determined from a comparison of the relative remanence of groups IIIa ($M_n \sim 0.06$ cgsm, $\chi \sim 1.6$ cgsm) and IIIb ($M_n \sim 0.07$ cgsm, $\chi \sim 1.7$ cgsm) (Guskova and Pochtarev, 1969).

The planetary origin interpretation of NRM could be ruled out if a consistent field estimate cannot be arrived at by comparing, say, the NRM of chondrites (for which cooling rates, depth of burial and size of parent body were estimated and of pallasites and mesosiderites, for which similar data exist (Wood, 1967; Sonett, 1971; Buseck

and Goldstein, 1964; Powell, 1969; Fricker et al., 1970).

(d) A laboratory determination of the temperature interval through which various meteorites must have cooled in order to acquire their NRM as (P)TRM in the field (<1 Oe) in their parent body, could help determine which among the calculated cooling curves (Wood, 1967; Sonett, 1971; Fricker et al., 1970) is best. It would thus be possible to select a self-consistent model for the origin of meteorites, which integrates magnetic remanence data with accretion temperatures, cooling histories, chemistry and petrology.

ACKNOWLEDGMENT

The author is much indebted to G. Arrhenius, who originally suggested this topic for investigation, for many helpful discussions. This work has been supported by NASA NGL 05-009-002.

REFERENCES

ALFVÉN, H., 1954. *On the Origin of the Solar System*, Oxford Univ. Press, London.

ALFVÉN, H., AND ARRHENIUS, G., 1970. Structure and evolutionary history of the solar system, *Astrophys. Space Sci.*, **1**, 186–271; **2**, 282–312.

ANDERS, E., 1971a. Meteorites and the early solar system, *Annual Rev. Astron. Astrophys.*, **9**, 1–34.

——, 1971b. Interrelations of meteorites, asteroids and comets, in *Physical Studies of Minor Planets*, edited by T. Gehrels, *NASA* **SP-267**, Supt. of Documents, U.S. Govt. Printing Office, Washington, 429–446.

ARRHENIUS, G., AND ALFVÉN, H., 1971. Fractionation and condensation in space, *Earth Planet. Sci. Lett.*, **10**, 253–267.

BANERJEE, S. K., 1970. Rockmagnetism today, *J. Appl. Phys.*, **41**, 966–973.

BANERJEE, S. K., AND HARGRAVES, R. B., 1971. Natural remanent magnetization of carbonaceous chondrites, *Earth Planet. Sci. Lett.*, **10**, 392–396.

BLANDER, M., AND ABDEL-GAWAD, M., 1969. The origin of meteorites and the constrained equilibrium condensation theory, *Geochim. Cosmochim. Acta*, **33**, 701–716.

BLANDER, M., AND KATZ, J. L., 1967. Condensation of primordial dust, *Geochim. Cosmochim. Acta*, **31**, 1025–1034.

BOZORTH, R. M., 1951. *Ferromagnetism*, Van Nostrand, New York.

BROWN, W. F., JR., 1960. Single domain particles: New uses of old theorems, *Amer. J. Phys.*, **28**, 542–551.

BUSECK, P. R., AND GOLDSTEIN, J. I., 1964. Pallasitic meteorites: Implications regarding the deep structure of asteroids, *Science*, **159**, 300–302.

CAMERON, A. G. W., 1963. Contraction of the Sun toward the main sequence, in *Origin of the Solar System*, edited by R. Jastrow and A. G. W. Cameron, Academic Press, New York, 55–61.

——, 1966. The accumulation of chondritic material, *Earth Planet. Sci. Lett.*, **1**, 93–96.

——, 1969. Physical conditions in the primitive solar nebula, in *Meteorite Research*, edited by P. M. Millman, D. Reidel Publ. Co., Dordrecht, Holland, 7–15.

——, 1973. The early evolution of the solar system, this volume.

CHATELAIN, A., KLINE, D., KOLOPUS, J. L., AND WEEKS, R. A., 1970. Electron and nuclear magnetic resonance of three chondrite meteorites, *J. Geophys. Res.*, **75**, 5681–5692.

DOELL, R. R., GROMMÉ, C. S., THORPE, A. N., AND SENFTLE, F. E., 1970. Magnetic studies of Apollo 11 lunar samples. *Proc. Apollo 11 Lunar Science Conf., Geochim. Cosmochim. Acta*, Suppl. **1**, 2097–2102.

DOELL, R. R., AND SMITH, P. J., 1969. On the use of magnetic cleaning in paleointensity studies, *J. Geomagn. Geoelec.*, **21**, 579–594.

DONN, B., AND SEARS, G. W., 1963. Planets and comets: Role of crystal growth in their formation, *Science*, **140**, 1208–1211.

DUNLOP, D. J., AND WEST, G. F., 1969. An experimental evaluation of single domain theories, *Rev. Geophys.*, **7**, 709–757.

EBERHARDT, T. P., GEISS, J., AND GRÖGLER, N., 1965. Further evidence on the origin of trapped gases in the meteorite Khor Temiki, *J. Geophys. Res.*, **70**, 4375–4378.

EVANS, M. E., AND WAYMAN, M. L., 1971. An investigation of small magnetic particles by means of electron microscopy, *Earth Planet. Sci. Lett.*, **9**, 365–370.

EVERITT, C. W. F., 1961. Thermoremanent magnetization. I. Experiments on single domain grains, *Phil. Mag.*, **6**, 713–726.

FRICKER, P. E., GOLDSTEIN, J. I., AND SUMMERS, A. L., 1970. Cooling rates and thermal histories of iron and stony-iron meteorites, *Geochim. Cosmochim. Acta*, **34**, 475–491.

GILLETT, F. C., STEIN, W. A., AND SOLOMON, P. M., 1970. The spectrum of VY Canis Majoris from 2.9 to 14 microns, *Astrophys. J.*, **160**, L173–L176.

GILMAN, R. C., 1969. On the composition of circumstellar grains, *Astrophys. J.*, **155**, L185–L187.

GOLDSTEIN, J. I., 1969. The classification of iron meteorites, in *Meteorite Research*, edited by P. M. Millman, D. Reidel Publ. Co., Dordrecht, Holland, 721–737.

GREEN, H. W., RADCLIFFE, S. V., AND HEUER, A. H., 1971. Allende meteorite: A high-voltage electron petrographic study, *Science*, **172**, 936–939.

GREENBERG, J. M., 1967. Small particles in space, in *The Zodiacal Light and the Interplanetary Medium*, edited by J. L. Weinberg, *NASA* **SP-150**, Supt. of Documents, U.S. Govt. Printing Office, Washington, 215–223.

——, 1968. Interstellar grains, in *Stars and Stellar Systems*, vol. VII, edited by B. M. Middlehurst and G. P. Kuiper, Univ. Chicago Press, 221–364.

——, 1970. Models of the zodiacal light, *Space Research X*, 225–232.

GUSKOVA, E. G., 1963. Investigation of natural remanent magnetization of stony meteorites, *Geomagnetizm i Aeronomiya*, **3**, 308–312.

GUSKOVA, E. G., AND POCHTAREV, V. I., 1967. Magnetic fields in space according to a study of the magnetic properties of meteorites, *Geomagnetizm i Aeronomiya*, **7**, 310–316 (*Geomagn. and Aeronom.*, **7**, 245–250).

GUSKOVA, E. G., AND POCHTAREV, V. I., 1969. Magnetic properties of meteorites of the Soviet collection (in Russian), in *Meteorite Research*, edited by P. M. Millman, D. Reidel Publ. Co., Dordrecht, Holland, 633–637.

HACKWELL, J. A., GEHRTZ, R. D., AND WOOLF, N. J., 1970. Interstellar silicate absorption bands, *Nature*, **227**, 822–823.

HAIGH, G., 1958. The process of magnetization by chemical change, *Phil. Mag.*, **3**, 267–286.

HARGRAVES, R. B., AND PERKINS, W. E., 1969. Investigations of the effect of shock on natural remanent magnetism, *J. Geophys. Res.*, **74**, 2576–2589.

HARPER, D. A., AND LOW, F. J., 1971. Far-infrared emission from H II regions, *Astrophys. J.*, **165**, L9–L13.

HARRIS, P. G., AND TOZER, D. C., 1967. Fractionation of iron in the solar system, *Nature*, **215**, 1449–1451.

HERBIG, G. H., 1970. VY Canis Majoris II. Interpretation of the energy distribution, *Astrophys. J.*, **162**, 557–570.

HOYLE, F., 1963. Formation of the planets, in *Origin of the Solar System*, edited by R. Jastrow and A. G. W. Cameron, Academic Press, New York, 63–71.

HOYLE, F., AND WICKRAMASINGHE, N. C., 1968. Condensation of the planets, *Nature*, **217**, 415–418.

IRVING, E., 1964. *Paleomagnetism and Its Application to Geological and Geophysical Problems*, J. Wiley and Sons, New York.

JAIN, A. V., AND LIPSCHUTZ, M. E., 1969. Shock histories of hexahedrites and Ga-Ge Group III octahedrites, in *Meteorite Research*, edited by P. M. Millman, D. Reidel Publ. Co., Dordrecht, Holland, 826–837.

JEFFERY, P. M., AND ANDERS, E., 1970. Origin of primordial noble gases in separated meteoritic minerals, I, *Geochim. Cosmochim. Acta*, **34**, 1175–1198.

JOKIPII, J. R., 1964. The distribution of gases in the protoplanetary nebula, *Icarus*, **3**, 248–252.

JONES, R. V., AND SPITZER, L., JR., 1967. Magnetic alignment of interstellar grains, *Astrophys. J.*, **147**, 943–964.

KELLOGG, K., LARSON, E. E., AND WATSON, D. E., 1970. Thermochemical remanent magnetization and thermal remanent magnetization: Comparison in a basalt, *Science*, **170**, 628–630.

KERN, J. W., 1961a. Effects of moderate stresses on directions of thermoremanent magnetization, *J. Geophys. Res.*, **66**, 3801–3805.

——, 1961b. The effect of stress on susceptibility and magnetization of a partially magnetized multidomain system, *J. Geophys. Res.*, **66**, 3807–3816.

——, 1961c. Stress stability of remanent magnetization, *J. Geophys. Res.*, **66**, 3817–3820.

KERRIDGE, J. F., 1967. The mineralogy and genesis of the carbonaceous meteorites, in *Mantles of the Earth and Terrestrial Planets*, edited by S. K. Runcorn, *Interscience*, London, 54–56.

——, 1970. Some observations on the nature of magnetite in the Orgueil meteorite, *Earth Planet. Sci. Lett.*, **9**, 299–306.

KIMOTO, K., KAMIYA, Y., NONOYAMA, M., AND UYEDA, R., 1963. An electron microscope study of fine metal particles prepared by evaporation in argon gas at low pressure, *Japan. J. Appl. Phys.*, **2**, 702–713.

KIMOTO, K., AND NISHIDA, I., 1967. An electron microscope and electron diffraction study of fine smoke particles prepared by evaporation in argon gas at low pressures (II), *Japan. J. Appl. Phys.*, **6**, 1047–1059.

KNELLER, E., 1969. Fine particle theory, in *Magnetism and Metallurgy*, vol. 1, edited by A. E. Berkowitz and E. Kneller, Academic Press, London, 366–464.

KOBAYASHI, K., 1959. Chemical remanent magnetization of ferromagnetic minerals and its application to rock magnetism, *J. Geomag. Geoelec.*, **10**, 99–117.

KOBAYASHI, K., AND FULLER, M., 1968. Stable remanence and memory of multi-domain materials, with special reference to magnetite, *Phil. Mag.*, **18**, 601–624.

KRISHNA SWAMY, K. S., AND DONN, B., 1968. An analysis of the infrared continuum of comets, *Astrophys. J.*, **153**, 291–300.

KUHI, L. V., 1964. Mass loss from T Tauri stars, *Astrophys. J.*, **140**, 1409–1433.

LAL, D., AND RAJAN, R. S., 1969. Observations on space irradiation of individual crystals of gas-rich meteorites, *Nature*, **223**, 269–271.

LARIMER, J. W., 1970. Chemical fractionation in meteorites III. Major element fractionations in chondrites, *Geochim. Cosmochim. Acta*, **34**, 367–387.

LARIMER, J. W., AND ANDERS, E., 1967. Chemical fractionation in meteorites—II. Abundance patterns and their interpretation, *Geochim. Cosmochim. Acta*, **31**, 1239–1270.

LEFÈVRE, J., 1970. An experimental study of the dust of iron, carbon, silicon carbide and silica, *Astron. Astrophys.*, **5**, 37–44.

LEHNERT, B., 1970. On the conditions for cosmic grain formation, *Cosmic Electrodynamics*, **1**, 218–232.

LEVIN, B. JU., 1969. Origin of meteorites and planetary cosmogony, in *Meteorite Research*, edited by P. M. Millman, D. Reidel Publ. Co., Dordrecht, Holland, 16–30.

LILLER, W., 1960. The nature of the grains in the tails of the comets 1956h and 1957d, *Astrophys. J.*, **132**, 867–882.

LORD, H. C., 1969. Possible solar primordial hydrogen in the Pesyanoe meteorite, *Earth Planet. Sci. Lett.*, **6**, 332–334.

LOW, F. J., JOHNSON, H. L., KLEINMANN, D. E., LATHAM, A. S., AND GEISEL, S. L., 1970. Photometric and spectroscopic observations of infrared stars, *Astrophys. J.*, **160**, 531–543.

LOW, F. J., AND SMITH, B. J., 1966. Infrared observations of a pre-planetary system, *Nature*, **212**, 675–676.

MAAS, R. W., NEY, E. P., AND WOOLF, N. J., 1970. The 10μ emission peak of comet Bennett 1969i, *Astrophys. J.*, **160**, L101–L104.

MACQUEEN, R. M., 1968. Infrared observations of the outer solar corona, *Astrophys. J.*, **154**, 1059–1076.

MARSHALL, M., AND COX, A., 1971. Effect of oxidation on the natural remanent magnetization of titano-magnetite in suboceanic basalt, *Nature*, **230**, 28–31.

MAURAIN, M. CH., 1901. Propriétés des dépots électrolytiques de fer obtenus dans un champ magnétique, *J. Phys. Radium*, **10**, 123–135.

MCCORD, T. E., ADAMS, J. B., AND JOHNSON, T. V., 1970. Asteroid Vesta: Spectral reflectivity and compositional implications, *Science*, **168**, 1445–1447.

MERRILL, R. T., 1970. Low temperature treatments of magnetite and magnetite-bearing rocks, *J. Geophys. Res.*, **75**, 3343–3349.

MEYER, CH., JR., 1971. An experimental approach to circumstellar condensation, *Geochim. Cosmochim. Acta*, **35**, 551–566.

NAGATA, T., ISHIKAWA, Y., KINOSHITA, H., KONO, M., SYONO, Y., AND FISHER, R. M., 1970. Magnetic properties of lunar crystalline rock and fines, *Science*, **167**, 703–704.

NAGATA, T., YAMA-AI, M., AND AKIMOTO, S., 1961. Memory of initial remanent magnetization and number of repeating heat-treatments in low-temperature behavior of haematite, *Nature*, **190**, 620–621.

ÖPIK, E. J., 1968. The cometary origin of meteorites, *Irish Astron. J.*, **8**, 185–208.

OZIMA, M., OZIMA, M., AND AKIMOTO, S., 1964. Low temperature characteristics of remanent magnetization of magnetite-self-reversal and recovery phenomena of remanent magnetization, *J. Geomagn. Geoelec.*, **16**, 165–177.

PELLAS, P., POUPEAU, G., LORIN, J. C., REEVES, H., AND AUDOUZE, J., 1969. Primitive low-energy particle irradiation of meteoritic crystals, *Nature*, **223**, 272–275.

POCHTAREV, V. I., 1967. Magnetic field of planets according to a study of the magnetic properties of meteorites, *Geomagnetizm i Aeronomiya*, **7**, 745–747 (*Geomagn. and Aeronom.*, **7**, 609–610).

POCHTAREV, V. I., AND GUSKOVA, E. G., 1962. The magnetic properties of meteorites, *Geomagnetizm i Aeronomiya*, **2**, 749–758 (*Geomagn. and Aeronom.*, **2**, 626–634).

POWELL, B. N., 1969. Petrology and chemistry on mesosiderites. I. Texture and composition of nickel iron, *Geochim. Cosmochim. Acta*, **33**, 789–810.

PURCELL, E. M., 1969. On the alignment of interstellar dust, *Physica*, **41**, 100–127.

SCHWARTZ, E. J., 1969. A discussion of thermal and alternating field demagnetization methods in the estimation of paleomagnetic field intensities, *J. Geomagn. Geoelec.*, **21**, 669–677.

SCHWARTZ, E. J., AND SYMONS, D. T. A., 1970. Paleomagnetic field intensity during cooling of the Sudbury Irruptive 1700 my ago, *J. Geophys. Res.*, **75**, 6631–6640.

SCHWARTZ, K., AND SCHUBERT, G., 1969. The early despinning of the Sun, *Astrophys. Space Sci.*, **5**, 444–447.

SENFTLE, F. E., THORPE, A. N., AND LEWIS, R. R., 1964. Magnetic properties of Ni-Fe spherules in tektites from Isabela, Philippine Islands, *J. Geophys. Res.*, **69**, 317–324.

SONETT, C. P., 1971. The relationship of meteoritic parent body thermal histories and electromagnetic heating by a pre-main sequence T-Tauri sun, in *Physical Studies of Minor Planets*, edited by T. Gehrels, *NASA* **SP–267**, Supt. of Documents, U.S. Govt. Printing Office, Washington, 239–246.

SONETT, C. P., COLBURN, D. S., SCHWARTZ, K., AND KEIL, K., 1970. The melting of asteroidal-sized bodies by unipolar dynamo induction from a primordial T-Tauri sun, *Astrophys. Space Sci.*, **7**, 446–488.

SPITZER, L., JR., 1963. Star formation, in *Origin of the Solar System*, edited by R. Jastrow and A. G. W. Cameron, Academic Press, New York, 39–53.

SPITZER, L., JR., AND TUKEY, J. W., 1949. Interstellar polarization, galactic magnetic fields and ferromagnetism, *Science*, **109**, 461–462.

STACEY, F. D., 1960a. Magnetic anisotropy of igneous rocks, *J. Geophys. Res.*, **65**, 2429–2442.

——, 1960b. Magnetic anisotropy of dispersed powders, *Australian J. Phys.*, **13**, 196–201.

STACEY, F. D., AND LOVERING, J. F., 1959. Natural magnetic moments of two chondritic meteorites, *Nature*, **183**, 529–530.

STACEY, F. D., LOVERING, J. F., AND PARRY, L. G., 1961. Thermomagnetic properties, natural magnetic moments and magnetic anisotropies of some chondritic meteorites, *J. Geophys. Res.*, **66**, 1523–1534.

STOTT, P. M., AND STACEY, F. D., 1960. Magnetostriction and paleomagnetism of igneous rocks, *J. Geophys. Res.*, **65**, 2419–2424.

STRANGWAY, D. W., LARSON, E. E., AND GOLDSTEIN, M., 1968. A possible cause of high magnetic stability in volcanic rocks, *J. Geophys. Res.*, **73**, 3787–3795.

STRANGWAY, D. W., LARSON, E. E., AND PEARCE, G. W., 1970. Magnetic properties of lunar samples, *Science*, **167**, 691–693.

STROM, K. M., STROM, S. E., AND YOST, J., 1971. Circumstellar shells in the young cluster NGC 2264, *Astrophys. J.*, **165**, 479–488.

SUTHERLAND, D. N., 1970. Chain formation of fine particle aggregates, *Nature*, **226**, 1241–1242.

TANAKA, T., AND TAMAGAWA, N., 1967. Magnetic properties of Fe-Co alloy fine particles, *Japan. J. Appl. Phys.*, **6**, 1096–1100.

THORPE, A. N., AND SENFTLE, F. E., 1964. Submicroscopic spherules and color of tektites, *Geochim. Cosmochim. Acta*, **28**, 981–994.

VERHOOGEN, J., 1959. The origin of thermoremanent magnetization, *J. Geophys. Res.*, **64**, 2441–2449.

WEAVING, B., 1961. Magnetic anisotropy in chondritic meteorites, *Geochim. Cosmochim. Acta*, **26**, 451–455.

——, 1962. The magnetic properties of the Brewster meteorite, *Geophys. J.*, **7**, 203–211.

WETHERILL, G. W., 1971. Cometary vs asteroidal origin of chondritic meteorites, in *Physical Studies of Minor Planets*, edited by T. Gehrels, *NASA* **SP–267**, Supt. of Documents, U.S. Govt. Printing Office, Washington, 447–460.

WHIPPLE, F. L., 1966. A suggestion as to the origin of chondrules, *Science*, **153**, 54–56.

WICKRAMASINGHE, N. C., AND NANDY, K., 1970. Interstellar extinction by graphite, iron and silicate grains, *Nature*, **227**, 51–53.

WOOD, J. A., 1962. Chondrules and the origin of terrestrial planets, *Nature*, **194**, 127–130.

——, 1967. Chondrites: Their metallic minerals, thermal histories and parent planets, *Icarus*, **6**, 1–49.

WOOLF, N. J., STEIN, W. A., AND STRITTMATTER, P. A., 1970. Infrared emission from Be stars, *Astron. Astrophys.*, **9**, 252–258.

Page intentionally left blank

34. The Cometary and Asteroidal Origins of Meteors

Ľubor Kresák
Astronomical Institute of the Slovak Academy of Sciences
Bratislava, Czechoslovakia

A quantitative examination of the gravitational and nongravitational changes of orbits shows that for larger interplanetary bodies the perturbations by Jupiter strongly predominate over all other effects, which include perturbations by other planets, splitting of comet nuclei and jet effects of cometary ejections. In an approximation to the restricted three-body problem, Sun-Jupiter-comet/asteroid, the value of the Jacobian integral represents a parameter of conspicuous stability which can be applied to delineate the evolutionary paths of the potential parent bodies of the meteoroids in the system of conventional orbital elements. Earth-crossing orbits can be reached along three main paths by the comets, and along two by the asteroids.

The structure of meteor streams, however, indicates that the mutual compensation of the changes in individual elements entering the Jacobian integral, which is characteristic for the comets, does not work among the meteoroids. It appears that additional forces of a different kind must exert appreciable influence on the motion of interplanetary particles of meteoroid size. Nevertheless, the distribution of the Jacobian constant in various samples of meteor orbits, from those of faint Super-Schmidt meteors up to those of meteorite-dropping fireballs, furnishes some information on the type of their parent bodies and on the relative contribution of individual sources.

The evolution of meteor orbits may be divided into three principal phases: (I) the evolution of the orbit of the parent body, (II) the differential acceleration at the moment of separation, and (III) the subsequent evolution. Under (II) we assume a separation from a sizeable body, with dimensions of the order of 10^4 cm and more, for which the dynamical effects of solar radiation and interplanetary magnetic fields are negligible. A progressive fragmentation can obviously continue in smaller particles as well.

The only unquestioned primordial source of meteoroids is comet nuclei. Another plausible but not definitely confirmed alternative source is the asteroids. An essential difference in the possibility of identification of these two sources consists in the distribution of their perihelion distances. Fifty-six percent of known comets have their perihelia situated within the orbit of the Earth; consequently, many meteors can be observed in orbits deviating very little from that of their parent comet, and they are easily related to it. This is practically impossible for normal asteroids, as only 0.2 percent of numbered asteroids come inside the Earth's orbit. Moreover, some or all of these peculiar objects may actually be extinct comet nuclei (Öpik, 1963).

Very important information on the evolution of meteoroids is furnished by meteor showers. The large proportion of meteors associated with showers indicates that the lifetime of individual meteoroids cannot be much longer than the life-

time of individual meteor streams, which evidently do not vanish through diffusion into the sporadic background. If there is indeed a significant contribution of asteroidal meteors, their ages would hardly be much greater than the ages of cometary meteors since interaction with the Earth's atmosphere does not indicate any striking difference in resistance to disintegration. The low age limit of small bodies reduces the potential significance of phase (III) as compared to phase (I), but only as far as gravitational effects are concerned. At the same time, the observed dispersion of meteor streams sets an upper limit to the effects of phase (II) on shower meteors, but this is still much higher than the expected effect of small ejection velocities.

From the dynamical point of view, the problem of cometary or asteroidal origin is essentially a problem of the aphelion distances of the parent bodies. If the aphelion distance is larger than, or at least approximately equal to, the heliocentric distance of Jupiter, a cometary origin appears beyond doubt even when the comet cannot be identified. If the aphelion is located distinctly inside the orbit of Jupiter, a direct identification of the parent body is generally impossible, and the possible evolutionary paths from the comet or asteroid system must be considered.

One meteor shower, the Geminids, is of particular interest in this respect. Most members of this shower, optically the strongest permanent shower in the northern hemisphere, have their aphelia concentrated within a range of r from 2.5 to 2.7, right in the middle of the asteroid belt. It is absolutely impossible to assume a displacement of this entire stream from a Jupiter-crossing orbit, and therefore an orbit of small aphelion distance must previously have been occupied by the parent body. It appears highly probable that this was a comet; but if this is true one has to explain how the aphelion has escaped from the comet system.

There are several additional streams for which parent comets are unknown, and some of them also have aphelia situated far inside the orbit of Jupiter. These streams are characterized by relatively small perihelion distances (δ Aquarids—0.08, Arietids—0.09, Geminids—0.14, ι Aquarids—0.21, ζ Perseids—0.34) compared with the streams of known comets (Draconids—0.99, Leonids—0.98, Perseids—0.95, Lyrids—0.92, Ursids—0.92, Andromedids—0.86, Orionids—0.58). Loosely dispersed streams of known parent comets show intermediate values (α Capricornids—0.56, Taurids—0.34, β Taurids—0.34). This evidence supports the explanation that the absence of a parent comet might be simply a consequence of its early extinction or disintegration in an orbit lying close to the Sun.

A considerable reduction of aphelion distance is a prerequisite of the effective operation of nongravitational forces in the third phase of evolution. For larger particles the gravitational perturbations by Jupiter make this rather difficult. According to Öpik (1951) and Whipple (1955) there is very little chance that particles with diameters exceeding 0.1 cm can be transported across the Jupiter barrier. However an important object, Comet Encke, proves that comets really can contract their orbits down to $Q=4.1$, at least. Comet Encke is a relatively large object which may have survived many more revolutions in its present orbit than has an average short-period comet. Even so its uniqueness demonstrates that a transition into an orbit of this type is a possible but very rare event, occurring perhaps once in 10^4 years.

THE TISSERAND INVARIANT

It follows from the general features of the solar system that the major orbital changes of the parent bodies of the meteoroids are due to perturbations by Jupiter. Approximating Jupiter's action by the restricted three-body problem, we can use a function of the elements of maximum stability, the simplified Jacobian integral or Tisserand invariant,

$$T=a^{-1}+2a_j^{-3/2}a^{1/2}(1-e^2)^{1/2}\cos i \qquad (1)$$

and consider the evolutionary paths along which this function maintains its constant value. Where the inclination remains low, $\cos i \simeq 1$, leaving a function of two variables

$$T_0=a^{-1}+2a_j^{-3/2}a^{1/2}(1-e^2)^{1/2} \qquad (2)$$

which is almost constant.

An analysis of available long-term integration of cometary orbits (Narin and Pierce, 1964; Kazimirchak-Polonskaya, 1967; Belyaev, 1967;

Marsden, 1968, 1969a, 1970a, 1970c; Everhart and Raghavan, 1970; etc.) enables us to obtain a general insight into the degree of stability of T and T_0, and on the relative importance of different sources of variations in these quantities.

Most serious is the effect of the eccentricity of Jupiter's orbit, neglected in the restricted three-body problem. This produces mean absolute changes in T of ± 0.001 after approaches to within 0.3 AU and ± 0.005 after approaches to 0.1 AU. The former case occurs, for an average short-period comet, once in about 200 years, the latter case once in about 1000 years. During a total integration time of about 10 000 years, no change exceeding ± 0.028 has been recorded. The mean cumulative effect can be estimated at ± 0.001 per century, with 2 to 3 percent probability of a change exceeding ± 0.010 per century. The changes due to perturbations by other major planets are generally smaller than the effect of Jupiter's eccentricity, the extreme value recorded being -0.007 after an approach to within 0.2 AU of Saturn. This obviously cannot happen to a comet of the Jupiter family.

The splitting of comet nuclei is found to introduce changes of the order of $\pm 10^{-5}$ to 10^{-4}; but after the tidal disruption of Sun-grazing comets changes of ± 0.001 to 0.002 have been observed. The present secular acceleration or deceleration of periodic comets by jet effects (Marsden, 1968) introduces changes of ± 0.001 in 10^3 to 10^4 years, with the extreme of $+0.001$ per 300 years for P/Honda-Mrkos-Pajdušáková and P/Encke. It is obviously possible that a rapid mass loss, especially for comets of very small perihelion distance, can make the changes appreciably higher and progressive.

The variations in T_0 for short-period comets, are, on the average, twice as large as those in T. The variations in a^{-1}, the Jacobian constant in the two-body problem or in the three-body problem with a fixed coordinate system, are as much as 20 times as large. No checks were attempted for the asteroids, but it is evident that in this case some of the above effects are absent, and the remaining ones much smaller than for the comets.

These quantitative estimates suggest that a crossing of the Jupiter barrier, and the subsequent transition into an orbit of the Geminid or Apollo type, is possible only if the original value of T is near 0.58. The limitations of this process can be shown in a diagram with paths of constant T_0 plotted as a function of semimajor axis and eccentricity (fig. 1). A comet starting from Oort's cloud could be observed from the Earth if the combined stellar and planetary perturbations significantly reduced its perihelion distance. Since T_0 is always smaller than $0.25q^{1/2}$ for $P>800$ yr, and T is always smaller than T_0, we can observe only long-period comets with the Jacobian constant far below the critical value of 0.58, for which $q>6$. From this source long-period meteor streams of random inclination are derived, such as the Lyrids (Comet 1861 I), Perseids (Comet 1862

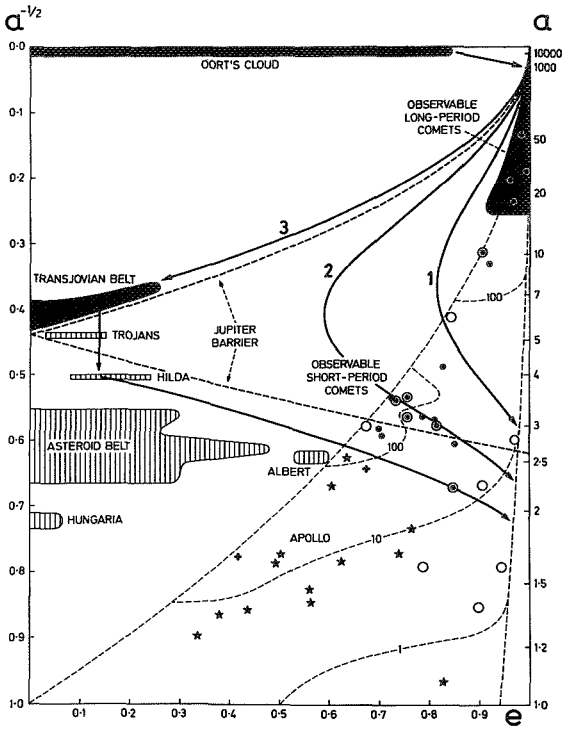

FIGURE 1.—Potential evolutionary paths of comets into short-period orbits. Heavy line (1) for $T_0=0.40$; (2) for $T_0=0.50$; (3) for $T_0=0.585$. Individual known objects are indicated only if the Earth-crossing condition $q<1$ (dashed curve close to the diagonal) is satisfied. Black dots are short-period comets; circles, meteor streams; stars, Apollo asteroids; crosses, meteorites. Thin dashed lines within the limits $q=0.06$ (curve at extreme right) and $q=1.00$ indicate the corrected relative abundances, 1, 10, and 100, of Super-Schmidt meteors for different combinations of $a^{-1/2}$ and e (Kresák, 1967).

III), Orionids and Aquarids (P/Halley), and Leonids (P/Tempel-Tuttle).

The capture of long-period comets, presumably with $q=3$ to 5, into Jupiter's family is characterized by $T_0=0.40$ to 0.50 (curves 1 and 2 in fig. 1) and low inclination. The aphelia of these comets concentrate near the Jupiter barrier and are not allowed to recede far from it toward the Sun. Examples of this type among meteor streams are the Andromedids (P/Biela), Draconids (P/Giacobini-Zinner), η Ursids (P/Pons-Winnecke), Bootids (P/Schwassmann-Wachmann 3), and α Capricornids (P/Honda-Mrkos-Pajdušáková). It may be noted that these streams tend to produce temporary displays of short duration, whereas the major long-period showers are of annual appearance and longer duration. Differences in total mass, geocentric velocity and strength of perturbations by Jupiter may be held responsible for this statistical distinction, without the necessity of assuming any differences in origin. The Ursids (P/Tuttle) represent a transition between the two groups.

The concentration of sporadic meteors in the two principal ranges of comet orbits is clearly recognized in every systematic meteor survey, thus presenting a satisfactory evidence of the cometary origin of these objects. On the other hand, a sharp cut-off of aphelia at the Jupiter barrier is missing, and the cisjovian orbits of some meteors have no counterpart in the system of comets. The only gap through which the aphelia can pass the barrier is situated at the highest eccentricities and smallest perihelion distances. These characteristics, best represented by the δ Aquarids and Arietids, would induce a rapid mass loss, and a comet in such an extreme situation would not survive long. Even the meteoroids following its orbit would be relatively short-lived, as confirmed by the sharp cut-off in the distribution of perihelion distances of meteors at about $q=0.06$, and by some physical peculiarities of meteors just above this limit (Kresák, 1968).

EVOLUTIONARY PATHS

The most promising evolutionary path (labeled 3 in fig. 1, $T_0=0.585$) leads along the outer edge of the Jupiter barrier. It requires first a capture from a low-inclination orbit, approaching Jupiter from outside ($q\simeq 6$), into a low-eccentricity orbit between Jupiter and Saturn. Accretion of comets in the solar nebula near the present orbits of Uranus and Neptune, with initial low-eccentricity orbits and some spiraling inward (Whipple, 1973) would make this step unnecessary. The latter alternative appears much more plausible from the dynamical point of view, however the long storage of comet-like objects at relatively small distances from the Sun may pose additional problems. In spite of the basic difference between these two processes, the ambiguity is rather irrelevant during the last phase of evolution, since we have satisfactory evidence that a Transjovian belt of comets does exist at present (Kresák, 1972). Members of this belt of comets are generally unobservable from the Earth, with the exception of the abnormally bright and active Comet Schwassmann-Wachmann 1. Nevertheless, long-term integrations indicate that at least three other comets (P/Oterma, P/Whipple and P/Shajn-Schaldach, the latter two probably being separated components of one primordial comet) have been captured from this belt since 1850, and one (P/Oterma) was ejected back into the belt. The frequency of documented events of this type is large compared with but one capture from a long-period orbit into the Jupiter family during the same period (P/Kearns-Kwee).

During close approaches to Jupiter, which are obviously of low relative velocity and long duration, members of the Transjovian belt can make a double crossing of the Jupiter barrier, from $q=a(1-e)>a_j$ to $Q=a(1+e)<a_j$. Subsequent evolution may permit them to change into orbits of the type of Comet Encke. A favorable interplay of perturbations is necessary, with several decelerating approaches to Jupiter, but the process is possible. An approximate $3/2$ resonance with Jupiter immediately after crossing of the barrier may trigger this trend of evolution if the initial mean motion is equal to, or slightly above, the exact resonance value. In its low-eccentricity stage the path touches the region of the Hilda asteroids. If any of them should happen to escape from the librating motion (according to Schubart, 1968, two of 21 numbered Hilda asteroids are not librating, but these are just objects of low eccentricity and small aphelion distance), it might evolve in a similar manner.

Non-gravitational effects would begin to act

much more effectively on an orbit situated entirely within the orbit of Jupiter; this refers not only to the jet effects of escaping matter on live comet nuclei but also the sunward drift of solid particles separated from them. The concentration of sporadic meteor orbits around $e\simeq0.65$, $a\simeq2.8$, $Q\simeq4.6$, adjoining the concentration of the Jupiter family around $e\simeq0.70$, $a\simeq3.3$, $Q\simeq5.6$, may be associated with this evolutionary path.

Also, not far from this area the Albert group of the asteroid belt comes closest to the Earth-crossing limit $q=1$. A definite displacement of the maximum concentration of the bright Prairie Network fireballs, including also the Příbram Meteorite, relative to that of the faint Super-Schmidt meteors (McCrosky, 1968) suggests than many larger meteoroids may have originated from asteroidal collisions. It may be noted that the size dependence of the drag effects of solar radiation would require just the reverse arrangement of orbits, with smaller particles situated inside the orbits of the larger ones.

Similar drag effects would also transport asteroidal meteoroids, produced by low-velocity collisions, from the main belt through the zodiacal cloud to the Sun. Since these effects tend to reduce the original eccentricities, most of the particles would reach the Earth with $e<0.10$, and only a very small fraction with $e>0.25$. This condition restricts the corresponding region of occurence of asteroidal meteors to the lower left edge of the diagram, and the Cyclid stream (Southworth and Hawkins, 1963) can be possibly a result of this process. The concentration of Apollo asteroids around $e\simeq0.40$, $a\simeq1.5$, $Q\simeq2.1$, including Eros as the largest representative with $q>1$, and the Lost City Meteorite, may be possibly related to the capture process of Mars investigated by Öpik (1963). The high-eccentricity asteroids of the type of Icarus or Apollo, and the unknown parent bodies of the Geminid, Arietid and other streams, may be extinct comets which may have experienced a similar evolution to what Comet Encke is now undergoing.

DISTRIBUTIONS IN THE JACOBIAN CONSTANT

Some insight into the relative contribution of meteors of different origin can be obtained by comparing the distribution of meteor orbits in T with that of their potential parent bodies. This is done in figure 2 for the asteroids, bright fireballs, faint meteors and comets. Percentages of T within ranges of special interest are listed in tables 1 and 2; for each type of object both the observed and corrected values are given.

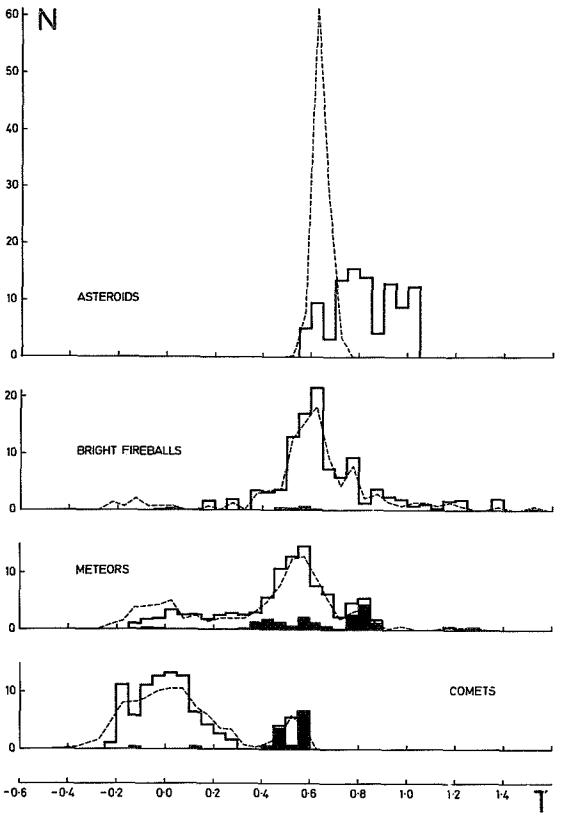

FIGURE 2.—Normalized distributions of different types of objects in the Jacobian constant T. Vertical scale, percentage for $\Delta T=0.05$. Broken lines, observed distribution; histograms, corrected distribution; black areas, contribution of shower meteors or comets associated with them.

The Asteroids

The observed distribution is taken from the list of 1746 numbered asteroids (Chebotarev, 1970). The corrected distribution includes 13 known asteroidal objects with $q<1$, both numbered and unnumbered (Chebotarev, 1970; Marsden, 1969b, 1970c, 1971; Van Houten et al.,

TABLE 1.—*Observed Abundance in Different Ranges of* T (*Percentages*)

Jacobian constant T characteristic objects	<0.30 long-period comets	0.30–0.55 short-period comets	0.55–0.60 transitional zone	0.60–0.75 normal asteroids	>0.75 Apollo asteroids
Asteroids	—	0.3	8	91	0.2
Comets	86	10	4	—	—
Sporadic meteors:					
Super-Schmidt meteors	29	24	11	17	19
Bright Super-Schmidt meteors	32	30	13	17	8
Small camera meteors	33	37	11	17	2
Bright fireballs	7	22	15	33	23
Brightest fireballs, $H_E>30$ km	12	38	12	19	19
Brightest fireballs, $H_E<30$ km	—	—	—	67	33
Meteorites	—	—	—	50	50
Shower meteors:					
Super-Schmidt meteors	34	18	7	8	33
Bright Super-Schmidt meteors	20	30	13	14	23
Small camera meteors	40	10	10	9	31
Bright fireballs	38	25	25	12	—
Meteor showers included	Leonids Orionids Perseids Lyrids	Quadrantids δ Aquarids Draconids ι Aquarids[a]	α Capricornids[a] N. Taurids[a]	S. Taurids[a]	Geminids

[a] Some shower meteors also in adjacent ranges of T.

1970). To account for the observational selection, this sample was corrected by a weighting factor

$$f_1=[2-a^{-1}-a(1-e^2)]^{1/4}$$
$$\times[3-a^{-1}-2a^{1/2}(1-e^2)^{1/2}\cos i]^{-1/4}\sin^{1/2}i \quad (3)$$

representing a square root of the inverse probability of impact per revolution according to Öpik (1951), in relative units. The square root was chosen as a reasonable compromise between the discovery probability of the smallest asteroids detected at very close approaches to the Earth (Apollo, Adonis, Hermes) and that of larger bodies detected at greater geocentric distances. The difference between the observed and corrected distribution is striking indeed, and displaces the values much farther from the critical limit $T=0.58$ into the asteroid region. On the other hand, we do not know how many, and which, Apollo objects are original asteroids.

The Comets

A total of 607 orbits of different comets (Porter, 1961; Marsden, 1966, 1970c) was used to find the observed distribution in T. The corrected distribution was determined from 220 returns of 162 different comets with $q<1$, observed during the last hundred years (1871 to 1971). It was attempted to make the resulting data directly comparable with meteor statistics corrected by Whipple's (1954) cosmic weight factors, involving the reciprocal probability of encounter per revolution and the magnitude-velocity dependence. All returns during which periodic comets should have been recovered, even without prediction, were counted. After comparing the distribution of peak apparent magnitudes for independent and predicted discoveries of the last hundred years, the following form of weighting factors was tentatively adopted:

$$\begin{aligned} f_2&=1 && \text{for } m\leq m_0 \\ f_2&=0.4^{m-m_0} && \text{for } m>m_0 \\ f_2&=0 && \text{for no recovery} \end{aligned} \quad (4)$$

Here m_0 denotes the maximum apparent magnitude of the comet during the discovery apparition, or the average from all apparitions during which the comet was located without prediction; m denotes the maximum apparent magnitude during the predicted return in question. The values

TABLE 2.—*Corrected Abundance in Different Ranges of* T (*Percentages*)

Jacobian constant T characteristic objects	<0.30 long-period comets	0.30–0.55 short-period comets	0.55–0.60 transitional zone	0.60–0.75 normal asteroids	>0.75 Apollo asteroids
Asteroids	—	—	5	27	68
Comets	83	10	7	—	—
Sporadic meteors:					
Super-Schmidt meteors	20	27	9	19	25
Bright Super-Schmidt meteors	24	36	16	17	7
Small camera meteors	23	47	9	19	2
Bright fireballs	4	23	17	32	24
Brightest fireballs, $H_E>30$ km	5	40	15	16	24
Brightest fireballs, $H_E<30$ km	—	—	—	74	26
Meteorites	—	—	—	50	50
Shower meteors:					
Super-Schmidt meteors	9	19	5	6	61
Bright Super-Schmidt meteors	6	29	11	11	43
Small camera meteors	14	7	7	8	64
Bright fireballs	8	47	35	10	—
Meteor showers included	Leonids Orionids Perseids Lyrids	Quadrantids δ Aquarids Draconids ι Aquarids[a]	α Capricornids[a] N. Taurids[a]	S. Taurids[a]	Geminids

[a] Some shower meteors also in the adjacent ranges of T.

of m_0 and m were extracted from Vsekhsvyatsky's (1958) summaries of observations up to 1955, and from various sources (e.g., Vsekhsvyatsky's Supplements, Porter's and Marsden's Annual Reports for the R.A.S.) for the last fifteen years. By this procedure, for example, a total weight of 12.9 was assigned to 29 observed returns and one missed return of P/Encke, a total weight of 6.5 to 10 observed and 10 missed returns of P/Grigg-Skjellerup, etc. Only the returns with $q<1$ were taken into account, e.g., prior to 1918 for P/Pons-Winnecke or prior to 1910 for P/Finlay. A separate solution was made for those comets for which associated meteor showers are known.

Bright Fireballs

The orbits are taken from a list of 141 Prairie Network meteors (McCrosky, 1968, 1970). The low proportion of shower meteors (black areas in fig. 2) is partly due to an intentional selection of sporadic meteors for reduction, and partly to an instrumental limitation by minimum duration. The correction factor reducing the observed numbers to the relative numbers of meteors colliding with the Earth per revolution, is Whipple's (1954) cosmic weight,

$$f_3 = V_G V_\infty^{-4}[2-a^{-1}-a(1-e^2)]^{1/2}\sin i \quad (5)$$

where V_G and V_∞ are the geocentric and no-atmosphere velocity, respectively. In contrast to the asteroids, the changes introduced by the corrections are relatively insignificant, except for a reduction of the contribution of high-velocity meteors associated with long-period comets. In the corresponding range of negative and small positive values of T, the effects of instrumental selection make the frequency rather indeterminate and seriously underestimated (Kresák, 1970). Even so the main feature of the distribution is a pronounced maximum at $T=0.55$ to 0.65 and $Q=3.5$ to 4.5, in a region adjacent to the Albert group of asteroids.

Faint Meteors

The orbits were taken from the list of 413 best measurable Super-Schmidt meteors (Jacchia and Whipple, 1961). Some selection effects, especially a preference for meteors of longer duration, are

involved. However, there is no substantial difference in the distribution of orbital elements compared with the complete list of the orbits of lower accuracy (McCrosky and Posen, 1961). Cosmic weight was introduced by relation (5), as in the preceding case, and the difference between the corrected and observed distribution in T was again found rather insignificant. In spite of a gross agreement, definite distinctions between faint meteors and bright fireballs can be recognized. As already pointed out by McCrosky (1968), the aphelia of Super-Schmidt meteors tend to concentrate farther from the Sun, approximately at the distance of Jupiter. This moderate difference is sufficient to shift the maximum occurrence of T from asteroidal values (above 0.58) to cometary ones (below 0.58). In the a/e diagram (fig. 1) this means a displacement from the neighborhood of the Albert asteroids to the evolutionary path via the Transjovian belt and to the Jupiter family. The long-period cometary contribution of $T<0.30$ is more pronounced for the faint meteors, the short-period Apollo-type contribution of $T>0.75$ for the bright fireballs, but these differences are affected by observational selection.

Observed and corrected numbers of meteors within five ranges of Jacobian constant T are intercompared in tables 1 to 3, where two additional meteor samples, 144 Harvard small-camera meteors (Whipple, 1954) and 359 randomly selected faint Super-Schmidt meteors (Hawkins and Southworth, 1961) are included. Two groups of the absolutely brightest fireballs (McCrosky, 1970; Ceplecha, 1970), selected according to the end heights, and two meteorites, Příbram and Lost City, are also added.

Two significant conclusions regarding meteor streams may be drawn from these data. First, meteor showers, in particular the Geminids, occur even in the range of a high asteroidal Jacobian constant, which obviously does not necessarily mean an asteroidal origin. Second, the dispersion in T within meteor streams is surprisingly large compared with the expected variations due to all perturbing effects considered in this paper. The mean deviations within individual showers range between ± 0.010 (Perseids, Quadrantids, Orionids) and ± 0.050 (Taurids, Aquarids). This dispersion is definitely not due to measuring errors, and is consistent with the observed radiant scatter which does not involve the inevitable errors in velocity determination. It may be noted that the mean differential velocities within most of the major showers range between 0.3 and 1.5 km/s, and that the relative velocities of the northern and southern components of the twin ecliptical streams (Taurids, δ Aquarids, ι Aquarids) are as high as 4 to 12 km/s (Kresák and Porubčan, 1970). In contrast to this, the separation velocities of persistent components of split cometary nuclei range between 0.002 and 0.04 km/s (Stefanik, 1966), and ejection velocities of small solid particles computed for the icy-conglomerate model (Whipple, 1951) are of the same order of magnitude. It is also interesting to note that even the dispersion of Jacobian constants within the asteroid families is one order of magnitude smaller than within compact meteor streams, ranging from ± 0.0006 for the Eos family to ± 0.006 for the Phocaea family.

It is essential that the mutual compensation of the two terms of equation (1), characteristic for perturbations by Jupiter and very clearly born out by the comets, is entirely absent in meteor streams. While the perturbational changes in T (the Jacobian integral in the rotating coordinate system of the restricted three-body problem) remain about 20 times smaller than those in a^{-1} (the Jacobian integral in the two-body problem) for the comets, the dispersion in both of these quantities is essentially equal in meteor streams. While the orbits of individual members of a stream appear much more alike than the orbits of one heavily perturbed comet at different epochs, the differences in the Jacobian constant are much greater in the former case.

This contradiction suggests that the evolution of meteor orbits cannot be satisfactorily interpreted in terms of gravitational effects alone. An identification of the additional forces with the drag effects of solar radiation would require a distinct magnitude separation at least within the showers whose parent comets are already inactive, and therefore unobservable. Although there are some observations indicating separation of this kind, this is always much less pronounced than the total non-selective dispersion. The drag effects would also require an increase of the mean Jacobian constant with decreasing particle size. However, a comparison of the Prairie Network

TABLE 3.—*Explanations and References to Tables 1 and 2*

Type of object	Mean absolute magnitude[a]	Number of objects			Source
		Total	$q<1$	In showers	
Numbered asteroids	+11.5	1743	3	—	Chebotarev, 1970
Unnumbered asteroids	+17.0	10	10	—	Different sources
Comets	+ 6.8	607	162	—	Porter, 1961; Marsden, 1966, 1970c
Super-Schmidt meteors	+ 1.2	359	343	61	Hawkins and Southworth, 1961
Bright Super-Schmidt meteors	+ 0.1	413	390	92	Jacchia and Whipple, 1961
Small camera meteors	− 4.2	144	143	58	Whipple, 1954
Bright fireballs	− 8.5	141	140	8	McCrosky, 1968, 1970
Brightest fireballs, $H_E>30$ km	−12.5	16	16	—	McCrosky, 1970; Ceplecha, 1970
Brightest fireballs, $H_E<30$ km	−18.0	9	9	—	
Meteorites	−15.5	2	2	—	

[a] At $r=1$, $\Delta=1$ for the asteroids (Gehrels scale) and comets (Vsekhsvyatsky scale); at $\Delta=100$ km for meteors (photographic, maximum light, Harvard scale).

fireballs with the faint Super-Schmidt meteors revealed just the opposite effect.

Attempts were also made to check the presence of librating motions among meteor orbits. These motions seem to be of considerable importance in the evolution of comets and asteroids (Marsden, 1970b; Kresák, 1972). For meteors there is a slight preference for $^3/_1$ and $^4/_1$ resonances with Jupiter (Kresák, 1969), but no simultaneous preference for any particular values of the libration argument, which would make this irregularity significant.

FIREBALL END HEIGHTS

Although the associated problems of meteor physics are beyond the scope of this paper, one correlation of the atmospheric phenomena with the Jacobian constant of the incident particle may be pointed out. Six years of operation of the Prairie Network and the European Network of all-sky cameras (McCrosky and Ceplecha, 1969) yielded a surprisingly low gain in the recovery of meteorites compared with the number of brilliant fireballs recorded. This disproportion may point to the existence of two or more types of meteor bodies of different resistances to atmospheric disintegration and possibly, but not necessarily, different types may come from parent bodies of different natures. The parameter for deciding whether we may or may not expect a meteorite fall from a fireball is the end height of the luminous trajectory H_E. Another important quantity involved both in the mass-brightness dependence and in the resulting end height is the no-atmosphere velocity V_∞.

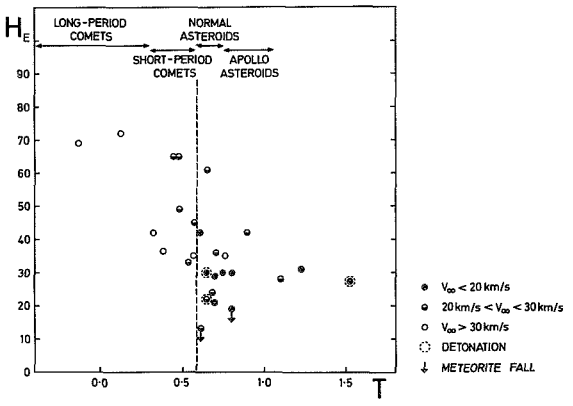

FIGURE 3.—A plot of meteor end height H_E against the Jacobian constant T for very bright fireballs ($M_p<-12$). The fireballs are identified by symbols based on the no-atmosphere velocity V_∞, and the presence of detonation and meteorite fall. The lower-end heights for asteroidal values of T ($T>0.58$, to the right of the vertical line) is clearly exhibited.

By courtesy of R. E. McCrosky and Z. Ceplecha, detailed data on the brightest fireballs recorded

by the Prairie Network and the European Network have been obtained. The brightness limit was set at $M_p = -12$, and values of the Jacobian constant computed from the orbital elements were plotted against the end heights. The result is shown in figure 3, with different velocity groups denoted by different symbols to show the possible role of the velocity effect. It is seen that fireballs with a higher extinction level, about 35 km and more, show a preponderance of cometary values, $T < 0.58$, entirely consistent with the situation among faint Super-Schmidt meteors. In contrast to this, a lower extinction level is, without exception, associated with asteroidal values of T. This dependence is definitely more pronounced than the obvious relation between V_∞ and H_E. A comparison with the ranges of T occupied by different types of larger objects (fig. 3) suggests that the H_E/T dependence may actually be connected with the nature of the parent body; if so, the asteroidal component should prevail slightly over the cometary component at $M_p < -12$. However, this assumption would not explain the disproportion between the frequency of bright fireball events and meteorite falls, and nonuniform physical properties within each of the two fundamental groups appear probable.

ACKNOWLEDGMENTS

The author is greatly indebted to B. G. Marsden, R. E. McCrosky and Z. Ceplecha for kindly putting at his disposal some of the orbital data used in this paper in advance of publication.

REFERENCES

Belyaev, N. A., 1967. The orbit evolution of comets Neujmin 2 (1916 II), Comas Sola (1927 III), Schwassmann-Wachmann 2 (1929 I) for 400 years (1660–2060), *Astron. Zh.*, **44**, 461–470.

Ceplecha, Z., 1970. private communication.

Chebotarev, G. A., 1970. *Ephemerides of minor planets for 1971*, Nauka, Leningrad, 166 pp.

Everhart, E., and Raghavan, N., 1970. Changes in total energy of long-period comets, 1800–1970, *Astron. J.*, **75**, 258–272.

Hawkins, G. S., and Southworth, R. B., 1961. Orbital elements of meteors, *Smithson. Contrib. Astrophys.*, **4**, 85–95.

Jacchia, L. G., and Whipple, F. L., 1961. Precision orbits of 413 photographic meteors, *Smithson. Contrib. Astrophys.*, **4**, 97–129.

Kazimirchak-Polonskaya, H. I., 1967. Evolution des orbites des comètes a courte période au cours des années 1660–2060 et le rôle des planètes extérieures dans cette évolution, *Astron. Zh.*, **44**, 439–460.

Kresák, Ľ., 1967. Relation of meteor orbits to the orbits of comets and asteroids, *Smithson. Contrib. Astrophys.*, **11**, 9–34.

——, 1968. The relation between orbits and physical characteristics of meteors, in *Physics and Dynamics of Meteors*, edited by Ľ. Kresák and P. M. Millman, D. Reidel Publ. Co., Dordrecht, Holland, 217–235.

——, 1969. The discrimination between cometary and asteroidal meteors. II. The orbits and physical characteristics of meteors, *Bull. Astron. Inst. Czech.*, **20**, 231–251.

——, 1970. On the orbits of bright fireballs, *Bull. Astron. Inst. Czech.*, **21**, 1–9.

——, 1972. On the dividing line between cometary and asteroidal orbits, in *The Motion, Evolution of Orbits and Origin of Comets* (I.A.U. Symposium No. 45), edited by G. A. Chebotarev, H. I. Kazimirchak-Polonskaya, and B. G. Marsden, D. Reidel Publ. Co., Dordrecht, Holland, 503–514.

Kresák, Ľ., and Porubčan, V., 1970. The dispersion of meteors in meteor streams, I. The size of the radiant areas, *Bull. Astron. Inst. Czech.*, **21**, 153–170.

Marsden, B. G., 1966. Supplementary catalogue of cometary orbits, *Mem. Brit. Astron. Assoc.*, **40**, No. 2, 19 pp.

——, 1968. Comets and nongravitational forces, I, *Astron. J.*, **73**, 367–379.

——, 1969a. Comets and nongravitational forces, II, *Astron. J.*, **74**, 720–734.

——, 1969b. Elements and ephemerides, *Minor Planet Circ.*, Nos. 3014–3016.

——, 1970a. Comets and nongravitational forces, III, *Astron. J.*, **75**, 75–84.

——, 1970b. On the relationship between comets and minor planets, *Astron. J.*, **75**, 206–217.

——, 1970c. private communication.

——, 1971. 1971 FA, *Circ. Bur. Central Telegr. Astron.*, No. 2320.

McCrosky, R. E., 1968. Orbits of photographic meteors, in *Physics and Dynamics of Meteors*, edicted by L. Kresák and P. M. Millman, D. Reidel Publ. Co., Dordrecht, Holland, 265–279.

——, 1970. private communication.

McCrosky, R. E., and Ceplecha, Z., 1969. Photographic networks for fireballs, in *Meteorite Research*, edited by P. M. Millman, D Reidel Publ. Co., Dordrecht, Holland, 600–612.

McCrosky, R. E., and Posen, A., 1961. Orbital elements of photographic meteors, *Smithson. Contrib. Astrophys.*, **4**, 15–84.

Narin, F., and Pierce, P. M., 1964. Perturbation, sighting and trajectory analysis for periodic comets, *Illinois Research Inst. Astro Sci. Center*, Rept. T–7, 107 pp.

Öpik, E. J., 1951. Collision probabilities with the planets and the distribution of interplanetary matter, *Proc. Roy. Irish Acad.*, **54A**, 165–199.

——, 1963. The stray bodies in the solar system, I. Survival of cometary nuclei and the asteroids, *Advan. Astron. Astrophys.*, **2**, 219–262.

Porter, J. G., 1961. Catalogue of cometary orbits, *Mem. Brit. Astron. Assoc.*, **39**, No. 3, 97 pp.

Schubart, J., 1968. Long-period effects in the motion of Hilda-type planets, *Astron. J.*, **73**, 99–103.

Southworth, R. B., and Hawkins, G. S., 1963. Statistics of meteor streams, *Smithson. Contrib. Astrophys.*, **7**, 261–285.

Stefanik, R. P., 1966. On thirteen split comets, *Mém. Soc. Roy. Sci. Liège*, **12/1**, 29–32.

Van Houten, J. C., Van Houten-Groeneveld, I., Herget, P., and Gehrels, T., 1970. The Palomar-Leiden survey of faint minor planets, *Advan. Astron. Astrophys. Suppl.*, **2**, 339–448.

Vsekhsvyatsky, S. K., 1958. *Fizicheskie kharakteristiki komet*, Gos. Izdatel'stvo fiziko-matematicheskoj literatury, Moskva, 575 pp.

Whipple, F. L., 1951. A comet model II. Physical relations for comets and meteors, *Astrophys. J.*, **113**, 464–474.

——, 1954. Photographic meteor orbits and their distribution in space, *Astron. J.*, **59**, 201–217.

——, 1955. A comet model. III. The zodiacal light, *Astrophys. J.*, **121**, 750–770.

——, 1973. Radial pressure in the solar nebula as affecting the motion of planetesimals, paper no. 38, this volume.

Page intentionally left blank

35. Cometary vs Asteroidal Origin of Chondritic Meteorites (Abstract)*

GEORGE W. WETHERILL
University of California, Los Angeles
Los Angeles, California

Monte Carlo calculations indicate excellent agreement between observed and predicted orbits of Prairie network fireballs, if it is assumed that fireballs are derived from remnants of short period comets of Jupiter's family. No such satisfactory agreement has been found for any other proposed source. The distribution of radiants and time of fall observed for chondrites will also be reproduced by this source, provided that consideration is given to the fact that the Earth's atmosphere will permit low velocity bodies to survive but will destroy high velocity bodies. Again, no other proposed source has been found to be adequate.

It now appears likely that the mean lifetime of chondrites is limited to $\sim 10^7$ yr by the high probability of complete fragmentation following impact by smaller bodies. This improves the agreement between the observed cosmic ray exposure ages and those predicted for a cometary source. This also requires some modification of the earlier discussions of alternative sources, but does not result in them becoming more satisfactory.

---

* The complete paper has been published in *Physical Studies of the Minor Planets*, NASA SP-267, edited by Tom Gehrels, pp. 447–460, 1971.

Page intentionally left blank

36. Accumulation of Chondrules on Asteroids (Abstract)*

FRED L. WHIPPLE
Smithsonian Astrophysical Observatory
and Harvard College Observatory
Cambridge, Massachusetts

It is shown that aerodynamic forces could have played a significant role in the selective accumulation of chondrules on asteroids that are moving with respect to the gas in a primeval solar nebula. Particles smaller than millimeter chondrules would sweep by an asteroid moving more slowly than a critical velocity, while larger particles could be accumulated by impact. Theory and calculation cover the case of subsonic velocity and asteroidal diameter up to 50 km independent of the nebular density from 10^{-8} to 10^{-6} g cm^{-3} or higher for smaller asteroids, as illustrated in table 1.

TABLE 1.—*Limiting Velocities and Reynolds Nos. for Small Asteroids under Consideration*

Diameter of asteroid (km)	Limiting velocity (km/s)	Reynolds no.
0.1	0.0034	0.04
1.0	0.034	0.4
10.0	0.34	4.0
100.0	3.4?	40.0

The calculations are based on a solar mixture of materials at T = 550° K and on Stokes' law of aerodynamic drag, which fails for nebular densities below about 10^{-8} g cm^{-3} for millimeter sized spheres. Below this limit the limiting velocity falls off proportionally to gas density. Note that the accretion rates for small particles can be severely restricted because of aerodynamic flow at small asteroidal velocities with respect to the gas. Near and above the critical velocity the asteroidal gravity does not materially add to the accretion rate regardless of asteroidal mass.

* The complete paper has been published in *Physical Studies of the Minor Planets*, NASA SP-267, edited by Tom Gehrels, pp. 251–256, 1971.

Page intentionally left blank

37. The Early Evolution of the Solar System

A. G. W. CAMERON
Yeshiva University and
Goddard Institute for Space Studies, NASA
New York, New York

The problems of relating collapse conditions in an interstellar cloud to a model of the primitive solar nebula are discussed. In such a nebula there is a radial force balance between gravity, the pressure gradient, and centrifugal forces due to the rotation. Approximate values are given for the combinations of temperature and density throughout the nebula, from a maximum of about 2000° K near the center to less than 200° K in the outer portion. These conditions are based upon the compression adiabats in the terminal stages of the collapse of an interstellar cloud. One general conclusion, of great importance for accumulation of bodies within the solar system, is that interstellar grains should not be completely evaporated at distances in the nebula beyond about one or two astronomical units.

DURING THE LAST FEW YEARS, I have been attempting to construct quantitative numerical models of the early solar nebula, which take into account some of the physics of star formation (for refs. see Cameron, 1970). It appears that star formation is initiated when a typical interstellar cloud undergoes collapse as a result of a prior compression to a higher-than-normal density in the interstellar medium. This compression can result in part from the shock transition undergone by the gas when it flows into the spiral arm of the galaxy, and it can also occur when hot stars, newly formed in the vicinity, reach the main sequence and ionize the surface layers of the interstellar cloud. Under these circumstances, the local pressure in the vicinity of the cloud becomes considerably increased, so that the interior of the cloud can become compressed and a dynamical collapse under the force of its own gravity can take place.

During the collapse of the cloud the interior becomes exceedingly cold. This results in part from a diminishing of heating by starlight and possibly by interstellar cosmic rays, and in part from the increased cooling efficiency of the gas. Temperatures of the order of 5 or 10° K may be reached. At these temperatures the speed of sound in the cloud is very small, so that pressure waves are unable to transmit from one part of the cloud to a more distant part any information about the current state of collapse of the first part of the cloud. This promotes the fragmentation of the cloud into smaller pieces, and progressive fragmentation should take place as the collapse proceeds.

The question of the angular momentum to be associated with the cloud fragments is a complicated problem. Since the collapse of the cloud should be initiated by compressive processes, then a great deal of turbulence should be present in it from the beginning of the collapse. The kinetic energy of the turbulence acts like a gas which compresses with a ratio of specific heats of $\frac{5}{3}$, while at the same time the temperature in the interior is decreasing as a result of the enhanced cooling efficiency. Hence, the relative energy

content in the turbulence will progressively increase until typical turbulent velocities become sonic. If these velocities were to become supersonic, they would be rapidly dissipated by shock phenomena. Hence the total internal energy in the form of turbulence will be comparable to the thermal energy of the cloud during the collapse phase. There will be a random turbulent component of the angular momentum in any given fragment of the cloud, which is likely to exceed the angular momentum that the fragment would have as a result of the initial rotation of the cloud itself. The turbulent component of the angular momentum will undergo a wide range of statistical variation.

Another complicating feature will be some redistribution of the angular momentum within a cloud fragment. A fragment presumably is formed as a result of a density fluctuation in the cloud, and hence it forms about some spot in the cloud where the density reaches a local maximum. As the fragment continues to collapse, the center will collapse more rapidly than the periphery of the fragment, so that the center will achieve a higher angular velocity than the periphery, and hence there can be a turbulent transfer of angular momentum from the central region to the exterior as the fragment collapse proceeds.

These general considerations lead me to believe that the fragments of the gas cloud will have both a wide variation in their total angular momentum, and also a considerable variation in the internal distribution of their angular momentum. Hence we have no good *a priori* basis for choosing a particular distribution of angular momentum within such a fragment, nor a total angular momentum for a fragment, in constructing any theory of the formation of the solar system. One should construct a theory which contains the angular momentum distribution as a parameter, or set of parameters, and then see whether the solar system corresponds to a particular set of such parameters. I believe that the model discussed below contains a reasonable angular momentum content to correspond to solar system conditions, but the theory described is incomplete, since at the present time the model is being used as a vehicle for the development of the necessary physical input toward further calculations.

The models which have been calculated have been based upon a spherical distribution of matter representing a fragment of an interstellar cloud. This spherical distribution of matter has been taken to be uniformly rotating, but it need not have a uniform density distribution in the interior. In fact, two cases have been taken: a uniform internal density distribution, and a density distribution which varies linearly from a central value to zero at the surface of the sphere. The model shown in figure 1 is based upon the latter assumption, but there is not a great deal of difference between the models which result from these assumptions. The total mass in the initial sphere, which is taken to collapse down to a thin disk, is two solar masses. This allows for the loss of a considerable amount of mass from the Sun in the T-Tauri phase solar wind, and also for the presence of mass in the nebula which will not be incorporated in the Sun, but which will be carried away by the T-Tauri solar wind.

When this program was started about three or four years ago, my first approach was to assume that the nebula would be very thin, so that the radial properties of the solar nebula could be considered as disconnected from the vertical properties. The radial properties were taken to be given

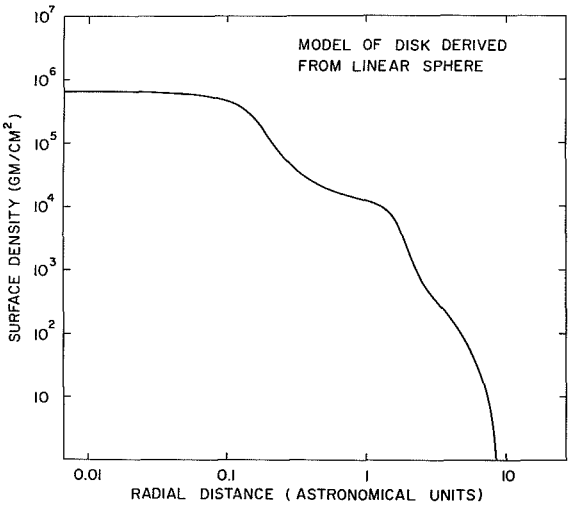

FIGURE 1.—Surface density of a two solar mass model of the primitive solar nebula, derived from a uniformly rotating sphere with a density varying linearly from a central value to zero at the surface. The radial pressure gradient has not been included in the force balance.

by a balance between gravity and the centrifugal force due to rotation, and the vertical properties were taken to be hydrostatic equilibrium, with a balance between gravity and the pressure gradient. In the latter case, any point in the nebula was considered to be part of an infinite plane having the same properties everywhere. While this proved to be a useful first orientation to the problem, both of the assumptions have proven to be inadequate, and at the present time the problem is being carried out with a partial recoupling of the vertical and radial properties in the disk.

The radial force balance in the disk is given by the following expression:

$$-\left\langle \frac{1}{\rho}\frac{dP}{dr}\right\rangle + r\Omega^2 - \frac{d\varphi}{dr} = 0 \qquad (1)$$

in which the terms represent, respectively, the average pressure gradient in the radial direction, the centrifugal force per unit mass, and the gravitational force per unit mass; ρ is the density, P the pressure, r the radial distance, Ω the angular velocity, and φ the gravitational potential.

For the vertical structure, if there were an infinite plane with the same properties everywhere, then the gravitational potential would be given by the following equation:

$$\frac{d^2\varphi}{dz^2} = -4\pi G\rho \qquad (2)$$

The hydrostatic equation, utilizing the perfect gas law, may be written in the following form:

$$-\frac{1}{\rho}\frac{dP}{dz} = \frac{N_0 kT}{\mu\rho}\frac{d\rho}{dz} \approx \frac{d\varphi}{dz} + \frac{z}{r}\frac{d\varphi}{dr} \qquad (3)$$

In the right hand side of this equation, we take the first term to be given by the solution of equation (2) for an infinite plane, and the second term is intended to represent the component of force due to a central gas concentration in the nebula which would be obtained from the equilibrium in the radial direction. The temperature gradient in the vertical direction is given by the requirement that energy be transported from the interior of the nebula to the surface, where it can be radiated away at the effective surface temperature. Radiative transfer will suffice to do this if the resulting temperature gradient proves to be subadiabatic, in which case we have

$$\frac{dT}{dz} = -\frac{3}{4ac}\frac{\kappa\rho}{T^3}L \qquad (4)$$

On the other hand, if radiative transfer would require a superadiabatic gradient, then convection will set in to transport energy in the vertical direction, and we can then assume an adiabatic temperature gradient:

$$\frac{dT}{dz} = \left(1 - \frac{1}{\gamma}\right)\frac{T}{P}\frac{dP}{dz} \qquad (5)$$

In these equations T is temperature, a is the Stefan-Boltzmann constant, c is the velocity of light, κ is the radiative opacity, L is the luminosity or rate of energy transfer, and γ is the ratio of specific heats. The rate of change of luminosity is equal to the rate at which gravitational potential energy is locally released by the contraction of the disk in the vertical direction, and is given by

$$\frac{dL}{dz} = -\rho\left(\frac{d\varphi}{dz} + \frac{z}{r}\frac{d\varphi}{dr}\right)\frac{dz}{dt} \qquad (6)$$

The solution of the vertical structure equations constitutes an eigenvalue problem, similar to that involved in the construction of a model of the stellar interior. Strictly speaking, one should follow the detailed evolution of every point in the nebula as one does for the evolution of a star, but this is far too complicated for the present approach. Instead, we assume that the relative height of the nebula at any point changes in a homologous fashion, as indicated by the following relation:

$$\frac{1}{z}\frac{dz}{dt} = \text{const} \qquad (7)$$

This allows the eigenvalue problem for the vertical structure to be solved independently of the previous history of the material.

At present the numerical solutions for the radial and vertical structure in the model of the primitive solar nebula are being carried out by Mr. Milton Pine, a graduate student at Yeshiva University. We have not yet succeeded in obtaining a full solution to the problem of the initial structure of the nebula, but we are close to it, and some of the numbers that I shall report here can be taken as correct in order of magnitude for such a model.

Figure 1 shows the structure of the two solar

mass disk in the absence of radial pressure gradients. This is the disk corresponding to the flattening of a uniformly rotating sphere in which the density varies linearly from the central value to zero at the surface. The angular momentum contained in the model happens to correspond to an assumption of corotation of the initial interstellar cloud, at the threshold of gravitational collapse, with the motion of the cloud about the center of the galaxy.

In this figure is plotted the surface density of the nebula in grams per square centimeter as a function of the radial distance in astronomical units. Notice that the dimension of the disk is comparable to the size of the solar system, so that this sort of model does not misrepresent the primitive solar nebula too badly. The surface density near the center of the disk is so small that there is no effective central body which can be called a star in the nebula. There is only a mild central density concentration in the disk.

Throughout the disk, except in the very central region, there is a large amount of shear. In this very wide range of radial distance the tangential velocity in the gas is roughly the same, about 10 km/s, so that the corresponding angular velocity varies roughly inversely as the radial distance.

This disk model is entirely two-dimensional in character. It is well known that disks of zero thickness are highly unstable against both radial and nonradial perturbations, so that rings would form in such disks if they were given a chance to do so. The method of calculation used to construct the model shown in figure 1 tends to suppress local ring instabilities in the disk but the convergence to the solution shown in the figure is a very slow one even on a very fast computer. In our earliest work I found rings in the solution near the exterior portion of the disk. These rings turned out to be solutions to the difference equations which resulted from the finite zoning used to construct the model, but they were not actual solutions to the problem. When the size of the zones was decreased, the rings disappeared. If the thickness of the nebula is sufficiently great, then the radial and nonradial instabilities are expected to be suppressed, so that no rings would be present.

The next step, which we initiated recently, was to add the radial gas pressure gradient to the force balance in the radial direction. When that was done, we found that the mathematical technique used to produce the gravitational self-consistent model in figure 1 no longer seemed to produce convergence at all. Thus in the last few months we have abandoned this method, and we have started to calculate the potential for a finite three-dimensional disk, taking into account the actual height of the disk at all points. The motivation in doing this has been to decrease the dependence of the potential calculation upon fluctuations in density on local distance scales, which tend to introduce instabilities into the problem. This potential calculation is considerably lengthier than it was in our two-dimensional approximation, and hence we have been seeking a method for solving the structure equations which does not involve an iteration procedure with matrix inversion at every step. We have not yet fully succeeded in accomplishing this, but we have produced models with approximate force balance, and these can be used to give some approximate ideas of the physical conditions to be expected in the initial solar nebula.

The introduction of the radial pressure gradient causes an expansion of the disk in the radial direction. This expansion is greater near the center of the disk than it is near the outside, and the central density is lowered to something in the vicinity of 10^5 grams per square centimeter column.

In order to determine the temperature gradient in the vertical direction, we need values for the radiative opacity. This opacity is a function of temperature and density. At the highest temperatures of interest in the nebula, opacities calculated for stellar interiors are available. At lower temperatures, the opacity is mainly due to small iron grains. The electrical conductivity of metallic iron allows the absorption of electromagnetic radiation of all wavelengths. Fortunately, the size of the grains is not important as long as the grains are small compared to the interesting wavelengths, since the opacity depends upon the total volume of the grains and not upon their total surface area. At higher pressures such triatomic molecules as water make an important contribution to the opacity, but these pressures are not encountered significantly in the model of the

initial solar nebula which we have constructed. The opacity which we have computed for this problem is shown in figure 2. The rapid changes in opacity occur at temperature and density combination where the iron grains condense out of the vapor phase. We have not taken into account the reduction in opacity that would occur if the iron should be transformed into magnetite at a temperature in the vicinity of 500° K.

One point of considerable interest is the minimum surface density required for convection to exist in the disk. We have calculated this as a function of the central temperature for the assumption that the vertical structure corresponds to a local portion of an infinite plane. This critical minimum surface density is shown in figure 3. The opacity of the iron grains dominates the determination of this critical density up to a temperature of about 1500° K. Above this, the iron disappears, and the opacity is mainly due to the H^- ion. Above 2000° K, the dissociation of hydrogen molecules sets in, which lowers the effective ratio of specific heats, so that the critical surface density is very considerably lowered once again, and it only recovers very slowly toward higher temperatures as shown in figure 3. It may be seen that in the lower temperature region, the critical surface density needed for convection is comparable to the surface densities throughout the inner regions of the disk.

There are a number of powerful dissipation mechanisms which will operate in the primordial solar nebula. In a convecting region, the very large turbulent viscosity due to the convection will cause a fairly rapid outward transport of angular momentum, which must be accompanied by an inward transport of matter and a fairly significant additional release of gravitational potential energy. However, the pressure in the middle of the plane is much greater than that in the upper vertical layers of the disk, and hence the pressure gradient near the middle is also greater than the pressure gradient near the surface. Consequently, a total force balance requires that the upper levels of the disk be rotating more rapidly than the central layers. This refers to any particular radial distance in the disk. However, in a convecting region it is required that the gas should approach a condition where the angular velocity is constant on a cylindrical surface

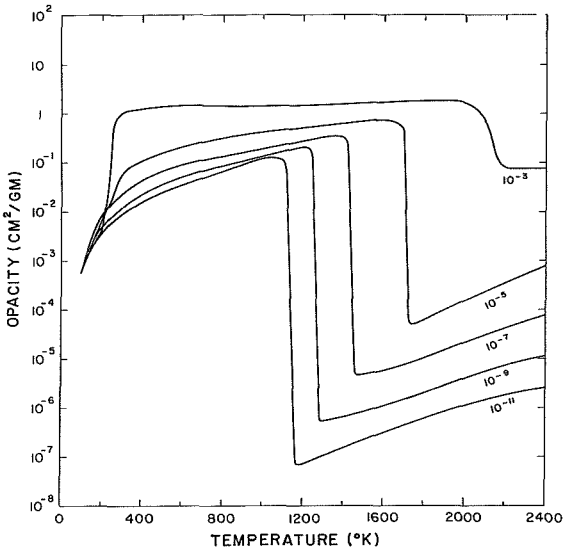

FIGURE 2.—Opacity of material of solar composition as a function of temperature for various pressures, assuming that the condensed iron grains are small compared to the important thermal wavelengths of light and that no transformation to magnetite occurs at low temperatures.

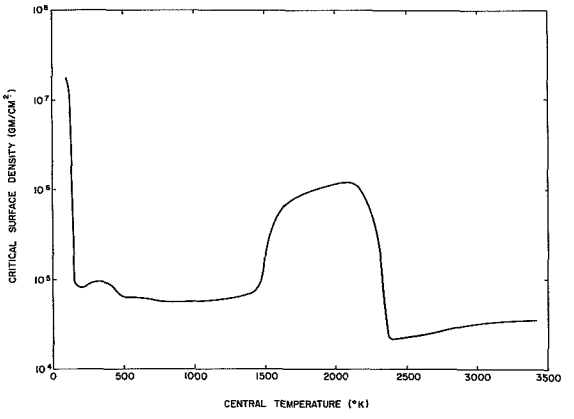

FIGURE 3.—Minimum surface densities required for convection, as a function of central temperature, for a part of an infinite plane distribution of material.

centered on the axis of rotation of the disk. This will give rise to large-scale currents in a convection zone which will rise and flow away from the center at high levels and will fall and flow inward near the center of the disk. These currents will also contribute to the rapid outward transport of angular momentum in the disk.

In a radiative region other effects take place. Here there is a force balance involving gas pressure gradients, centrifugal forces, and gravitational potential gradients. The "level surfaces" are not perpendicular to the gravitational potential gradients. Nevertheless, for a completely static situation we would require that the pressure, density, and temperature should all be constant on level surfaces. The divergence of the radiative energy flux should also be zero everywhere on a level surface, in the absence of internal energy sources. However, it is not possible to satisfy all of these conditions, and hence we cannot have a fully static solution. The divergence of the radiative energy flux can only be constant on the average over a level surface. Nearer the axis of rotation, where the temperature is higher, the excess temperature gradient will give rise to an outward flowing motion of gas, in which the divergence of the energy flux is balanced by the adiabatic expansion of the gas. Near the mid-plane of the disk on the same level surface, the negative value of the divergence of the energy flux is balanced by the adiabatic compression of the gas. This gives rise to Eddington-Sweet circulation currents. The theory of such currents has been discussed only in the limit where the centrifugal force perturbations are small compared to gravity, not comparable as in the present case. A proper theory for the present case would require full development of higher order terms, and this has not been carried out. However, I estimate that the Eddington-Sweet circulation currents in the radiative part of the solar nebula probably have velocities which are a substantial fraction of the velocity of sound.

All of these dissipation mechanisms lead to a rapid outward transport of angular momentum, and a very short dissipation time for the gas in the disk. Hence we must expect that whatever accumulation of large bodies is to take place with the assistance of the gas in the disk, must take place quickly before the Sun is formed by the dissipation of the disk, and the T-Tauri phase solar wind then sweeps away the remaining gas.

Table 1 shows some rough estimates for the physical conditions in the initial solar nebula. The combinations of temperature and density shown in the table are intended to represent values at the center of the disk. These combinations of temperature and density correspond to the final compressive adiabat to be expected in the interior of a fragment of an interstellar cloud as estimated by Larson (1969). In using this adiabat, I have ignored the alterations in it that might be produced by the shock which decelerates the material as it falls inward to form the disk through collapse of the interstellar gas fragment.

As shown in table 1, the temperature will have a maximum value in the vicinity of 2000° K near the center of the nebula, and will progressively decrease until a value of less than 200° K is reached near the outer part of the disk. The central pressure is about one millibar, and decreases to about a microbar in the outer parts of the disk. The thickness of the disk near the center is about half an AU, and this increases to become slightly more than an astronomical unit in the outer portion. Perhaps of greatest interest in terms of the accumulation of bodies in the disk are the ratios of the radial pressure gradient to the centrifugal forces at the mid-point in the plane of the disk.

TABLE 1.—*Very Approximate Initial Conditions in the Solar Nebula*

Radial distance (AU)	Surface density (g/cm^2)	Temperature (° K)	Pressure (atm)	Thickness (AU)	$\frac{\left(\frac{1}{\rho}\frac{dP_c}{dr}\right)}{r\Omega^2}$
0	1×10^{5}	2000	1×10^{-3}	0.5	1
1	5×10^{4}	1500	3×10^{-4}	0.6	0.5
5	1.8×10^{4}	640	3×10^{-5}	0.8	0.1
20	4×10^{3}	170	1.5×10^{-6}	1.1	0.03

This ratio is near unity near the center of the disk, and is still several percent in the outer portions. The significance in this ratio lies in the fact that the gas in the disk, which is partially supported by a pressure gradient, will rotate at less than Keplerian orbital velocity, whereas solid particles of significant size in the disk will not be supported by the gas radial pressure gradient, and hence will suffer a continuing gas drag, and will gradually spiral in toward the center of the nebula. This would be a general tendency which would be superimposed upon the migrations of the particles produced by the fairly strong currents which would exist in different parts of the disk.

The disk temperatures shown are probably comparable to the highest temperatures to which particles will be subjected in various parts of the disk. The disk will cool as a function of time, thus lowering the temperatures over the initial values shown in table 1. At the center of the disk, the temperature is high enough to evaporate iron and silicate materials, and hence we would expect that the interstellar grains which accompany the gas in its collapse would be destroyed inside a radial distance of 1 or 2 AU. However, the grains will not be completely evaporated at larger radial distances in the disk. The more volatile substances will be evaporated from them, but they will remain as centers of condensation for these volatiles when the temperature falls once again. Sulfur should remain in the form of troilite at distances of about 5 AU and greater. The common ices should remain in the grains at distances of the order of 20 AU and greater. This is where we should expect cometary accumulation to occur, and it is likely that cometary accumulation occurring at 20 AU and beyond has been responsible for providing the basic material which led to the accumulation of the planets Uranus and Neptune. I would not expect the ices to be present in the particles which would initially accumulate at the distance of the asteroids, Jupiter, and Saturn. I believe it more likely that rocky bodies should form at these distances, and grow in size until they are able to capture appreciable amounts of gas from the solar nebula, thus leading eventually to bodies which largely resemble the Sun in composition. In the inner solar system the large turbulent and circulatory motions of the gas are probably sufficient to limit greatly the amount of gas accumulation that can take place on forming bodies, and the subsequent T-Tauri phase solar wind should then be able to remove not-too-massive primitive atmospheres on the inner terrestrial planets.

ACKNOWLEDGMENT

This work has been supported in part by grants from the National Science Foundation and the National Aeronautics and Space Administration.

REFERENCES

CAMERON, A. G. W., 1970. Formation of the Earth-Moon system, *EOS, Trans. Am. Geophys. Union*, **51**, 628–633.

LARSON, R. B., 1969. Numerical calculations of the dynamics of a collapsing proto-star, *Monthly Notices Roy. Astron. Soc.*, **145**, 271–295.

Page intentionally left blank

38. Radial Pressure in the Solar Nebula as Affecting the Motions of Planetesimals

FRED L. WHIPPLE
Smithsonian Astrophysical Observatory and
Harvard College Observatory
Cambridge, Massachusetts

In the classical rotating Laplacian-type nebula, pressure gradients can develop radially to the protosun because of central radiation, particle ejection, and magnetic-field expansion or because of radial temperature or total gas density gradients. Except for the last two effects, the acting central acceleration for the gas is reduced from the gravitational value; the pressure gradient in the gas caused by temperature or density gradients may either add to or subtract from the gravitational acceleration, depending on the sense of the pressure gradient. Planetesimals in the nebula may thus experience tangential accelerations (+ or −) with respect to the gas because of the differential radial accelerations acting on the particles and the gas. As a consequence, the planetesimals may spiral outward or inward with respect to the protosun. The present paper deals with growing planetesimals and a range of drag laws depending on the Reynolds number and on the ratio of particle size to mean free path.

Particles spiral in the direction of positive pressure gradient, thus being concentrated toward toroidal concentrations of gas. The effect increases with decreasing rates of particle growth, i.e., with increasing time scales of planet formation by accretion. In the outer regions, where evidence suggests that comets were formed and Uranus and Neptune were so accumulated, the effect of the pressure gradient is to clear the forming comets from those regions. The large mass of Neptune may have developed because of this effect, perhaps Neptune's solar distance was reduced from Bode's "law," and perhaps no comet belt exists beyond Neptune. In the asteroid belt, on a slow time scale, the effect may have spiraled planetesimals toward Mars and Jupiter, thus contributing to the lack of planet formation in this region.

BASIC PRINCIPLES

LET US ASSUME THAT DURING PLANETARY FORMATION in our solar system, gas and dust grains constitute a Laplacian-type nebular disk rotating about a central mass, roughly that of the Sun today. The grains or planetesimals are generally accreting in all size ranges from atomic and molecular to large bodies. For smaller bodies, the gas, presumed to be approximately a solar mix, acts as a buffer against high velocities of encounter that might cause collisional destruction. The motions are fairly circular, controlled by a nearly inverse-square law of central force, while the gas and, at first, the grains are spread about the fundamental plane, held by the gas pressure against the surface gravity in the plane and the perpendicular component of the central force.

In such a system the gas pressure varies from

point to point, depending on gravity and possible magnetohydrodynamic effects if a plasma is present. Radial variations in gas pressure affect the net central radial acceleration on the gas, causing the gas to deviate from the motion appropriate to the local gravitational acceleration and therefore appropriate to the motions of the solid grains, as shown in figure 1. The grains thus meet a resisting medium and tend to move in toward the protosun or are accelerated radially outward, depending on the sense of the effective radial acceleration acting on the gas.

Let Δg be the deviation from the central gravitational acceleration acting on the gas, whether caused by spiraling magnetic fields or by a radial pressure gradient in neutral gas, dP/dr, where P is the total gas pressure and r is the radial distance to the center of the protosun. For a gas of density ρ, the radial correction to the central acceleration is, by the classical formula,

$$\Delta g = + \frac{1}{\rho} \frac{dP}{dr} \tag{1}$$

Note that in equation (1) the sign is reversed from that for stellar interiors because the gas in the nebula is held in radial equilibrium by its motion in the central gravitational field for $dP/dr = 0$. A positive pressure gradient outward from the center increases the effective central acceleration from that of gravity alone and causes the gas in equilibrium motion to rotate more rapidly. In that case, the gas accelerates the grains in their near-circular motion and causes them to move radially outward. The opposite is true for $dP/dr < 0$.

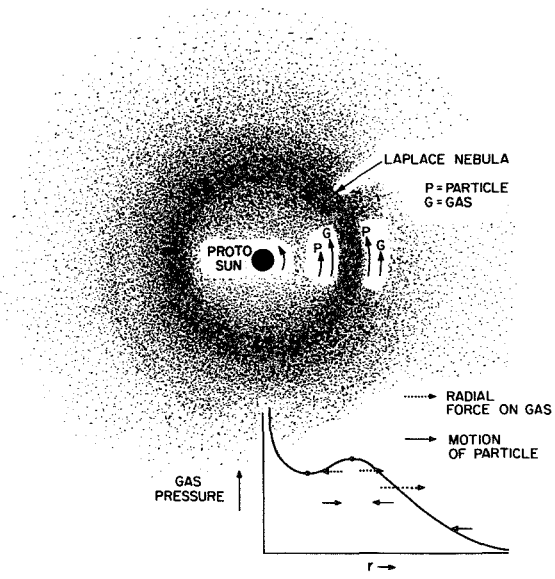

FIGURE 1.—Effect of gas pressure gradient on particle motion.

To determine the quantitative motion of the grains, note that the near-circular velocity change ΔV in the gas under a central acceleration g follows from the velocity law

$$V = g^{1/2} r^{1/2} \tag{2}$$

by differentiation, to the form

$$\Delta V = \frac{r^{1/2} \Delta g}{2 g^{1/2}} \tag{3}$$

A spherical grain of radius s, density ρ_s, and mass m will experience a drag $(-)$ or accelerating $(+)$ force F by interaction with the gas at relative velocity v, where $v < \Delta V$. The drag equation in a neutral gas is formally stated as

$$F = \frac{C_D}{2} \pi s^2 \rho v^2 \tag{4}$$

where C_D is the dimensionless drag coefficient dependent on the Reynolds number R_e if the mean free path L of the gas atoms or molecules is small compared to s.

For gases the Reynolds number is defined by

$$R_e = \frac{2 \rho v s}{\eta} \tag{5}$$

where η is the viscosity of the gas, given approximately by $\eta = \frac{1}{2} \rho \bar{v} L$, in which $\bar{v}$ is the mean kinetic speed of the atoms or molecules.

In case $L < s$, following the approximations by Probstein and Fassio (1969),

$$C_D = 24 R_e^{-1} \quad \text{for} \quad R_e < 1 \tag{6a}$$

$$C_D = 24 R_e^{-3/5} \quad \text{for} \quad 1 < R_e < 10^3 \tag{6b}$$

$$C_D = \tfrac{4}{9} \quad \text{for} \quad R_e > 10^3 \tag{6c}$$

where equation (6a) represents Stokes' law of drag and (6c) the Newtonian case, which holds fairly well for supersonic velocities $(v > \bar{v})$.

For the subsonic case when $L \geq s$, the drag

equation becomes generally complicated, but for $v \ll \bar{v}$, the Epstein approximation has some validity:

$$F(\text{Epstein}) = A\bar{v}\rho s^2 v \qquad (7)$$

where $A \simeq 4\pi/3$ if the accommodation coefficient of atoms or molecules on the moving sphere is unity.

For our purposes, the various forms of the drag equation can be simplified by the introduction of the quantity *stopping time* t_e, which is the ratio of the body's speed to the absolute value of the deceleration from drag. Equations (6a), (6b), (6c), and (7), respectively, can then be expressed as follows:

$$R_e < 1 \qquad t_e = \frac{2\rho_s s^2}{9\eta} \qquad (6'a)$$

$$1 < R_e < 10^3 \qquad t_e = \frac{2^{3/5}\rho_s s^{8/5}}{9\eta^{3/5}\rho^{2/5}v^{2/5}} \qquad (6'b)$$

$$R_e > 10^3 \qquad t_e = \frac{6\rho_s s}{\rho v} \qquad (6'c)$$

$$\text{Epstein} \qquad t_e = \frac{\rho_s s}{\rho \bar{v}} \qquad (7')$$

where for all, the drag law becomes simply

$$\frac{F(v)}{m} = \frac{v}{t_e} \qquad (8)$$

In the case of equations (6'b) and (6'c), t_e has been changed from the e-folding decay time by a factor of less than 2 to produce the generality of equation (8), which is correct for all cases. Stokes' law (eq. (6'a)) attains an error of only a factor of 3 up to $R_e = 10^2$.

The motion of the spherical grain or planetesimal in the solar nebula under influence of the gas "wind" is generally complicated. The present paper will deal in detail with only two extreme and simple illustrative cases: (A) where the "drag" force F for $v \sim \Delta V$ is large so that the grain at velocity ΔV with respect to the gas would be stopped in a small fraction of the period of revolution T_p, i.e., $t_e \ll T_p/2\pi$; and (B) where the grain or planetesimal at relative velocity $v = \Delta V$ would not be stopped for a time comparable to or greater than the period of revolution, i.e., $t_e \gg T_p/2\pi$.

In case A, where $t_e \ll T_p/2\pi$, the grain will largely follow the rotational motion of the gas and thus experience a central acceleration reduced or increased by Δg. Hence, it will execute a radial motion at velocity v with respect to the gas derived from $F(v) \simeq m\ \Delta g$.

In case B, where $t_e \gg T_p/2\pi$, the much larger grain or planetesimal will experience a tangential drag or an accelerating force at velocity $\sim \Delta V$ and slowly spiral radially in or out with respect to the rotating system of gas according to the modified equations of motion in a central force.

EQUATIONS OF MOTION

Case A.—Grains carried along with the gas, $t_e \ll T_p/2\pi$. The relative velocity v of the grain in the gas is smaller than ΔV and very much smaller than the speed of sound. Thus, case A divides into only two subcases: case A1, when the mean free path L is larger than the particle radius s, requiring Epstein's law (eqs. (7), (7'), and (8)); and case A2, when $L \leq s$ and R_e is small, requiring Stokes' law (eqs. (6'a) and (8)).

Case A1.—$v \ll \Delta V$, $v \ll \bar{v}$, $L > s$, and $t_e \ll T_p/2\pi$. For a grain (radius s, mass m, density ρ_s) the terminal radial speed in the cloud under the acceleration Δg becomes from Epstein's law (eqs. (7') and (8))

$$\frac{dr}{dt} = t_e\ \Delta g = \frac{\rho_s s}{\rho \bar{v}}\ \Delta g \qquad (9)$$

where Δg is given by eq. (1) for a radial pressure gradient in the gas or by the effect of a radial acceleration on the gas from some other source such as a magnetic field.

Case A2.—$v \ll \Delta V$, $v \ll \bar{v}$, $L \leq s$, and $t_e \ll T_p/2\pi$. Here the terminal radial speed of the grain is derived from Stokes' law (eqs. (6'a) and (8)), so that

$$\frac{dr}{dt} = t_e \Delta g = \frac{2\rho_s s^2\ \Delta g}{9\eta} \qquad (10)$$

where η is the viscosity of the gas.

Equation (10) is independent of the gas density so long as $L \leq s$ and holds fairly well to $R_e = 10$ and within a factor of 3 to $R_e = 10^2$.

Case B.—Grains and planetesimals meeting a resisting medium at $v \simeq \Delta V \ll V$. Here, $t_e \geq T_p$ and generally $L < s$, $v \ll \bar{v}$, while R_e may become

appreciable for large bodies, although in most cases of interest R_e is small. Tisserand (1896) solved this two-body problem for small orbital eccentricity e and constant $v=\Delta V \ll V$. To the first order in e, $de/dt=0$, so that a small orbital eccentricity is retained either under resistance or acceleration for gas in nearly circular motion.

For circular velocity V of mass m at distance r from the effective center of mass M, and a resisting or accelerating force F, the classical two-body solution takes the form

$$\frac{1}{r}\frac{dr}{dt} = \frac{2F(\Delta V)}{mV} = \frac{2\Delta V}{t_e V} = \frac{1}{t_e}\frac{\Delta g}{g} \qquad (11)$$

by equations (2), (3), (5) and (8).

The appropriate expression for t_e can be chosen from equation (6'a), (6'b), or (6'c), depending on the value of R_e for $v=\Delta V$ (eqs. (5) and (4)). Since the spiraling rate is extremely small for large bodies with large values of R_e, only the Stokes' law (eq. (6'a)) equation will be presented explicitly, viz:

$$\frac{dr}{dt} = \frac{9\eta r}{2\rho_s s^2}\frac{\Delta g}{g} \qquad (12)$$

The intermediate case between A and B, when $t_e \sim T_p/2\pi$, has been solved by F. Franklin (private communication) for Epstein's and Stokes' laws, the drag being proportional to v. The maximum rate of orbital change is $dr/dt=0.5\Delta V$ at $t_e=0.8T_p/2\pi$. When $t_e=T_p$, dr/dt equals 0.8 the value given by equation (11), approaching equation (11) as a limit for larger values of t_e. For $t_e<T_p/30$, equations (9) and (10) are correct within about 20 percent and improve for smaller t_e. The intermediate case thus gives values of dr/dt varying from $0.3\Delta V$ at $t_e=T_p/30$ to a maximum of $0.5\Delta V$ at $t_e=T_p/8$ and dropping to $0.3\Delta V$ at $t_e=T_p$. Near but outside these limits, equations (9) and (10) or equation (11) gives fairly satisfactory values for dr/dt.

EFFECTS OF GRAIN GROWTH ON RADIAL MOTION

We wish to consider grains that are growing by the accretion of atoms and molecules from the nebula. For atoms or molecules that can "freeze" on the grain, constituting a fraction f_i of the total density by weight, with an accommodation coefficient α_i, a mean molecular velocity $\bar{v}_i$, and a mean diffusion coefficient D_i, a spherical grain of radius s and density ρ_s grows at a rate

$$\frac{ds}{dt} = \frac{\alpha_i f_i \bar{v}_i \rho}{4\rho_s}\left(1+\frac{\bar{v}_i s}{4D_i}\right)^{-1} \qquad (13)$$

The second term becomes significant when the grain has reached such a size that for a velocity v through the gas small compared to $\bar{v}_i$, grain growth is inhibited by gas diffusion of the appropriate atoms and molecules. Approximately, $D_i=1.4\eta_i/\rho$, where η_i is the viscosity appropriate to the "freezing" atoms and molecules. Hence, from the second term of equation (13), the grain growth rate slows when $s \gg 5.6\eta_i/\bar{v}_i\rho$, and is given by

$$\frac{ds}{dt} = \frac{1.4\alpha_i f_i \eta_i}{\rho_s s} \qquad (14)$$

becoming independent of the general gas density and varying inversely as the radius of the grain.

The transition from rapid grain growth (first term of eq. (13); e.g., Kuiper, 1951) to diffusion-limited grain growth (eq. (14)) begins when the mean free path L_i becomes small compared to s, or roughly when the drag law at low grain velocities changes from the Epstein law (eq. (9)) to Stokes' law (eq. (10) or (12)). Hence, for the Epstein case (A1) we keep only the first term in equation (13), so that a very small grain grows to radius s_1 in time t_1 given by

$$t_1 = \frac{4\rho_s}{\alpha_i f_i \bar{v}_i \rho} s_1 \qquad (15)$$

Again for the Epstein case, by equations (9) and (15), the change in radial distance from r_0 at $t=0$ to r_1 at t_1 and s_1 becomes

$$r_1 - r_0 = \frac{\alpha_i f_i \bar{v}_i \Delta g}{8\bar{v}} t_1^2 = \frac{2\rho_s^2 \Delta g s_1^2}{\alpha_i f_i \bar{v}_i \bar{v} \rho^2} \qquad (16)$$

applicable when $v \ll \bar{v}$, $t_e \ll T_p/2\pi$, and $L \leq s$ and when changes in ρ and g with r are neglected. Equation (16) applies well in the assumed low-density region of the solar nebula beyond Uranus, where cometary accretion is expected. Note that exhaustion of condensable gas slows the growth rates and thereby increases the total amount of spiraling.

Within Jupiter's orbit, the relatively high gas density usually assumed and the consequent rapid growth rates carry the grain through the regimes

of Epstein's and Stokes' laws rather quickly. Thus, equation (12) can be used if applicable, and we will introduce the equations for large Reynolds numbers (t_e from eq. (6'c) and dr/dt from eq. (11)) and larger bodies, even though the relative velocity ΔV (eq. (3)) may be small. On this basis, the slow growth from s_2 to s_3 will take place by equation (14) in time t_3-t_2 given by

$$t_3-t_2=\frac{\rho_s(s_3^2-s_2^2)}{2.8\alpha_i f_i \eta_i} \tag{17}$$

while

$$\frac{1}{r}\frac{dr}{dt}=\frac{\rho(\Delta V)^2}{3\rho_s V}\frac{1}{s} \tag{18}$$

where the sign of dr/dt is that of ΔV, given by equation (3), $\Delta V=2^{-1}r^{1/2}g^{-1/2}\,\Delta g$.

APPLICATION IN THE "COMETARY REGION"

Let us arbitrarily define the "cometary region" at $r=25$ AU, with a typical density in the plane of $10^{-11.4}$ g cm^{-3}, $T=55°$ K, $P=10^{-2.1}$ dyn cm^{-2}, giving a total areal density across the plane of $10^{2.3}$ g cm^{-2} (2×10^{-5} solar mass per square AU) for a solar mixture by weight of gases (H, He, Ne, Ar) 0.9803, ices (C, N, O plus H) 0.0175, and Earthy materials (heavy elements) 0.0022. The corresponding viscosity will be $\eta=10^{-4.3}$ cgs, $\bar{v}=10^{4.85}$ cm s^{-1} for a mean molecular weight of 2.34, and $\bar{v}_i=10^{4.41}$ cm s^{-1} for the ices plus Earthy material of mean molecular weight 18.4 and a mass fraction $f_i=0.0197$.

The peak of the gas pressure and density will have been farther out, near $r=30$ AU at Neptune's present solar distance, but the order-of-magnitude calculations at $r=25$ AU will illustrate the nature of the spiraling phenomena caused by a negative pressure gradient outward near the edge of the nebula. Suppose the pressure falls linearly with r to 0 at 50 AU. Then $dP/dr=-10^{-16.7}$ cgs, while $\Delta g=10^{-5.3}$ cm s^{-2} by equation (1) and $\Delta V=10^{3.2}$ cm s^{-1} by equation (3) for a central solar mass. A forming icy grain of radius s and density 0.1 g cm^{-3} thus meets a resisting velocity of 16 m s^{-1}, small compared to molecular velocities. The Reynolds number for equation (5) becomes $R_e=10^{-3.6}\,s$ (cm), so that we are in the realm of Epstein's and Stokes' laws of drag up to "cometesimals" of radius 100 m or larger at great solar distances. Correspondingly, the mean free path of the gas molecules is of the order of 1 m or more so that little error is made in applying Epstein's law up to perhaps $s=10$ m, while to about the same limit the diffusion slowing of the accretion rate by the second term of equation (13) can be neglected. Hence, by equation (15), the time t_1 for a tiny grain to grow to a radius s_1 becomes

$$t_1=6.3s_1(\text{cm})\,\text{yr} \tag{19}$$

if we accept an accommodation coefficient $\alpha_i=1.0$.

Thus, our cometesimal will grow to a radius of 10 m in some 10^4 yr. Its loss of solar distance from r_0 to r_1, given by equation (16), then becomes

$$r_0-r_1=1.2\times10^{-5}\,s_1^2\ \text{AU} \tag{20}$$

so that the cometesimal spirals in "nominally 12 AU" by the time it has grown to a radius of 10 m, neglecting significant changes in density and other quantities depending on solar distance.

Note that the time varies inversely as the nebular density ρ and that the amount of spiraling varies as ρ^{-2}, so that the inward spiraling for a constant $\Delta g=dP/dr\rho$ is increased for cometesimals of a given size at greater solar distances or at lower solar densities, even though the time scale increases as ρ^{-1}. Reduction in growth rates by any cause increases the total amount of spiraling for a given gas density and gradient.

The sizable magnitude of the spiraling rate for cometesimals growing at the edge of the solar nebula may explain three facets of the present solar system: (a) the comparable masses of Neptune and Uranus, (b) the reduction of Neptune's solar distance from Bode's "law," and (c) the still unobservable "comet belt" beyond Neptune, expected by the writer (Whipple, 1964).

If we assume (Kuiper, 1951; Cameron, 1962; Whipple, 1964) that Uranus and Neptune are aggregates of cometesimals, then it is otherwise surprising that there should have been enough material at Neptune's distance to make a planet as large as Uranus. The spiraling effect, however, could bring in the cometesimals to a solar distance where the pressure gradient was smaller and pile up the cometary material from greater distances for accretion at Neptune, producing no sizable planet (Pluto?) beyond. Neptune's mean solar distance may also have been reduced. Thus, my

expectation of a comet belt beyond Neptune is perhaps unwarranted. In fact, the observations indicate that less than one Earth mass exists in a ring beyond Neptune to a solar distance of 50 AU (Hamid, Marsden, and Whipple, 1968).

APPLICATION IN THE ASTEROIDAL REGION

We may take a "typical" asteroidal region at $r=2.5$ AU, with density in the plane of $10^{-8.4}$ g cm^{-3} or a pressure of $10^{-4.1}$ atm, $T=550°$ K, $P=10^{+1.9}$ dyn cm^{-2}, giving a total areal density across the plane of $10^{4.3}$ g cm^{-2} (2×10^{-3} solar mass per square AU), $\eta=10^{-3.8}$ cgs, $\bar{v}=10^{5.35}$ cm s^{-1}, and $\bar{v}_i=10^{4.78}$ cm s^{-1} for Earthy molecules of mean molecular weight 33.5 and a mass fraction $f_i=0.0022$. The assumed temperature is that derived by Larimer and Anders (1967), supported by the further conclusions of Keays, Ganapathy, and Anders (1971) that in 13 chondrites at formation, $T=530^{\circ}{}^{+80^{\circ}}_{-60^{\circ}}$ K and $P=10^{-4\pm2}$ atm. The atmospheric model is here calculated to allow for one central solar mass plus the additional surface pressure derived from the gravitational attraction of the gas on itself.

Suppose, for illustration, that the gas pressure doubles in 1 AU toward the Sun so that $dP/dr=-10^{-11.3}$ cgs, $\Delta g=-10^{-2.9}$ cm s^{-2} by equation (1), and $\Delta V=10^{4.1}$ cm s^{-1} by equation (3). In the gas the mean free path is 0.2 cm and $R_e=0.64s$. This puts us squarely in the Newtonian range of drag (eq. (6′c)) and the range of slow grain growth (eq. (15)) for sizable planetesimals of $s\gtrsim10$ m. Growth to such sizes for $\rho_s=3$ occurs rapidly, ~1.4 cm yr^{-1}, for a short time and then slows. As we have seen, the radial spiraling rate for a change approximately fifty fold in radius by Stokes' law averages about 0.3 ΔV or $dr/dt=10^{-2.1}$ AU yr^{-1}. Thus, the reduction in r is a fraction of 1 AU while the planetesimal is growing to meter dimensions.

For larger bodies, $s>10$ m, we can apply equation (18) (Newtonian drag and the classical resisting medium) to find the spiraling distance Δr in time Δt for constant s (cm)

$$\frac{\Delta r}{r}=-\frac{1.22}{s}\Delta t(\mathrm{yr}) \qquad (21)$$

Appreciable change of solar distance occurs when Δt in years becomes comparable to the radius of the planetesimal measured in centimeters and varies directly as the nebular density (eq. (18)). The growth rate, however, is really quite uncertain. The assumed value of ΔV is still small (less than 1 percent) compared to the orbital velocity but is some 7 percent of the mean molecular velocity. Turbulent motion of the gas might easily produce random relative velocities of the order of 1 km s^{-1} so that the faster growth rate might be applicable (first term of eq. (13)). In that case, the change of r for a further growth to kilometers might not be significant. The slow growth rate, however, would make a significant change in r quite likely.

We may conclude, therefore, that effects of pressure gradients in the asteroid belt could be very important in shifting planetesimals toward Mars or Jupiter, provided the growth rates of the asteroids are not too rapid. For the basic development of the asteroids on a short time scale of 10^3 to 10^4 yr, the effect would be minor. However, should the nebular density be 10^{-5} atm or less in the asteroid region and the growth time 10^6 to 10^8 yr, pressure gradients could well have decimated the asteroid region by spiraling the planetesimals toward Mars or Jupiter, depending on the distribution of gas and the location of original grain growth. Possibly this effect contributed to the failure of an Earth-sized planet to develop between Mars and Jupiter.

GENERAL REMARKS

My attention was first directed to systematic interactions between gas motions and growing planetesimals in a postulated solar nebula by Hoyle's (1960) theory involving the expansion of a centrally condensed nebula by the outward force of spiraling magnetic fields from the Sun. In this process, the plasma would be pressed outward from the Sun, carrying with it the neutral gas and, according to Hoyle, also the planetesimals. In fact (Whipple, 1964), the reduced effective gravity on the gas will, following the arguments of this paper, cause the planetesimals to spiral inward toward the Sun rather than outward.

Cameron (1969) mentions the effect of a radial pressure gradient in producing an inward spiraling of planetesimals but does not discuss the alterna-

tive possibility, viz, outward spiraling, should a positive outward pressure gradient occur. Generally, if a toroid of higher density occurs in the solar nebula, the growing planetesimals are drawn toward it from the inside as well as from the outside, increasing the growth rate of an accreting planet. The importance of the effect, as we have seen above, depends mostly upon the nebular density and the time rates of chemical condensation. For a short time scale ($\sim 10^3$ to 10^4 yr) such as Cameron envisages, the pressure-gradient effect would not be important.

For long time scales of planetary formation, 10^6 to 10^8 yr, as are frequently postulated, the pressure-gradient effect could be highly significant. It may well have drawn in the cometary material from far beyond Neptune, adding materially to Neptune's mass and reducing the solar distance from Bode's "law." It may have greatly reduced the comet production in these regions of space so that no significant comet belt exists beyond Neptune. Conceivably, the pressure-gradient effect may have assisted in the building of Mars and Jupiter, at the expense of the asteroid belt. A lower surface gas density between the regions of Mars and Jupiter might not, in itself, have prevented the accretion of a sizable terrestrial planet between Mars and Jupiter without the action of the pressure-gradient effect.

ACKNOWLEDGMENT

I am indebted to Fred A. Franklin for his assistance with regard to the mathematical solutions noted in this paper.

REFERENCES

CAMERON, A. G. W., 1962. The formation of the Sun and planets, *Icarus*, **1**, 13–69.

CAMERON, A. G. W., 1969. Physical conditions in the primitive solar nebula, in *Meteorite Research*, edited by P. M. Millman, D. Reidel Publ. Co., Dordrecht-Holland, 7–15.

HAMID, S. E., MARSDEN, B. G., AND WHIPPLE, F. L., 1968. Influence of a comet belt beyond Neptune on the motions of periodic comets, *Astron. J.*, **73**, 727–729.

HOYLE, F., 1960. On the origin of the solar nebula, *Quart. J. Roy. Astron. Soc.*, **1**, 28–55.

KEAYS, R. R., GANAPATHY, R., AND ANDERS, E., 1971. Chemical fractionations in meteorites—IV. Abundances of fourteen trace elements in L-chondrites; implications for cosmothermometry, *Geochim. Cosmochim. Acta*, **35**, 337–363.

KUIPER, G. P., 1951. On the origin of the solar system, in *Astrophysics*, edited by J. A. Hynek, McGraw-Hill Book Co., New York, 357–424.

LARIMER, J. W., AND ANDERS, E., 1967. Chemical fractionations in meteorites. II. Abundance patterns and their interpretation, *Geochim. Cosmochim. Acta*, **31**, 1239–1270.

PROBSTEIN, R. F., AND FASSIO, F., 1969. Dusty hypersonic flows, Fluid Mechanics Lab., Publ. No. 69–2, Massachusetts Institute of Technology, Cambridge, Mass.

TISSERAND, F., 1896. *Mécanique Céleste*, Gauthier-Villars, Paris, vol. IV, 216.

WHIPPLE, F. L., 1964. The history of the solar system, *Proc. Nat. Acad. Sci.*, **52**, 565–594.

Page intentionally left blank

39. Current Evolution of Meteoroids

J. S. DOHNANYI
Bellcomm, Inc.
Washington, D.C.

The observed mass distribution of meteoroids at 1 AU from the Sun is briefly reviewed in a survey that ranges over the bulk of the mass spectrum from micrometeoroids to meteorite parent objects. The evolution of meteoroids under the influence of collisions, planetary perturbations, the Poynting-Robertson effect and radiation pressure is then discussed.

Most micrometeoroids are expelled from the solar system by radiation pressure shortly after their production as secondary ejecta during impact by larger objects or as dust ejected by comets. Particles that survive will eventually be swept out by the Poynting-Robertson effect.

Meteoroids in the radio and photographic ranges are destroyed in collisions faster than they can be replaced by the production of secondary fragments during collisions between larger objects. The source of new particles needed to maintain the population of these meteoroids in a stationary distribution may be material expelled by comets.

The survival of large objects is limited by gravitational scattering during close planetary encounters and by collisions as well, if they spend sufficient time in the asteroid belt. The observed radiation-exposure ages of chondrites are shown to be consistent with this model.

THE DISTRIBUTION OF THE MASSES of meteoroids is governed by several processes (Whipple, 1967). Large numbers of new objects are injected into the solar system by comets. Many small objects are removed by the Poynting-Robertson effect (Robertson, 1937; Wyatt and Whipple, 1950); particles are destroyed by interparticle collisions and their shattering into fragments creates new particles (Whipple, 1967; Dohnanyi, 1967). The influence of these collisions on the distribution of meteoroid masses has recently been discussed by Dohnanyi (1970; to be referred to as D-I in this paper), who showed that the distribution of meteoroids in the photographic range and of fainter ones is not likely to be stationary unless many of the particles, destroyed by collisions, are replaced by new ones given off by comets; the influence of radiation pressure on the size distribution of such cometary debris was also stressed (D-I).

The orbital elements of meteoroids undergo frequent and random changes caused by planetary perturbations (Öpik, 1951; Arnold, 1965). The influence of this process on the radiation exposure age distribution of meteorites has recently been discussed by Wetherill (1967) and Wetherill and Williams (1968). This age distribution was found to be sensitive to the survival times of meteorite-producing objects with respect to catastrophic collisions and to the rate at which these objects can "diffuse" through the solar system as a result of random gravitational perturbations caused by close planetary encounters (Öpik, 1966).

In this paper we shall discuss some aspects of the current evolution of the mass distribution of meteoroids; orbits will only be considered to the extent that they may influence the mass distribution. This will be shown to lead to a self-consistent description of the dominating processes controlling the mass distribution of meteoroids with masses ranging from micrometeoroids to meteorite-producing objects having masses of tens of tons.

OBSERVATIONAL EVIDENCE

This section is a discussion of the observed distribution of sporadic meteoroids ranging in size from micrometeoroids to large objects.

The flux $n(m)\ dm$ of meteoroids having a mass in the range m to dm incident on a unit area per 2π sr per unit time will be taken as:

$$n(m)\ dm = am^{-\alpha}\ dm \qquad (1)$$

where a and α are constants in different mass ranges; α is known as the population index.

Figure 1 is a plot of the cumulative flux $N(m)$ of meteoroids into Earth's atmosphere per meter^2 per sec per 2π steradians having a mass of m kg or greater.

$$N(m) = \int_m^{M_\infty} n(M)\ dM \qquad (2)$$

where M_∞ is the mass of the largest object included among meteoroids. Near the small mass limit of the distribution, I used the results of the Pioneer 8 and 9 data obtained by Berg and Gerloff (1970), multiplied by two to correct for the Earth's focusing effect. These authors have found an indication of a "cutoff" in the population of meteoroids, at a mass of about 5×10^{-15} kg, which sets the effective upper limit to the flux of penetrating particles, as seen in figure 1.

The points labelled Explorer XXIII and Pegasus are the influx rates measured by these satellites, and are based on calibrations by Naumann (1968) and Naumann et al. (1969). The penetration sensors aboard Explorer XXIII and Pegasus were calibrated in the laboratory by firing particles at meteoric velocities into sensors similar to those actually flown. Since many of these particles were accelerated gas dynamically, a fraction of their

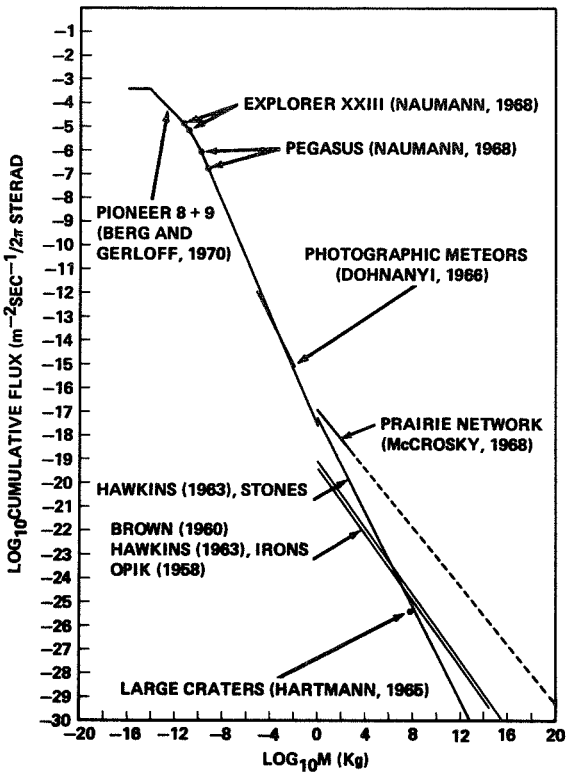

FIGURE 1.—Cumulative flux ($m^{-2}\ s^{-1}/2\pi$ sr) of meteoroids into Earth's atmosphere having a mass of m (kg) or greater.

masses may have ablated during the acceleration, so that the indicated flux is likely an upper limit. Some micrometeoroids may, however, be fluffy and of low density (Soberman, 1971) and would be less penetrating than were the laboratory particles of equal mass, so that the indicated flux may also be a lower limit. The nominal flux is, however, in agreement with the penetration flux measured by the Ariel II satellite (Jennison et al., 1967). Since it is difficult to estimate precisely the uncertainties involved, an order of magnitude approximation may be the most accurate estimate that can be attained at the present time.

Data from visual, radar and photographic observations as well as zodiacal light studies have been considered before (Whipple, 1967; Dohnanyi, 1965). A best estimate to fit these data has been obtained in D-I; it has the form of equation (1) with

$\alpha = 1.5$, for micrometeoroids, $m \leq 10^{-10}$ kg

$\alpha = 1\frac{3}{6}$, for larger meteoroids but smaller than meteorite producing objects, $10^{-10}\ \text{kg} \leq m < 1\ \text{kg}$ (3)

This simple model gives a good fit to the data, as can be seen from the appropriate portions of the curve in figure 1. Numerical flux values are given in table 1.

Mass distributions obtained from satellite microphone measurements have been discussed by Kerridge (1970) and McDonnell (1971); because of calibration difficulties, many of these data are difficult to interpret. In those cases where calibration difficulties have likely been overcome, the results are comparable to the penetration data (Kerridge, 1970).

Mass fluxes of micrometeoroids estimated from particle collection experiments on board rockets and satellites are subject to uncertainties arising from contamination and identification difficulties (see Fechtig et al., 1968; Dohnanyi, 1971a, for an annotated bibliography) and will not be employed in this study. Many of these particles are comparable to or smaller than the wavelength of light; a discussion of the interaction of such small particles with the solar radiation field requires a discussion of interference effects and is beyond the scope of this paper.

The influx rate of meteorite-producing objects has been estimated variously by Brown (1960), Hawkins (1963), and Öpik (1958); their estimates are plotted in figure 1. These data are based on the mass distribution of recovered meteorites and their estimated rates of fall. Hartmann's (1965) estimate of the flux rate of large crater-producing objects is also indicated.

Precise photographic observation of fireballs from the Prairie Network Project led McCrosky (1968b) to obtain as the cumulative flux (in MKS units) for these objects:

$$N(m) = 10^{-16.96}\, m^{-0.62} \qquad 1 \leq m \leq 10^{4}\ \text{kg} \quad (4)$$

As can be seen from figure 1, this flux is about an order of magnitude higher than that of Hawkins' (1963) stones and about two orders of magnitude higher than the other earlier estimates. Extrapolation (dashed line in fig. 1) of the Prairie Network data leads to an even greater difference. Uncertainties in the photometric masses of these objects are not believed to span this discrepancy

TABLE 1.—*Differential Flux of Meteoroids* $n(m) = am^{-\alpha}$ *for Different Mass Ranges*[a]

Mass range	a, $m^{-2}\ s^{-1}\ kg^{\alpha-1}/2\pi$ sr	α
$m < 5\times10^{-15}$ kg		<3/2
$5\times10^{-15}\ \text{kg} \leq m \leq 10^{-10}$ kg	1.4×10^{-11}	3/2
$10^{-10}\ \text{kg} \leq m < 1$ kg	3×10^{-18}	13/6

[a] See equation (1) in text.

(McCrosky and Ceplecha, 1970); low density, fragile objects whose fragments do not survive atmospheric entry are believed responsible for the higher flux of fireballs than had been estimated earlier for meteorite producing objects.

INFLUENCE OF COLLISIONS

Meteoroids frequently undergo mutual collisions. Since these collisions are inelastic, the target particles may either lose a small portion of their mass (erosive collisions) or be completely broken up (catastrophic collisions). The net result is a change in the meteoroid distribution.

The equation that expresses the dependence of the population on collisions can be written as

$$\frac{\partial f(m,t)}{\partial t}\,dm = \frac{\partial f(m,t)}{\partial t}\,dm\,\Big|_{\text{erosion}} + \frac{\partial f(m,t)}{\partial t}\,dm\,\Big|_{\text{catastrophic collisions}} + \frac{\partial f(m,t)}{\partial t}\,dm\,\Big|_{\text{creation by fragmentation}} \quad (5)$$

where $f(mt)\ dm$ is the particle number density function, i.e., the number of particles per unit volume of space in the mass range m to $m+dm$. The number density $f(m, t)\ dm$ is perpetually altered by erosive and catastrophic collisions and the creation of fragments in the mass range m to $m+dm$ by the crushing of larger objects during inelastic collisions.

It has been shown (Dohnanyi, 1969 and D-I) that, for a distribution with a population index $\alpha = 1\frac{3}{6}$ the contribution of particle creation, expressed by the last term in equation (5), is

minor compared with the other two processes. The influence of collisions on the distribution of small particles is then dominated by catastrophic collisions, while erosion dominates the distribution of large particles (D-I).

The influence of catastrophic collisions on the particle population is readily calculated. We take for the number density of small objects in the mass range m to $m+dm$ at 1 AU from the Sun

$$f(m) = \frac{1}{2}\frac{4}{V_\infty} n(m) \qquad (6)$$

Here V_∞ is the average Earth entry velocity and $n(m)$ is given in table 1; the factor $\frac{1}{2}$ is included to correct for the Earth's gravitational focusing effect, the factor 4 results from averaging the velocity distribution over all directions and $n(m)$ is given by table 1.

Using earlier results from photographic meteors (Dohnanyi, 1966) we take $V_\infty = 20.6$ km/s and an average collision velocity for sporadic meteoroids equal to their mean geocentric velocity of 17.3 km/s. In D-I, the largest meteoroid mass, Γ', that is catastrophically disrupted by impact of a projectile meteoroid of unit mass, was estimated (Moore and Gault, 1965; Moore and Robertson, 1966). The result is $\Gamma' \approx 7.5 \times 10^4$ for basalt particles and about an order of magnitude smaller for pumice particles.

Assuming a steady state distribution, one can readily calculate how many particles in this environment will survive catastrophic collisions after a time t. The result is shown in figure 2, which is a plot, for basalt-like particles, of the number density of particles that survive disruption after various time intervals, as indicated.

It is readily seen, from figure 2, that the heaviest toll is taken from particles in the faint radiometeor range: less than 0.1 percent of these particles survive disruptive collisions in the mass range 10^{-9} kg$<m<10^{-5}$ kg during a time interval of about 10^5 yr. Larger particles survive longer because the number of projectile masses lethal to larger objects decreases; micrometeoroids, on the other hand, have a longer survival time for disruptive collisions because the distribution of small objects that disrupt them tapers off.

The true number of surviving micrometeoroids is smaller than indicated in figure 2, since the Poynting-Robertson effect will cause many of these particles to spiral in toward the Sun. This is indicated as a function of particle mass in figure 3, which is a plot of meteoroid survival times with respect to removal and destruction processes.

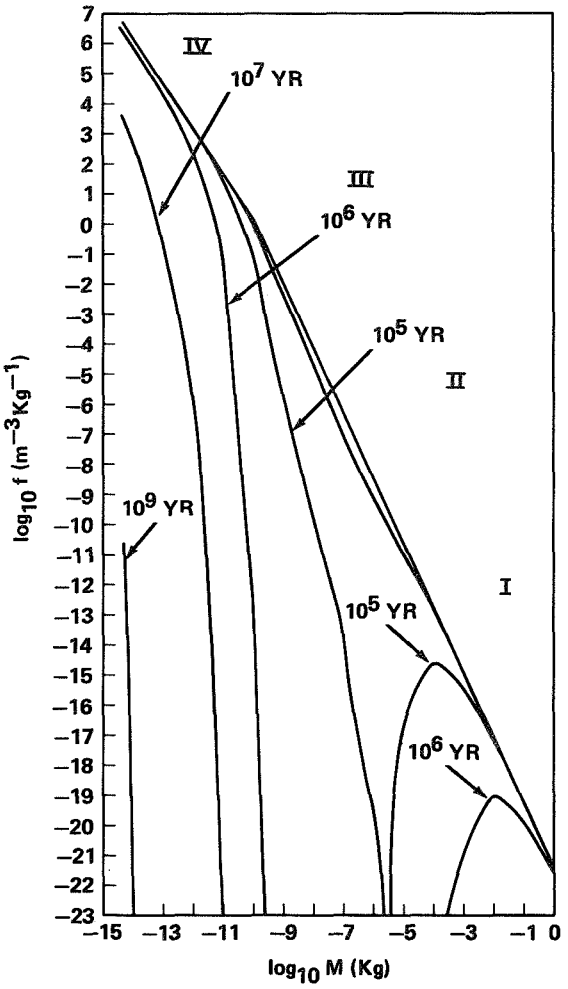

FIGURE 2.—Number density, $f(m, t)dm$, per meter^3 of meteoroids having masses in the range m to $m+dm$ (kg) is plotted for different times t, as indicated, for particles surviving disruptive collisions in a stationary population $f(m, o)$.

The survival time with respect to catastrophic collisions is made up of two main contributions:

$$1/\tau = 1/\tau_{cc} + 1/\tau_s \qquad (7)$$

where

$$1/\tau_{cc}(m) = km^{2/3} \int_{m/\Gamma'}^{M_\infty} f(M)\, dM \qquad (8)$$

and

$$1/\tau_s(m) = k \int_{m/\Gamma'}^{M_\infty} M^{2/3} f(M)\, dM \qquad (9)$$

$\tau_{cc}(m)$ is the survival time of a particle with respect to fragmentation by a comparatively small projectile particle, and $\tau_s(m)$ is the survival time of a particle with respect to being swept up by larger objects. The quantity K is defined in (D-I) as

$$K = (3\pi^{1/2}/4\rho)^{2/3}\langle V\rangle \qquad (10)$$

where ρ is the material density of the particles and $\langle V\rangle$ is the average encounter speed.

Figure 3 also shows a plot of the particle lifetime τ_{PR} with respect to the Poynting-Robertson effect for a particle of material density of 3.5 g cm^{-3} like that of basalt, and a material density of $\frac{1}{3}$ g cm^{-3} which resembles pumice.

The time for a particle to erode to $\frac{1}{2}$ of its radius τ_E is plotted for a meteoroid with a density 3.5 g cm^{-3} resembling basalt in composition for two linear erosion rates: 100 Å yr^{-1}, which is an upper limit obtained earlier by Whipple (1967), and 1 Å yr^{-1}, a recent estimate based on cosmic ray track densities in glass removed from Surveyor 3 spacecraft, as well as in some lunar samples (Fleischer et al., 1971).

The line labelled "gravitational lifetime" is the effective survival time of a particle in an Earth-crossing orbit with respect to being swept up by the Earth (Öpik, 1966). The actual time a particle is expected to spend in Earth-crossing orbit is considerably shorter (Wetherill, 1968); multiple near encounters give rise to a random walk process causing the particle to "diffuse" out of the region where its motion may be perturbed by the gravitational field of the Earth.

Comparison of survival times with respect to the various dynamic processes plotted in figure 3 indicates that the Poynting-Robertson effect determines the survival times for micrometeoroids. Also, the survival times for disruptive collisions of micrometeoroids with masses $m < 10^{-12}$ kg is dominated by the sweeping-up action of larger particles. Erosion is negligible for small objects. Catastrophic collisions with relatively small projectile particles dominate the survival times of particles in a mass range of 10^{-10} kg $< m < 10^{3}$ kg; larger objects will be dispersed by random walk from the vicinity of Earth's orbit long before they may be destroyed there by collisions.

Survival times with respect to catastrophic collisions of asteroids in the asteroid belt

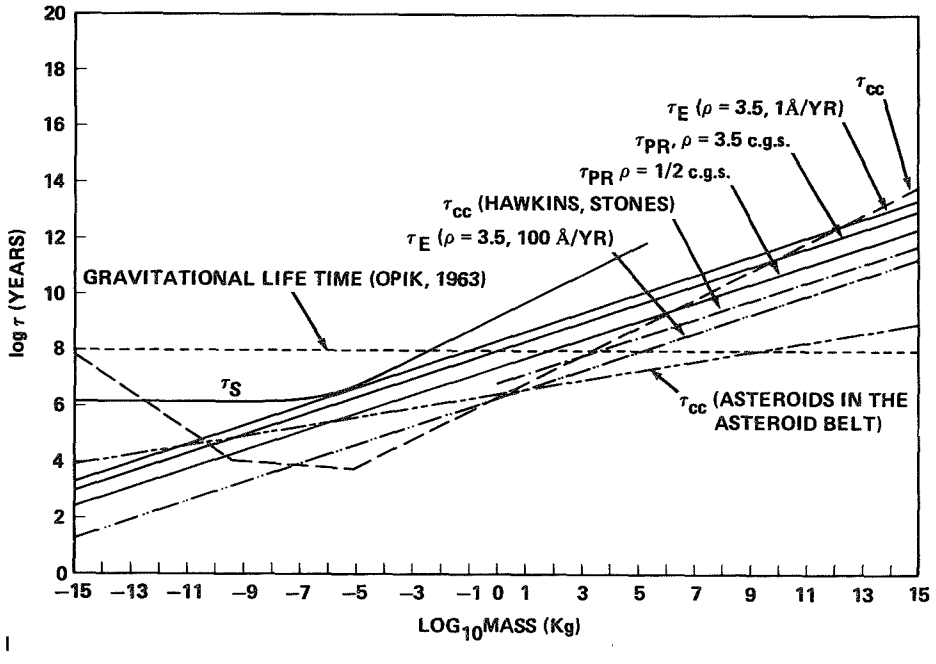

FIGURE 3.—Survival times as a function of mass of stray objects with respect to different loss processes, as indicated.

(Dohnanyi, 1969) and the extrapolated values of these survival times for small masses are indicated in figure 3 for the sake of comparison.

INFLUENCE OF RADIATION PRESSURE ON THE DISTRIBUTION OF METEOROID MASSES

A certain amount of radiation pressure, in a direction away from the Sun, is exerted by the Sun's light on all objects in the solar system (Robertson, 1937; van de Hulst, 1962). The result is a decrease, with decreasing particle radius, in the central force attracting the particle to the Sun. For particle radii smaller than a certain critical value, the electromagnetic force exceeds the gravitational force and the particle is blown out of the solar system. This critical radius is a function of the material density of the particle and its optical properties.

Consequently, the size distributions of particles injected by a comet into orbits about the Sun with an initial angular momentum equal to that of the comet will have a "cutoff" below a certain critical size due to radiation pressure. This problem was discussed in D-I (also Harwit, 1963), and the results are summarized in figure 4. This figure is a plot of the critical particle mass just blown away by radiation pressure when ejected at the perihelion of some parent comet having an eccentricity e, as indicated. The particles are assumed opaque and particle material densities of $\frac{1}{2}$, 1, 2, and 3.5×10^3 kg/m^3 have been considered. The eccentricities of some major showers are also indicated. One may assume that each comet that presumably gave rise to a major shower had, at the time it created the shower, an eccentricity similar to that of the shower. The intersection of each horizontal line, representing the eccentricity of the shower, with any line labelled by a density gives the smallest particle mass with the given density that can be present in the shower, according to geometric optics.

It is readily seen, from figure 4, that none of the major showers would initially contain particles smaller than about 10^{-9} to 10^{-12} kg having a density of $\frac{1}{2}\times10^3$ kg/m^3. The radiation pressure cutoff on the shower masses occurs in the range of 10^{-11} to 10^{-13} kg for meteoroids having a density similar to basalt (3.5×10^3 kg/m^3). For particles having a mass of about 10^{-15} kg or smaller, interference effects come into play and a discussion of

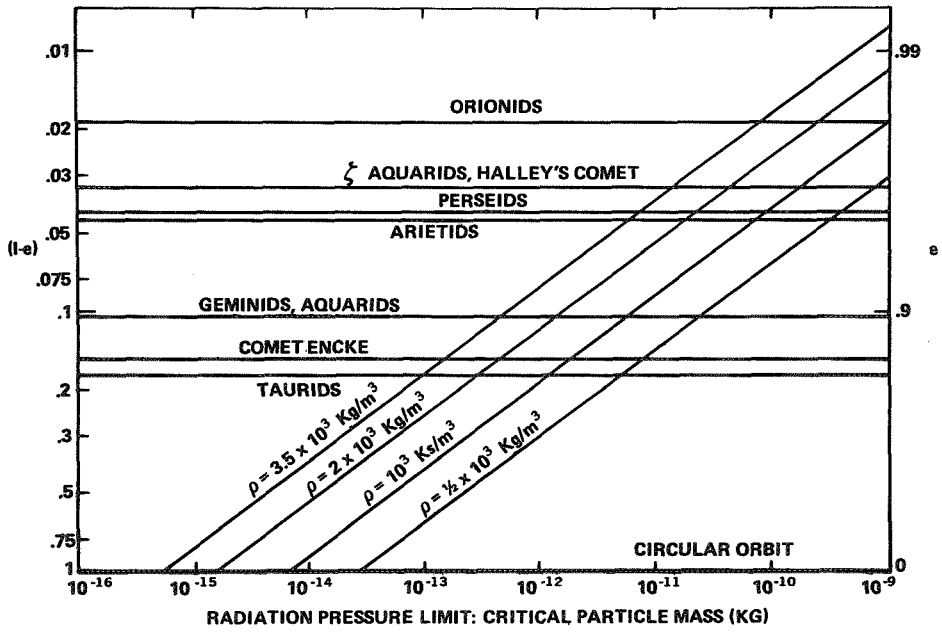

FIGURE 4.—Radiation pressure limit for particles of different material densities ρ ejected by some parent object at perihelion; e is the eccentricity of the parent object.

the stability of those very small particles is beyond the scope of this paper.

Similar considerations apply to fragments ejected from a parent body after an inelastic collision with another, smaller, meteoroid. In order to see, in detail, the effect under discussion, we consider the eccentricity E and semimajor axis A of a fragment ejected from a parent body with eccentricity e and semimajor axis a. Following D-I we denote by ν the ratio of the total central force on the fragment particle, i.e., the force of gravity reduced by radiation pressure, to the gravitational force acting on it. Since typical ejection velocities are small compared with the velocity of parent objects (Gault et al., 1963; Dohnanyi, 1971b) we take the heliocentric velocity of the ejecta equal to that of the parent objects immediately after impact. Assuming conservation of angular momentum, it can then be shown that

$$A=\nu a/[1-2a(1-\nu)/r] \qquad (11)$$

where r is the radial distance from the Sun to the point of collision. Since $\nu \leq 1$, by definition, it can be shown from equation (11) that the semimajor axis, A, of the ejecta is always greater than the semimajor axis of the parent object.

It is readily seen from equation (11) that if

$$a/r \geq 2/(1-\nu) \qquad (12)$$

the ejecta will be expelled from the solar system by radiation pressure.

According to equation (12), elimination from the solar system by radiation pressure is favored for collisions near perihelion (i.e., small a/r) and since the particle number density as well as the encounter velocity increases rapidly toward the Sun (D-I), we may expect most collisions to occur near the perihelion of the colliding objects and hence figure 4 may also be applied to collisions, as a rough approximation.* It may then be concluded that the contribution to the micrometeoroid population of fragments created during collisions by larger objects is much reduced by the elimination of these ejecta by radiation pressure.

The smaller the density of the fragment, the stronger is the effect of radiation pressure under discussion; this would seem to create a natural selection favoring the elimination of fluffy particles.

It has been shown in D-I that a population of objects with a mass distribution having a population index of $1\frac{3}{6}$ is not stable; because of collisions, particles in any mass range are destroyed faster than they can be replaced by the creation of fragments of the same mass range. Hence, if the present distribution of meteoroids has reached an approximately steady state configuration, it is necessary to have a source of meteoroids replenishing the particles destroyed by collisions but not replaced by fragments. If meteor showers are indeed the required source which replenishes the population of sporadic meteoroids, and if the known major showers and comets are representative of the source of meteoroids, one would expect a drop in the population of sporadic meteoroids with masses smaller than 10^{-9} to 10^{-11} kg, depending on their density. This conclusion appears to be borne out by observation, as is indicated in the changing slope of the sporadic meteoroid mass spectrum around 10^{-10} kg.

RADIATION AGES OF METEORITES

The survival time of large meteoroids with respect to catastrophic collisions increases monotonically with mass (fig. 3); the survival time of sufficiently large objects, therefore, will be dominated by the dispersive effects of gravitational perturbations. Taking the mean dispersal time of an object τ_d to be shorter than 10^2 million years, which is the lifetime of objects with respect to being swept up by the Earth, we see from figure 3 that the survival time of objects with masses of hundreds of kg will be limited by τ_d. This, however, does not necessarily hold for objects whose orbits cross the asteroid belt; depending on the relative time spent in the asteroid belt as well as on the average encounter velocity with asteroids, the survival time of these objects may still be collision dominated.

Figure 5 is a plot of the observed rate of fall of chondritic meteorites, as given by Wetherill (1969) in different cosmic ray exposure age ranges. It can be seen, in figure 5, that few objects have

* An exception occurs for objects having a node through the asteroid belt; depending on their orbital elements, it may then be physically possible for such objects to experience a more severe collisional environment in the asteroid belt than at perihelion.

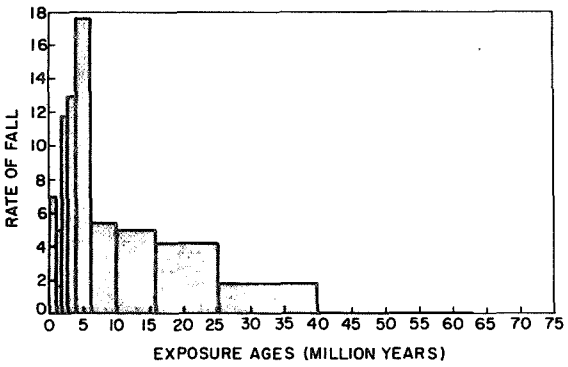

FIGURE 5.—Observed cosmic-ray exposure ages of chondritic meteorites (Wetherill, 1969).

ages smaller than a million years. Under steady state conditions it appears, therefore, that most of these objects originated in a region of the solar system far away from Earth's orbit, and spent some time on their way to the Earth's vicinity. Consequently, very few newly created meteorites are present.

We therefore consider a simplified model for meteorite producing objects. We shall assume that the meteorite producing objects have orbits (cf., Wetherill and Williams, 1968; Wetherill, 1969; and Anders, 1971, for a more general discussion) with nodes that do not intersect Earth's orbit, but do intersect the asteroid belt. This latter assumption is reasonable if we assume that the orbits of these objects resemble somewhat those of the Prairie Network fireballs (McCrosky, 1968a). Using typical orbital elements for these objects, we have

$$\begin{aligned} q' &\sim 4 \text{ AU} \\ e &\sim 0.7 \\ i &\sim 10^\circ \end{aligned} \tag{13}$$

where q is the aphelion distance, e is the eccentricity of the orbit and i is the inclination. It is readily shown that such an object spends about 75 percent of its time at a solar distance between 2.2 AU and aphelion. If all this time is spent within the asteroid belt, then use of a steady state asteroidal mass distribution (Dohnanyi, 1969) together with a mean encounter velocity with asteroids of about 11 km s^{-1} (as suggested by the orbital elements of equation (13)) leads, for an object with a mass of 10^4 kg, to

$$\tau_{cc} \sim 1 \text{ million years} \tag{14}$$

where τ_{cc} is the survival time of the object with respect to catastrophic collisions with asteroids. We chose a mass of 10^4 kg as a typical meteorite parent object; much smaller objects are likely to produce few, if any, meteorites after atmospheric entry and larger objects are comparatively so scarce that their contribution to the production of meteorites will be neglected here. The value of 1 million yr for τ_{cc} is an underestimate, since our test object is not likely to spend all of its time near the center of the asteroid belt; indeed, having an aphelion distance of 4 AU, it will spend about 40 percent of its time beyond 3.5 AU from the Sun. Thus, taking 3.5 AU as the outer bound of the asteroid belt,

$$\tau_{cc} \sim 2 \cdot 10^6 \text{ yr} \tag{15}$$

appears a more reasonable estimate.

The cumulative number of 10^4 kg objects, $h(T)$, having an age of T million years or longer is then

$$h(T) = h_0 e^{-T/\tau_{cc}} \tag{16}$$

where h_0 is the total number of our meteorite parent objects with masses of 10^4 kg. It is assumed, in equation (16), that these objects are in a steady state distribution and h_0 and $h(T)$ are therefore independent of time.

We now assume that these objects are occasionally perturbed into Earth crossing orbits with node(s) oscillating around 1 AU so that collision with the Earth becomes possible and the objects may then be recovered as meteorites. In order for this to happen, one or both of the nodes must be at a distance of 1 AU from the Sun which means that, for non-zero inclinations, the aphelion of the orbit will be some distance above the ecliptic and thus above the central region of the asteroid belt. The collisional survival time will be correspondingly lengthened for objects in such Earth-crossing orbits. As a first approximation, we assume, therefore, that these Earth-crossing objects will have survival times determined by the random gravitational scattering in close encounters with the Earth, i.e., the collisional survival times of these Earth-crossing orbits are relatively long.

We may then write

$$\frac{\partial n_e'(t)}{\partial t} \approx -\frac{n_e'(t)}{y} + \frac{h(t)}{x} \tag{17}$$

where $n_e'(t)$ is the number density per unit volume of 10-ton objects in Earth-crossing orbit at a time t, and $h(t)$ is the number density per unit volume of 10-ton objects in previous, non-Earth-crossing orbits. Quantity $1/y$ is the *a priori* probability, per unit time, for any Earth-crossing object to be scattered out of Earth-crossing orbit by a close encounter with the Earth and $1/x$ is the *a priori* probability per unit time for a non-Earth-crossing meteorite parent object to be scattered into an Earth-crossing orbit.

We assume steady state conditions:

$$\partial n_e'(t)/\partial t = 0 \tag{18}$$

and hence

$$n_e' = (y/x)h \tag{19}$$

as one would expect.

To calculate the distribution of the ages T of these objects, we replace t by T in Equation (17) and get

$$\partial n_e(T)/\partial T = -n_e(T)/y + h(T)/x \tag{20}$$

where $[\partial n_e(T)/\partial T]\,dT$ is the number density per unit volume of 10-ton objects with ages in the range of T to $T+dT$, and $n_e(T)$ and $h(T)$ are the number of Earth-crossing and non Earth-crossing objects, respectively, per unit volume with ages greater than T. Because of the imposition of steady state conditions, n_e and h are given by equation (19), for $T=0$, i.e., the number of objects for all ages is given by equation (19). Using equations (16), (19) and (20) we get:

$$\frac{\partial n_e(T)}{\partial T} = n_e(0)\,(e^{-T/\tau_{cc}} - e^{-T/y})/(\tau_{cc} - y),\ \tau_{cc} \neq y \tag{21}$$

and

$$\frac{\partial n_e(T)}{\partial T} = n_e(0)\,T(e^{-T/y})/y^2,\ \tau_{cc} = y \tag{22}$$

The expression for $[\partial n_e(T)/\partial T]\,dT$ determined by equation (21) or (22), gives the number of meteorite producing objects having an age of T to $T+dT$ and is therefore proportional to the number of meteorites in that cosmic ray exposure-age range. It is readily seen, from equations (21) and (22), that the number of "young" meteorites having ages much smaller than y and τ_{cc} is zero. This happens because a finite time is required for an object, which has just been created in a non-Earth-crossing orbit, to "find its way" to an Earth-crossing orbit.

A comparison of equation (21) with the observed cosmic ray exposure ages of chondritic meteorites based on a compilation by Wetherill (1969) is plotted in figure 6. The data published by Wetherill (1969) appear in the form of histograms (fig. 5) representing the rates of fall for meteorites in various ranges of cosmic ray exposure ages. In figure 6, Wetherill's data are reduced to represent the differential distribution $\partial n_e(T)/\partial T$ of cosmic ray exposure ages per unit exposure-age range. Taking

$$n_e(0) = 68.95 \tag{23}$$

which is the total rate of fall for all exposure ages given by Wetherill (1969), $\partial n_e(T)/\partial T$ from equation (21) is then plotted in figure 6 for several combinations of the survival times τ_{cc} and y.

It can be seen from equations (21) and (22) that $\partial n_e(T)/\partial T$ is symmetric with respect to τ_{cc} and y. This means that if either τ_{cc} or y is very short, there will be a peak in the distribution of meteorites with very short exposure ages. This happens because if τ_{cc} is short, young objects are favored and if y is short, meteorites do not have enough time to "grow old" in Earth-crossing orbits. If, on the other hand, either τ_{cc} or y is long, the distribution has a long exponential tail containing many old meteorites. This happens because relatively many objects escape catastrophic collisions if τ_{cc} is long, which results in a corresponding abundance of old objects. If y is long, then meteorites in Earth crossing orbits stay around long enough for many of them to age there. If τ_{cc} is comparable to y, then most objects have an age of that same order of magnitude, i.e., a narrowly peaked distribution of radiation ages.

It can be seen, from figure 5, that the best estimate of 2×10^6 yr for τ_{cc} (eq. (15)) combined with a gravitational survival time in Earth-crossing orbit of about 2×10^6 yr provides a reasonable fit to the observational data.

We now consider the frequency of meteorite falls. According to the results of the Prairie

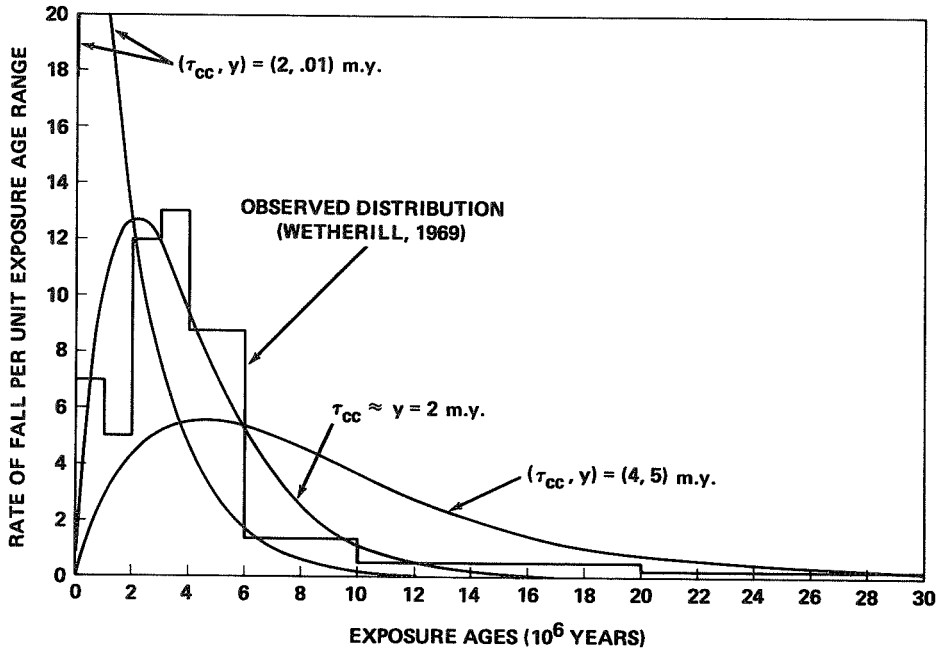

FIGURE 6.—Observed and theoretical distribution of cosmic ray exposure ages per unit exposure-age range of chondritic meteorites for different survival times τ_{cc} and y discussed in the text.

Network Project (McCrosky, 1968b), the flux of objects per unit mass range having a mass of 10 tons that enter the Earth's atmosphere is 2.25×10^{-24} kg^{-1} m^{-2} s^{-1}. Using equation (6) and a mean Earth entry velocity of 20 km s^{-1}, we obtain a number density of 2.25×10^{-28} particles/(kg m^3).

We now assume that the original meteorite parent objects in non-Earth-crossing orbits are objects in Mars-crossing orbits. For the number density per m^3 kg of Mars-crossing objects having a mass of 10^4 kg, we employ the results of Kessler (1970), who estimated the number density of large objects at a distance of about 1.5 AU from the Sun to be about 1 percent of the peak number density of the asteroidal belt. Assuming the latter to be about double the average number density (Narin, 1966) and using the results of Dohnanyi (1969), we then get a value of 2.22×10^{-28} for the number density h per (kg m^3) of 10^4 kg objects at a distance of 1.5 AU from the Sun (i.e., Mars-crossing orbits). This number is, however, an underestimate, since these Mars-crossing objects spend most of their time away from perihelion and near aphelion. A best estimate for the number density of Mars crossing meteorite parent objects is perhaps an order of magnitude greater.

Using equation (19), we can now calculate the survival time x; the result is

$$x=y(h/n_e)\approx10\times2(2.22\times10^{-28}/2.25\times10^{-28})$$
$$\approx2\times10^7 \text{ yr} \quad (24)$$

which is surprisingly short. On the other hand, if we used Hawkins' (1963) estimate for the flux of stone meteorite-producing objects, then the number density n_e of 10^4 kg objects near Earth would be 6.4×10^{-30}/(kg m^3) and we would have

$$x=2\times10(2.2\times10^{-28}/6.4\times10^{-30})10^6 \text{ yr}$$
$$=\approx7\times10^8 \text{ yr} \quad (25)$$

It therefore appears that a diffusion time x ranging from as short a value as 2×10^7 yr up to about 6×10^9 yr can explain the data, depending on the flux law employed, or more specifically, depending on the extent meteorite producing bodies are assumed to contribute to the Prairie Network flux of fireballs.

DISCUSSION AND CONCLUSION

The considerations of the section on radiation pressure suggest the difficulty of creating micrometeoroids in substantial quantities, either by cometary emission or by the production of second-

ary ejecta during collisions: Radiation pressure is likely to expel most of the small objects shortly after their creation, while those that initially survive radiation pressure will spiral into the Sun as a result of the Poynting-Robertson effect. While a detailed mathematical formulation of this problem has not been developed, the "bending over" of the flux curve for micrometeoroids (fig. 1) is probably caused by this process.

Meteoroids in the radio and photographic meteor range have survival times limited by catastrophic collisions. Fragments from the disruption of relatively large objects are not produced in sufficient quantities to maintain the population of these meteoroids in steady state (D-I), hence it is necessary that a steady supply of cometary debris be available to replenish the destroyed particles.

Large objects, of the meteorite producing class, have survival times limited by collisions as well as gravitational dispersal. If the latter were unimportant, most meteorites would have a very young radiation exposure age corresponding to the curve in figure 6, labelled $(\tau_{cc}, y) = (2, .01)$ m.y.; also, if collisions were very rare and the survival time were dominated by gravitational dispersal alone, a similar exponential type curve would be obtained. The data support neither of these distributions but suggest that the gravitational dispersal time is comparable to the collisional survival time of these objects prior to their having been scattered into Earth-crossing orbits. This is consistent with a model in which the meteorite parent objects have Mars-crossing orbits and aphelia in the asteroid belt or somewhat beyond (Wetherill, 1968, 1969; Anders, 1971). These objects are then scattered, during close encounters with Mars or perhaps Jupiter, into Earth-crossing orbits. This simple model is found to predict a distribution of meteorite radiation exposure ages consistent with observation (Wetherill, 1969). While a precise identification of these original objects is still under discussion (Wetherill, 1969; Anders, 1971), results derived from this simple statistical model may provide additional clues concerning their identity.

ACKNOWLEDGMENTS

Thanks are due to M. Liwshitz, R. E. McCrosky, and G. W. Wetherill for some important suggestions and valuable discussions.

REFERENCES

ANDERS, E., 1971. Interrelations of meteorites, asteroids and comets, in *Physical Studies of Minor Planets*, edited by T. Gehrels, *NASA* **SP–267**, Supt. of Documents, U.S. Govt. Printing Office, Washington, 429–446.

ARNOLD, J. R., 1965. The origin of meteorites as small bodies. II. The model. III. General considerations, *Astrophys. J.*, **141**, 1536–1556.

BERG, O. E., AND GERLOFF, U., 1970. Orbital elements of micrometeoroids derived from Pioneer 8 measurements, *J. Geophys. Res.*, **75**, 6932–6939.

BROWN, H., 1960. Density and mass distribution of meteorites, *J. Geophys. Res.*, **75**, 1679–1683.

DOHNANYI, J. S., 1965. The meteoroid environment of the Apollo program, *Bellcomm Rept.*, TR–66–340–1.

——, 1966. Model distribution of photographic meteors, *Bellcomm Rept.*, TR–66–340–1.

——, 1967. Collision model of meteoroids, in *The Zodiacal Light and the Interplanetary Medium*, edited by J. L. Weinberg, *NASA* **SP–150**, Supt. of Documents, U.S. Govt. Printing Office, Washington, 315–319.

——, 1969. Collisional model of asteroids and their debris, *J. Geophys. Res.*, **74**, 2531–2554; also in *Bellcomm Rept.* TR–68–710–4, 1968.

——, 1970. On the origin and distribution of meteoroids, *J. Geophys. Res.*, **75**, 3468–3493.

——, 1971a. Micrometeoroids, *EOS Trans. Am. Geophys. Union*, **52**, *IUGG*, 459–464.

——, 1971b. The lunar micrometeoroid experiment, LO 33, *Bellcomm Rept.* TM-71-2015-2.

FECHTIG, H., GERLOFF, U., AND WEIHRAUCH, J. H., 1968. Results of cosmic dust collection on Luster 1965, *J. Geophys. Res.*, **73**, 5029–5037.

FLEISCHER, R. L., HART, H. R., JR., AND COMSTOCK, G. M., 1971. Very heavy solar cosmic rays: energy spectrum and implications for lunar erosion, *Science*, **171**, 1240–1242.

GAULT, D. E., SHOEMAKER, E. M., AND MOORE, J. H., 1963. Spray ejected from the lunar surface by meteoroid impact, *NASA Tech. Note* **D–1767**.

HARTMANN, W. K., 1965. Terrestrial and lunar flux of large meteorites in the last two billion years, *Icarus*, **4**, 157–165.

HARWIT, M., 1963. Origins of the zodiacal dust cloud, *J. Geophys. Res.*, **68**, 2171–2180.

HAWKINS, G. S., 1963. Impacts on the earth and moon, *Nature*, **197**, 781.

JENNISON, R. C., MCDONNELL, J. A. M., AND RODGER, I., 1967. The Ariel II micrometeorite penetration measurements, *Proc. Roy. Soc. London*, **A300**, 251–269.

KERRIDGE, J. F., 1970. Micrometeorite environment at the Earth's orbit, *Nature*, **228**, 616–619.

KESSLER, D. J., 1970. Meteoroid environment model-170 (interplanetary and planetary), *NASA Special Rept.* **SP-8038**.

MCCROSKY, R. E., 1968a. Orbits of photographic meteors, *Physics and Dynamics of Meteors*, edited by Ľ. Kresák and P. M. Millman, Springer-Verlag, New York, 265–279.

——, 1968b. Distributions of large meteoric bodies, *Smithson. Astrophys. Obs. Spec. Rept.* No. 280, 1–13.

MCCROSKY, R. E., AND CEPLECHA, Z., 1970. Fireballs and the physical theory of meteors, *Bull. Astron. Inst. Czech.*, **21**, 271–296.

MCDONNELL, J. A. M., 1971. Review of in situ measurements of cosmic dust particles in space, *Space Res.*, **9**, 415–435.

MOORE, H. J., AND GAULT, D. E., 1965. The fragmentation of spheres by projectile impact, *Astrogeologic Studies, U.S. Geol. Surv. Ann. Progr. Rept.*, 127–150.

MOORE, H. J., AND ROBERTSON, F. G., 1966. Hypervelocity impact craters in pumice, *Astrogeologic Studies, U.S. Geol. Surv. Ann. Progr. Rept.*, 107–125.

NARIN, F., 1966. Spatial distribution and motion of the known asteroids, *J. Spacecraft Rockets*, **3**, 1438–1440.

NAUMANN, R. J., 1968. Calibration of Pegasus and Explorer XXIII detector panels, presented at OART–OSSA Meteoroid Environment Workshop, NASA Headquarters, 342.

NAUMANN, R. J., JEX, D. W., AND JOHNSON, C. L., 1969. Calibration of Pegasus and Explorer XXIII detector panels, *NASA Tech. Rept.* **R-321**, 1–37.

ÖPIK, E. J., 1951. Collision probabilities with the planets and the distribution of interplanetary matter, *Proc. Roy. Irish. Acad.*, **54A**, 165–199.

——, 1958. On the catastrophic effects of collisions with celestial bodies, *Irish Astrophys. J.*, **5**, 34–36.

——, 1966. The stray bodies in the solar system. II. The cometary origin of meteorites, *Advan. Astron. Astrophys.*, Academic Press, New York, 301–336.

ROBERTSON, H. P., 1937. Dynamical effects of radiation on the solar system, *Mon. Not. Roy. Astron. Soc.*, **97**, 423–438.

SOBERMAN, R. K., 1971. The terrestrial influx of small meteoric particles, *Rev. Geophys. Space Phys.*, **9**, 239–258.

VAN DE HULST, H. C., 1962. *Light Scattering by Small Particles*, J. Wiley and Sons, New York.

WETHERILL, G. W., 1967. Collisions in the asteroid belt, *J. Geophys. Res.*, **72**, 2429–2444.

——, 1968. Dynamical studies of asteroidal and cometary orbits and their relation to the origin of meteorites, in *Origin and Distribution of the Elements*, edited by L. H. Ahrens, Pergamon Press, London, 423–443.

——, 1969. Relationships between orbits and sources of chondritic meteorites, *Meteorite Res.*, edited by P. M. Millman, Springer-Verlag, New York, 573–589.

WETHERILL, G. W., AND WILLIAMS, J. G., 1968. Evaluation of the Apollo asteroids as sources of stone meteorites, *J. Geophys. Res.*, **73**, 635–648.

WHIPPLE, F. L., 1967. On maintaining the meteoritic complex, in *The Zodiacal Light and the Interplanetary Medium*, edited by J. L. Weinberg, *NASA* **SP-150**, Supt. of Documents, U.S. Govt. Printing Office, Washington, 409–426.

WYATT, S. P., AND WHIPPLE, F. L., 1950. The Poynting-Robertson effect on meteor orbits, *Astrophys. J.*, **111**, 134–141.

40. Possible Interaction of Interstellar Particles With the Solar and Terrestrial Environment

J. MAYO GREENBERG
State University of New York at Albany and Dudley Observatory
Albany, New York

The possibility for detection of interstellar particles in the Earth's environment is considered on the basis of the passage of the solar system through the interstellar medium. Among the forces which inhibit interstellar particle penetration, the deflection by the solar magnetic field and the repulsive force due to the radiation from the Sun are by far the most important.

IT IS VARIOUSLY ESTIMATED that the number density of small particles in the solar system at one AU is of the order of 10^{-12} cm^{-3}. If we use an average interstellar extinction per unit distance in the solar neighborhood as 1 mag/kpc we obtain an average number density for 0.1μ radius interstellar particles of $N_{IP} \cong 10^{-12}$ cm^{-3} which is the same order of magnitude.

While it is true that the interstellar particles are generally smaller than the interplanetary particles, nevertheless the small particle component of the interplanetary space which contributes particularly to the polarization of the zodiacal light is suggestively similar in typical size (Giese and Dziembowski, 1967, Aller et al., 1967). It is therefore not unreasonable to examine further the question of the interstellar component of the interplanetary particle distribution (Greenberg, 1969, 1970). We must consider first the chance for passage of the Sun through an interstellar cloud and further we must consider the effects of repulsive forces exerted by the solar system on the incoming interstellar particles.

PASSAGE OF THE SUN THROUGH AN INTERSTELLAR CLOUD

The space between the stars appears to consist mainly of cool neutral hydrogen clouds imbedded in a hot neutral hydrogen medium of quite low density. The cool clouds vary in size typically between 1 pc and 10 pc in radius. We picture a spherical shape for illustrative purposes only. The larger clouds may have a hydrogen number density of $N_H = 10$ cm^{-3} and the smaller ones may have a density of $N_H = 10^3$ cm^{-3} or higher. Neither the distribution of cloud size nor the appropriate densities is firmly established. For our purposes it will be useful to make some crude assumptions to get order of magnitude estimations of the probability that the Sun may be passing through some cloud. It should be noted that with the hydrogen densities chosen above the respective particle densities in small and large clouds would be the order of 4000×10^{-12} cm^{-3} and 40×10^{-12} cm^{-3} which are larger than the number density of small zodiacal light particles.

If all the clouds are of 10 pc radius, the number density of such clouds would be 6×10^3 kpc^{-3} and if all are 1 pc radius clouds the number density would be 6×10^4 kpc^{-3}. Using random cloud velocities of 10 km/sec (10 pc in one million years) we see that the time of passage through the large and small clouds are 10^6 and 10^5 years respectively. Based on the cloud number densities the time spent between the clouds is, for the former, 5×10^6 yrs. and, for the latter, 2.5×10^6 yrs. Thus the fraction of time spent inside a cloud

is bracketed between $\frac{1}{5}$ and $\frac{1}{25}$. Neither of these probabilities—certainly not the former—is sufficiently small to exclude the chance that some of the interplanetary particles are of interstellar origin. It should be pointed out on the other hand that there is apparently no convincing evidence that we are now passing through a cloud.

DUST REPELLING MECHANISMS

Three obvious mechanisms for repelling the interstellar dust from entering the solar system are magnetic fields, the solar wind and solar radiation pressure. The first is applicable only if the dust particles are charged. The effects of the second are stronger if the dust particles are charged but exists even when the grains are uncharged.

Solar Wind

Let us estimate the distance over which an interstellar grain will penetrate the solar system under the assumption that it meets the solar wind head-on. We assume that the solar wind consists of 3 protons cm^{-3} moving with a speed of 400 km sec^{-1}. The penetration distance d is obtained by requiring that the total energy imparted to the grain by the colliding protons equal the initial grain kinetic energy. We may write this condition approximately as $\frac{1}{2}m_g V^2 = m_H v_H^2 n_H \pi a^2 d$. Using grain density $s=1$ and radius $a=10^{-5}$ cm we find that $d \approx 50$ AU if the speed of passage of the solar system through the cloud is 10 km/sec. This is so large insofar as the solar wind is concerned that the interstellar grains should pass through unaffected. In view of the fact that we have assumed a constant solar wind intensity throughout the solar system in this simplified calculation, we have greatly overestimated the solar wind effect. Even taking into account the fact that a charged grain would have a greater collision cross section, the average rate of momentum transfer for the distant collisions is not sufficient to change our conclusions.

Magnetic Field

As an illustration we consider the effect on a "typical sized" $a=0.1\mu$ grain. Larger grains would be less deflected than smaller grains so the criticality derived is an upper limit insofar as larger grains are concerned.

Rather than calculating the radius of curvature of a typical entering grain we calculate its deflection. The calculation is simplified by assuming the net effect will not be large. The final result will indicate the consistency of this assumption.

Consider the worst possible case that the grain enters normal to the magnetic field in the solar system. The field will be represented by its transverse component B_t, (Ness, 1968) having a field strength of the order of 6×10^{-5} gauss at 1 AU.

The force on the grains is qVB and the acceleration is $a_\perp = qVB_t/m_g$ where $B_t = B_0(1\text{ AU}/R)$ and $B_0 = 6\times10^{-5}$ gauss. The deflection may be calculated simply by assuming a very large radius of curvature. We get the lateral deflection as

$$\Delta = \int_0^t a_\perp t\, dt$$

We let $t=x/V$ where x is measured from some outer point in the solar system. We shall choose this outer point as $R_0 = 10$ AU. Then:

$$\Delta = \frac{qVB_0(1\text{ AU})^2}{m_g V^2} \int_{R_1}^{R_0} \frac{(R_0 - R)\, dR}{R}$$

where R_1 is chosen as the distance from the Sun where the deflection is defined. If we let $R_1 = 1$ AU and let the charge on the grain be such as to give it a one volt potential we get $\Delta \approx 10^3$ AU for $V=20$ km/s! This is enormous. It is only for grains with potentials $\leq 10^{-3}$ volts that the angle of deflection becomes moderate. For $a=10^{-5}$ cm this implies less than one electron charge. We note that, for fixed potential, $\Delta \sim a^{-2}$ so that interstellar grains in the one micron size range might sweep through.

Radiation Pressure

The criterion we use here is whether the net repulsive force is such that an incoming grain at 10 km/sec turns around at 1 AU. We therefore equate the initial kinetic and final potential energy where the latter is defined in terms of an effective repulsive gravitational constant ϵG. Thus $\epsilon \equiv (\frac{1}{2}V^2)/(GM_0/R_1)$. This gives $\epsilon \approx 0.05$, i.e., the radiation force need be only slightly greater than

the gravitational force. For a 6000 K blackbody the radiation force on a 0.1μ dirty ice grain is $\approx 10^{-10}$ dynes. The gravitational force is equivalently 4.3×10^{-10} dynes. Thus a 0.1μ ice grain should penetrate. It can be shown that somewhat smaller grains will also penetrate. However it is clear that the dominant factor in preventing the penetration of dust particles from interstellar space is the radiation of the Sun.

ACKNOWLEDGMENT

Work supported in part by NASA Grant No. NGR-33-011-043.

REFERENCES

ALLER, L. H., DUFFNER, G., DWORETSKY, M., GUDEHUS, D., KILSTON, S., LECKRONE, D., MONTGOMERY, J., OLIVER, J., AND ZIMMERMAN, E., 1967. Some models of the zodiacal cloud, *The Zodiacal Light and the Interplanetary Medium*, edited by J. L. Weinberg, *NASA* **SP-150,** Supt. of Documents, U.S. Govt. Printing Office, Washington, 243–256.

GIESE, R. H., AND DZIEMBOWSKI, C. V., 1967. On optical models approximating observations of the zodiacal light outside the ecliptic, *The Zodiacal Light and the Interplanetary Medium*, edited by J. L. Weinberg, *NASA* **SP-150,** Supt. of Documents, U.S. Govt. Printing Office, Washington, 271–276.

GREENBERG, J. M., 1969. A possible inter-relation between interstellar and interplanetary cosmic dust, *Space Research IX*, 111–115.

GREENBERG, J. M., 1970. Models of the zodiacal light, *Space Research X*, 225–232.

NESS, N. F., 1968. Observed properties of the interplanetary plasma, *Ann. Rev. Astron. Astrophys.*, **6,** 79–114.

List of Participants

Albers, H., Vassar College
Alvarez, J. M., NASA Langley Research Center
Blanchard, M. B., NASA Ames Research Center
Brecher, A., University of California at San Diego
Brett, P. R., NASA Manned Spacecraft Center
Brownlee, D., University of Washington, Seattle
Cameron, A. G. W., Yeshiva University
Ceplecha, Z., Ondřejov Observatory, Czechoslovakia
Collins, J. G., University of Western Ontario
Cook, A. F., Harvard College Observatory and Smithsonian Astrophysical Observatory
Di Benedetto, F., University of Rome, Italy
Dohnanyi, J. S., Bellcomm, Inc.,
Dubin, M., NASA, Washington, D.C.
Fechtig, H., Max-Planck Institut, Heidelberg
Fleischer, R. L., General Electric Co. Research and Development Center, Schenectady
Forti, G., Harvard College Observatory and Smithsonian Astrophysical Observatory
Friichtenicht, J., TRW Systems, Redondo Beach, Calif.
Giese, R. H., Ruhr-Universität, Bochum
Gill, J. R., NASA, Washington, D.C.
Greenberg, J. M., State University of New York at Albany and Dudley Observatory
Hallgren, D. S., Dudley Observatory
Halliday, I., National Research Council of Canada
Hanner, M. S., Dudley Observatory
Hartung, J. B., NASA Manned Spacecraft Center
Harvey, G. A., NASA Langley Research Center
Hemenway, C. L., Dudley Observatory and State University of New York at Albany
Hindley, B., Vanderbilt University
Jones, J. V., University of Western Ontario
Kresák, L., Astronomical Institute, Bratislava, Czechoslovakia
Leinert, C., Landessternwarte Heidelberg
Lindblad, B. A., Lunds Universitet
Millman, P. M., National Research Council of Canada
McCrosky, R. E., Harvard College Observatory and Smithsonian Astrophysical Observatory
McIntosh, B. A., National Research Council of Canada
Naumann, R. J., NASA Marshall Space Flight Center
Patashnick, H., Dudley Observatory
Peterson, A. W., University of New Mexico, Albuquerque
Richardson, M. B., State University of New York at Albany
Roosen, R. G., NASA Goddard Space Flight Center
Roy, N. L., TRW Systems, Redondo Beach, Calif.
Russell, J. A., University of Southern California, Los Angeles
Savage, H. F., NASA Ames Research Center
Schmalberger, D. C., State University of New York at Albany and Dudley Observatory
Sekanina, Z., Harvard College Observatory and Smithsonian Astrophysical Observatory
Shao, C. Y., Harvard College Observatory and Smithsonian Astrophysical Observatory
Soberman, R. K., General Electric Co. Space Sciences Laboratory, Philadelphia
Southworth, R. B., Harvard College Observatory and Smithsonian Astrophysical Observatory
Swider, A. L., State University of New York at Albany
Theisinger, P., Jet Propulsion Laboratory, California Institute of Technology
Utech, K., Gesellschaft für Weltraumforschung, Bad Godesberg
Weinberg, J. L., Dudley Observatory
Wetherill, G. W., University of California, Los Angeles
Whipple, F. L., Harvard College Observatory and Smithsonian Astrophysical Observatory
Wilson, L., University of Lancaster
Wright, F. W., Harvard College Observatory and Smithsonian Astrophysical Observatory

☆ U.S. GOVERNMENT PRINTING OFFICE: 1973 O—499-153

"The aeronautical and space activities of the United States shall be conducted so as to contribute . . . to the expansion of human knowledge of phenomena in the atmosphere and space. The Administration shall provide for the widest practicable and appropriate dissemination of information concerning its activities and the results thereof."

—NATIONAL AERONAUTICS AND SPACE ACT OF 1958

NASA SCIENTIFIC AND TECHNICAL PUBLICATIONS

TECHNICAL REPORTS: Scientific and technical information considered important, complete, and a lasting contribution to existing knowledge.

TECHNICAL NOTES: Information less broad in scope but nevertheless of importance as a contribution to existing knowledge.

TECHNICAL MEMORANDUMS: Information receiving limited distribution because of preliminary data, security classification, or other reasons. Also includes conference proceedings with either limited or unlimited distribution.

CONTRACTOR REPORTS: Scientific and technical information generated under a NASA contract or grant and considered an important contribution to existing knowledge.

TECHNICAL TRANSLATIONS: Information published in a foreign language considered to merit NASA distribution in English.

SPECIAL PUBLICATIONS: Information derived from or of value to NASA activities. Publications include final reports of major projects, monographs, data compilations, handbooks, sourcebooks, and special bibliographies.

TECHNOLOGY UTILIZATION PUBLICATIONS: Information on technology used by NASA that may be of particular interest in commercial and other non-aerospace applications. Publications include Tech Briefs, Technology Utilization Reports and Technology Surveys.

Details on the availability of these publications may be obtained from:

SCIENTIFIC AND TECHNICAL INFORMATION OFFICE

NATIONAL AERONAUTICS AND SPACE ADMINISTRATION

Washington, D.C. 20546